BEILSTEIN JOURNAL OF ORGANIC CHEMISTRY

Carbon-rich materials: from polyaromatic molecules to fullerenes and other carbon allotropes

Edited by Hiroko Yamada and Yoko Yamakoshi

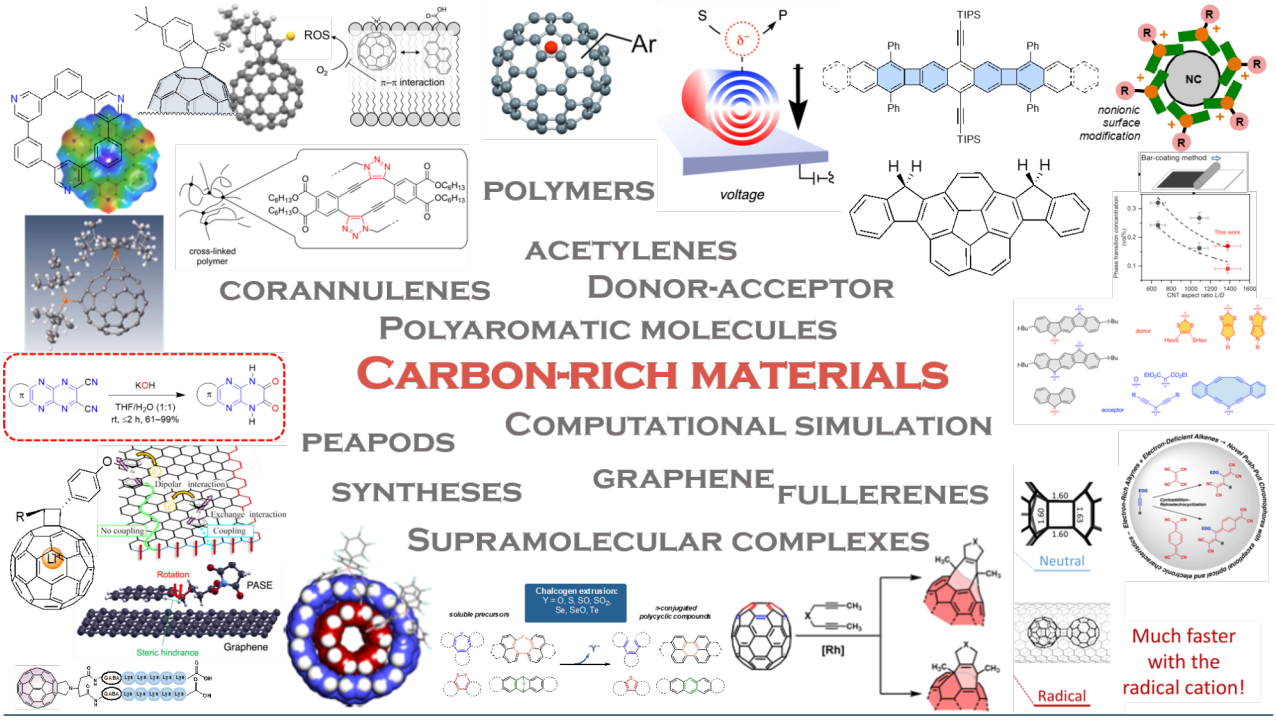

Generated on 07 February 2026, 20:04

Imprint

Beilstein Journal of Organic Chemistry
www.bjoc.org
ISSN 1860-5397
Email: journals-support@beilstein-institut.de

The *Beilstein Journal of Organic Chemistry* is published by the Beilstein-Institut zur Förderung der Chemischen Wissenschaften.

Beilstein-Institut zur Förderung der Chemischen Wissenschaften
Trakehner Straße 7–9
60487 Frankfurt am Main
Germany
www.beilstein-institut.de

BEILSTEIN JOURNAL OF ORGANIC CHEMISTRY

Carbon-rich materials: from polyaromatic molecules to fullerenes and other carbon allotropes

Hiroko Yamada[*1] and Yoko Yamakoshi[*2]

Editorial

Open Access

Address:
[1]Institute for Chemical Research, Kyoto University, Gokasho, Uji, Kyoto, 611-0011, Japan and [2]Department of Chemistry and Applied Biosciences, ETH Zürich, Zürich CH8093, Switzerland

Email:
Hiroko Yamada[*] - hyamada@scl.kyoto-u.ac.jp; Yoko Yamakoshi[*] - yamakoshi@org.chem.ethz.ch

* Corresponding author

Keywords:
carbon allotropes; carbon-rich materials; fullerenes; polyaromatic molecules

Beilstein J. Org. Chem. **2025,** *21,* 798–799.
https://doi.org/10.3762/bjoc.21.62

Received: 11 February 2025
Accepted: 25 February 2025
Published: 17 April 2025

This article is part of the thematic issue "Carbon-rich materials: from polyaromatic molecules to fullerenes and other carbon allotropes".

Guest Editors: H. Yamada and Y. Yamakoshi

In addition to diamond and graphite, traditional carbon allotropes in our old high-school textbook, new types of carbon allotropes, molecular carbons, were discovered in the last decades. These include fullerenes (1985) [1], carbon nanotubes (1991) [2], and graphene (2004) [3]. Due to their unique electronic and photophysical properties, research in the area of carbon-rich molecules and polyaromatic molecules became explosive in their activity and a numerous new studies and directions have emerged. Because of dramatic expansion and development of these research areas, these molecules became targets of Nobel Prizes in Chemistry (in 1996 to Carl, Kroto, and Smalley for the discovery of C_{60}) and in Physics (in 2010 to Geim and Noboselov for the discovery of graphene).

Prior to the celebration of the 40th anniversary of the discovery of fullerene in 2025, we planned this thematic issue on carbon-rich materials. We highly appreciate that so many of our colleagues and friends – researchers with a variety of backgrounds working on these special molecules – agreed to contribute to this project.

The authors hail from diverse research areas, including synthetic organic chemistry, surface chemistry, computational chemistry, physics, electrochemistry, polymer chemistry, supramolecular chemistry, and biochemistry. All are working on fascinating topics associated with these exciting molecules. Furthermore, the authors come from all over the world, not only from Switzerland and Japan but also from China, Denmark, Estonia, France, Spain, Turkey, and USA.

We hope that the readers will enjoy this thematic issue and be inspired to further develop their own research in the near future.

Hiroko Yamada and Yoko Yamakoshi

Kyoto, Zurich, February 2025

ORCID® iDs

Hiroko Yamada - https://orcid.org/0000-0002-2138-5902
Yoko Yamakoshi - https://orcid.org/0000-0001-8466-0118

Data Availability Statement

Data sharing is not applicable as no new data was generated or analyzed in this study.

References

1. Kroto, H. W.; Heath, J. R.; O'Brien, S. C.; Curl, R. F.; Smalley, R. E. *Nature* **1985,** *318,* 162–163. doi:10.1038/318162a0
2. Iijima, S. *Nature* **1991,** *354,* 56–58. doi:10.1038/354056a0
3. Novoselov, K. S.; Geim, A. K.; Morozov, S. V.; Jiang, D.; Zhang, Y.; Dubonos, S. V.; Grigorieva, I. V.; Firsov, A. A. *Science* **2004,** *306,* 666–669. doi:10.1126/science.1102896

License and Terms

BEILSTEIN JOURNAL OF ORGANIC CHEMISTRY

Controlling the reactivity of La@C_{82} by reduction: reaction of the La@C_{82} anion with alkyl halide with high regioselectivity

Yutaka Maeda*[1], Saeka Akita[1], Mitsuaki Suzuki[2], Michio Yamada[1], Takeshi Akasaka[3], Kaoru Kobayashi[4] and Shigeru Nagase[4]

Full Research Paper

Open Access

Address:
[1]Department of Chemistry, Tokyo Gakugei University, Koganei, Tokyo 184-8501, Japan, [2]Department of Chemistry, Josai University, Sakado, Saitama 350-0295, Japan, [3]Tsukuba Advanced Research Alliance, University of Tsukuba, Ibaraki 305-8577, Japan and [4]Department of Theoretical Studies, Institute for Molecular Science, Okazaki 444-8585, Japan

Email:
Yutaka Maeda* - ymaeda@u-gakugei.ac.jp

* Corresponding author

Keywords:
electron transfer; metallofullerene; radical; reduction

Beilstein J. Org. Chem. **2023,** *19,* 1858–1866.
https://doi.org/10.3762/bjoc.19.138

Received: 11 October 2023
Accepted: 22 November 2023
Published: 11 December 2023

This article is part of the thematic issue "Carbon-rich materials: from polyaromatic molecules to fullerenes and other carbon allotropes".

Guest Editor: Y. Yamakoshi

Abstract

Endohedral metallofullerenes have excellent redox properties, which can be used to vary their reactivity to certain classes of molecules, such as alkyl halides. In this study, the thermal reaction of the La@C_{2v}-C_{82} anion with benzyl bromide derivatives **1** at 110 °C afforded single-bonded adducts **2**–**5** with high regioselectivity. The products were characterized by matrix-assisted laser desorption/ionization time-of-flight mass spectrometry and visible–near infrared spectroscopy. The reaction of La@C_{2v}-C_{82} with alkyl halides using the same conditions showed no consumption of La@C_{2v}-C_{82}, indicating that the reactivity of La@C_{2v}-C_{82} toward alkyl halides was effectively increased by one-electron reduction. Single-crystal X-ray diffraction analysis of the single-bonded adduct **3a** revealed the addition site of the *p*-methoxybenzyl group on La@C_{2v}-C_{82}. Theoretical calculations indicated that the addition site carbons in neutral La@C_{2v}-C_{82} have high spin density, whereas those in the La@C_{2v}-C_{82} anion do not have high charge densities. Thus, the reaction is believed to occur via electron transfer, followed by the radical coupling of La@C_{2v}-C_{82} and benzyl radicals, rather than by bimolecular nucleophilic substitution reaction of La@C_{2v}-C_{82} anion with **1**.

Introduction

Fullerenes, the third carbon allotrope, have unique spherical molecular structures and exhibit high reactivity as electron-deficient polyolefins. The excellent redox properties of fullerenes are useful for their chemical derivatization and practical applications [1-5]. Fullerene anions can be easily produced chemically or electrochemically. C_{60}^{2-} is a strong electron donor and potential nucleophile that reacts with electrophiles [6-11]. The mechanism for the reaction of C_{60}^{2-} with alkyl halides has been studied in detail by Fukuzumi et al., who found that the reaction occurs via electron transfer, followed by bimolecular nucleophilic substitution (S_N2) reaction [8].

Endohedral metallofullerenes, wherein one or more metal atoms are encapsulated inside a fullerene cage, have garnered research interest [12-15]. The encapsulation of metal atoms can result in electron transfer from the metal atoms to the fullerene cage. Because of this intramolecular electron transfer, the characteristic properties of metallofullerenes, such as their redox potentials, are significantly different from those of empty fullerenes. For example, La@C_{82} has paramagnetic properties, and its formal electronic structure is described as $La^{3+}C_{82}^{3-}$. We previously investigated the reaction of M@C_{2v}-C_{82} ions (M = Y, La, Ce) with disilirane, which possesses high reactivity toward electron acceptors [16,17]. Interestingly, the reactivity of M@C_{2v}-C_{82} toward disilirane was increased by the one-electron oxidation of M@C_{2v}-C_{82}. Moreover, the reaction was suppressed by the one-electron reduction of M@C_{2v}-C_{82}. These results suggest that oxidation and reduction reactions are useful for tuning the reactivity of metallofullerenes. Recently, remarkable reactivity of $[M_3N@I_h\text{-}C_{80}]^{2-}$ (M = Lu, Sc) toward benzal bromide was reported, demonstrating one possible reaction of the anion species of closed-shell endohedral metallofullerenes [18]. Although $[Lu_3N@I_h\text{-}C_{80}]^{2-}$ reacts with benzal bromide to afford a methanofullerene, $[Sc_3N@I_h\text{-}C_{80}]^{2-}$ did not react under the same conditions (E_{ox} $[Lu_3N@I_h\text{-}C_{80}]^{2-}$ = 1.80 V vs Fc^+/Fc; E_{ox} $[Sc_3N@I_h\text{-}C_{80}]^{2-}$ = −1.62 V vs Fc^+/Fc; C_{60}^{2-} = −1.50 V vs Fc^+/Fc)). The different reactivity of $[M_3N@I_h\text{-}C_{80}]^{2-}$ was explained by theoretical calculations. The charge density of the highest occupied molecular orbital (HOMO) was more highly localized on the fullerene cage for $[Lu_3N@I_h\text{-}C_{80}]^{2-}$, whereas it was more localized on the inside of the cluster for $[Sc_3N@I_h\text{-}C_{80}]^{2-}$.

A previous study reported that thermal treatment of La@C_{2v}-C_{82} in the presence of 3-triphenylmethyl-5-oxazolidinone in toluene afforded four different benzylated La@C_{2v}-C_{82} isomers [19]. Benzyl radicals may have been generated due to the involvement of azomethine ylide; however, the detailed mechanism has not been elucidated. In this article, we describe the thermal reaction of the La@C_{2v}-C_{82} anion, activated by one-electron reduction, with benzyl bromide derivatives.

Results and Discussion

The La@C_{2v}-C_{82} anion [20] was prepared by chemical reduction [21] using a degassed tetrabutylammonium hexafluorophosphate (TBAF) pyridine solution. After stirring for 3 h, a dark green solution was obtained. CS_2 was added to precipitate TBAF, and the solution was filtered to collect the La@C_{2v}-C_{82} anion solution. The solvent was then removed under reduced pressure and replaced with 1,2-dichlorobenzene (ODCB). The characteristic absorption peak at 1000 nm assigned to La@C_{2v}-C_{82} decreased, and the new absorption peak at 934 nm assigned to the La@C_{2v}-C_{82} anion increased. Reactions of the La@C_{2v}-C_{82} anion with 4-methylbenzyl bromide (**1a**) were conducted at 110 °C for 2 h (Scheme 1). Figure 1 depicts the changes in the visible–near infrared (vis–NIR) absorption spectra during the reaction, showing gradual changes with isosbestic points. Since the electrolyte interferes with the high-performance liquid chromatography (HPLC) separation and anionic species may not be eluted under typical fullerene HPLC separation conditions, trifluoroacetic acid was added to the reaction mixture. Notably, La@C_{2v}-C_{82} is produced after the addition of trifluoroacetic acid to the La@C_{2v}-C_{82} anion [20]. After removing the solvent under vacuum, the electrolyte was removed by adding CS_2 and then filtering. Subsequent HPLC separation of the reaction mixture with **1a** afforded products **2a**, **3a**, **4a**, and **5a** in yields of 40, 37, 9, and 1%, respectively, based on the consumption of La@C_{2v}-C_{82} (Figure 2a and Supporting Information File 1, Figure S1). The yield was estimated from the absorption intensity ratio at 330 nm. On the other hand, no consumption of La@C_{2v}-C_{82} was observed in the reaction of La@ C_{2v}-C_{82} with **1a** (Figure 2b). The reaction of the La@C_{2v}-C_{82} anion toward **2a**–**5a** requires heating, therefore the reactivity of La@$C_{2v}C_{82}$ anion is lower than that of the

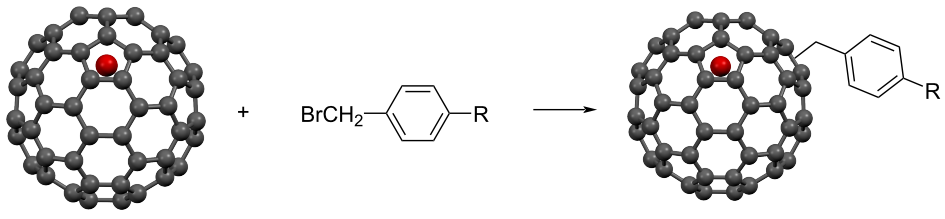

Scheme 1: Reaction of the La@C_{2v}-C_{82} anion with benzyl bromide derivatives.

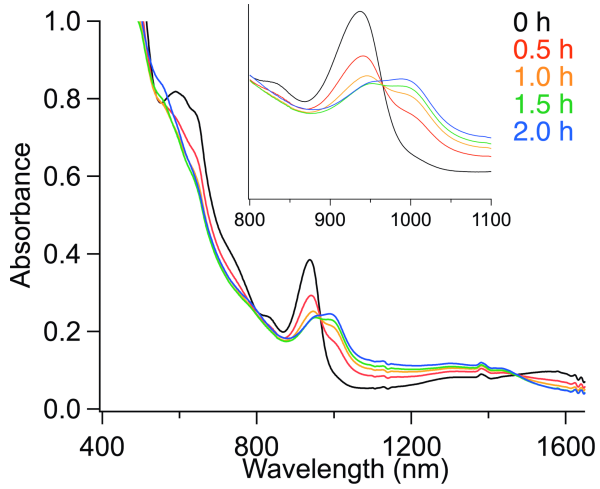

Figure 1: Changes in absorption spectra during the reaction of La@C_{2v}-C_{82} anion with **1a**.

C_{60}^{2-} and C_{60} anion radicals [10,11], which react even at room temperature. However, the one-electron reduction of La@C_{2v}-C_{82} is effective for the activating its reactivity toward alkyl halides in the thermal reaction. Recently, Zhou et al. reported that the reaction of Gd@C_{2v}-C_{82} with benzyl bromide requires a three-electron reduction of Gd@C_{2v}-C_{82} for the addition reaction to occur at room temperature [22].

Supporting Information File 1, Figure S1 depicts the three HPLC separation steps including recycling for the isolation. The matrix-assisted laser desorption/ionization time-of-flight (MALDI–TOF) mass spectra of **2a**–**5a** displayed the molecular ion peaks at *m*/*z* 1229, as expected for the 1:1 adducts of La@C_{2v}-C_{82} and the 4-methylbenzyl group $[MH]^+$ (Figure 3). Fragment peaks were observed at *m*/*z* 1123, corresponding to the mass of the fragment ion $[La@C_{2v}\text{-}C_{82}]^+$. Similarly, the reaction of **1b** gave **2b**–**5b** in yields of 39, 42, 5, and 5%, respectively, and that of **1c** gave **2c**–**5c** in yields of 34, 33, 16, and 10%, respectively, based on the consumption of La@C_{2v}-C_{82} (see Supporting Information File 1, Figures S2–S6).

For the comparison, the photoreaction of the La@C_{2v}-C_{82} anion with **1a** was performed in ODCB using a high-pressure mercury arc lamp (cutoff < 350 nm, 1 h). The HPLC profile after the photoreaction indicates that several products other than **2a**–**5a** were present (Figure 2c), similar to the photoreaction of La@C_{2v}-C_{82} with **1a** (Figure 2d). A previous study reported that the reaction of La@C_{2v}-C_{82} with benzyl bromide under photolytic conditions affords eight monoadducts [19]. Therefore, one-electron reduction and the subsequent thermal reac-

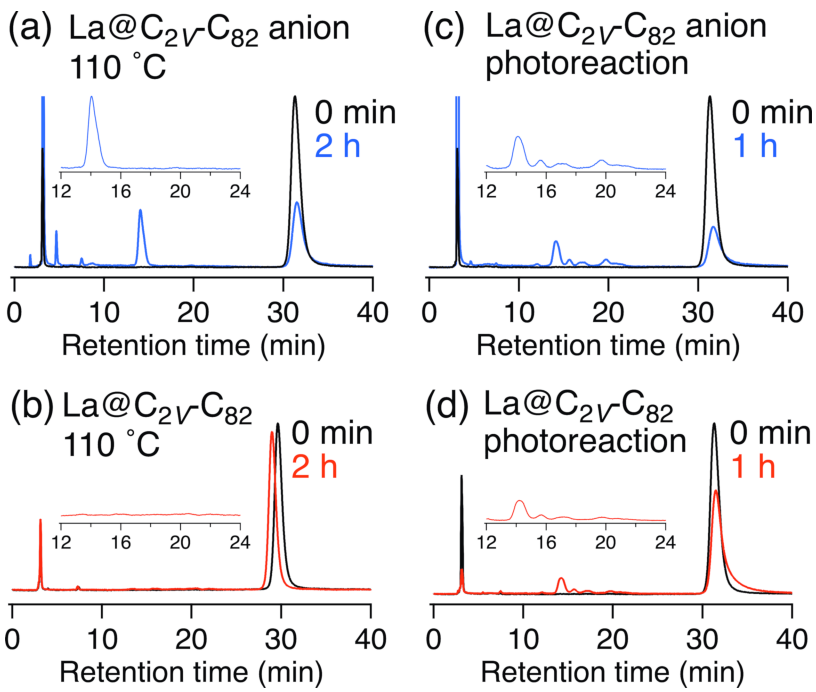

Figure 2: HPLC profiles of the reaction mixture. Conditions: Buckyprep column (⌀ = 4.6 × 250 mm); eluent, toluene; flow rate, 1 mL/min; UV detector, 330 nm. (a) La@C_{2v}-C_{82} anion with **1a**. 110 °C, 2 h. (b) La@C_{2v}-C_{82} with **1a**. 110 °C, 2 h. (c) La@C_{2v}-C_{82} anion with **1a**. *hv* > 350 nm, 1 h. (d) La@C_{2v}-C_{82} with **1a**. *hv* > 350 nm, 1 h. Black line is the HPLC profiles of La@C_{2v}-C_{82} at the same concentration as the reaction. Reaction mixtures with La@C_{2v}-C_{82} anions were treated with dichloroacetic acid before injection.

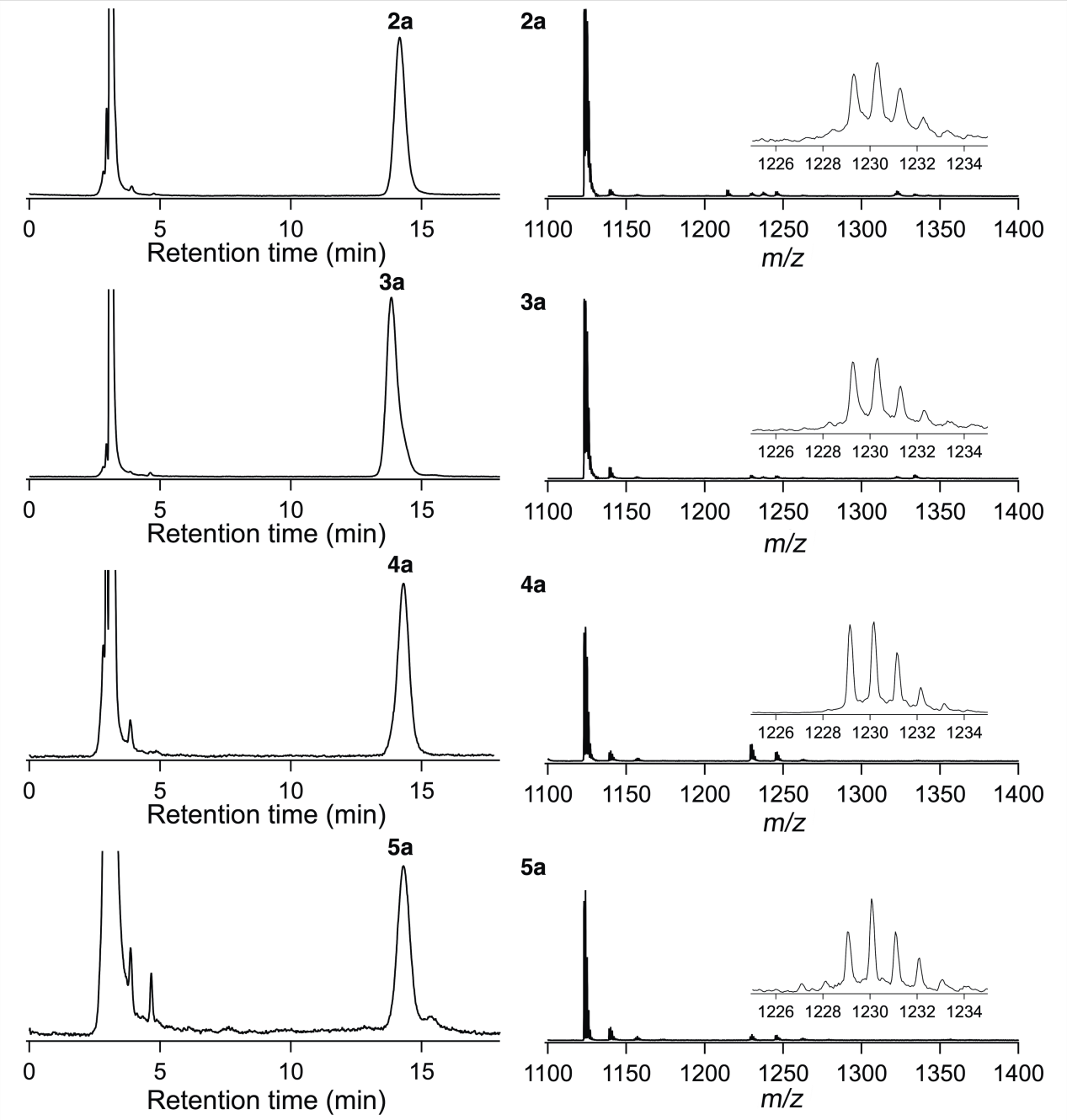

Figure 3: HPLC profiles (Buckyprep column (⌀ = 4.6 × 250 mm); eluent, toluene; flow rate, 1.0 mL/min; UV detector, 330 nm.) and MALDI–TOF mass spectra (matrix: dithranol, positive mode) of **2a**–**5a**.

tion of La@C_{2v}-C_{82} were effective for its functionalization in terms of both regioselectivity and reactivity compared to the thermal and photoreactions of La@C_{2v}-C_{82} reported previously [19].

Figure 4 shows the absorption spectra of **2**–**5**. Their absorption onsets move to shorter wavelengths relative to those of La@C_{2v}-C_{82}, which are characteristic features of single-bonded La@C_{2v}-C_{82} derivatives [19,23], indicating that **2**–**5** have larger HOMO–lowest unoccupied molecular orbital energy gaps owing to their closed shell structures. As previous studies have shown that the absorption spectra of fullerene derivatives sensitively reflect the addition site, the absorption spectra can be regarded as powerful tools to determine the addition site in fullerene adducts [19,23-25]. Regardless of the substituents (**a**–**c**) of benzyl bromide, **2**, **3**, **4**, and **5** exhibited similar characteristic absorption features, respectively, supporting that the addition site of each isomer (e.g., **2a**–**c**) are the same.

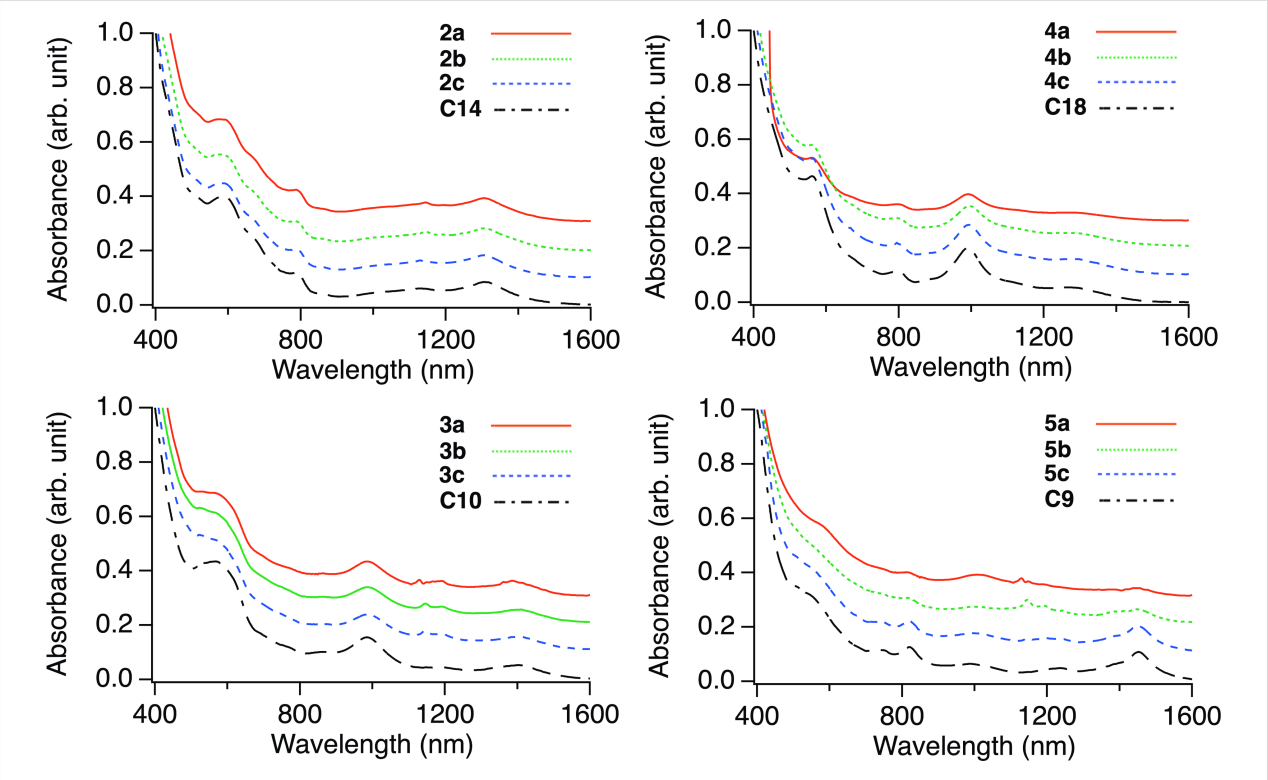

Figure 4: Absorption spectra of **2**, **3**, **4**, and **5** in CS_2 and absorption spectra of C14, C10, C18, and C9 in Ce@C_{2v}-C_{82}($CH_2C_6H_3Me_2$), which is attributed to the **1b**, **1d**, **1c**, and **1a** isomers in [25]. The carbon atom numbers correspond to that shown in Figure 6d.

We determined the addition sites of the single-bonded La@C_{2v}-C_{82} derivatives, La@C_{2v}-C_{82}($CHClC_6H_3Cl_2$) [19] and La@C_{2v}-C_{82}($CBr(CO_2Et)_2$) [23], by single-crystal X-ray diffraction (SC-XRD) analysis. Based on the similarity in the absorption spectra of La@C_{2v}-C_{82}($CHClC_6H_3Cl_2$), the addition site of **3a**–**c** was expected to be at the C10 (for the numbering of carbon atoms in La@C_{2v}-C_{82}; see Figure 6d). Takano et al. estimated the addition sites of the 3,5-dimethylphenylmethyl group on Ce@C_{2v}-C_{82} (Ce@C_{2v}-C_{82}($CH_2C_6H_3Me_2$)) through temperature-dependent paramagnetic shifts of its nuclear magnetic resonance signals [25]. The similarity in the HPLC separation behavior and absorption spectra between the La@C_{2v}-C_{82} adducts (**2a**–**c**, **3a**–**c**, and **4a**–**c**) [19] and the Ce@C_{2v}-C_{82}($CH_2C_6H_3Me_2$) isomers [25] reported by Takano et al. was observed. Based on this observation, the plausible addition sites of **2a**–**c**, **3a**–**c**, and **4a**–**c** were estimated to be at the C14, C10, and C18 positions. The molecular structure of **3a** was confirmed by the SC-XRD analysis, which showed that the addition site of addendum was indeed at the C10 position of La@C_{2v}-C_{82} (Figure 5).

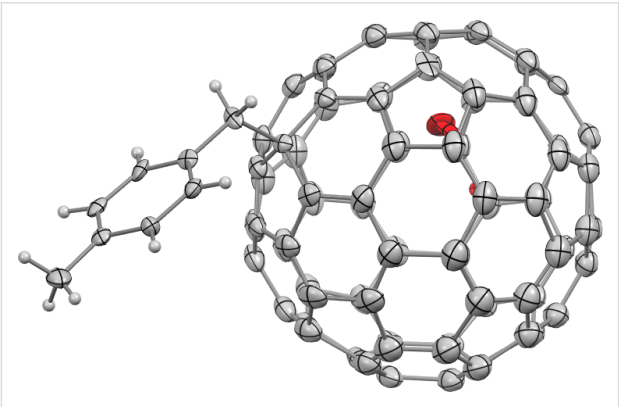

Figure 5: ORTEP drawing of **3a** with thermal ellipsoids shown at 50% probability level. Only an independent unit of **3a** is shown. This crystal has two independent units of **3a** and three CS_2 molecules as guest solvents. The difference between the two independent units is the direction of the tolyl group in the crystal (Supporting Information File 1, Figure S7).

The La@C_{2v}-C_{82} anion can act as an electron donor and a nucleophile. To confirm the reaction mechanism, charge density and the p-orbital axis vector (POAV) values [26] of the carbon atoms ($\theta_{\sigma\pi}$-90°) of the La@C_{2v}-C_{82} anion were calculated using density functional theory (DFT) [27-33]. As shown in Table 1 and Figure 6, the C1, C2, and C3 atoms have large negative charge densities (C1: −0.1498, C2: −0.1828, C3: −0.1126), and C1 and C2 atoms have high POAV values (C1: 11.2, C2: 11.3) in the La@C_{2v}-C_{82} anion. Meanwhile, the C10, C14, and C18 atoms have moderate or small negative charge densities (C10: −0.0317, C14: −0.0137, C18: −0.0128) and high

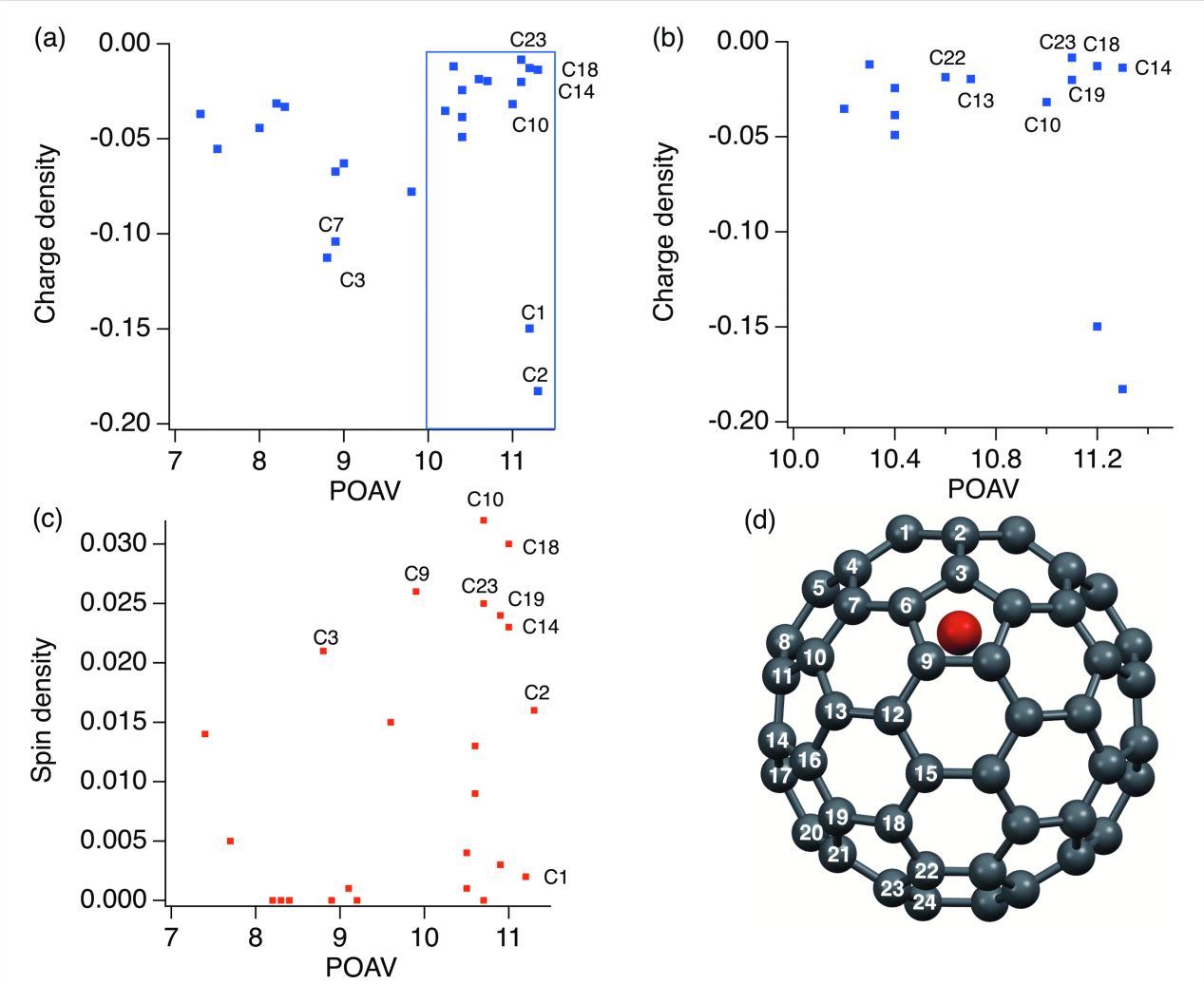

Figure 6: (a) Charge density of La@C_{2v}-C_{82} anion as a function of its POAV values and (b) an enlarged part view of blue region in (a). (c) Spin density of La@C_{2v}-C_{82} as a function of its POAV values [34,35]. (d) Molecular structure of La@C_{2v}-C_{82} and numbering carbon atoms.

POAV values (C10: 11.0, C14: 11.3, C18: 11.2) in the La@C_{2v}-C_{82} anion. On the other hand, the C10, C14, and C18 atoms have larger spin densities (C10: 0.032, C14: 0.023, C18: 0.030) [34,35] than the C1 and C2 atoms (C1: 0.002, C2: 0.016) in La@C_{2v}-C_{82} (Figure 6b). These results suggest that the reaction mechanism involving the electron transfer from the La@C_{2v}-C_{82} anion to benzyl bromide derivatives followed by the radical coupling reaction is more plausible for the formation of the corresponding adducts rather than the S_N2 reaction mechanism of the La@C_{2v}-C_{82} anion with benzyl bromide derivatives.

Conclusion

The reaction of La@C_{2v}-C_{82} anion with benzyl bromide derivatives **1** at 110 °C afforded the corresponding single-bonded adducts **2**–**5** with high regioselectivity. One-electron reduction of La@C_{2v}-C_{82} increased its reactivity during thermal reaction relative to that of neutral La@C_{2v}-C_{82}. Structural analysis of the two major products indicated that the characteristic absorption features were strongly affected by the addition sites. Based on theoretical studies and considering the identified addition sites, a plausible reaction mechanism for the reaction is the electron transfer from La@C_{2v}-C_{82} anion to benzyl bromide, followed by radical coupling. This demonstrates that one-electron reduction of La@C_{2v}-C_{82} is an easy and effective method for controlling its reactivity and selectivity via ionization for the production of La@C_{2v}-C_{82} derivatives.

Experimental

General: All chemicals and solvents were obtained from Wako, TCI, and Aldrich and were used without further purification unless otherwise stated. ODCB was distilled over P_2O_5 under vacuum prior to use. HPLC was performed on an LC-9201 instrument (Japan Analytical Industry Co., Ltd.) by

Table 1: Charge densities and POAV values of carbon atoms for La@C_{2v}-C_{82} anion, and spin densities and POAV values of carbon atoms for La@C_{2v}-C_{82} [34,35]. The carbon atom numbers correspond to that shown in Figure 6d.

Carbon atom number	La@C_{2v}-C_{82} anion		La@C_{2v}-C_{82} [34,35]	
	POAV	Charge density	POAV	Spin density
1	11.2	−0.1498	11.2	0.002
2	11.3	−0.1828	11.3	0.016
3	8.8	−0.1126	8.8	0.021
4	9.8	−0.0778	9.6	0.015
5	9.0	−0.0629	9.2	0.000
6	10.4	−0.0491	10.5	0.004
7	8.9	−0.1041	9.1	0.001
8	8.9	−0.0672	8.9	0.000
9	10.2	−0.0353	9.9	0.026
10	11.0	−0.0317	10.7	0.032
11	10.4	−0.0386	10.6	0.009
12	7.5	−0.0554	7.7	0.005
13	10.7	−0.0196	10.9	0.003
14	11.3	−0.0137	11.0	0.023
15	7.3	−0.0369	7.4	0.014
16	10.4	−0.0244	10.6	0.013
17	8.0	−0.0443	8.2	0.000
18	11.2	−0.0128	11.0	0.030
19	11.1	−0.0201	10.9	0.024
20	8.3	−0.0332	8.4	0.000
21	10.3	−0.0119	10.5	0.001
22	10.6	−0.0186	10.7	0.000
23	11.1	−0.0084	10.7	0.025
24	8.2	−0.0314	8.3	0.000

monitoring the UV absorption at 330 nm with toluene as the eluent. Mass spectrometry was performed using a Bruker AUTOFLEX III smart beam with dithranol as the matrix. Optical absorption spectra were recorded using a Pyrex cell with a 10 mm path length and a spectrophotometer (V-670; Jasco Corp.).

Preparation of La@C_{2v}-C_{82}

As described in [19], soot containing endohedral metallofullerenes were produced through the standard arc vaporization method using a composite anode rod containing graphite and metal oxide. The composite rod was subjected to an arc discharge under a He atmosphere at 50 Torr. Raw soot was collected and suspended in 1,2,4-trichlorobenzene (TCB). The mixture was refluxed for 16 h. The TCB solution was collected and injected into the HPLC instrument to separate the endohedral metallofullerenes using a PBB column (⌀ 20 mm × 250 mm; Cosmoses, Nacalai Tesque Inc.) with chlorobenzene as the mobile phase in the first step and a Buckyprep column (⌀ 20 mm × 250 mm × 2; Cosmoses, Nacalai Tesque Inc.) with toluene as the mobile phase in the second step.

Preparation of the La@C_{2v}-C_{82} anion

As described in [21], La@C_{2v}-C_{82} (0.34×10^{-6} mol) was dissolved in 10 mL of a pyridine solution containing TBAF (0.54×10^{-3} mol) and then stirred for 2 h under an Ar atmosphere. The resulting green solution was concentrated to 2.0 mL. CS_2 was added to the solution to precipitate excess TBAF which was then removed by filtration. The La@C_{2v}-C_{82} anion ([La@C_{2v}-C_{82}]PF_6) was collected as the filtrate (with a 78% yield estimated from the molar absorbance coefficient). This step was repeated to ensure a sufficient amount of La@C_{2v}-C_{82} anions for the next step.

Reaction of the La@C_{2v}-C_{82} anion with **1a**

1a was added to 12 mL of the La@C_{2v}-C_{82} anion (0.89×10^{-6} mol) ODCB solution. The solution was degassed using freeze-pump-thaw cycles. The solution was then heated at 110 °C for 2 h. After the reaction, dichloroacetic acid was added to recover the unreacted La@C_{2v}-C_{82} in its neutral form. Four isomers, **2a**, **3a**, **4a**, and **5a**, and La@C_{2v}-C_{82} were isolated from the reaction mixture using multistep HPLC, as shown in Supporting Information File 1, Figures S2, S4, and S6. The yields were calculated from the HPLC peak areas monitored at

330 nm, assuming that La@C_{2v}-C_{82} and the monoadducts have the same absorption coefficients.

X-ray crystallography

Black crystalline rods of **3a** were obtained using the liquid–liquid bilayer diffusion method with **3a** in a CS_2 solution and an *n*-hexane solution in a glass tube (⌀ = 7 mm) at room temperature. The SC-XRD measurement was performed at 90 K on a Bruker AXS instrument equipped with an Apex II CCD detector with Mo *Kα* radiation (λ = 0.71073 Å). The multi-scan method was used for absorption corrections. Structures were solved using direct methods and refined using SHELXL-2014/7 [36-38]. Deposition Number 2299232 (for **3a**) contains the supplementary crystallographic data for this study. This data was provided free of charge by the joint Cambridge Crystallographic Data Centre and Fachinformationszentrum Karlsruhe Access Structures Service.

Theoretical calculations

POAV ($\theta_{\sigma\pi}$–90°) and charge densities values were calculated using the Gaussian 03 program with DFT at the B3LYP/3-21G for C and H [33], and the LanL2DZ basis set and effective core potential (ECP) for La [29,32].

La@C_{2v}-C_{82}($CH_2C_6H_4CH_3$) (**2a**): vis–NIR (CS_2): λ_{max} = 572, 741, 1304 nm; MALDI–TOF MS (*m*/*z*): $[MH]^+$ calcd for $LaC_{90}H_9$, 1228.98; found, 1229.04.

La@C_{2v}-C_{82}($CH_2C_6H_4CH_3$) (**3a**): vis–NIR (CS_2): λ_{max} = 560, 851, 991, 1271 nm; MALDI–TOF MS (*m*/*z*): $[MH]^+$ calcd for $LaC_{90}H_9$, 1228.98; found, 1228.99.

La@C_{2v}-C_{82}($CH_2C_6H_4CH_3$) (**4a**): vis–NIR (CS_2): λ_{max} = 525, 986, 1410 nm; MALDI–TOF MS (*m*/*z*): $[MH]^+$ calcd for $LaC_{90}H_9$, 1228.98; found, 1229.15.

La@C_{2v}-C_{82}($CH_2C_6H_4CH_3$) (**5a**): vis–NIR (CS_2): λ_{max} = 809, 997, 1454 nm; MALDI–TOF MS (*m*/*z*): $[MH]^+$ calcd for $LaC_{90}H_9$, 1228.98; found, 1229.04.

La@C_{2v}-C_{82}($CH_2C_6H_4CCSi(CH_3)_3$) (**2b**): vis–NIR (CS_2): λ_{max} = 568, 762, 1307 nm; MALDI–TOF MS (*m*/*z*): $[MH]^+$ calcd for $LaC_{94}H_{16}Si$, 1311.01; found, 1311.25.

La@C_{2v}-C_{82}($CH_2C_6H_4CCSi(CH_3)_3$) (**3b**): vis–NIR (CS_2): λ_{max} = 559, 883, 995, 1242 nm; MALDI–TOF MS (*m*/*z*): $[MH]^+$ calcd for $LaC_{94}H_{16}Si$, 1311.01; found, 1311.37.

La@C_{2v}-C_{82}($CH_2C_6H_4CCSi(CH_3)_3$) (**4b**): vis–NIR (CS_2): λ_{max} = 521, 986, 1410 nm; MALDI–TOF MS (*m*/*z*): $[MH]^+$ calcd for $LaC_{94}H_{16}Si$, 1311.01; found, 1311.29.

La@C_{2v}-C_{82}($CH_2C_6H_4CCSi(CH_3)_3$) (**5b**): vis–NIR (CS_2): λ_{max} = 809, 998, 1447 nm; MALDI–TOF MS (*m*/*z*): $[MH]^+$ calcd for $LaC_{94}H_{16}Si$, 1311.01; found, 1311.25.

La@C_{2v}-C_{82}($CH_2C_6H_5$) (**2c**): vis–NIR (CS_2): λ_{max} = 583, 786, 1305 nm; MALDI–TOF MS (*m*/*z*): $[MH]^+$ calcd for $LaC_{89}H_7$, 1214.97; found, 1214.83.

La@C_{2v}-C_{82}($CH_2C_6H_5$) (**3c**): vis–NIR (CS_2): λ_{max} = 561, 891, 993, 1270 nm; MALDI–TOF MS (*m*/*z*): $[MH]^+$ calcd for $LaC_{89}H_7$, 1214.97; found, 1214.96.

La@C_{2v}-C_{82}($CH_2C_6H_5$) (**4c**): vis–NIR (CS_2): λ_{max} = 521, 986, 1410 nm; MALDI–TOF MS (*m*/*z*): $[MH]^+$ calcd for $LaC_{89}H_7$, 1214.97; found, 1214.82.

La@C_{2v}-C_{82}($CH_2C_6H_5$) (**5c**): vis–NIR (CS_2): λ_{max} = 818, 999, 1451 nm; MALDI–TOF MS (*m*/*z*): $[MH]^+$ calcd for $LaC_{89}H_7$, 1214.97; found, 1214.98.

Supporting Information

Supporting Information features HPLC chromatographs and MS spectra of fullerene derivatives, changes in absorption spectra during the reaction of La@C_{2v}-C_{82} with **1b** and **1c**, X-ray crystallographic data of **3a**, and ORTEP drawings of the independent unit of **3a**.

Supporting Information File 1

Additional experimental data.
[https://www.beilstein-journals.org/bjoc/content/supplementary/1860-5397-19-138-S1.pdf]

Funding

This work was supported by JSPS KAKENHI Grants Number 21H01759 and 20K05469.

ORCID® iDs

Yutaka Maeda - https://orcid.org/0000-0003-0502-5621
Mitsuaki Suzuki - https://orcid.org/0000-0001-7226-2665
Michio Yamada - https://orcid.org/0000-0002-6715-4202
Takeshi Akasaka - https://orcid.org/0000-0002-4073-4354

References

1. Hirsch, A.; Brettreich, M. *Fullerenes: Chemistry and Reactions;* Wiley-VCH: Weinheim, Germany, 2004. doi:10.1002/3527603492
2. Kadish, K. M.; Ruoff, R. S., Eds. *Fullerenes: Chemistry, Physics, and Technology;* John Wiley & Sons: New York, NY, USA, 2000.
3. Prato, M.; Maggini, M. *Acc. Chem. Res.* **1998,** *31,* 519–526. doi:10.1021/ar970210p

4. Thilgen, C.; Diederich, F. *Chem. Rev.* **2006,** *106,* 5049–5135. doi:10.1021/cr0505371
5. Vostrowsky, O.; Hirsch, A. *Chem. Rev.* **2006,** *106,* 5191–5207. doi:10.1021/cr050561e
6. Caron, C.; Subramanian, R.; D'Souza, F.; Kim, J.; Kutner, W.; Jones, M. T.; Kadish, K. M. *J. Am. Chem. Soc.* **1993,** *115,* 8505–8506. doi:10.1021/ja00071a093
7. Subramanian, R.; Boulas, P.; Vijayashree, M. N.; D'Souza, F.; Jones, M. T.; Kadish, K. M. *J. Chem. Soc., Chem. Commun.* **1994,** 1847–1848. doi:10.1039/c39940001847
8. Fukuzumi, S.; Suenobu, T.; Hirasaka, T.; Arakawa, R.; Kadish, K. M. *J. Am. Chem. Soc.* **1998,** *120,* 9220–9227. doi:10.1021/ja9815430
9. Allard, E.; Rivière, L.; Delaunay, J.; Dubois, D.; Cousseau, J. *Tetrahedron Lett.* **1999,** *40,* 7223–7226. doi:10.1016/s0040-4039(99)01467-7
10. Wabra, I.; Holzwarth, J.; Hauke, F.; Hirsch, A. *Chem. – Eur. J.* **2019,** *25,* 5186–5201. doi:10.1002/chem.201805777
11. Maeda, Y.; Sanno, M.; Morishita, T.; Sakamoto, K.; Sugiyama, E.; Akita, S.; Yamada, M.; Suzuki, M. *New J. Chem.* **2019,** *43,* 6457–6460. doi:10.1039/c9nj01043b
12. Akasaka, T.; Nagase, S., Eds. *Endofullerenes: A New Family of Carbon Clusters;* Kluwer Academic Publisher: Dordrecht, Netherlands, 2002.
13. Maeda, Y.; Tsuchiya, T.; Lu, X.; Takano, Y.; Akasaka, T.; Nagase, S. *Nanoscale* **2011,** *3,* 2421–2429. doi:10.1039/c0nr00968g
14. Lu, X.; Feng, L.; Akasaka, T.; Nagase, S. *Chem. Soc. Rev.* **2012,** *41,* 7723–7760. doi:10.1039/c2cs35214a
15. Popov, A. A.; Yang, S.; Dunsch, L. *Chem. Rev.* **2013,** *113,* 5989–6113. doi:10.1021/cr300297r
16. Akasaka, T.; Kato, T.; Kobayashi, K.; Nagase, S.; Yamamoto, K.; Funasaka, H.; Takahashi, T. *Nature* **1995,** *374,* 600–601. doi:10.1038/374600a0
17. Maeda, Y.; Miyashita, J.; Hasegawa, T.; Wakahara, T.; Tsuchiya, T.; Feng, L.; Lian, Y.; Akasaka, T.; Kobayashi, K.; Nagase, S.; Kako, M.; Yamamoto, K.; Kadish, K. M. *J. Am. Chem. Soc.* **2005,** *127,* 2143–2146. doi:10.1021/ja043986b
18. Li, F.-F.; Rodríguez-Fortea, A.; Poblet, J. M.; Echegoyen, L. *J. Am. Chem. Soc.* **2011,** *133,* 2760–2765. doi:10.1021/ja110160j
19. Takano, Y.; Yomogida, A.; Nikawa, H.; Yamada, M.; Wakahara, T.; Tsuchiya, T.; Ishitsuka, M. O.; Maeda, Y.; Akasaka, T.; Kato, T.; Slanina, Z.; Mizorogi, N.; Nagase, S. *J. Am. Chem. Soc.* **2008,** *130,* 16224–16230. doi:10.1021/ja802748q
20. Akasaka, T.; Wakahara, T.; Nagase, S.; Kobayashi, K.; Waelchli, M.; Yamamoto, K.; Kondo, M.; Shirakura, S.; Okubo, S.; Maeda, Y.; Kato, T.; Kako, M.; Nakadaira, Y.; Nagahata, R.; Gao, X.; Van Caemelbecke, E.; Kadish, K. M. *J. Am. Chem. Soc.* **2000,** *122,* 9316–9317. doi:10.1021/ja001586s
21. Tsuchiya, T.; Wakahara, T.; Lian, Y.; Maeda, Y.; Akasaka, T.; Kato, T.; Mizorogi, N.; Nagase, S. *J. Phys. Chem. B* **2006,** *110,* 22517–22520. doi:10.1021/jp0650679
22. Zhou, X.; Yao, Y.-R.; Hu, Y.; Yang, L.; Yang, S.; Zhang, Y.; Zhang, Q.; Peng, P.; Jin, P.; Li, F.-F. *Inorganics* **2023,** *11,* 349. doi:10.3390/inorganics11090349
23. Feng, L.; Nakahodo, T.; Wakahara, T.; Tsuchiya, T.; Maeda, Y.; Akasaka, T.; Kato, T.; Horn, E.; Yoza, K.; Mizorogi, N.; Nagase, S. *J. Am. Chem. Soc.* **2005,** *127,* 17136–17137. doi:10.1021/ja055484j
24. Hirsch, A.; Grösser, T.; Skiebe, A.; Soi, A. *Chem. Ber.* **1993,** *126,* 1061–1067. doi:10.1002/cber.19931260428
25. Takano, Y.; Tashita, R.; Suzuki, M.; Nagase, S.; Imahori, H.; Akasaka, T. *J. Am. Chem. Soc.* **2016,** *138,* 8000–8006. doi:10.1021/jacs.6b04037
26. Haddon, R. C. *J. Am. Chem. Soc.* **1990,** *112,* 3385–3389. doi:10.1021/ja00165a020
27. Maeda, Y.; Matsunaga, Y.; Wakahara, T.; Takahashi, S.; Tsuchiya, T.; Ishitsuka, M. O.; Hasegawa, T.; Akasaka, T.; Liu, M. T. H.; Kokura, K.; Horn, E.; Yoza, K.; Kato, T.; Okubo, S.; Kobayashi, K.; Nagase, S.; Yamamoto, K. *J. Am. Chem. Soc.* **2004,** *126,* 6858–6859. doi:10.1021/ja0316115
28. *Gaussian 03,* Revision C.02; Gaussian, Inc.: Wallingford, CT, 2004.
29. Lee, C.; Yang, W.; Parr, R. G. *Phys. Rev. B* **1988,** *37,* 785–789. doi:10.1103/physrevb.37.785
30. Becke, A. D. *Phys. Rev. A* **1988,** *38,* 3098–3100. doi:10.1103/physreva.38.3098
31. Becke, A. D. *J. Chem. Phys.* **1993,** *98,* 5648–5652. doi:10.1063/1.464913
32. Hay, P. J.; Wadt, W. R. *J. Chem. Phys.* **1985,** *82,* 299–310. doi:10.1063/1.448975
33. Binkley, J. S.; Pople, J. A.; Hehre, W. J. *J. Am. Chem. Soc.* **1980,** *102,* 939–947. doi:10.1021/ja00523a008
34. Sato, S.; Maeda, Y.; Guo, J.-D.; Yamada, M.; Mizorogi, N.; Nagase, S.; Akasaka, T. *J. Am. Chem. Soc.* **2013,** *135,* 5582–5587. doi:10.1021/ja309763f
35. Maeda, Y.; Sato, S.; Inada, K.; Nikawa, H.; Yamada, M.; Mizorogi, N.; Hasegawa, T.; Tsuchiya, T.; Akasaka, T.; Kato, T.; Slanina, Z.; Nagase, S. *Chem. – Eur. J.* **2010,** *16,* 2193–2197. doi:10.1002/chem.200902512
36. Sheldrick, G. M. *Acta Crystallogr., Sect. A: Found. Crystallogr.* **2008,** *64,* 112–122. doi:10.1107/s0108767307043930
37. Sheldrick, G. M. *Acta Crystallogr., Sect. A: Found. Adv.* **2015,** *71,* 3–8. doi:10.1107/s2053273314026370
38. Sheldrick, G. M. *Acta Crystallogr., Sect. C: Struct. Chem.* **2015,** *71,* 3–8. doi:10.1107/s2053229614024218

License and Terms

BEILSTEIN JOURNAL OF ORGANIC CHEMISTRY

Anion–π catalysis on carbon allotropes

M. Ángeles Gutiérrez López, Mei-Ling Tan, Giacomo Renno, Augustina Jozeliūnaitė, J. Jonathan Nué-Martinez, Javier Lopez-Andarias, Naomi Sakai and Stefan Matile*

Review

Open Access

Address:
Department of Organic Chemistry, University of Geneva, Geneva, Switzerland

Email:
Stefan Matile* - stefan.matile@unige.ch

* Corresponding author

Keywords:
anion–π interactions; autocatalysis; catalysis; carbon nanotubes; Diels–Alder reactions; electric-field-induced catalysis; electromicrofluidics; enolate addition; ether cyclizations; fullerenes

Beilstein J. Org. Chem. **2023,** *19,* 1881–1894.
https://doi.org/10.3762/bjoc.19.140

Received: 13 October 2023
Accepted: 29 November 2023
Published: 12 December 2023

This article is part of the thematic issue "Carbon-rich materials: from polyaromatic molecules to fullerenes and other carbon allotropes".

Guest Editor: Y. Yamakoshi

Abstract

Anion–π catalysis, introduced in 2013, stands for the stabilization of anionic transition states on π-acidic aromatic surfaces. Anion–π catalysis on carbon allotropes is particularly attractive because high polarizability promises access to really strong anion–π interactions. With these expectations, anion–π catalysis on fullerenes has been introduced in 2017, followed by carbon nanotubes in 2019. Consistent with expectations from theory, anion–π catalysis on carbon allotropes generally increases with polarizability. Realized examples reach from enolate addition chemistry to asymmetric Diels–Alder reactions and autocatalytic ether cyclizations. Currently, anion–π catalysis on carbon allotropes gains momentum because the combination with electric-field-assisted catalysis promises transformative impact on organic synthesis.

Introduction

Anion–π catalysis was introduced ten years ago [1]. The idea is to stabilize anionic transition states on electron-deficient, π-acidic aromatic surfaces (Figure 1A). The true beginning is arguably in 2015 because it took some time to find the benchmark reaction needed to develop the catalysts (Figure 2) [2]. With this operational enolate chemistry in hand, it quickly became clear that increasing π acidity at the same time decreases the stability of the catalyst [3-5]. This suggested that induced rather than intrinsic anion–π interactions should provide access to really strong catalysts [3]. They have been predicted theoretically to occur on π-stacks [6], and confirmed recently to exist and apply to anion–π catalysis on π-stacked foldamers (Figure 1B) [7] and micelles [8]. However, due to their unique polarizability [9-11], the dream scaffolds for induced anion–π interactions are carbon allotropes. Anionic transition states placed on C_{60} fullerenes **1** will drive the 60 π electrons toward the other side, thus inducing a transient macrodipole that will stabilize the same transition state that induced its formation (Figure 1C) [12]. This intriguing mechanism of catalysis should be further intensified on single-walled carbon nanotubes **2** (SWCNTs, Figure 1D) and multi-walled carbon nanotubes **3** (MWCNTs, Figure 1E) [13]. Multiple substrate/transition-state

binding should reduce particularly in-plane polarization of the π system and thus induced anion–π interactions. Since the polarization caused by substrate/transition-state binding hinders additional binding, this effect should occur only at high concentrations.

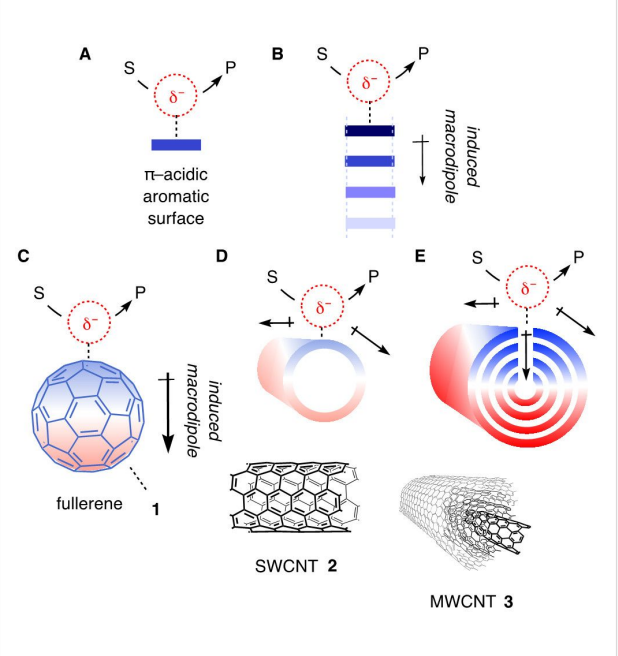

Figure 1: (A) Anion–π catalysis: Stabilization of anionic transition states from substrate S to product P on π-acidic aromatic surfaces. (B) Anion–$(π)_n$–π catalysis: Stabilization of anionic transition states by polarization of π stacks to induce oriented macrodipoles. (C–E) Anion–π catalysis on (C) C_{60} fullerenes **1**, (D) SWCNTs **2** and (E) MWCNTs **3**. Part E of Figure 1 was adapted from [44] (© 2023 M. A. Gutiérrez López et al., published by the American Association for the Advancement of Science, distributed under the terms of the Creative Commons Attribution 4.0 International License, https://creativecommons.org/licenses/by/4.0).

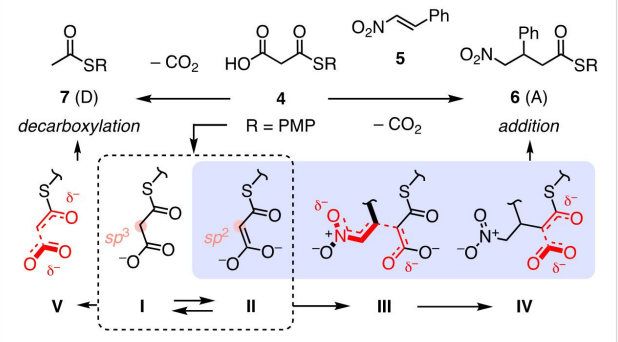

Figure 2: Bioinspired enolate addition chemistry to benchmark anion–π catalysts: Stabilization of "enol" intermediate **II** over "keto" intermediate **I** and nitronate transition state **III** by anion–π interactions (blue) selectively catalyzes the formation of the intrinsically disfavored enolate addition (A) product **6** over decarboxylation (D) product **7**. A/D product ratios are used to characterize anion–π catalysis, increasing A/D ratios indicate increasing anion–π catalysis. PMP = *para*-methoxyphenyl.

These expectations were first explored with anion–π catalysis on fullerenes in 2017 [12], followed by SWCNTs and MWCNTs two years later [13]. Particularly MWCNTs have the potential to couple anion–π and cation–π catalysis with electric-field-assisted catalysis [14]. While anion–π (and cation–π [15,16]) catalysis, compared to other unorthodox interactions, has been less impactful than expected [3,4,17-31], this combination has the potential to revolutionize organic catalysis [32-43]. These high expectations have never been realized for technical reasons. However, recent breakthroughs suggest that these methodological problems are now solved [44]. In electrochemical microfluidic reactors, electric-field-assisted anion–π catalysis on MWCNTs **3** is in place to lift anion–π catalysis on a level of general practical significance. For this reason, it appeared timely to recapitulate the results available so far on anion–π catalysis on carbon allotropes.

Review

Anion–π catalysis on fullerenes

The use of fullerenes in catalysis is surprisingly underdeveloped [45-51]. Anion–π and cation–π interactions on fullerenes attract similarly little attention until today [52-57]. Anion–π catalysis on fullerenes has been introduced in 2017 [12]. Fullerene anion–π catalysts were developed with the benchmark reaction introduced two years earlier (Figure 2) [2]. In this reaction, at the beginning of all biosynthesis, finetuned malonic acid half thioesters **4** [58-60] are deprotonated, and tautomers **I** and **II** add to an enolate acceptor. For anion–π catalysis, nitroolefins like **5** [60] were convenient acceptors because they are compatible with asymmetric catalysis, and because stabilization of intermediate **III** by privileged nitronate-π interactions drives the reaction forward. Decarboxylation of the resulting intermediate **IV** then affords the chiral addition product **6**. This enolate addition is in kinetic competition with simple decarboxylation, yielding thioacetate **7**. Under most conditions, this decarboxylation is favored. Anion–π catalysis selectively accelerates the intrinsically disfavored but significant enolate addition by stabilizing the planar sp^2 intermediate **II** that has to add before decarboxylation can occur [2,61]. The non-planar sp^3 keto intermediate **I** that can decarboxylate through intermediate **V** without preceding enolate addition is less stabilized on the planar π surfaces of anion–π catalysts. The A/D product ratio is thus a convenient measure for anion–π catalysis, the larger the better, with A/D > 1, the intrinsic selectivity for decarboxylation has been inverted [2,3,18].

Applying lessons from simpler anion–π catalysts, trialkylamines were tethered to C_{60} fullerenes [12]. These amines function as bases, their position next to the aromatic surface is essential to turn on anion–π interactions as soon as substrate **4** is deprotonated. Fullerene derivatization with the Bingel reaction

installs a cyclopropane that continues with one or two acid derivatives. In fullerene **8**, this is an amide with a short ethylene tether for the tertiary amine (Figure 3).

Fullerene **8** catalyzed the formation of the addition product **6** with high selectivity over the decarboxylation product **7** [12]. The experimental product ratio A/D_{8} was divided by the product ratio A/D_{9} measured with the fullerene-free **9**. The resulting $A/D_{8/9}$ = 2.6 reports the isolate contribution of the fullerene to catalysis in a comparable manner. This high value supported that the high polarizability of fullerenes provides access to strong induced anion–π interactions for efficient anion–π catalysis (Figure 1C).

Elongation of the tether in fullerenes **10** and **11** reduced product ratios to still significant $A/D_{10/9} \sim A/D_{11/9}$ = 2.1. The origin of this decrease in anion–π catalysis is likely to include increasing entropy losses in pseudo-macrocyclic transition states. Normalized against the fullerene-free control **12**, a secondary Bingel amide in **13** caused a drop to $A/D_{13/12}$ = 1.6. Similarly, low $A/D_{14/12}$ = 1.5 for an ester in **14** supported that removal of the hydrogen-bond donor in **5** rather than steric constraints account for the decrease in anion–π catalysis. Elongation of the tether in the ester series **14**–**16** was as in the amide series from **8** and thus supported entropic contributions to anion–π catalysis. Steric increase of the secondary amide in **17** impeded anion–π catalysis, presumably because the catalytic π surface next to the ammonium cation became inaccessible for anions paired with the tethered ammonium cation. Normalized against the fullerene-free control **18**, an electron-withdrawing cyano group on the cyclopropane in **19** gave similarly poor $A/D_{19/18}$ = 1.5.

At constant tether length as short as possible, strong increases in anion–π catalysis were found by further minimizing entropy losses in pseudo-macrocyclic transition states, bound non-covalently to both the active π surface and the ammonium cation of the tether. Normalized against the fullerene-free control **20**, the most preorganized dyad **21** gave a new record $A/D_{21/20}$ = 4.1. This value was much higher than the previous best $A/D_{8/9}$ = 2.6 with a freely rotating tether. Further increasing activity with fullerene **22** should not be overrated because $A/D_{22/23}$ = 4.6 was recorded against triethylamine (**23**), which is a less precise control compared to the exactly matching **20**.

Asymmetric anion–π catalysis on fullerenes

The best fullerene catalyst **21** was applied to other reactions. Diels–Alder reactions are of special interest for anion–π catalysis because of the promise to accelerate an intrinsically disfavored but relevant pathway, like in the benchmark enolate addition (Figure 2) [62]. Namely, in solution, the *endo* transition state **VI** is preferred to maximize orbital overlap (Figure 4) [63]. For π-acidic surfaces, the *exo* transition state **VII** is more completely accessible (Figure 4). The 3-hydroxy-2-pyrone (**24**) was selected as representative diene for the anionic [4 + 2] cycloaddition with maleimide **25** as standard dienophile to afford *endo* product **26** and *exo* product **27** [64-66]. With the less powerful fullerene catalyst **14**, the increase of the *exo*/*endo* selectivity compared to the fullerene-free control **12**, i.e., $exo/endo_{14/12}$ = 1.1, was negligible [12]. With the best fullerene catalyst **21**, the presence of the fullerene made the diastereoselectivity ratio with $exo/endo_{21/20}$ = 1.9 nearly doubled. The same was true for the enantioselectivity, which increased from 23% ee for control **20** to 55% ee for anion–π catalyst **21**.

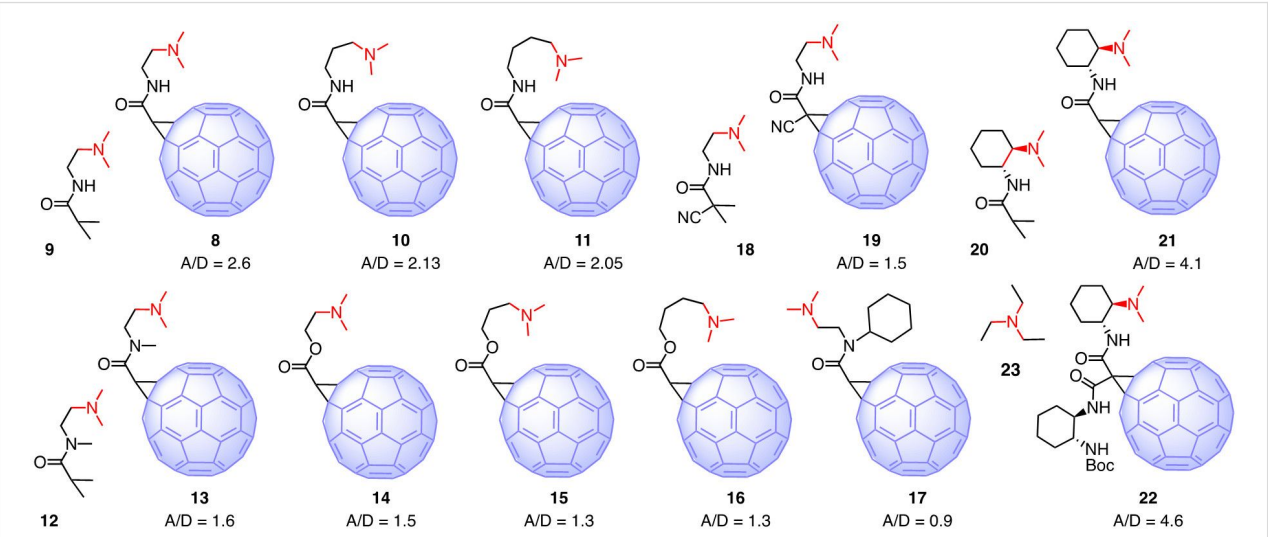

Figure 3: Structure and activity of fullerene-amine dyads to catalyze the intrinsically disfavored but biologically relevant enolate addition chemistry in Figure 2. A/D ratios of fullerene catalysts are normalized against the A/D_0 ratios of the fullerene-free controls (**9**, **12**, **18**, **20**, **23**), increasing A/D ratios indicate increasing anion–π catalysis on fullerenes.

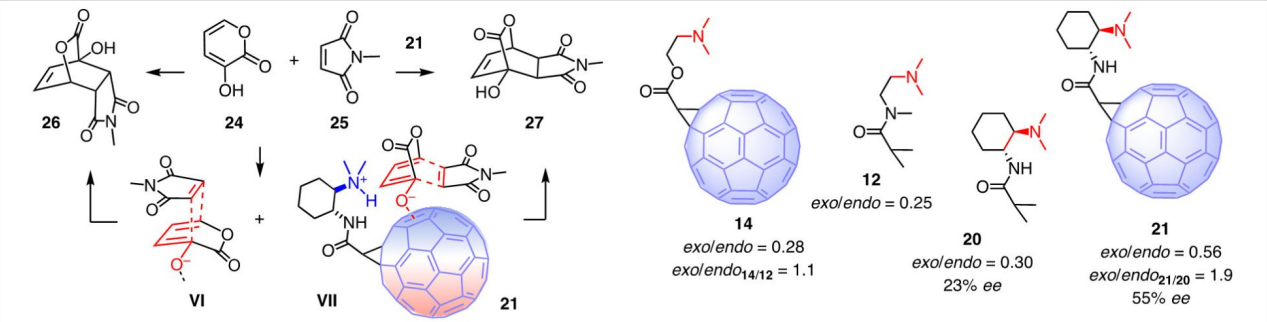

Figure 4: Asymmetric anion–π catalysis of intrinsically disfavored *exo*-selective Diels–Alder reactions on fullerene catalyst **21**, with notional *endo* and *exo* transition states **VI** and **VII**, respectively.

These results were in support that stabilization of the intrinsically disfavored *exo* transition state **VII** on the polarizable surface of carbon allotropes can increase diastereo- and enantioselectivity of Diels–Alder reactions.

The direct formation of 1,3-nonadjacent stereocenters is a topic of concern in asymmetric catalysis [67]. To explore compatibility with anion–π catalysis, the addition of ethyl 2-cyano-2-phenylacetate (**28**) to 2-chloroacrylonitrile (**29**) was selected (Figure 5) [68]. In the presence of 5 mol % of the best fullerene catalyst **21**, conversion into dicyanide **30** reached 72% within 5 days at ambient temperature [67]. While enantioselectivity was negligible, dr 5.3:1 was the best diastereoselectivity among all tested anion–π catalysts. This result was consistent with the stabilization of the anionic intermediates **IX** and **X** and the respective transition states on the polarized fullerene surface.

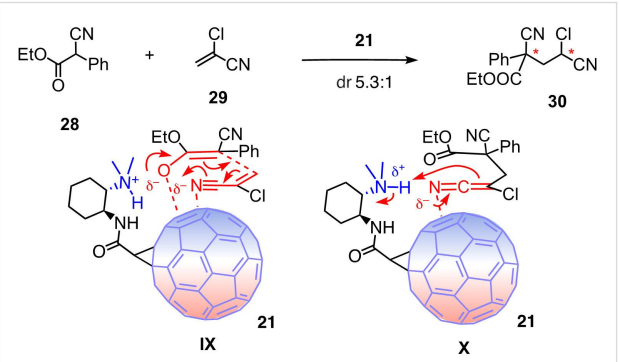

Figure 5: Asymmetric anion–π catalysis to install remote stereogenic centers on fullerene catalyst **21**, with notional transition states **IX** and **X**.

Anion–π autocatalysis on fullerenes

The autocatalysis of epoxide-opening ether cyclization on π-acidic aromatic surfaces has been identified in 2018 as an emergent property of anion–π catalysis [69]. In this series, fullerene catalyst **31** was found to catalyze the cyclization of epoxide **32** into THF **33** (Figure 6). The rate enhancement for catalysis was 270, whereas autocatalysis accelerated the reaction by 1045 M^{-1}. The origin of autocatalysis on π-acidic surfaces was clarified only this year because the involvement of two molecules of water in the decisive transition state **XI** complicated the situation [70].

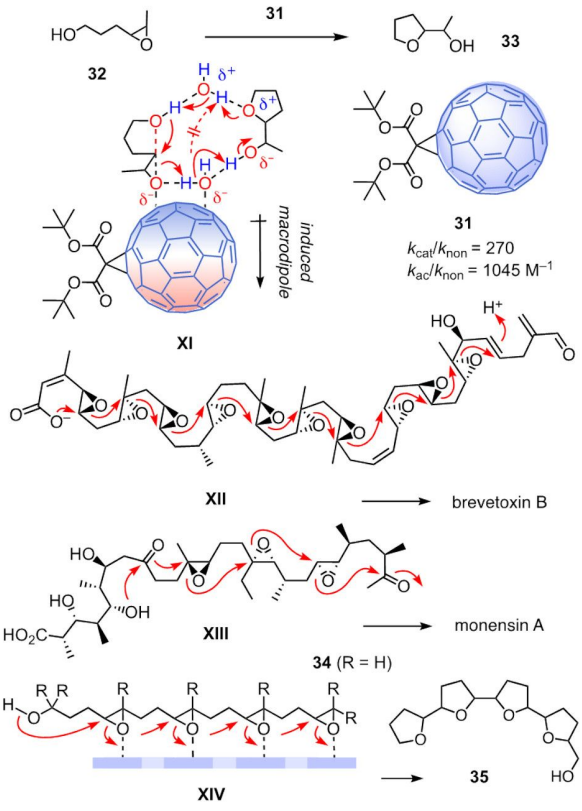

Figure 6: Primary anion–π autocatalysis on monofunctional fullerene **31**, with catalytic and autocatalytic rate enhancements, representative cascade cyclizations with anti-Baldwin (**XII**) and Baldwin (**XIII**) selectivity in nature, and primary anion–π autocatalysis of cascade cyclization **XIV** on catalysts other than carbon allotropes.

This reaction was intriguing for reasons beyond autocatalysis. It is the only example so far where fullerenes act as anion–π cata-

lyst without additional activating groups, usually a tethered base to inject a negative charge into the substrate directly on top of the catalytic π surface [69]. The *tert*-butyl esters in Bingel fullerene **31** serve only to improve solubility and are not expected to participate in catalysis. Moreover, epoxide opening polyether cyclizations are among the most impressive cascade reactions in nature [71-73]. Best known is the hypothetical cascade **XII** in the biosynthesis of brevetoxin B [74]. It affords eleven fused ethers by violating the Eschenmoser–Dunitz–Baldwin guidelines [75-78] in every step. Among the Baldwin compatible examples from nature, the cascade **XIII** leading to monensin A is arguably the most popular [79]. On anion–π catalysts other than carbon allotropes, up to four epoxides **34** have been cyclized into the monensin-like tetra-THF **35** as outlined in intermediate **XIV** [24,25]. Thus, this reaction can be considered as the anion–π catalysis counterpart of the steroid cyclizations catalyzed in nature with the charge inverted, conventional cation–π interactions [15].

Anion–π catalysis on fullerene dimers

The strength of anion–π interactions increases with face-to-face π stacking because the delocalized π electrons move within the stack away from the charge, which induces a macrodipole along the stack that supports the binding of the anion (Figure 1B) [61]. What works for anion–$(\pi)_n$–π catalysis on π-stacked foldamers [61] and micelles [8] should apply to fullerenes as well. The unique polarizability of fullerene monomers like **1** is thought to induce strong anion–π interactions and thus account for the observed catalytic activity (Figure 7A) [12]. This polarizability should further increase in fullerene dimers like **36** [80].

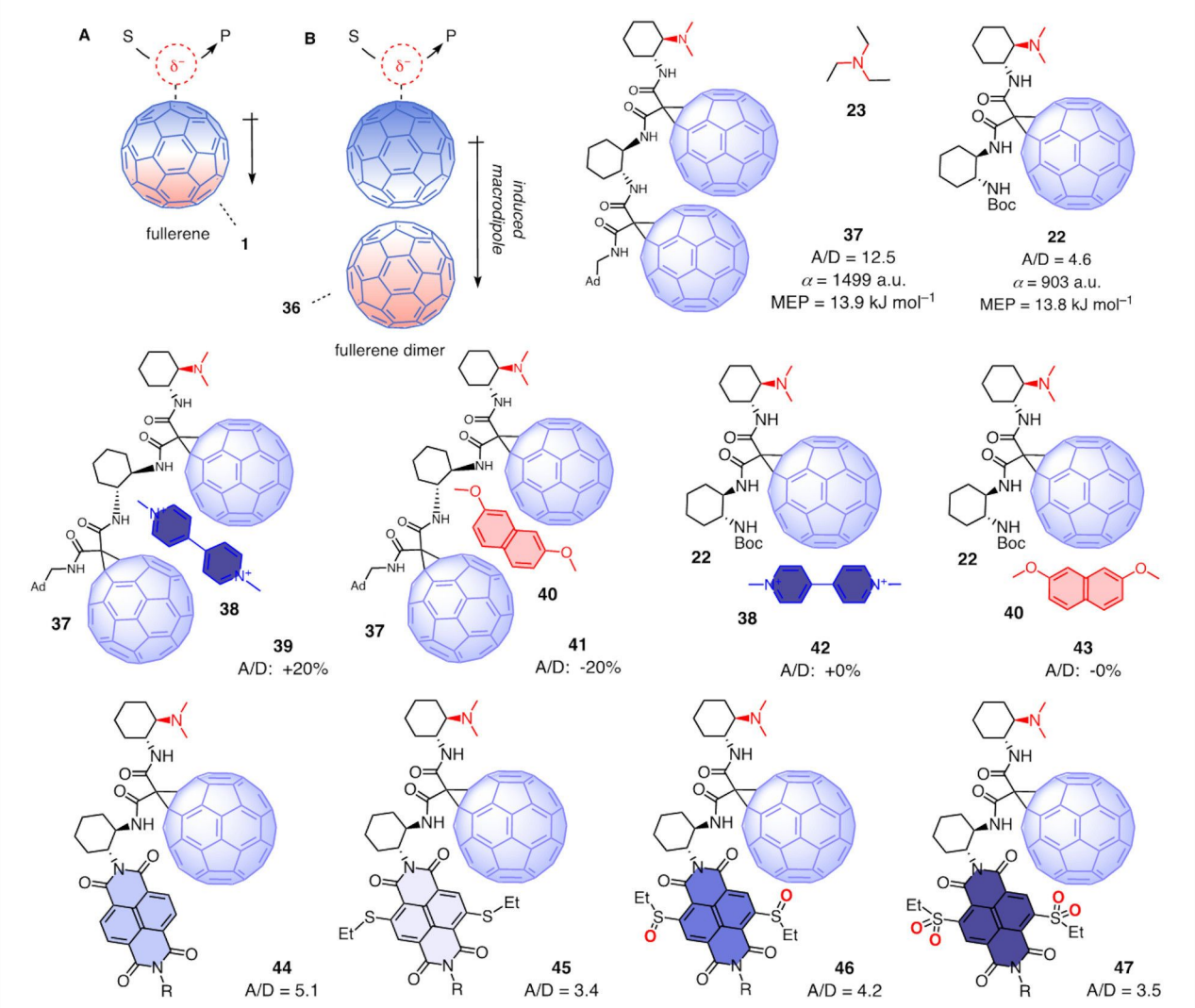

Figure 7: (A) Macrodipoles induced by anionic transition states account for anion–π catalysis on fullerenes. (B) Fullerene dimers double polarizability of the π system and thus anion–π catalysis, with structure of fullerene dimer **37**, intercalating activators and inactivators, monomeric fullerene and fullerene-NDI controls, and A/D ratios for products **6** and **7** normalized against the A/D_0 ratio of the fullerene-free control **23**, increasing A/D ratios indicate increasing anion-π catalysis.

Anions, anionic reactive intermediates and anionic transition states on top of fullerenes dimers should thus induce a larger macrodipole which should in turn strengthen their binding to the expanded π system and thus increase anion–π catalysis (Figure 1B).

Fullerene dimer **37** was equipped with the tethered tertiary amine needed to deprotonate the substrate **4** and produce the conjugate bases **I** and **II** as the first reactive intermediates directly on the active π surface (Figure 2 and Figure 7) [80]. Calibrated against triethylamine **23**, fullerene dimer **37** catalyzed enolate addition with an $A/D_{\mathbf{37/23}}$ = 12.5. This is more than twice the $A/D_{\mathbf{22/23}}$ = 4.6 of the respective monomer **22**, which was already best among fullerene monomers. In computational simulations, the positive maximum of the MEP surface next to the amine base was the same for dimer **37** (+13.9 kJ mol^{-1}) and monomer **22** (+13.8 kJ mol^{-1}), supporting that the dramatic increase in activity did not originate from a change in intrinsic anion–π interactions. The computed polarizability of dimer **37** (α = 1499 a.u.) was almost twice as high as that of monomer **22** (α = 903 a.u.), confirming that powerful induced anion–π interactions account for the high catalytic activity.

Twenty equivalents of the π-acidic intercalator **38** increased the catalytic activity of fullerene dimer **37** by 20%. This increase was consistent with the formation of the π-stacked complex **39** with increased polarizability and electron deficiency. With the π-basic intercalator **40**, the catalytic activity of fullerene dimer **37** decreased by 20%. This complementary decrease supported the formation of complex **41** with decreased electron deficiency. Control experiments with fullerene monomer **22** gave unchanged catalytic activity with intercalators **38** or **40**, which suggested that complexes **42** and **43** do not form. The insensitivity of fullerene monomers **22** thus supported that **38** and **40** activate and inactivate fullerene dimers **37** by intercalation in-between the two fullerenes.

Replacement of the second fullerene in dimer **37** with a poorly polarizable naphthalenediimide (NDI) in **44** increased the catalytic activity of fullerene monomer **22** much less significantly. With less electron-deficient NDIs carrying two sulfide donors in the core, the catalytic activity of **45** dropped below that of fullerene monomer **22**. Oxidation of the sulfide donors into sulfoxide acceptors increased the catalytic activity much less than expected, resting below that of unsubstituted NDIs despite stronger π acidity. Supported by experimental and computational data, this poor performance of dyad **46** was explained by lone-pair π interactions of the fullerene with the donating oxygens. These lone-pair π interactions were even more impactful on the sulfone level. Compared to the sulfoxides in **46**, the catalytic activity of dyad **47** decreased rather than increased despite stronger π acidity.

Supported by computational predictions [80,81], record activities in anion–π catalysis with fullerene dimers called for higher oligomers. However, synthetic efforts were not fruitful, mostly due to poor solubility.

Anion–π catalysis on carbon nanotubes

With fullerenes confirmed as privileged scaffold for induced anion–π catalysis but higher oligomers inaccessible [12,67,80], the obvious next move was to switch to carbon nanotubes. Compared to the sixty free electrons rushing toward one side of a C_{60} fullerene **1** to create a large macrodipole in response to an anionic transition state, the number of electrons available to maximize polarizability already in SWCNTs **2** is much higher (Figure 1D) [9-11]. Continuing in this series to increase polarizability with carbon allotropes, MWCNTs **3** emerge as privileged scaffold for anion–π catalysis because polarizability is possible not only along the tubes but also between the nanotubes, like in π-stacked foldamers (Figure 1E).

Numerous reports on catalysis with carbon nanotubes have appeared [45,46,82-94]. They serve as catch-and-release scaffolds in different variations, and, less frequently, as (photo)redox partners. Although they might contribute to these activities, anion–π interactions have not been considered. Anion–π catalysis on carbon nanotubes has been introduced explicitly in 2019 [13]. Already in the presence of pristine SWCNTs **2**, the ability of TEA **23** to catalyze enolate addition with **4** increased to $A/D_{\mathbf{48/23}}$ = 1.2 for a virtual catalytic complex **48** between the two (Figure 8). Covalent modification of SWCNTs with tertiary amines as in **49** further increased activity to $A/D_{\mathbf{49/23}}$ = 2.0. Suppression of this increase in a virtual complex **50** with a competitive inhibitor **51** further supported that the observed activity originates from anion–π catalysis.

With $A/D_{\mathbf{52/23}}$ = 1.3, pristine MWCNTs **3** failed to increase the activity of TEA **23** much more than SWCNTs **2**. This is not surprising because virtual complexes **52** and **48** are not expected to exist to an appreciable extent. With covalent modification, MWCNTs **53** with $A/D_{\mathbf{53/23}}$ = 7.3 outperformed the corresponding SWCNTs **49** with $A/D_{\mathbf{49/23}}$ = 2.0 clearly. This significant increase in activity was consistent with the increase in polarizability from SWCNTs **2** to MWCNTs **3** (Figure 1). Compared to fullerene monomers and dimers, this activity cannot be overestimated because MWCNTs operate in suspension rather than solution, that is as formal heterogenous rather than homogenous catalysts.

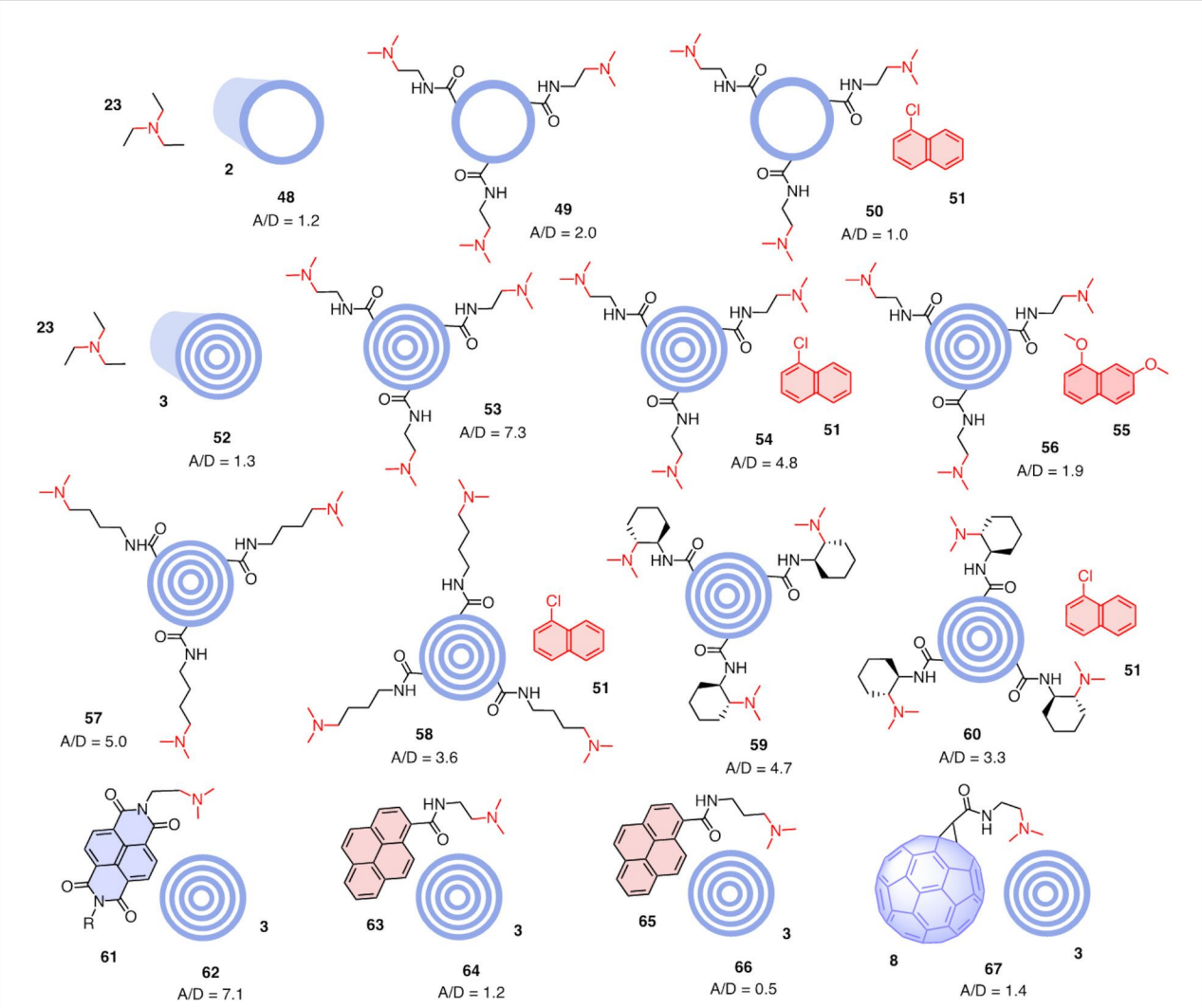

Figure 8: Structure and activity of covalently and non-covalently modified SWCNTs and MWCNTs, with A/D ratios for products **6** and **7** normalized against the A/D_0 ratios of the CNT-free controls, increasing A/D ratios indicate increasing anion–π catalysis.

Inhibition of the covalently modified MWCNT **53** with inhibitor **51** in complex **54** was supported by a drop from $A/D_{53/23}$ = 7.3 to $A/D_{54/23}$ = 4.8. Under identical conditions, the much more π-basic inhibitor **55** inhibited enolate addition by the MWCNT **53** almost completely, i.e., $A/D_{56/23}$ = 1.9 for the formal catalyst-inhibitor complex **56**. Increasing inhibition with the π basicity of the inhibitor was consistent with powerful anion–π interactions accessible on MWCNTs for efficient anion–π catalysis.

Like in the fullerene series, elongation of the tether in **57** decreased catalytic activity to still important $A/D_{57/23}$ = 5.0, presumably due to entropic reasons. The activity of inhibitor **51** remained detectable under standard conditions, thus supporting the formation of complex **58** with $A/D_{58/23}$ = 3.6. Unlike the fullerene series, preorganization of the tight tether in MWCNT **59** with $A/D_{59/23}$ = 4.7 did not give the best activity. This suggested that with the fully rigid and tight tether, small differences in local environment turned an advantageous match with the most convex surface of fullerene **21** into a slight mismatch with MWCNTs **59**. However, activities remained high and inhibition with inhibitor **51** in formal complex **60** was with $A/D_{60/23}$ = 3.3 preserved, also with this mildly mismatched tether.

The π-acidic NDI **61** with a Leonard-turned tertiary amine is a privileged small-molecule anion–π catalyst that catalyzes the enolate addition of malonate **4** with an activity that, however, does not reach that of the best carbon allotropes [95]. In the presence of pristine MWCNTs **3**, the activity of the NDI catalyst **61** increased significantly, implying the formation of complex **62** with $A/D_{62/61}$ = 7.1. While the reaction presumably still

occurred on the NDI surface, this very high A/D value suggested that efficient face-to-face stacking connected the active NDI surfaces to the nanotube to increase intrinsic anion–π interactions with the highest polarizability.

For interfacing with CNTs, the π-basic pyrenes rather than the π-acidic NDIs are most popular [82,88,90,96-99]. Equipped with a tertiary amine, the catalytic activity of dyad **63** increased only slightly in the presence of MWCNTs **3**, suggesting that the formed π-basic complex **64** is with $A/D_{64/63}$ = 1.2 much less active than the π-acidic NDI complex **62** with $A/D_{62/61}$ = 7.1, which is as expected for operational anion–π catalysis. With a longer tether, the already weak activity of pyrene **65** even decreased rather than increased in the presence of MWCNTs **3**, with a formal complex **66** operating with $A/D_{66/65}$ = 0.5. The activity of the fullerene catalyst **8** did not increase much in the presence of MWCNTs **3**, giving formal complex **67** with $A/D_{67/8}$ = 1.4. This was meaningful because the high activity of fullerene **8** with $A/D_{8/9}$ = 2.6 (Figure 3) leaves little room to improve, and the interaction between convex aromatic surfaces is not favorable.

Taken together, anion–π catalysis on multiwalled carbon nanotubes (**53**, A/D = 7.3) is better than on single-walled carbon nanotubes (**49**, A/D = 2.0) and monomeric fullerenes (**22**, A/D = 4.6) but weaker than on fullerene dimers (**37**, A/D = 12.5). The true activity is presumably much higher because MWCNTs, and SWCNTs, are heterogenous catalysts that operate as suspensions with only a minor fraction of the total π surface accessible for function. Fullerene monomers and dimers, in contrast, are homogenous catalysts that are fully dissolved and thus fully accessible. Anion–π catalysis thus increases roughly with the polarizability of the carbon allotrope. The overall less convincing activities found with SWCNTs could originate from more favorable weakening of the exclusively in-plane polarization by multiple substrate/transition-state binding under the selected experimental conditions. Besides these overall minor reservations for SWCMTs, the found activities are among the best observed [3], confirming the promise of induced anion–π interactions on carbon allotropes for catalysis.

In contrast to these conclusions made with modified carbon nanotubes, epoxide-opening ether cyclization of **32** occurred on undermodified fullerene **31** (Figure 6) but not on pristine MWCNTs **3** (Figure 9). Modified carbon nanotubes exert their catalytic power because the tethered base injects the negative charge into the substrate right on top of the polarizable π surface of the tube. Inability of pristine MWCNTs **3** to open and cyclize epoxide **32** thus implied insufficient substrate binding to form substrate-catalyst complexes that can proceed to transition state **XV** (Figure 9A). To increase binding, substrates would have to be equipped with interfacers. For MWCNTs **3**, interfacing with pyrene is most popular [82,88,90,96-99]. A pyrene interfacer was thus attached to substrate **32** [44]. Binding of the pyrene in the resulting substrate **68** to the MWCNT catalyst **3** should then afford a substrate-catalyst complex strong enough to access the interfaced transition state **XVI** and yield product **69**. Already the presence of 9 wt % of MWCNT suspensions gave rate enhancements of 390. They increased with increasing MWCNT concentrations.

In the presence of 25 mol % of inhibitor **70**, rate enhancements dropped to 11. This decrease was consistent with the formation of the formal inhibitor-catalyst complex **71**, where the π-basic DANs **70** stacked onto MWCNTs hinder the access of substrate **68**, physically, electrostatically, or both. The addition of 25 mol % product **69** at the beginning of the reaction decelerated rather than accelerated the cyclization from rate enhancements of 390 down to 5. The formal product-catalyst complexes **72** were, however, weak enough not to interfere with full substrate conversion, that is turnover. They provided support for the occurrence of anion–π catalysis but not autocatalysis on MWCNTs. The disappearance of autocatalysis on MWCNTs provided consistent support that the polarization of the extended π system induced by substrate/transition-state binding hinders additional binding. An anionic transition state on the extended π surface thus not only induces its own stabilization by polarization, i.e., self-creates its own catalyst, but also self-protects against its destruction by multiple binding at sufficiently low concentrations (Figure 1).

Rate enhancements for the conversion of substrate **73** into product **74** in the presence of 9 wt % pristine MWCNTs **3** were not as high as with substrate **68**. This result was consistent with pyrene as best interfacers for MWCNTs. For anion–π catalysis on NDI stacks, the reversed order was obtained, consistent with the preferred formation of DAN-NDI charge transfer complexes [8,100-106].

The efficient conversion of interfaced substrates **68** and **73** on pristine MWCNTs **3** was of particular interest with regard to catalysis initiated by oriented external electric fields (OEEFs, Figure 9B). The idea of OEEF catalysis has been around for a long time as a promising, bioinspired concept to revolutionize organic synthesis on the broadest sense [32-35]. Indeed, every chemical transformation can be seen as a directional displacement of point charges, electrons. Control over speed and direction of this charge translocation by OEEFs should allow to generally manipulate molecular transformation, from speed to selectivity and access to completely new reactions. Internal electric fields have been shown to account for much of the

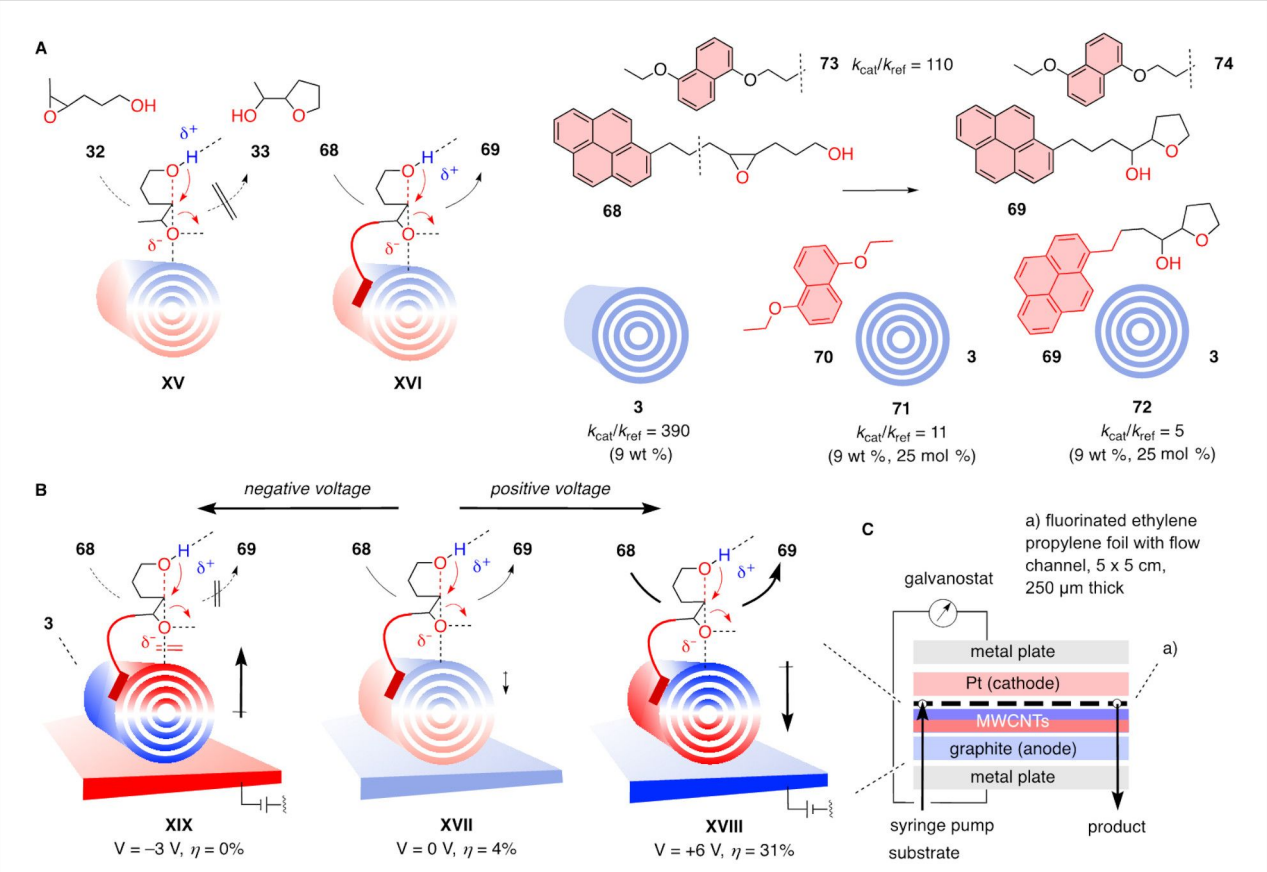

Figure 9: (A) Epoxide-opening ether cyclization on pristine carbon nanotubes occurs with (**XVI**) but not without (**XV**) interfacers such as pyrene in **68** or DAN in **73**, catalyst inactivation with **70** in formal complex **71** and product **69** in formal complex **72** supports anion-π catalysis but not autocatalysis. (B) Electric-field-induced anion–π catalysis on MWCNTs **3** in electrochemical microfluidic reactors, with reactor design (C) and notional transition states for ether cyclization of **68** at positive (**XVIII**), zero (**XVII**) and negative voltage (**XIX**). Parts B and C of Figure 9 were adapted from [44] (© 2023 M. A. Gutiérrez López et al., published by the American Association for the Advancement of Science, distributed under the terms of the Creative Commons Attribution 4.0 International License, https://creativecommons.org/licenses/by/4.0).

power of enzymes [41-43]. The translation of these lessons from nature into OEEF catalysis has so far been slow for a series of most demanding challenges [32-40]. It has been shown that anion–π catalysis with NDIs on ITO electrodes could solve some but not all of these challenges, and relevance for practice remained negligible [14].

Operational anion–π catalysis on MWCNTs fundamentally changed this situation. Integrated into electrochemical microfluidic reactors [107-110], this breakthrough promised to solve all problems obstructing the use of OEEF catalysis in a remarkably straightforward manner. Electrochemical microfluidic reactors should provide access to strong fields at voltages low enough to avoid electron transfer, offer high enough effective catalyst to substrate ratios and work without interfering electrolytes (Figure 9C). MWCNTs drop casted on graphite anodes [111] then should translate the applied OEEFs into strong local macrodipoles. These oriented macrodipoles, depending on the sign of the applied voltages, should then enable strong anion–π and cation–π interactions [112-115] and accelerate and direct the electron displacement during the reaction. Possible limitations at high concentrations in suspension from catalyst depolarization by multiple binding (Figure 1) naturally do not apply to permanent polarization by OEEFs (Figure 9B).

To elaborate on these great expectations, pristine MWCNTs **3** were drop casted on the graphite anodes of electrochemical microfluidic reactors [44]. The substrate was injected by a syringe pump, the product was collected at the other end of the microflow channel and analyzed by HPLC (Figure 9C). Without applied voltage, the reaction essentially did not occur under these heterogenous conditions. This inactivity indicated that transition state **XVII**, characterized by interfacing and induced MWCNT polarization by the transition state itself but not from OEEFs, is hardly accessible (Figure 9B). With increasing positive voltage applied, conversion increased in a pseudo-linear manner. At 6 V, the conversion after one passage through the system at a flow rate Q_v = 25 µL min^{-1} increased to 31%. The

emergence of conversion in response to applied voltage was consistent with operational OEEF catalysis, that is the stabilization of transition state **XVIII** by the local oriented macrodipole of MWCNTs that are polarized by the OEEF applied. Inversion of the applied voltage to –3 V removed the minimal activity present without voltage. This result was important because it was not only consistent with the existence of OEEF catalysis with a destabilized transition state **XIX**. It also disfavored contributions from S_N1-type mechanisms and, most important, from electron transfer.

Anion–π catalysis on graphite

Beginning with spherical fullerenes, expansion of the aromatic surface of carbon allotropes leads to SWCNTs and MWCNTs. Further expansion by unrolling nanotubes into infinite sheets leads to graphene **75** as formal homolog of SWCNTs **2** and graphite **76** as formal homolog of MWCNTs **3** (Figure 10) [112,114-123]. Graphite is the oldest, most common carbon allotrope composed of sp^2 hybridized atoms, complementary to diamond as the archetypal sp^3 carbon allotrope. Conductive because of the delocalized electrons of the giant π system, graphite is commonly used as electrode. With this giant π system, graphite qualifies as potential anion–π and cation–π catalyst, depending on the orientation of the planes in the solid.

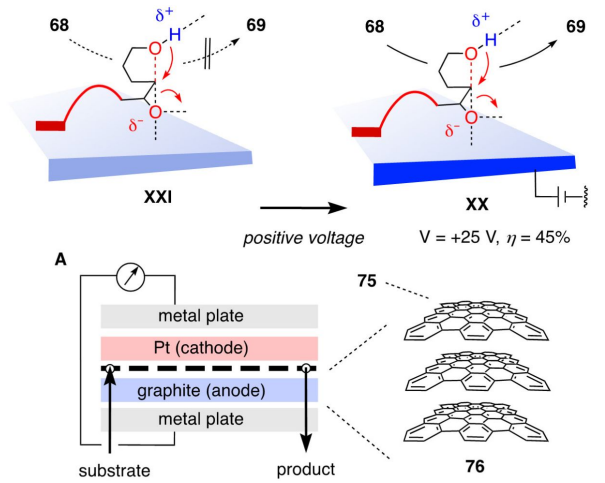

Figure 10: Electric-field-induced anion–π catalysis on MWCNTs **3** on graphite **76** in electrochemical microfluidic reactors, with reactor design (A) and notional transition states for ether cyclization of **68** at positive (**XX**) and zero voltage (**XXI**) on graphite **76**. Figure 10 was adapted from [44] (© 2023 M. A. Gutiérrez López et al., published by the American Association for the Advancement of Science, distributed under the terms of the Creative Commons Attribution 4.0 International License, https://creativecommons.org/licenses/by/4.0).

Also in electromicrofluidic reactors, graphite electrodes are used. It was thus tempting to try OEEF-induced anion–π catalysis in the absence of MWCNTs, directly on graphite. However, without MWCNTs drop casted on the graphite electrode, the conductivity of the reactor was much lower [44]. This meant that already small currents produce high voltage. Despite this undesirable situation, conversion of **68** was observed to increase with increasing voltage. This observation was particularly intriguing because electric-field-induced anion–π catalysis on graphite might be relevant with regard to early steps in the origin of life [124,125].

Conclusion

Anion–π catalysis on carbon allotropes originates from the observation that access to strong anion–π interactions by increasing the intrinsic π acidity of aromatic surfaces is not realistic. Any permanent withdrawal of electron density destabilizes the aromatic system before anion–π interactions would become really attractive for catalysis [3]. This observation called for a shift of attention from intrinsic to induced anion–π interactions. Polarizability of the aromatic system has been predicted since the beginning to provide access to really strong anion–π interactions [61]. For anion–π catalysis, the shift from intrinsic to induced anion–π interactions suggests that the anionic transition state will induce the formation of its own catalyst. Close to a polarizable π surface, such an anionic transition state will drive all movable electrons away. This induced charge relocation will generate strong macrodipoles which are oriented to stabilize the same anionic transition state that induces their formation (Figure 1).

The shift of attention from intrinsic to induced anion–π interactions thus called for aromatic systems of highest polarizability, that is carbon allotropes [9-11]. This account recapitulates how anion–π catalysis on carbon allotropes was explored first on fullerene monomers, then fullerene dimers, SWCNTs and MWCNTs. Studies mainly focusing on enolate addition chemistry showed that selectivity generally increases with the polarizability of the carbon allotrope. Other reactions like asymmetric anion Diels-Alder reactions, the construction of 1,3-nonadjacent stereocenters and bioinspired ether cyclizations have been realized as well.

The emerging combination with oriented external electric fields changes the mechanism of anion–π catalysis on carbon allotropes [44]. Rather than an anionic transition state creating its own catalyst, the OEEF polarizes the carbon allotrope in advance. The resulting macrodipoles then should enable strong anion–π and cation–π interactions depending on their orientation, and accelerate and direct electron displacement during the reaction. This translation of the external field into local oriented macrodipoles solves one important challenge that has delayed progress with OEEF-induced catalysis. Namely, the fields predicted to accelerate and direct the flow of electrons during a

reaction are much larger than the voltage needed to turn-on electron transfer and redox chemistry. This dilemma is overcome by carbon allotropes. They translate voltages weak enough to avoid electron transfer into oriented local molecular macrodipoles that are strong enough to access significant anion–π and cation–π interactions and thus accelerate electrons movement during a reaction.

The rich collection of additional problems holding back progress with OEEF-induced catalysis could be addressed with electrochemical microfluidic reactors. Most important are high effective catalyst to substrate ratios, high fields from small voltages, and no need to add electrolytes. These electrochemical microfluidic reactors have been constructed for a completely different purpose, that is practical access to organic redox chemistry [107-110]. Our results suggest that there might be more to win before the electrons jump. Being general and easy to use, the introduced supramolecular organocatalytic systems promise to lift all involved topics to a new level of significance. Essentially every reaction consists of the movement of electrons, from nucleophile to electrophile. To accelerate and direct this charge displacement, any electron-rich motif in transition states and reactive intermediates should be stabilizable by induced anion–π interactions with MWCNTs that are polarized by an electric field. Inversion of the applied voltage should allow to stabilize the respective electron-poor motifs by induced cation–π interactions, and the combination with co-catalysts interfaced on MWCNTs should provide general access to asymmetric catalysis. OEEF-induced anion–π and cation–π catalysis on carbon allotropes, affordable, clean and general, thus have the potential to non-covalently electrify organic synthesis in the broadest sense.

Acknowledgements

We thank all collaborators and co-workers who contributed to this research.

Funding

We thank the University of Geneva, the National Centre of Competence in Research (NCCR) Molecular Systems Engineering (51NF40-205608) and the Swiss NSF for financial support (Excellence Grant 200020 204175; Swiss-ERC Advanced Grant TIMEUP, TMAG-2_209190).

ORCID® iDs

M. Ángeles Gutiérrez López - https://orcid.org/0009-0007-4606-8392
Mei-Ling Tan - https://orcid.org/0000-0001-7983-3432
Augustina Jozeliūnaitė - https://orcid.org/0000-0003-1643-7373
J. Jonathan Nué-Martinez - https://orcid.org/0000-0001-6483-6892
Naomi Sakai - https://orcid.org/0000-0002-9460-1944
Stefan Matile - https://orcid.org/0000-0002-8537-8349

References

1. Zhao, Y.; Domoto, Y.; Orentas, E.; Beuchat, C.; Emery, D.; Mareda, J.; Sakai, N.; Matile, S. *Angew. Chem., Int. Ed.* **2013,** *52,* 9940–9943. doi:10.1002/anie.201305356
2. Zhao, Y.; Benz, S.; Sakai, N.; Matile, S. *Chem. Sci.* **2015,** *6,* 6219–6223. doi:10.1039/c5sc02563j
3. Zhao, Y.; Cotelle, Y.; Liu, L.; López-Andarias, J.; Bornhof, A.-B.; Akamatsu, M.; Sakai, N.; Matile, S. *Acc. Chem. Res.* **2018,** *51,* 2255–2263. doi:10.1021/acs.accounts.8b00223
4. Luo, N.; Ao, Y.-F.; Wang, D.-X.; Wang, Q.-Q. *Chem. – Eur. J.* **2022,** *28,* e202103303. doi:10.1002/chem.202103303
5. Miros, F. N.; Zhao, Y.; Sargsyan, G.; Pupier, M.; Besnard, C.; Beuchat, C.; Mareda, J.; Sakai, N.; Matile, S. *Chem. – Eur. J.* **2016,** *22,* 2648–2657. doi:10.1002/chem.201504008
6. Frontera, A.; Quiñonero, D.; Garau, C.; Costa, A.; Ballester, P.; Deyà, P. M. *J. Phys. Chem. A* **2006,** *110,* 9307–9309. doi:10.1021/jp062176e
7. Keshri, S. K.; Ishizuka, T.; Kojima, T.; Matsushita, Y.; Takeuchi, M. *J. Am. Chem. Soc.* **2021,** *143,* 3238–3244. doi:10.1021/jacs.0c13389
8. Tan, M.-L.; Ángeles Gutiérrez López, M.; Sakai, N.; Matile, S. *Angew. Chem., Int. Ed.* **2023,** *62,* e202310393. doi:10.1002/anie.202310393
9. Sabirov, D. S. *RSC Adv.* **2014,** *4,* 44996–45028. doi:10.1039/c4ra06116k
10. Zhang, Y.; Wang, D.; Wang, W. *Comput. Theor. Chem.* **2018,** *1128,* 56–59. doi:10.1016/j.comptc.2018.02.011
11. Sabirov, D. S.; Tukhbatullina, A. A. *Nanomaterials* **2022,** *12,* 4404. doi:10.3390/nano12244404
12. López-Andarias, J.; Frontera, A.; Matile, S. *J. Am. Chem. Soc.* **2017,** *139,* 13296–13299. doi:10.1021/jacs.7b08113
13. Bornhof, A.-B.; Vázquez-Nakagawa, M.; Rodríguez-Pérez, L.; Ángeles Herranz, M.; Sakai, N.; Martín, N.; Matile, S.; López-Andarias, J. *Angew. Chem., Int. Ed.* **2019,** *58,* 16097–16100. doi:10.1002/anie.201909540
14. Akamatsu, M.; Sakai, N.; Matile, S. *J. Am. Chem. Soc.* **2017,** *139,* 6558–6561. doi:10.1021/jacs.7b02421
15. Kennedy, C. R.; Lin, S.; Jacobsen, E. N. *Angew. Chem., Int. Ed.* **2016,** *55,* 12596–12624. doi:10.1002/anie.201600547
16. Kutateladze, D. A.; Strassfeld, D. A.; Jacobsen, E. N. *J. Am. Chem. Soc.* **2020,** *142,* 6951–6956. doi:10.1021/jacs.0c02665
17. Luo, N.; Ao, Y.-F.; Wang, D.-X.; Wang, Q.-Q. *Angew. Chem., Int. Ed.* **2021,** *60,* 20650–20655. doi:10.1002/anie.202106509
18. Maynard, J. R. J.; Galmés, B.; Stergiou, A. D.; Symes, M. D.; Frontera, A.; Goldup, S. M. *Angew. Chem., Int. Ed.* **2022,** *61,* e202115961. doi:10.1002/anie.202115961
19. Luo, N.; Ao, Y.-F.; Wang, D.-X.; Wang, Q.-Q. *Chem. – Asian J.* **2021,** *16,* 3599–3603. doi:10.1002/asia.202100920
20. Giese, M.; Albrecht, M.; Rissanen, K. *Chem. Commun.* **2016,** *52,* 1778–1795. doi:10.1039/c5cc09072e
21. Neel, A. J.; Hilton, M. J.; Sigman, M. S.; Toste, F. D. *Nature* **2017,** *543,* 637–646. doi:10.1038/nature21701
22. Guo, S.-Y.; Guo, Q.-H.; Tong, S.; Wang, M.-X. *Angew. Chem., Int. Ed.* **2020,** *59,* 8078–8083. doi:10.1002/anie.201915839
23. Cotelle, Y.; Lebrun, V.; Sakai, N.; Ward, T. R.; Matile, S. *ACS Cent. Sci.* **2016,** *2,* 388–393. doi:10.1021/acscentsci.6b00097
24. Paraja, M.; Matile, S. *Angew. Chem., Int. Ed.* **2020,** *59,* 6273–6277. doi:10.1002/anie.202000579
25. Paraja, M.; Hao, X.; Matile, S. *Angew. Chem., Int. Ed.* **2020,** *59,* 15093–15097. doi:10.1002/anie.202000681

26. Gini, A.; Paraja, M.; Galmés, B.; Besnard, C.; Poblador-Bahamonde, A. I.; Sakai, N.; Frontera, A.; Matile, S. *Chem. Sci.* **2020,** *11,* 7086–7091. doi:10.1039/d0sc02551h
27. Chen, H.; Frontera, A.; Ángeles Gutiérrez López, M.; Sakai, N.; Matile, S. *Helv. Chim. Acta* **2022,** *105,* e202200119. doi:10.1002/hlca.202200119
28. Chen, H.; Li, T.-R.; Sakai, N.; Besnard, C.; Guénée, L.; Pupier, M.; Viger-Gravel, J.; Tiefenbacher, K.; Matile, S. *Chem. Sci.* **2022,** *13,* 10273–10280. doi:10.1039/d2sc03991e
29. Hao, X.; Li, T.-R.; Chen, H.; Gini, A.; Zhang, X.; Rosset, S.; Mazet, C.; Tiefenbacher, K.; Matile, S. *Chem. – Eur. J.* **2021,** *27,* 12215–12223. doi:10.1002/chem.202101548
30. Humeniuk, H. V.; Gini, A.; Hao, X.; Coelho, F.; Sakai, N.; Matile, S. *JACS Au* **2021,** *1,* 1588–1593. doi:10.1021/jacsau.1c00345
31. Akamatsu, M.; Yamanaga, K.; Tanaka, K.; Kanehara, Y.; Sumita, M.; Sakai, K.; Sakai, H. *Langmuir* **2023,** *39,* 5833–5839. doi:10.1021/acs.langmuir.3c00127
32. Shaik, S.; Danovich, D.; Joy, J.; Wang, Z.; Stuyver, T. *J. Am. Chem. Soc.* **2020,** *142,* 12551–12562. doi:10.1021/jacs.0c05128
33. Ciampi, S.; Darwish, N.; Aitken, H. M.; Díez-Pérez, I.; Coote, M. L. *Chem. Soc. Rev.* **2018,** *47,* 5146–5164. doi:10.1039/c8cs00352a
34. Kareem, S.; Vali, S. R.; Reddy, B. V. S. *Eur. J. Org. Chem.* **2023,** e202300103. doi:10.1002/ejoc.202300103
35. Shaik, S.; Ramanan, R.; Danovich, D.; Mandal, D. *Chem. Soc. Rev.* **2018,** *47,* 5125–5145. doi:10.1039/c8cs00354h
36. Delley, M. F.; Nichols, E. M.; Mayer, J. M. *J. Am. Chem. Soc.* **2021,** *143,* 10778–10792. doi:10.1021/jacs.1c05419
37. Yu, L.-J.; Coote, M. L. *J. Phys. Chem. A* **2019,** *123,* 582–589. doi:10.1021/acs.jpca.8b11579
38. Zhang, B.; Schaack, C.; Prindle, C. R.; Vo, E. A.; Aziz, M.; Steigerwald, M. L.; Berkelbach, T. C.; Nuckolls, C.; Venkataraman, L. *Chem. Sci.* **2023,** *14,* 1769–1774. doi:10.1039/d2sc06411a
39. Gorin, C. F.; Beh, E. S.; Bui, Q. M.; Dick, G. R.; Kanan, M. W. *J. Am. Chem. Soc.* **2013,** *135,* 11257–11265. doi:10.1021/ja404394z
40. Blyth, M. T.; Noble, B. B.; Russell, I. C.; Coote, M. L. *J. Am. Chem. Soc.* **2020,** *142,* 606–613. doi:10.1021/jacs.9b12186
41. Fried, S. D.; Boxer, S. G. *Annu. Rev. Biochem.* **2017,** *86,* 387–415. doi:10.1146/annurev-biochem-061516-044432
42. Vaissier Welborn, V.; Head-Gordon, T. *Chem. Rev.* **2019,** *119,* 6613–6630. doi:10.1021/acs.chemrev.8b00399
43. Warshel, A.; Sharma, P. K.; Kato, M.; Xiang, Y.; Liu, H.; Olsson, M. H. M. *Chem. Rev.* **2006,** *106,* 3210–3235. doi:10.1021/cr0503106
44. Gutiérrez López, M. Á.; Ali, R.; Tan, M.-L.; Sakai, N.; Wirth, T.; Matile, S. *Sci. Adv.* **2023,** *9,* eadj5502. doi:10.1126/sciadv.adj5502
45. Campisciano, V.; Gruttadauria, M.; Giacalone, F. *ChemCatChem* **2019,** *11,* 90–133. doi:10.1002/cctc.201801414
46. Garrido, M.; Gualandi, L.; Di Noja, S.; Filippini, G.; Bosi, S.; Prato, M. *Chem. Commun.* **2020,** *56,* 12698–12716. doi:10.1039/d0cc05316c
47. Toganoh, M.; Matsuo, Y.; Nakamura, E. *J. Organomet. Chem.* **2003,** *683,* 295–300. doi:10.1016/s0022-328x(03)00465-0
48. Vidal, S.; Marco-Martínez, J.; Filippone, S.; Martín, N. *Chem. Commun.* **2017,** *53,* 4842–4844. doi:10.1039/c7cc01267e
49. Sun, Y.-B.; Cao, C.-Y.; Yang, S.-L.; Huang, P.-P.; Wang, C.-R.; Song, W.-G. *Chem. Commun.* **2014,** *50,* 10307–10310. doi:10.1039/c4cc04891a
50. Sun, Y.; Cao, C.; Huang, P.; Yang, S.; Song, W. *RSC Adv.* **2015,** *5,* 86082–86087. doi:10.1039/c5ra16011a
51. Nierengarten, J.-F. *Chem. Commun.* **2017,** *53,* 11855–11868. doi:10.1039/c7cc07479d
52. Yamada, M. *ChemPlusChem* **2023,** *88,* e202300062. doi:10.1002/cplu.202300062
53. Li, C.-Z.; Chueh, C.-C.; Yip, H.-L.; Ding, F.; Li, X.; Jen, A. K.-Y. *Adv. Mater. (Weinheim, Ger.)* **2013,** *25,* 2457–2461. doi:10.1002/adma.201204543
54. Sun, X.; Chen, W.; Liang, L.; Hu, W.; Wang, H.; Pang, Z.; Ye, Y.; Hu, X.; Wang, Q.; Kong, X.; Jin, Y.; Lei, M. *Chem. Mater.* **2016,** *28,* 8726–8731. doi:10.1021/acs.chemmater.6b04056
55. Sun, X.; Ji, L. Y.; Chen, W. W.; Guo, X.; Wang, H. H.; Lei, M.; Wang, Q.; Li, Y. F. *J. Mater. Chem. A* **2017,** *5,* 20720–20728. doi:10.1039/c7ta06335k
56. Yamada, M.; Sahara, K.; Koizumi, M.; Maeda, Y.; Suzuki, M. *Chem. – Eur. J.* **2023,** *29,* e202300877. doi:10.1002/chem.202300877
57. Sun, S.; Liu, Z.; Colombo, F.; Gao, R.; Yu, Y.; Qiu, Y.; Su, J.; Gan, L. *Angew. Chem., Int. Ed.* **2022,** *61,* e202212090. doi:10.1002/anie.202212090
58. Kobuke, Y.; Yoshida, J.-i. *Tetrahedron Lett.* **1978,** *19,* 367–370. doi:10.1016/s0040-4039(01)85127-3
59. Sakai, N.; Sordé, N.; Matile, S. *Molecules* **2001,** *6,* 845–851. doi:10.3390/61100845
60. Lubkoll, J.; Wennemers, H. *Angew. Chem., Int. Ed.* **2007,** *46,* 6841–6844. doi:10.1002/anie.200702187
61. Bornhof, A.-B.; Bauzá, A.; Aster, A.; Pupier, M.; Frontera, A.; Vauthey, E.; Sakai, N.; Matile, S. *J. Am. Chem. Soc.* **2018,** *140,* 4884–4892. doi:10.1021/jacs.8b00809
62. Liu, L.; Cotelle, Y.; Bornhof, A.-B.; Besnard, C.; Sakai, N.; Matile, S. *Angew. Chem., Int. Ed.* **2017,** *56,* 13066–13069. doi:10.1002/anie.201707730
63. Hoffmann, R.; Woodward, R. B. *J. Am. Chem. Soc.* **1965,** *87,* 4388–4389. doi:10.1021/ja00947a033
64. Suzuki, T.; Watanabe, S.; Kobayashi, S.; Tanino, K. *Org. Lett.* **2017,** *19,* 922–925. doi:10.1021/acs.orglett.7b00085
65. Okamura, H.; Shimizu, H.; Nakamura, Y.; Iwagawa, T.; Nakatani, M. *Tetrahedron Lett.* **2000,** *41,* 4147–4150. doi:10.1016/s0040-4039(00)00555-4
66. Chatelet, B.; Dufaud, V.; Dutasta, J.-P.; Martinez, A. *J. Org. Chem.* **2014,** *79,* 8684–8688. doi:10.1021/jo501457d
67. Zhang, X.; Liu, L.; López-Andarias, J.; Wang, C.; Sakai, N.; Matile, S. *Helv. Chim. Acta* **2018,** *101,* e1700288. doi:10.1002/hlca.201700288
68. Wang, Y.; Liu, X.; Deng, L. *J. Am. Chem. Soc.* **2006,** *128,* 3928–3930. doi:10.1021/ja060312n
69. Zhang, X.; Hao, X.; Liu, L.; Pham, A.-T.; López-Andarias, J.; Frontera, A.; Sakai, N.; Matile, S. *J. Am. Chem. Soc.* **2018,** *140,* 17867–17871. doi:10.1021/jacs.8b11788
70. Gutiérrez López, M. Á.; Tan, M.-L.; Frontera, A.; Matile, S. *JACS Au* **2023,** *3,* 1039–1051. doi:10.1021/jacsau.2c00656
71. Sittihan, S.; Jamison, T. F. *J. Am. Chem. Soc.* **2019,** *141,* 11239–11244. doi:10.1021/jacs.9b04696
72. Liu, H.; Lin, S.; Jacobsen, K. M.; Poulsen, T. B. *Angew. Chem., Int. Ed.* **2019,** *58,* 13630–13642. doi:10.1002/anie.201812982
73. Li, F.-X.; Ren, S.-J.; Li, P.-F.; Yang, P.; Qu, J. *Angew. Chem., Int. Ed.* **2020,** *59,* 18473–18478. doi:10.1002/anie.202007980
74. Nakanishi, K. *Toxicon* **1985,** *23,* 473–479. doi:10.1016/0041-0101(85)90031-5
75. Tenud, L.; Farooq, S.; Seibl, J.; Eschenmoser, A. *Helv. Chim. Acta* **1970,** *53,* 2059–2069. doi:10.1002/hlca.19700530816

76. Bürgi, H. B.; Dunitz, J. D.; Lehn, J. M.; Wipff, G. *Tetrahedron* **1974,** *30,* 1563–1572. doi:10.1016/s0040-4020(01)90678-7
77. Baldwin, J. E. *J. Chem. Soc., Chem. Commun.* **1976,** 734–736. doi:10.1039/c39760000734
78. Gilmore, K.; Mohamed, R. K.; Alabugin, I. V. *Wiley Interdiscip. Rev.: Comput. Mol. Sci.* **2016,** *6,* 487–514. doi:10.1002/wcms.1261
79. Cane, D. E.; Celmer, W. D.; Westley, J. W. *J. Am. Chem. Soc.* **1983,** *105,* 3594–3600. doi:10.1021/ja00349a040
80. López-Andarias, J.; Bauzá, A.; Sakai, N.; Frontera, A.; Matile, S. *Angew. Chem., Int. Ed.* **2018,** *57,* 10883–10887. doi:10.1002/anie.201804092
81. Panneerselvam, M.; Akash, H.; Patnaik, A. *Phys. Chem. Chem. Phys.* **2023,** *25,* 10647–10660. doi:10.1039/d2cp06017e
82. Tasis, D.; Tagmatarchis, N.; Bianco, A.; Prato, M. *Chem. Rev.* **2006,** *106,* 1105–1136. doi:10.1021/cr050569o
83. Liu, D.; Lungerich, D.; Nakamuro, T.; Harano, K.; Nakamura, E. *Micron* **2022,** *160,* 103316. doi:10.1016/j.micron.2022.103316
84. Blanco, M.; Nieto-Ortega, B.; de Juan, A.; Vera-Hidalgo, M.; López-Moreno, A.; Casado, S.; González, L. R.; Sawada, H.; González-Calbet, J. M.; Pérez, E. M. *Nat. Commun.* **2018,** *9,* 2671. doi:10.1038/s41467-018-05183-8
85. Kitanosono, T.; Xu, P.; Kobayashi, S. *Science* **2018,** *362,* 311–315. doi:10.1126/science.aap7883
86. Gholinejad, M.; Naghshbandi, Z.; Nájera, C. *ChemCatChem* **2019,** *11,* 1792–1823. doi:10.1002/cctc.201802101
87. Chen, Z.; Guan, Z.; Li, M.; Yang, Q.; Li, C. *Angew. Chem., Int. Ed.* **2011,** *50,* 4913–4917. doi:10.1002/anie.201006870
88. Xing, L.; Xie, J.-H.; Chen, Y.-S.; Wang, L.-X.; Zhou, Q.-L. *Adv. Synth. Catal.* **2008,** *350,* 1013–1016. doi:10.1002/adsc.200700617
89. Li, H.; Zhong, M.; Li, C.; Ren, Y.; Chen, J.; Yang, Q. *ChemCatChem* **2019,** *11,* 3952–3958. doi:10.1002/cctc.201900311
90. Zhang, L.; Zhang, W.; Serp, P.; Sun, W.-H.; Durand, J. *ChemCatChem* **2014,** *6,* 1310–1316. doi:10.1002/cctc.201301063
91. Ding, Q.; Yu, Y.; Huang, F.; Zhang, L.; Zheng, J.-G.; Xu, M.; Baell, J. B.; Huang, H. *Chem. – Eur. J.* **2020,** *26,* 4592–4598. doi:10.1002/chem.201905468
92. Chronopoulos, D. D.; Kokotos, C. G.; Karousis, N.; Kokotos, G.; Tagmatarchis, N. *Nanoscale* **2015,** *7,* 2750–2757. doi:10.1039/c4nr06543c
93. Hajipour, A. R.; Khorsandi, Z. *ChemistrySelect* **2017,** *2,* 8976–8982. doi:10.1002/slct.201700847
94. Mercadante, A.; Campisciano, V.; Morena, A.; Valentino, L.; La Parola, V.; Aprile, C.; Gruttadauria, M.; Giacalone, F. *Eur. J. Org. Chem.* **2022,** e202200497. doi:10.1002/ejoc.202200497
95. Cotelle, Y.; Benz, S.; Avestro, A.-J.; Ward, T. R.; Sakai, N.; Matile, S. *Angew. Chem., Int. Ed.* **2016,** *55,* 4275–4279. doi:10.1002/anie.201600831
96. Li, F.; Zhang, B.; Li, X.; Jiang, Y.; Chen, L.; Li, Y.; Sun, L. *Angew. Chem., Int. Ed.* **2011,** *50,* 12276–12279. doi:10.1002/anie.201105044
97. Das, A.; Stahl, S. S. *Angew. Chem., Int. Ed.* **2017,** *56,* 8892–8897. doi:10.1002/anie.201704921
98. Glanzer, S.; Sax, A. F. *Mol. Phys.* **2013,** *111,* 2427–2438. doi:10.1080/00268976.2013.831499
99. Garrido, M.; Volland, M. K.; Mũnich, P. W.; Rodríguez-Pérez, L.; Calbo, J.; Ortí, E.; Herranz, M. Á.; Martín, N.; Guldi, D. M. *J. Am. Chem. Soc.* **2020,** *142,* 1895–1903. doi:10.1021/jacs.9b10772
100. Hagihara, S.; Tanaka, H.; Matile, S. *J. Am. Chem. Soc.* **2008,** *130,* 5656–5657. doi:10.1021/ja801094p
101. Talukdar, P.; Bollot, G.; Mareda, J.; Sakai, N.; Matile, S. *Chem. – Eur. J.* **2005,** *11,* 6525–6532. doi:10.1002/chem.200500516
102. Gabriel, G. J.; Iverson, B. L. *J. Am. Chem. Soc.* **2002,** *124,* 15174–15175. doi:10.1021/ja0275358
103. Cougnon, F. B. L.; Sanders, J. K. M. *Acc. Chem. Res.* **2012,** *45,* 2211–2221. doi:10.1021/ar200240m
104. Iijima, T.; Vignon, S. A.; Tseng, H.-R.; Jarrosson, T.; Sanders, J. K. M.; Marchioni, F.; Venturi, M.; Apostoli, E.; Balzani, V.; Stoddart, J. F. *Chem. – Eur. J.* **2004,** *10,* 6375–6392. doi:10.1002/chem.200400651
105. Ikkanda, B. A.; Samuel, S. A.; Iverson, B. L. *J. Org. Chem.* **2014,** *79,* 2029–2037. doi:10.1021/jo402704z
106. Mukhopadhyay, P.; Iwashita, Y.; Shirakawa, M.; Kawano, S.-i.; Fujita, N.; Shinkai, S. *Angew. Chem., Int. Ed.* **2006,** *45,* 1592–1595. doi:10.1002/anie.200503158
107. Elsherbini, M.; Wirth, T. *Acc. Chem. Res.* **2019,** *52,* 3287–3296. doi:10.1021/acs.accounts.9b00497
108. Noël, T.; Cao, Y.; Laudadio, G. *Acc. Chem. Res.* **2019,** *52,* 2858–2869. doi:10.1021/acs.accounts.9b00412
109. Folgueiras-Amador, A. A.; Philipps, K.; Guilbaud, S.; Poelakker, J.; Wirth, T. *Angew. Chem., Int. Ed.* **2017,** *56,* 15446–15450. doi:10.1002/anie.201709717
110. Gnaim, S.; Bauer, A.; Zhang, H.-J.; Chen, L.; Gannett, C.; Malapit, C. A.; Hill, D. E.; Vogt, D.; Tang, T.; Daley, R. A.; Hao, W.; Zeng, R.; Quertenmont, M.; Beck, W. D.; Kandahari, E.; Vantourout, J. C.; Echeverria, P.-G.; Abruna, H. D.; Blackmond, D. G.; Minteer, S. D.; Reisman, S. E.; Sigman, M. S.; Baran, P. S. *Nature* **2022,** *605,* 687–695. doi:10.1038/s41586-022-04595-3
111. Gabriel, G.; Gómez-Martínez, R.; Villa, R. *Physiol. Meas.* **2008,** *29,* S203–S212. doi:10.1088/0967-3334/29/6/s18
112. Foroutan-Nejad, C.; Marek, R. *Phys. Chem. Chem. Phys.* **2014,** *16,* 2508–2514. doi:10.1039/c3cp52671b
113. Novák, M.; Foroutan-Nejad, C.; Marek, R. *J. Chem. Theory Comput.* **2016,** *12,* 3788–3795. doi:10.1021/acs.jctc.6b00586
114. Farajpour, E.; Sohrabi, B.; Beheshtian, J. *Phys. Chem. Chem. Phys.* **2016,** *18,* 7293–7299. doi:10.1039/c5cp07710a
115. Chen, J.; Li, J.; Liu, X.; He, Z.; Shi, G. *Phys. Chem. Chem. Phys.* **2023,** *25,* 13260–13264. doi:10.1039/d3cp00986f
116. Hu, H.; Xin, J. H.; Hu, H.; Wang, X.; Kong, Y. *Appl. Catal., A* **2015,** *492,* 1–9. doi:10.1016/j.apcata.2014.11.041
117. Zhou, K.; Xu, Z. *Phys. Rev. Res.* **2020,** *2,* 042034. doi:10.1103/physrevresearch.2.042034
118. Chen, L.; Liu, S.; Xu, Z.; Yang, X. *J. Phys. Chem. Lett.* **2019,** *10,* 5735–5741. doi:10.1021/acs.jpclett.9b02074
119. Dai, L. *Acc. Chem. Res.* **2013,** *46,* 31–42. doi:10.1021/ar300122m
120. Acocella, M. R.; Mauro, M.; Guerra, G. *ChemSusChem* **2014,** *7,* 3279–3283. doi:10.1002/cssc.201402770
121. Bian, S.; Scott, A. M.; Cao, Y.; Liang, Y.; Osuna, S.; Houk, K. N.; Braunschweig, A. B. *J. Am. Chem. Soc.* **2013,** *135,* 9240–9243. doi:10.1021/ja4042077
122. Sun, P. Z.; Xiong, W. Q.; Bera, A.; Timokhin, I.; Wu, Z. F.; Mishchenko, A.; Sellers, M. C.; Liu, B. L.; Cheng, H. M.; Janzen, E.; Edgar, J. H.; Grigorieva, I. V.; Yuan, S. J.; Geim, A. K. *Proc. Natl. Acad. Sci. U. S. A.* **2023,** *120,* e2300481120. doi:10.1073/pnas.2300481120
123. Su, D. S.; Qi, W.; Wen, G. Carbon and Graphite for Catalysis. *Industrial Carbon and Graphite Materials;* Wiley-VCH: Weinheim, Germany, 2021; Vol. I, pp 457–490. doi:10.1002/9783527674046.ch8

124. Liu, Z.; Wu, L.-F.; Kufner, C. L.; Sasselov, D. D.; Fischer, W. W.; Sutherland, J. D. *Nat. Chem.* **2021,** *13,* 1126–1132. doi:10.1038/s41557-021-00789-w
125. Muchowska, K. B.; Varma, S. J.; Moran, J. *Chem. Rev.* **2020,** *120,* 7708–7744. doi:10.1021/acs.chemrev.0c00191

License and Terms

BEILSTEIN JOURNAL OF ORGANIC CHEMISTRY

Biphenylene-containing polycyclic conjugated compounds

Cagatay Dengiz

Review

Open Access

Address:
Department of Chemistry, Middle East Technical University, 06800 Ankara, Turkey

Email:
Cagatay Dengiz - dengizc@metu.edu.tr

Keywords:
acenes; biphenylene; [N]phenylenes; polycyclic aromatic compounds

Beilstein J. Org. Chem. **2023,** *19,* 1895–1911.
https://doi.org/10.3762/bjoc.19.141

Received: 01 September 2023
Accepted: 30 November 2023
Published: 13 December 2023

This article is part of the thematic issue "Carbon-rich materials: from polyaromatic molecules to fullerenes and other carbon allotropes".

Guest Editor: Y. Yamakoshi

Abstract

There has been a growing emphasis on the synthesis of polycyclic conjugated compounds, driven by their distinct structural characteristics that make them valuable candidates for use in cutting-edge technologies. In particular, acenes, a subgroup of polycyclic aromatic compounds, are sought-after synthetic targets due to their remarkable optoelectronic properties which stem from their π-conjugation and planar structure. Despite all these promising characteristics, acenes exhibit significant stability problems when their conjugation enhances. Various approaches have been developed to address this stability concern. Among these strategies, one involves the incorporation of the biphenylene unit into acene frameworks, limiting the electron delocalization through the antiaromatic four-membered ring. This review gives a brief overview of the methods used in the synthesis of biphenylenes and summarizes the recent studies on biphenylene-containing polycyclic conjugated compounds, elucidating their synthesis, and distinct optoelectronic properties.

Introduction

Acenes represent an important category of carbon-rich polycyclic aromatic hydrocarbons (PAHs) characterized by the presence of linearly fused benzene rings [1,2]. Investigating the electronic properties of acenes is essential for understanding the correlations between structure and electronic properties, as these units serve as fundamental building blocks in graphite and carbon nanotubes [3]. The limited stability of this particular class of PAHs arises as a key challenge, primarily attributed to their extended conjugation. The longer acenes exhibit increased reactivity, readily undergoing processes of oxidation and dimerization, consequently disrupting the molecular conjugation [4]. This instability poses a significant obstacle in their widespread application across various devices [4]. The decline in stability seen in larger acenes can be attributed to Clar's rule, which considers the increasing number of non-sextet rings throughout the acene series as a contributing factor (Figure 1) [5,6].

Numerous approaches have been developed to address the challenges arising from the instability and solubility issues encountered in acenes. These include the incorporation of heteroatoms

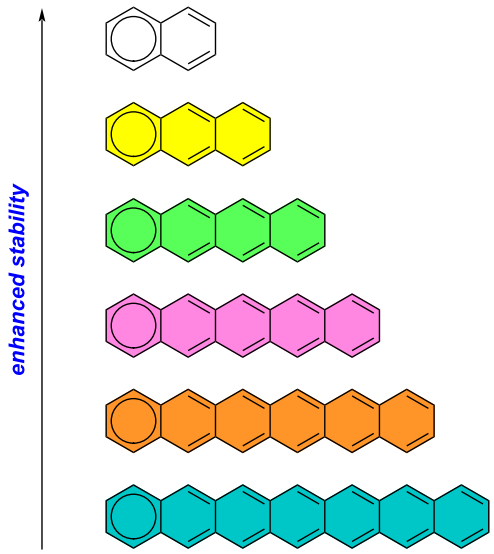

Figure 1: The correlation between stability and Clar's rule in acenes.

within the acene backbone [7,8], stabilization of the acene core structure through the integration of diverse units [9,10], and the introduction of bulky substituents [11]. These approaches aim to maintain the desirable electronic properties of acenes while mitigating the aforementioned challenges to the best possible extent. Our focus in this review is primarily on exploring the role of biphenylenes in stabilizing the core structures of acenes and other PAHs.

Review

Biphenylenes and [N]phenylenes

Biphenylene (**1**), which consists of two aromatic benzene rings connected with a four-membered ring, is a highly intriguing compound in terms of its structure. It possesses a planar configuration and consists of 4*n* π-electrons, rendering it antiaromatic. However, despite being antiaromatic, biphenylene is more stable than other known antiaromatic compounds [12]. Research using computational methods to investigate how benzo and benzocyclobutadiene annulations impact the ring current density of biphenylene derivatives reveals that the antiaromatic (paratropic) current density in the 4-ring structure can range widely, shifting from highly antiaromatic to nonaromatic limits based on the annulation modes employed [13,14]. Since Lothrop's initial successful synthesis of biphenylene in 1941 [15], numerous studies have been carried out, highlighting four prominent synthetic approaches. These methods include flash vacuum pyrolysis [16-18], [2 + 2] cycloaddition [19,20], [2 + 2 + 2] cycloaddition [21], and the Ullmann reaction [15,22] (Scheme 1). Due to the observed low yields in flash vacuum pyrolysis, the difficulty in synthesizing starting materials, such as **3**, and the impractical nature of scaling up the method for large quantities, the other three approaches have gained popularity for synthesizing biphenylene derivatives [23]. The utilization of in-situ aryne synthesis to generate biphenylene through the dimerization of arynes **2** from diverse substrates has gained popularity. However, this approach occasionally gives rise to the production of high-energy intermediates, such as benzenediazonium-2-carboxylate, and yields that are comparatively low [20]. After the Ullmann reaction was successfully employed for the first reported synthesis of biphenylene [15], subsequent studies have explored various transition-metal-mediated coupling reactions using 2,2'-dihalogenated biphenyls **4** as starting materials [24,25]. Although the cobalt-mediated alkyne trimerization route frequently used by Vollhardt and co-workers is not the first choice for the synthesis of the biphenylene itself, it has led to the synthesis of structurally demanding substituted biphenylenes and the emergence of a family of polycyclic hydrocarbons called [N]phenylenes.

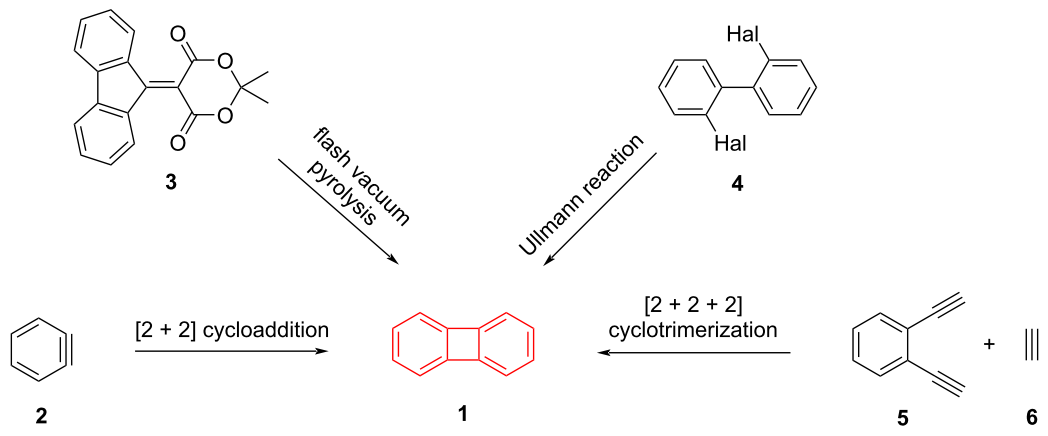

Scheme 1: General synthetic strategies to access the biphenylene core **1**.

The utilization of cobalt-mediated alkyne trimerization facilitated the synthesis of [N]phenylenes exhibiting diverse structural configurations, including linear **7**, angular **8**, zig-zag **9**, bent **10**, branched **11**, and cyclic **12** topologies (Figure 2) [26-30]. In [N]phenylene structures, the presence of a formally antiaromatic four-membered ring leads to the localization of π-electrons on the benzene rings [31]. Despite this phenomenon, the oligomer series demonstrates a decreasing band gap, indicating the ability of electrons to transmit through the four-membered rings [32].

Phenylene-containing oligoacenes (POAs)

The localization of π-electrons and the consequent decrease in band gaps observed in the [N]phenylene series have sparked interest in exploring acene–biphenylene hybrid structures. If this trend could be maintained in practical applications, it would offer the opportunity to retain the desirable electronic properties while mitigating the inherent stability concerns associated with acenes. The underlying principle guiding the design is to maximize stability by incorporating the largest possible number of Clar sextets, while concurrently minimizing any adverse impact on electronic properties resulting from reduced electron delocalization. In 1983, McOmie and co-workers reported the first synthesis of phenylene-containing oligoacenes (POAs) [33]. The primary objective of their work was to establish an alternative synthetic approach to the existing methods for biphenylene synthesis described in the literature, rather than focusing on the optoelectronic properties of the resulting compounds. Small quantities of the key starting material benzocyclobutene-1,2-dione (BBD, **13**) were obtained through the pyrolysis of indane-1,2,3-trione. When BBD **13** was subjected to reflux conditions with bis(cyanomethyl) compounds **14a** (a benzene derivative) and **14b** (a naphthalene derivative) in acetonitrile, the desired POAs **15a** and **15b** were obtained with yields of 25% and 48%, respectively (Scheme 2). It was also reported in the same study that the yield of **15b** increased up to 62% when the water formed during the reaction was removed with CaH_2.

The initial results on biphenylene and its more extensively fused counterparts led to another notable study conducted by Jensen and Coleman in 1959 [34]. By subjecting α,α,α′,α′-tetra-

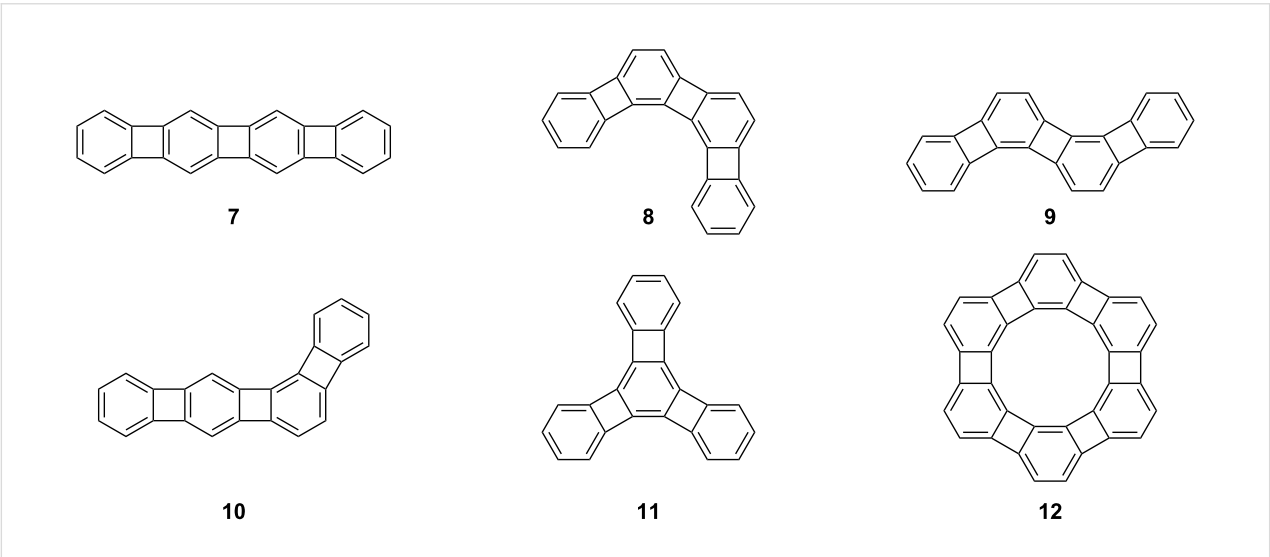

Figure 2: [N]Phenylenes **7**–**12** with different topologies.

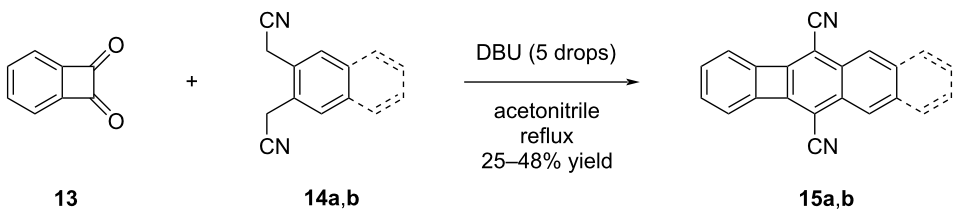

Scheme 2: Synthesis of POAs **15a** and **15b** via reactions of BBD **13** and bis(cyanomethyl) compounds **14a** and **14b**.

bromo-*o*-xylene (**16**) to *t*-BuOK to anhydrous conditions, biphenylene derivative **17** was obtained with a yield of 69% (Scheme 3). In the final step of the synthesis, a halogen–lithium exchange was carried out, followed by treatment with MeOH, resulting in a 79% yield of benzo[*b*]biphenylene (**18**).

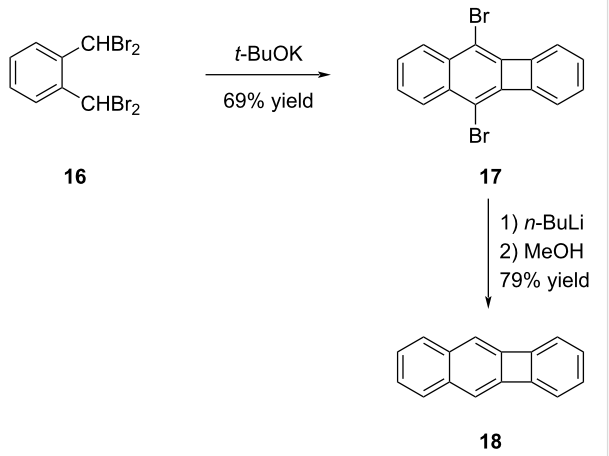

Scheme 3: Synthesis of benzo[*b*]biphenylene (**18**).

In their efforts to find a more general method for the synthesis of benzo[*b*]biphenylenes, Barton and co-workers were able to synthesize benzo[*b*]biphenylene (**18**) in 71% yield by the reaction of equal molar amounts of tetrabromo compound **16** and 1,1,2,2-tetrabromo-1,2-dihydrobenzocyclobutene (**19**) in the presence of activated zinc dust in THF (Scheme 4) [35]. By making minor adjustments to the reaction conditions, such as employing DMF as the solvent and raising the temperature to 100 °C, along with utilizing compound **20** as the starting material, Barton and his team achieved the synthesis of POA **21**. This POA featured an extended conjugation and was obtained in 30% yield.

In a study released by Swager and Parkhurst in 2012 [36], the term POA has been used for the first time in the literature. In this study, they successfully synthesized POAs **25a** and **25b** by employing sequential Diels–Alder reactions (Scheme 5). Furthermore, the researchers conducted a comprehensive investigation into the optical and electrochemical characteristics of these compounds. The key component employed in the production process, known as 3,4-bis(methylene)cyclobutene, was generated through the application of flash vacuum pyrolysis to 1,5-hexadiyne. When 3,4-bis(methylene)cyclobutene undergoes a reaction with dienes like 1,3-diphenylisobenzofuran and 1,3-diphenylisonaphthofuran, it selectively produces compounds **22a** and **22b**. In the subsequent step, the exocyclic methylidene groups react with bisarynes, which are in situ formed from **23**, resulting in the formation of symmetric polycyclic structures **24a** and **24b**. These isomers obtained as a mixture are then subjected to treatment with *p*-TsOH in acetic acid, without the need for further purification, to yield the desired products **25a** and **25b** in 71 and 42% yields, respectively. When comparing compounds **25a** and **25b**, UV–vis and fluorescence studies (λ_{max} = 500 nm, λ_{em} = 502 nm, Φ_{em} = 0.45 for **25a**; λ_{max} = 513 nm, λ_{em} = 517 nm, Φ_{em} = 0.26 for **25b**; λ_{max} = 442 nm, λ_{em} = 444 nm, Φ_{em} = 0.97 for 9,10-bis((triisopropylsilyl)ethynyl)anthracene – blue-colored) provide clear evidence of a bathochromic shift and a reduction in the optical band gap. These results support the idea that the introduction of biphenylene linkages may decrease delocalization in the structure. However, despite this reduction, there is still communication between the acene units evident from the decreased band gaps in compounds **25a** and **25b**.

Despite the achievements in the synthesis of [N]phenylene and POAs, the challenges of low yield and stability issues, particularly with the starting materials employed in the syntheses, prompted researchers to explore alternative and improved methods. In this context, Xia and co-workers drew inspiration

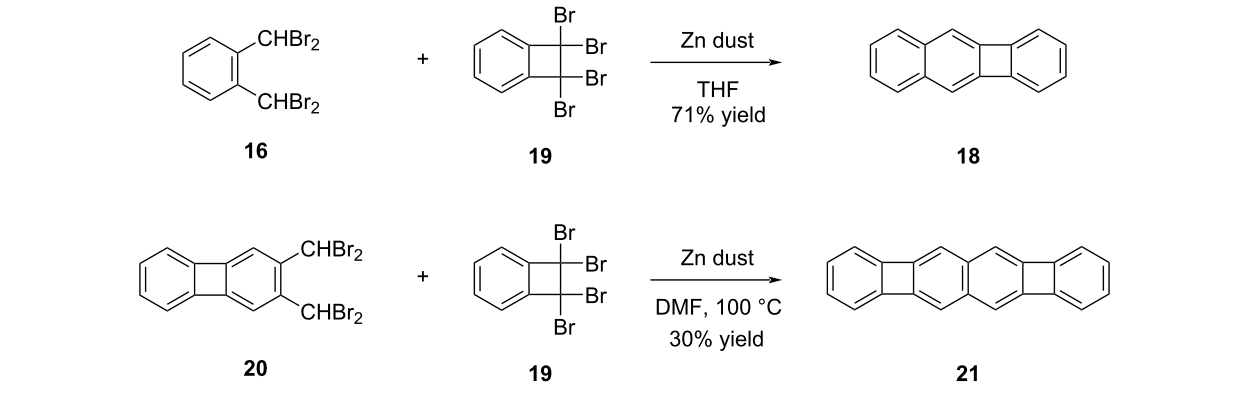

Scheme 4: Synthesis of benzobiphenylene **18** and POA **21**.

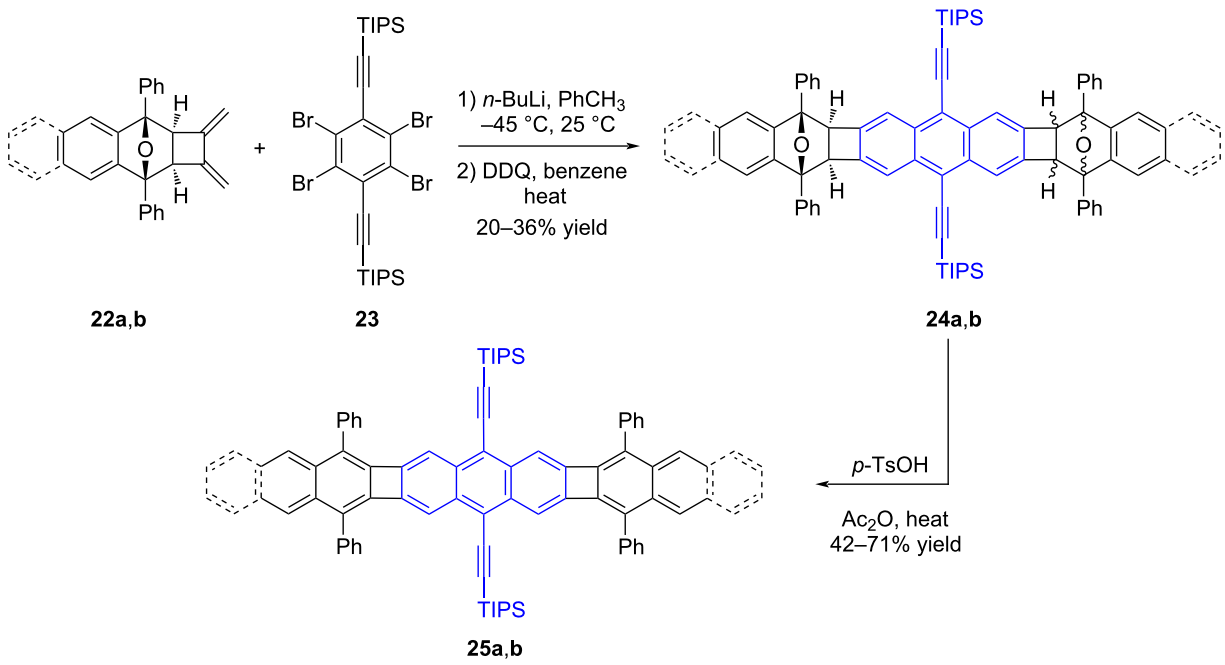

Scheme 5: Synthesis of symmetric POAs **25a** and **25b**.

from their prior investigations on palladium-catalyzed annulation reactions concerning ladder polymers [37]. They envisioned that by making minor modifications to the starting materials, they could readily access structurally complex POAs. The researchers efficiently conducted palladium-catalyzed C–H activated annulation reactions, involving oxanorbornadiene derivative **26** and aryl bromides including dibromoanthracene **27** [38]. Subsequent aromatization reactions were then carried out, resulting in the successful synthesis of the target POAs with high yields. The study involved the synthesis of numerous polycyclic hydrocarbons containing both electron-withdrawing and -donating side groups. Among the various compounds synthesized, a particularly noteworthy achievement was the successful synthesis of acene-type compound **29** using 2,6-dibromo-9,10-bis(triisopropylsilylethynyl)anthracene (**27**), which was accomplished with high yields (Scheme 6).

The presence of two methyl groups in the bridge-head positions of compound **26** is crucial in these annulation reactions. These groups play a vital role in preventing undesired side reaction pathways, as their absence would lead to the failure in the formation of the desired target products. Upon comparing the UV–vis absorbance graphs of compounds **28** and **29**, POA **29** (λ_{max} = 500 nm), which was obtained through the aromatization of compound **28**, exhibited a significant bathochromic shift. These observations further support the hypothesis that electrons can indeed be delocalized through the 4-membered ring system in the POAs.

Following their work reported in 2017 [38], Xia and his group directed their attention towards refining the electronic properties of POAs through structural variations [39]. Using catalytic annulation reactions involving 1,4-dibromo-2,5-dichlorobenzene (**31**) and substituted oxanorbornenes (**26** and **30b**,**c**), products **32a**–**c**, with R groups representing (a) H, (b) F, and (c) –OCH_2O–, were successfully synthesized, albeit with moderate yields (Scheme 7).

Following that, compounds **32a**–**c** underwent derivatization through Sonogashira cross-coupling reactions with alkynes featuring different protecting groups such as TIPS, TES, and TIBS. Scheme 7 illustrates the derivatization process using one of the chosen examples, specifically the TIPS group. Accordingly, the cross-coupling products **33a**–**c** were obtained in yields ranging between 45% and 60%. The last step of the sequential reactions is the aromatization step and the target POAs **34a**–**c** were obtained in yields between 80–84%. UV–vis investigations conducted on compounds **34a**–**c** revealed absorption bands that align well with acene structures. While **34a** and **34b** displayed nearly identical absorption profiles with a maximum absorption at λ_{max} = 515 nm, the incorporation of donor groups in compound **34c** led to a noteworthy bathochromic shift with a maximum absorption at λ_{max} = 534 nm. Additionally, it was reported that all three compounds, **34a**–**c**, demonstrated remarkable stability, showing no signs of degradation over an extended period when kept in the dark, both in solid form and in solution under air. In the final phase of the

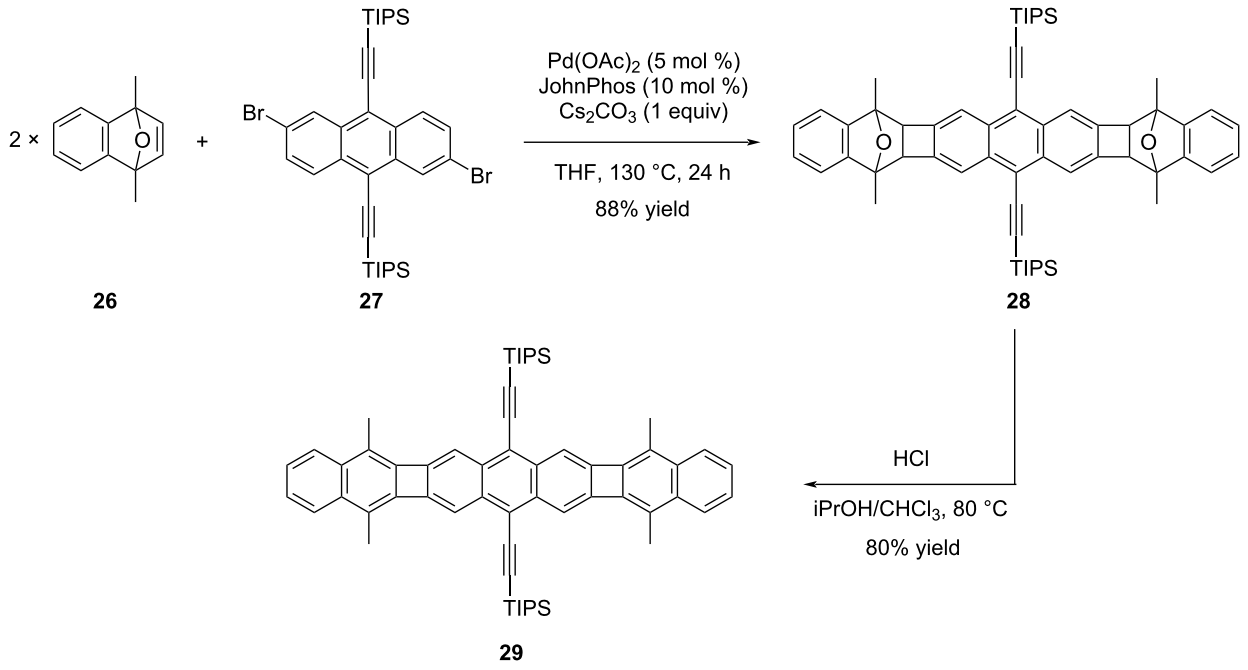

Scheme 6: Synthesis of POA **29** via palladium-catalyzed annulation/aromatization reaction.

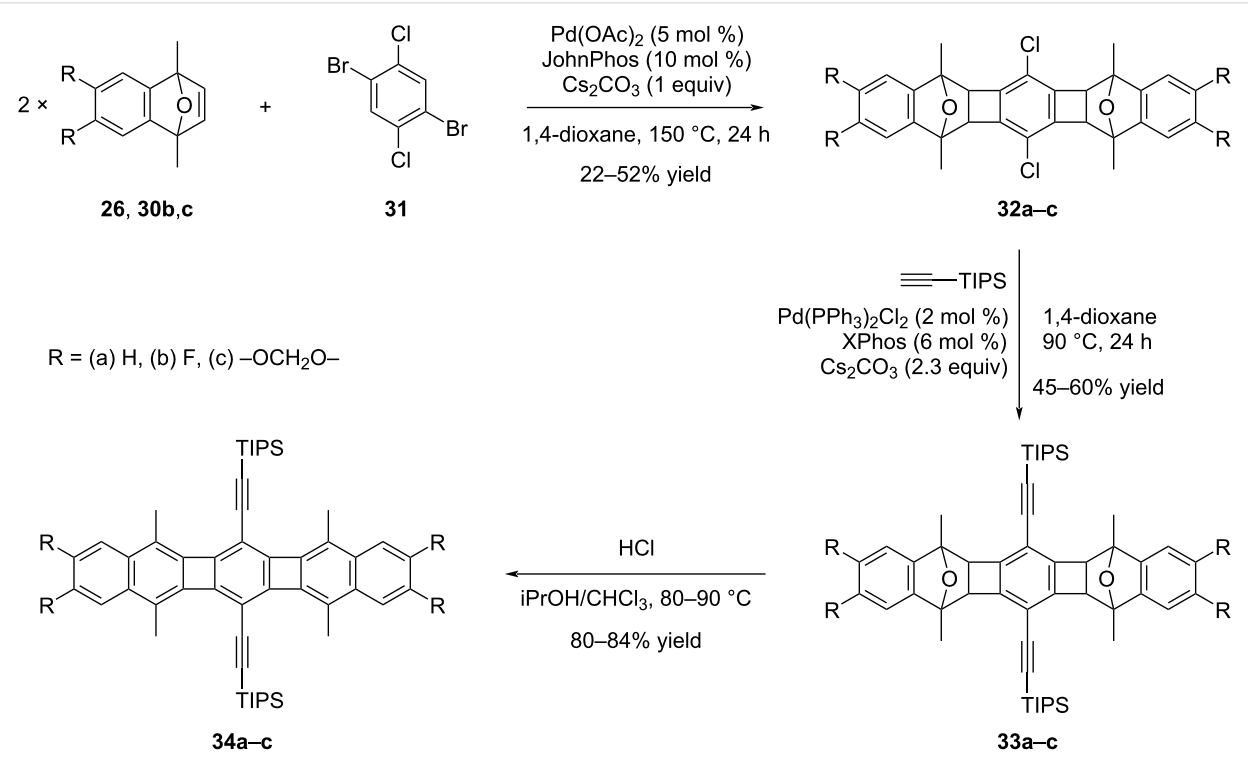

Scheme 7: Synthesis of bisphenylene-containing structures **34a–c**.

study, the authors investigated the charge-transport properties of compound **34a** in OFET. Since the charge-transport properties are significantly affected by the molecular packing, they have modified compound **34a** using different protecting groups. In this context, triethylsilyl (TES), triisopropylsilyl (TIPS), and triisobutylsilyl (TIBS) groups were incorporated into

the structure considering the increased dimensions. Thus, derivatives **34a**-TES and **34a**-TIPS showed hole mobilities of 0.075 $cm^2 V^{-1} s^{-1}$ and 0.19 $cm^2 V^{-1} s^{-1}$, respectively, while the highest value was noted with **34a**-TIBS at 0.52 $cm^2 V^{-1} s^{-1}$.

Later on, Xia and his colleagues demonstrated that curved PAH structures can be synthesized by employing their own developed palladium-catalyzed arene–oxanorbornadiene annulation reactions [40]. This study involved converting PAHs obtained through annulation and aromatization steps into curved PAH structures using metal-catalyzed cycloaddition reactions pioneered by Vollhart [41] and Kotora [42]. Unlike previous studies that reported cycloadditions from bay regions of [N]phenylenes, metal-catalyzed cycloadditions with diphenylacetylene occurred exclusively in the non-bay region, which allowed for straightforward syntheses of curved structures. Moreover, the presence of methyl groups in the structure facilitated the controlled activation of desired cyclobutadiene units, enabling precise modifications. A selected example from the study is summarized in Scheme 8. The angular structure **36** was prepared through annulation reaction between oxanorbornene **26** and 1,8-dibromobiphenylene (**35**), followed by aromatization via treatment with HCl in $CHCl_3$ and iPrOH, resulting in the formation of compound **37** in 49% yield. In the final step, Ir-catalyzed cycloaddition reaction with diphenylacetylene (tolane) led to PAH **38** in 47% yield.

According to the X-ray analysis results, it is evident that the structure of compound **38** is far from planarity, and the phenanthrene moiety exhibits a dihedral angle of approximately 22°. Upon comparing the UV–vis spectra of the angular structures **37** and **38**, it was observed that after the Ir-catalyzed cycloaddition reaction, the λ_{max} of product **38** considerably blue shifted in comparison to the λ_{max} of **37**.

Xia et al. also conducted a synthesis of [3]naphthylene regioisomers through Pd-catalyzed annulation reactions, employing 2,7-, 1,5-, and 1,7-dibromonaphthalenes (Scheme 9) [43].

These annulation reactions involving 2,7-, 1,5-, and 1,7-dibromonaphthalene with different benzoxanorbornadienes (R = (a) TIPSA, (b) 2,6-$(CH_3)_2C_6H_3$, (c) H), followed by aromatization in acidic conditions, resulted in the formation of three [3]naphthalene regioisomers **43a–c**, **44a–c**, and **45a–c** with excellent yields of up to 94%. The synthesized PAHs **43a**, **44a**, and **45a** with diverse geometries exhibited interesting absorption and emission characteristics, making them highly intriguing for further study and potential applications. Among the regioisomers in the series, the linear isomer **43a** displayed the highest quantum yield (Φ_{em} = 0.64). Additionally, its absorption and emission max values (λ_{max} and $\lambda_{max,em}$) were determined to be 476 and 477 nm, respectively. Compound **44a** exhibited no alteration in the absorption maxima; however, there was a considerable bathochromic shift in the emission maxima (λ_{max} = 476 nm and $\lambda_{max,em}$ = 587 nm for **44a**). In contrast to compound **43a**, Φ_{em} of compound **44a** decreased significantly to 0.08. Likewise, compound **45a** (λ_{max} = 402 nm, $\lambda_{max,em}$ = 524 nm, Φ_{em} = 0.16) also demonstrated a substantially reduced quantum yield when compared to compound **43a**. Theses regioisomers with varying geometric structures provided strong evidence that the antiaromaticity of the cyclobutadiene (CBD) ring can be tuned up with appropriate structural designs. NICS (nucleus independent chemical shift) analysis revealed that the linear structures within the series exhibited

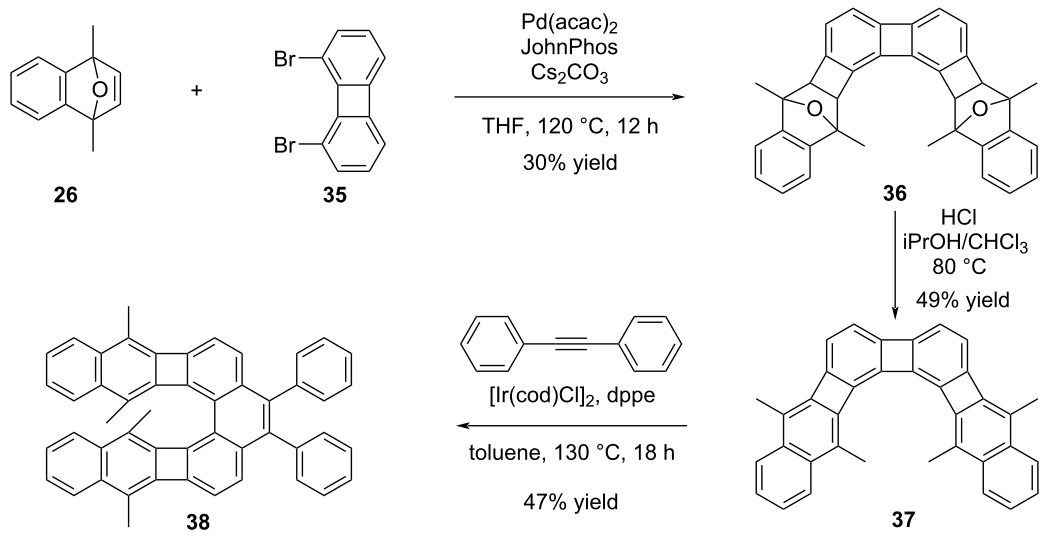

26 35 36 37 38

Scheme 8: Synthesis of curved PAH **38** via Pd-catalyzed annulation and Ir-catalyzed cycloaddition reactions.

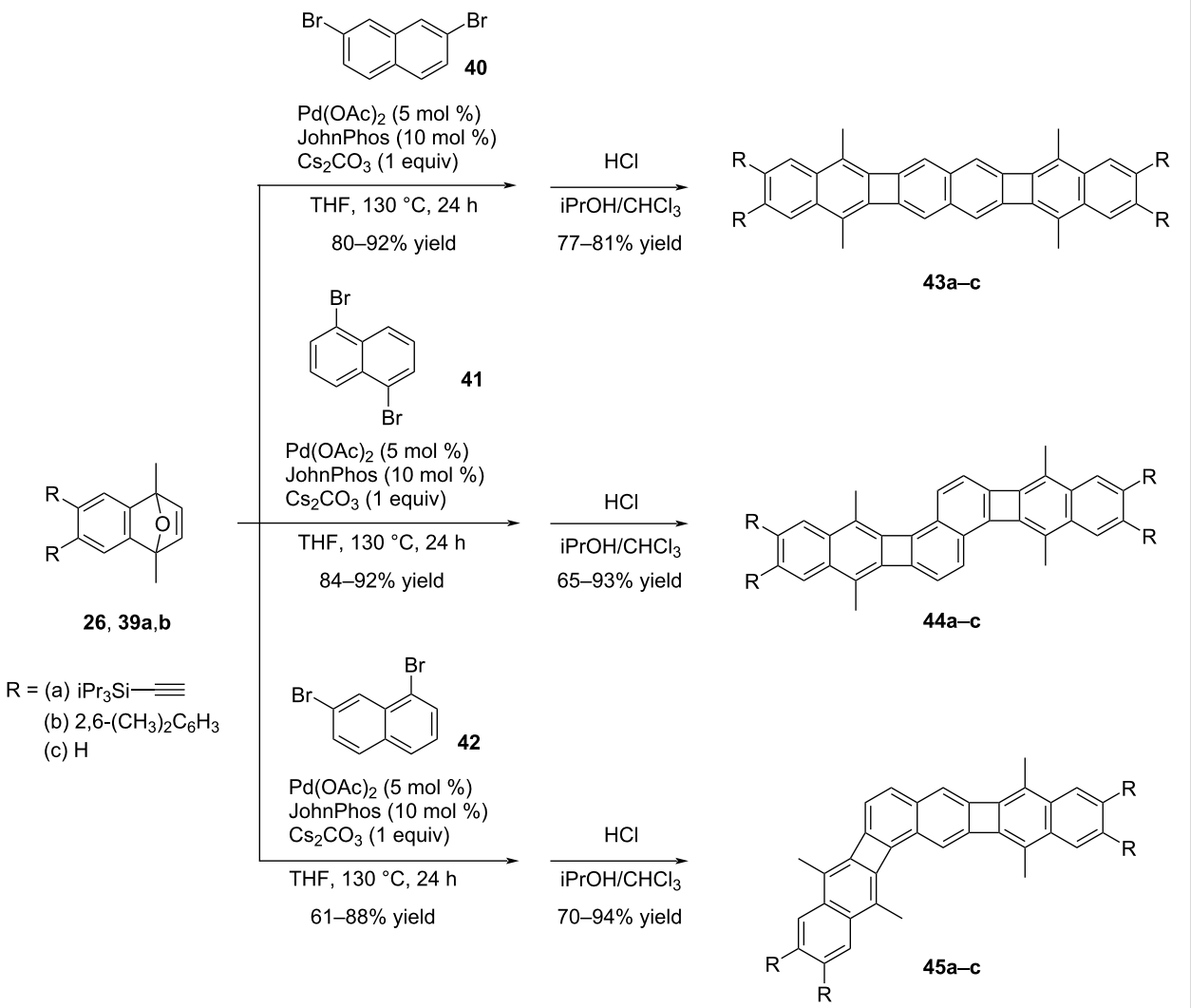

Scheme 9: Synthesis of [3]naphthylenes.

reduced antiaromaticity in the CBD ring compared to other structural arrangements.

By employing a methoxy group on the oxonorbornene, the methyl ether moiety can be removed and the phenol subsequently converted to a triflate. The Pd-catalyzed annulation approach can be conducted sequentially, facilitating the synthesis of polyaromatic hydrocarbons, particularly unsymmetrical ones (Scheme 10) [44]. In this way, compound **48** was synthesized through a two-step process involving the Pd-catalyzed annulation between compounds **46** and **47**, followed by aromatization in the presence of PPTS. The methoxy group was then cleaved using HBr in Aliquat-336, and the resulting product was converted to the triflate under basic conditions, resulting in a regioisomeric mixture of **49** with a yield of 81% over the two steps. To obtain the PAH **51**, a second Pd-catalyzed annulation and subsequent aromatization of **50** were performed in an acidic medium. Ultimately, the desired compound, PAH **51** bearing TIPS groups, was obtained in 82% yield as the final product. UV–vis and fluorescence studies were conducted to gather insights into the optoelectronic characteristics of PAH **51**. The obtained data revealed that the synthesized compound possesses a unique absorption and emission profile, highlighting its distinctive optical properties (λ_{max} = 470 nm, $\lambda_{max,em}$ = 470 nm, Φ_{em} = 0.12).

Biphenylene-containing azaacenes

Bunz and co-workers incorporated biphenylene units into azaacene structures to enhance their stability [45]. Initially, their early attempts focused on synthesizing unsymmetrical azaacenes containing biphenylene units. Through the condensation of *ortho*-diamine compounds **53a–c** derived from benzene (**53a**), naphthalene (**53b**), and anthracene (**53c**) with compound **52**, the desired target azaacenes **54a–c** were successfully ob-

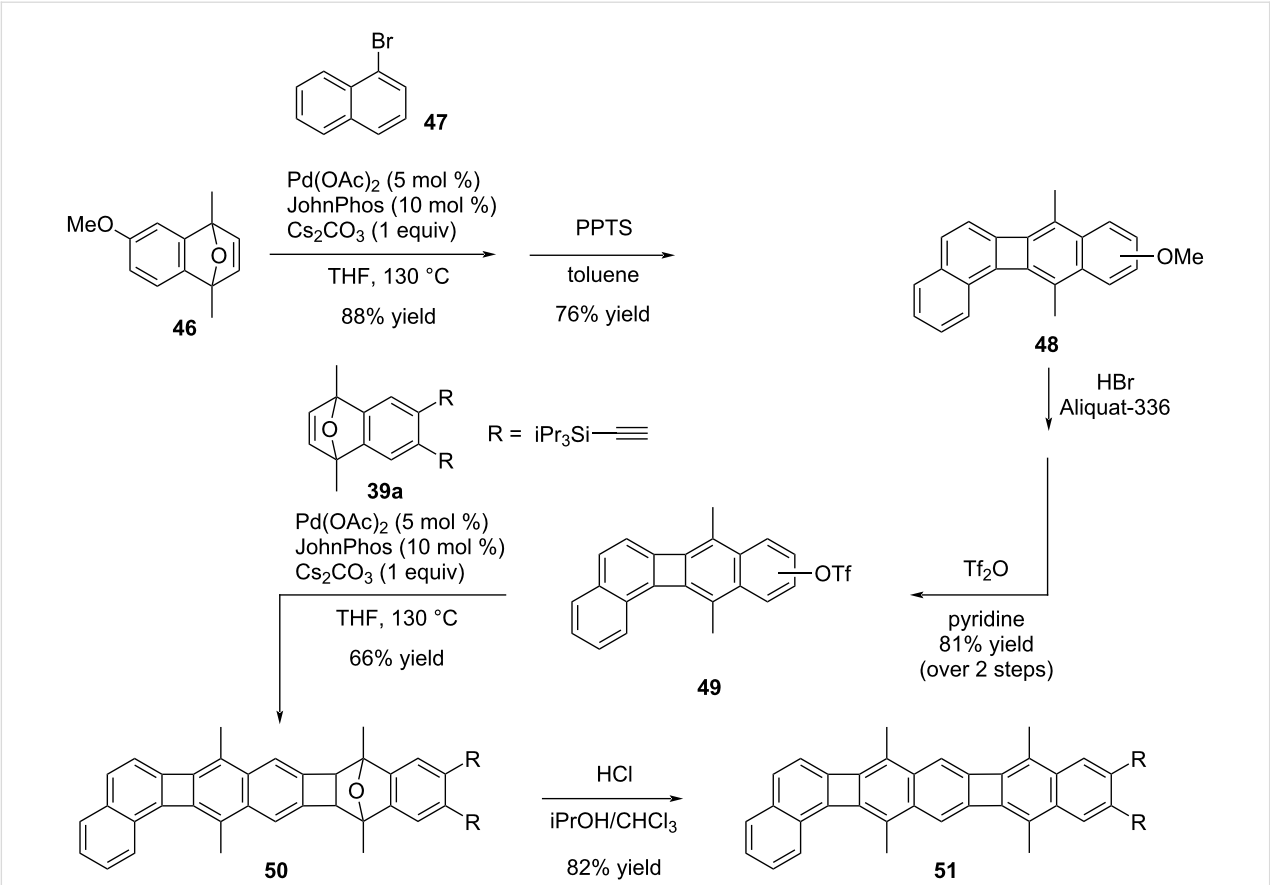

Scheme 10: Sequential Pd-catalyzed annulation reactions.

tained in yields ranging from 68% to 84% (Scheme 11). As anticipated, there was a notable red shift observed from **54a** to **54c**, which can be attributed to the expansion of the acene structure (λ_{max} = 441 nm, $\lambda_{max,em}$ = 444 nm for **54a**; λ_{max} = 541 nm, $\lambda_{max,em}$ = 550 nm for **54b**; λ_{max} = 648 nm, $\lambda_{max,em}$ = 655 nm for **54c**).

Next, the Bunz group focussed on symmetric azaacenes, which present a greater challenge in synthesis compared to their non-symmetric counterparts (Scheme 12) [46]. This complexity arises from factors such as limited substrate versatility and the difficulty in incorporating solubilizing groups into the symmetric azaacene framework. In the initial stage, the condensation reactions between biphenylene-2,3-dione (**52**) and diaminothiadiazoles **55a**,**b** resulted in the formation of polycyclic structures **56a** and **56b** containing thiadiazole units, in yields of 57% and 34%, respectively. Subsequently, by selectively cleaving the thiadiazole ring using $LiAlH_4$, followed by further conden-

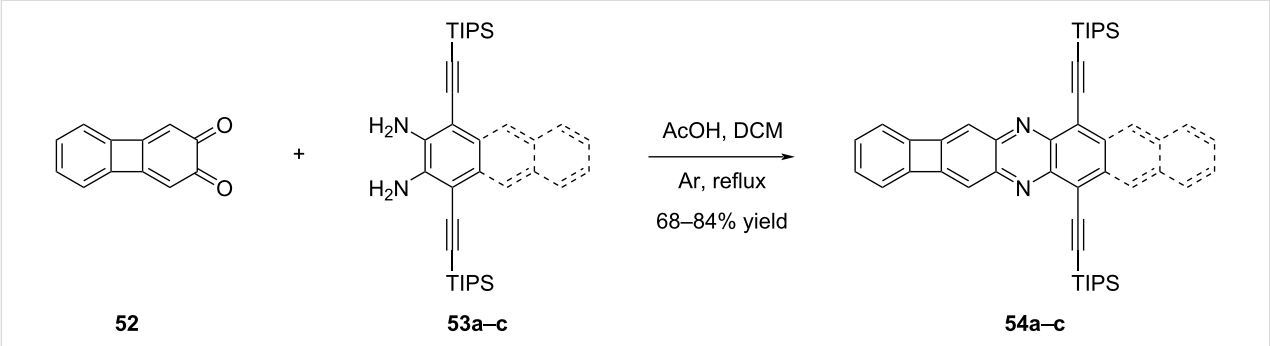

Scheme 11: Synthesis of biphenylene-containing unsymmetrical azaacenes **54a–c**.

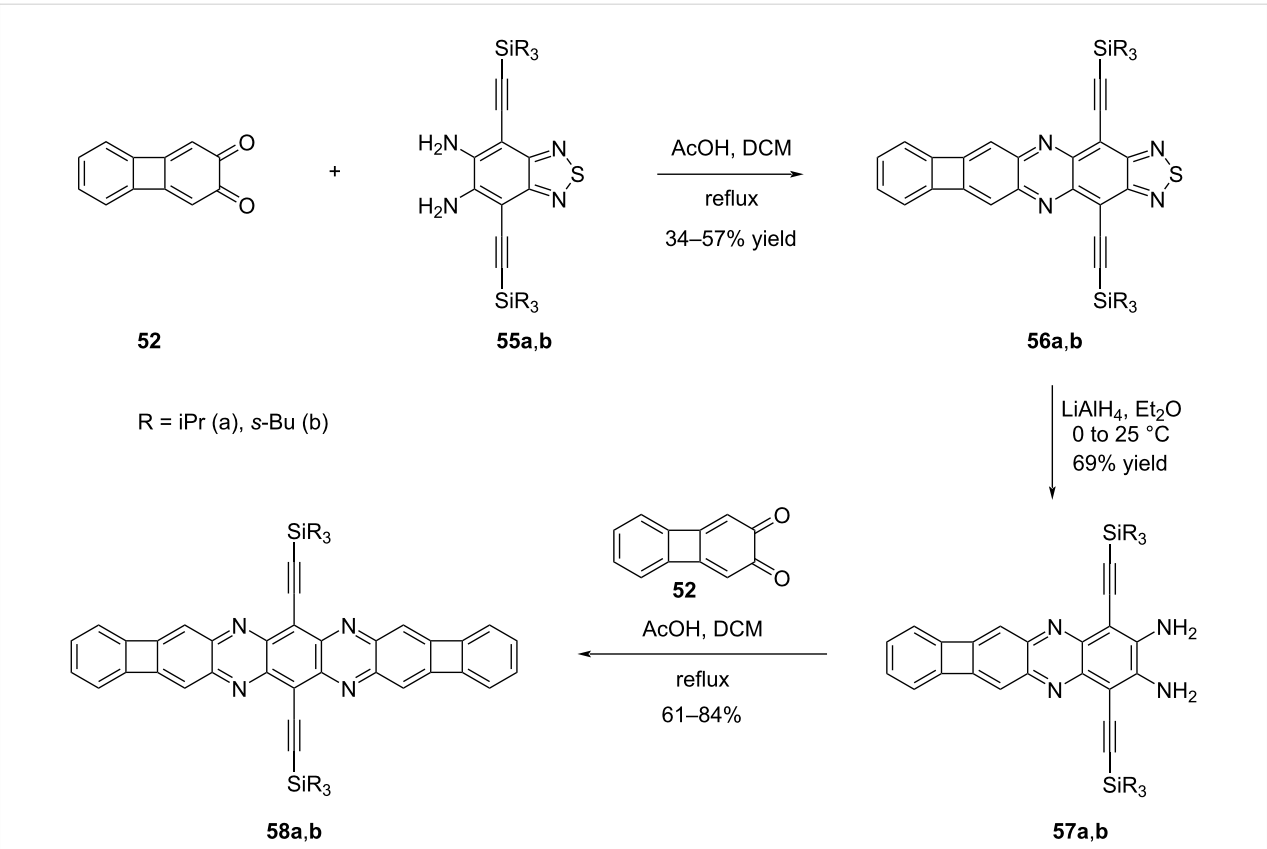

Scheme 12: Synthesis of biphenylene containing symmetrical azaacenes **58a**,**b**.

sation reaction with dione **52**, the desired symmetric azaacenes **58a** and **58b** with R groups representing (a) isopropyl and (b) *sec*-butyl, were successfully obtained in 84% and 61% yields, respectively. The incorporation of a biphenylene group into the azaacene structure did not result in any significant impact on the electrochemical properties. The electrochemical analysis revealed the presence of two reduction potentials commonly observed in azaacenes, suggesting that the modification did not alter this characteristic feature. For compound **58a**, λ_{max} was observed at 600 nm, and $\lambda_{max,em}$ was at 614 nm. On the other hand, for compound **58b**, λ_{max} was found at 606 nm, and $\lambda_{max,em}$ occurred at 616 nm. Based on the photophysical properties of compounds **54a** and **54b**, which were synthesized in the previous study (Scheme 11), it is evident that the addition of the second biphenylene-fused pyrazine group to the structure leads to a substantial red shift towards the NIR region. This observation indicates that the incorporation of biphenylene-containing groups has a positive impact on the optoelectronic properties of these structures, while also promoting their stability.

With appropriate substrate choices, Xia and co-workers were able to apply the Pd-catalyzed annulation strategy that they developed for the synthesis of biphenylene-containing azaacene structures [47] (Scheme 13). The methodology used in this study closely resembled their previous work (Scheme 9) [43].

The method used offered a distinct advantage compared to previous approaches [45], as it enabled the synthesis of not only linear azaacene structures but also non-linear structures as shown in Scheme 13. This versatility allowed for a broader range of conjugated molecules to be successfully prepared. The target azaacene analogues **62**–**64**, featuring 2,6-$(CH_3)_2C_6H_3$ groups were obtained in yields ranging from 50 to 85% through a series of steps. First, Pd-catalyzed annulation reactions of oxanorbornene **39b** and dibromophenazine derivatives **59**–**61** were carried out. Subsequently, aromatization reactions were performed in the presence of HCl to yield the desired products. The conjugated structures with distinct geometries demonstrated significant absorption and fluorescence characteristics. Among the synthesized compounds, linear derivative **62** exhibited the most intense absorption peak (λ_{max} = 503 nm), whereas the other two compounds **63** and **64** possessed slightly blue-shifted absorption maxima at 487 nm and 501 nm, respectively. When the fluorescence properties of compounds **62**, **63**, and **64** were examined, it was observed that compound **62** exhibited

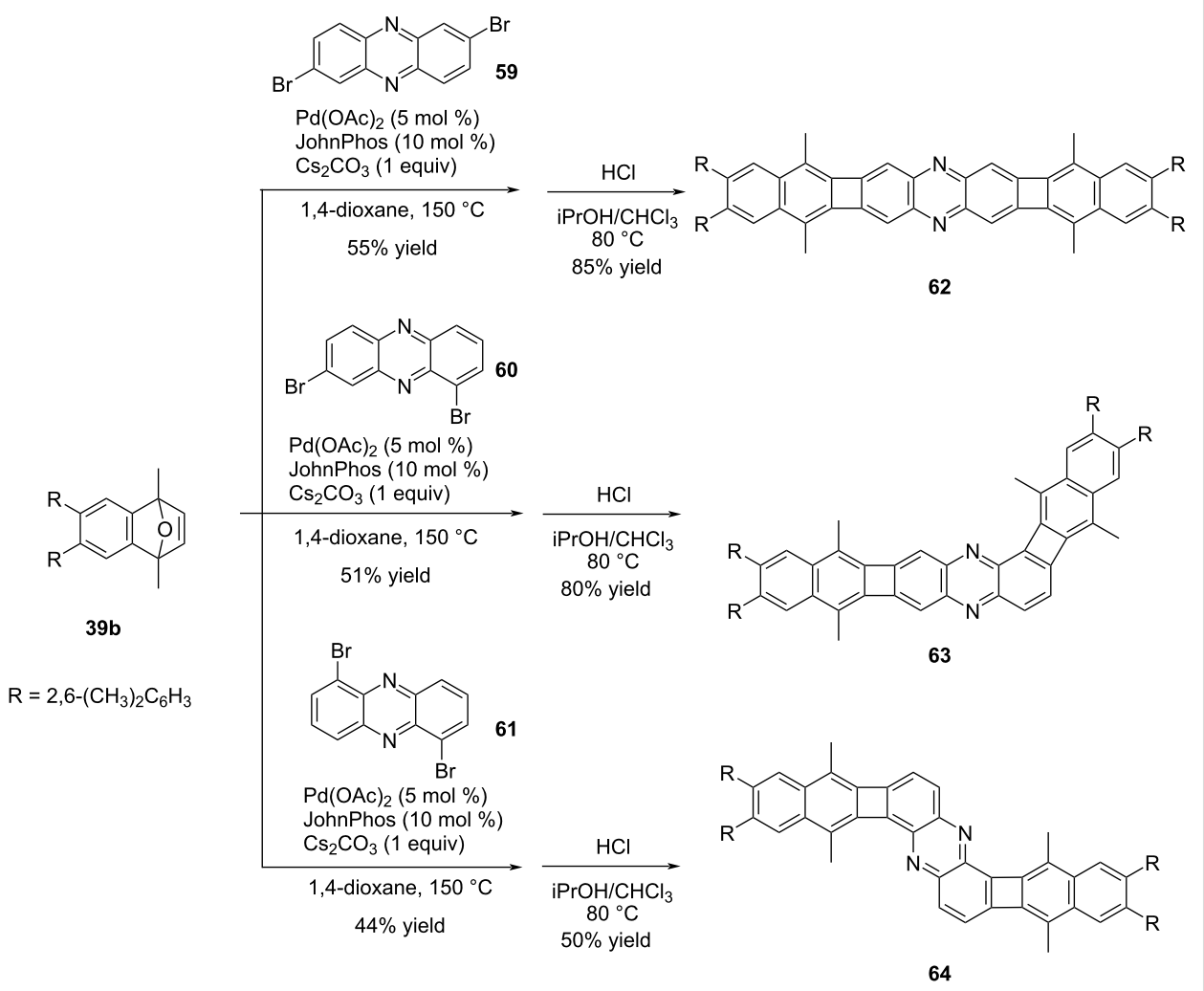

Scheme 13: Synthesis of azaacene analogues **62–64**.

strong fluorescence, making it an excellent fluorophore ($\lambda_{max,em}$ = 508 nm, Φ_{em} = 0.58) . On the other hand, compound **63** showed weaker fluorescence compared to **62** ($\lambda_{max,em}$ = 666 nm, Φ_{em} = 0.07), and compound **64** displayed almost no fluorescence emission ($\lambda_{max,em}$ = 497 nm, Φ_{em} = NA).

Naphthazarin–biphenylene hybrid structures

Taking the advantage of naphthazarin's bifunctional Diels–Alder reactivity, Swager and his team succeeded in the synthesis of POA-type structures incorporating naphthazarin and triptycene units (Scheme 14) [48]. Naphthazarin derivatives are known to complex with boron moieties and metals to form electron-poor acene units. Through the Diels–Alder reaction involving dienophile **66**, which was formed via the tautomerization of compound **65**, and diene **67**, compound **68** was successfully obtained in 30% yield. In the final step, the target POA-type structure containing naphthazarin **69** was synthesized by aromatization under acidic conditions. The attempts to conduct complexation experiments using $BF_3{\cdot}OEt_2$ to obtain a stable BF_2 complex were unsuccessful, primarily due to solubility problems encountered with substrate **69** and its BF_2 complex. Based on the UV–vis analysis of compounds **65** and **69**, it was observed that compound **65** displayed a low-energy absorption band at λ_{max} = 568 nm, whereas compound **69** exhibited absorption at λ_{max} = 557 nm. Unfortunately, the unsuccessful BF_2 complexation step to isolate stable BF_2 complex of **69**, likely attributable to solubility issues encountered with substrate **69**, prevented the incorporation of the acene backbone into the structure. Consequently, the anticipated red-shift in the absorption spectrum could not be observed as expected.

Boron-doped phenylene-containing oligoacenes

Following the evaluation of the POA concept combined with azaacenes and naphthazarin derivatives, the impact of boron doping on the optoelectronic properties of POA structures was

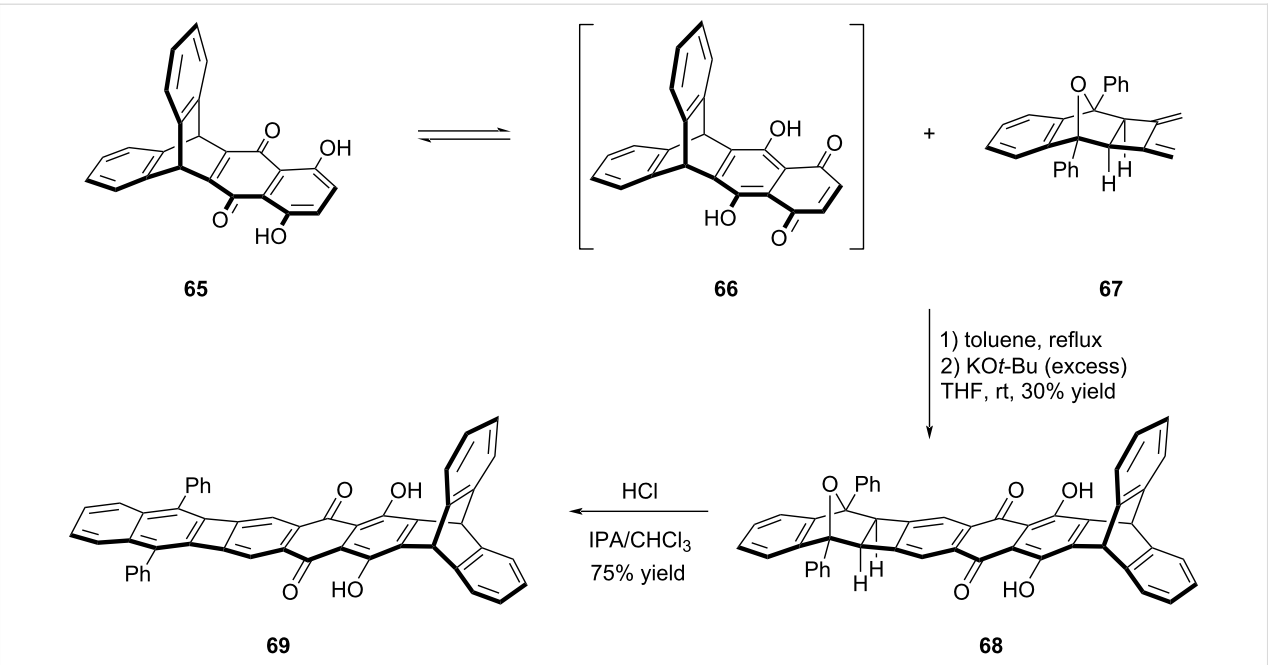

Scheme 14: Synthesis of POA-type structure **69**.

also targeted [49]. In the study, the envisaged POA **73** was successfully synthesized in three steps (Scheme 15). The initial step involved the synthesis of compound **71** in 64% yield using a cobalt-catalyzed cyclotrimerization reaction between 1,2-diethynylbenzene (**5**) and bis(trimethylsilyl)acetylene (**70**), a method commonly employed in [N]phenylene synthesis. Subsequently, treatment of compound **71** with excess BBr_3 in *n*-hexane, dibrominated intermediate **72** was obtained in 57% yield. In the final step, mesitylation was conducted utilizing mesitylcopper, leading to the successful access of the desired boron-doped POA **73** in 80% yield.

The red-colored POA **73** is noted for its absence of well-resolved absorption bands above 450 nm. Instead, the compound's color is attributed to plateau-shaped weak absorption bands, extending to approximately 570 nm. Surprisingly, POA **73** exhibited nonfluorescent behavior, in contrast to previously known POAs described in the literature. The hypothesis

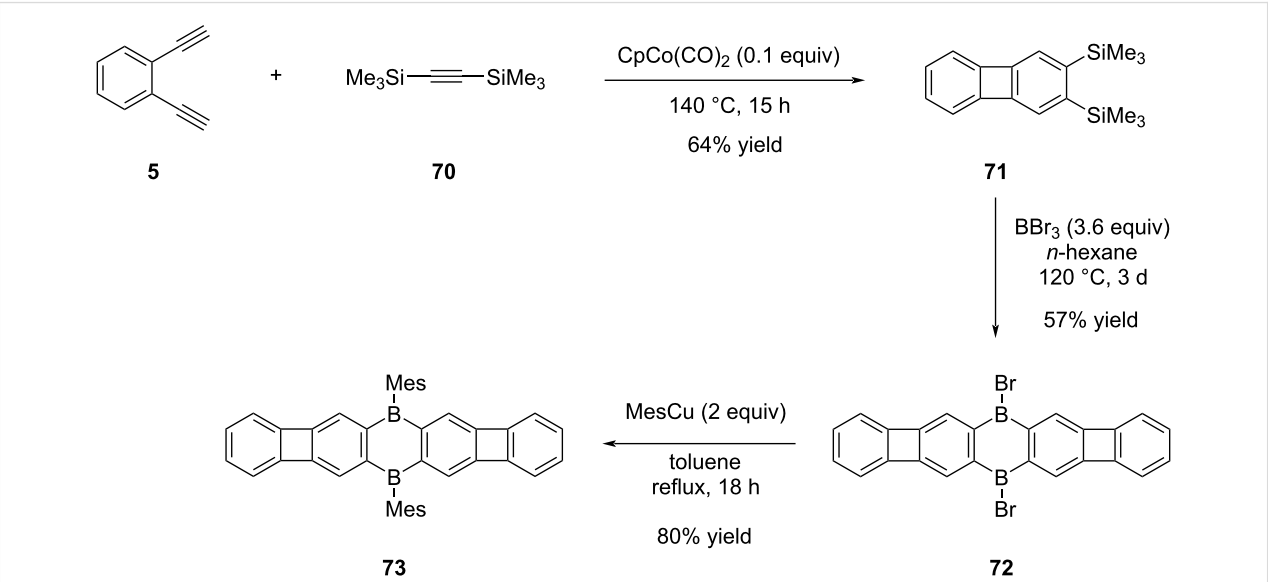

Scheme 15: Synthesis of boron-doped POA **73**.

suggesting that this phenomenon is a result of non-radiative deactivation was corroborated by detailed computational chemistry studies.

In continuation of the aforementioned work by Wagner and co-workers [49], they have synthesized also "v" and "z"-shaped POAs, wherein biphenylene groups are angularly incorporated into the 1,4-dibora-2,5-cyclohexadiene structure (Scheme 16) in addition to a π-extended linear POA (Scheme 17) [50]. The preparation of v- and z-shaped POAs **77** and **78** was carried out starting from 2-bromobiphenylene (**74**). Initial steps involved *ortho*-directed lithiation and subsequent treatment with Me_3SiCl, resulting in the formation of compound **75**. Further transformation through lithium–halogen exchange, followed by reaction with Me_3SiCl, yielded bis(trimethylsilylated) intermediate **76** in a 90% yield. By utilizing the conditions outlined in the prior investigation [49], compound **76** was subjected to a reaction with BBr_3. In the final step, the integration of mesityl

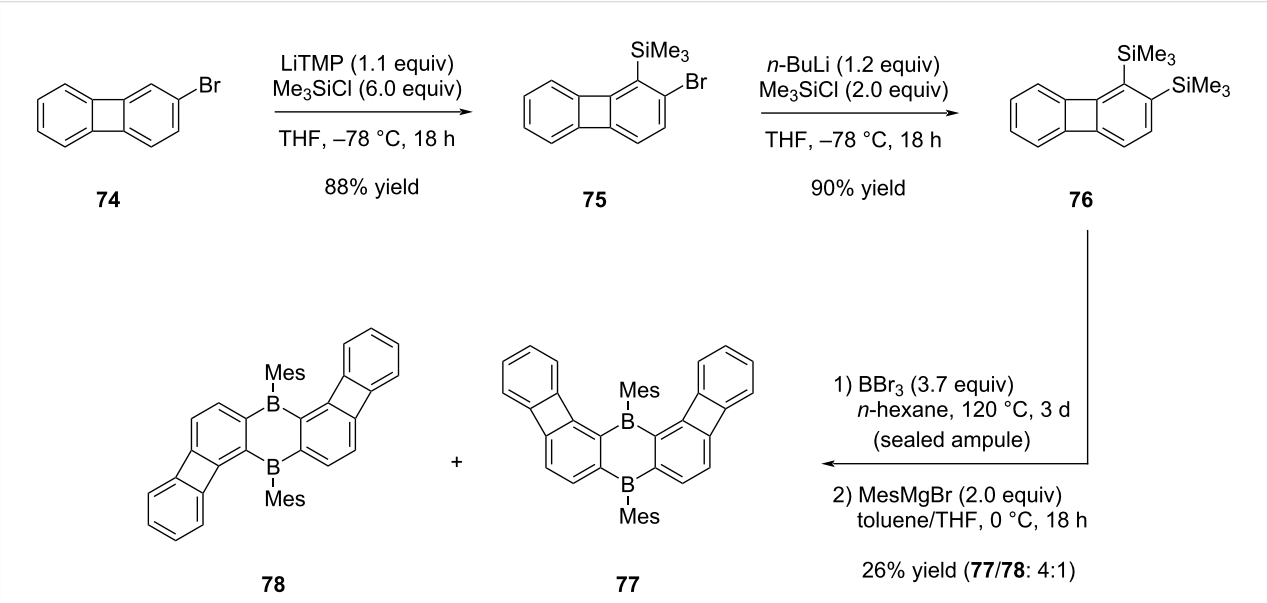

Scheme 16: Synthesis of “v”- and “z”-shaped B-POAs **77** and **78**.

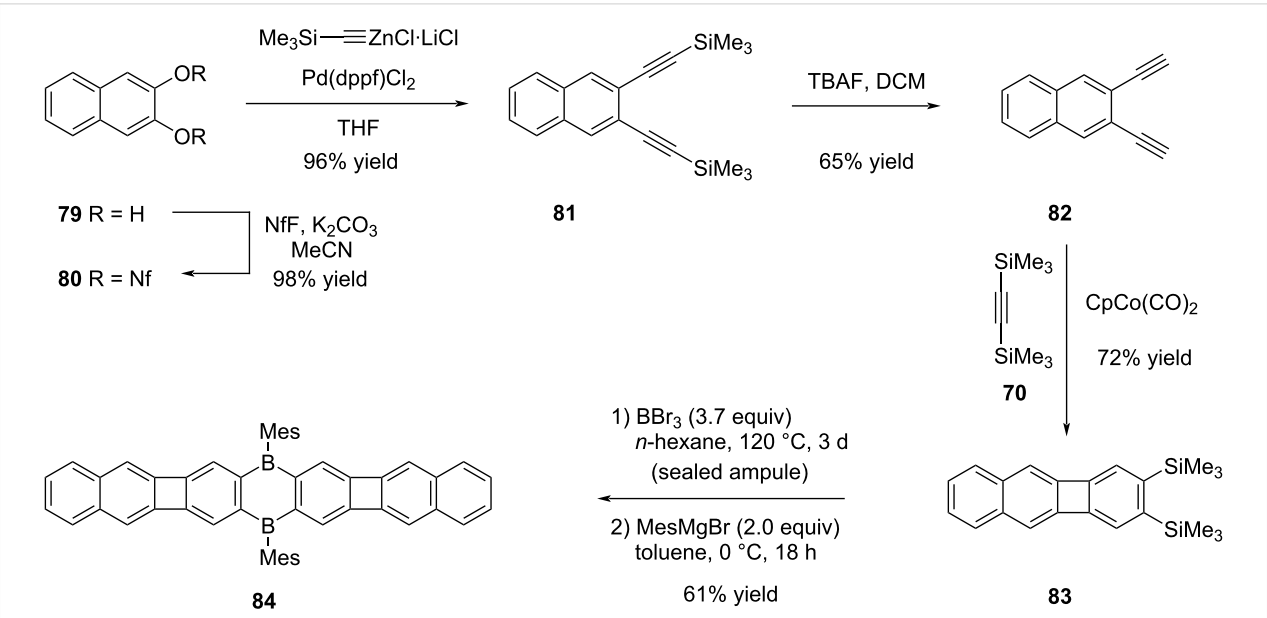

Scheme 17: Synthesis of boron-doped extended POA **84**.

groups into the molecular structure, resulted in the production of both compounds **77** and **78**, adopting v and z-configurations, respectively, in a 4 to 1 ratio.

The synthesis of linear compound **84**, characterized by a more extensive conjugated system in comparison to the boron-modified POA **73** outlined in Scheme 15, was accomplished through a sequence of five steps, starting from 2,3-dihydroxynaphthalene (**79**, Scheme 17). Following the successful synthesis of the nonaflate during the initial phase starting from **79**, the subsequent step involved the synthesis of compound **81** through the utilization of the Negishi cross-coupling reaction and then the removal of TMS groups from this intermediate was achieved using TBAF, resulting in the formation of diyne **82** in 65% yield. The progression towards the synthesis of biphenylene-containing substrate **83** was achieved through a Co-mediated alkyne trimerization process. Finally, the synthesis of the targeted boron-doped extended POA **84** was carried out with a yield of 61%, following a series of reactions including cyclocondensation with BBr_3 and mesitylation.

Since the "v" and "z"-shaped POAs could not be separated by physical methods, it was not possible to study their photophysical properties separately. Nonetheless, comparison of the properties of POAs **73** and **84** has provided essential data. Closely resembling compound **73**, the red color of POA **84** is attributed to an extensively broad absorption band, with an onset wavelength at around 570 nm. Although POA **73** does not exhibit any fluorescence characteristics, compound **84** displays a red emission, which can be attributed to the presence of two benzene rings integrated within its structure ($\lambda_{max,em}$ = 646 nm, Φ_{em} = 0.12). The fluorescence properties of the mixture **77**/**78** were markedly enhanced in comparison to those of linear POAs **73** and **84**, owing to the distinctive geometric arrangement inherent in their structures ($\lambda_{max,em}$ = 506 nm, Φ_{em} = 0.65).

On-surface synthesis of phenylene-containing oligoacenes

The POA syntheses discussed in this review thus far have predominantly involved solution chemistry. However, recent reports have demonstrated the feasibility of producing biphenylene-containing polycyclic aromatic compounds through on-surface chemistry techniques. One of the initial examples was documented by Fasel and Meunier in 2017 [51]. In their study, they effectively synthesized POA **87** utilizing 2,3-dibromotetracene (**85**) as substrate at a temperature of 430 K, employing ultra high vacuum conditions on Ag(111).

Subsequent scanning tunneling microscopy (STM) analyses unveiled not only the linear POA **87** resulting from surface-catalyzed formal [2 + 2] cycloaddition reactions but also the emergence of tetracene trimer **86** and tetramer **88** stemming from [2 + 2 + 2] cycloaddition reactions (Scheme 18). It is proposed that an aryne intermediate is formed after thermal activation and that the observed end products are formed from arynes via [2 + 2] and [2 + 2 + 2] cycloadditions.

In a closely related study conducted by Grill et al., the behavior of 2,3-dibromoanthracene (**89**) was examined on two distinct surfaces [Au(100) and Au(111)] (Scheme 19) [52]. Notably, on

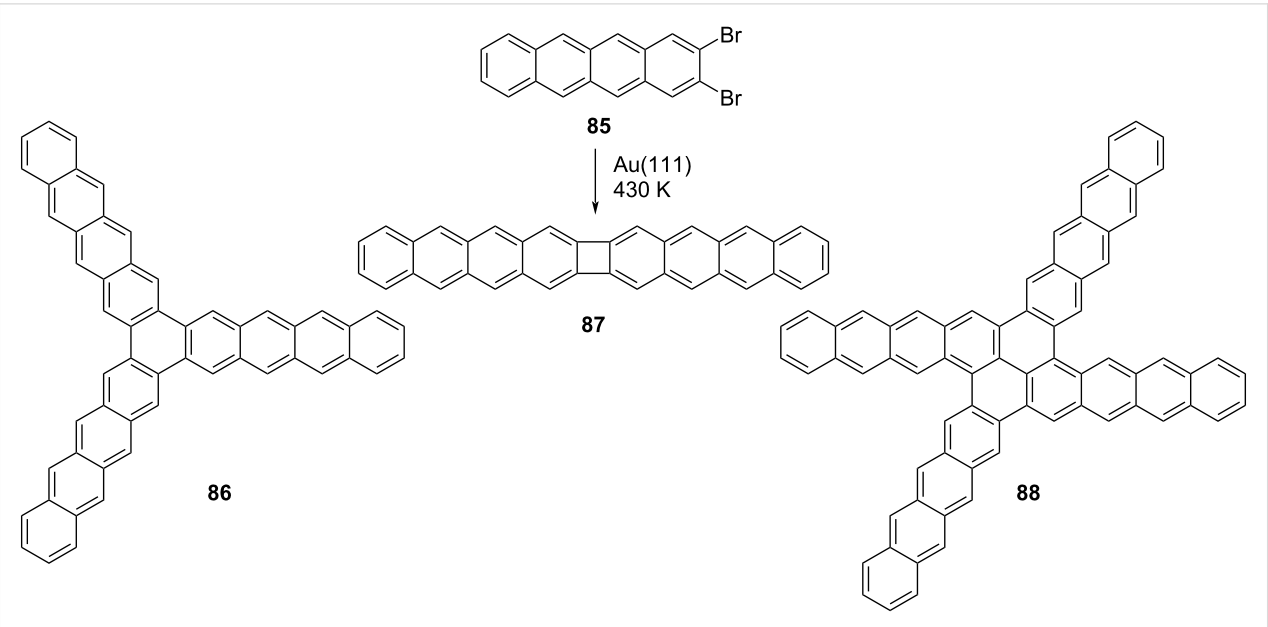

Scheme 18: Ag(111) surface-catalyzed synthesis of POA **87**.

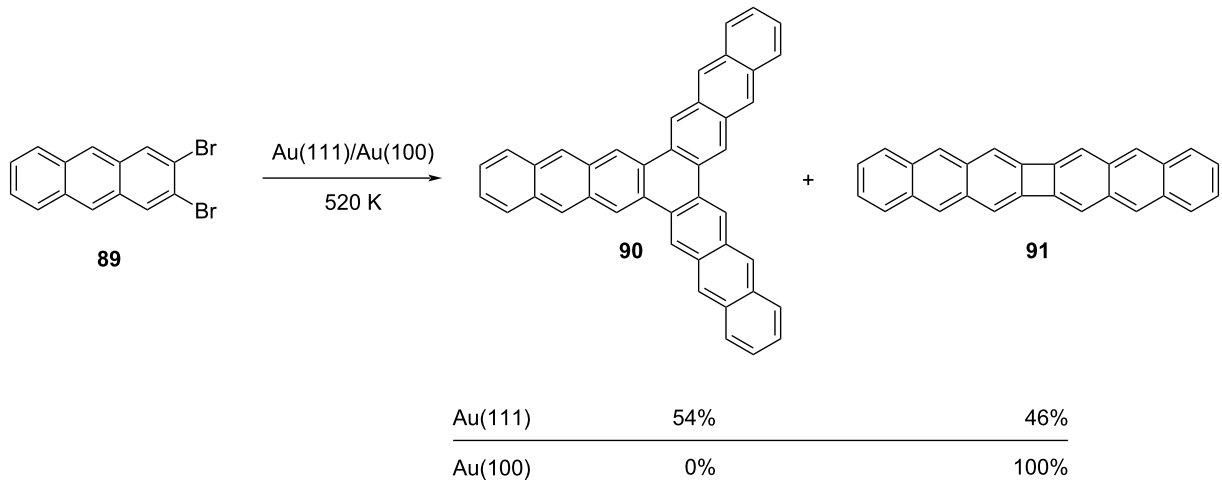

Scheme 19: Au(100) and Au(111) surface-catalyzed synthesis of POA **91**.

the Au(111) substrate, nearly equivalent quantities of dimer **91** resulting from a [2 + 2] cycloaddition and trimer **90** formed via a [2 + 2 + 2] cycloaddition pathway were observed. In contrast, when applied to Au(100), only the dimer structure **91** was generated through the [2 + 2] cycloaddition process.

In a recent study in this field, Izydorczyk et al. were able to selectively synthesize compound **87** through a hybrid approach involving the integration of both solution and surface chemistry techniques [53]. The key compound **96** to be used in the synthesis of POA **87** was synthesized in two steps. In the first step, **94** was obtained using a double Sonogashira cross-coupling reaction, followed by a Au(I)-catalyzed [4 + 2] cycloaddition reaction to afford the target substrate **96** and its regioisomer **95** in a 2:1 ratio (Scheme 20). POA **87** was obtained on Au(111) at 610 K after Ullmann-type coupling and aromatic dehydrogena-

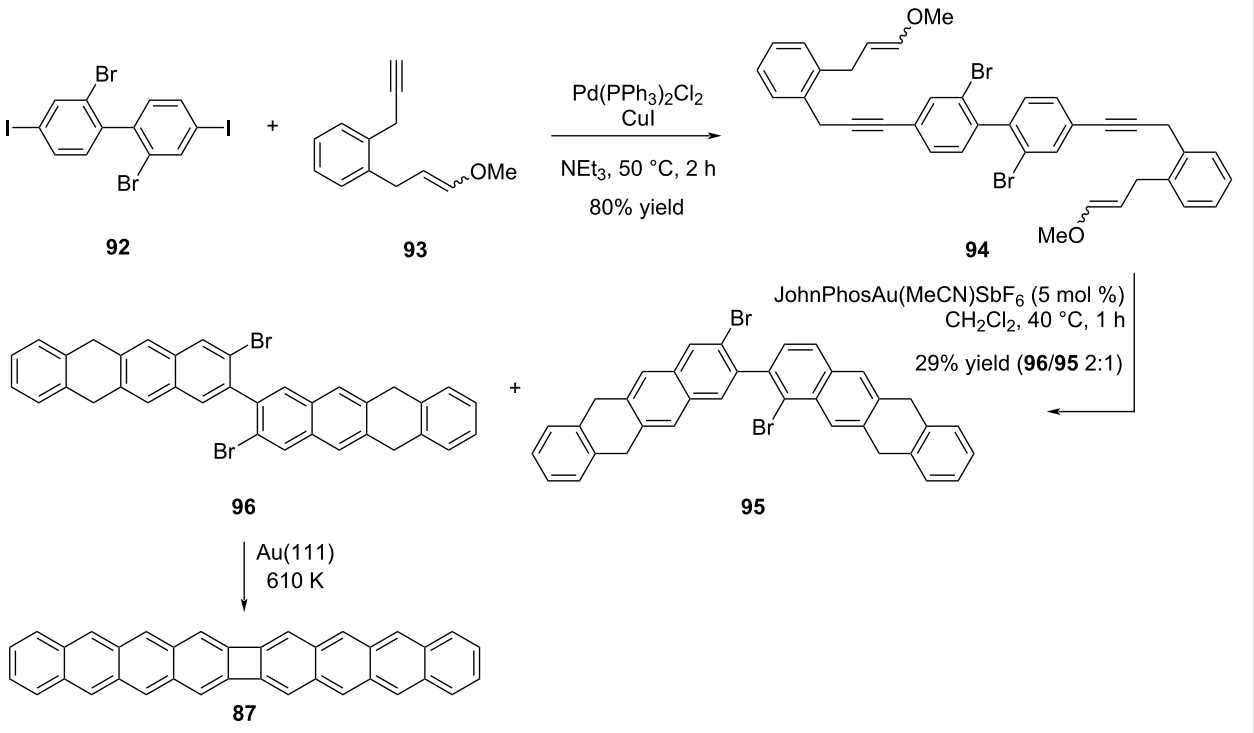

Scheme 20: Au(111) on-surface synthesis of POA **87**.

tion of compound **96**. Apart from these studies, the synthesis of smaller POA units has been accomplished by similar methods starting from naphthalene percursors on the Ag(111) surface [54]. The synthesis of nanoribbons containing biphenylene units was also achieved on the Ag(111) surface at 475 K by using 2,3,8,9-tetrabromotetracene as the substrate [55].

Conclusion

In conclusion, even though considerable time has elapsed since its initial synthesis in 1941, biphenylene continues to be a significant synthetic target, with a notable increase in research activity in recent times. Despite this long history, the synthetic methods used in the synthesis of biphenylene are largely limited to flash vacuum pyrolysis, [2 + 2] cycloaddition, [2 + 2 + 2] cycloaddition, and the Ullmann reaction. This shows how open this field is to further development and indicates the significant potential for new methodologies to be developed. In particular, the utilization of biphenylene units for stabilizing polycyclic aromatic compounds, along with the instances elucidated in this review where the electron delocalization occurs through the 4-membered ring, amplifies the intrinsic value of these structures. Methods that combine heteroatoms with biphenylene moieties have also been employed to alter the electronic characteristics and enhance the stability of polycyclic aromatic (POA) structures. Over the recent years, it has been shown that synthetically demanding biphenylene-containing polycyclic aromatic compounds can be achieved in a controlled manner not only by solution chemistry but also by on-surface chemistry. All these results, which are open for further development, confirm that biphenylene structures are very important synthetic units and will be used as tools for the synthesis of more complex structures in the future.

Funding

CD acknowledges the financial support provided by the GEBIP Award of the Turkish Academy of Sciences.

ORCID® iDs

Cagatay Dengiz - https://orcid.org/0000-0002-8238-6941

References

1. Tönshoff, C.; Bettinger, H. F. *Chem. – Eur. J.* **2021,** *27,* 3193–3212. doi:10.1002/chem.202003112
2. Anthony, J. E. *Chem. Rev.* **2006,** *106,* 5028–5048. doi:10.1021/cr050966z
3. Bendikov, M.; Wudl, F.; Perepichka, D. F. *Chem. Rev.* **2004,** *104,* 4891–4946. doi:10.1021/cr030666m
4. Anthony, J. E. *Angew. Chem., Int. Ed.* **2008,** *47,* 452–483. doi:10.1002/anie.200604045
5. Von Ragué Schleyer, P.; Manoharan, M.; Jiao, H.; Stahl, F. *Org. Lett.* **2001,** *3,* 3643–3646. doi:10.1021/ol016553b
6. Solà, M. *Front. Chem. (Lausanne, Switz.)* **2013,** *1,* 22. doi:10.3389/fchem.2013.00022
7. Bunz, U. H. F. *Acc. Chem. Res.* **2015,** *48,* 1676–1686. doi:10.1021/acs.accounts.5b00118
8. Bunz, U. H. F. *Chem. – Eur. J.* **2009,** *15,* 6780–6789. doi:10.1002/chem.200900990
9. Wang, J.; Chu, M.; Fan, J.-X.; Lau, T.-K.; Ren, A.-M.; Lu, X.; Miao, Q. *J. Am. Chem. Soc.* **2019,** *141,* 3589–3596. doi:10.1021/jacs.8b12671
10. Ong, A.; Tao, T.; Jiang, Q.; Han, Y.; Ou, Y.; Huang, K.-W.; Chi, C. *Angew. Chem., Int. Ed.* **2022,** *61,* e202209286. doi:10.1002/anie.202209286
11. Müller, M.; Ahrens, L.; Brosius, V.; Freudenberg, J.; Bunz, U. H. F. *J. Mater. Chem. C* **2019,** *7,* 14011–14034. doi:10.1039/c9tc04843j
12. Takano, H.; Ito, T.; Kanyiva, K. S.; Shibata, T. *Eur. J. Org. Chem.* **2019,** 2871–2883. doi:10.1002/ejoc.201900111
13. Radenković, S.; Tošović, J.; Havenith, R. W. A.; Bultinck, P. *ChemPhysChem* **2015,** *16,* 216–222. doi:10.1002/cphc.201402468
14. Gershoni-Poranne, R.; Stanger, A. *Chem. – Eur. J.* **2014,** *20,* 5673–5688. doi:10.1002/chem.201304307
15. Lothrop, W. C. *J. Am. Chem. Soc.* **1941,** *63,* 1187–1191. doi:10.1021/ja01850a007
16. Brown, R. F. C.; Coulston, K. J.; Eastwood, F. W. *Tetrahedron Lett.* **1996,** *37,* 6819–6820. doi:10.1016/s0040-4039(96)01488-8
17. Brown, R. F. C.; Browne, N. R.; Coulston, K. J.; Eastwood, F. W.; Irvine, M. J.; Pullin, A. D. E.; Wiersum, U. E. *Aust. J. Chem.* **1989,** *42,* 1321–1344. doi:10.1071/ch9891321
18. Toda, F.; Garratt, P. *Chem. Rev.* **1992,** *92,* 1685–1707. doi:10.1021/cr00016a001
19. Campbell, C. D.; Rees, C. W. *J. Chem. Soc. C* **1969,** 742–747. doi:10.1039/j39690000742
20. Logullo, F. M.; Seitz, A. H.; Friedman, L. *Org. Synth.* **1968,** *48,* 12. doi:10.15227/orgsyn.048.0012
21. Berris, B. C.; Lai, Y.-H.; Vollhardt, K. P. C. *J. Chem. Soc., Chem. Commun.* **1982,** 953–954. doi:10.1039/c39820000953
22. Mondal, S. *ChemTexts* **2016,** *2,* 17. doi:10.1007/s40828-016-0036-2
23. Schaub, T.; Radius, U. *Tetrahedron Lett.* **2005,** *46,* 8195–8197. doi:10.1016/j.tetlet.2005.09.124
24. Iyoda, M.; Kabir, S. M. H.; Vorasingha, A.; Kuwatani, Y.; Yoshida, M. *Tetrahedron Lett.* **1998,** *39,* 5393–5396. doi:10.1016/s0040-4039(98)01082-x
25. Wang, S.-L.; Pan, M.-L.; Su, W.-S.; Wu, Y.-T. *Angew. Chem., Int. Ed.* **2017,** *56,* 14694–14697. doi:10.1002/anie.201708892
26. Diercks, R.; Vollhardt, K. P. C. *J. Am. Chem. Soc.* **1986,** *108,* 3150–3152. doi:10.1021/ja00271a080
27. Holmes, D.; Kumaraswamy, S.; Matzger, A. J.; Vollhardt, K. P. C. *Chem. – Eur. J.* **1999,** *5,* 3399–3412. doi:10.1002/(sici)1521-3765(19991105)5:11<3399::aid-chem3399>3.0.co;2-v
28. Berris, B. C.; Hovakeemian, G. H.; Lai, Y.-H.; Mestdagh, H.; Vollhardt, K. P. C. *J. Am. Chem. Soc.* **1985,** *107,* 5670–5687. doi:10.1021/ja00306a013
29. Diercks, R.; Vollhardt, K. P. C. *Angew. Chem., Int. Ed. Engl.* **1986,** *25,* 266–268. doi:10.1002/anie.198602661
30. Schulman, J. M.; Disch, R. L. *J. Am. Chem. Soc.* **1996,** *118,* 8470–8474. doi:10.1021/ja9611811
31. Schleifenbaum, A.; Feeder, N.; Vollhardt, K. P. C. *Tetrahedron Lett.* **2001,** *42,* 7329–7332. doi:10.1016/s0040-4039(01)01425-3

32. Dosche, C.; Löhmannsröben, H.-G.; Bieser, A.; Dosa, P. I.; Han, S.; Iwamoto, M.; Schleifenbaum, A.; Vollhardt, K. P. C. *Phys. Chem. Chem. Phys.* **2002,** *4,* 2156–2161. doi:10.1039/b109342h
33. Buckland, P. R.; Hacker, N. P.; McOmie, J. F. W. *J. Chem. Soc., Perkin Trans. 1* **1983,** 1443–1448. doi:10.1039/p19830001443
34. Jensen, F. R.; Coleman, W. E. *Tetrahedron Lett.* **1959,** *1* (20), 7–11. doi:10.1016/s0040-4039(01)99477-8
35. Barton, J. W.; Shepherd, M. K.; Willis, R. J. *J. Chem. Soc., Perkin Trans. 1* **1986,** 967–971. doi:10.1039/p19860000967
36. Parkhurst, R. R.; Swager, T. M. *J. Am. Chem. Soc.* **2012,** *134,* 15351–15356. doi:10.1021/ja3043883
37. Liu, S.; Jin, Z.; Teo, Y. C.; Xia, Y. *J. Am. Chem. Soc.* **2014,** *136,* 17434–17437. doi:10.1021/ja5110415
38. Jin, Z.; Teo, Y. C.; Zulaybar, N. G.; Smith, M. D.; Xia, Y. *J. Am. Chem. Soc.* **2017,** *139,* 1806–1809. doi:10.1021/jacs.6b12888
39. Jin, Z.; Yao, Z.-F.; Barker, K. P.; Pei, J.; Xia, Y. *Angew. Chem., Int. Ed.* **2019,** *58,* 2034–2039. doi:10.1002/anie.201812581
40. Yin, X.; Zheng, K.; Jin, Z.; Horst, M.; Xia, Y. *J. Am. Chem. Soc.* **2022,** *144,* 12715–12724. doi:10.1021/jacs.2c02457
41. Gu, Z.; Boursalian, G. B.; Gandon, V.; Padilla, R.; Shen, H.; Timofeeva, T. V.; Tongwa, P.; Vollhardt, K. P. C.; Yakovenko, A. A. *Angew. Chem., Int. Ed.* **2011,** *50,* 9413–9417. doi:10.1002/anie.201103428
42. Korotvička, A.; Císařová, I.; Roithová, J.; Kotora, M. *Chem. – Eur. J.* **2012,** *18,* 4200–4207. doi:10.1002/chem.201103888
43. Jin, Z.; Teo, Y. C.; Teat, S. J.; Xia, Y. *J. Am. Chem. Soc.* **2017,** *139,* 15933–15939. doi:10.1021/jacs.7b09222
44. Jin, Z.; Teo, Y. C.; Teat, S. J.; Xia, Y. *Synlett* **2018,** *29,* 2547–2551. doi:10.1055/s-0037-1610261
45. Biegger, P.; Schaffroth, M.; Patze, C.; Tverskoy, O.; Rominger, F.; Bunz, U. H. F. *Chem. – Eur. J.* **2015,** *21,* 7048–7052. doi:10.1002/chem.201500319
46. Biegger, P.; Schaffroth, M.; Tverskoy, O.; Rominger, F.; Bunz, U. H. F. *Chem. – Eur. J.* **2016,** *22,* 15896–15901. doi:10.1002/chem.201602675
47. Teo, Y. C.; Jin, Z.; Xia, Y. *Org. Lett.* **2018,** *20,* 3300–3304. doi:10.1021/acs.orglett.8b01190
48. Dengiz, C.; Luppino, S. P.; Gutierrez, G. D.; Swager, T. M. *J. Org. Chem.* **2017,** *82,* 7470–7480. doi:10.1021/acs.joc.7b01170
49. Kirschner, S.; Mewes, J.-M.; Bolte, M.; Lerner, H.-W.; Dreuw, A.; Wagner, M. *Chem. – Eur. J.* **2017,** *23,* 5104–5116. doi:10.1002/chem.201700056
50. Kirschner, S.; Uecker, I.; Bolte, M.; Lerner, H.-W.; Wagner, M. *Organometallics* **2019,** *38,* 2818–2823. doi:10.1021/acs.organomet.9b00330
51. Sánchez-Sánchez, C.; Nicolaï, A.; Rossel, F.; Cai, J.; Liu, J.; Feng, X.; Müllen, K.; Ruffieux, P.; Fasel, R.; Meunier, V. *J. Am. Chem. Soc.* **2017,** *139,* 17617–17623. doi:10.1021/jacs.7b10026
52. Koch, M.; Gille, M.; Hecht, S.; Grill, L. *Surf. Sci.* **2018,** *678,* 194–200. doi:10.1016/j.susc.2018.05.014
53. Izydorczyk, I.; Stoica, O.; Krawiec, M.; Blieck, R.; Zuzak, R.; Stępień, M.; Echavarren, A. M.; Godlewski, S. *Chem. Commun.* **2022,** *58,* 4063–4066. doi:10.1039/d2cc00479h
54. Kawai, S.; Takahashi, K.; Ito, S.; Pawlak, R.; Meier, T.; Spijker, P.; Canova, F. F.; Tracey, J.; Nozaki, K.; Foster, A. S.; Meyer, E. *ACS Nano* **2017,** *11,* 8122–8130. doi:10.1021/acsnano.7b02973
55. Sánchez-Sánchez, C.; Dienel, T.; Nicolaï, A.; Kharche, N.; Liang, L.; Daniels, C.; Meunier, V.; Liu, J.; Feng, X.; Müllen, K.; Sánchez-Valencia, J. R.; Gröning, O.; Ruffieux, P.; Fasel, R. *Chem. – Eur. J.* **2019,** *25,* 12074–12082. doi:10.1002/chem.201901410

License and Terms

BEILSTEIN JOURNAL OF ORGANIC CHEMISTRY

Facile access to pyridinium-based bent aromatic amphiphiles: nonionic surface modification of nanocarbons in water

Lorenzo Catti*, Shinji Aoyama and Michito Yoshizawa*

Full Research Paper

Open Access

Address:
Laboratory for Chemistry and Life Science, Institute of Innovative Research, Tokyo Institute of Technology, 4259 Nagatsuta, Midori-ku, Yokohama 226-8503, Japan

Email:
Lorenzo Catti* - catti.l.aa@m.titech.ac.jp; Michito Yoshizawa* - yoshizawa.m.ac@m.titech.ac.jp

* Corresponding author

Keywords:
aromatic micelle; nanocarbon; nonionic surface modification; pyridinium; water-solubilization

Beilstein J. Org. Chem. **2024,** *20,* 32–40.
https://doi.org/10.3762/bjoc.20.5

Received: 13 October 2023
Accepted: 04 December 2023
Published: 08 January 2024

This article is part of the thematic issue "Carbon-rich materials: from polyaromatic molecules to fullerenes and other carbon allotropes".

Guest Editor: Y. Yamakoshi

Abstract

Efficient water-solubilization of nanocarbons is desirable for both their biological and material applications, but so far has mainly relied on covalent modifications or amphiphiles featuring ionic side-chains. Here, we report a facile 2–4-step synthesis of pyridinium-based, bent aromatic amphiphiles with modular *nonionic side-chains* (i.e., CH_3 and $CH_2CH_2(OCH_2CH_2)_2$–Y (Y = OCH_3, OH, and imidazole)). The new amphiphiles quantitatively self-assemble into ≈2 nm-sized aromatic micelles in water independent of the side-chain. Importantly, efficient water-solubilization and *nonionic* surface modification of various nanocarbons (e.g., fullerene C_{60}, carbon nanotubes, and graphene nanoplatelets) are achieved through noncovalent encircling with the bent amphiphiles. The resultant imidazole-modified nanocarbons display a pH-responsive surface charge, as evidenced by NMR and zeta-potential measurements. In addition, solubilization of a nitrogen-doped nanocarbon (i.e., graphitic carbon nitride) in the form of 10–30 nm-sized stacks is also demonstrated using the present amphiphiles.

Introduction

Nanocarbons, such as fullerenes, graphenes, and carbon nanotubes, are continuing to attract global attention due to their unique chemical and physical properties [1,2]. Facile water-solubilization and modifications of nanocarbons with various sizes and shapes are desirable for both their biological and materials applications, but so far have mainly relied on i) covalent modifications, leading to irreversible property changes (Figure 1a, left) [3,4] and noncovalent wrapping with ii) linear/planar amphiphiles bearing ionic side-chains [5,6] or iii) amphiphilic/polar polymers, displaying low to moderate interactions and debundling efficiency (Figure 1a, center and right) [7-11]. The development of new amphiphiles with large polyaromatic panels for strong aromatic–aromatic interactions and nonionic side-chains on the other hand would grant access to water-

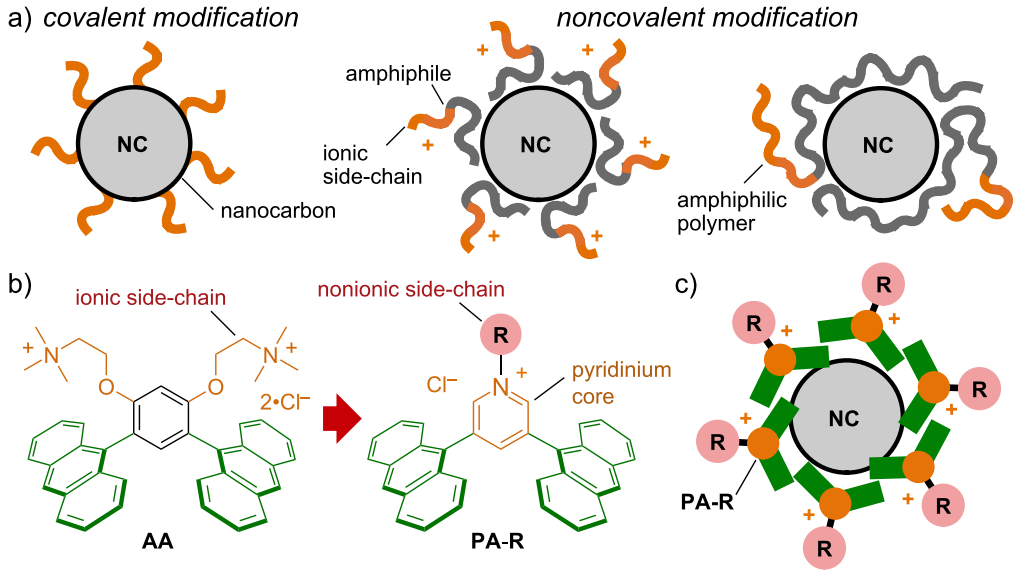

Figure 1: a) Previous methods for the water-solubilization and modification of nanocarbons (NCs). b) Bent aromatic amphiphiles **AA** and **PA-R** (R = CH_3 and $CH_2CH_2(OCH_2CH_2)_2$–Y (Y = OCH_3, OH, and imidazole)). c) Nonionic surface modification of NCs via noncovalent encircling with **PA-R**s.

soluble nanocarbons with tunable surface properties, which could expand noncovalent nanocarbon chemistry and technology.

We here report pyridinium-based, bent aromatic amphiphiles **PA-R**, featuring a pyridinium salt (Py-R^+·Cl^-) as the key motif, capable of providing both a cationic hydrophilic hinge and a variety of nonionic side-chains (i.e., CH_3 and $CH_2CH_2(OCH_2CH_2)_2$–Y (Y = OCH_3, OH, and imidazole); Figure 1b). The present amphiphile is originated from bent aromatic amphiphile **AA** [12,13], composed of two anthracene panels linked by a *m*-phenylene spacer with two cationic side-chains, which assembles into an aqueous ≈2 nm-sized aromatic micelle with broad host functions [14-21]. Replacement of the *m*-phenylene unit with an *N*-functionalized pyridinium core reduces the synthetic steps from 6 to 2–4, while at the same time enabling the use of various nonionic side-chains. Amphiphiles **PA-R** quantitatively self-assemble into aromatic micelles (**PA-R**)$_n$, with outer diameters of ≈2 nm, independent of the side-chain present. Importantly, efficient water-solubilization and nonionic surface modification of nanocarbons (i.e., fullerene C_{60} (**C_{60}**), single/multi-walled carbon nanotubes (***s/m*-CNT**), and graphene nanoplatelets (**GN**)) can be achieved through noncovalent encircling with the present pyridinium-based amphiphiles (Figure 1c). The noncovalent modification of **C_{60}** with multiple imidazole side-chains is found to yield a pH-responsive surface charge, as evidenced by NMR and zeta-potential measurements. A nitrogen-doped nanocarbon, i.e., graphitic carbon nitride (**g-C_3N_4**), is likewise solubilized by **PA-R** in water and subsequently deposited onto a cellulose filter using a simple filtration protocol.

Results and Discussion

Synthesis of pyridinium-based amphiphiles

Synthesis of the pyridinium-based amphiphiles **PA-R** was achieved in 2–4 steps starting from commercially available 3,5-dibromopyridine. Negishi cross-coupling with 9-anthrylzinc chloride in the presence of $PdCl_2(PhCN)_2$/P(*t*-Bu)$_3$ as catalyst afforded the common precursor 3,5-dianthrylpyridine (**prePA**), a simple yet novel bent building block, in 81% yield. For the synthesis of the methyl derivative, **prePA** was *N*-alkylated with excess methyl iodide yielding **PA-CH_3'**, followed by ion exchange using an exchange resin to provide **PA-CH_3** as a yellow solid (74% yield over 2 steps; Figure 2a). Despite its large aromatic framework with a monocationic core, **PA-CH_3** was found to be soluble in water up to ≈0.9 mM. Using similar procedures, amphiphiles **PA-OCH_3** and **PA-OH** were synthesized by reacting **prePA** under neat conditions with 1-(2-bromoethoxy)-2-(2-methoxyethoxy)ethane (67% yield over 2 steps after ion-exchange) and 2-[2-(2-chloroethoxy)ethoxy]ethanol (42% yield), respectively (Figure 2b). Imidazole-functionalized amphiphile **PA-Im** was obtained by first reacting **prePA** with 1,2-bis(iodoethoxy)ethane to yield a reactive iodo-derivative, which was subsequently quaternized with imidazole and converted to the chloride salt (42% yield over 3 steps). All three $CH_2CH_2(OCH_2CH_2)_2$-containing

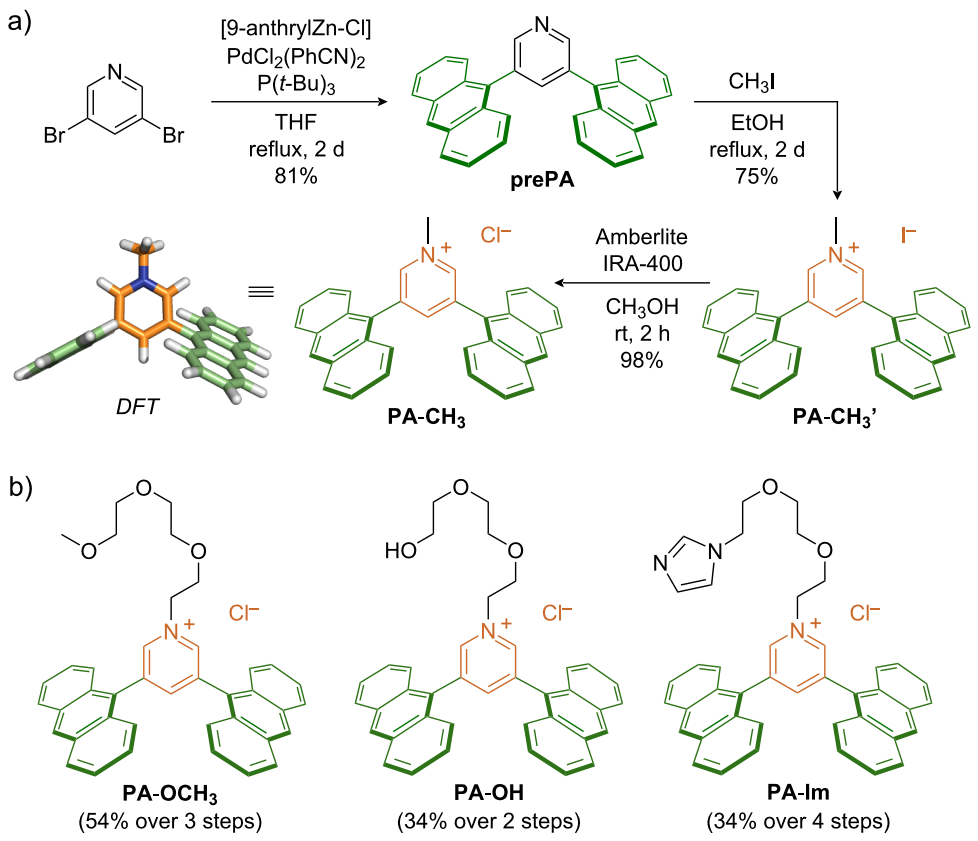

Figure 2: a) Synthetic route toward **prePA** and **PA-CH$_3$**, including the optimized structure (DFT) of **PA-CH$_3$**. b) Structures of **PA-OCH$_3$**, **PA-OH**, and **PA-Im**.

amphiphiles were found to display good-to-high water-solubilities. It is noteworthy that an **AA** derivative featuring three nonionic $-O(CH_2CH_2O)_2CH_3$ side-chains on the phenylene spacer is insoluble in water (see Figure S45 in Supporting Information File 1), emphasizing the importance of the hydrophilic pyridinium core for the observed water-solubility.

Formation and structure of aromatic micelles

Aromatic micelle (**PA-CH$_3$**)$_n$ was facilely generated via dissolution of **PA-CH$_3$** (2.1 mg, 4.3 µmol) in water (8.6 mL). The ^{1}H NMR spectrum of **PA-CH$_3$** in D_2O showed significantly upfield-shifted signals ($\Delta\delta$ = −2.73 ppm for H_b) compared to the spectrum in CD_3OD, in a manner similar to **AA** [12,13], indicating self-assembly via the hydrophobic effect and π-stacking interactions (Figure 3a,b). The self-assembly in water was further supported by UV–visible analysis, displaying slight red-shifts of the anthracene absorption bands relative to the spectrum in methanol ($\Delta\lambda_{max}$ = +3; Figure S36 in Supporting Information File 1). The formation of spherical particles with narrow size distribution and an average diameter of ≈2 nm was confirmed by DLS and DOSY NMR measurements (Figure 3e and Figure S27 in Supporting Information File 1). Based on molecular modeling, these data suggested the self-assembly of in average six **PA-CH$_3$** amphiphiles into a small aromatic micelle (Figure 3g). In a similar way, the generation of micelles (**PA-OCH$_3$**)$_n$, (**PA-OH**)$_n$, and (**PA-Im**)$_n$ was confirmed via NMR, UV–visible, and DLS analyses upon dissolution of the corresponding amphiphiles in water (Figure 3c,d,f and Figure S30–S36 in Supporting Information File 1). It is noteworthy that all four amphiphiles formed similar sized micelles (d_{av} ≈ 2 nm), independent of the attached side-chain.

NMR dilution experiments with **PA-CH$_3$** and **PA-OCH$_3$** indicated that their critical micelle concentrations (CMCs) are below 0.1 mM (Figures S28 and S32, Supporting Information File 1), which is around 10 times lower than that of **AA** [12,13]. The increased stability against dilution likely arises from reduced electrostatic repulsion and increased anthracene-based π-stacking interactions due to the absence of *o*-alkoxy groups. Aromatic micelle (**PA-CH$_3$**)$_n$ was furthermore found to be stable for at least six days at room temperature in the dark (see Figure S37 in Supporting Information File 1).

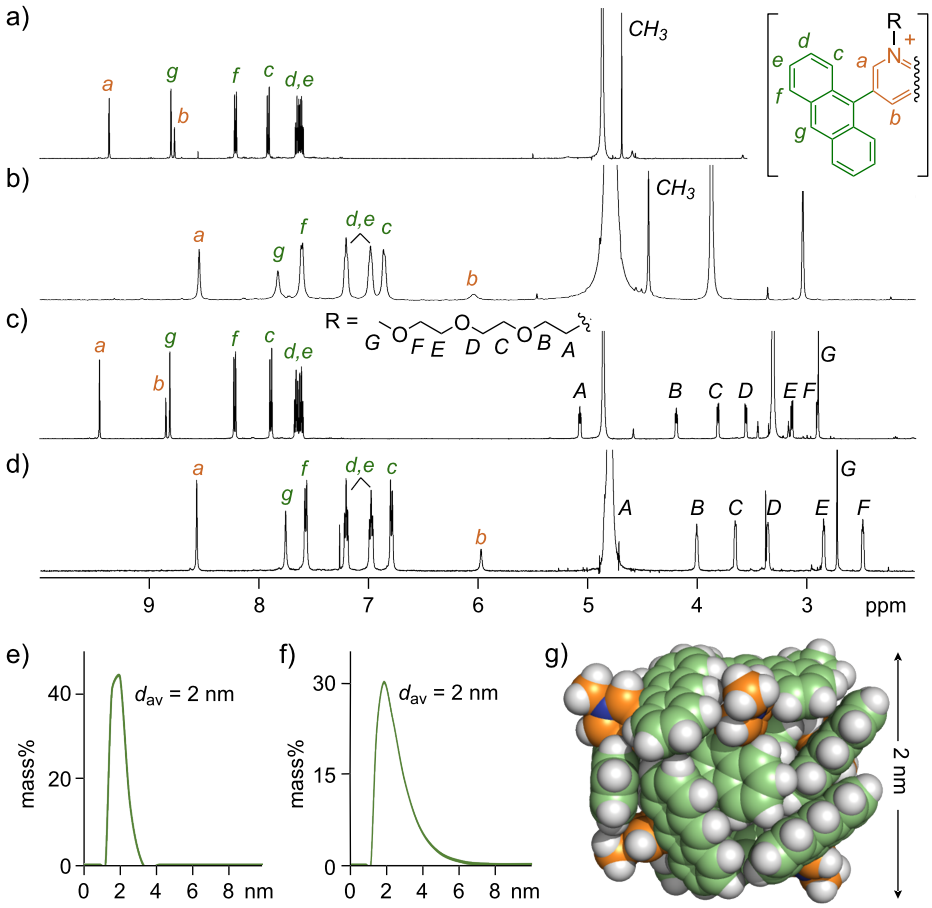

Figure 3: ^{1}H NMR spectra (500 MHz, rt, 0.5 mM and 1.0 mM based on **PA-CH$_3$** and **PA-OCH$_3$**, respectively, TMS in $CDCl_3$ as external standard) of a) **PA-CH$_3$** in CD_3OD, b) (**PA-CH$_3$**)$_n$ in D_2O, c) **PA-OCH$_3$** in CD_3OD, and d) (**PA-OCH$_3$**)$_n$ in D_2O. DLS charts (rt, H_2O, 0.5 mM and 1.0 mM based on **PA-CH$_3$** and **PA-OCH$_3$**, respectively) of e) (**PA-CH$_3$**)$_n$ and f) (**PA-OCH$_3$**)$_n$. g) Optimized structure (MM) of (**PA-CH$_3$**)$_6$.

Noncovalent encircling of various nanocarbons in water

By employing a simple grinding–sonication protocol, various nanocarbons could be efficiently solubilized in water via noncovalent encircling by newly synthesized amphiphiles **PA-R** [22]. A mixture of solid **PA-OCH$_3$** (1.7 mg, 2.7 μmol) and water-insoluble **C$_{60}$** (1.4 mg, 1.9 μmol) was manually ground for 3 min using an agate mortar and pestle (Figure 4a) [23]. Following addition of H_2O (2.7 mL), the suspension was sonicated with a probe sonicator (40 kHz, 150 W, 10 min), centrifuged (16,000*g*, 10 min), and then filtrated (200 nm pore-size membrane filter) to yield a clear brown solution containing host–guest composite (**PA-OCH$_3$**)$_n$·(**C$_{60}$**)$_m$. The UV–visible analysis clearly showed new guest-derived absorption bands around 340 nm and 420–650 nm, confirming the solubilization of **C$_{60}$** in water (Figure 4b). Similar host–guest composites were also obtained using **PA-CH$_3$**, **PA-OH**, and **PA-Im** under the same conditions. It is noteworthy that the **C$_{60}$**-solubilization efficiency varied depending on the employed **PA-R** side-chain, likely due to the difference in water-solubility of the corresponding amphiphiles. The efficiency was found to be in the order of **PA-Im** > **PA-OH** > **PA-OCH$_3$** >> **PA-CH$_3$**, as judged by the guest absorbance at 525 nm (Figure 4c). Importantly, **PA-OCH$_3$**, **PA-OH**, and **PA-Im** displayed an improved **C$_{60}$**-solubilization efficiency (up to 1.6-fold), compared to previous amphiphile **AA** bearing ionic side-chains [17]. The improvement presumably stems from the increased flexibility of the anthracene panels and decreased electrostatic repulsion between the cationic moieties, allowing for tighter and more adaptable aromatic–aromatic stacking interactions. The aliphatic amphiphile sodium dodecyl sulfate (SDS) showed a 10-times lower efficiency compared to **PA-Im** under the same conditions (Figure S38 in Supporting Information File 1). The concentration of **C$_{60}$** in the solution of (**PA-Im**)$_n$·(**C$_{60}$**)$_m$ was roughly estimated to be 0.1 mg mL^{-1}. The DLS measurement of (**PA-Im**)$_n$·(**C$_{60}$**)$_m$ displayed an average particle diameter of

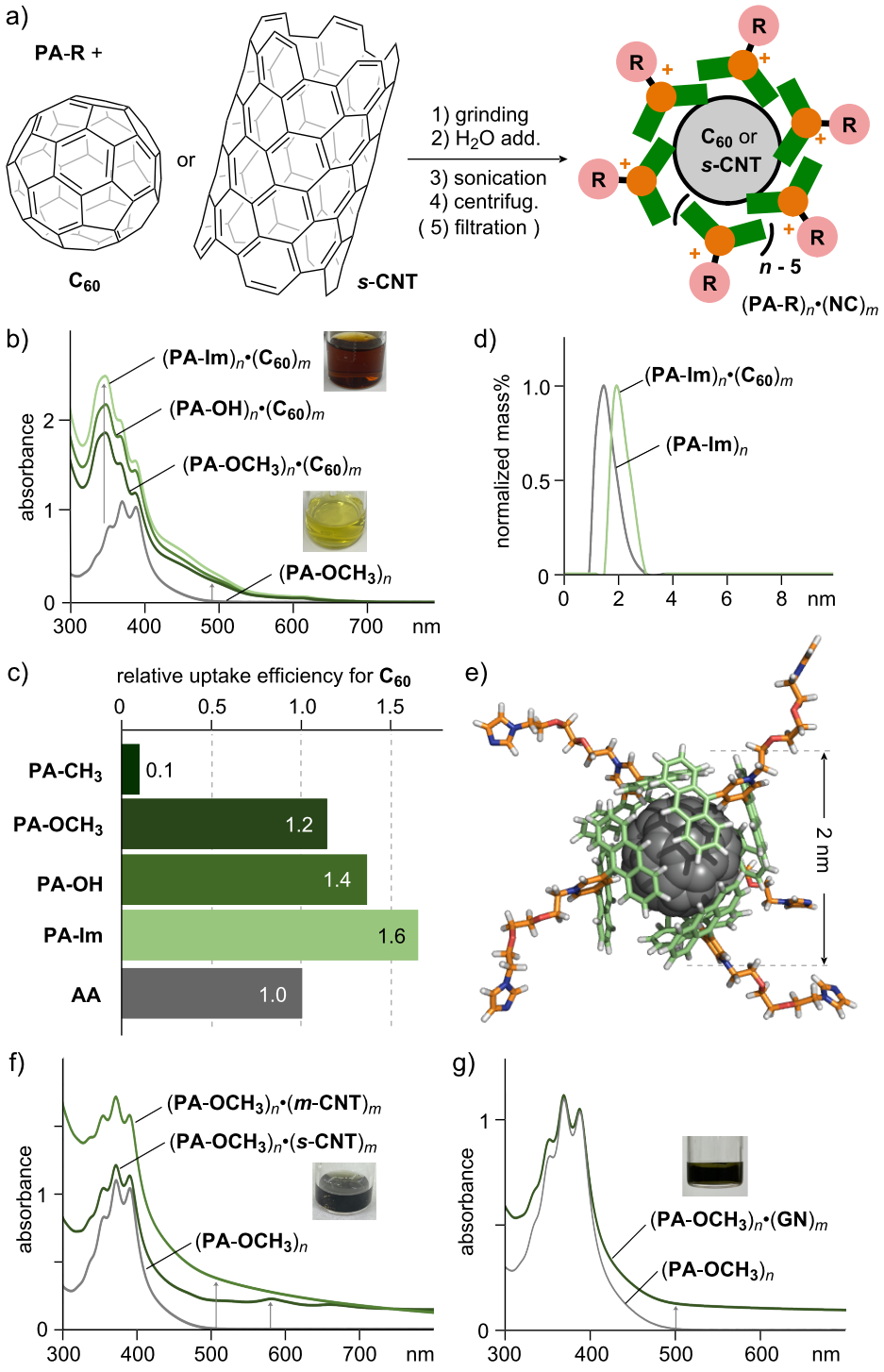

Figure 4: a) General protocol for the noncovalent encircling of C_{60} and ***s*-CNT** by **PA-R**. b) UV–visible spectra (H_2O, rt, 1.0 mM based on **PA-R**) of $(\textbf{PA-OCH}_3)_n$, $(\textbf{PA-OCH}_3)_n{\cdot}(\textbf{C}_{60})_m$, $(\textbf{PA-OH})_n{\cdot}(\textbf{C}_{60})_m$, and $(\textbf{PA-Im})_n{\cdot}(\textbf{C}_{60})_m$. c) Relative uptake efficiencies (λ_{det} = 525 nm) of C_{60} by **PA-R** and **AA**. d) DLS charts (rt, H_2O, 1.0 mM based on **PA-Im**) of $(\textbf{PA-Im})_n{\cdot}(\textbf{C}_{60})_m$ and $(\textbf{PA-Im})_n$. e) Optimized structure (MM) of $(\textbf{PA-Im})_5{\cdot}\textbf{C}_{60}$. UV–visible spectra ($H_2O$, rt, 1.0 mM based on $\textbf{PA-OCH}_3$) of f) $(\textbf{PA-OCH}_3)_n$ and $(\textbf{PA-OCH}_3)_n{\cdot}$(***s*-CNT** or ***m*-CNT**)$_m$, and g) $(\textbf{PA-OCH}_3)_n$ and $(\textbf{PA-OCH}_3)_n{\cdot}(\textbf{GN})_m$.

≈2 nm, which, in combination with molecular modeling, indicated a noncovalent surface functionalization of a single C_{60} molecule by five **PA-Im** amphiphiles (Figure 4d,e).

Besides spherical C_{60}, planar **GN** (2–10 nm thick, 5 µm wide) and tubular ***s*-CNT** and ***m*-CNT** (0.7–0.9 and 9–11 nm thick, ≥0.7 and 3–6 µm long, respectively) were also solubilized in

water using **PA-OCH$_3$** as a representative **PA-R** amphiphile, in a similar way as described above (Figure 4f,g) [23]. Due to the large size of these nanocarbons, the resultant host–guest composites were subjected to UV–visible analysis without further filtration following centrifugation (16,000*g*, ≈10 min). The obtained UV–visible spectra of the blackish, clear solutions of (**PA-OCH$_3$**)$_n$·(**GN**)$_m$, (**PA-OCH$_3$**)$_n$·(***s*-CNT**)$_m$, and (**PA-OCH$_3$**)$_n$·(***m*-CNT**)$_m$ showed broad, featureless absorption bands, with a characteristic small peak at ≈580 nm for the E_{22} transition only in the case of the ***s*-CNT** host–guest composite (Figure 4f,g) [24]. The concentration of **GN** in the aqueous solution of (**PA-OCH$_3$**)$_n$·(**GN**)$_m$ was estimated to be ≈0.03 mg mL^{-1}. Amphiphile **PA-OCH$_3$** thus enabled the efficient water-solubilization of nanocarbons independent of their size and shape (i.e., spherical, planar, and tubular objects).

Electrostatic surface properties of hosts and host–guest composites

Zeta potential (ZP) measurements were employed to further study the electrostatic surface properties of the aromatic micelles (**PA-R**)$_n$ and their host–guest composites including nanocarbons in water. The ZP of self-assembled nanoparticles evaluates their structural stability in solution against aggregation through electrostatic repulsion [25]. Solutions of the micelles in Milli-Q water (0.5 mM based on **PA-R**) gave ZPs significantly varying with the attached side-chains. Aqueous solutions of (**PA-CH$_3$**)$_n$, (**PA-OCH$_3$**)$_n$, and (**PA-OH**)$_n$ provided ZPs of 7.3 mV, 18.8 mV, and 20.3 mV, respectively, suggesting an increase in stability upon introduction of the long hydrophilic side-chains (Table 1). As expected, previous aromatic micelle (**AA**)$_n$ (1.0 mM based on **AA**) featuring multiple ionic side-chains showed a significantly higher ZP of 48.9 mV.

The ZP of (**PA-OCH$_3$**)$_n$ largely increased upon encapsulation of **C$_{60}$** (46.7 mV) and ***s*-CNT** (43.2 mV), due to the stabilization of the host–guest composites through the template effect of the hydrophobic nanocarbon guests (Table 2). Moreover, aromatic micelle (**PA-Im**)$_n$ and its host–guest composite (**PA-Im**)$_n$·(**C$_{60}$**)$_m$ were anticipated to provide pH-dependent ZPs via imidazole-based protonation/deprotonation. Micelle (**PA-Im**)$_n$ showed a significantly higher ZP (41.7 mV) compared to the other derivatives in neutral water, owing to the basic imidazole groups (Table 1). The protonation behavior of the imidazole groups on (**PA-Im**)$_n$·(**C$_{60}$**)$_m$ in D_2O (0.5 mM based on **PA-Im**) was monitored by ^{1}H NMR spectroscopy, showing significant down-field shifts of the imidazole ring protons upon addition of HCl (40 equiv based on **PA-Im**; Figure 5a,b). These properties enabled a pH-responsive surface charge of its host–guest composite (Table 2). Accordingly, (**PA-Im**)$_n$·(**C$_{60}$**)$_m$ displayed a ZP

Table 1: Zeta potentials (ZP) of aromatic micelles (**PA-R**)$_n$ and (**AA**)$_n$ [23].

aromatic micelle	ZP [mV]
(**PA-CH$_3$**)$_n$	7.3
(**PA-OCH$_3$**)$_n$	18.8
(**PA-OH**)$_n$	20.3
(**PA-Im**)$_n$	41.7
(**AA**)$_n$	48.9

Table 2: Zeta potentials of (**PA-OCH$_3$**)$_n$·(**C$_{60}$** or ***s*-CNT**)$_m$ and (**PA-Im**)$_n$·(**C$_{60}$**)$_m$ under neutral/acidic conditions [23].

	ZP [mV]	
host–guest composite	neutral	acidic
(**PA-OCH$_3$**)$_n$·(**C$_{60}$**)$_m$	46.7	47.7
(**PA-OCH$_3$**)$_n$·(***s*-CNT**)$_m$	43.2	n.d.
(**PA-Im**)$_n$·(**C$_{60}$**)$_m$	52.8	60.3

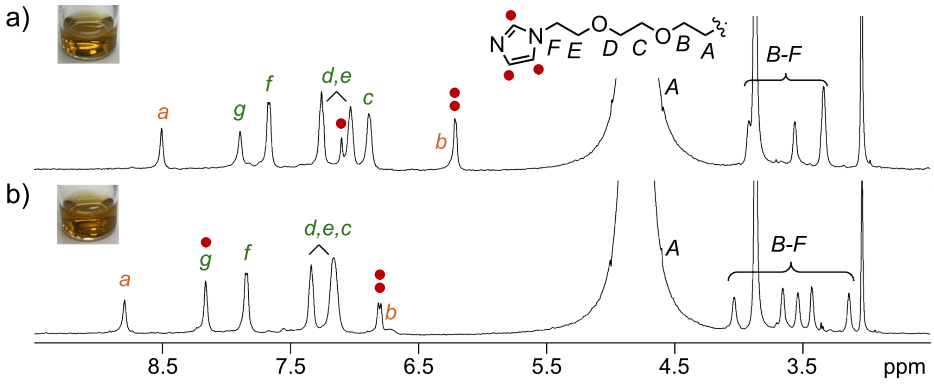

Figure 5: ^{1}H NMR spectra (500 MHz, D_2O, rt, 0.5 mM based on **PA-Im**) of (**PA-Im**)$_n$·(**C$_{60}$**)$_m$ a) before and b) after addition of 40 equiv HCl.

of 60.3 mV at pH 2.8 contrary to 52.8 mV at pH 6.8 (ΔZP = +7.5 mV) [26]. Control experiments using $(\mathbf{PA\text{-}OCH_3})_n{\cdot}(\mathbf{C_{60}})_m$ showed only a minor change in the ZP (ΔZP = +1.0 mV) under similar conditions, confirming the importance of the noncovalent imidazole functionalities [27].

Solubilization and AFM analysis of a nitrogen-doped nanocarbon

Finally, water-solubilization and aqueous processing of nitrogen-doped nanocarbon **g-C_3N_4** was achieved using aromatic micelle $(\mathbf{PA\text{-}OCH_3})_n$ (Figure 6a). The multiple N-atoms bestow **g-C_3N_4** with unique properties that are responsible for its widespread use in catalysis [28]. Subjecting yellow solid **PA-OCH_3** (1.2 mg, 1.9 μmol) and pale yellow solid **g-C_3N_4** (1.0 mg) to the grinding (3 min) and sonication (30 min) protocol provided a clear yellow aqueous solution of $(\mathbf{PA\text{-}OCH_3})_n{\cdot}(\mathbf{g\text{-}C_3N_4})_m$. The formation of the host–guest structure was confirmed by UV–visible analysis, which showed a new absorption band around 312 nm (Figure 6b). This result showcased the ability of amphiphile **PA-OCH_3** to solubilize not only conventional nanocarbons but also heteroatom-containing ones. To obtain direct structural information of the encircled $(\mathbf{g\text{-}C_3N_4})_m$, dry-state AFM measurements (on mica) were conducted using an aqueous solution of $(\mathbf{PA\text{-}OCH_3})_n{\cdot}(\mathbf{g\text{-}C_3N_4})_m$. The obtained AFM images showed large sheets with thicknesses of 10–30 nm and widths of 150–300 nm (Figure 6c,d), indicating solubilization of $(\mathbf{g\text{-}C_3N_4})_m$ as 20–60 stacks.

The encircled **g-C_3N_4**-based host–guest composite was subsequently deposited onto a mixed cellulose ester (MCE) filter (50 nm pore-size) using a simple filtration protocol (Figure 6a, right). Filtration of the aqueous solution of $(\mathbf{PA\text{-}OCH_3})_n{\cdot}(\mathbf{g\text{-}C_3N_4})_m$ and washing with water to remove **PA-OCH_3** generated a yellow solid $(\mathbf{g\text{-}C_3N_4})_m$ ($d \approx 0.5$ cm) on the filter [29]. We thus successfully demonstrated the application of $(\mathbf{PA\text{-}OCH_3})_n$ toward aqueous processing of carbon/nitrogen-rich materials.

Conclusion

We have developed new pyridinium-based bent amphiphiles **PA-R** that can be facilely accessed from simple yet novel building block 3,5-dianthrylpyridine in 1–3 steps. The amphiphiles quantitatively self-assembled into ≈2 nm-sized aromatic micelles $(\mathbf{PA\text{-}R})_n$ via the hydrophobic effect and π-stacking interactions, and displayed high stability against dilution (CMC < 0.1 mM). The molecular design allowed installation of various nonionic side-chains (i.e., CH_3 and $CH_2CH_2(OCH_2CH_2)_2$–Y (Y = OCH_3, OH, and imidazole)) via

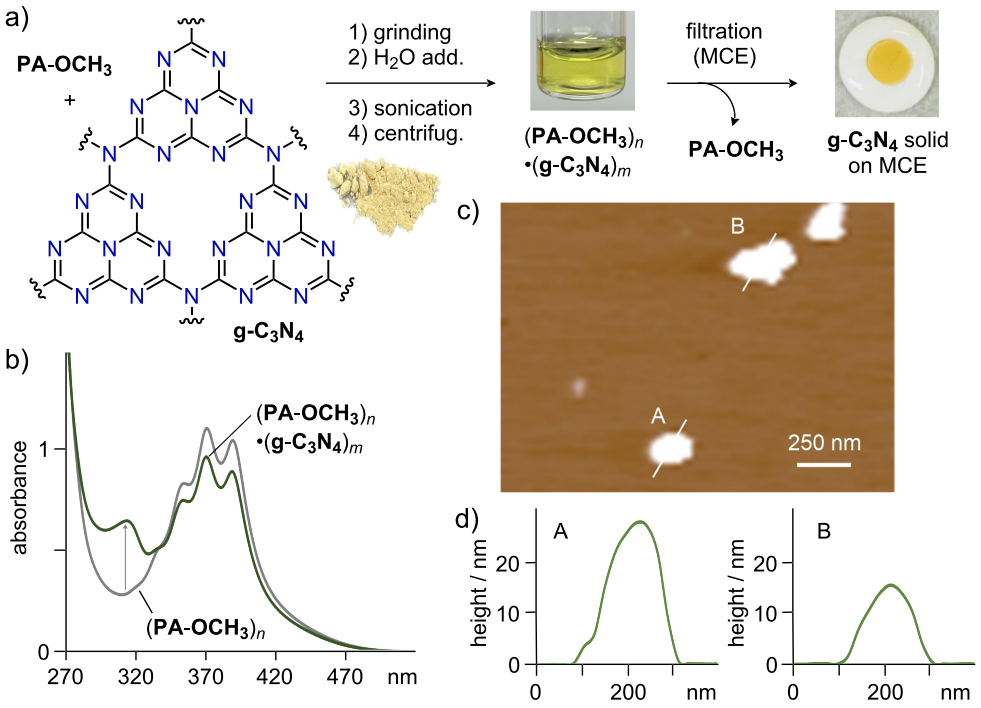

Figure 6: a) Protocol for the noncovalent encircling of **g-C_3N_4** by **PA-OCH_3** and subsequent deposit of **g-C_3N_4** on a filter. b) UV–visible spectra (H_2O, rt, 1.0 mM based on **PA-OCH_3**) of $(\mathbf{PA\text{-}OCH_3})_n$ and $(\mathbf{PA\text{-}OCH_3})_n{\cdot}(\mathbf{g\text{-}C_3N_4})_m$. c) AFM image (dry, rt, mica) of $(\mathbf{PA\text{-}OCH_3})_n{\cdot}(\mathbf{g\text{-}C_3N_4})_m$ and d) its selected size profiles.

simple *N*-alkylation, enabling the nonionic surface modification of nanocarbons via their encircling by the present amphiphiles in water. For example, utilizing the imidazole-functionalized amphiphile, an aqueous fullerene-based host–guest composite with pH-responsive surface charge was generated. In addition, water-solubilization of graphitic carbon nitride and subsequent deposition onto a filter was achieved through a simple filtration protocol. We hope that the facile access and high modularity of **PA**-**R** will promote the widespread application of aromatic micelles, an emergent new class of soft molecular host compounds [14,15,30,31].

Supporting Information

Supporting Information File 1

General information, experimental procedures, characterization data, and copies of spectra.
[https://www.beilstein-journals.org/bjoc/content/supplementary/1860-5397-20-5-S1.pdf]

Acknowledgements

Zeta potential measurements were performed with the help of Prof. Takafumi Ueno and Dr. Satoshi Abe (Tokyo Institute of Technology). We thank Takayuki Iijima and Dr. Kei Kondo for their synthetic support in this work.

Funding

This work was supported by JSPS KAKENHI (Grant No. JP22H00348/JP23K17913/JP22H05560/JP23K13760). S.A. thanks the Tokyo Tech Advanced Human Resource Development fellowship.

ORCID® iDs

Lorenzo Catti - https://orcid.org/0000-0003-0727-0620

References

1. Martín, N.; Nierengarten, J.-F., Eds. *Supramolecular Chemistry of Fullerenes and Carbon Nanotubes;* Wiley-VCH: Weinheim, Germany, 2012. doi:10.1002/9783527650125
2. Arnault, J.-C.; Eder, D., Eds. *Synthesis and Applications of Nanocarbons;* Wiley-VCH: Weinheim, Germany, 2020. doi:10.1002/9781119429418
3. Dugan, L. L.; Turetsky, D. M.; Du, C.; Lobner, D.; Wheeler, M.; Almli, C. R.; Shen, C. K.-F.; Luh, T.-Y.; Choi, D. W.; Lin, T.-S. *Proc. Natl. Acad. Sci. U. S. A.* **1997,** *94,* 9434–9439. doi:10.1073/pnas.94.17.9434
4. Georgakilas, V.; Kordatos, K.; Prato, M.; Guldi, D. M.; Holzinger, M.; Hirsch, A. *J. Am. Chem. Soc.* **2002,** *124,* 760–761. doi:10.1021/ja016954m
5. Nakashima, N.; Tomonari, Y.; Murakami, H. *Chem. Lett.* **2002,** *31,* 638–639.
6. Peng, X.; Yuan, Y.; Wang, H.; Liang, C. *J. Environ. Sci.* **2016,** *42,* 89–96. doi:10.1016/j.jes.2015.05.026
7. Yamakoshi, Y. N.; Yagami, T.; Fukuhara, K.; Sueyoshi, S.; Miyata, N. *J. Chem. Soc., Chem. Commun.* **1994,** 517–518. doi:10.1039/c39940000517
8. O'Connell, M. J.; Boul, P.; Ericson, L. M.; Huffman, C.; Wang, Y.; Haroz, E.; Kuper, C.; Tour, J.; Ausman, K. D.; Smalley, R. E. *Chem. Phys. Lett.* **2001,** *342,* 265–271. doi:10.1016/s0009-2614(01)00490-0
9. Zheng, M.; Jagota, A.; Semke, E. D.; Diner, B. A.; Mclean, R. S.; Lustig, S. R.; Richardson, R. E.; Tassi, N. G. *Nat. Mater.* **2003,** *2,* 338–342. doi:10.1038/nmat877
10. Wang, J.; Musameh, M.; Lin, Y. *J. Am. Chem. Soc.* **2003,** *125,* 2408–2409. doi:10.1021/ja028951v
11. Bai, Y.; Lin, D.; Wu, F.; Wang, Z.; Xing, B. *Chemosphere* **2010,** *79,* 362–367. doi:10.1016/j.chemosphere.2010.02.023
12. Kondo, K.; Suzuki, A.; Akita, M.; Yoshizawa, M. *Angew. Chem., Int. Ed.* **2013,** *52,* 2308–2312. doi:10.1002/anie.201208643
13. Kondo, K.; Klosterman, J. K.; Yoshizawa, M. *Chem. – Eur. J.* **2017,** *23,* 16710–16721. doi:10.1002/chem.201702519
14. Yoshizawa, M.; Catti, L. *Acc. Chem. Res.* **2019,** *52,* 2392–2404. doi:10.1021/acs.accounts.9b00301
15. Yoshizawa, M.; Catti, L. *Proc. Jpn. Acad., Ser. B* **2023,** *99,* 29–38. doi:10.2183/pjab.99.002
16. Kondo, K.; Akita, M.; Nakagawa, T.; Matsuo, Y.; Yoshizawa, M. *Chem. – Eur. J.* **2015,** *21,* 12741–12746. doi:10.1002/chem.201501414
17. Wang, Y.; Kai, H.; Ishida, M.; Gokulnath, S.; Mori, S.; Murayama, T.; Muranaka, A.; Uchiyama, M.; Yasutake, Y.; Fukatsu, S.; Notsuka, Y.; Yamaoka, Y.; Hanafusa, M.; Yoshizawa, M.; Kim, G.; Kim, D.; Furuta, H. *J. Am. Chem. Soc.* **2020,** *142,* 6807–6813. doi:10.1021/jacs.0c01824
18. Tsuchida, Y.; Aratsu, K.; Hiraoka, S.; Yoshizawa, M. *Angew. Chem., Int. Ed.* **2021,** *60,* 12754–12758. doi:10.1002/anie.202101453
19. Catti, L.; Narita, H.; Tanaka, Y.; Sakai, H.; Hasobe, T.; Tkachenko, N. V.; Yoshizawa, M. *J. Am. Chem. Soc.* **2021,** *143,* 9361–9367. doi:10.1021/jacs.0c13172
20. Liu, S.-Y.; Kishida, N.; Kim, J.; Fukui, N.; Haruki, R.; Niwa, Y.; Kumai, R.; Kim, D.; Yoshizawa, M.; Shinokubo, H. *J. Am. Chem. Soc.* **2023,** *145,* 2135–2141. doi:10.1021/jacs.2c08795
21. Aoyama, S.; Catti, L.; Yoshizawa, M. *Angew. Chem., Int. Ed.* **2023,** *62,* e202306399. doi:10.1002/anie.202306399
22. Besides nanocarbons, **PA**-**R** amphiphiles also allowed the water-solubilization of hydrophobic dyes (Figure S46 in Supporting Information File 1).
23. See Supporting Information File 1. While water-solubilization of $\mathbf{C_{60}}$ by **PA**-**R** is also possible using only grinding, sonication improves the efficiency. Zeta potential measurements were conducted using Milli-Q H_2O at room temperature at 0.5 mM or 1.0 mM concentration based on **PA**-**R** or **AA**, respectively.
24. Bachilo, S. M.; Strano, M. S.; Kittrell, C.; Hauge, R. H.; Smalley, R. E.; Weisman, R. B. *Science* **2002,** *298,* 2361–2366. doi:10.1126/science.1078727
25. White, B.; Banerjee, S.; O'Brien, S.; Turro, N. J.; Herman, I. P. *J. Phys. Chem. C* **2007,** *111,* 13684–13690. doi:10.1021/jp070853e
26. The stability of $(\mathbf{PA\text{-}Im})_n{\cdot}(\mathbf{C_{60}})_m$ under acidic conditions was confirmed by UV–visible analysis (Figure S39 in Supporting Information File 1).
27. Preliminary tests indicated the metal-coordination abilities of $(\mathbf{PA\text{-}Im})_n{\cdot}(\mathbf{C_{60}})_m$ toward $PdCl_2(CH_3CN)_2$ in water [23].

28. Zhao, Z.; Sun, Y.; Dong, F. *Nanoscale* **2015,** *7,* 15–37. doi:10.1039/c4nr03008g
29. In a similar way, free-standing ***m*-CNT** films were obtained from (**PA-OCH$_3$**)$_n$·(***m*-CNT**)$_m$ after dissolution of the MCE membrane filter in acetone.
30. Toyama, K.; Tanaka, Y.; Yoshizawa, M. *Angew. Chem., Int. Ed.* **2023,** *62,* e202308331. doi:10.1002/anie.202308331
31. Hashimoto, Y.; Katagiri, Y.; Tanaka, Y.; Yoshizawa, M. *Chem. Sci.* **2023,** *14,* 14211–14216. doi:10.1039/d3sc04613c

License and Terms

BEILSTEIN JOURNAL OF ORGANIC CHEMISTRY

Preparing a liquid crystalline dispersion of carbon nanotubes with high aspect ratio

Keiko Kojima[1], Nodoka Kosugi[1,2], Hirokuni Jintoku[1], Kazufumi Kobashi[1] and Toshiya Okazaki[*1,2]

Full Research Paper

Open Access

Address:
[1]Nano Carbon Device Research Center, National Institute of Advanced Industrial Science and Technology (AIST), 1-1-1 Higashi, Tsukuba 305-8565, Japan and [2]Department of Chemistry, University of Tsukuba, 1-1-1 Tennodai, Tsukuba 305-8571, Japan

Email:
Toshiya Okazaki[*] - toshi.okazaki@aist.go.jp

* Corresponding author

Keywords:
aqueous dispersion; bar-coating; carbon nanotube; coffee-ring effect; liquid crystal

Beilstein J. Org. Chem. **2024,** *20,* 52–58.
https://doi.org/10.3762/bjoc.20.7

Received: 15 October 2023
Accepted: 29 December 2023
Published: 11 January 2024

This article is part of the thematic issue "Carbon-rich materials: from polyaromatic molecules to fullerenes and other carbon allotropes".

Guest Editor: Y. Yamakoshi

Abstract

We successfully prepared a surfactant-assisted carbon nanotube (CNT) liquid crystal (LC) dispersion with double-walled CNTs (DWCNTs) having a high aspect ratio (≈1378). Compared to dispersions of single-walled CNTs (SWCNTs) with lower aspect ratio, the transition concentrations from isotropic phase to biphasic state, and from biphasic state to nematic phase are lowered, which is consistent with the predictions of the Onsager theory. An aligned DWCNT film was prepared from the DWCNT dispersion by a simple bar-coating method. Regardless of the higher aspect ratio, the order parameter obtained from the film is comparable to that from SWCNTs with lower aspect ratios. This finding implies that precise control of the film formation process, including a proper selection of substrate and deposition/drying steps, is crucial to maximize the CNT-LC utilization.

Introduction

Carbon nanotubes (CNTs) are cylindrical carbon structures with high electrical conductivity and tensile strength in the direction of the tube, anticipated as durable and highly conductive fibers. However, the properties of produced fibers are often inferior to the inherent properties of CNTs. For instance, the wet-spinning method has resulted in CNT fibers with electrical conductivity up to 109,000 S/cm [1], which is about 1/4 that of Al, while individual single-walled CNTs (SWCNTs) have been estimated to have a conductivity of 900,000 S/cm [2]. The electrical conductivity of CNT fibers is primarily determined by the density of the fibers and the length of their constituent CNTs [3,4]. Therefore, enhancing CNT alignment is crucial for producing CNT fibers to endow inherent CNT properties, as greater alignment leads to higher density and consequently improved electrical conductivity.

One effective technique for producing high-performance wet-spun CNT fibers is to utilize liquid crystal (LC) CNT aqueous

dispersions as spinning dopes [1,5-10]. The CNT LCs are formed by condensing the dispersed rod-like CNTs, either isolated or bundled [5,7,9-23]. In previous studies, we prepared surfactant-stabilized aqueous dispersions of SWCNT LC and evaluated their dispersion states using the differential centrifugal sedimentation (DCS) method [22,23]. The transition concentrations from the isotropic phase to the biphasic state, and from the biphasic state to the nematic phase were inversely proportional to the aspect ratio (*L*/*D*) of the SWCNT, following the same trend as the Onsager theory [7,9,11,15,20,23,24]. By using dispersions with higher SWCNT aspect ratio, a film of SWCNTs with a higher order parameter was prepared by the bar-coating method [23]. Therefore, it is essential to prepare CNT LCs that contain rod-like CNTs with a high *L*/*D* to fabricate well-ordered CNT materials.

Here, stable double-walled CNT (DWCNT) LC dispersions with a higher *L*/*D* were successfully prepared utilizing highly crystalline DWCNTs. Indeed, the transition concentrations from the isotropic phase to the biphasic coexisting state and from the biphasic coexisting state to the nematic phase were found to be lower than those in the previous study. In addition, the shapes of the spindle-shaped nematic LC, or so-called tactoids, in the biphasic state were examined. The transition from homogeneous tactoids to bipolar tactoids occurred at a larger tactoid volume than that previously observed [23]. This can be ascribed to the higher *L*/*D* of the DWCNTs in this study. On the other hand, despite higher *L*/*D*, the CNT orientation in the film prepared from the dispersion was comparable to the previous study. This suggests that further optimization of the deposition process is necessary to create highly oriented CNT films.

Results and Discussion

To prepare carbon nanotube dispersions with high aspect ratios, we utilized DWCNTs obtained from Shenzhen Nanotech Port Co. Ltd. Supporting Information File 1 provides characterization details. Briefly, the Raman G/D ratio was approximately 37 (Supporting Information File 1, Figure S1d), indicating high crystallinity [25]. The far-infrared spectrum exhibited a plateau in the lower wavenumber region around 12 cm^{-1}, suggesting that a significant amount of DWCNTs have effective lengths (CNT channels consisted of some condutive paths affected by defects or kinks) longer than 4 μm (Supporting Information File 1, Figure S1e) [26].

The DWCNT powder was dispersed with a surfactant of sodium cholate (SC) in water by a two-step process [22,23] (see the Experimental section). The size distribution of the DWCNTs in the dispersion was estimated by DCS method (Figure 1a). The observed intense peak at approximately 9 nm suggests that DWCNTs were mainly dispersed as isolated or bundle forms based on the previous studies [22,23]. Besides, DCS analysis also identified a smaller peak at around 0.1 μm (Figure 1a, inset). The signal can be attributed to DWCNT agglomerates that are 10 μm in size, taking into account the buoyancy resulting from particle porosity [22,23,27,28]. Indeed, the DWCNT agglomerates having corresponding size can be seen in the optical microscope image of the dispersion (Figure 1b).

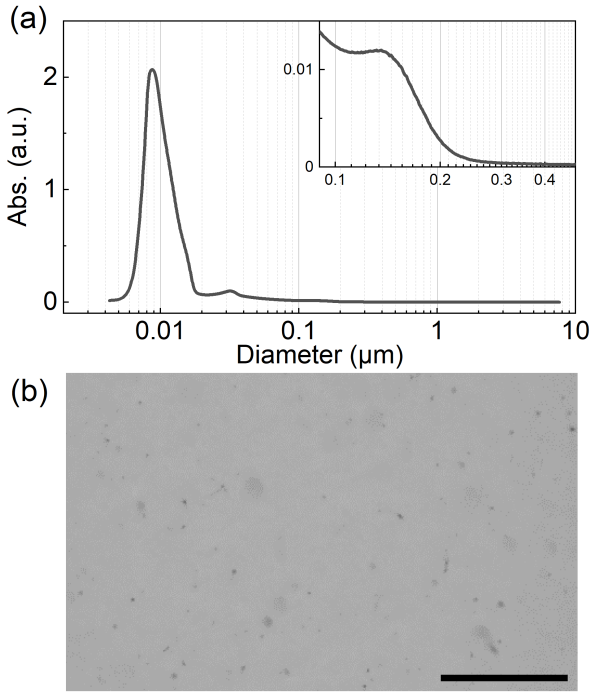

Figure 1: (a) Size distribution of DWCNTs in dispersion by DCS measurements. (b) Optical microscopy image of the DWCNT dispersion. Scale bar is 100 μm.

The shapes of DWCNTs in the dispersion were examined by scanning electron microscopy (SEM) and atomic force microscopy (AFM) (see Supporting Information File 1, Figure S2). In both images, rod-like DWCNTs were observed, while spaghetti-like agglomerates were hardly observed. The average length (*L*) and diameter (*D*) of the DWCNT samples were ≈2.9 μm and ≈2.1 nm, respectively. The *L*/*D* of the DWCNTs was 1378, which was larger than the value reported in previous research (*L*/*D* = 1088) [23]. Based on the transmission electron microscope (TEM) images, the average diameter of DWCNTs was ≈1.8 nm (Supporting Information File 1, Figure S1a). Since the observed DWCNT diameter based on the SEM images is ≈2.1 nm, the dispersion is likely composed mostly of isolated DWCNTs.

To investigate the liquid crystal behavior, the DWCNT dispersion was concentrated by ultra-filtration (Figure 2a). As the concentration of DWCNTs increased, the isotropic phases

(Figure 2d, the DWCNT concentration = 0.078 vol %) changed to the nematic phase (Figure 2b, the DWCNT concentration = 0.41 vol %). At intermediate concentrations, biphasic states appeared where the nematic droplets, tactoid, coexisted in the isotropic phase (Figure 2c, the DWCNT concentration = 0.16 vol %) [15,17,22,23,29,30]. The nematic phase shows disturbed textures similar to the previously reported SWCNTs in sodium deoxycholate (SDOC) and sodium taurodeoxycholate (TDOC) aqueous dispersions [23]. The average diameter of DWCNTs in the present study was 2.1 nm, which was almost the same as that of SWCNTs in SDOC and TDOC [23]. Thus, the effect of stiffness of DWCNTs does not seem to affect the domain size of LC very much.

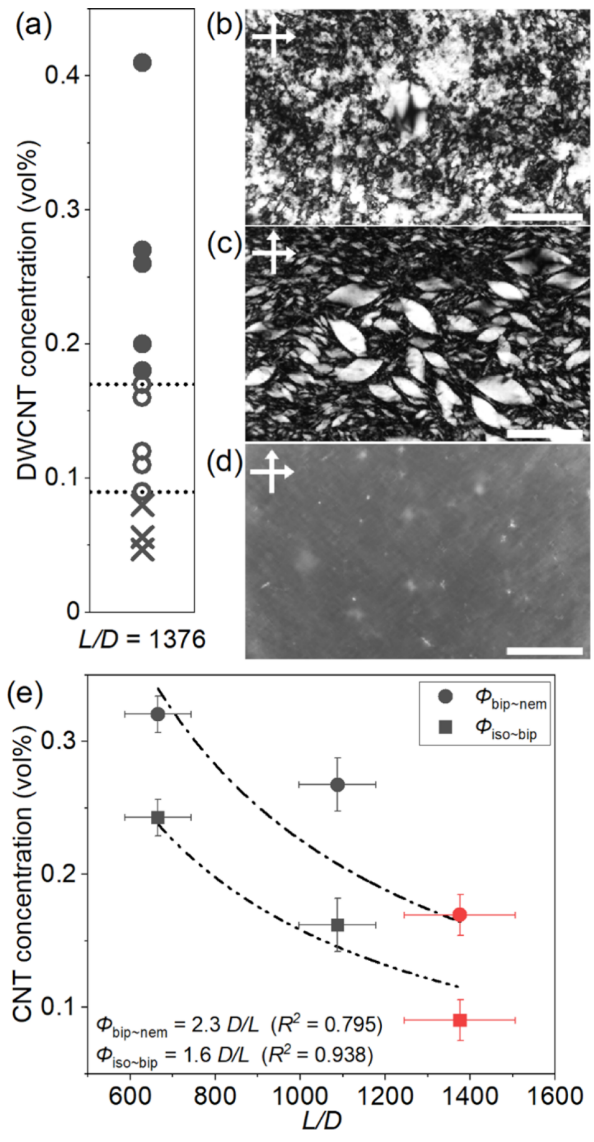

Figure 2: (a) Phase diagram of the DWCNT dispersion. The nematic phase, biphasic state and isotropic phase are marked by filled circle, open circle and cross mark, respectively. (b-d) POM images of the dispersions. DWCNT concentrations are (b) 0.41 vol %, (c) 0.16 vol % and (d) 0.078 vol %. Scale bars are 200 µm. (e) The plot of the phase transition concentration against the CNT aspect ratio *L*/*D* of three CNT-SC aqueous dispersions [22,23]. Dashed lines indicate the results of curve fitting by inverse function in each phase transition, from isotropic phase to biphasic state and from biphasic state to nematic phase.

The phase transition concentrations from isotropic phase to biphasic state, $\phi_{iso\sim bip}$, and from biphasic state to nematic phase, $\phi_{bip\sim nem}$, were estimated by sigmoid curve fitting. The values were found to be 0.090 vol % and 0.17 vol %, respectively, as shown in Supporting Information File 1, Figure S3, which were lower than those previously obtained in the surfactant-assisted SWCNT aqueous dispersions [22,23]. Figure 2e shows the phase transition concentrations obtained in this study (L/D = 1378, red symbols) together with the previously obtained values for the SWCNT-SC dispersions (L/D = 1088 and = 665, black symbols) [22,23]. The Onsager theory predicts that the phase transition concentration for rod-like particles with aspect ratio L/D is $\phi_{iso\sim bip} = 3.34\ D/L$ and $\phi_{bip\sim nem} = 4.49\ D/L$ [24]. The L/D dependence of each phase transition concentration shows the inverse proportional relationship.

On the other hand, the surface charge is an important factor for the transition concentrations. In fact, the surfactant dependence can be explained by this effect [23]. The ζ-potential of the DWCNTs was −52.3 ± 0.77 mV (Supporting Information File 1, Figure S4), the repulsive force between the DWCNTs was slightly larger than the previously reported SWCNT-SC dispersions [23]. Although the lower ζ-potential of the DWCNT-SC should lead to higher transition concentration, those of DWCNT-SC were slightly lower than expected based on the fitting curve (Figure 2e). This indicates that the L/D had a greater impact on the transition concentrations than the ζ-potential.

In the biphasic state, the spindle nematic phase droplets, tactoids, were observed (Figure 2c). These were classified into two types depending on the orientation of the DWCNT [22,23,29,30]. If the DWCNTs align parallel to the long axis of the spindle droplet, it is referred to as a homogenous tactoid. Conversely, if the DWCNTs align from one pole to another, it is called a bipolar tactoid. Figure 3 illustrates the aspect ratio of the tactoids (R/r) as a function of the tactoid volume (Rr^2). We analyzed 100 tactoids in this study. The homogenous tactoids transformed into bipolar tactoids during the volume growth at around $Rr^2 = 15310\ \mu m^3$ (dashed line in Figure 3, and Supporting Information File 1, Figure S5). Previous research has shown that the transition volume of tactoids increases with larger L/D ratios of the SWCNTs [23]. The findings in this study align with these previous results, as the tactoid transition volume and DWCNT aspect ratio were larger compared to previous SWCNT-SC dispersions [23].

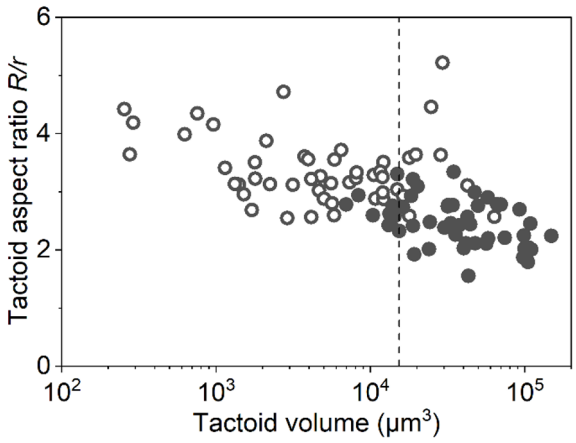

Figure 3: Observed tactoid aspect ratio R/r as a function of tactoid volume Rr^2. Filled circle and open circle indicate bipolar tactoid and homogenous tactoid respectively. Dashed line denotes the estimated transition volume from homogenous to bipolar tactoids (=15310 μm^3).

A thin film was produced utilizing a bar-coating method with DWCNT LC dispersion. The polarizing optical microscopy (POM) images exhibited alignment of the DWCNTs along the shear direction (Figure 4a,b). To estimate the order parameter, the polarized optical absorption measurement was conducted at different sample angles ranging from 0° to 90° at intervals of 10° (Figure 4c). The sample rotation led to gradual changes in absorption intensities, and the average order parameter was calculated to be ≈0.23 from the spectra of 0° ($A_{\parallel}$) and 90° ($A_{\perp}$) using Equation 1 [21,23].

$$S = \frac{A_{\parallel} - A_{\perp}}{A_{\parallel} + 2A_{\perp}} \quad (1)$$

Generally, it is anticipated that rod-shaped particles with larger L/D will produce a highly aligned film [23,31,32]. However, the value obtained is almost identical to the previous ones with SWCNTs having a smaller L/D (≈0.22) [23]. Figure 4d shows a typical SEM image of the prepared DWCNT film. One μm wide DWCNT bundles on the film's surface align along the shear direction, while the remaining DWCNTs beneath the thick bundles form mesh-like structures. The shear force exerted by the bar may not sufficiently align the DWCNTs located near the substrate. Thus, optimizing the interaction between the DWCNTs and substrate is necessary to improve the alignment.

To further investigate the low alignment, the film thickness was analyzed by laser confocal microscopy (Figure 5a, Table 1). The average thickness was ≈393 nm, whereas the edge of the film was much thicker (≈999 nm). In earlier studies, the CNTs

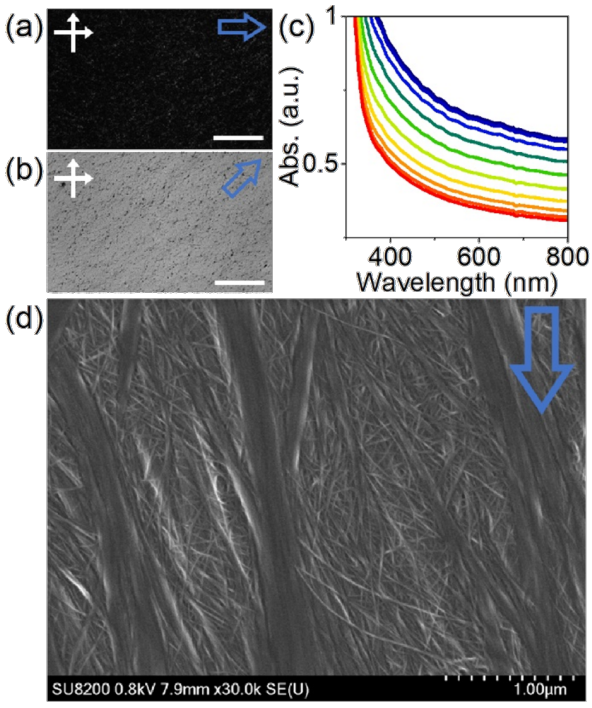

Figure 4: (a, b) POM images of the DWCNT film at (a) 0° and (b) 45° under crossed polarizers (white double arrows). Scale bars are 400 μm. (c) Polarized optical absorption spectra with different angles ranging from 0° (red) to 90° (blue). The sear direction and polarizer are parallel at 0°. (d) SEM image of the DWCNT film. Blue outlined arrows indicate the shear direction of bar-coating.

in the dispersions were observed to flow and accumulate along the droplet's edge due to the coffee ring effect [15,33,34]. As a result, the volume fraction of DWCNTs at the edge increased. Notably, the widths of bundled DWCNTs at the edge were larger than in the inner region (Figure 5b,c). The direction of the bundled DWCNTs near the film surface were parallel to the shear direction in both regions. Due to the randomly oriented DWCNTs beneath the surface, the densification of aligned DWCNTs toward the edge region could account for the similar orientation degree to the previous lower L/D SWCNT film [23]. To obtain highly aligned CNT films, the condition of drying step [33], the surfactant concentration of the dispersion, the materials of the substrate [34], and the viscosity of the dispersions should be adjusted. For instance, Headrick et al. fabricated highly aligned films by immersing the substrate in a solidifying solution immediately after the SWCNTs were aligned by applying shear stress to the dispersion [35].

Conclusion

We here investigated the LC behavior of the rod-like DWCNTs having a high L/D. Because the aspect ratio was 1.3 times larger than that of the low L/D SWCNTs, the phase transition concentrations, $\phi_{iso\sim bip}$ and $\phi_{bip\sim nem}$ became lower than those re-

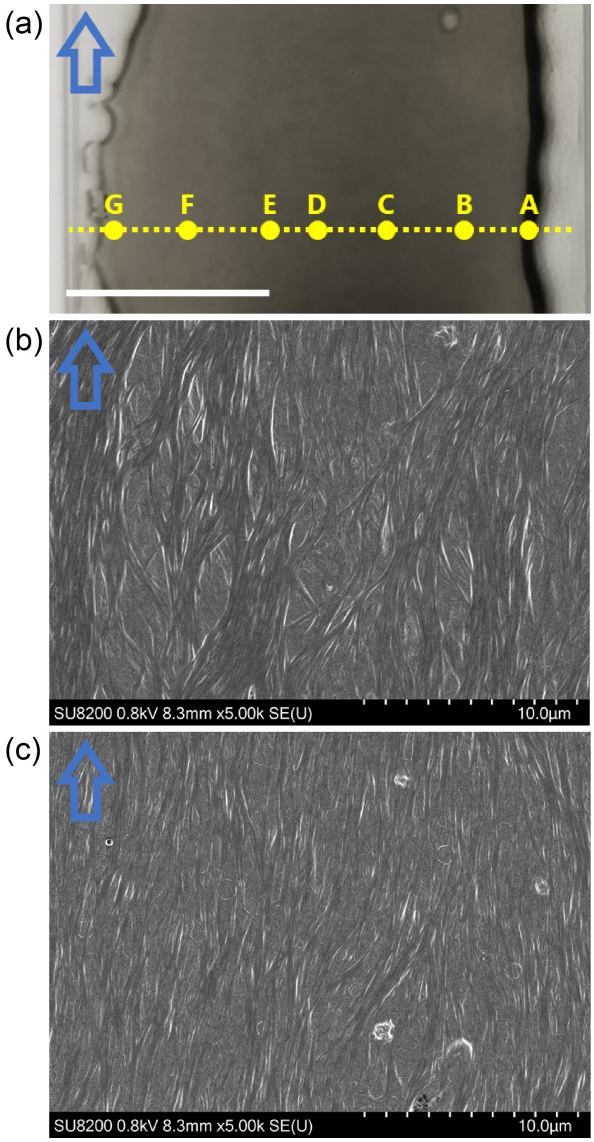

Figure 5: (a) Photograph of the DWCNT film. Thicknesses were measured at 7 spots along the yellow dashed line. Scale bar is 1 cm. SEM image at spot (b) A and (c) D. Blue outlined arrows indicate the shear direction of bar-coating.

Table 1: The list of the thickness at each spot in Figure 5a.

Spot	Thickness [nm]
A	999
B	339
C	320
D	343
E	301
F	252
G	200

ported previously, which is consistent with the Onsager theory. On the other hand we found that the order parameter of the DWCNT film, obtained from the LC dispersion, was nearly identical to that of the film composed of lower *L*/*D* SWCNTs [23]. Further optimization of experimental conditions, including viscosity of the dispersion and substrate, is necessary to fully utilize CNT-LC dispersions.

Experimental

Characterization of DWCNT

DWCNTs were purchased from Shenzhen Nanotech Port Co. Ltd. (NTP9112, Product Number DW220817). For the transmission electron microscope observations (Topcon Corporation, EM-002B), DWCNTs were suspended in acetone using a bath-type sonicator and were put onto a copper grid with carbon mesh. To perform thermogravimetric analysis (TGA), a TG/DTA7300 instrument from SII Nano Technology Inc. was utilized. The DWCNT powder was preheated at 180 °C for ten minutes under vacuum and subsequently measured under flowing air (200 mL/min) at a ramping rate of 1 °C/min. The Raman and absorption spectra were obtained from DWCNT thin film on a silicon substrate. The DWCNT thin film was prepared using vacuum filtration. Raman measurements were conducted using a HORIBA T64000 532 nm laser, while far-infrared (FIR) absorption measurements were carried out using a Fourier-transform infrared spectroscopy (Bruker, VERTEX 80v) and a THz time domain spectroscopy (THz-TDS) system (Otsuka Electronics, TR-1000).

Preparation of the DWCNT dispersion

The dispersion of DWCNTs was prepared using a two-step process in accordance with previous studies [22,23]. Initially, 100 mg of DWCNT powder was pre-dispersed in 100 mL of Wako glycerol with a stirrer (ASONE, HPS-100PD) rotating at 500 rpm for 18 hours. During the stirring, the DWCNTs were defibrated by the shear stress of the high-viscosity glycerol [36]. After suspension in 200 mL of water, the DWCNT-glycerol mixture was filtered through a 1.0 μm pore size polytetrafluoroethylene (PTFE) membrane (Merck, Omnipore 47mm). To ensure complete removal of glycerol from the DWCNTs, we repeated the washing process until 2 L of water had passed through the membrane, resulting in the formation of a DWCNT wet cake. In the second step, the cake was placed in a 50 mL solution of 10 mg/mL sodium cholate (SC) (Wako) and sonicated for 50 minutes using a 500 W tip-type sonicator (Sonics, VCX500) with a titanium alloy tip (TI-6AL-4V). Centrifugation at 4,000*g* for 30 minutes (KOKUSAN, H-36) and then 20,000*g* for 20 minutes (Hitachi-Koki, CS100GXII) effectively removed the large DWCNT agglomerates and impurities remaining in the dispersion. The dispersion states of DWCNTs were assessed using optical microscopy (OLYMPUS, DSX510)

and differential centrifugal sedimentation (DCS) analysis (CPS Instruments, CPS 24000UHR (CR-39)). The shape and size of the DWCNTs in dispersion were observed by settling them on a silicon substrate, washed with acetone, and exposed to UV light for 20 minutes using an ozone cleaner (Meiwafosis, PC-450 plus) via dip-coating. The structures of DWCNTs were examined using scanning electron microscopy (SEM) (HITACHI High-Tech, SU8200) and atomic force microscopy (AFM) (OLYMPUS, OLS-4500). Additionally, the ζ-potential of the DWCNTs was determined by measuring the ζ potential analyzer (Malvern Panalytical, ZETASIZER Pro Red label) in a disposable cell (Malvern Panalytical, DTS1070).

Concentration of the DWCNT dispersion and measurement of liquid crystal phase transitions

The DWCNT dispersion was concentrated by a centrifugal ultrafiltration method (SARTORIUS, VIVASPIN Turbo 15, molecular weight cut-off (MWCO) = 3,000 Da). The value of MWCO was chosen to eliminate only SC and water molecules. The DWCNT dispersion was repeatedly subjected to centrifugation at 1,000*g* for 5 minutes (KOKUSAN H-36) and stirred with a pipette to prevent DWCNT re-aggregation, resulting in the production of the condensed DWCNT dispersion. The dispersions' concentrations were adjusted by adding 10 mg/mL of SC aqueous solution and then estimated from the optical absorption intensity at 750 nm by using a Shimazu UV-3100 spectrometer. Subsequently, each dispersion was enclosed within a Vitro TubeTM 5012-050 glass capillary (cavity size: 0.1 mm × 2 mm × 50 mm) from VITROCOM, and the edges were sealed by UV resin. After the samples were left for one week, the liquid phases were observed using an OLYMPUS BX51 polarized optical microscope (POM).

Preparation and characterization of DWCNT film

The DWCNT film was prepared from the dispersion with nematic phase by bar-coating method. Initially, the glass slide was washed with acetone and then irradiated with UV light for a duration of 1 hour via an ozone cleaner (Meiwafosis, PC-450 plus). Later, the substrate was coated using a bar coater (OSG SYSTEM PRODUCTS Co., LTD, Select-Roller L60, OSP-10 (bar groove pitch: 0.2 mm, depth: 24 μm)) with the dispersion. The specimen was air-dried until the film was completely dried. The DWCNT orientations of the film were observed by POM (OLYMPUS, BX51) and SEM (HITACHI High-Tech, SU8200). The degree of alignment was determined through analysis of the polarized optical absorption spectra by a Jasco V-770 spectrometer. The film's thicknesses were measured using a laser confocal microscope (OLYMPUS, OLS-4500).

Supporting Information

Supporting Information File 1

Additional experimental information and figures.
[https://www.beilstein-journals.org/bjoc/content/supplementary/1860-5397-20-7-S1.pdf]

Acknowledgements

The authors thank Dr. Y. Kuwahara (AIST), Dr. M. Aizawa (Tokyo Institute of Technology), Dr. T. Yamamoto (AIST), Dr. S. Muroga (AIST), Dr. H. Kihara (AIST) and Dr. N. Koumura (AIST) for their helpful discussions.

ORCID® iDs

Keiko Kojima - https://orcid.org/0000-0003-3498-3140
Hirokuni Jintoku - https://orcid.org/0000-0001-5009-0663
Kazufumi Kobashi - https://orcid.org/0000-0002-7122-7638
Toshiya Okazaki - https://orcid.org/0000-0002-5958-0148

Preprint

A non-peer-reviewed version of this article has been previously published as a preprint: https://doi.org/10.3762/bxiv.2023.44.v1

References

1. Taylor, L. W.; Dewey, O. S.; Headrick, R. J.; Komatsu, N.; Peraca, N. M.; Wehmeyer, G.; Kono, J.; Pasquali, M. *Carbon* **2021,** *171,* 689–694. doi:10.1016/j.carbon.2020.07.058
2. Kong, J.; Zhou, C.; Morpurgo, A.; Soh, H. T.; Quate, C. F.; Marcus, C.; Dai, H. *Appl. Phys. A: Mater. Sci. Process.* **1999,** *69,* 305–308. doi:10.1007/s003390051005
3. Tajima, N.; Watanabe, T.; Morimoto, T.; Kobashi, K.; Mukai, K.; Asaka, K.; Okazaki, T. *Carbon* **2019,** *152,* 1–6. doi:10.1016/j.carbon.2019.05.062
4. Watanabe, T.; Yamazaki, S.; Yamashita, S.; Inaba, T.; Muroga, S.; Morimoto, T.; Kobashi, K.; Okazaki, T. *Nanomaterials* **2022,** *12,* 593. doi:10.3390/nano12040593
5. Davis, V. A.; Ericson, L. M.; Parra-Vasquez, A. N. G.; Fan, H.; Wang, Y.; Prieto, V.; Longoria, J. A.; Ramesh, S.; Saini, R. K.; Kittrell, C.; Billups, W. E.; Adams, W. W.; Hauge, R. H.; Smalley, R. E.; Pasquali, M. *Macromolecules* **2004,** *37,* 154–160. doi:10.1021/ma0352328
6. Ericson, L. M.; Fan, H.; Peng, H.; Davis, V. A.; Zhou, W.; Sulpizio, J.; Wang, Y.; Booker, R.; Vavro, J.; Guthy, C.; Parra-Vasquez, A. N. G.; Kim, M. J.; Ramesh, S.; Saini, R. K.; Kittrell, C.; Lavin, G.; Schmidt, H.; Adams, W. W.; Billups, W. E.; Pasquali, M.; Hwang, W.-F.; Hauge, R. H.; Fischer, J. E.; Smalley, R. E. *Science* **2004,** *305,* 1447–1450. doi:10.1126/science.1101398
7. Davis, V. A.; Parra-Vasquez, A. N. G.; Green, M. J.; Rai, P. K.; Behabtu, N.; Prieto, V.; Booker, R. D.; Schmidt, J.; Kesselman, E.; Zhou, W.; Fan, H.; Adams, W. W.; Hauge, R. H.; Fischer, J. E.; Cohen, Y.; Talmon, Y.; Smalley, R. E.; Pasquali, M. *Nat. Nanotechnol.* **2009,** *4,* 830–834. doi:10.1038/nnano.2009.302

8. Behabtu, N.; Young, C. C.; Tsentalovich, D. E.; Kleinerman, O.; Wang, X.; Ma, A. W. K.; Bengio, E. A.; ter Waarbeek, R. F.; de Jong, J. J.; Hoogerwerf, R. E.; Fairchild, S. B.; Ferguson, J. B.; Maruyama, B.; Kono, J.; Talmon, Y.; Cohen, Y.; Otto, M. J.; Pasquali, M. *Science* **2013,** *339,* 182–186. doi:10.1126/science.1228061
9. Maillaud, L.; Headrick, R. J.; Jamali, V.; Maillaud, J.; Tsentalovich, D. E.; Neri, W.; Bengio, E. A.; Mirri, F.; Kleinerman, O.; Talmon, Y.; Poulin, P.; Pasquali, M. *Ind. Eng. Chem. Res.* **2018,** *57,* 3554–3560. doi:10.1021/acs.iecr.7b03973
10. Headrick, R. J.; Williams, S. M.; Owens, C. E.; Taylor, L. W.; Dewey, O. S.; Ginestra, C. J.; Liberman, L.; Ya'akobi, A. M.; Talmon, Y.; Maruyama, B.; McKinley, G. H.; Hart, A. J.; Pasquali, M. *Sci. Adv.* **2022,** *8,* 10.1126/sciadv.abm3285. doi:10.1126/sciadv.abm3285
11. Badaire, S.; Zakri, C.; Maugey, M.; Derré, A.; Barisci, J. N.; Wallace, G.; Poulin, P. *Adv. Mater. (Weinheim, Ger.)* **2005,** *17,* 1673–1676. doi:10.1002/adma.200401741
12. Rai, P. K.; Pinnick, R. A.; Parra-Vasquez, A. N. G.; Davis, V. A.; Schmidt, H. K.; Hauge, R. H.; Smalley, R. E.; Pasquali, M. *J. Am. Chem. Soc.* **2006,** *128,* 591–595. doi:10.1021/ja055847f
13. Moulton, S. E.; Maugey, M.; Poulin, P.; Wallace, G. G. *J. Am. Chem. Soc.* **2007,** *129,* 9452–9457. doi:10.1021/ja072160h
14. Lu, L.; Chen, W. *ACS Nano* **2010,** *4,* 1042–1048. doi:10.1021/nn901326m
15. Zhang, S.; Li, Q.; Kinloch, I. A.; Windle, A. H. *Langmuir* **2010,** *26,* 2107–2112. doi:10.1021/la902642f
16. Ao, G.; Nepal, D.; Aono, M.; Davis, V. A. *ACS Nano* **2011,** *5,* 1450–1458. doi:10.1021/nn103225r
17. Puech, N.; Blanc, C.; Grelet, E.; Zamora-Ledezma, C.; Maugey, M.; Zakri, C.; Anglaret, E.; Poulin, P. *J. Phys. Chem. C* **2011,** *115,* 3272–3278. doi:10.1021/jp1102077
18. Tardani, F.; La Mesa, C.; Poulin, P.; Maugey, M. *J. Phys. Chem. C* **2012,** *116,* 9888–9894. doi:10.1021/jp300691w
19. Zakri, C.; Blanc, C.; Grelet, E.; Zamora-Ledezma, C.; Puech, N.; Anglaret, E.; Poulin, P. *Philos. Trans. R. Soc., A* **2013,** *371,* 20120499. doi:10.1098/rsta.2012.0499
20. Wang, P.; Barnes, B.; Wu, X.; Qu, H.; Zhang, C.; Shi, Y.; Headrick, R. J.; Pasquali, M.; Wang, Y. *Adv. Mater. (Weinheim, Ger.)* **2019,** *31,* 1901641. doi:10.1002/adma.201901641
21. Jintoku, H.; Matsuzawa, Y. *ACS Appl. Nano Mater.* **2022,** *5,* 2195–2203. doi:10.1021/acsanm.1c03894
22. Kojima, K.; Aizawa, M.; Yamamoto, T.; Muroga, S.; Kobashi, K.; Okazaki, T. *Langmuir* **2022,** *38,* 8899–8905. doi:10.1021/acs.langmuir.2c01024
23. Kojima, K.; Jintoku, H.; Kuwahara, Y.; Aizawa, M.; Yamamoto, T.; Muroga, S.; Kobashi, K.; Okazaki, T. *Appl. Phys. Express* **2022,** *15,* 125003. doi:10.35848/1882-0786/aca23c
24. Onsager, L. *Ann. N. Y. Acad. Sci.* **1949,** *51,* 627–659. doi:10.1111/j.1749-6632.1949.tb27296.x
25. Kobashi, K.; Ata, S.; Yamada, T.; Futaba, D. N.; Okazaki, T.; Hata, K. *ACS Appl. Nano Mater.* **2019,** *2,* 4043–4047. doi:10.1021/acsanm.9b00941
26. Morimoto, T.; Joung, S.-K.; Saito, T.; Futaba, D. N.; Hata, K.; Okazaki, T. *ACS Nano* **2014,** *8,* 9897–9904. doi:10.1021/nn505430s
27. Kato, Y.; Morimoto, T.; Kobashi, K.; Yamada, T.; Okazaki, T.; Hata, K. *J. Phys. Chem. C* **2019,** *123,* 21252–21256. doi:10.1021/acs.jpcc.9b04667
28. Kato, Y.; Morimoto, T.; Kobashi, K.; Yamaguchi, T.; Mori, T.; Sugino, T.; Okazaki, T. *Powder Technol.* **2022,** *407,* 117663. doi:10.1016/j.powtec.2022.117663
29. Puech, N.; Grelet, E.; Poulin, P.; Blanc, C.; van der Schoot, P. *Phys. Rev. E* **2010,** *82,* 020702. doi:10.1103/physreve.82.020702
30. Jamali, V.; Behabtu, N.; Senyuk, B.; Lee, J. A.; Smalyukh, I. I.; van der Schoot, P.; Pasquali, M. *Phys. Rev. E* **2015,** *91,* 042507. doi:10.1103/physreve.91.042507
31. Babaei-Ghazvini, A.; Acharya, B. *Carbohydr. Polym. Technol. Appl.* **2022,** *3,* 100217. doi:10.1016/j.carpta.2022.100217
32. Babaei-Ghazvini, A.; Acharya, B.; Korber, D. R. *Carbohydr. Polym.* **2022,** *275,* 118709. doi:10.1016/j.carbpol.2021.118709
33. Majumder, M.; Rendall, C. S.; Eukel, J. A.; Wang, J. Y. L.; Behabtu, N.; Pint, C. L.; Liu, T.-Y.; Orbaek, A. W.; Mirri, F.; Nam, J.; Barron, A. R.; Hauge, R. H.; Schmidt, H. K.; Pasquali, M. *J. Phys. Chem. B* **2012,** *116,* 6536–6542. doi:10.1021/jp3009628
34. Howard, N. S.; Archer, A. J.; Sibley, D. N.; Southee, D. J.; Wijayantha, K. G. U. *Langmuir* **2023,** *39,* 929–941. doi:10.1021/acs.langmuir.2c01691
35. Headrick, R. J.; Tsentalovich, D. E.; Berdegué, J.; Bengio, E. A.; Liberman, L.; Kleinerman, O.; Lucas, M. S.; Talmon, Y.; Pasquali, M. *Adv. Mater. (Weinheim, Ger.)* **2018,** *30,* 1704482. doi:10.1002/adma.201704482
36. Kobashi, K.; Sekiguchi, A.; Yamada, T.; Muroga, S.; Okazaki, T. *ACS Appl. Nano Mater.* **2020,** *3,* 1391–1399. doi:10.1021/acsanm.9b02252

License and Terms

BEILSTEIN JOURNAL OF ORGANIC CHEMISTRY

Multi-redox indenofluorene chromophores incorporating dithiafulvene donor and ene/enediyne acceptor units

Christina Schøttler[1,2], Kasper Lund-Rasmussen[1], Line Broløs[1], Philip Vinterberg[1], Ema Bazikova[1], Viktor B. R. Pedersen[1] and Mogens Brøndsted Nielsen[*1]

Full Research Paper

Open Access

Address:
[1]Department of Chemistry, University of Copenhagen, Universitetsparken 5 DK-2100 Copenhagen Ø, Denmark and [2]Sino-Danish College (SDC), University of Chinese Academy of Sciences, Beijing, China

Email:
Mogens Brøndsted Nielsen[*] - mbn@chem.ku.dk

* Corresponding author

Keywords:
alkynes; chromophores; fused-ring systems; heterocycles; redox chemistry

Beilstein J. Org. Chem. **2024,** *20,* 59–73.
https://doi.org/10.3762/bjoc.20.8

Received: 13 October 2023
Accepted: 28 December 2023
Published: 15 January 2024

This article is part of the thematic issue "Carbon-rich materials: from polyaromatic molecules to fullerenes and other carbon allotropes".

Guest Editor: Y. Yamakoshi

Abstract

Large donor–acceptor scaffolds derived from polycyclic aromatic hydrocarbons (PAHs) with tunable HOMO and LUMO energies are important for several applications, such as organic photovoltaics. Here, we present a large selection of PAHs based on central indenofluorene (IF) or fluorene cores and containing various dithiafulvene (DTF) donor units that gain aromaticity upon oxidation and a variety of acceptor units, such as vinylic diesters, enediynes, and cross-conjugated radiaannulenes (RAs) that gain aromaticity upon reduction. In some cases, the DTF units are expanded by pyrrolo annelation. The optical and redox properties of these compounds, in some cases carbon-rich, were studied by UV–vis absorption spectroscopy and cyclic voltammetry. Synthetically, the work explores IF diones or fluorenone as central building blocks by subjecting the carbonyl groups to a variety of reactions; that are, phosphite- or Lawesson's reagent-mediated olefination reactions (to introduce DTF motifs), Ramirez/Corey–Fuchs dibromo-olefinations followed by Sonogashira couplings (to introduce enediynes motifs), and Knoevenagel condensations (to introduce the vinylic diester motif). By a subsequent Glaser–Hay coupling reaction, a RA acceptor unit was introduced to provide a DTF-IF-RA donor–acceptor scaffold with a low-energy charge-transfer absorption and multi-redox behavior.

Introduction

Tetrathiafulvalene (TTF, Figure 1) is a redox-active molecule that has been widely explored in materials chemistry and supramolecular chemistry [1-8]. TTF reversibly undergoes two sequential one-electron oxidations, generating first a radical cation ($TTF^{+\bullet}$) and subsequently a dication (TTF^{2+}) containing two 6π-aromatic 1,3-dithiolium rings. The redox properties and geometries of the redox states have been finely tuned by extending the conjugated system with various cores, such as

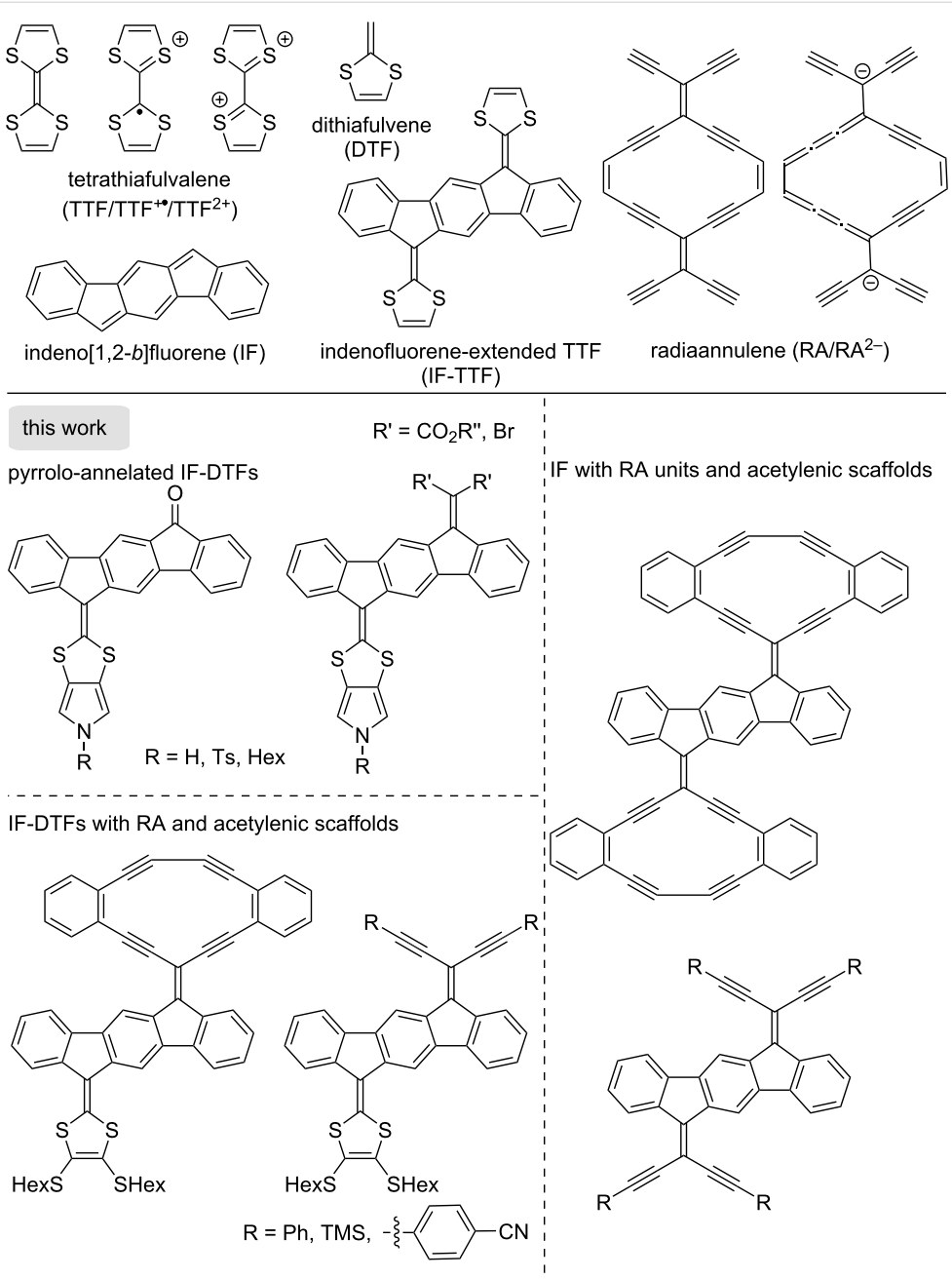

Figure 1: Overview of structural motifs relevant for the work described herein.

polycyclic aromatic hydrocarbons (PAHs), resulting in so-called extended TTFs [9-12]. One example of this is the introduction of an indeno[1,2-*b*]fluorene (IF) core [13], providing indenofluorene-extended TTFs (IF-TTFs) of the general structure shown in Figure 1. The π-system can be further expanded as well at the dithiole rings. For example, we have recently developed a synthetic protocol for fusing a pyrrole unit to one of the dithiole rings of an IF-TTF, allowing for dimerization of extended TTFs via the nitrogen atom by different linkers [14].

Donor–acceptor chromophores can be obtained by replacing one of the dithiafulvene (DTF) rings of the IF-TTF by an electron acceptor. Cyclic and acyclic acetylenic scaffolds comprised of enediyne units are known to behave as good electron acceptors [15,16], and we became interested in combining the IF-DTF scaffold with such motifs to generate novel multi-redox systems. For example, the radiaannulene moiety RA shown in Figure 1 (or its truncated counterpart with one of the exocyclic enediyne units removed) [17,18] is a particularly good electron acceptor as it gains 14π-aromaticity upon reduction. In this

work, we also want to further explore pyrrolo-annelated IF-DTFs with different substituents on the nitrogen atom, and the functionalization at the other end of the IF core with electron-accepting moieties. An overview of general motifs targeted in this work is shown in Figure 1.

Results and Discussion

Synthesis

The synthetic building blocks **1**–**8** used in this work are shown in Figure 2. The dione **1** and the ketones **4** and **6** were synthesized according to literature procedures [14,19,20], as were the 1,3-dithiole-2-thiones **2** and **3** [21]. Fluorenone **5** is commercially available. The new building blocks **7** and **8** were prepared according to related literature procedures [21], as described in Supporting Information File 1.

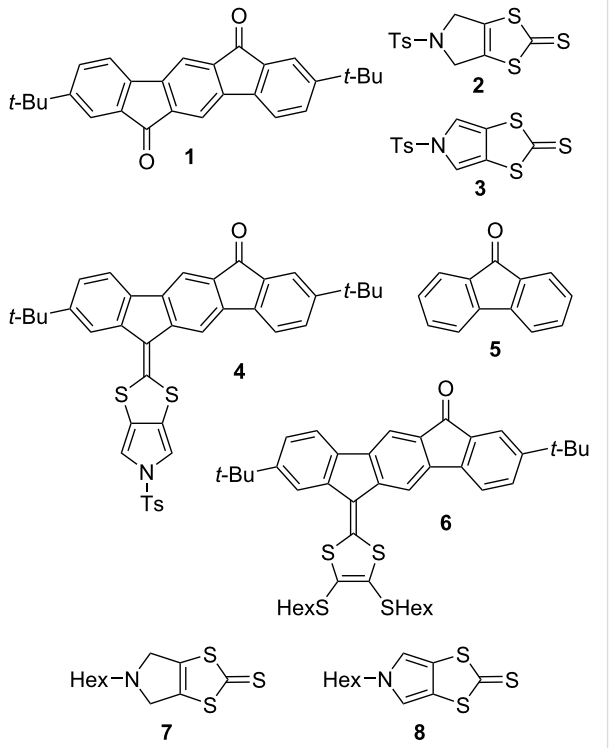

Figure 2: Dione/ketones **1**, **4**–**6** and 1,3-dithiole-2-thione compounds **2**, **3**, **7**, and **8** are building blocks used in this work.

Our first objective was to explore further annellation of dihydropyrrole and pyrrole units at the DTF moiety of an IF-DTF. A phosphite-mediated coupling of either 1,3-dithiole-2-thione **2**, **7**, or **8** with IF dione **1** afforded IF-DTFs **9**–**11**, as shown in Scheme 1. Compound **11** was also obtained from building block **4** via the pyrrolo-annelated IF-DTF **12** by removal of the tosyl (Ts) group under alkaline conditions, followed by nucleophilic substitution to incorporate the hexyl chain on the pyrrole. Furthermore, treatment of the IF-DTF ketone **4** with Lawesson's reagent (using a recently established protocol [20]) yielded the large dimer **13** as a mixture of *E* and *Z* isomers (ca. 4:1). Further functionalization of the IF-DTF ketone **11** was obtained by Ramirez/Corey–Fuchs dibromo-olefination and Knoevenagel condensation to yield vinylic dibromide **14** and diester **15**, respectively, as illustrated in Scheme 2. We noted that the dibromo-olefination reaction was first discov-

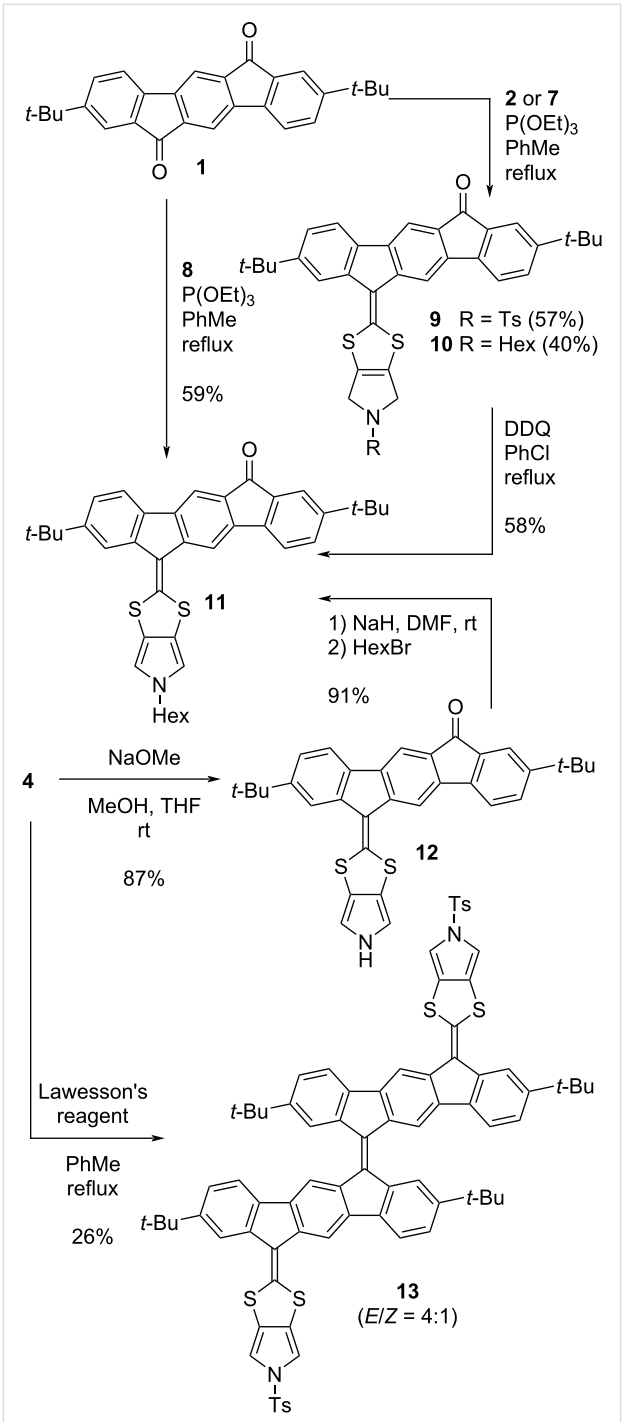

Scheme 1: Synthesis of IF-DTF ketones **9–12** and dimer **13**.

ered by Ramirez and co-workers [22] and used in the first step of the Corey–Fuchs reaction that ultimately provides an alkyne [23].

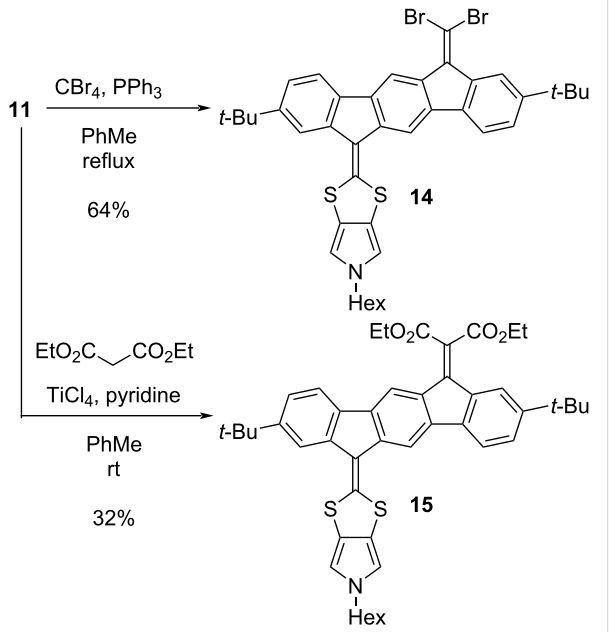

Scheme 2: Further functionalization of the IF-DTF ketone **11** via Ramirez/Corey–Fuchs dibromo-olefination and Knoevenagel condensation.

To elucidate the properties of the donor part itself of the pyrrolo-annelated IF-DTF systems, we prepared compounds **16** and **17** containing a smaller fluorene PAH. These compounds were prepared by a Lawesson's reagent-promoted coupling between fluorenone **5** and the Ts-protected 1,3-dithiole-2-thione building blocks **2** and **3**, respectively, shown in Scheme 3 (albeit in modest yields). Fluorene-based DTF compounds have previously been explored in various elaborate systems [24-27].

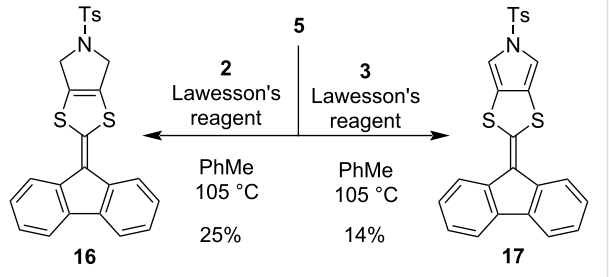

Scheme 3: Coupling of 1,3-dithiole-2-thione building blocks **2** and **3** with fluorenone **5** to afford fluorene-extended DTFs **16** and **17**.

Next, we wanted to explore IF-DTFs as motifs for acetylenic scaffolding (Scheme 4). Starting from IF-DTF building block **6**, dibromo-olefinated compound **18** was obtained by a Ramirez/Corey–Fuchs reaction. Two-fold Sonogashira couplings with trimethylsilylacetylene, ethynylbenzene, or 4-ethynylbenzonitrile yielded compounds **19**–**21**, while two-fold Sonogashira coupling with ((2-ethynylphenyl)ethynyl)triisopropylsilane resulted in compound **22**. Desilylation of the alkynes of compound **22** with tetrabutylammonium fluoride (TBAF) and subsequent intramolecular Glaser–Hay coupling of the terminal alkynes afforded the macrocyclic DTF-IF-RA scaffold **23**. Molecular sieves (4 Å) were added to the reaction mixture as this has previously been shown to significantly promote the Glaser–Hay coupling [28]. Compounds **20** and **21** were unfortunately very sensitive compounds that were found to easily degrade, which made their characterization somewhat difficult (vide infra).

We also targeted other enediyne acetylenic scaffolds with IF as central core as shown in Scheme 5. Starting from IF dione **1**, compounds **24** and **25** were synthesized via Ramirez/Corey–Fuchs dibromo-olefinations. Four-fold Sonogashira couplings of compound **25** with triisopropylsilylacetylene and ((2-ethynylphenyl)ethynyl)triisopropylsilane yielded compounds **26** and **27**, respectively. A two-fold, intramolecular Glaser–Hay coupling of compound **27** (after desilylation) was attempted under the conditions that were successful in the synthesis of compound **23** (Scheme 4). A compound that may tentatively be assigned to **28** was observed by MALDI–MS analysis of the reaction mixture, but less than needed for an NMR sample was isolated. Furthermore, the isolated compound proved quite insoluble in all investigated deuterated solvents, and therefore it was not possible to determine the purity of the product by this method.

In an initial attempt to investigate other synthetic pathways to extended IF compounds, the reduced IF **29** was synthesized from IF dione **1** by a Wolff–Kishner reduction of the two ketones as shown in Scheme 6. Compound **29** could potentially after deprotonation be reacted with electrophiles as previously established [29] for the parent structure [30] without *tert*-butyl substituents.

UV–vis absorption spectroscopy

UV–vis absorption spectra of the known compound **4** [14] and new compounds **9**–**12** and **15** are depicted in Figure 3, and the data are presented in Table 1. A redshift of the longest-wavelength absorption maximum is observed for all new compounds compared to that of **4**. For compounds **11** and **12**, this indicates that the inductive electron-withdrawing or -donating influences of the substituent group (Ts group in **4** and Hex group in **11**) on the nitrogen atom in the pyrrole ring have an effect on the absorption in the visible spectrum of pyrrolo-annelated IF-DTF ketones. Interestingly, the absorption of the dihydropyrrole

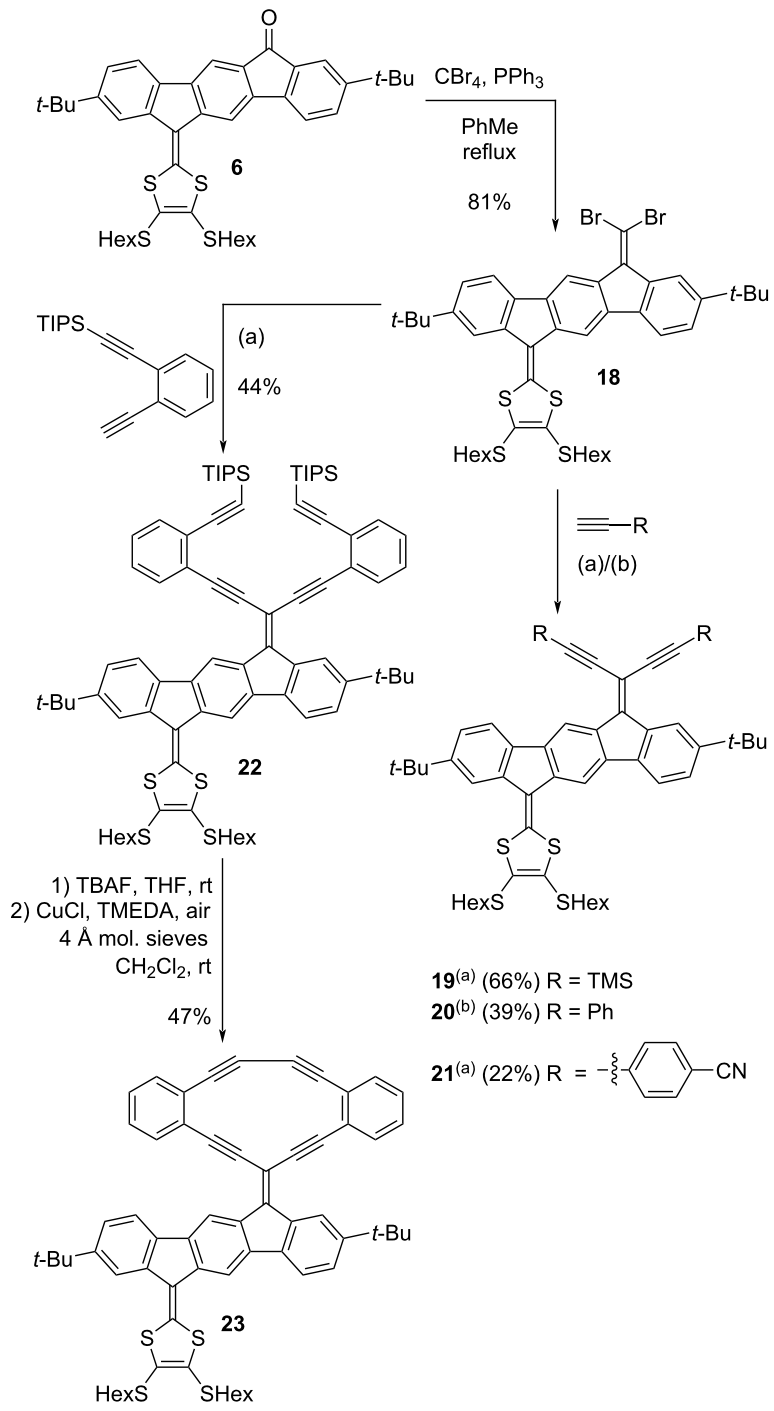

Scheme 4: Synthesis of acetylenic scaffolds based on IF-DTF. Conditions: (a) $Pd(PPh_3)_2Cl_2$, CuI, THF, Et_3N, rt. (b) Pd_2dba_2, P(*t*-Bu)$_3$, CuI, THF, Et_3N, rt.

IF-DTF **9** is redshifted relative to that of the pyrrole IF-DTF **4**, while the absorption does not change significantly when comparing IF-DTFs **10** and **11**, indicating that the extent to which the absorption changes upon oxidation from a dihydropyrrole to a pyrrole unit depends on the substituent on the N of the dihydropyrrole/pyrrole ring. Introducing the diester electron-acceptor in compound **15** does not change the absorption significantly, compared to compound **11**. When changing the solvent from PhMe to CH_2Cl_2, we observed a redshift of the longest-wavelength absorption maximum for compounds **10** and **11**, indicating some charge-transfer character of the absorption (see Figure S1 in Supporting Information File 1).

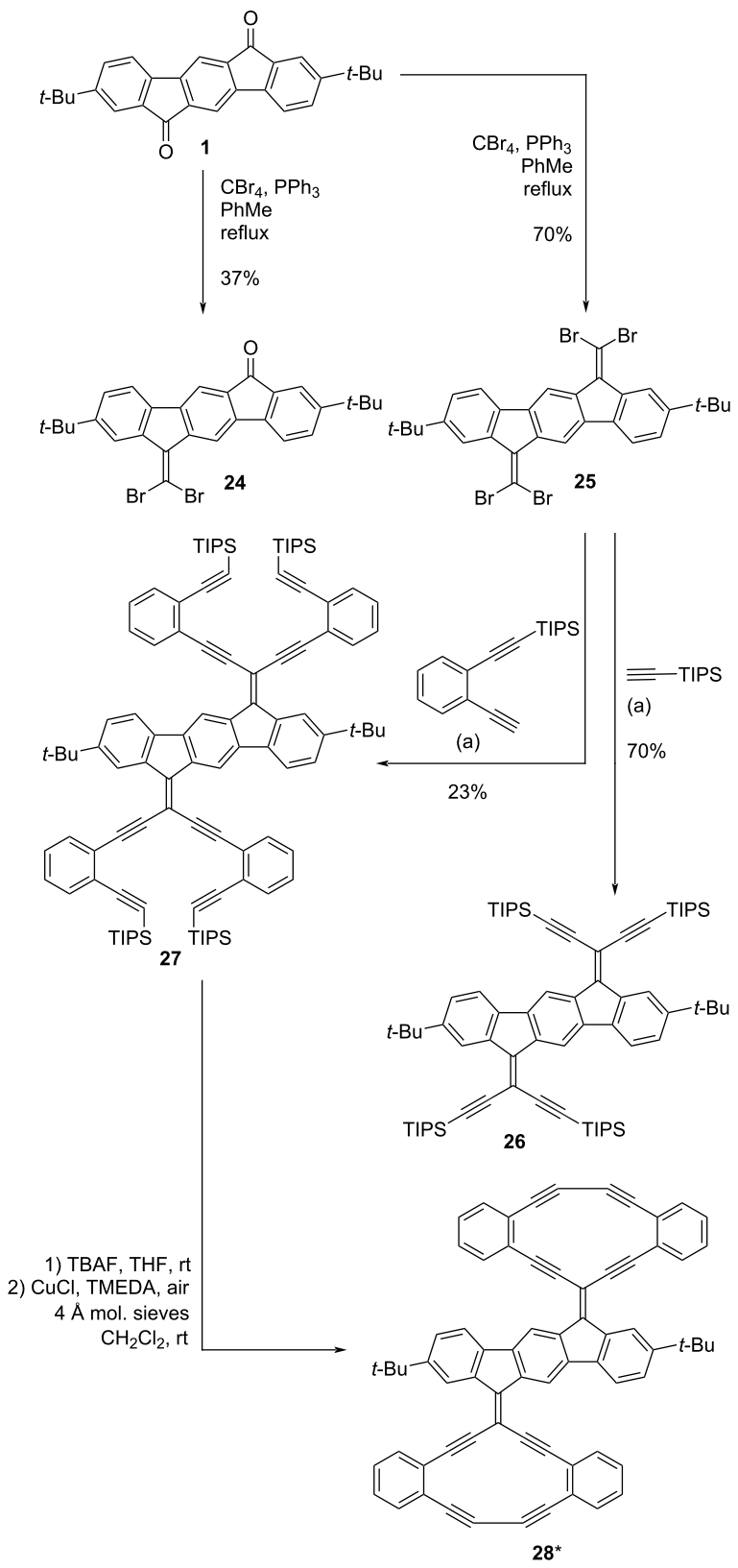

Scheme 5: Synthesis of acetylenic scaffolds with IF as central core. *Not fully characterized due to poor solubility. Conditions: (a) $Pd(PPh_3)_2Cl_2$, CuI, THF, Et_3N, rt.

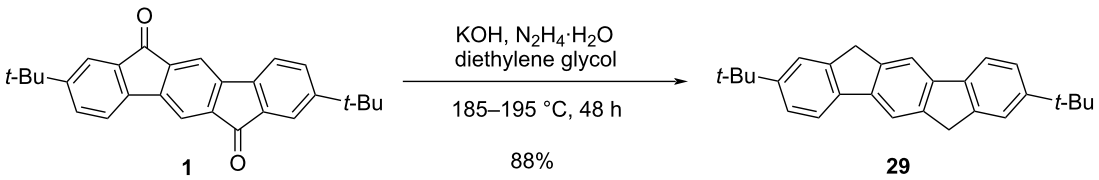

Scheme 6: Reduction of IF dione **1** to dihydro-IF **29**.

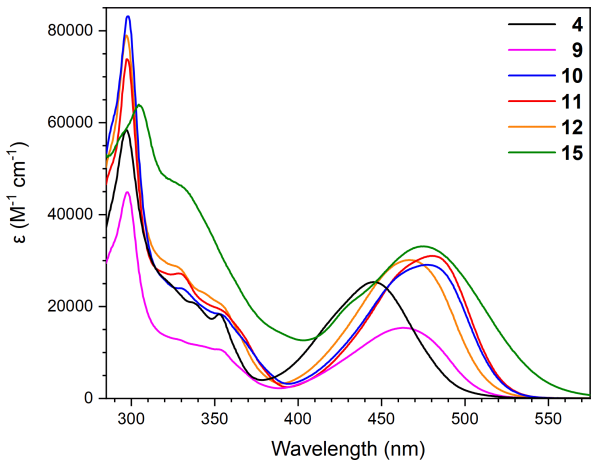

Figure 3: UV–vis absorption spectra of compounds **4**, **9**–**12**, and **15** in PhMe at 25 °C.

UV–vis absorption spectra of the known compound **30** [20] and new compounds **13**, **16**, and **17** are shown in Figure 4, and the data are presented in Table 1. Compared to compound **30**, the longest-wavelength absorption maximum of compound **16** is slightly blueshifted while the absorption maximum of compound **17** is significantly blueshifted. This indicates that annelation of the dihydropyrrole ring to the DTF moiety does not change the absorption maximum significantly compared to the two SHex substituents, while annelation of a pyrrole ring results in an absorption maximum at significantly shorter wavelength. These compounds have blueshifted longest-wavelength absorptions relative to the donor–acceptor scaffolds incorporating a pyrrolo-annelated DTF unit. Of these compounds, the large dimer **13** stands out with a significantly redshifted and intense longest-wavelength absorption maximum (λ_{max} at 574 nm) expanding to ca. 680 nm.

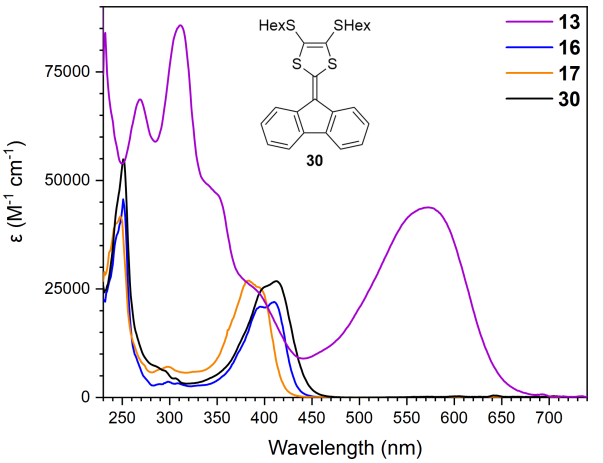

Figure 4: UV–vis absorption spectra of compounds **13**, **16**, **17**, and **30** in CH_2Cl_2 at 25 °C.

UV–vis absorption spectra of compounds **22**, **23**, **26**, and **27** are depicted in Figure 5. By comparing donor–acceptor chromophores **22** and **23**, it is observed that the RA moiety of DTF-IF-RA scaffold **23** induces a significant redshift, presumably due to the stronger electron-accepting character of the RA unit

Table 1: UV–vis absorption data of compounds in PhMe or CH_2Cl_2 at 25 °C (absorption maxima λ_{max} and molar absorptivities ε).

Compound	λ_{max} [nm] (ε [10^3 M^{-1} cm^{-1}])	Compound	λ_{max} [nm] (ε [10^3 M^{-1} cm^{-1}])
4[a]	297 (58), 445 (25)	**16**[b]	297 (3.6), 395 (21)*, 409 (22)
9[a]	297 (45), 462 (20)	**17**[b]	297 (7.1), 383 (27), 393 (25)*
10[a]	298 (68), 478 (24)	**22**[b]	262 (51), 300 (55), 402 (17) (broad), 489 (27)
11[a]	298 (74), 480 (31)	**23**[b]	297 (95), 401 (21)*, 426 (24), 444 (23)*, 529 (34)
12[a]	297 (79), 466 (30)	**26**[b]	296 (76), 413 (52), 440 (70)
13[b,c]	269 (69), 312 (84), 574 (43)	**27**[b]	306 (46), 444 (24)*, 461 (25), 534 (1.8) (broad)
15[a]	304 (60), 475 (34)	**30**[b,d]	251, 400*, 412

[a]PhMe; [b]CH_2Cl_2; [c]*E*/*Z* ratio of 4:1; [d]reference [14]; *shoulder peak.

(and hence a lower-energy LUMO) compared to the acyclic acetylenic scaffold of compound **22** (in line with first reduction potentials, vide infra). For compound **27**, a shorter longest-wavelength absorption maximum at 461 nm is observed; this is a symmetric compound for which no donor–acceptor "push–pull" system is present (albeit a broad tail to the absorption is observed), in contrast to **22** and **23**. The absorption maxima of compound **26** are significantly blueshifted, presumably due to the smaller conjugated system. The same trend with a shorter longest-wavelength absorption maximum that was observed for compound **27** was also observed for this compound.

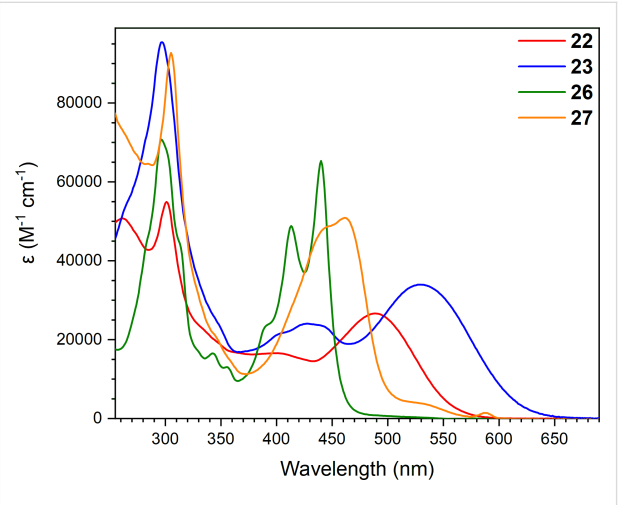

Figure 5: UV–vis absorption spectra of compounds **22**, **23**, **26**, and **27** in CH_2Cl_2 at 25 °C.

The degradation of compound **20** in the presence of light and oxygen is visible as a color change upon leaving a sample of the compound in solution in an open vial, unshielded from light (Figure S2 in Supporting Information File 1). This degradation was investigated by UV–vis absorption spectroscopy; the absorption spectrum was measured over time for three different samples, and a notable change in the longest-wavelength absorption maximum was only observed for the sample that was exposed to both light and oxygen (see Figures S3 and S4 in Supporting Information File 1). We speculate that this degradation is due to the reaction with singlet oxygen generated by the compound as a photosensitizer; indeed, we have recently shown [31] that IF-TTF compounds are reactive towards singlet oxygen at the central fulvene bond but, in contrast, IF-TTFs (without an acetylenic moiety as in **20**) are themselves poor photosensitizers for singlet oxygen.

Electrochemistry

Cyclic voltammograms of compounds **11**, **13**, **15**, **16**, and **17** (in MeCN for compounds **11** and **15** and in CH_2Cl_2 for compounds **13**, **16**, and **17**, all with 0.1 M Bu_4NPF_6 as supporting electrolyte) are shown in Figure 6, and potentials against ferrocene (Fc/Fc^+) (obtained from differential pulse voltammetry, see Supporting Information File 1) are summarized in Table 2. Compounds **11** and **15** showed two irreversible first oxidations at +0.34 V and +0.38 V vs Fc/Fc^+, showing that replacing the ketone with the stronger electron withdrawing vinylic diester renders the first oxidation more difficult (by 40 mV). An anodic shift of 40 mV was also observed for the second oxidation. Oppositely, compound **15** underwent a significantly easier first reduction than **11** (−1.00 V vs −1.35 V), and it also underwent a second reduction. The pyrrolo-annelated dimer **13** showed a reversible oxidation at +0.42 V followed by an irreversible oxidation at +1.01 V, and two reversible reductions at −1.48 V and −1.81 V. Here, the acceptor properties are not promoted by incorporating an acceptor unit as in **15**, but instead by the bifluorenylidene motif [32] obtained by dimerizing two pyrrolo-annelated IF-DTF units. Notably, the dimer **13** underwent a first oxidation more readily (by as much as 0.14 V) than the corresponding fluorene-DTF donor **17** (both containing the same *N*-tosylated pyrrolo-DTF unit). The low electrochemical

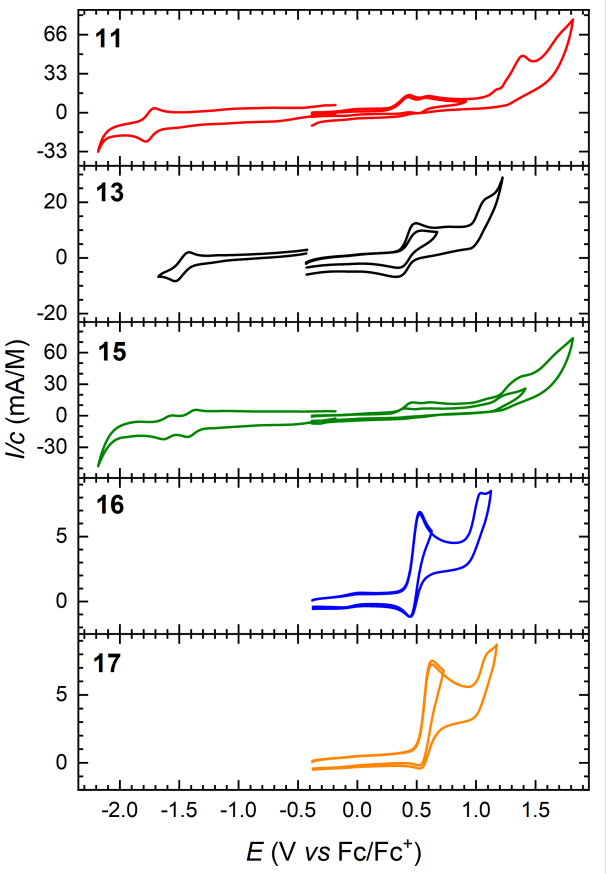

Figure 6: Cyclic voltammograms of compounds **11** (in MeCN), **13** (in CH_2Cl_2), **15** (in MeCN), **16** (in CH_2Cl_2), and **17** (in CH_2Cl_2); supporting electrolyte: 0.1 M Bu_4NPF_6, scan rate: 0.1 V/s. All potentials are depicted against the Fc/Fc^+ redox couple.

HOMO–LUMO gap of **13** is paralleled by a low-energy longest-wavelength absorption maximum (vide supra, Figure 7).

Table 2: Electrochemical data from differential pulse voltammetry of compounds in CH_2Cl_2 (with 0.1 M Bu_4NPF_6) if not otherwise stated; potentials in volts vs Fc/Fc^+.

Compound	E^1_{ox}	E^2_{ox}	E^1_{red}	E^2_{red}
11[a]	+0.34	+0.52	−1.35	–
13[b]	+0.42	+1.01	−1.48	−1.81
15[a]	+0.38	+0.56	−1.00	−1.21
16	+0.47	+0.99	–	–
17	+0.56	+1.07	–	–
22	+0.41	+0.76	−1.80	–
23	+0.41	+0.81	−1.50	−1.78
26	+0.84	–	−1.64	−1.98
27	+0.85	–	−1.63	−1.89

[a]In MeCN. [b]*E*/*Z* ratio of 4:1.

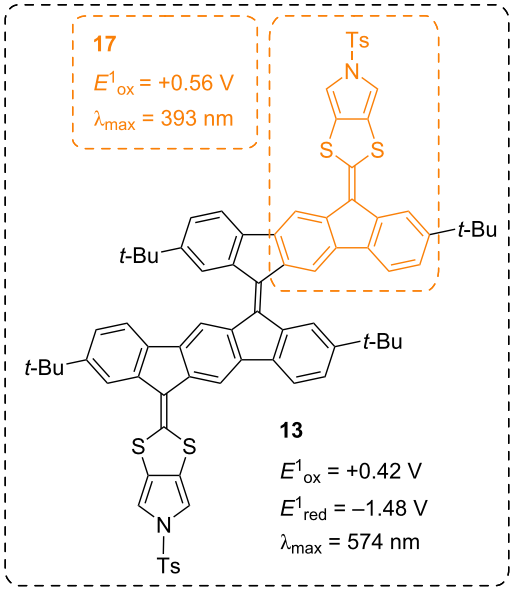

Figure 7: Comparison of properties of compounds **13** and **17**.

A quasi-reversible first oxidation was observed at +0.47 V for the fluorene compound **16** and an irreversible oxidation at +0.99 V. Compound **17** experienced a quasi-reversible first oxidation at +0.56 V and an irreversible oxidation at +1.07 V. Thus, the dihydropyrrolo-annelated DTF compound is more easily oxidized than the pyrrolo-annelated DTF compound. These fluorene compounds did not experience a reduction within the potential window.

Cyclic voltammograms of the acetylenic scaffolds **22**, **23**, **26**, and **27** (in CH_2Cl_2 with 0.1 M Bu_4NPF_6 as supporting electrolyte) are shown in Figure 8. Quasi-reversible one-electron oxidations of the two DTF-functionalized compounds **22** and **23** are observed at +0.41 V followed by irreversible oxidations at +0.76 V (**22**) and +0.81 V (**23**), respectively. One reversible oxidation at +0.84 V and one reversible reduction at −1.64 V were observed for compound **26**, along with one irreversible reduction at −1.98 V. These oxidation and reduction potentials are not significantly different from the potentials observed for compound **27**, namely one quasi-reversible oxidation at +0.85 V and two one-electron reductions at −1.63 V and −1.89 V, indicating that the larger conjugated system of compound **27** does not significantly change the redox properties of the compound. Compounds **26** and **27** lack the DTF donor part and are hence oxidized at significantly higher potentials than the other compounds. On the other hand, they are stronger acceptors than the acetylenic scaffold **22** containing the DTF donor. We have previously [33] studied a related compound in which all four triisopropylsilylethynyl substituents of **26** are replaced by cyano groups; this compound showed superior acceptor properties, being reduced at −0.81 V and −1.09 V vs Fc/Fc^+ (similar conditions), but no donor properties (thereby contrasting **26** and **27**).

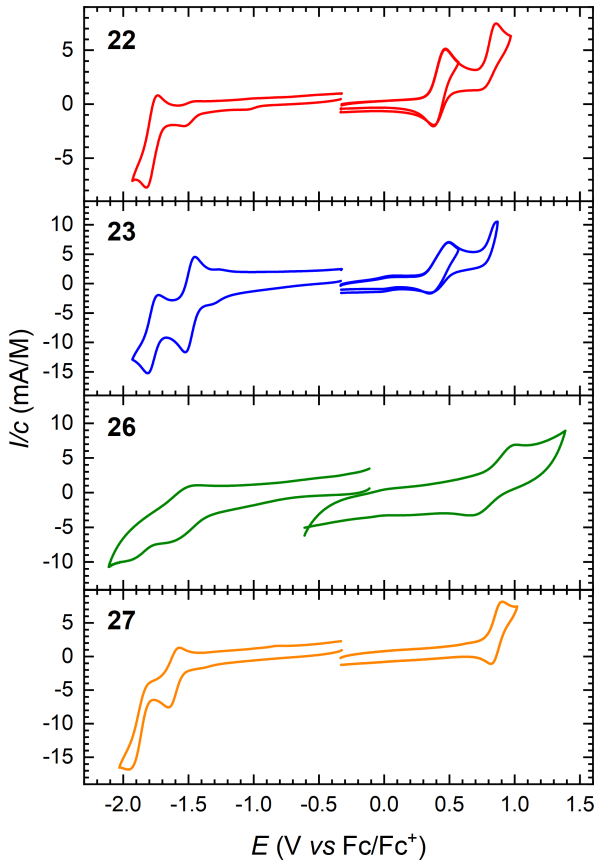

Figure 8: Cyclic voltammograms of compounds **22**, **23**, **26**, and **27** in CH_2Cl_2; supporting electrolyte: 0.1 M Bu_4NPF_6, scan rate: 0.1 V/s. All potentials are depicted against the Fc/Fc^+ redox couple.

Of the acetylenic scaffolds studied, DTF-IF-RA **23** containing an RA moiety is the strongest acceptor, which we ascribe to gain of 14π_z-aromaticity of the cyclic moiety of the reduced species (in line with previously studied RA scaffolds [17,18,34]). Indeed, it is reduced more easily by as much as 0.3 V than its corresponding acyclic counterpart, compound **22**, although it contains a π-system of the same size, and it is even reduced more easily by 0.13 V than the acetylenic scaffold **27** containing acetylenic acceptor motifs at both ends of the IF core and hence no DTF donor unit. Compound **23** also undergoes a reversible, second reduction to form the dianion. This compound should gain aromaticity upon either reduction or oxidation as illustrated in Figure 9.

X-ray crystallographic analysis

Crystals suitable for single-crystal X-ray diffraction studies were obtained for compounds **25**, **26**, and **29**. Their structures are shown in Figure 10, top, and their respective crystal packings below. All three compounds pack in a herringbone manner in the crystal structure, with the major difference that com-

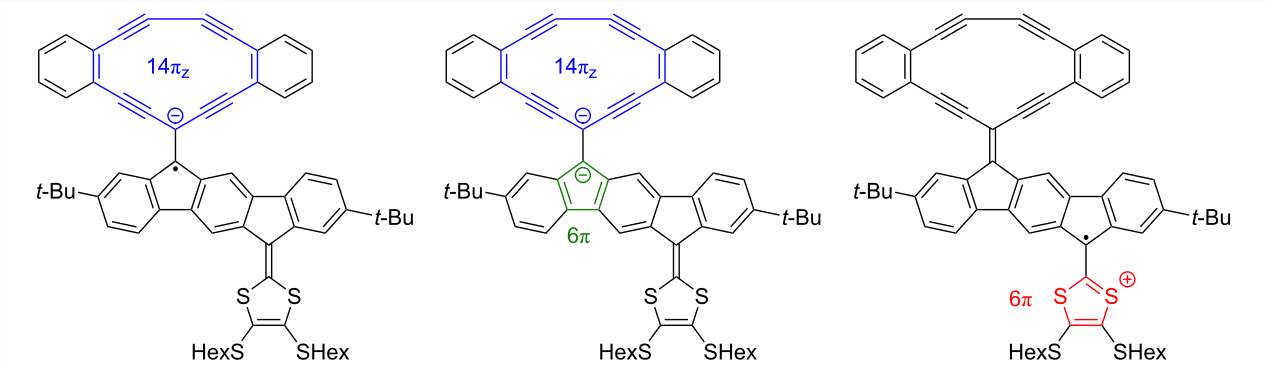

Figure 9: Radical anion (left), dianion (middle), and radical cation (right) of compound **23**; the radical anion has a 14π_z-aromatic ring (highlighted in blue; only counting 2π-electrons of each triple bond, here defined as those in π_z orbitals), the dianion has an additional 6π-aromatic cyclopentadienyl anion (highlighted in green), while the cation has a 6π-aromatic 1,3-dithiolium ring (highlighted in red).

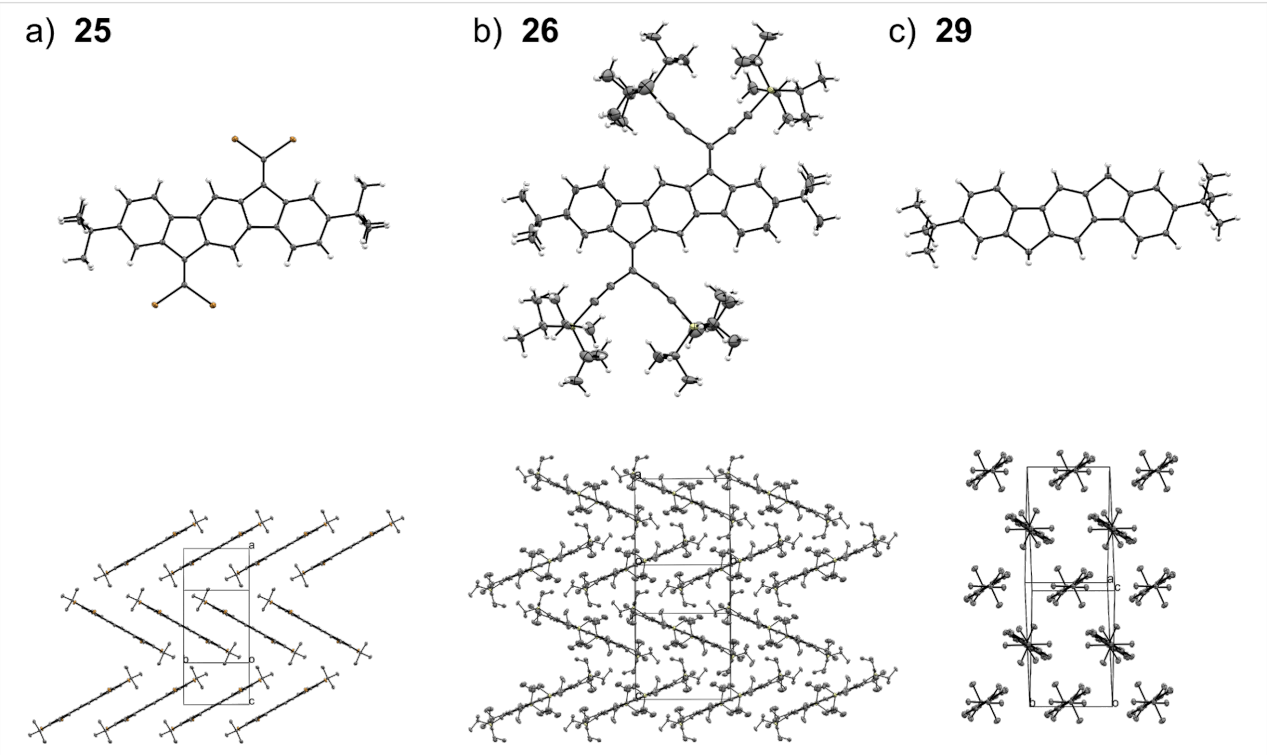

Figure 10: ORTEP plots (50% probability) and crystal packing of compounds a) **25**, b) **26**, and c) **29**. The respective crystal packing of each compound is shown below, in which the hydrogen atoms are omitted for clarity. Atoms are colored grey (carbon), white (hydrogen), brown (bromine), pale-yellow (silicon).

pound **29** is perpendicular with respect to the herringbone pattern and the related structures (see Figure 10, bottom). Compound **25** packs with an intramolecular distance of 3.41 Å between the planes of the π-systems. Neither compound **26** nor **29** shows π–π interactions in the crystal packing. The large bulkiness of the TIPS groups along with the *tert*-butyl groups in compound **26** prevent these interactions, while for compound **29**, the lack of π–π interactions can be ascribed to the methylene bridges as the hydrogens along with the *tert*-butyl groups prevent good overlap of the π-systems.

Table 3 lists the lengths of the bonds (*b*–*f*) within the five-membered rings of the cores as well as the exocyclic C=C double bond (*a*) that is present in compounds **25** and **26** (for bond labels, see Figure 11). A small difference in the exocyclic C=C bond length is observed between **25** and **26**, with the bond in **26** being slightly longer. Bonds *b* and *f* are affected by the moiety X, with the less π-delocalized structure **29** having the longest bonds of 1.51 Å, while only minor differences are observed for bonds *c*, *d*, and *e*.

Table 3: Bond lengths (Å) within five-membered rings and of exocyclic C=C double bond (for bond assignments, see Figure 11).

Bond	Compound **25**	Compound **26**	Compound **29**
a	1.343(3)	1.362(2)	–
b	1.495(3)	1.478(2)	1.5102(15)
c	1.408(3)	1.405(2)	1.4030(15)
d	1.463(3)	1.468(2)	1.4690(15)
e	1.412(3)	1.410(2)	1.4103(15)
f	1.495(2)	1.474(2)	1.5090(15)

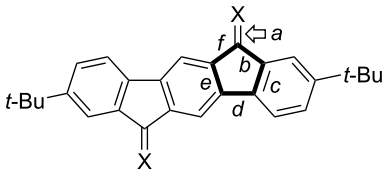

Figure 11: Labels of bonds within five-membered ring.

Conclusion

In summary, various redox-active chromophores based on the indenofluorene scaffold were synthesized, incorporating different dithiafulvenes and acetylenic scaffolds, such as acetylenic radiaannulenes. The compounds have strong absorptions in the visible region and undergo reversible (or quasi-reversible) oxidations and reductions. We have also presented two new fluorene-extended dithiafulvenes, which also absorb strongly in the visible region and undergo one reversible oxidation, while no reductions were observed for these compounds. Systematic studies show that by small structural modifications, the optical and electrochemical HOMO–LUMO gaps can be finely tuned – with first oxidations and reductions that can be adjusted by several hundreds of millivolts for donor–acceptor IF scaffolds. Introduction of both the dithiafulvene and radiaannulene units along the indenofluorene scaffold provided a donor–acceptor compound covering a particularly broad absorption profile and with a redshifted longest-wavelength absorption maximum relative to most of the compounds (529 nm in dichloromethane), which can be related to the fact that it is both a good donor and a good acceptor as shown electrochemically. This compound stands out as gaining aromaticity in one of its appendages along the IF core upon either reduction (generation of $14\pi_z$-aromatic ring) or oxidation (generation of 1,3-dithiolium ring).

Synthetically, the work relies on using indenofluorene diones as key building blocks for performing olefination reactions, such as phosphite- or Lawesson's reagent-mediated couplings, Ramirez/Corey–Fuchs dibromo-olefinations, and Knoevenagel condensations. In particular, the acetylenic scaffolds presented in this work may be useful precursors for even more elaborate, conjugated and carbon-rich structures in future work.

Experimental

Anhydrous MeOH was obtained by distillation from activated Mg and stored over 3 Å molecular sieves, or by drying over 3 Å molecular sieves. All remaining anhydrous solvents were obtained from a solvent drying tower (IT model PS-MD-05). HPLC grade solvents were used unless otherwise specified. Purification by chromatography was performed using silica gel (flash: 40–63 μm, Sepacore® Flash Systems X10/X50: 40–63 μm). TLC was performed using aluminum sheets covered with silica gel coated with fluorescent indicator. NMR spectra were recorded on a Bruker instrument at 500 MHz and 126 MHz for ^{1}H and ^{13}C NMR, respectively. Deuterated chloroform ($CDCl_3$, ^{1}H = 7.26 ppm, ^{13}C = 77.16 ppm), deuterated CH_2Cl_2 (CD_2Cl_2, ^{1}H = 5.32 ppm, ^{13}C = 54.00 ppm), deuterated DMSO ($(CD_3)_2SO$, ^{1}H = 2.50 ppm, ^{13}C = 39.53 ppm), deuterated acetone ($(CD_3)_2CO$, ^{1}H = 2.05 ppm, ^{13}C = 29.84 ppm), or deuterated benzene (C_6D_6, ^{1}H = 7.16 ppm, ^{13}C = 128.39 ppm) were used as solvents and internal references. Chemical shift values are referenced to the ppm scale and coupling constants are expressed in Hertz (Hz). HRMS analysis was performed on a Bruker SolariX XR MALDI-FT-ICR instrument with dithranol as matrix. Melting points are not corrected.

UV–vis absorption spectroscopy

UV–vis absorption spectra were recorded on a Varian Cary 50 UV–vis spectrophotometer scanning between 800 and 200 nm.

All spectra were recorded with baseline correction in CH_2Cl_2 or toluene (HPLC grades) at 25 °C in a quartz cuvette with a 10 mm path length.

Electrochemistry

Cyclic voltammograms (CV) and differential pulse voltammograms (DPV) were obtained using an Autolab PGSTAT12 instrument and Nova 1.11 software with a scan rate of 0.1 V/s for the CVs. A silver wire immersed in a 0.1 M Bu_4NPF_6 solution in CH_2Cl_2 separated from the analyte solution by a frit was used as the reference electrode, a Pt wire was used as the counter electrode, and a platinum disk (diameter = 1.6 mm) or a glassy carbon disk (3 mm) was used as the working electrode. The reference electrode was separated from the solution containing the substrate by a ceramic frit. Measured potentials were referenced to ferrocene/ferrocenium (Fc/Fc^+) redox couple, measured before and after the experiment. A 0.1 M solution of NBu_4PF_6 was used as electrolyte. All solutions were purged with Ar prior to measurements.

Crystallography

All single crystal X-ray diffraction data for compounds **25**, **26**, and **29** were collected on a Bruker D8 VENTURE diffractometer equipped with a Mo Kα X-ray (λ = 0.71073 Å). The data collections were done at 100 K. All data were integrated with SAINT and a multi-scan absorption correction using SADABS was applied [35,36]. The structure was solved by direct methods using SHELXT and refined by full-matrix least-squares methods against *F*2 by SHELXL-2019/2 [37,38]. The data for the compounds have been deposited with the Cambridge Crystallographic Data Centre [39]. The CIF files (Supporting Information Files 2–4) and reports were generated using FinalCIF [40].

Synthesis

Compounds **1** [19], **2** [21], **3** [21], **4** [14], and **6** [20] were synthesized according to literature procedures, and compounds **7** and **8** were synthesized according to modified literature procedures [21]. Representative synthetic protocols are provided below, while protocols for **7**, **8**, **10**–**12**, **14**, **15**, **17**, **20**–**22**, **24**–**27** are included in Supporting Information File 1.

Compound 9

A solution of **1** (139 mg, 352 μmol) and **2** (176 mg, 534 μmol) in anhydrous toluene (5 mL) and $P(OEt)_3$ (10 mL) was heated to reflux for 5 h, resulting in a color change from orange to dark red. The reaction mixture was then allowed to cool to rt before it was concentrated under reduced pressure. The resulting dark red solid was purified by flash column chromatography (SiO_2, 20% EtOAc/heptane), and recrystallization from CH_2Cl_2/MeOH followed by centrifugation yielded **9** (136 mg, 57%) as an orange solid. R_f = 0.18 (70% CH_2Cl_2/heptane); mp 178–181 °C; ^{1}H NMR (500 MHz, $CDCl_3$) δ 7.99 (s, 1H), 7.80 (d, *J* = 8.4 Hz, 2H), 7.76 (s, 1H), 7.72–7.71 (m, 2H), 7.68 (d, *J* = 8.0 Hz, 1H), 7.58–7.44 (m, 2H), 7.44–7.35 (m, 3H), 4.50 (s, 4H), 2.44 (s, 3H), 1.43 (s, 9H), 1.36 (s, 9H) ppm; ^{13}C NMR (126 MHz, $CDCl_3$) δ 194.1, 152.7, 151.1, 148.7, 148.0, 144.7, 143.5, 142.3, 142.3, 138.8, 137.1, 135.5, 135.1, 133.6, 132.3, 131.4, 130.4, 129.1, 128.8, 127.7, 121.0, 123.4, 121.6, 120.0, 119.7, 119.6, 115.7, 114.5, 52.7, 52.6, 35.4, 35.2, 31.9, 31.4, 21.8 ppm; five sp^2 signals missing, presumably due to overlap. HRMS (MALDI$^+$, FT-ICR, dithranol, *m*/*z*) [M + H$^+$] calcd for $C_{40}H_{38}NO_3S_3^+$, 676.2008; found, 676.2019.

Compound 13

A solution of **4** (62.0 mg, 92.0 μmol) and Lawesson's reagent (23.1 mg, 57.0 μmol) in anhydrous, N_2-degassed toluene (20 mL) was heated to reflux for 21 h. The reaction mixture was then allowed to cool to rt, diluted with toluene (50 mL), washed with 1 M NaOH (3 × 50 mL), and then with H_2O (3 × 50 mL). The organic phase was dried over $MgSO_4$ and concentrated under reduced pressure. The residue was purified by flash column chromatography (SiO_2, 20% EtOAc/heptane), yielding **13** (15.5 mg, 26%) as a purple solid. R_f = 0.23 (20% EtOAc/heptane); ^{1}H NMR (500 MHz, $CDCl_3$) δ 8.64 (s, 2H), 8.50 (s, 2H), 8.12 (s, 2H), 7.96 (s, 2H), 7.83 (d, *J* = 8.4 Hz, 4H), 7.64 (d, *J* = 8.0 Hz, 2H), 7.50 (d, *J* = 8.0 Hz, 2H), 7.34 (m, 6H), 7.29 (d, *J* = 8.4 Hz, 2H), 7.23 (s, 2H), 7.20 (s, 2H), 2.42 (s, 6H), 1.44 (s, 18H), 1.27 (s, 18H) ppm (*E*:*Z* ratio 4:1; ^{1}H NMR signals reported for the *E* isomer); ^{13}C NMR (126 MHz, $CDCl_3$) δ 150.2, 149.9, 145.8, 143.6, 140.7, 140.5, 139.1, 139.0, 138.6, 137.9, 137.4, 137.0, 136.4, 135.5, 130.4, 127.2, 126.7, 126.6, 126.1, 125.4, 124.1, 123.7, 120.8, 119.2, 119.1, 117.9, 115.0, 111.5, 111.4, 55.7, 35.3, 35.2, 35.2, 35.1, 32.0, 31.9, 31.8, 31.7, 31.6, 29.9, 29.5, 29.1, 22.8, 21.8, 14.3 ppm (*E*:*Z* ratio 4:1; sp^2-C signals missing, presumably due to overlap): HRMS (MALDI$^+$, FT-ICR, dithranol, *m*/*z*) [M$^{\bullet+}$] calcd for $C_{80}H_{70}N_2O_4S_6^{\bullet+}$, 1314.3654; found, 1314.3631.

Compound 16

To a flame-dried vial equipped with a magnetic stir bar were added **2** (69 mg, 209 μmol), **5** (28 mg, 153 μmol), and Lawesson's reagent (63 mg, 155 μmol). Dry toluene (5 mL) degassed with N_2 for 15 min was added, and the solution was heated to 105 °C for 18.5 h. The reaction mixture was then allowed to cool to rt, diluted with toluene (20 mL), and washed with 1 M NaOH (3 × 20 mL), and then with H_2O (20 mL). The yellow precipitate in the aqueous phase was isolated by filtration and washed with H_2O before it was purified by flash column chromatography (SiO_2, 50%–100% CH_2Cl_2/heptane) yielding **16** (18 mg, 39 μmol, 25%) as a yellow solid. R_f = 0.18 (50% CH_2Cl_2/heptane); mp > 260 °C; ^{1}H NMR (500 MHz,

CD_2Cl_2) δ 7.84 (d, *J* = 7.5 Hz, 2H), 7.77 (d, *J* = 8.1 Hz, 2H), 7.75 (d, *J* = 7.5 Hz, 2H), 7.41 (td, *J* = 7.5, 1.1 Hz, 2H), 7.39 (d, *J* = 8.1 Hz, 2H), 7.34 (td, *J* = 7.5, 1.1 Hz, 2H), 4.46 (s, 4H), 2.42 (s, 3H) ppm; ^{13}C NMR (126 MHz, CD_2Cl_2) δ 145.0, 138.5, 137.3, 134.0, 130.6, 128.8, 128.0, 127.5, 126.4, 123.4, 120.2, 21.7 ppm; two sp^2-C carbon signals missing, presumably due to overlap; HRMS (MALDI$^+$, FT-ICR, dithranol, *m*/*z*) [$M^{\bullet+}$] calcd for $C_{25}H_{19}NO_2S_3^{\bullet+}$, 461.0572; found, 461.0577.

Compound **18**

To an Ar-degassed solution of PPh_3 (845 mg, 3.22 mmol) and CBr_4 (560 mg, 1.69 mmol) in anhydrous toluene (20 mL) was added **6** (250 mg, 0.351 mmol). The reaction mixture was heated to reflux and stirred under a N_2 atmosphere for 30 h before it was cooled to rt and filtered through a plug of SiO_2 (CH_2Cl_2 as eluent) and concentrated in vacuum. Flash column chromatography (10% CH_2Cl_2/heptane) yielded **18** (246 mg, 81%) as an orange solid. R_f = 0.29 (10% CH_2Cl_2/heptane); ^{1}H NMR (500 MHz, $CDCl_3$) δ 8.99 (d, *J* = 0.7 Hz, 1H), 8.71 (d, *J* = 1.5 Hz, 1H), 7.94 (d, *J* = 0.7 Hz, 1H), 7.76–7.75 (m, 2H), 7.71 (d, *J* = 8.0 Hz, 1H), 7.48 (dd, *J* = 8.0, 1.5 Hz, 1H), 7.38 (dd, *J* = 8.0, 1.5 Hz, 1H), 3.01–2.96 (m, 4H), 1.85–1.68 (m, 4H), 1.51–1.47 (m, 4H), 1.45 (s, 9H), 1.40 (s, 9H), 1.37–1.30 (m, 8H), 0.92–0.88 (m, 6H) ppm; ^{13}C NMR (126 MHz, $CDCl_3$) δ 150.5, 150.4, 139.8, 139.6, 138.8, 138.5, 138.3, 138.1, 137.6, 137.3, 136.1, 135.8, 129.5, 128.4, 126.6, 123.3, 123.2, 121.4, 120.1, 119.2, 118.9, 117.3, 113.8, 89.1, 36.9, 36.8, 35.3, 35.3, 31.9, 31.7, 31.6, 31.5, 30.1, 30.0, 28.5, 22.7, 14.2, 14.2 ppm; two sp^3-C signals missing, presumably due to overlap; HRMS (MALDI$^+$, FT-ICR, dithranol, *m*/*z*) [$M^{\bullet+}$] calcd for $C_{44}H_{52}Br_2S_4^{\bullet+}$, 868.1293; found, 868.1287.

Compound **19**

To a N_2-degassed solution of **18** (90 mg, 0.10 mmol) in anhydrous THF (5 mL) and Et_3N (5 mL) were added N_2-degassed trimethylsilylacetylene (0.20 mL, 1.4 mmol), $Pd(PPh_3)_2Cl_2$ (15 mg, 0.021 mmol), and CuI (5.0 mg, 0.026 mmol). The reaction mixture was stirred at rt under a N_2 atmosphere for 4 h before it was filtered through a plug of SiO_2 (CH_2Cl_2 as eluent) and concentrated under reduced pressure. Purification by flash column chromatography (SiO_2, 10–15% CH_2Cl_2/heptane) yielded **19** (62 mg, 66%) as a purple solid (red in solution). R_f = 0.31 (15% CH_2Cl_2/heptane); ^{1}H NMR (500 MHz, $CDCl_3$) δ 9.07 (s, 1H), 8.81 (d, *J* = 1.7 Hz, 1H), 7.91 (s, 1H), 7.76 (d, *J* = 1.7 Hz, 1H), 7.72 (d, *J* = 8.0 Hz, 1H), 7.65 (d, *J* = 8.0 Hz, 1H), 7.41 (dd, *J* = 8.0, 1.7 Hz, 1H), 7.37 (dd, *J* = 8.0, 1.7 Hz, 1H), 3.01–2.96 (m, 4H), 1.79–1.72 (m, 4H), 1.54–1.48 (m, 4H), 1.45 (s, 9H), 1.40 (s, 9H), 1.35–1.32 (m, 8H), 0.92–0.89 (m, 6H), 0.44 (s, 9H), 0.35 (s, 9H) ppm; ^{13}C NMR (126 MHz, $CDCl_3$) δ 150.6, 150.2, 146.7, 139.6, 138.8, 138.3, 138.0, 137.6, 137.5, 136.0, 135.5, 129.5, 128.5, 126.9, 123.2, 123.2, 121.8, 120.1, 119.0, 118.8, 117.3, 113.9, 104.9, 104.5, 104.5, 104.3, 99.5, 36.9, 36.8, 35.3, 35.3, 31.9, 31.8, 31.6, 31.5, 30.1, 30.0, 28.5, 22.7, 22.7, 14.2, 14.2, 0.3, 0.1 ppm; one sp^2-C signal and one sp^3-C signal missing, presumably due to overlap; HRMS (MALDI$^+$, FT-ICR, dithranol, *m*/*z*) [$M^{\bullet+}$] calcd for $C_{54}H_{70}S_4Si_2^{\bullet+}$, 903.3972; found, 903.3985.

Compound **23**

In a manner similar to [41], TBAF (1 M in THF, 0.2 mL, 0.2 mmol) was added to a solution of **22** (93 mg, 0.073 mmol) in THF (10 mL), and the reaction mixture was stirred at rt for 45 min before it was filtered through a plug of SiO_2 (CH_2Cl_2 as eluent) and concentrated under reduced pressure to a volume of approx. 2 mL. The resulting solution was diluted with CH_2Cl_2 (50 mL). A solution of CuCl (7.0 mg, 0.070 mmol) in CH_2Cl_2 (5 mL) and TMEDA (0.10 mL, 0.67 mmol) was added along with 4 Å molecular sieves, and the reaction mixture was stirred in an open flask at rt for 3 days before it was filtered through a plug of SiO_2 (CH_2Cl_2 as eluent) and concentrated under reduced pressure. Flash column chromatography (30% CH_2Cl_2 (technical grade stabilized with 0.2% EtOH)/heptane) yielded **23** (33 mg, 47%) as a dark green solid. R_f = 0.20 (40% CH_2Cl_2/heptane); ^{1}H NMR (500 MHz, $CDCl_3$) δ 9.17 (s, 1H), 8.83 (d, *J* = 1.7 Hz, 1H), 7.89 (d, *J* = 7.8 Hz, 1H), 7.88 (s, 1H), 7.80 (d, *J* = 7.8 Hz, 1H), 7.76–7.71 (m, 2H), 7.60 (d, *J* = 8.0 Hz, 1H), 7.51–7.28 (m, 8H), 3.02–2.97 (m, 4H), 1.80–1.73 (m, 4H), 1.52–1.50 (m, 4H), 1.48 (s, 9H), 1.47 (s, 9H), 1.37–1.32 (m, 8H), 0.96–0.85 (m, 6H) ppm; ^{13}C NMR (126 MHz, $CDCl_3$) δ 150.5, 150.1, 148.3, 140.0, 139.0, 138.7, 138.7, 138.5, 137.8, 137.4, 136.0, 135.8, 131.4, 131.4, 130.6, 129.7, 129.5, 129.5, 129.0, 129.0, 128.8, 128.6, 128.6, 128.5, 127.0, 125.2, 125.0, 123.2, 123.1, 121.8, 120.2, 119.0, 117.9, 114.1, 99.6, 96.9, 95.9, 95.4, 94.5, 88.0, 87.8, 82.4, 81.2, 36.9, 36.8, 35.3, 35.2, 32.0, 31.9, 31.6, 31.5, 30.1, 30.0, 28.5, 22.7, 22.7, 14.2, 14 ppm; one signal missing in the aromatic region and one signal missing in the aliphatic region, presumably due to overlap; HRMS (MALDI$^+$, FT-ICR, dithranol, *m*/*z*) [$M^{\bullet+}$] calcd for $C_{82}H_{102}S_4Si_2^{\bullet+}$, 956.3572; found, 956.3620.

Compound **29**

To a 250 mL round-bottomed flask equipped with a reflux condenser and containing a magnetic stir bar, diethylene glycol (125 mL) and KOH (2.67 g, 47.7 mmol) were added. The solution was degassed with Ar for 30 min after which **5** (461 mg, 1.17 mmol) was added. Then, $N_2H_4{\cdot}H_2O$ (2.4 mL, 50.0 mmol) was added slowly, resulting in a color change to black within 30 min. The reaction was carried out under inert N_2 atmosphere. The reaction mixture was then heated to 185–190 °C for 48 h after which it was cooled to 100 °C, poured onto ice (400 mL), and acidified with aq HCl (20 mL, 6 M), resulting in an

orange precipitate. The ice was allowed to melt, and the precipitate was filtered, washed with H2O (100 mL), and dissolved in EtOAc (200 mL), after which the volatiles were removed under reduced pressure yielding compound **29** as a light orange crystalline solid (375 mg, 1.02 mmol, 88%). mp > 250 °C; ^{1}H NMR (500 MHz, CDCl3) δ 7.89 (s, 2H), 7.71 (d, *J* = 8.0, 2H), 7.59 (s, 2H), 7.42 (d, *J* = 8.0, 2H), 3.95 (s, 4H), 1.39 (s, 18H) ppm; ^{13}C NMR (126 MHz, $CDCl_3$) δ 149.8, 143.8, 142.5, 140.6, 139.5, 124.1, 122.1, 119.2, 116.3, 37.0, 35.0, 31.8 ppm; HRMS (MALDI$^+$, FT-ICR, dithranol, *m*/*z*) [$M^{\bullet+}$] calcd for $C_{28}H_{30}^{\bullet+}$, 366.2342; found, 366.2344.

Supporting Information

Supporting Information File 1

Synthetic protocols, UV–vis and NMR spectra, differential pulse voltammograms, and X-ray crystallographic data.
[https://www.beilstein-journals.org/bjoc/content/supplementary/1860-5397-20-8-S1.pdf]

Supporting Information File 2

Crystallographic information file of compound **25**.
[https://www.beilstein-journals.org/bjoc/content/supplementary/1860-5397-20-8-S2.cif]

Supporting Information File 3

Crystallographic information file of compound **26**.
[https://www.beilstein-journals.org/bjoc/content/supplementary/1860-5397-20-8-S3.cif]

Supporting Information File 4

Crystallographic information file of compound **29**.
[https://www.beilstein-journals.org/bjoc/content/supplementary/1860-5397-20-8-S4.cif]

Funding

The Novo Nordisk Foundation (NNF20OC0061574) and Sino-Danish College (SDC) are acknowledged for financial support.

ORCID® iDs

Christina Schøttler - https://orcid.org/0000-0001-6068-8343
Kasper Lund-Rasmussen - https://orcid.org/0009-0008-3973-5991
Viktor B. R. Pedersen - https://orcid.org/0000-0003-0661-6351
Mogens Brøndsted Nielsen - https://orcid.org/0000-0001-8377-0788

Data Availability Statement

The data that supports the findings of this study is available from the corresponding author upon reasonable request.

Preprint

A non-peer-reviewed version of this article has been previously published as a preprint: https://doi.org/10.3762/bxiv.2023.43.v1

References

1. Canevet, D.; Sallé, M.; Zhang, G.; Zhang, D.; Zhu, D. *Chem. Commun.* **2009,** 2245–2269. doi:10.1039/b818607n
2. Martín, N. *Chem. Commun.* **2013,** *49,* 7025–7027. doi:10.1039/c3cc00240c
3. Bergkamp, J. J.; Decurtins, S.; Liu, S.-X. *Chem. Soc. Rev.* **2015,** *44,* 863–874. doi:10.1039/c4cs00255e
4. Azov, V. A. *Tetrahedron Lett.* **2016,** *57,* 5416–5425. doi:10.1016/j.tetlet.2016.10.082
5. Jana, A.; Ishida, M.; Park, J. S.; Bähring, S.; Jeppesen, J. O.; Sessler, J. L. *Chem. Rev.* **2017,** *117,* 2641–2710. doi:10.1021/acs.chemrev.6b00375
6. Jana, A.; Bähring, S.; Ishida, M.; Goeb, S.; Canevet, D.; Sallé, M.; Jeppesen, J. O.; Sessler, J. L. *Chem. Soc. Rev.* **2018,** *47,* 5614–5645. doi:10.1039/c8cs00035b
7. Yamada, H.; Yamashita, M.; Hayashi, H.; Suzuki, M.; Aratani, N. *Chem. – Eur. J.* **2018,** *24,* 18601–18612. doi:10.1002/chem.201802744
8. Schröder, H. V.; Schalley, C. A. *Beilstein J. Org. Chem.* **2018,** *14,* 2163–2185. doi:10.3762/bjoc.14.190
9. Bryce, M. R. *J. Mater. Chem.* **1995,** *5,* 1481–1496. doi:10.1039/jm9950501481
10. Roncali, J. *J. Mater. Chem.* **1997,** *7,* 2307–2321. doi:10.1039/a703956e
11. Brunetti, F. G.; López, J. L.; Atienza, C.; Martín, N. *J. Mater. Chem.* **2012,** *22,* 4188–4205. doi:10.1039/c2jm15710a
12. Hammerich, O.; Nielsen, M. B. *J. Mater. Chem. C* **2019,** *7,* 2809–2822. doi:10.1039/c9tc00120d
13. Christensen, M. A.; Parker, C. R.; Sørensen, T. J.; de Graaf, S.; Morsing, T. J.; Brock-Nannestad, T.; Bendix, J.; Haley, M. M.; Rapta, P.; Danilov, A.; Kubatkin, S.; Hammerich, O.; Nielsen, M. B. *J. Mater. Chem. C* **2014,** *2,* 10428–10438. doi:10.1039/c4tc02178a
14. Broløs, L.; Nielsen, M. B. *RSC Adv.* **2020,** *10,* 15030–15033. doi:10.1039/d0ra02787a
15. Nielsen, M. B.; Diederich, F. *Chem. Rev.* **2005,** *105,* 1837–1868. doi:10.1021/cr9903353
16. Diederich, F.; Kivala, M. *Adv. Mater. (Weinheim, Ger.)* **2010,** *22,* 803–812. doi:10.1002/adma.200902623
17. Lincke, K.; Floor Frellsen, A.; Parker, C. R.; Bond, A. D.; Hammerich, O.; Brøndsted Nielsen, M. *Angew. Chem., Int. Ed.* **2012,** *51,* 6099–6102. doi:10.1002/anie.201202324
18. Kilde, M. D.; Murray, A. H.; Andersen, C. L.; Storm, F. E.; Schmidt, K.; Kadziola, A.; Mikkelsen, K. V.; Hampel, F.; Hammerich, O.; Tykwinski, R. R.; Nielsen, M. B. *Nat. Commun.* **2019,** *10,* 3714. doi:10.1038/s41467-019-11700-0
19. Broløs, L.; Kilde, M. D.; Hammerich, O.; Nielsen, M. B. *J. Org. Chem.* **2020,** *85,* 3277–3286. doi:10.1021/acs.joc.9b03118
20. Bliksted Roug Pedersen, V.; Granhøj, J.; Erbs Hillers-Bendtsen, A.; Kadziola, A.; Mikkelsen, K. V.; Brøndsted Nielsen, M. *Chem. – Eur. J.* **2021,** *27,* 8315–8324. doi:10.1002/chem.202100984
21. O'Driscoll, L. J.; Andersen, S. S.; Solano, M. V.; Bendixen, D.; Jensen, M.; Duedal, T.; Lycoops, J.; van der Pol, C.; Sørensen, R. E.; Larsen, K. R.; Myntman, K.; Henriksen, C.; Hansen, S. W.; Jeppesen, J. O. *Beilstein J. Org. Chem.* **2015,** *11,* 1112–1122. doi:10.3762/bjoc.11.125

22. Desai, N. B.; McKelvie, N.; Ramirez, F. *J. Am. Chem. Soc.* **1962,** *84,* 1745–1747. doi:10.1021/ja00868a057
23. Corey, E. J.; Fuchs, P. L. *Tetrahedron Lett.* **1972,** *13,* 3769–3772. doi:10.1016/s0040-4039(01)94157-7
24. Mysyk, D. D.; Perepichka, I. F.; Perepichka, D. F.; Bryce, M. R.; Popov, A. F.; Goldenberg, L. M.; Moore, A. J. *J. Org. Chem.* **1999,** *64,* 6937–6950. doi:10.1021/jo990100r
25. Amriou, S.; Wang, C.; Batsanov, A. S.; Bryce, M. R.; Perepichka, D. F.; Ortí, E.; Viruela, R.; Vidal-Gancedo, J.; Rovira, C. *Chem. – Eur. J.* **2006,** *12,* 3389–3400. doi:10.1002/chem.200501326
26. Pérez, E. M.; Sierra, M.; Sánchez, L.; Torres, M. R.; Viruela, R.; Viruela, P. M.; Ortí, E.; Martín, N. *Angew. Chem., Int. Ed.* **2007,** *46,* 1847–1851. doi:10.1002/anie.200604327
27. Dekhtiarenko, M.; Krykun, S.; Carré, V.; Aubriet, F.; Canevet, D.; Allain, M.; Voitenko, Z.; Sallé, M.; Goeb, S. *Org. Chem. Front.* **2020,** *7,* 2040–2046. doi:10.1039/d0qo00641f
28. Vilhelmsen, M. H.; Jensen, J.; Tortzen, C. G.; Nielsen, M. B. *Eur. J. Org. Chem.* **2013,** 701–711. doi:10.1002/ejoc.201201159
29. Tan, G.; Li, S.; Chen, S.; Sui, Y.; Zhao, Y.; Wang, X. *J. Am. Chem. Soc.* **2016,** *138,* 6735–6738. doi:10.1021/jacs.6b04081
30. Merlet, S.; Birau, M.; Wang, Z. Y. *Org. Lett.* **2002,** *4,* 2157–2159. doi:10.1021/ol025972l
31. Henke, P.; Rindom, C.; Kanta Aryal, U.; Frydenlund Jespersen, M.; Broløs, L.; Mansø, M.; Turkovic, V.; Madsen, M.; Mikkelsen, K. V.; Ogilby, P. R.; Brøndsted Nielsen, M. *ChemSusChem* **2023,** *16,* e202202320. doi:10.1002/cssc.202202320
32. Eakins, G. L.; Cooper, M. W.; Gerasimchuk, N. N.; Phillips, T. J.; Breyfogle, B. E.; Stearman, C. J. *Can. J. Chem.* **2013,** *91,* 1059–1071. doi:10.1139/cjc-2013-0074
33. Andersen, D.; Nygaard, D. B.; Kragh, R. R.; Broløs, L.; Nielsen, M. B. *Tetrahedron Lett.* **2020,** *61,* 151939. doi:10.1016/j.tetlet.2020.151939
34. Jiang, H.; Mazzanti, V.; Parker, C. R.; Broman, S. L.; Wallberg, J. H.; Lušpai, K.; Brincko, A.; Kjaergaard, H. G.; Kadziola, A.; Rapta, P.; Hammerich, O.; Nielsen, M. B. *Beilstein J. Org. Chem.* **2015,** *11,* 930–948. doi:10.3762/bjoc.11.104
35. *SAINT,* V8.40A; Bruker AXS Inc.: Madison, Wisconsin, USA.
36. Krause, L.; Herbst-Irmer, R.; Sheldrick, G. M.; Stalke, D. *J. Appl. Crystallogr.* **2015,** *48,* 3–10. doi:10.1107/s1600576714022985
37. Sheldrick, G. M. *Acta Crystallogr., Sect. A: Found. Adv.* **2015,** *71,* 3–8. doi:10.1107/s2053273314026370
38. Sheldrick, G. M. *Acta Crystallogr., Sect. C: Struct. Chem.* **2015,** *71,* 3–8. doi:10.1107/s2053229614024218
39. Groom, C. R.; Bruno, I. J.; Lightfoot, M. P.; Ward, S. C. *Acta Crystallogr., Sect. B: Struct. Sci., Cryst. Eng. Mater.* **2016,** *72,* 171–179. doi:10.1107/s2052520616003954
40. Kratzert, D. *FinalCif, V113*, https://dkratzert.de/finalcif.html
41. Broløs, L.; Kilde, M. D.; Brock-Nannestad, T.; Nielsen, M. B. *Eur. J. Org. Chem.* **2021,** 3537–3544. doi:10.1002/ejoc.202100514

License and Terms

BEILSTEIN JOURNAL OF ORGANIC CHEMISTRY

Electron-beam-promoted fullerene dimerization in nanotubes: insights from DFT computations

Laura Abella[‡1], Gerard Novell-Leruth[‡1,2], Josep M. Ricart[1], Josep M. Poblet[1] and Antonio Rodríguez-Fortea[*1]

Full Research Paper

Open Access

Address:
[1]Departament de Química Física i Inorgànica, Universitat Rovira i Virgili, C/Marcel·lí Domingo 1, 43007 Tarragona, Spain and [2]Hydrogen and Power-to-X Department, Iberian Center for Research in Energy Storage (CIIAE), FUNDECYT-PCTEx, Polytechnic School of Caceres Building, Office CIIAE-C7, Av. Universidad s/n, 10003 Cáceres, Spain

Email:
Antonio Rodríguez-Fortea[*] - antonio.rodriguezf@urv.cat

* Corresponding author ‡ Equal contributors

Keywords:
DFT; dimerization; fullerene; molecular dynamics; peapods

Beilstein J. Org. Chem. **2024,** *20,* 92–100.
https://doi.org/10.3762/bjoc.20.10

Received: 13 October 2023
Accepted: 04 January 2024
Published: 17 January 2024

This article is part of the thematic issue "Carbon-rich materials: from polyaromatic molecules to fullerenes and other carbon allotropes".

Guest Editor: Y. Yamakoshi

Abstract

Fullerene dimerization inside a peapod is analyzed at DFT level by characterizing the stationary points and deriving the energy profile of the initial and reversible process named phase 1. We find that the barriers for the radical cation mechanism are significantly lower than those found for the neutral pathway. The peapod is mainly providing one-dimensional confinement for the reaction to take place in a more efficient way. Car–Parrinello metadynamics simulations provide hints on structures for the initial steps of the irreversible phase 2 where bond formation and breaking lead to important structural reorganizations within the coalescence process.

Introduction

Transmission electron microscopy (TEM) is a technique that has been used for a long time to provide images of molecules, but also to monitor the reactions triggered by the energy transfer of the electron beam to the atoms that build the molecules. In particular, the advances in TEM as well as in methods to anchor molecules on surfaces like graphene or carbon nanotubes have allowed the scientific community to visualize at atomic resolution the structural changes of molecules in situ by single-molecule atomic-resolution real-time TEM imaging (SMART-TEM) [1-5]. Since the initial discovery [2], many movies have been published that record the dynamic behavior of a wide range of molecules and chemical reactions. One such process was the dimerization of C_{60} fullerene in a carbon nanotube peapod, i.e., hybrid structures consisting of fullerene molecules encapsulated in single-walled carbon nanotubes (SWCNT) [6-8]. Different stages of dimerization of C_{60} molecules inside a peapod, a reaction confined within a one-dimensional nanoscale space, have been detected in the last decade [3,4,7,9]. Nakamura and co-workers termed ‘phase 1’ the stage with reversible bond formation and ‘phase 2’ the stage with irreversible C–C fusions

[7]. In phase 1, a [2 + 2] cycloadduct C_{120} dimer is formed, which was initially proposed to be with C_s symmetry, in contrast to the X-ray structure for the C_{120} dimer that shows D_{2h} symmetry [3,9]. In phase 2, irreversible structural rearrangements occur leading to a nanotubular-shaped fullerene inside the peapod. Kinetic analysis with the variable-temperature (VT) SMART-TEM method for the aforementioned C_{60} dimerization has also been reported by these authors [9]. They concluded that the SWCNT, which accumulates energy by the interaction with the electron beam, activates the reaction either via singlet excitation or via radical cation formation (Scheme 1). Estimation of the activation barrier for the [2 + 2] cycloaddition when the nanotube acts as a sensitizer is 33.5 ± 6.8 kJ mol^{-1}. This value agrees with computational predictions for the reaction via an excited singlet state [10].

Although only a few analyses of the reaction mechanisms have been studied due to the complexity of the system, several intermediates inside the CNT have been proposed [3,11,12], which may be different from those proposed to take place in the gas phase or in the solid state at high pressures and high temperatures [13-15]. We aim to shed light in these reaction mechanisms and energy profiles by using complementary methodologies as standard density functional theory (DFT) calculations and first-principles Car–Parrinello molecular dynamics (CPMD) simulations. Firstly, we have analyzed the interaction between C_{60} and the nanotube within the peapod. Next, we have found that some dimeric C_{60}–C_{60} fullerene structures inside the carbon nanotube are thermodynamically favorable. Experiments indicate that, besides C_{60} sensitization via a singlet excited state, the [2 + 2] cycloaddition can also be activated through the formation of $C_{60}^{+\bullet}$ radical cation [3,9]. This mechanistic proposal for phase 1, which to our knowledge has not yet been explored in detail inside a carbon nanotube, is analyzed here and compared to the non-activated C_{60} dimerization. Finally, some intermediates for the subsequent irreversible C–C fusions occurring in phase 2 are proposed with the help of accelerated Car–Parrinello MD simulations.

Results and Discussion

Nanotube-C_{60} interaction: stabilization of the peapod

First, we estimated the size of the stabilizing interaction that holds the peapod, that is, the interaction between the C_{60} surface and the walls of the armchair (10,10) CNT. The interaction or encapsulation energy of a fullerene inside the CNT, defined as $E_{encap} = E_{Fuller@CNT} - E_{Fuller} - E_{CNT}$, amounts to −3.23 eV for C_{60} at our present computational settings (PBE/plane waves, see section Computational methods). This significant amount of energy, which could be overestimated, comes from the π–π interactions between the C_{60} surface and the CNT wall and is modelled in a first approximation using Grimme's corrections to the dispersion energy [16]. This interaction energy is comparable to those in similar systems with π–π interactions, as for example a "buckyball catcher" complex with C_{60} or the interlayer interaction between graphene sheets [16]. It is found to be significantly smaller than for $C_{60}@C_{240}$ [17], but larger than for $C_{60}@C_{540}$ and $C_{60}@C_{960}$ nanoonions [18]. The encapsulation energy of two separated C_{60} molecules essentially doubles that of a single molecule (−6.48 eV, see Figure S1 in Supporting Information File 1). For different C_{60} dimers (Figure 1), the interaction energies range between −6.45 and −6.50 eV (Figure S1 in Supporting Information File 1), a range which is around 1% of the total encapsulation energy. As a consequence of the effective π–π interactions, the larger the contact between the fullerene dimer surface and the CNT wall the larger the encapsulation energy. This significant interaction

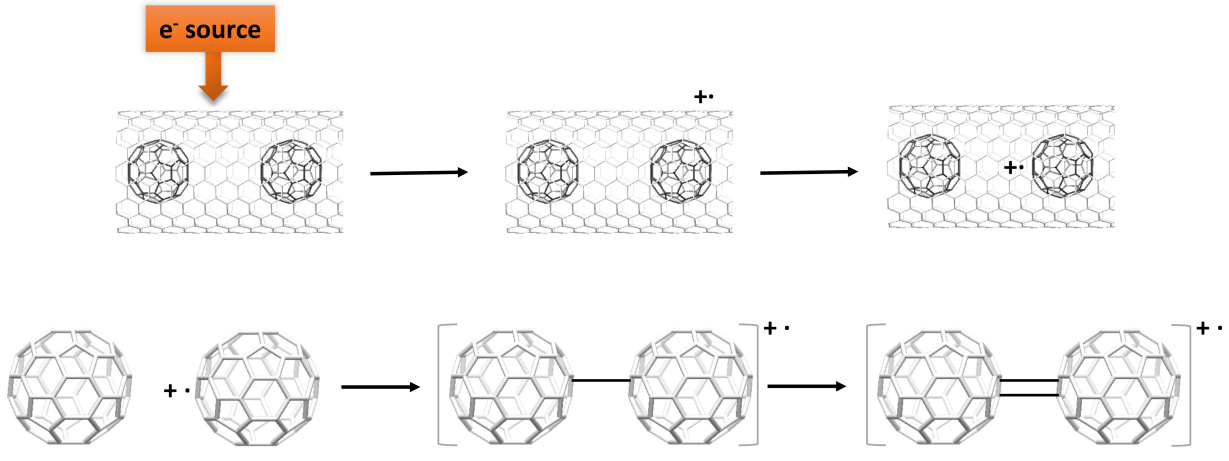

Scheme 1: Proposed radical cation mechanism for the dimerization of two C_{60} cages inside a metallic carbon nanotube.

is also apparent from an inspection of the electronic structure of the peapod, where we can observe some molecular orbitals with non-spurious contributions from each of the CNT and C_{60} fragments (Figures S2–S4 in Supporting Information File 1).

Relative stabilities of C_{60}–C_{60} dimers

We computed the reaction energies for the dimerization of two C_{60} molecules in the one-dimensional space within the CNT and compared the results with those for the same reaction in the gas phase. We assumed that the cation radical mechanism takes place, that is, the ionized CNT generates a radical cation $C_{60}^{\bullet+}$ that reacts with a C_{60} molecule to yield different $C_{120}^{\bullet+}$ dimers. The energies for the dimerization of two neutral C_{60} molecules were also computed for comparison (Table 1). As products, we have considered dimer **1-*D*$_{2h}$** and dimer **1-*C*$_s$**, which are products of reversible [2 + 2] cycloadditions (phase 1) between two [6,6]-bonds in the former case and, between a [6,6]-bond and a [6,5]-bond in the latter (Figure 1). Dimer **1-*C*$_s$** is at our computational settings (PBE/PW), more than 15 kcal mol^{-1} higher in energy than dimer **1-*D*$_{2h}$**, the one characterized by X-ray crystallography in the solid state, both in the gas phase and inside the CNT. Similar lower stabilities for dimer **1-*C*$_s$** are also found for the radical cation products, especially in the gas phase (second column in Table 1). The reaction energies are, however, notably more negative for the radical cation products. Besides, radical cations **1-*C*$_s$**$^{\bullet+}$ and **1-*D*$_{2h}$**$^{\bullet+}$ show comparable energies. Finally, for the nanotubular-shaped **C_{120}-NT-*D*$_{5d}$** isomer, the formation energies with respect to C_{60} + C_{60} are up to −300 kcal mol^{-1}, which reflects the high degree of C–C bond reorganization needed to obtain this fullerene isomer that satisfies the so-called isolated pentagon rule (IPR) [19]. We corroborated our results for the gas-phase products using somewhat different computational settings with a non-periodic electronic structure code as ADF, see values in parenthesis in the two first columns of Table 1 (also at PBE level, but using atomic orbitals instead of plane waves as basis sets, see Computational methods). Although reaction energies are predicted to be somewhat more exothermic in most of the cases, relative energies between isomers are very similar, both for the neutral as well as for the radical cation dimers, what confirms the reliability of the computational settings used in the periodic VASP code.

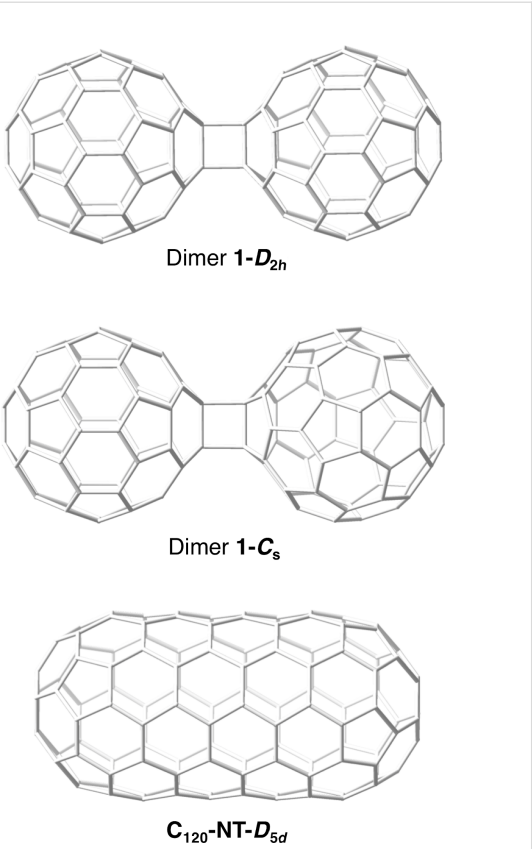

Figure 1: DFT-optimized structures of C_{60} dimers **1-*D*$_{2h}$**, **1-*C*$_s$** and nanotubular **C_{120}-NT-*D*$_{5d}$** fullerene.

Table 1: Reaction energies for the dimerization of two neutral C_{60} molecules and one neutral C_{60} and one radical cation $C_{60}^{\bullet+}$ to yield different C_{120} dimers.[a]

	Gas-phase		@SWCNT	
	C_{60} + C_{60}	C_{60} + $C_{60}^{\bullet+}$	C_{60} + C_{60}	C_{60} + $C_{60}^{\bullet+}$
dimer **1-*D*$_{2h}$**	−6.1	-23.6	-5.7	−8.9
	(−9.9)	(−23.4)		
dimer **1-*C*$_s$**	+11.3	−10.0	+10.6	−6.6
	(+7.6)	(−10.7)		
C_{120}-NT-*D*$_{5d}$	−296.3	−329.3	−308.3	−332.2
	(−298.6)	(−327.5)		

[a]Energies referred to 2 C_{60} and C_{60} + $C_{60}^{\bullet+}$ (in kcal mol^{-1}) for the dimers represented in Figure 1 in the gas phase and inside the carbon nanotube (@SWCNT). Energies calculated using VASP package (PBE/PW-PAW). Energies in parenthesis were obtained with the ADF code (PBE/TZP).

Energy profile for the reversible [2 + 2] cycloaddition in phase 1

We analyzed in detail the energy profile for the first step in the dimerization process, that is, the reversible [2 + 2] cycloaddition to obtain dimers **1-C_s** and **1-D_{2h}**. We initially considered dimerization in the gas phase to check the reliability of our methodology (periodic calculations using VASP code) by comparing with other more standard procedures (non-periodic calculations using ADF code; see Computational methods for details) when computing the energy profile for the radical cation C_{60} + C_{60}^{+}. Besides, we computed the profile for the neutral dimerization C_{60} + C_{60} to assess the effect ionization produced by the electron beam has in the process. Before the reaction takes place, a stabilizing van der Waals complex between the two C_{60} molecules was formed (Figure 2), with an interdimer distance around 3 Å (slightly larger for the neutral profile). For dimer **1-C_s**, the stabilization of this complex is significantly more important for the radical cation (around 20 kcal mol^{-1}) than for the neutral complex (less than 10 kcal mol^{-1}). To reach intermediate **I-1**, the singly-bonded dimer, a transition state **TS-1** has to be overcome. The barrier for the radical cation is much smaller (6–7 kcal mol^{-1}) than for the neutral dimer (28.8 kcal mol^{-1}), so we confirm that the process is activated for the cation. The interdimer C···C distance is smaller than 2 Å for the radical cation and for the neutral species. Once intermediate **I-1** is formed, the interdimer C–C distance is around 1.60–1.70 Å. Formation of the second C–C bond to yield dimer **1-C_s** requires to overcome a second transition state **TS-2** with energy barriers that range between 10–13 kcal mol^{-1} from the immediate intermediate depending on the profile. The interdimer C···C distance of the forming bond is slightly larger than 2 Å in all three cases. Finally, formation of dimer **1-C_s** is exothermic for the radical cation profile, but moderately endothermic for the neutral dimer, as

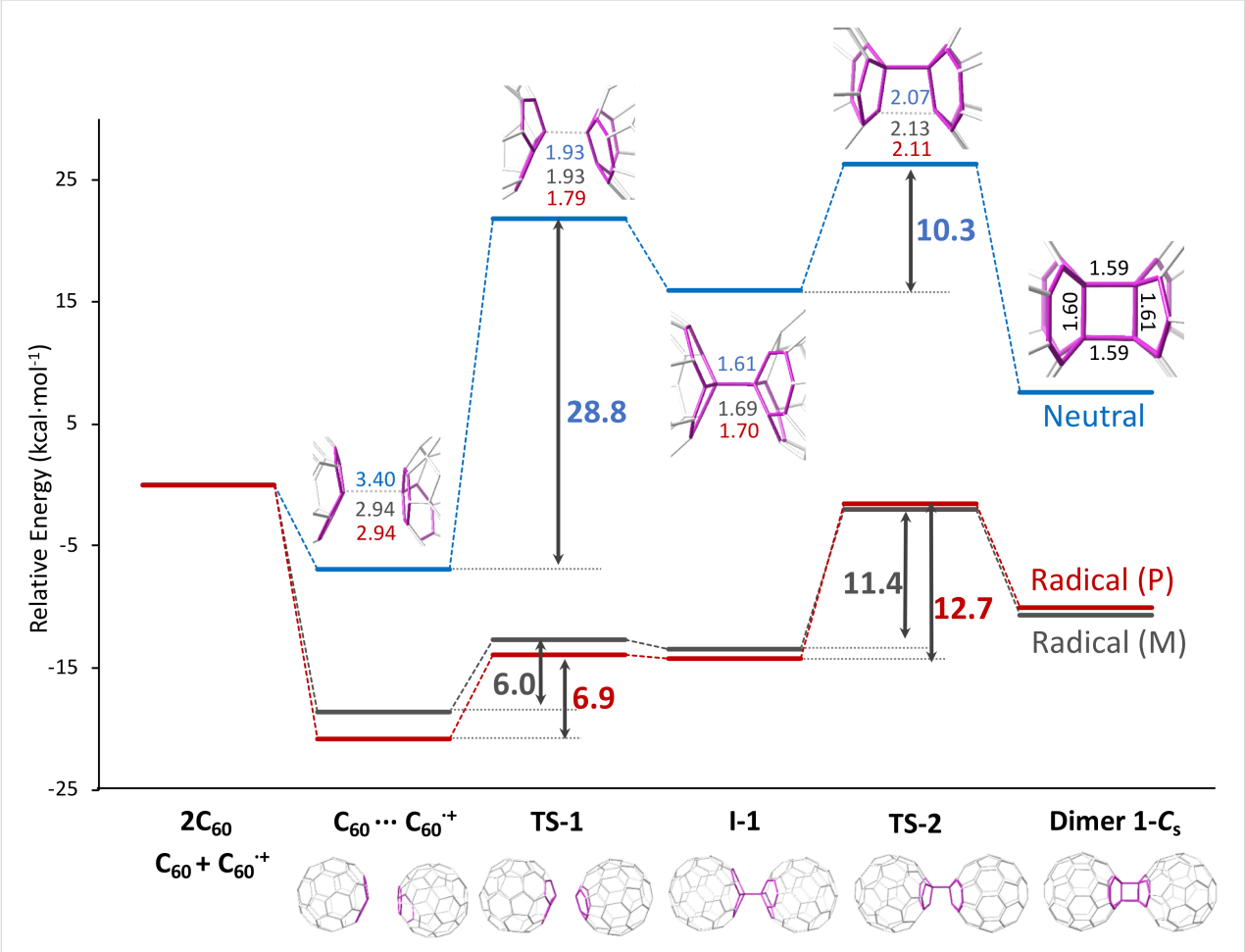

Figure 2: Energy profiles for the dimerization of 2 C_{60} and C_{60} + $C_{60}^{\bullet+}$ fullerenes in the gas phase. All energy barriers are in kcal mol^{-1} and distances of the most relevant bonds for the different structures are represented in Å in a zoomed image. Energy profile for C_{60} + $C_{60}^{\bullet+}$ radical dimerization (phase 1) computed with the periodic (P) approximation (plane waves, VASP) is represented in red, while energy profiles for C_{60} + $C_{60}^{\bullet+}$ radical and C_{60} + C_{60} neutral dimerizations computed with the standard molecular (M) approach (atomic basis functions, ADF) are represented in grey and blue, respectively.

previously observed. As general trends, we find that the radical cation profiles are qualitatively parallel with some minimal differences, which corroborates the validity of our periodic approximation to study the dimerization of the radical cation inside the CNT (see below). The rate-determining transition state for the radical cation and for the neutral dimer is the same (TS2) as well as the lowest-energy intermediate (van der Waals complex), so the two profiles are not that different, according to the energetic spam model by Kozuch and Shaik [20]. In any case, the mechanism via radical cation is the most favorable, both kinetically and thermodynamically. For dimer **1-D$_{2h}$**$^{\bullet+}$, the energy profile up to **I-1** is very similar to that of dimer **1-C$_s$**$^{\bullet+}$ (see Supporting Information File 1, Figure S9). However, **TS-2** is significantly lower in energy. Therefore, in gas phase, dimer **1-*D*$_{2h}$**$^{\bullet+}$ is predicted to be the thermodynamic and the kinetic product.

Once our methodology was validated, the energy profile for the formation of dimer **1-*C*$_s$** inside the CNT was analyzed. In contrast to the gas phase reaction, we now only found the initial van der Waals complex and a single transition state **TS** for both the neutral and the radical cation profiles (Figure 3). The van der Waals complex shows an interdimer C···C distance of 2.86 Å, slightly shorter than the one observed for the gas phase reaction. The transition state **TS** corresponds now to the formation of the second interdimer C···C distance, around 2.15 Å (Figure 3), once the first C–C bond is already formed. All the attempts to obtain an intermediate with a single C–C interdimer bond failed. The energy barrier to overcome the **TS** is predicted to be 29.1 kcal mol^{-1} for the neutral dimer, but only 2.0 kcal mol^{-1} for the radical cation. Therefore, the first step of the C_{60} dimerization is significantly faster for the radical cation than for the neutral system. Formation of dimer **1-*C*$_s$**@CNT is appreciably endothermic for the neutral profile (>10 kcal mol^{-1}), but fairly exothermic (−25 kcal mol^{-1}, Figure 3) for the radical cation dimer (C_{60}-C_{60})$^{\bullet+}$@CNT. Albeit some differences are present, the general features of the energy profiles inside the CNT are not that different from those in the gas phase; the C_{60} + C_{60} dimerization is slightly endothermic with a barrier around 30 kcal mol^{-1}, whereas dimerization for the radical cation is exothermic with a tiny (or almost nil) barrier, which makes this initial step of the reaction drastically faster. Therefore, the main function of the CNT is to *constrain* the translation of C_{60} molecules to a one-dimensional space to maximize the rate of collisions between them. Finally, we would like to point out that in the reversible phase 1, radical

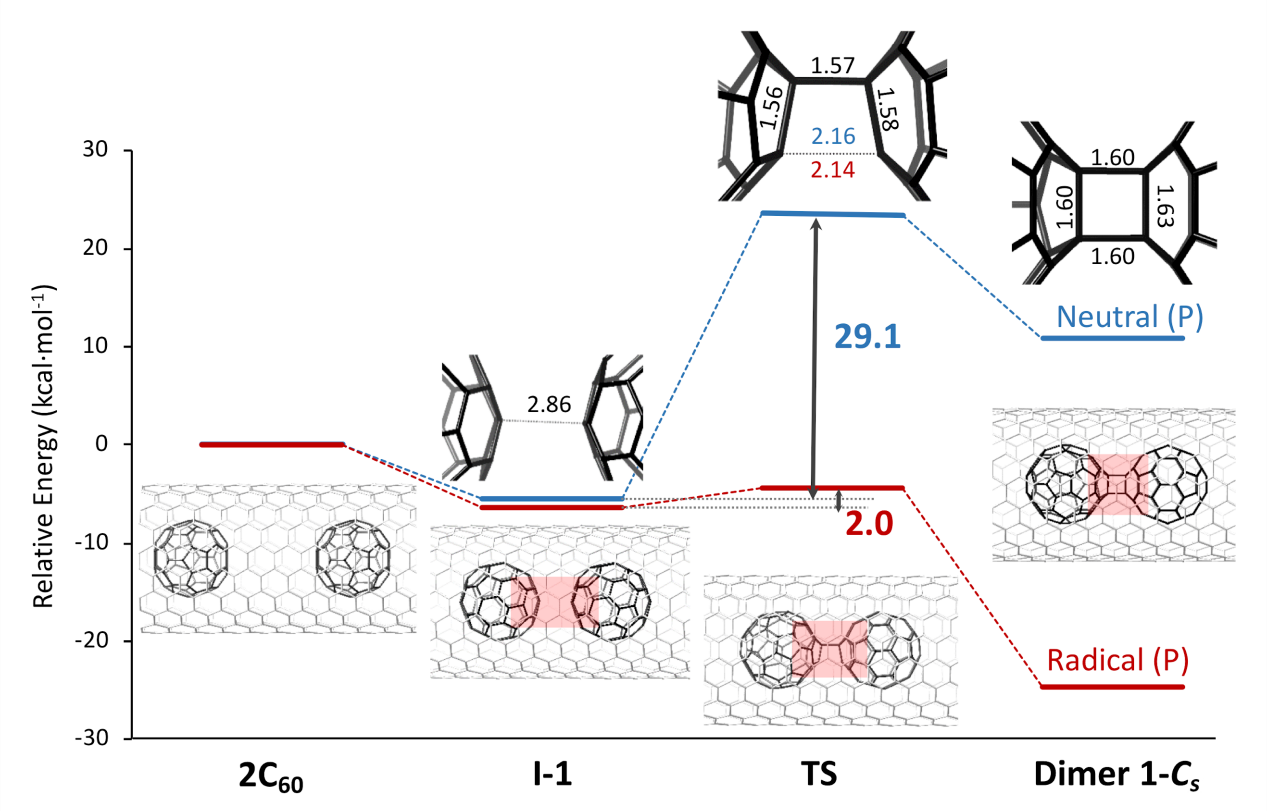

Figure 3: Energy profiles for the dimerization of 2 C_{60} (neutral) and C_{60} + $C_{60}^{\bullet+}$ (radical cation) fullerenes inside the SWCNT computed with the periodic (P) approximation (plane waves, VASP). Energy barriers are in kcal mol^{-1} and distances of the most relevant bonds for the different structures are in Å.

cation (**1-D_{2h}**)$^{\bullet+}$@CNT, which shows slightly lower energy than (**1-C_s**)$^{\bullet+}$@CNT (2 kcal mol^{-1} with our settings) is also predicted to be formed. Free energy difference between the two isomers, estimated in the gas phase, is somewhat reduced when increasing temperature (see Supporting Information File 1, Table S1). Therefore, the molar fraction of (**1-C_s**)$^{\bullet+}$@CNT would increase slightly at higher temperatures.

Mechanistic insights on the irreversible phase 2: first steps

Once phase 1 was analyzed in detail, we studied the irreversible formation of C–C bonds in the interdimer region, known as phase 2 in the dimerization process. Due to the large number of possible pathways to be investigated, we made use of a simulation technique that allowed us to explore the free energy surface in a fast and efficient way. In particular, we performed Car–Parrinello metadynamics simulations by choosing collective variables (CVs) that describe the formation and breaking of C–C bonds in the interdimer region (see Computational methods for more details). It is not the goal of the present work to explain all the steps up to the formation of fullertube C_{120}, but the steps that follow the formation of dimers **1-C_s**$^{\bullet+}$ and **1-D_{2h}**$^{\bullet+}$. We first run a metadynamics simulation for dimer **1-C_s**$^{\bullet+}$ using as CV the coordination number of nine carbon atoms of one C_{60} molecule (those of contiguous hexagon and pentagon) with respect to nine carbon atoms in the other C_{60}, all of them in the interdimer region (see Supporting Information File 1). Choosing this single CV, we aim to rapidly and efficiently explore the region of the free energy surface that describes the formation of irreversible C–C bonds. Molecular dynamics simulations were done in the radical C_{120} dimer alone; we did not consider the interaction with the CNT. After a 4 ps metadynamics, we observed the sequential formation of C–C bonds between the two C_{60} cages up to a number of six in structures that we have called dimer **3B-C_s**$^{\bullet+}$ (three bonds), dimer **4B-C_s**$^{\bullet+}$ (four bonds), dimer **5B-C_s**$^{\bullet+}$ (five bonds) and finally dimer **HPR-C_s**$^{\bullet+}$ (six bonds, see Figure 4). In the latter, one hexagon from each C_{60} face each other with six interdimer bonds formed between the C atoms at the vertexes of each hexagon forming a hexagonal prism (HPR). Several authors have already proposed this HPR structure for the dimerization of two neutral C_{60} cages [13-15]. We characterized this structure as a minimum of the potential energy surface at 49.2 kcal mol^{-1} (PBE/TZP) higher than dimer **1-C_s**$^{\bullet+}$ (Table 2). The C–C distances of the six new bonds are 1.597 Å and the six C–C distances within each hexagon have been elongated from 1.41–1.49 in C_{60} to 1.55–1.57 Å (Table S2). Dimers **3B-C_s**$^{\bullet+}$ and **4B-C_s**$^{\bullet+}$ are also characterized as minima at 18.7 and 34.3 kcal mol^{-1} with respect to dimer **1-C_s**$^{\bullet+}$ (Table 2). Structure of dimer **5B-C_s**$^{\bullet+}$ found in the metadynamics, however, is not a minimum and leads to dimer **3B-C_s**$^{\bullet+}$ upon geometry optimization. C–C distances of the new bonds are within the range 1.53–1.71 Å. For dimer **1-C_s**$^{\bullet+}$, the two distances are equivalent (1.587 Å) as they are the six distances for **HPR-C_s**$^{\bullet+}$ (1.597 Å); for dimers **3B-C_s**$^{\bullet+}$ and **4B-C_s**$^{\bullet+}$, however, more asymmetry in the distances is found. Similar C–C distances within the interacting hexagons exist, all of them within the range 1.55–1.60 Å (Supporting Information File 1, Table S2). A second metadynamics run for dimer **1-D_{2h}**$^{\bullet+}$ was also done using as CV the coordination number of ten carbon atoms of one C_{60} molecule (two contiguous hexagons) with respect to ten carbon atoms in the other C_{60}, analogous to the first run. After 7 ps, we also observed the sequential formation of C–C bonds between the two cages in structures now called dimer **3B-D_{2h}**$^{\bullet+}$ (three bonds),

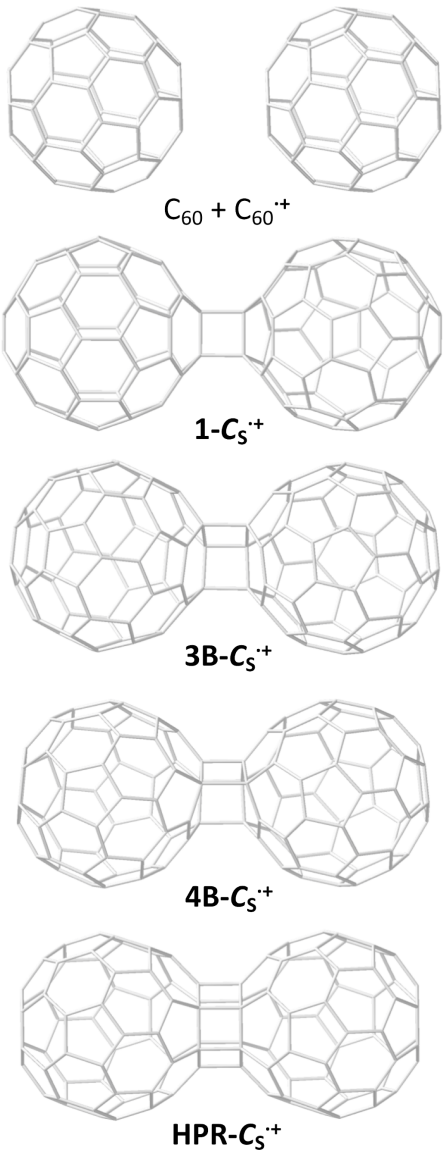

Figure 4: Proposed sequence of C_{60} dimers up to the formation of dimer **HPR-C_s**$^{\bullet+}$.

dimer **4B-D_{2h}**$^{\bullet+}$ (four bonds), dimer **5B-D_{2h}**$^{\bullet+}$ (five bonds) and finally dimer **HPR-D_{2h}**$^{\bullet+}$ (six bonds, see Figure S10). Dimers **3B-D_{2h}**$^{\bullet+}$, **4B-D_{2h}**$^{\bullet+}$ and **HPR-D_{2h}**$^{\bullet+}$ are characterized as minima at 32.7, 39.3 and 63.3 kcal mol^{-1} with respect to dimer **1-D_{2h}**$^{\bullet+}$ (Table 2). The C–C bond distances are very similar to those of the corresponding C_s dimers (Supporting Information File 1, Table S2).

Table 2: Relative energies for several dimers during the reaction of one neutral C_{60} and one radical cation $C_{60}^{\bullet+}$.[a]

	$C_s$$^{\bullet+}$	$D_{2h}$$^{\bullet+}$
dimer **1**	12.7	0.0
dimer **3B**$^{\bullet+}$	31.4	32.7
dimer **4B**$^{\bullet+}$	47.0	39.3
dimer **HPR**$^{\bullet+}$	61.9	63.3

[a]Relative energies with respect to dimer **1-D_{2h}**$^{\bullet+}$ (in kcal mol^{-1}). Corresponding dimers are shown in Figure 4 and Supporting Information File 1, Figure S10.

Conclusion

Two different computational methodologies, molecular approach versus periodic solid-state approach provide analogous and consistent results, which gives strong support and reliability to the predictions. In general, the reaction of two C_{60} molecules to yield different dimers is exothermic and the exothermicity is enhanced when radical cation dimers are formed. The thermodynamics of dimerization inside the nanotube is not that different as found in the gas phase; the nanotube mainly provides a 1D confinement for the reaction to proceed. The barriers for the reversible phase 1 are found to be easily surmountable at ambient temperature for both the forward and the inverse processes, especially for the dimerization of radical cation fullerenes. For the initial steps of irreversible phase 2, up to six C–C bonds in the interdimer region are formed leading to a hexagonal prism shared by the two cages, with significantly larger barriers than in phase 1, and the processes, consequently, slower. Next steps of radical cation dimerization inside the CNT (phase 2), which are under study, combined with new SMART-TEM images and movies will provide us a deeper understanding of fullerene coalescence processes in peapods.

Computational Methods

The Amsterdam Density Functional (ADF) code [21,22] was used for the electronic structure calculations and to optimize reactants, products, intermediates and transition states. The Perdew, Burke and Ernzerhoff (PBE) functional provided the electronic density [23]. Electrons were described with Slater-type basis functions of triple-ζ + polarization quality. We have included scalar relativistic corrections using the zeroth-order regular approximation (ZORA) formalism. Grimme3 BJ-DAMP dispersion corrections have also been included in all calculations [24]. Stationary points were fully characterized by computing the Hessian matrix.

Car–Parrinello molecular dynamics (CPMD) simulations were performed by means of the CPMD program [25,26]. The description of the electronic structure was based on the expansion of the valence electronic wave functions in a plane wave (PW) basis set, which was limited by an energy cutoff of 40 Ry. The interaction between the valence electrons and the ionic cores was treated through the pseudopotential (PP) approximation (Martins–Troullier type) [27]. The PBE functional was selected as the density functional. Dispersion corrections were also considered in the calculations. We used a fictitious electron mass of 800 a.u. The simulations were carried out using periodic boundary conditions in a tetragonal cell (side length of 11 Å and height of 20 Å) and a time step of 0.144 fs. We used the metadynamics technique to analyze the dimerization reaction mechanism [28-30]. The collective variable (CV) considered for the exploration of the free-energy surface was the coordination number of nine C atoms of one C_{60} (those that are involved in a hexagon fused with a pentagon) with respect to the nine C atoms (hexagon-pentagon) on the other C_{60} molecule (see Supporting Information File 1 for details). The armchair-type single-wall carbon nanotube (SWCNT) (10,10) with a length of 22.14 Å and a diameter of 13.65 Å was employed in the calculations.

The fullerene dimerization mechanism inside a SWCNT was also studied by density functional theory applied to periodic systems through VASP code [31]. The exchange-correlation functional used was PBE with the zero damping DFT-D3 method of Grimme et al. [16]. Inner electrons were replaced by PAW pseudopotentials [16] while valence electron density was expanded in plane waves with a maximum kinetic energy of 400 eV. The model of SWCNT was 29.61 Å long and with a diameter of 13.65 Å, embedded in a box of 30 × 30 Å of vacuum in the plane perpendicular to the nanotube axis. The gas-phase structures were in a cubic box of 30 Å side. The k-point sampling was performed through the Gamma–Pack scheme with one point. Transition states were obtained through the climbing image version of the nudged elastic band algorithm [32] and dimer method [33]. These structures showed a single imaginary frequency or with some negligible imaginary frequencies (under 10 cm^{-1}). The projected density of states was calculated and own code estimated the bands that belong to fullerene or SWCNT. The excited states of the fullerene dimer inside the SWCNT were studied with a single-point energy calculation of a given band structure where one electron of the highest-occupied band of the fullerene is excited to the lowest-unoccupied band of SWCNT.

Supporting Information

Supporting Information File 1

Additional details of the computational settings and results: encapsulation energies, molecular orbitals (MO), MO diagrams, intermediate structures in metadynamics and optimized xyz coordinates for the dimers.
[https://www.beilstein-journals.org/bjoc/content/supplementary/1860-5397-20-10-S1.pdf]

Funding

A.R.-F. and J.M.P. thank the Spanish Ministry of Science and Innovation for grant PID2020-112762GB-I00 funded by MCIN/AEI/10.13039/501100011033. J.M.R. thanks grant PID2021-128128NB-I00 funded by MICIN/AEI/10.13039/501100011033 and by "ERDF A way of making Europe". The authors also thank the Generalitat de Catalunya (grant 2021SGR00110) and the URV for support.

ORCID® iDs

Laura Abella - https://orcid.org/0000-0003-2188-248X
Gerard Novell-Leruth - https://orcid.org/0000-0001-9626-1720
Josep M. Ricart - https://orcid.org/0000-0002-2610-5535
Josep M. Poblet - https://orcid.org/0000-0002-4533-0623
Antonio Rodríguez-Fortea - https://orcid.org/0000-0001-5884-5629

References

1. Chuvilin, A.; Khlobystov, A. N.; Obergfell, D.; Haluska, M.; Yang, S.; Roth, S.; Kaiser, U. *Angew. Chem., Int. Ed.* **2010,** *49,* 193–196. doi:10.1002/anie.200902243
2. Koshino, M.; Tanaka, T.; Solin, N.; Suenaga, K.; Isobe, H.; Nakamura, E. *Science* **2007,** *316,* 853. doi:10.1126/science.1138690
3. Nakamura, E. *Angew. Chem., Int. Ed.* **2013,** *52,* 236–252. doi:10.1002/anie.201205693
4. Nakamura, E. *Acc. Chem. Res.* **2017,** *50,* 1281–1292. doi:10.1021/acs.accounts.7b00076
5. Skowron, S. T.; Chamberlain, T. W.; Biskupek, J.; Kaiser, U.; Besley, E.; Khlobystov, A. N. *Acc. Chem. Res.* **2017,** *50,* 1797–1807. doi:10.1021/acs.accounts.7b00078
6. Hernández, E.; Meunier, V.; Smith, B. W.; Rurali, R.; Terrones, H.; Buongiorno Nardelli, M.; Terrones, M.; Luzzi, D. E.; Charlier, J.-C. *Nano Lett.* **2003,** *3,* 1037–1042. doi:10.1021/nl034283f
7. Koshino, M.; Niimi, Y.; Nakamura, E.; Kataura, H.; Okazaki, T.; Suenaga, K.; Iijima, S. *Nat. Chem.* **2010,** *2,* 117–124. doi:10.1038/nchem.482
8. Smith, B. W.; Monthioux, M.; Luzzi, D. E. *Nature* **1998,** *396,* 323–324. doi:10.1038/24521
9. Okada, S.; Kowashi, S.; Schweighauser, L.; Yamanouchi, K.; Harano, K.; Nakamura, E. *J. Am. Chem. Soc.* **2017,** *139,* 18281–18287. doi:10.1021/jacs.7b09776
10. Zobač, V.; Lewis, J. P.; Abad, E.; Mendieta-Moreno, J. I.; Hapala, P.; Jelínek, P.; Ortega, J. *J. Phys.: Condens. Matter* **2015,** *27,* 175002. doi:10.1088/0953-8984/27/17/175002
11. Han, S.; Yoon, M.; Berber, S.; Park, N.; Osawa, E.; Ihm, J.; Tománek, D. *Phys. Rev. B* **2004,** *70,* 113402. doi:10.1103/physrevb.70.113402
12. Shimizu, T.; Lungerich, D.; Harano, K.; Nakamura, E. *J. Am. Chem. Soc.* **2022,** *144,* 9797–9805. doi:10.1021/jacs.2c02297
13. Adams, G. B.; Page, J. B.; Sankey, O. F.; O'Keeffe, M. *Phys. Rev. B* **1994,** *50,* 17471–17479. doi:10.1103/physrevb.50.17471
14. Laranjeira, J.; Strutyński, K.; Marques, L.; Martínez-Núñez, E.; Melle-Franco, M. *Carbon* **2023,** *213,* 118209. doi:10.1016/j.carbon.2023.118209
15. Liu, F.-L.; Zhao, X.-X. *J. Mol. Struct.: THEOCHEM* **2007,** *804,* 117–121. doi:10.1016/j.theochem.2006.10.018
16. Grimme, S.; Antony, J.; Ehrlich, S.; Krieg, H. *J. Chem. Phys.* **2010,** *132,* 154104. doi:10.1063/1.3382344
17. Grimme, S.; Mück-Lichtenfeld, C.; Antony, J. *J. Phys. Chem. C* **2007,** *111,* 11199–11207. doi:10.1021/jp0720791
18. Stasyuk, A. J.; Stasyuk, O. A.; Solà, M.; Voityuk, A. A. *J. Phys. Chem. C* **2019,** *123,* 16525–16532. doi:10.1021/acs.jpcc.9b02354
19. Fowler, P. W.; Manolopoulos, D. E. *An Atlas of Fullerenes;* Oxford University Press: Oxford, UK, 1995.
20. Kozuch, S.; Shaik, S. *Acc. Chem. Res.* **2011,** *44,* 101–110. doi:10.1021/ar1000956
21. *ADF 2019, SCM, Theoretical Chemistry;* Vrije Universiteit: Amsterdam, The Netherlands, http://www.scm.com.
22. te Velde, G.; Bickelhaupt, F. M.; Baerends, E. J.; Fonseca Guerra, C.; van Gisbergen, S. J. A.; Snijders, J. G.; Ziegler, T. *J. Comput. Chem.* **2001,** *22,* 931–967. doi:10.1002/jcc.1056
23. Perdew, J. P.; Burke, K.; Ernzerhof, M. *Phys. Rev. Lett.* **1996,** *77,* 3865–3868. doi:10.1103/physrevlett.77.3865
24. Grimme, S.; Ehrlich, S.; Goerigk, L. *J. Comput. Chem.* **2011,** *32,* 1456–1465. doi:10.1002/jcc.21759
25. Car, R.; Parrinello, M. *Phys. Rev. Lett.* **1985,** *55,* 2471–2474. doi:10.1103/physrevlett.55.2471
26. *CPMD 4.1;* IBM Corp.: Armonk, NY, USA, 2015.
27. Troullier, N.; Martins, J. L. *Phys. Rev. B* **1991,** *43,* 1993–2006. doi:10.1103/physrevb.43.1993
28. Iannuzzi, M.; Laio, A.; Parrinello, M. *Phys. Rev. Lett.* **2003,** *90,* 238302. doi:10.1103/physrevlett.90.238302
29. Laio, A.; Parrinello, M. *Proc. Natl. Acad. Sci. U. S. A.* **2002,** *99,* 12562–12566. doi:10.1073/pnas.202427399
30. Laio, A.; Rodriguez-Fortea, A.; Gervasio, F. L.; Ceccarelli, M.; Parrinello, M. *J. Phys. Chem. B* **2005,** *109,* 6714–6721. doi:10.1021/jp045424k
31. Kresse, G.; Hafner, J. *Phys. Rev. B* **1993,** *47,* 558–561. doi:10.1103/physrevb.47.558
32. Henkelman, G.; Uberuaga, B. P.; Jónsson, H. *J. Chem. Phys.* **2000,** *113,* 9901–9904. doi:10.1063/1.1329672
33. Henkelman, G.; Jónsson, H. *J. Chem. Phys.* **1999,** *111,* 7010–7022. doi:10.1063/1.480097

License and Terms

BEILSTEIN JOURNAL OF ORGANIC CHEMISTRY

Perspectives on push–pull chromophores derived from click-type [2 + 2] cycloaddition–retroelectrocyclization reactions of electron-rich alkynes and electron-deficient alkenes

Michio Yamada

Review

Open Access

Address:
Department of Chemistry, Tokyo Gakugei University, Nukuikitamachi 4-1-1, Koganei, Tokyo 184-8501, Japan

Email:
Michio Yamada - myamada@u-gakugei.ac.jp

Keywords:
click chemistry; donor–acceptor conjugate; intramolecular charge transfer; photoluminescence; photoinduced electron transfer

Beilstein J. Org. Chem. **2024,** *20,* 125–154.
https://doi.org/10.3762/bjoc.20.13

Received: 12 October 2023
Accepted: 04 January 2024
Published: 22 January 2024

This article is part of the thematic issue "Carbon-rich materials: from polyaromatic molecules to fullerenes and other carbon allotropes".

Guest Editor: Y. Yamakoshi

Abstract

Various push–pull chromophores can be synthesized in a single and atom-economical step through [2 + 2] cycloaddition–retroelectrocyclization (CA–RE) reactions involving diverse electron-rich alkynes and electron-deficient alkenes. In this review, a comprehensive investigation of the recent and noteworthy advancements in the research on push–pull chromophores prepared via the [2 + 2] CA–RE reaction is conducted. In particular, an overview of the physicochemical properties of the family of these compounds that have been investigated is provided to clarify their potential for future applications.

Introduction

Push–pull chromophores, wherein both electron-donating and electron-accepting substituents are incorporated into a π-electron-conjugated system, exhibit exceptional optical and electronic properties. They hold significant promise for applications in diverse fields, particularly materials science (specifically in optoelectronics) [1,2]. The synthesis of push–pull chromophores is often achieved through click-type reactions between electron-rich alkynes and electron-deficient alkenes, which is a reliable and atom-economical method. Diverse chromophores can be obtained via this method, depending upon the choice of alkynes and alkenes. The pioneering work by Bruce et al. in 1981 revealed that the cleavage of tetracyanoethylene (TCNE) under mild conditions via its reaction with metal acetylides yields metal complexes featuring the tetracyanobuta-1,3-diene (TCBD) structural motif [3]. Subsequently, numerous researchers have explored the synthesis of various push–pull chromophores, primarily via reactions between alkynes and alkenes. Several comprehensive reviews of nonplanar push–pull chromophores have since enriched the scientific literature [4-6]. In 2018, Michinobu and Diederich provided an exemplary overview of click-type [2 + 2] cycloaddition (CA)–retroelectrocyclization (RE) reactions, offering means for preparing these

coveted push–pull chromophores [7]. A review conducted in 2023 comprehensively explored the optoelectronic properties of TCBDs along with their photovoltaic applications [8]. The landscape of [2 + 2] CA–RE reactions for the preparation of push–pull chromophores is rapidly evolving and expanding. This evolution necessitates an update on the latest insights for materials science researchers. Furthermore, the diverse research advancements related to the distinctive physicochemical properties of push–pull chromophores remain fragmented. Thus, the primary objective of this review is to consolidate the developments in the research on push–pull chromophores prepared via [2 + 2] CA–RE reactions between electron-rich alkynes and electron-deficient alkenes across various domains of chemistry. This endeavor aims to delineate new directions for prospective applications of push–pull chromophores. Notably, in polymer chemistry, significant progress has been made in employing [2 + 2] CA–RE reactions for polymers as a valuable post-functionalization treatment [9,10]. However, this topic lies beyond the scope of this review.

Review

Click-type [2 + 2] CA–RE reactions

Click-type [2 + 2] CA–RE and associated reactions were comprehensively elucidated in a previous review [7]. Succinctly, the [2 + 2] CA reaction is postulated to be a stepwise process, whereas RE is postulated to be a concerted process. The [2 + 2] CA–RE sequence proceeds successively, as depicted in Scheme 1, where electron-donating groups are denoted as EDGs. During the [2 + 2] CA process, the nucleophilic attack by the terminal alkyne carbon of an electron-rich alkyne on an electron-deficient alkene, such as TCNE and 7,7,8,8-tetracyano-*p*-quinodimethane (TCNQ), results in the formation of a zwitterionic intermediate, wherein the negative charge evolves into a stabilized carbanion (dicyanomethide anion). Subsequently, the ring closure of the zwitterionic intermediate generates the corresponding cyclobutene intermediate. Finally, the ensuing RE process yields the corresponding TCBD derivatives. The resulting TCBDs and related products exhibit strong light absorption, resulting from the intramolecular charge transfer (ICT) in the visible region; they also exhibit a rich redox chemistry [11]. In the [2 + 2] CA–RE reaction of TCNQ with electron-rich alkynes, the alkyne terminal carbon executes a nucleophilic attack on the exocyclic carbon of the dicyanovinyl (DCV) group of TCNQ, affording dicyanoquinodimetanes (DCNQs) [12,13]. Intense ICT bands of TCBD and DCNQ are observed at around 450–470 nm and 680–710 nm, respectively. A study confirmed that with appropriate molecular design, the π-conjugation relationship between the donor and acceptor moieties in TCBDs and DCNQs can be retained despite their non-planarity [14]. Diederich et al. synthesized a plethora of push–pull chromophores by employing anilino groups as EDGs [4,5,7]. Notably, the *N*,*N*-dimethylanilino (DMA) moiety activates the reactivity of the neighboring alkyne moiety so strongly that the [2 + 2] CA–RE reactions

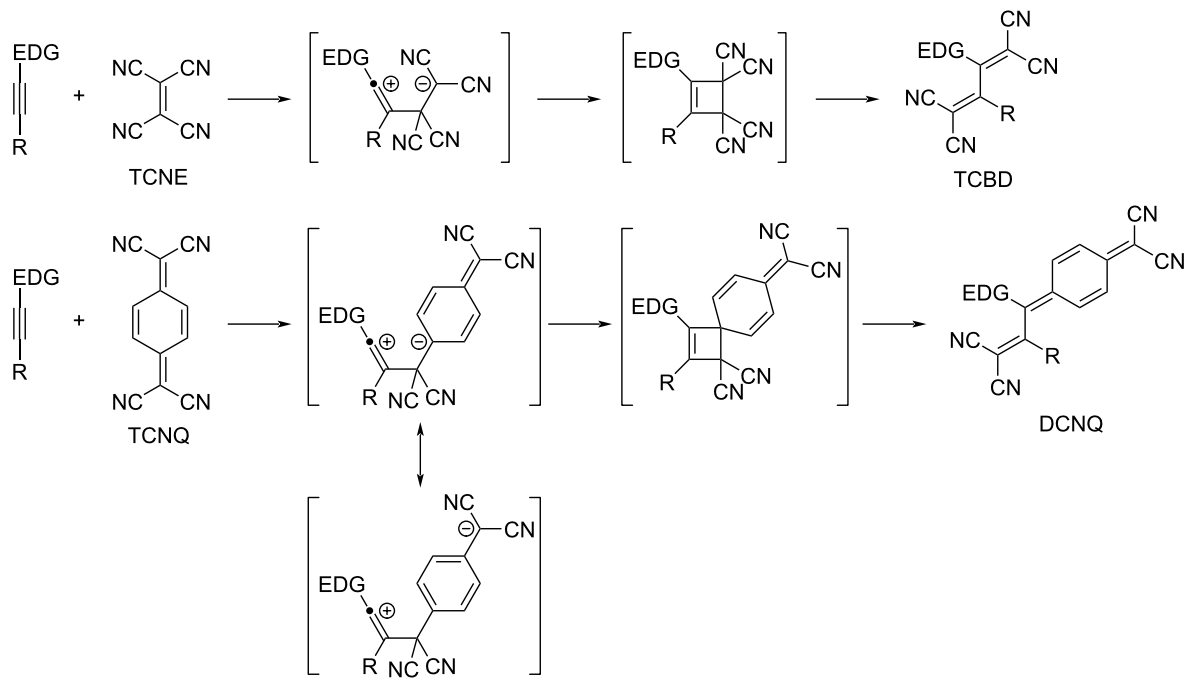

Scheme 1: Pathway of the [2 + 2] CA–RE reaction of an electron-rich alkyne with TCNE or TCNQ. EDG = electron-donating group.

with electron-deficient olefins proceed seamlessly [15,16] even when the terminus of the alkyne moiety is substituted by a cyano group [17]. In addition to anilino groups, a myriad of donor entities, including urea-substituted phenyl groups [18,19], carbazoles [20], phenothiazines [21,22], thiophenes [23-26], tetrathiafulvalenes (TTFs) [27], extended TTFs [28], ferrocenes [27,29-46], azulenes and their homologous compounds [32,47-58], boron dipyrromethenes (BODIPYs) [41,59-61], porphyrins [62-64], chlorophylls [65,66], triazenes [67,68], ynamides [69-71], arylynamines [72], indoles [73], and γ-pyranylidenes [74], have been identified as effective donor components for [2 + 2] CA–RE reactions. Concerning electron-deficient alkenes, 2,3,5,6-tetrafluoro-7,7,8,8-tetracyano-*p*-quinodimethane [75], DCV derivatives [76-80], tricyanovinyl derivatives [79,80], polyenic DCVs [81], *N*,*N*′-dicyanoquinone diimides [82], and 6,6-dicyanopentafulvenes (DCFs) [83,84] have been employed. Notably, the [2 + 2] CA–RE reaction of DMA-ethynyl-appended porphyrin with TCNQ is observed to occur on a metal surface (specifically Au(111)) under high-vacuum conditions, with successful visualization achieved through scanning tunneling microscopy [85]. For TCBDs bearing unsubstituted anilino (*p*-$H_2NC_6H_4$–) groups, their conversion into the *p*-iodophenyl derivatives via the Sandmeyer reaction and subsequent post-functionalization via the Suzuki and Sonogashira coupling reactions are achieved [86]. In the reaction of bisanilino-end-capped buta-1,3-diynes with TCNE, simultaneous [2 + 2] CA–RE reactions proceed for each of the two alkyne moieties of the buta-1,3-diyne skeletons, forming octacyano[4]dendralene molecules corresponding to TCBD dimers [87,88]. A well-recognized potent electron acceptor, 2,3-dichloro-5,6-dicyano-1,4-benzoquinone, and its homologous compounds have been employed in chemical transformation reactions involving electron-rich alkynes. In particular, a [2 + 2] CA adduct was prepared through the [2 + 2] CA–RE reaction. Studies have shown that the thermal treatment of the [2 + 2] CA adduct leads to the formation of a spiro compound [89-94]. Ester-substituted, electron-deficient alkenes have also been employed in [2 + 2] CA–RE reactions involving electron-rich alkynes. Alkenes featuring either one or two ester substitutions exclusively catalyze [2 + 2] CA–RE reactions, yielding multicyanated ethenes [95]. Contrarily, alkenes bearing three or four ester substitutions partake in a [4 + 2]-type hetero-Diels–Alder (DA) reaction, yielding a third product, presumably through a [3 + 2] cycloaddition reaction, followed by rearrangement. The [2 + 2] CA–RE reactions involving cumulenes and TCNE also present noteworthy chemical transformation reactions [96-99]. However, the chemistry of cumulenes is not discussed in detail here; please refer to a previous review [7] for comprehensive insights.

Upon replacing TCNE with tetracyanoethylene oxide (TCNEO), the [2 + 2] CA–RE reaction is extremely slow when applied to mono-substituted alkynes bearing an DMA group. Conversely, for bis-substituted alkynes, the reaction occurs readily at room temperature, yielding the corresponding TCBD products, as shown in Scheme 2. This reaction required the presence of two equivalents of TCNEO relative to the alkyne substrate for the generation of the TCBD products [100]. For the reaction, the formal [3 + 2] cycloaddition reaction is postulated to initiate through the initial nucleophilic attack of the alkyne carbon on the electrophilic TCNEO carbon, yielding a

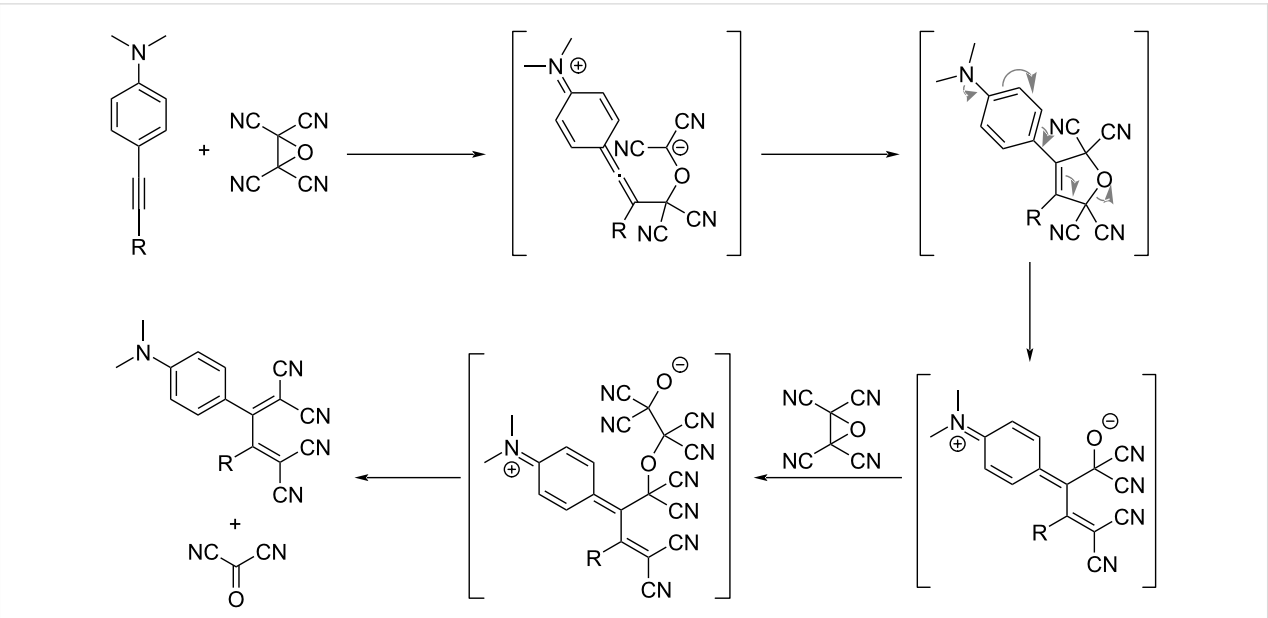

Scheme 2: Reaction pathway for DMA-appended acetylene and TCNEO.

zwitterionic intermediate. Subsequently, following the production of an oxide ion through the ring-opening reaction of the 2,5-dihydrofuran ring, the oxide ion attacks another TCNEO molecule. This sequence culminates in the elimination of the tetracyanodioxetane moiety (either as dioxetane or carbonyl dicyanide molecules in the form of degraded fragments), affording the TCBD products.

A distinguishing feature of the [2 + 2] CA–RE reaction involving electron-rich alkynes and DCFs is the alternation of regioselectivity, which is contingent upon the specific substituents incorporated onto the cyclopentadienyl moiety of the DCF molecule [83,84], as shown in Scheme 3. In the reaction between 4-ethynyl-*N*,*N*-dimethylaniline (**1**) and triisopropylsilylethynyl-substituted DCF **2a**, heating at 80 °C in acetonitrile selectively yields the corresponding adduct **3a** with 64% yield. In **3a**, the anilino group forms a covalent linkage, engaging in conjugation with the fulvene moiety. Conversely, the reaction of phenyl-substituted DCF **2b** with **1** under the same reaction conditions selectively affords the corresponding adduct **3b** with 64% yield. In **3b**, the anilino group is conjugated with the DCV group rather than the fulvene moiety. This variation in the products arises from the difference in the initial reaction step, in particular, whether the nucleophilic attack of the alkyne carbon in **1** occurs at C(6) or C(1) of the DCF framework. This differentiation can be attributed to the efficient electron conjugation between the alkyne and cyclopentadiene moieties.

TCBD **4**, obtained through the [2 + 2] CA–RE reaction, continues to function as an electron-accepting alkene, as shown in Scheme 4. Subsequent [2 + 2] CA–RE reactions involving electron-rich alkynes yield tetracyano-1,3,5-hexatrienes

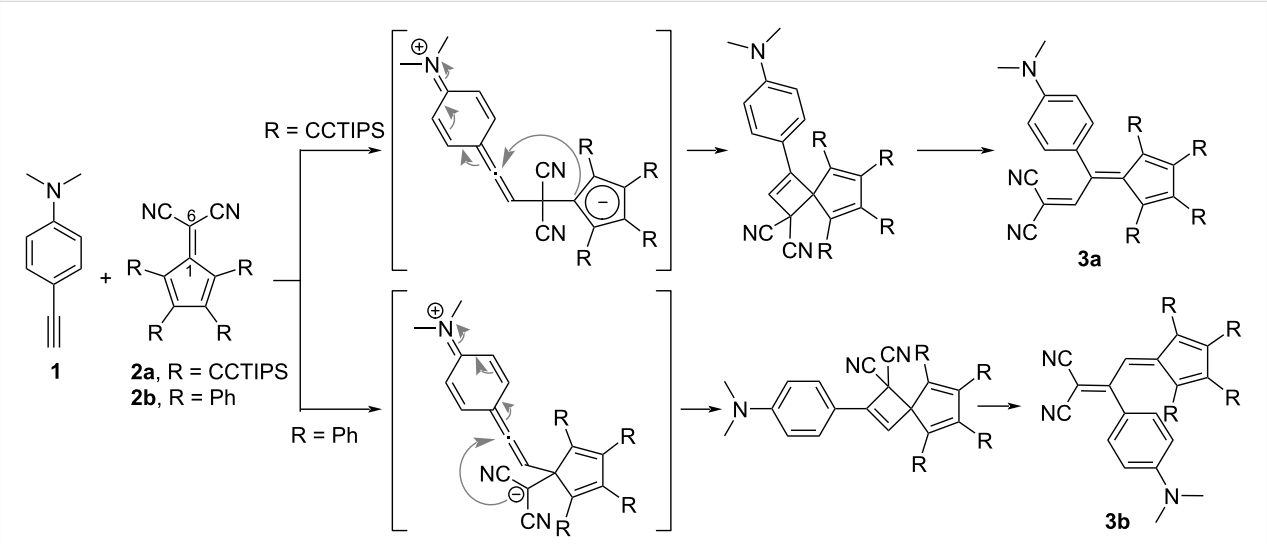

Scheme 3: Pathway of the [2 + 2] CA–RE reaction between **1** and DCFs.

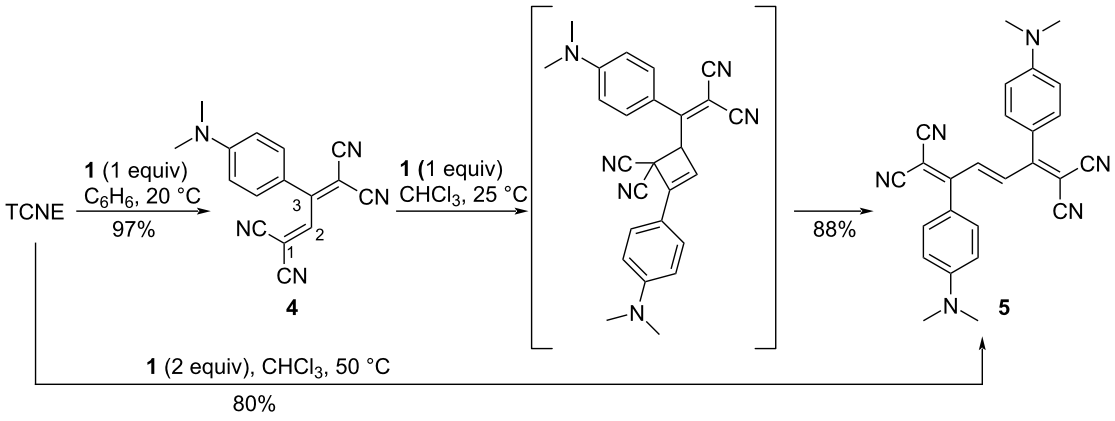

Scheme 4: Sequential double [2 + 2] CA–RE reactions between **1** and TCNE.

(TCHTs). These reactions occur seamlessly in a one-pot fashion. For instance, the reaction of one equivalent of TCNE with two equivalents of **1** in chloroform at 50 °C for 36 h yields the corresponding TCHT **5** with 80% yield [101]. In this reaction, the nucleophilic attack of the alkyne carbon of **1** occurs at the C(2) carbon of **4**. Moreover, when TCBD **6**, exhibiting enhanced electron-accepting capabilities, reacts with **1**, it displays a more intricate reaction profile compared with that of **4** (Scheme 5). In addition to pentacyano-1,3-5-hexatriene (PCHT) compound **7**, compounds **8** and **9** are generated [102]. This reaction is notably influenced by the different conditions, particularly the solvent employed. For instance, when toluene is used as the reaction solvent, a reaction at 100 °C for 15 h affords an *E*/*Z* mixture of **7** (*E*/*Z* ≈ 1:1) with 90% yield, **8** with 10% yield, and **9** with 0% yield. In contrast, a reaction at 25 °C for 15 h in *N*,*N*-dimethylformamide (DMF) affords **7** with 16% yield, **8** with 25% yield, and **9** with 46% yield. Furthermore, **7** and **8** are efficiently converted into **10** and **11**, respectively, with high yields (80% and 95%, respectively) via column chromatography employing silica gel in acetonitrile, thereby instigating further molecular transformation reactions. In these reactions, the nucleophilic attack of the alkyne carbon of **1** occurs at the C(1) carbon of **6**. When the formal [2 + 2] cycloaddition, as delineated in path A, occurs for the zwitterionic intermediate featuring the 1,1,3-tricyanoallyl anion obtained through the nucleophilic attack, subsequent RE affords **7**. Conversely, if the formal [4 + 2] cycloaddition occurs along the course elucidated in path B, the generation of **8** is expected. Similarly, when the formal [4 + 2] cycloaddition follows the course depicted in path C, the generation of **9** is envisaged. Among these compounds, **10** features a DCF structure and is amenable to further molecular transformations through a reaction with **1** [103].

Considering the structure of **7**, the possibility of a multistep [2 + 2] CA–RE reaction via a reaction with **1** becomes feasible. To execute such a multistep [2 + 2] CA–RE reaction, it becomes imperative to suppress the generation of **8** and **9**, as well as the conversion reaction of **7** into **10**. Therefore, it is im-

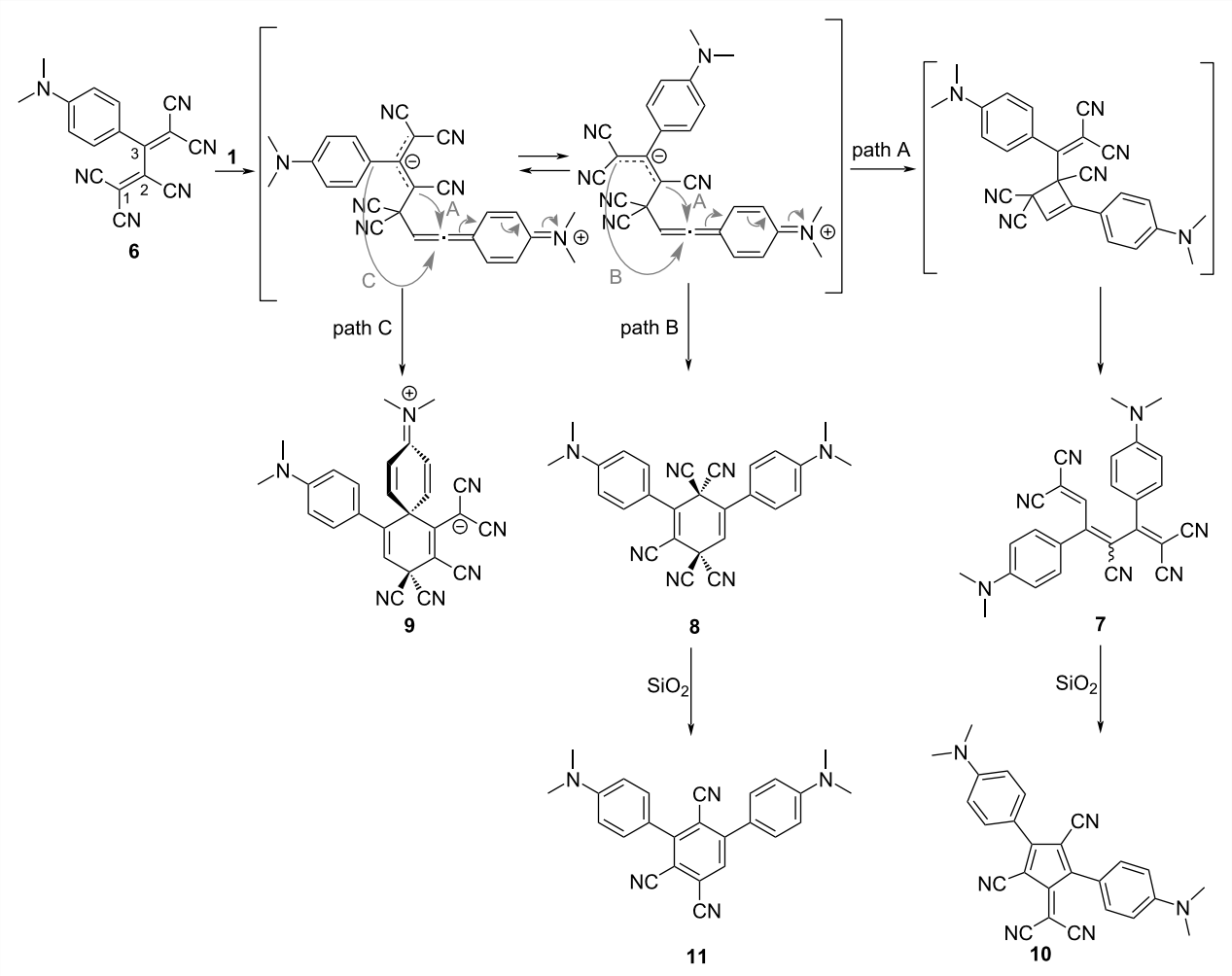

Scheme 5: Divergent chemical transformation pathways of TCBD **6**.

portant to use toluene as the solvent. Accordingly, pentacyanoocta-1,3,5,7-tetraene (PCOT) **12** was synthesized with 75% yield as a mixture of 3*Z*,5*E*/3*E*,5*E* isomers in the ratio of 71:29 via a one-pot reaction involving TCNE and one equivalent of 3-(4-(dimethylamino)phenyl)propionitrile in toluene at 90 °C for 24 h. Subsequently, one equivalent of **1** was added at 90 °C for 24 h (Scheme 6) [101]. While the separation of the isomers was not achieved, the structure of the 3*Z*,5*E* isomer was successfully characterized through single-crystal X-ray crystallography.

A mechanistic investigation of the [2 + 2] CA–RE reactions involving DCV compounds was undertaken by Diederich et al. in 2010 [77]. Their investigation unveiled that the reaction between **1** and arylated DCV derivatives followed second-order kinetics, indicating a bimolecular process. Furthermore, their findings elucidated a compelling linear free-energy relationship between the rate constants and electronic characteristics of the *para*-substituents of the DCV electrophiles, implying a dipolar, zwitterionic mechanism. The researchers also performed theoretical calculations, unveiling that the ring-opening step presented a higher energy barrier compared with the ring-formation step, particularly when the DCV compounds lacked aryl substituents. Subsequently, they successfully isolated the corresponding cyclobutene intermediate **13** through the reaction of **1** with 1,1-dicyanoethene (**14**). They demonstrated that this intermediate was converted into the corresponding TCBD **15** upon further heating, as depicted in Scheme 7. The kinetics of the RE step conformed well to that of a first-order reaction. However, notably, they underscored that generalizing the elucidated reaction mechanism to other [2 + 2] CA–RE reactions involving TCNE and TCNQ as electrophiles might be difficult. They emphasized the significance of considering a pre-equilibrium state of the charge-transfer complexes between the alkynes and alkenes and mentioned that the positioning of the [2 + 2] CA or RE step as the rate-determining step may depend upon the structural attributes of the electrophiles and nucleophiles.

In 2023, Nielsen et al. conducted an exhaustive kinetic analysis of the [2 + 2] CA–RE reaction involving 4-trimethylsilylethynylaniline and TCNE by leveraging ^{1}H nuclear magnetic resonance (NMR) spectroscopy. Their investigation revealed that the product plays a pivotal role as an autocatalyst in the kinetics, as illustrated in Scheme 8 [104-106]. The traditional model posits that an alkyne (**A**) and TCNE (designated as **B** in Scheme 8) initially form a charge-transfer complex **AB**. Subsequently, this complex forms a zwitterion intermediate (**C1**), followed by the formation of a cyclobutene intermediate (**C2**), ulti-

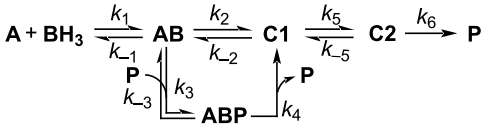

Scheme 8: Autocatalytic model proposed by Nielsen et al.

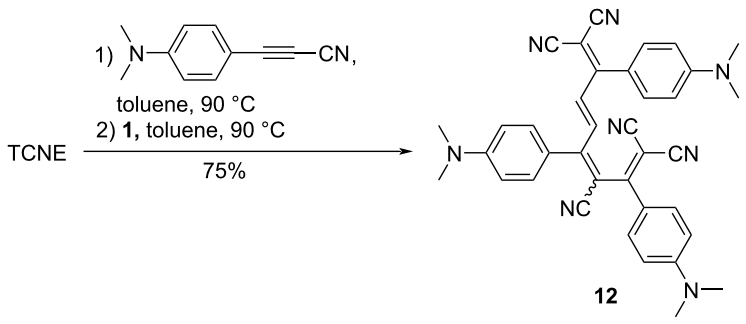

Scheme 6: Synthesis of **12**.

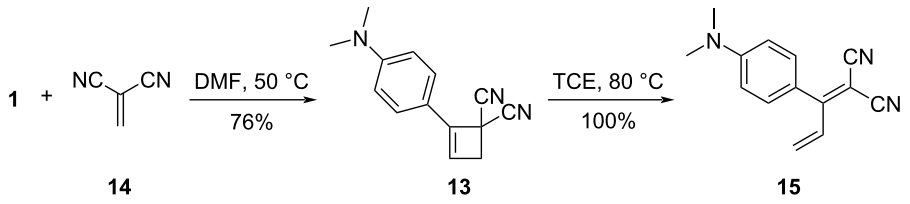

Scheme 7: [2 + 2] CA–RE reaction of **1** with **14**. TCE = 1,1,2,2-tetrachloroethane.

mately forming the product **P**. However, the researchers strongly advocated for an alternative pathway, which entails the formation of a complex between **AB** and **P**, from which **C1** is generated. Notably, this additional route significantly accelerates the overall reaction. The researchers reported that the conversion of the **ABP** complex into **C1** transpired at a markedly accelerated rate compared with the conversion of **AB** alone, with a kinetic constant ratio of $k_4/k_2 = 62$. Consequently, it is posited that **P** assumes the role of a template, directing the arrangement of reactants in a precise manner conducive to the generation of **C1**.

Leveraging the irreversibility inherent in the [2 + 2] CA–RE reaction, **1** can be adeptly employed as a proficient trapping agent for TCNE. Anthracene-based ynamide **16** offers two potential reactive sites for TCNE, one residing at the anthracene moiety and other at the alkyne moiety, as shown in Scheme 9 [71]. As exemplified by Trolez et al., the introduction of one equivalent of TCNE to **16** at room temperature initiates a [4 + 2] cycloaddition reaction with the anthracene moiety, yielding the DA cycloadduct **17**. To achieve the conversion of the alkyne moiety of **16** into TCBD, the addition of five equivalents of TCNE to **16** or one equivalent of TCNE to **17** is required. This results in the formation of TCBD compound **18** bearing a derivatized anthracene moiety. Subsequently, to restore the anthracene structure of **18**, the retro-DA reaction must occur efficiently. Therefore, through the addition of **1**, followed by heating, the generated TCNE is effectively captured by **1**. This maneuver concurrently suppresses the progression of the DA reaction, leading to the efficient generation of the anthracenyl TCBD **19**.

Concerning [2 + 2] CA–RE reactions, studies have shown that alkynes exhibiting angular distortion exhibit high reactivity toward electron-deficient alkenes independent of the presence or absence of electron-donating substituents on the alkynes. The remarkable reactivity displayed by angle-strained alkynes makes them highly valuable tools in biorthogonal chemistry [107-109]. The reaction between dibenzo-fused cyclooctyne **20** and TCNE was observed to occur at room temperature, quantitatively yielding **22**, wherein the TCBD moiety was effectively integrated, as shown in Scheme 10 [110]. During this reaction, an intermediate **21** was successfully captured experimentally along with the occurrence of only the [2 + 2] CA reaction. Similarly, the reaction involving cyclooctadiyne (**23**) and TCNE progressed in a stepwise manner, ultimately affording **27** with 90% yield. The formation of intermediates **24**, **25**, and **26** was elucidated through ^{1}H NMR analysis, of which **24** and **26** were successfully isolated and characterized. A comprehensive analysis of the [2 + 2] CA–RE reaction activation parameters via ^{1}H NMR spectroscopy revealed that the rate-determining step in the transformation of **20** into **22** was the first-order RE step, which was primarily governed by enthalpy changes. Furthermore, it was observed that the ring strain significantly accelerated the second-order [2 + 2] CA step. The rate enhancement in the [2 + 2] CA step was approximately 3300 times that for an acyclic model compound, at 298 K. Regarding the conversion reaction from **23** to **27**, the rate-determining step was identified to be the final RE step: the conversion of **26** to **27**. Comparative analysis using a linear model compound revealed rate enhancements of 5500 times that for the initial [2 + 2] CA step and 80 times that for the subsequent [2 + 2] CA step at 298 K, which was attributable to the ring strain.

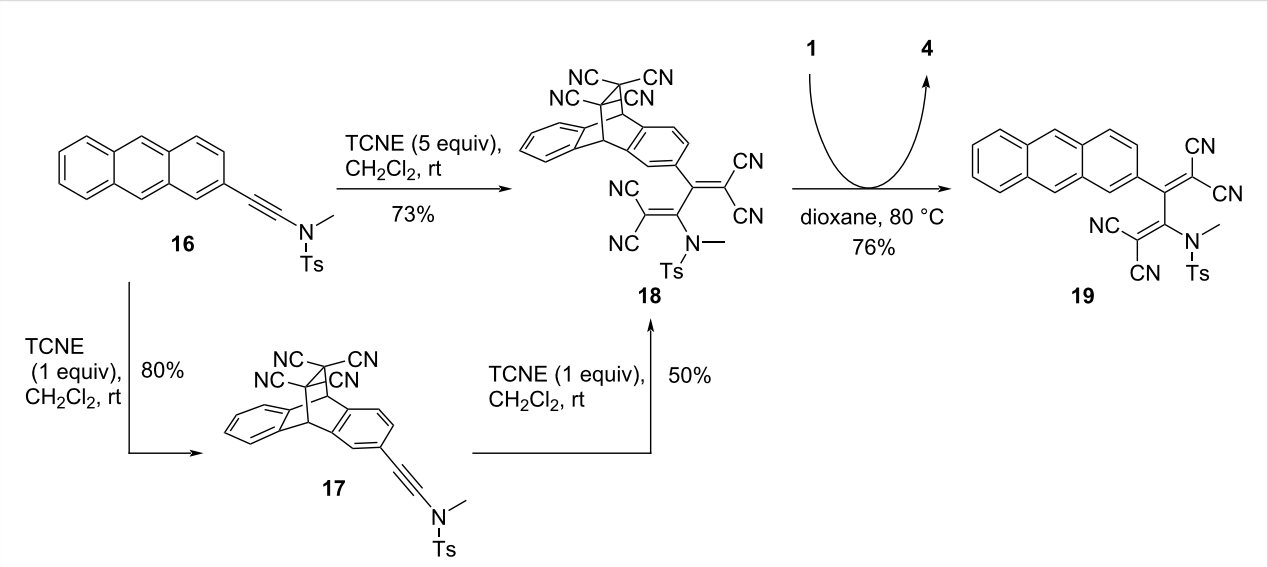

Scheme 9: Synthesis of anthracene-embedded TCBD compound **19**.

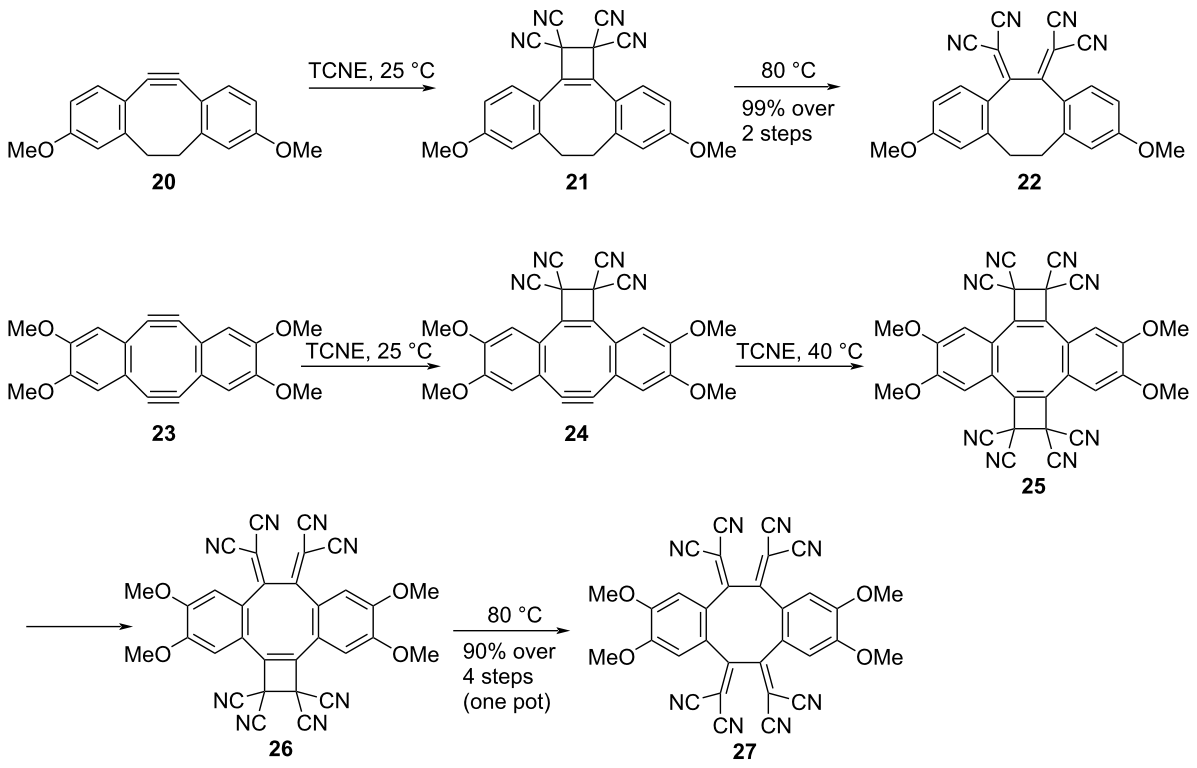

Scheme 10: Sequence of the [2 + 2] CA–RE reaction between dibenzo-fused cyclooctyne or cyclooctadiyne and TCNE. All reactions were performed in TCE-d_2.

Jasti et al. synthesized an array of cycloparaphenylenes (CPPs) that incorporated alkyne moieties (**28a–c**) within their ring structures and investigated their reactions with TCNE (Scheme 11) [111]. In these reactions, CPP derivatives **30a–c**, featuring TCBD moieties, were obtained with 59–97% yields. The magnitude of the ring strain exerted a profound effect on the reactivity of the compounds. Notably, the largest macrocycle **28c** required heating to 100 °C to generate **30c**. Conversely, the transformation of **28b** proceeded at 45 °C, and the smallest macrocycle **28a** reacted with TCNE at 0 °C. Kinetic investigations revealed that the rate-determining step in the reaction involving **28a–c** with TCNE was the second-order [2 + 2] CA step, succeeded by the rapid RE step; the result is in contrast to those obtained for **20** and **23**. This divergence in the reactivity may be attributed to the pronounced steric repulsion between the DCV group and the aryl hydrogen, particularly discernible for **21** and **26** during the RE step. Conversely, for **29a**, it is reasonable to posit that the phenyl rings possess a degree of rotational freedom, thereby circumventing steric repulsions.

The steric congestion surrounding TCBD moieties can also induce further skeletal rearrangement. For instance, the spatial constraints proximal to the surface of fullerene derivatives lead

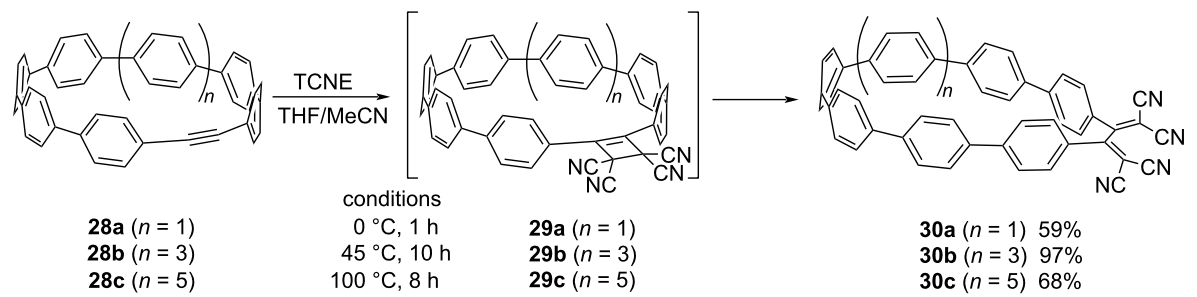

Scheme 11: [2 + 2] CA–RE reaction between the CPP derivatives and TCNE. THF = tetrahydrofuran.

to novel reactions arising from steric congestion. In a reaction involving ethynylfullerene derivatives featuring a DMA group (**31**) and TCNE, the conventional [2 + 2] CA–RE reaction was observed to transpire at 20 °C, yielding the corresponding TCBD derivatives **32**, as shown in Scheme 12. Conversely, upon refluxing in chlorobenzene, a rearrangement ensued, yielding tetrakis-substituted fullerene derivatives **33** [112]. During this rearrangement, it was postulated that a zwitterionic intermediate was formed from the nucleophilic attack of the carbon of the dicyanomethylidene adjacent to the DMA group on the fullerene sphere. This was followed by a nucleophilic attack of the fullerene carbanion on one of the cyano groups, ultimately yielding **33**. Computational calculations also suggested that the rearrangement was facilitated by the destabilization of the reactant due to steric interactions.

Additional skeletal transformation reactions in TCBD structures, such as those shown in Scheme 12, have also been reported [113-116], which enable the construction of a wide array of push–pull chromophore structures. For instance, Shoji et al. reported that the reaction between 3(4-(*N*,*N*-dimethylanilino))prop-2-yn-1-ol (**34**) and TCNE in dichloromethane at room temperature yielded **35**, which was characterized by a furan skeleton (Scheme 13) [116]. This transformation occurred through the intermediate formation of the corresponding TCBD with a high yield of 85%. Furthermore, when **35** reacted with pyrrolidine at 0 °C, the pentafulvene derivative **36** was obtained with 63% yield via an additional ring-opening process. Similar skeletal transformation reactions were observed for azulene derivatives bearing similar substructures.

The reaction of **1** with TCNE in an aqueous medium containing a surfactant results in the formation of a 6,6-dicyanoheteropentafulvene derivative **37** as an additional byproduct along with the typical TCBD adduct **4** (Scheme 14) [117]. The yields and formation ratios of **4** and **37** depend on the type and concentration of the surfactant employed. For instance, when the nonionic surfactant, Brij 30, was used as the reaction solvent at a concentration of 20 mM, exceeding the critical micelle concentration, **4** and **37** were obtained in a ratio of 53:47, with 64% yield. Notably, **37** exhibits instability in silica gel and polar solvents. In particular, when **37** is kept in ethyl acetate or acetonitrile for 8 h, **38** is obtained with 98% yield. Microscopic observations suggest that the vesicle structure, with water as the

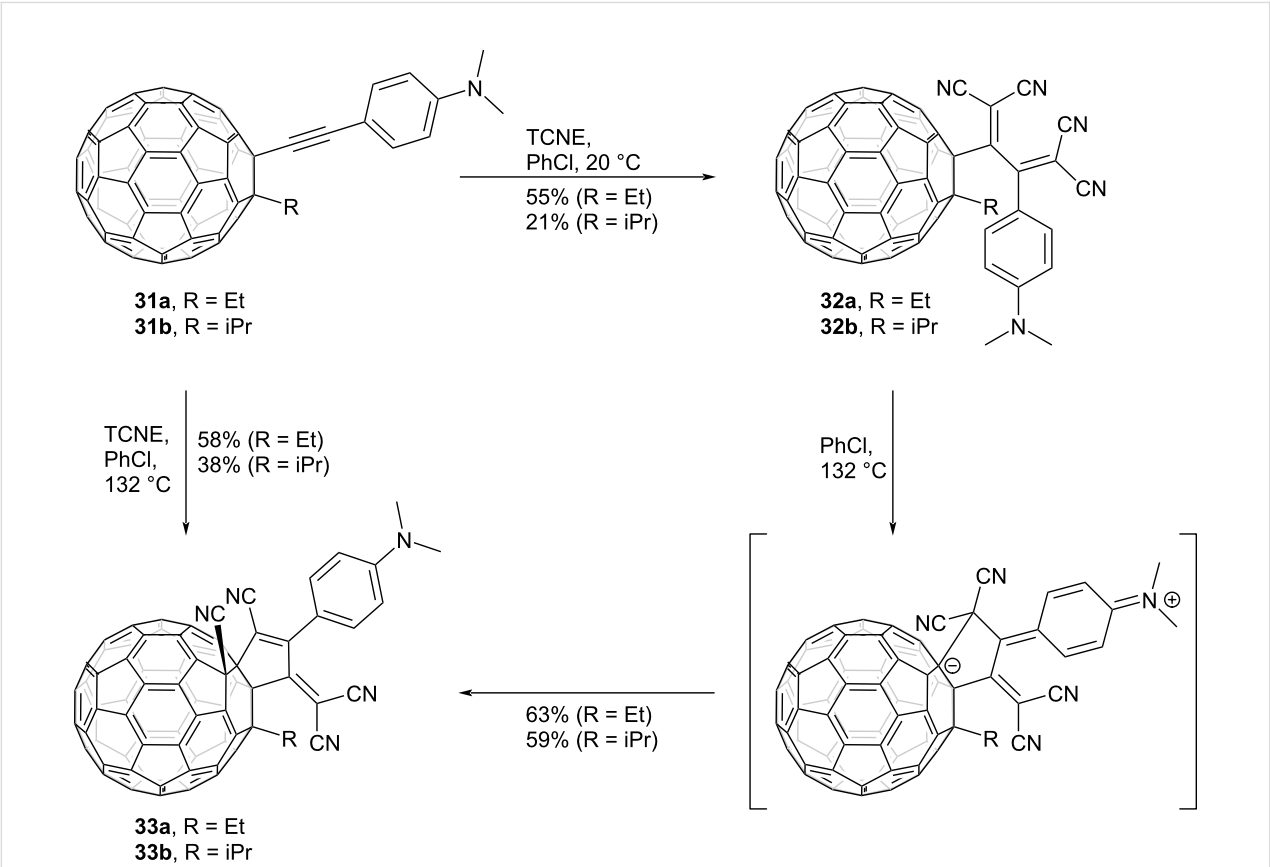

Scheme 12: [2 + 2] CA–RE reaction between ethynylfullerenes **31** and TCNE and subsequent thermal rearrangement.

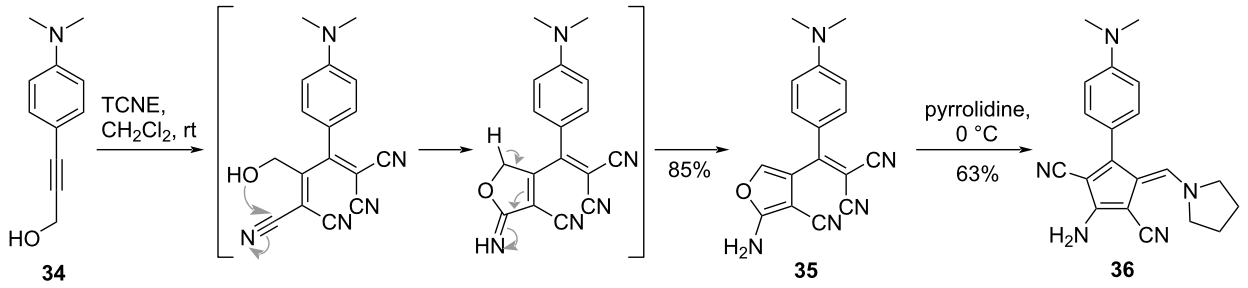

Scheme 13: Pathway of the [2 + 2] CA–RE reaction between TCNE and **34**, followed by additional skeletal transformation.

core, plays a pivotal role in the transformation of **4** into **37**. A similar reaction of TCBD with water was also reported by Bruce et al. [118].

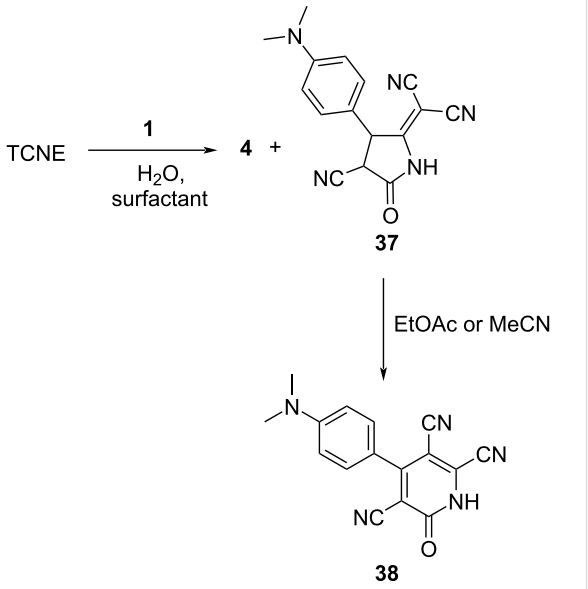

Scheme 14: Synthesis scheme for heterocycle **38** from the reaction between TCNE and **1** in water and a surfactant.

The reaction of the anthracene derivative **39**, wherein a DMA–ethynyl group is introduced at the 9-position, with TCNE at 40 °C in THF yielded the corresponding TCBD **40** with 91% yield. Subsequent heating of **40** in toluene at 70 °C led to an intramolecular cyano-DA (CDA) reaction, which quantitatively afforded the CDA product **41** (Scheme 15) [119]. The quantitative CDA reaction progression was attributed to be due to the presence of multiple cyano groups on the skeleton, which increased the dienophile character of the cyano groups and stabilized the structure of the product. The thermal conversion of **40** to **41** was also accelerated by the addition of $B(C_6H_5)_3$, which may be due to the enhancement of the dienophilic nature of the cyano group due to coordination with borane.

Rotaxane synthesis

Push–pull chromophores with nonplanar configurations have been reported as effective stoppering motifs for rotaxane synthesis. A rational approach toward rotaxane synthesis involves affixing stoppers at both termini substituents and threading a molecular thread through a macrocycle. In this threading–stoppering strategy, a mild yet high-yield reaction is required for the stoppering process. The [2 + 2] CA–RE reaction, which yields push–pull chromophores, is the preferred method for stoppering. Accordingly, Li et al. synthesized a rotaxane **44** terminated using push–pull chromophores by incorporating concise

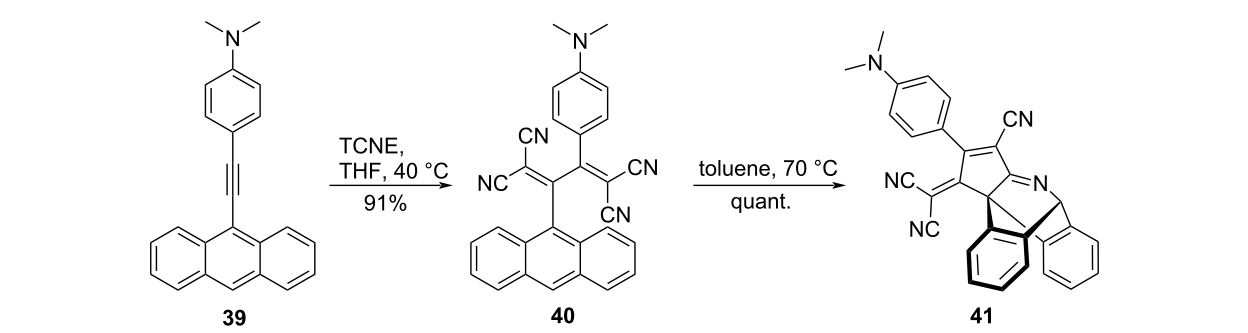

Scheme 15: Synthesis scheme of the CDA product **41**.

peptide and DCNQ moieties and employing the threading–stoppering method (Scheme 16). In **44**, the rod moiety and macrocycle feature short peptide substructures. Consequently, the macrocycle was tethered to the peptide segment through amide–amide hydrogen bonding, and **44** was obtained with 30% yield. The generation of **44** was accompanied by the formation of the corresponding free thread with 62% yield, resulting from the reaction between the thread precursor **42** and macrocycle **43**, followed by an additional reaction of the alkyne moiety with TCNQ [120]. Rotaxane **46** terminated using push–pull chromophores, which exhibited a solvent-driven molecular shuttling phenomenon, was synthesized from the thread precursor **45** using a clipping approach; however, the yield for the ring-formation process was modest at 5% (see Scheme 16) [121,122]. The macrocycle in **46** was observed to engage with the peptide segment in low-polarity solvents. In contrast, ^{1}H NMR analysis suggested that the macrocycle disengaged from the peptide segment and relocated along the alkyl chain in dimethyl sulfoxide. Furthermore, the solvent-driven shuttling motion of the macrocycle was observed to exert a discernible effect on the aggregation of the amphiphilic molecular system. In particular, changing the solvent led to the generation of interlaced nanofibers, perforated capsules, and wormlike nanoparticles.

In rotaxanes, the utilization of metal–ligand bonding involving Cu^I is a common strategy for immobilizing a thread moiety within a macrocycle. However, the efficacy of such a bonding is

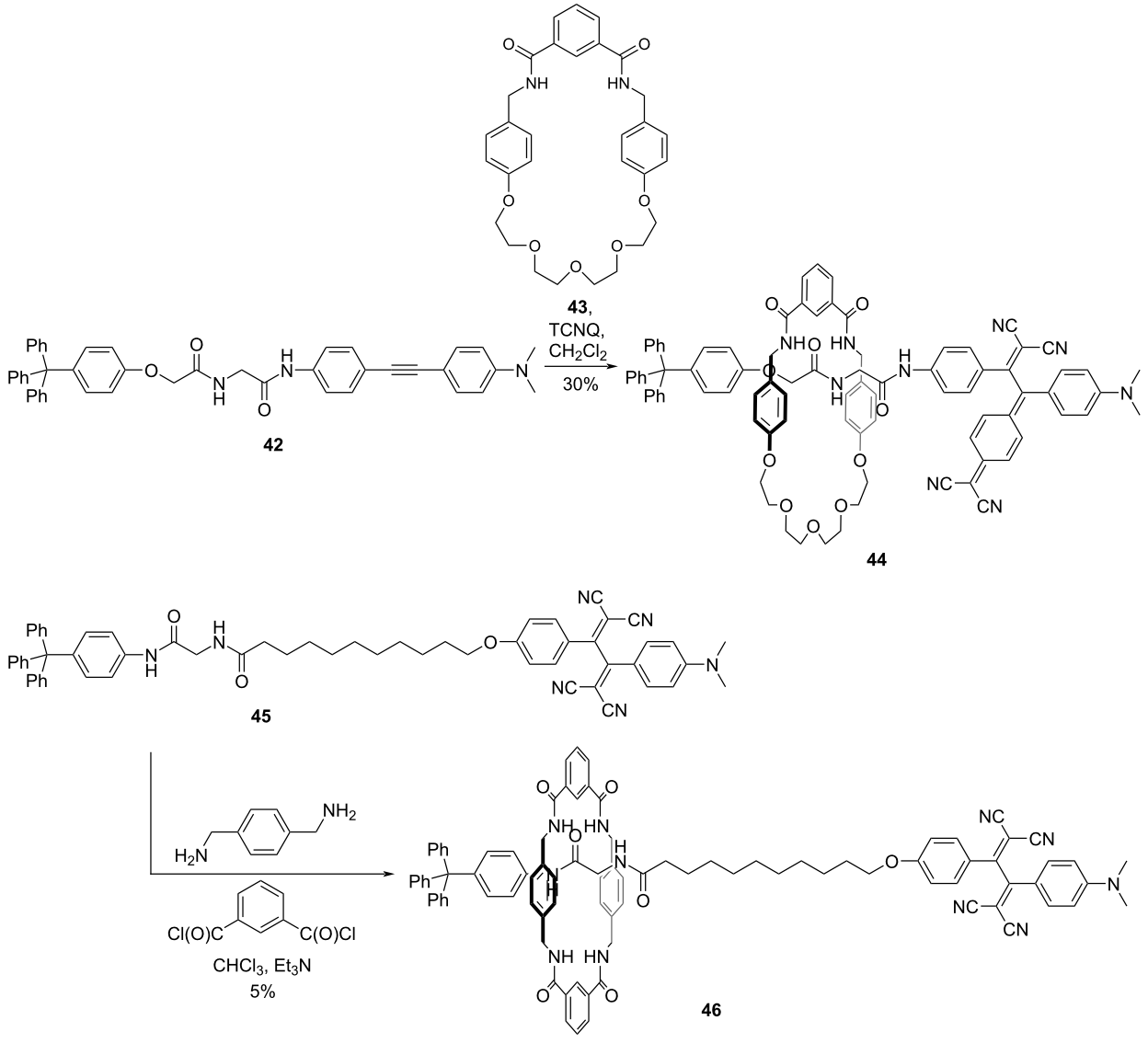

Scheme 16: Synthesis of rotaxanes **44** and **46** via the [2 + 2] CA–RE reaction.

compromised when catalysts are used in stoppering reactions, e.g., the copper-catalyzed azide–alkyne cycloaddition reaction. Consequently, a [2 + 2] CA–RE reaction that can yield push–pull chromophores without the use of a catalyst is exceedingly valuable as a stoppering method, even for systems featuring metal–ligand bonding. Accordingly, Diederich et al. demonstrated the synthesis of a Cu^{I} bis-phenanthroline-based rotaxane **50** by employing the [2 + 2] CA–RE reaction, as shown in Scheme 17 [123]. The initial threading reaction involving the rod molecule **47** and macrocycle **48**, constructed using $[Cu(MeCN)_4]PF_6$, resulted in the formation of the pseudorotaxane **49**. The ensuing [2 + 2] CA–RE reaction of **49** with TCNQ in dichloromethane at room temperature afforded **50** with an impressive yield of 84%.

Chiroptical properties

Push–pull chromophores synthesized through the [2 + 2] CA–RE reaction can, in certain cases, exhibit distinct chiroptical properties, attributable to their nonplanar geometry and steric congestion. In previous studies, chiral induction in TCBD structures was accomplished by introducing chiral allene (**51**) [124,125] or binaphthyl (**52** and **53**) [126,127] moieties, as shown in Figure 1. These molecules exhibited Cotton effects related to ICT absorptions, and chiral induction in TCBD moieties resulted from optically active constituents. Compound **53**, due to its elongated rigid structure, holds potential for use as a chiral dopant in nematic liquid crystals (LCs); however, the helical twisting powers of **53** within nematic LCs are limited. Recently, Alonso-Gómez et al. reported the synthesis and optical resolutions of spirobifluorenes featuring two TCBD units located at the 2,2'-positions, designated as **54** [128]. Furthermore, Autschbach et al. prepared chiral carbo[6]helicene–TCBD derivatives **55** and **56** from enantiopure precursors [129]. For such intricate molecular systems, the presence of multiple chromophore units induces complexity in the interpretation of the resulting circular dichroism (CD) spectra because of the overlap of several exciton couplets. Thus, exciton coupling CD signals were not discernible for **51**–**55**. Further, regarding **56**, the exciton coupling CD signal in the ICT region may not be apparent at a glance. Nevertheless, comprehensive computational analyses employing the matrix method suggest that the intense long-wavelength CD signal observed for **56** is due to the coupling of individual helicene-to-TCBD electric-transition dipole moments.

The emergence of axial chirality in TCBDs and DCNQs and their optical resolutions were first realized in 2010 through their conjugation with methylated fullerenes, as shown in Figure 2 [130]. The optical resolution was realized using a chiral high-performance liquid chromatography (HPLC) system equipped with an (*S*,*S*)-*WHELK-O*1 column. The absolute configurations of the axially chiral TCBD and DCNQ derivatives were ascertained by a comparative analysis of the experimental CD spectra against the spectra derived from time-dependent density functional theory (TD-DFT) calculations. The axial chirality was stabilized by the steric congestion on the surface of fuller-

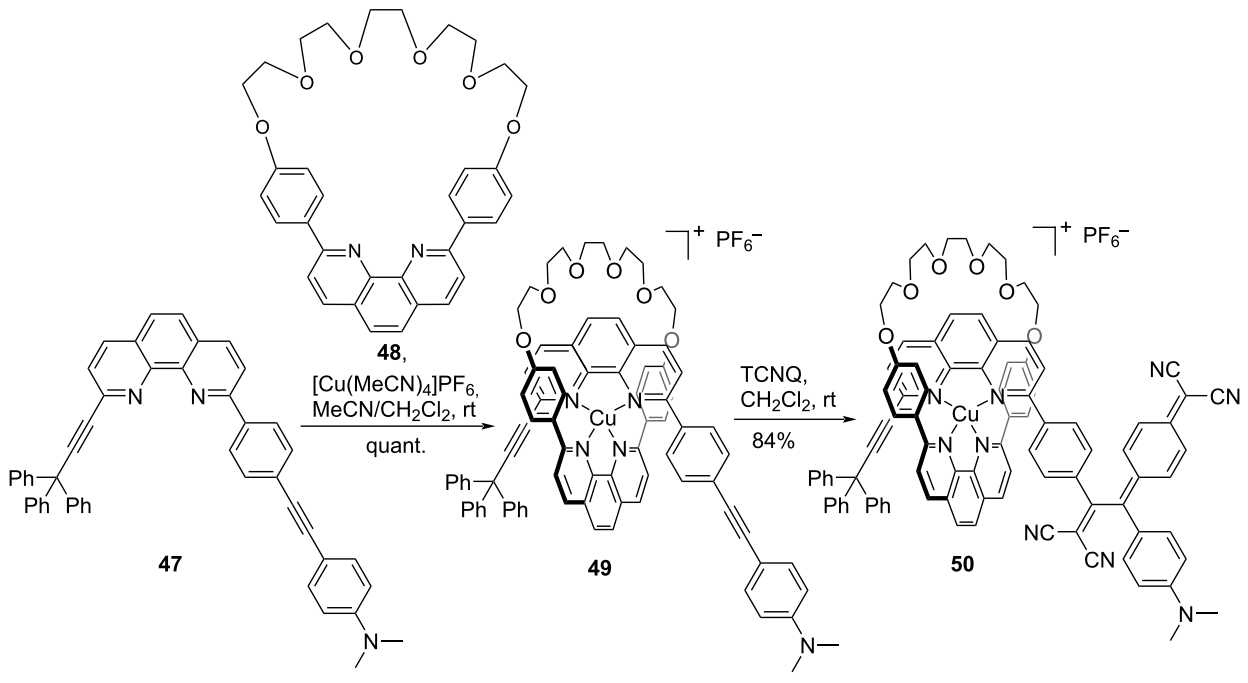

Scheme 17: Synthesis of a Cu^{I} bisphenanthroline-based rotaxane **50**.

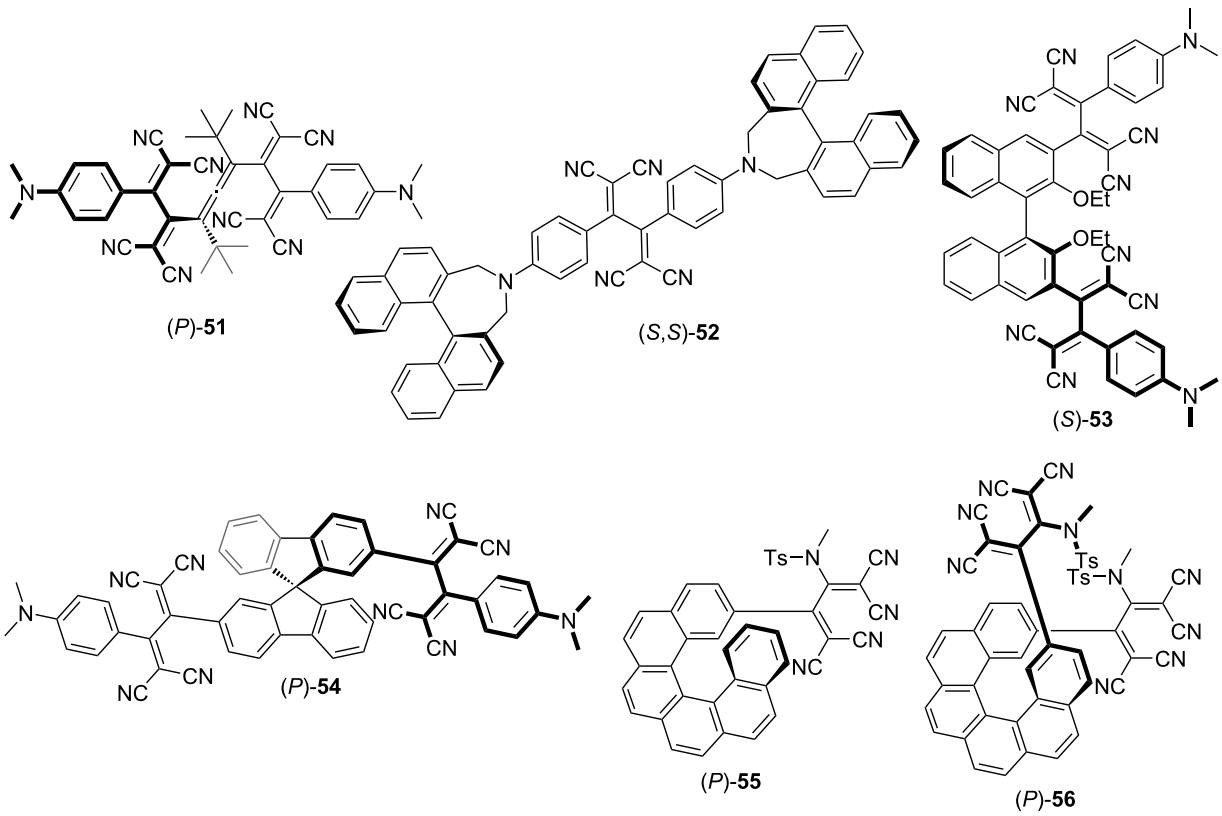

Figure 1: Structures of the chiral push–pull chromophores **51**–**56**.

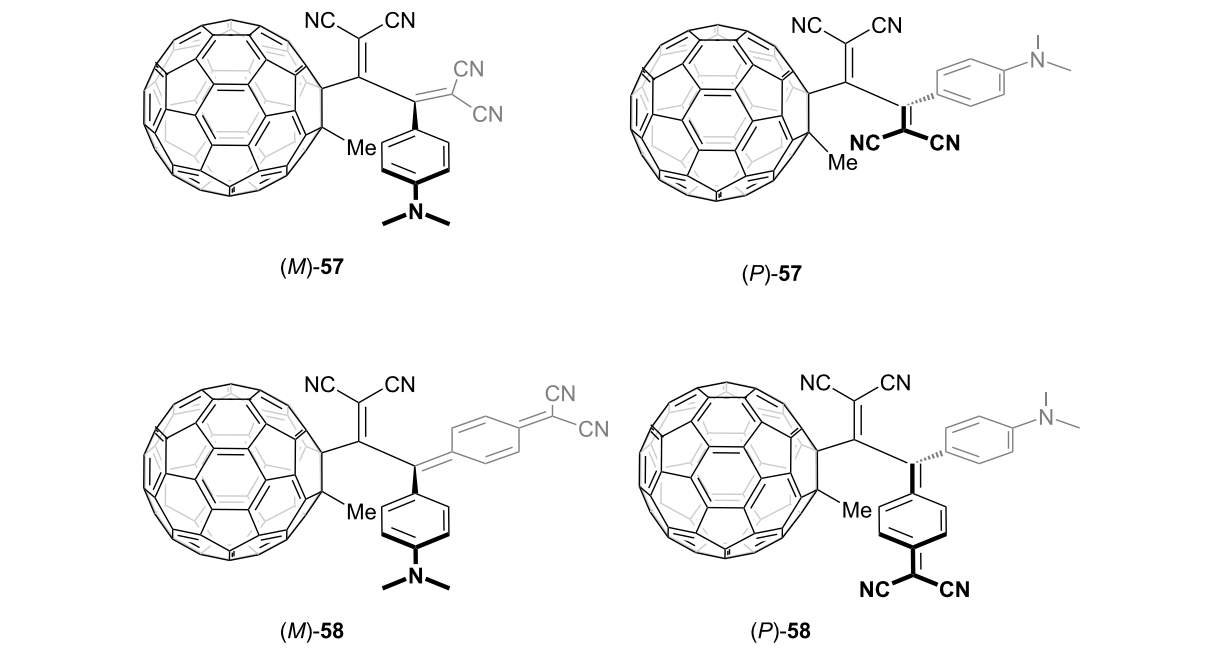

Figure 2: Structures of the axially chiral TCBD **57** and DCNQ **58** bearing a C_{60} core.

ene, with its endurance contingent upon the bulkiness of the substituent incorporated onto the fullerene core. This observation was supported by the absence of axial chirality in molecules where an additional alkyne moiety is intercalated between the C_{60} core and TCBD or DCNQ unit or where a methyl group on the C_{60} surface is replaced by a hydrogen atom. The C_{60}–TCBD conjugate **57** and C_{60}–DCNQ conjugate **58** exhibited substantial optical rotations at 589 nm, presenting +770 for (*P*)-**57** and +5,800 for (*P*)-**58**. In concordance, robust Cotton effects related to ICT absorption in the visible region were evident in their CD spectra. Using the Arrhenius and Eyring formalisms, the kinetic parameters for the thermal racemization of **57** and **58** were obtained. The activation free enthalpy ($\Delta G^{\ddagger}$) for the racemization of **57** ($\Delta G^{\ddagger}_{298\ K}$ = 24.8 kcal mol^{-1}) was ≈1.5 kcal mol^{-1} larger than that for **58** ($\Delta G^{\ddagger}_{298\ K}$ = 23.3 kcal mol^{-1}), indicating that the cylohexa-2,5-diene-1,4-diylidene moiety is more flexible and its distortion by out-of-plane bending is energetically less favored compared to the DCV moiety.

Guldi et al. reported that the atropisomerism in the TCBD structure was observed when the TCBD moiety was incorporated at the axial position of the subphthalocyanine (SubPc) core (Figure 3) [131]. Axially chiral SubPc–TCBD–aniline conjugates **59** and **60** were characterized via optical-resolution analysis through chiral HPLC using a Chiralpak IC column. The researchers unequivocally determined the absolute configurations of these atropisomers through the X-ray crystallographic analyses of (S_a)-**59** and (R_a)-**60**. Surprisingly, heating the enantiomers of **69** and **60** at 80 °C for 3 h resulted in negligible thermally induced racemization. Meanwhile, in O_2-free toluene solution under illumination, the racemization was observed at 80 °C. Torres et al. performed detailed theoretical calculations and showed that the racemization observed in **59** and **60** is caused by triplet-state photogeneration, which leads to the rotation around the sterically hindered buta-1,3-diene chiral axis [132]. In fact, the estimated energy barrier of ≈37 kcal mol^{-1} is reduced to ≈15 kcal mol^{-1} upon the electronic excitation of **59** and **60** to the T_1 state. It is reasonable to consider that the phototriggered racemization is inhibited in the presence of O_2 because O_2 acts as a triplet-state scavenger. Osuka et al. synthesized two types of subporphyrin derivatives **61** and **62**, wherein the subporphyrin skeleton was functionalized at its *meso* or axial position with the TCBD moiety (Figure 3). Although the optical resolution of **61** failed, they succeeded in achieving the optical resolution of **62** via chiral HPLC using a Chiralpak IC column. In **62**, unlike **59** and **60**, thermally induced racemization was observed and kinetic parameters were obtained ($\Delta G^{\ddagger}_{298\ K}$ = 25.4 kcal mol^{-1}), which were similar to those reported for **57** and **58** [133].

Photoluminescence properties

Most anilino-substituted TCBD molecules exhibit negligible fluorescence in chloroform, while only a few exhibit weak fluo-

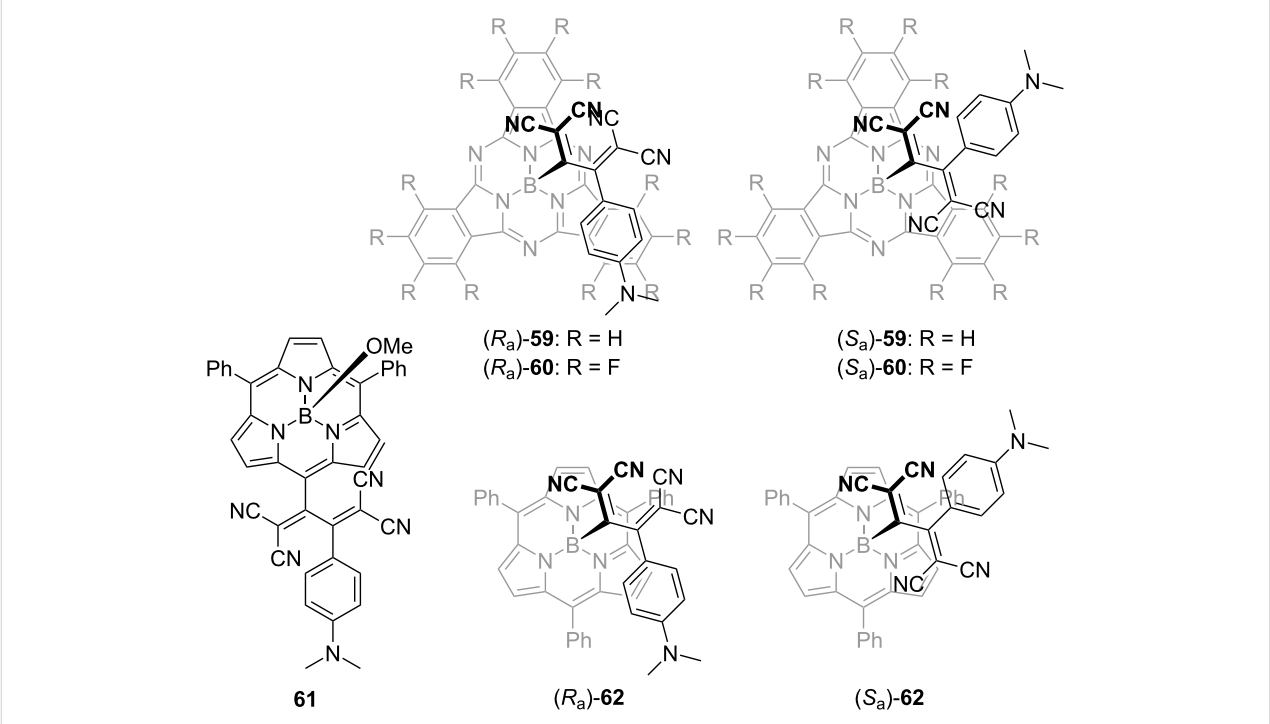

Figure 3: Structures of the axially chiral SubPc–TCBD–aniline conjugates **59** and **60** and the subporphyrin–TCBD–aniline conjugates **61** and **62**.

rescence in hexane [15]. These nonluminescence characteristics are attributable to the low-energy state of the twisted ICT (TICT) state, which is capable of deactivating the ground state through accessible conical intersections (CIs) [15,134-136]. In particular, Diederich et al. conducted a theoretical investigation on the photophysical properties of 1,1,2,4,4-pentacyanobuta-1,3-diene (PCBD) (**63**) [134]. Compound **63** and the TCBD **64** demonstrated no discernible luminescence at room temperature and 77 K (Figure 4). Transient absorption spectral measurements of **63** in toluene revealed that the lowest singlet excited state (S_1) decays mono-exponentially to the ground state (S_0) within approximately 1 ps, suggesting the existence of an accessible CI between S_1 and S_0. In the S_1 minimum conformation of **63**, the PCBD moiety adopted a planar orientation perpendicular to that of the aniline moiety. The calculations indicated the presence of accessible S_1/S_0 CIs. In the lowest-energy S_1/S_0 CI geometry, the aniline moiety exhibited a pronounced quinoidal character and the carbon atom directly linked to the butadiene moiety exhibited a conspicuous radical nature. Concurrently, the excited electron was extensively delocalized over the entire pentacyanobutadiene moiety. The researchers postulated the following description for the photophysical properties of **64**: a nonradiative deactivation process occurred via a CI, which was similar to that observed in the case of **63**.

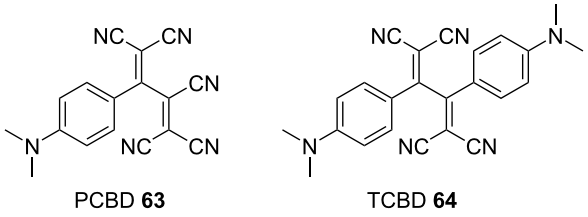

Figure 4: Structures of **63** and the TCBD **64**.

Notably, a rigid molecular environment, which induces constraints on molecular motions, serves to mitigate nonradiative losses in push–pull chromophores. Li et al. synthesized an oligo(*p*-phenylenevinylene)-based TCBD derivative denoted as **65**, which is noteworthy for its lack of photoluminescence in solution as well as contradictory propensity to form luminescent nanostructure suspensions in hexane (Figure 5) [137]. It was posited that **65** features hollow vesicles, with vesicle fusion releasing curvature energy, leading to a thermodynamically more stable tubular structure. Such aggregation-induced-emission (AIE)-active aggregates exhibit emissive behavior in hexane, with an emission peak at 679 nm and a shoulder at 717 nm along with a fluorescence quantum yield of 8.5%. This luminescence phenomenon can be aptly considered to be AIE, considering the pronounced constraints imposed on molecular rotation in the aggregate state, including rotation around the central single bond of the TCBD moiety.

Regarding the anthracene-embedded TCBD **19** in dichloromethane, no emission signal was observed. However, in the powdered form or sparsely distributed rigid matrices, a broad emission spectrum was observed. In particular, the powders of **19** exhibited photoluminescence in the near-infrared (NIR) region centered at 865 nm, with a long tail extending up to 1,550 nm. This enhancement in photoluminescence can be attributed to the restriction of molecular motion, resulting in the inhibition of nonradiative processes. Analogously, the TCBDs **66** and **67**, consisting of pyrene and perylene moieties, respectively, have been reported to exhibit luminescence in the NIR

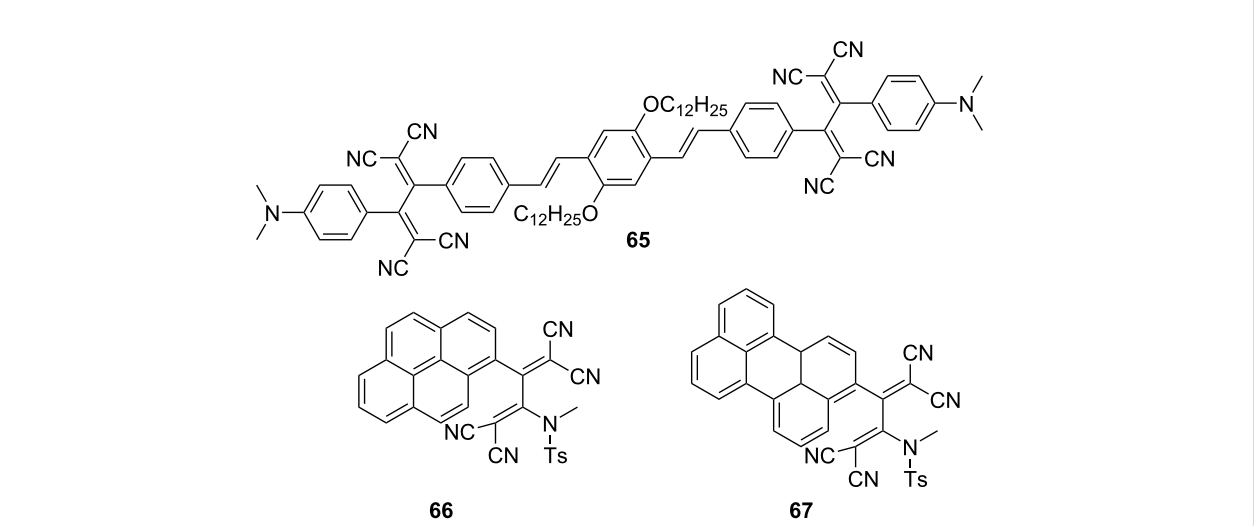

Figure 5: Structures of the fluorophore-containing TCBDs **65**–**67**.

region in their powdered forms, with the maxima at 810 nm and 890 nm for **66** and **67**, respectively, despite their nonemissive behavior in dichloromethane [138].

Compounds **55** and **56** remain devoid of emissive characteristics even when in a solution or a solid state [129]. When compound **50** was characterized using a standard steady-state fluorimeter, no emission signals were observed across the visible and NIR regions extending up to 1,600 nm, both in a room-temperature solution (dichloromethane) and as a frozen matrix at 77 K [123]. This is in contrast with the typical homoleptic phenanthroline-based CuI complexes renowned for their emissions from a triplet metal-to-ligand charge transfer excited state. The absence of luminescence may be attributed to the presence of competitive processes, such as energy or electron transfer.

Trolez et al. investigated the photoluminescence properties of various fluorophore-containing TCBDs synthesized via reactions between ynamides and TCNE [139]. The study revealed that numerous fluorenyl derivatives and their phenanthrenyl and terphenyl counterparts exhibited noteworthy emission behavior in solid form and in solutions (Figure 6). For instance, the fluorenyl derivatives **68** and **69**, phenanthrenyl derivative **70**, and terphenyl derivative **71** exhibited fluorescence characterized by emission peaks at 596, 595, 639, and 594 nm, with fluorescence quantum yields of 6.1%, 7.5%, 1.6%, and 7.8%, respectively, when dissolved in cyclohexane. Notably, the photoluminescence characteristics of these compounds depend on the solvent polarities, as evidenced by the observed decrease in the fluorescence quantum yields in toluene. This phenomenon aligns with the notion that the TICT states experience stabilization with increasing solvent polarity. Conversely, in contrast to **68**–**70**, and **71**, a TCBD derivative **72** incorporating a tetraphenylethylene (TPE) moiety exhibited no emission in toluene, possibly due to the presence of intramolecular motion within the propeller core of TPE, which promoted nonradiative decay [140].

A subgroup of compounds that exhibit exceptional luminescence in solution includes **73**, **74**, and **75**, each containing urea-substituted phenyl groups (Figure 7) [18,19]. When excited at 380 nm, these compounds show broad emission spectra encompassing the entire visible region, featuring two peaks centered at 430–472 and 633 nm. The fluorescence quantum yields estimated for **73**, **74**, and **75** in acetonitrile are 3.4%, 3.3%, and 4.3%, respectively. Notably, in the case of **74** and **75**, the intensity of the long-wavelength emission increases when they are excited at 420 nm, resulting in white-light emission. The underlying mechanism governing these luminescence properties remains unknown. It has been established that **75** does not exhibit luminescence in its solid-state form, which is attributed to the quenching effects arising from hydrogen bonding and π–π stacking interactions. In contrast, when **75** is incorporated into a nanocomposite with polystyrene serving as the matrix, luminescent properties are observed [141].

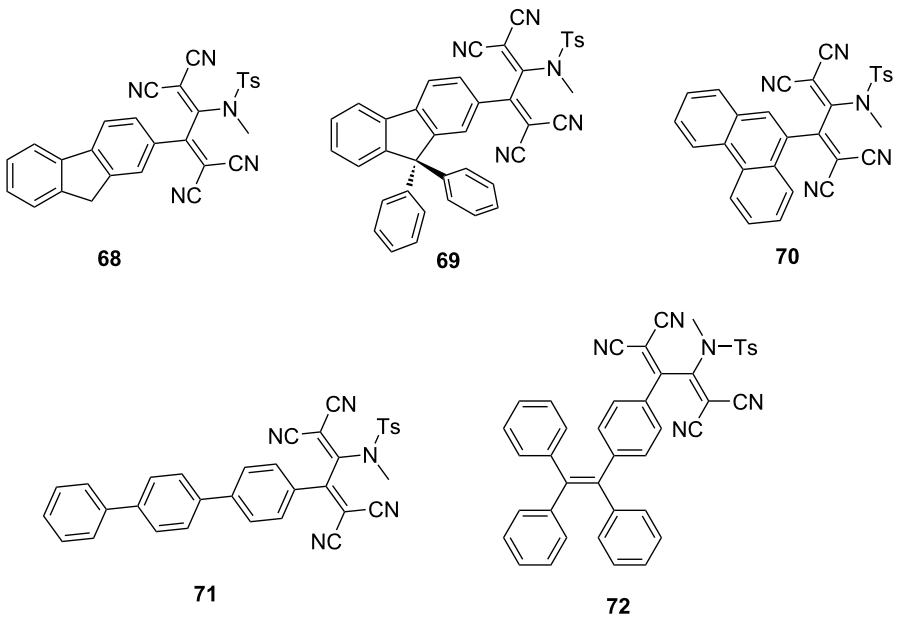

Figure 6: Structures of the fluorophore-containing TCBDs **68**–**72**.

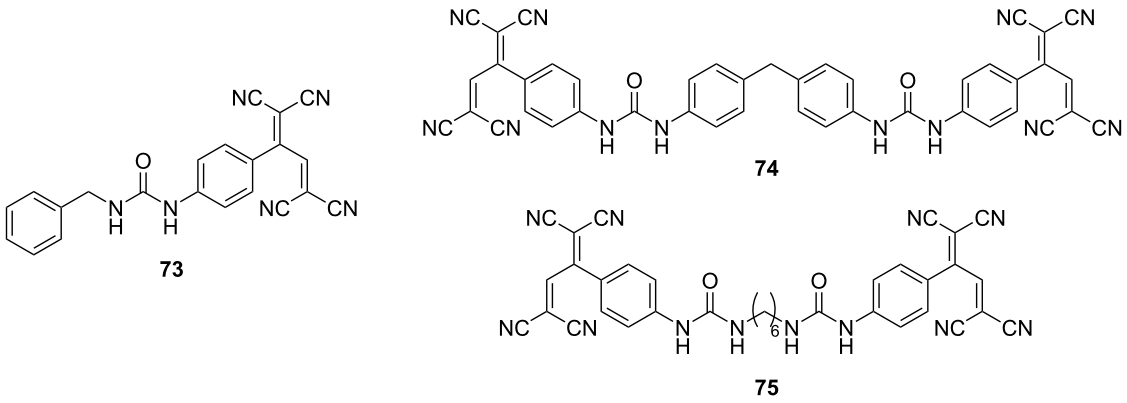

Figure 7: Structures of the urea-containing TCBDs **73**–**75**.

Photoinduced intramolecular energy and electron transfer

Exploiting the electron-accepting property of TCBD, donor–acceptor conjugated systems have been systematically developed by coupling the TCBD motif with an electron donor, resulting in the experimental observation of photoinduced electron- and energy-transfer events. In 2014, comprehensive investigations on the photophysical properties of conjugates featuring diethylamino groups and TCBD or DCNQ structures covalently linked to C_{60} (**76** and **77**) and conjugates incorporating octamethylferrocenyl (OEF) groups and TCBD or DCNQ structures bonded to C_{60} (**78** and **79**) in addition to their respective reference compounds (**80**–**83**) were reported (Figure 8) [142]. In these conjugates, the push–pull chromophores and the C_{60} unit were effectively spatially isolated from each other – a feat achieved through the strategic incorporation of a pyrrolidine ring as the connecting bridge. Thorough examinations via steady-state fluorescence spectroscopy in toluene unequivocally demonstrated that compounds **77**–**83** exhibited negligible emissions upon excitation in the charge-transfer (CT) band. In contrast, compound **76** emitted radiations corresponding to fluorescence exhibited by fullerenes, with a peak wavelength of 708 nm, upon CT-band excitation. This observation confirms the plausible energy transfer from the local charge-separated (CS) state of the push–pull chromophore (namely *N*,*N*-diethylanilino (DEA)$^{\bullet+}$–TCBD$^{\bullet-}$) to the singlet excited state of C_{60} ($^1C_{60}$*). In transient absorption spectral measurements conducted via the femtosecond laser-flash photolysis of compound **80** in toluene, the occurrence of CT-band bleaching along with increased absorption in the 500–700 nm spectral range and a net decrease in absorption within the 850–1,200 nm region has been observed upon excitation at 420 nm, which is proximate to the CT band. For compound **76**, in addition to the CT-band bleaching and increased absorption within the 500–700 nm range, an increase in the absorption intensity at 1,021 nm, corresponding to the characteristics of the C_{60} radical anion, was observed initially (20 ps), indicating the formation of the DEA$^{\bullet+}$–$C_{60}^{\bullet-}$ CS state. Furthermore, an increase in the absorption intensity at 700 nm, corresponding to the triplet excited state of C_{60} ($^3C_{60}$*), was observed along with the decay of the CS state with a lifetime of 1,380 ps. Conversely, for compound **77**, excitation at 387 nm was required for the formation of the CS state and an increase in the absorption intensity at 890 nm, indicating the emergence of $^1C_{60}$* state with a lifetime of 115 ps, was accompanied by a subsequent increase in the absorption intensity at 1,021 nm, corresponding to the formation of the C_{60} radical anion. The lifetimes of the charge separation and charge recombination events were determined to be 2 and 165 ps, respectively, via multiwavelength analyses. The excitation at 640 nm, a wavelength proximate to the CT band, failed to induce any discernible electron or energy transfer from the DEA moiety to the C_{60} core. When compound **77** underwent photoexcitation at 640 nm, the CT band exhibited bleaching along with an increase in the absorption intensity at 523 nm and a decrease in the NIR region, similar to the trend observed for **80**. Notably, no other distinctive changes were observed. The photoexcitation of **78** at 420 nm caused CT band excitation, leading to charge separation. This was exemplified by the emergence of a maximum absorption peak at 1,024 nm, indicating the one-electron reduced form of C_{60}. Although the observation of the oxidation process of the ferrocene unit was obstructed by the more substantial absorption changes associated with fullerene reduction, the lifetimes of the formation and decay of the CS state, OEF$^{\bullet+}$–$C_{60}^{\bullet-}$, were determined to be 13 and 82 ps, respectively. For **79**, the excitation of C_{60} at 387 nm was essential for the development of the CS state, similar to that observed for **77**. In this case, the lifetimes of the charge separation and recombination events were determined to be 2 and 58 ps, respectively. The observed longer lifetimes attributed to DEA substitution could be due to the larger distance and the Marcus inverted region [143] character, compared with the results obtained for OEF substitution.

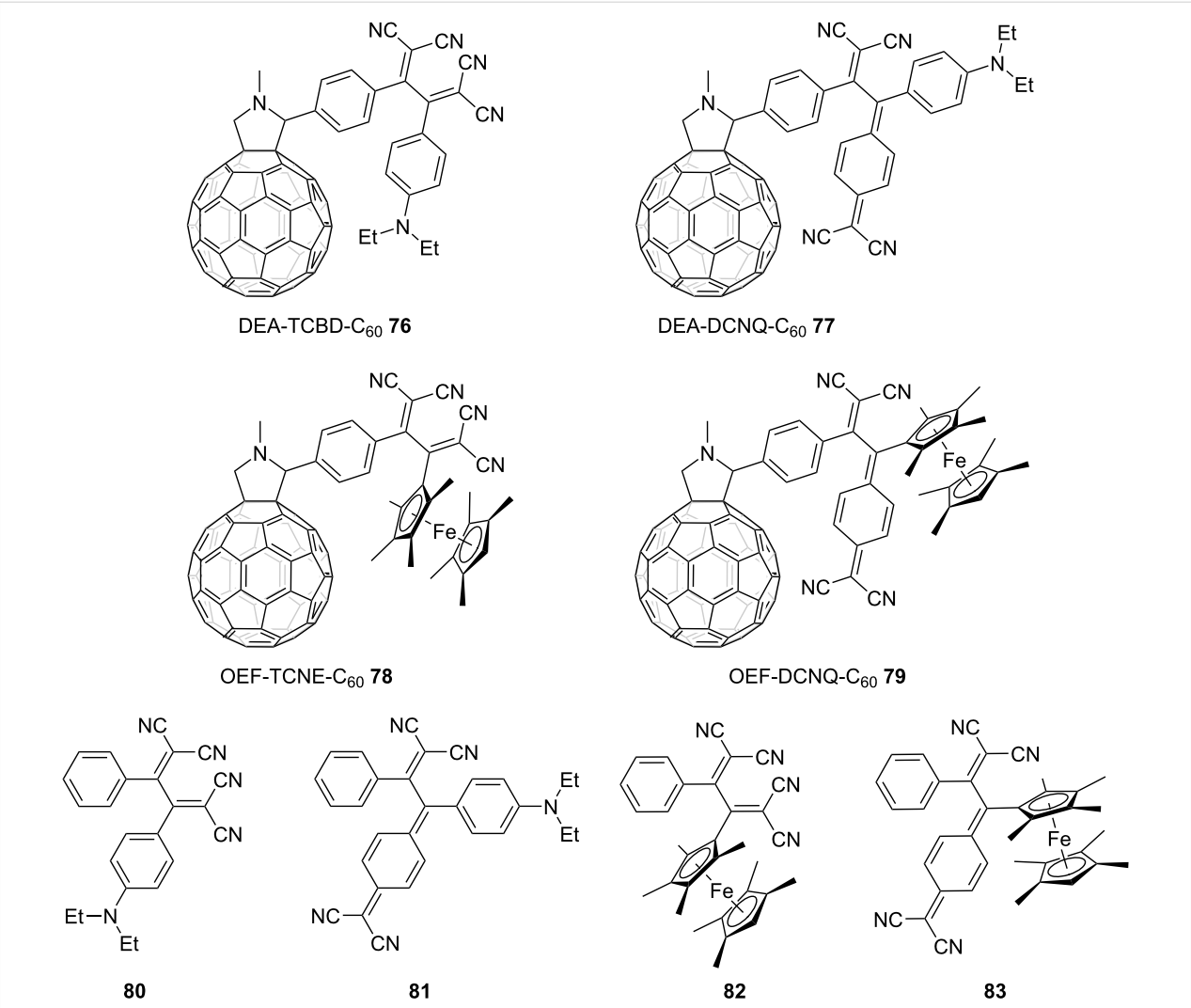

Figure 8: Structures of the fullerene–TCBD and DCNQ conjugates **76–79** and their reference compounds **80–83**.

Guldi et al. synthesized zinc phthalocyanine (ZnP_C) covalently linked with anilino-TCBD molecules, denoted as **84** and **85**, and investigated their optical properties (Figure 9). They observed robust low-energy ICT absorption peaks at 752/753 nm, along with the distinctive high-energy ICT absorption peaks at 470 nm, which are characteristic of anilino-TCBD. Furthermore, they identified B-band (355/361 nm) and Q-band (660/685 nm) transitions, which are hallmarks of phthalocyanines in benzonitrile, and elicit panchromatic optical absorption properties [144]. In **84** and **85**, the two DCV structures comprising TCBD are primarily contorted and exhibit limited conjugation. Consequently, these two structures could independently contribute to the emergence of two distinct and robust ICT bands in close proximity to those of their neighboring electron-rich ZnPc and DMA groups. Notably, in the transient absorption spectra of **84**, acquired upon excitation at 775 nm (an excitation wavelength corresponding to the low-energy CT absorption), the direct formation of a CS state, characterized as $ZnPc^{\bullet+}$–$TCBD^{\bullet-}$, can be observed.

SubPc–TCBD–aniline conjugates **59** and **60** exhibited distinct physicochemical properties, depending on whether the peripheral substituents introduced into the SubPcs consisted of hydrogen (as in **59**) or fluorine (as in **60**) atoms [131]. For **59**, the emergence of a metastable radical ion-pair state ($H_{12}SubPc^{\bullet+}$–$TCBD^{\bullet-}$–aniline) was realized after the generation of the $H_{12}SubPc$ singlet excited state via 550 nm and 458 nm excitations, corresponding to the Q-band of $H_{12}SubPc$ and the ICT band, respectively. This indicates that similar ultrafast charge-separation and charge-recombination dynamics will also be observed in toluene. For **60**, the emergence of new maxima at 500, 660, and 742 nm and minima at 460 nm accompanied the decay of the excited singlet state of $F_{12}SubPc$, which was first generated by 550 nm

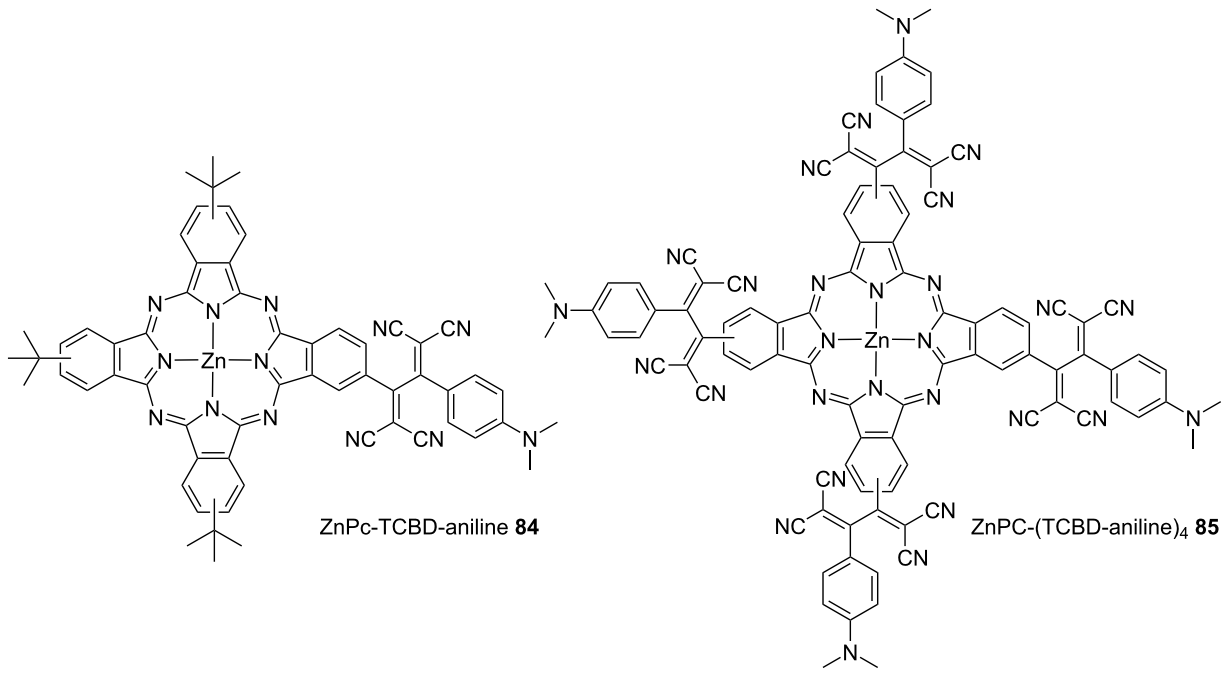

Figure 9: Structures of the ZnPc–TCBD–aniline conjugates **84** and **85**.

excitation in toluene. The transients at 500 and 742 nm were considered to result from the $F_{12}SubPc^{\bullet-}$ radical anion, that at 660 nm was considered to result from the $TCBD^{\bullet-}$ radical anion, and the minimum at 460 nm corresponded to the bleaching of the ICT absorption band. This suggests that exciplexes ($[(F_{12}SubPc–TCBD)^{\delta-}–aniline^{\delta+}]^*$) are generated where the negative charge is delocalized over $F_{12}SubPc$ and TCBD. The radiative exciplex formation was also confirmed by time-resolved fluorescence measurements. In fact, in toluene, **60** showed maximum emission at 675 nm and a shoulder emission at 612 nm. When the solvent was changed from toluene to benzonitrile and the polarity of the solvent increased, the emission at 612 nm remained almost unchanged, while the emission at 675 nm significantly quenched with a red shift of 35 nm. In the transient absorption spectra of **60** in benzonitrile, the formation of an exciplex was not observed and it was considered that the CS state ($(F_{12}SubPc–TCBD)^{\bullet-}–aniline^{\bullet+}$) was formed from the singlet excited state of $F_{12}SubPc$ before returning to the singlet ground state. The aforementioned phenomenon, characterized by the switch in the exciplex or the CS-state formation for **60** depending on the solvent, was also observed for excitation at 458 nm corresponding to the ICT band.

A series of multicomponent systems consisting of anilino-substituted TCBD or PCBD coupled with zinc porphyrins (ZnPs) were synthesized, and their photophysical properties were investigated by Diederich et al. [145]. The representative molecules among these are shown in Figure 10. In **86**, wherein ZnP and anilino-PCBD are linked using a spacer, the excitation of the porphyrin chromophore (at 560 nm, corresponding to the Q-band) generated an excited singlet state of ZnP (^{1}ZnP*) with a lifetime of 71 ps in toluene. Meanwhile, the absorption at 640 nm, corresponding to the ZnP radical cation, was not observed. The results obtained from Rehm–Weller's equation [146] suggested that photoinduced electron transfer was thermodynamically permitted in **86**. However, ultrafast energy transfer from ^{1}ZnP* to the PCBD moiety was considered to have occurred. In **87**, the energy transfer from ^{1}ZnP* to the TCBD moiety was not thermodynamically allowed. Conversely, the CS state ($ZnP^{\bullet+}$-S-$TCBD^{\bullet-}$) was estimated to be approximately isoenergetic. The lifetime of ^{1}ZnP* was estimated to be 1,080 ps. However, the emergence of the weak absorption band of the ZnP radical cation at 640 nm was hindered by the overwhelming absorption intensity of the residual porphyrin. The transient absorption spectra of **87** were obtained in benzonitrile solvent, which was expected to stabilize the CS state. Absorption corresponding to the ZnP radical cation was clearly observed with a lifetime of 2.3 μs. The occurrence of such a long-living CS state can be rationally associated with the Marcus-inverted-region [143] behavior of the charge-recombination process. For **88**, which has no spacer between ZnP and TCBD, as opposed to the case for **87**, the excitation of the porphyrin chromophore in toluene led to the formation of ^{1}ZnP* with a lifetime of 6.6 ps. This was followed by the emergence of the

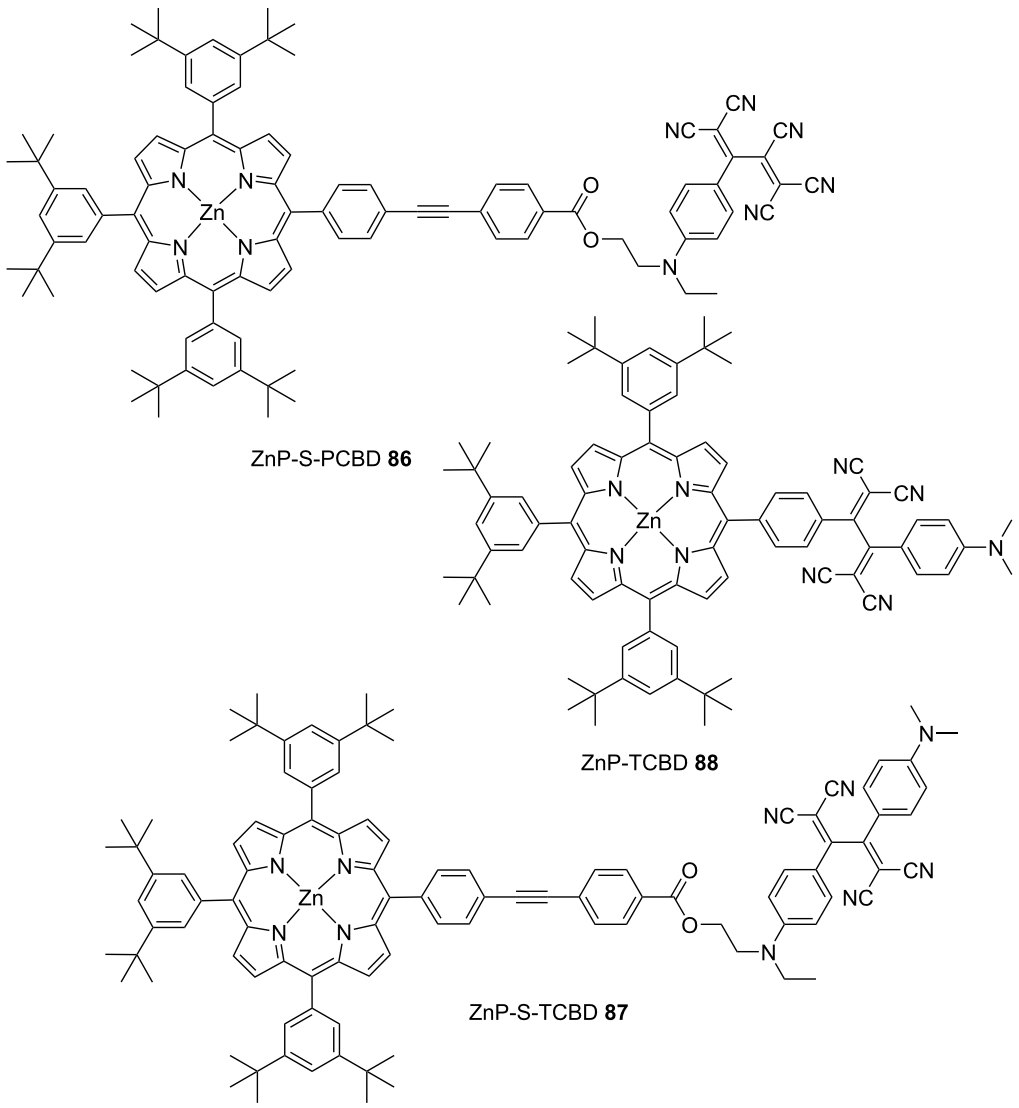

Figure 10: Structures of the ZnP–PCBD and TCBD conjugates **86**–**88**.

CS state and subsequent charge recombination within 20 ps. Thus, the results indicate that a separating bridge is essential for guaranteeing long-lived CS states.

Guldi et al. synthesized 16 distinct donor–acceptor conjugated molecules, denoted as **89**–**104** (Figure 11). These molecules comprised ZnP as an electron donor and push–pull chromophores with varying reduction potentials as electron acceptors interconnected by various rigid spacers [147,148]. Comprehensive analyses and characterizations of the photoinduced electron-transfer processes in these conjugates were conducted. In these molecular designs, the center-to-center distances of the electron donor and acceptor ranged from 13.9 Å to 25.1 Å. Marcus curves were obtained by measuring the charge-separation and charge-recombination lifetimes of these molecules by laser-flash photolysis (excitation wavelength = 420 nm) and the resulting electron-transfer rates were plotted. In the measurements in toluene, the lifetimes of the CS states and charge-recombination events differed significantly depending on the type of spacer and acceptor moiety, with the CS-state lifetimes ranging from 3 (for **98**) to 931 ps (for **103**) and the charge-recombination lifetimes ranging from 12 (for **98**) to 24,000 ps (for **101**). The obtained plot is consistent with the Marcus curves obtained using the semi-empirical approach, which includes the nuclear factor, particularly the electron-vibration coupling. This indicates that the consideration of quantum chemical vibrational effects is important in explaining the electron-transfer processes in these conjugates. For these molecules, the dynamics of the charge-recombination processes were found to be located in the Marcus inverted region. The total reorgani-

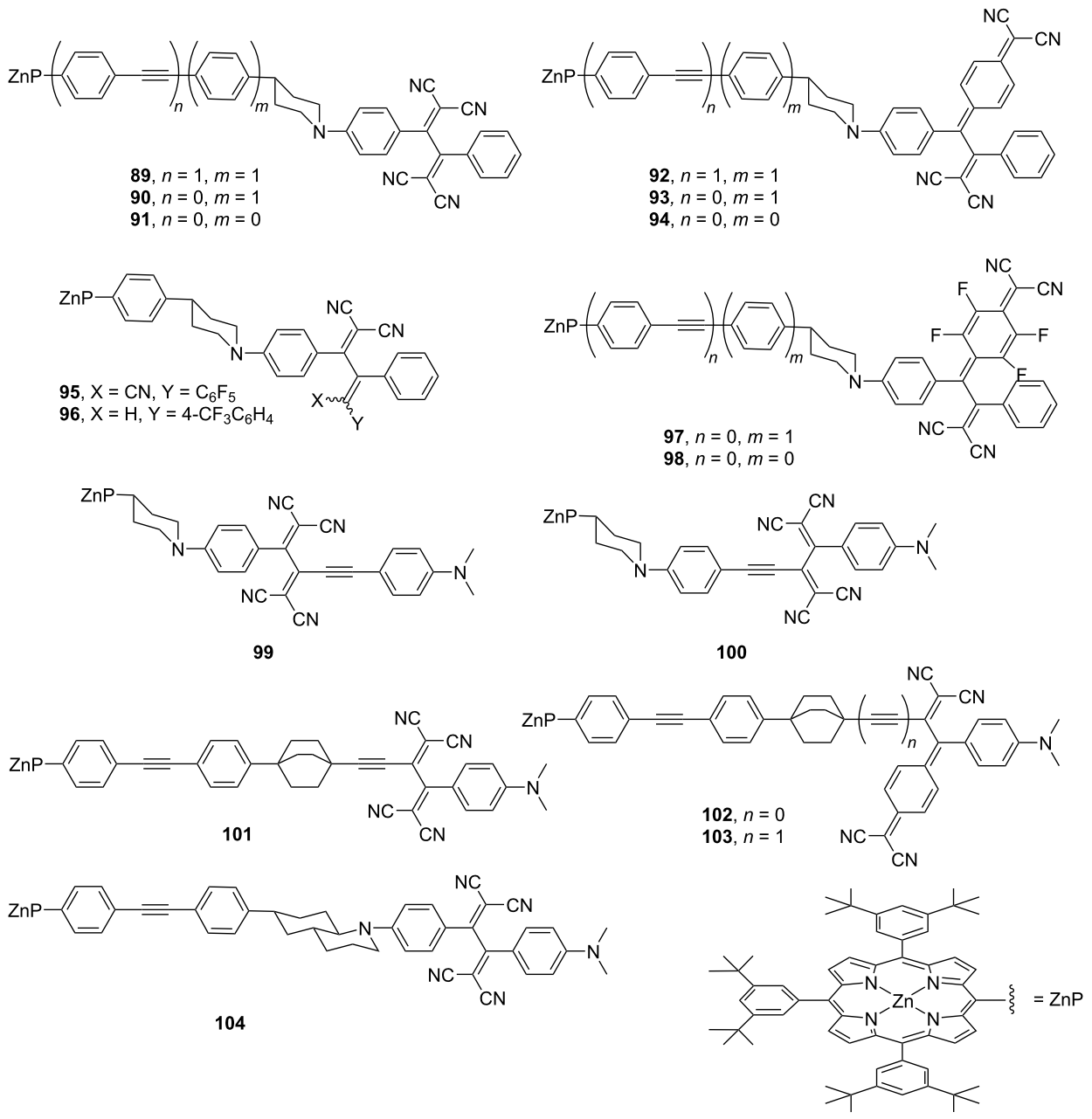

Figure 11: Structures of the porphyrin-based donor–acceptor conjugates (**89**–**104**).

zation energies and electronic coupling matrix elements estimated from the fitting of the Marcus curve were determined to be 0.66–0.79 eV and 13.9–30.9 cm^{-1}, respectively. Using a molecular design similar to that of **102**, the rectification property of a compound wherein TTF and DCNQ are linked by a rigid spacer has also been reported [149].

Misra et al. designed and synthesized a series of chromophore molecules **105**–**112** featuring porphyrin moieties and investigated their photophysical properties. They found that the introduction of the TCBD structures switched the role of porphyrins in photoevents (Figure 12) [150]. In molecules **105**, **106**, **109**, and **110** without the TCBD structure, when the metalloporphyrin moiety (MP) was subjected to Soret-band excitation (426 nm) in benzonitrile, the emergence of the S_2 state was observed; the subsequent internal conversion of S_2 into the S_1 state was also observed, from which the CS state ($MP^{\bullet-}$–$D^{\bullet+}$) emerged. Here, since the triplet state $^3MP^*$ is energetically lower than the CS

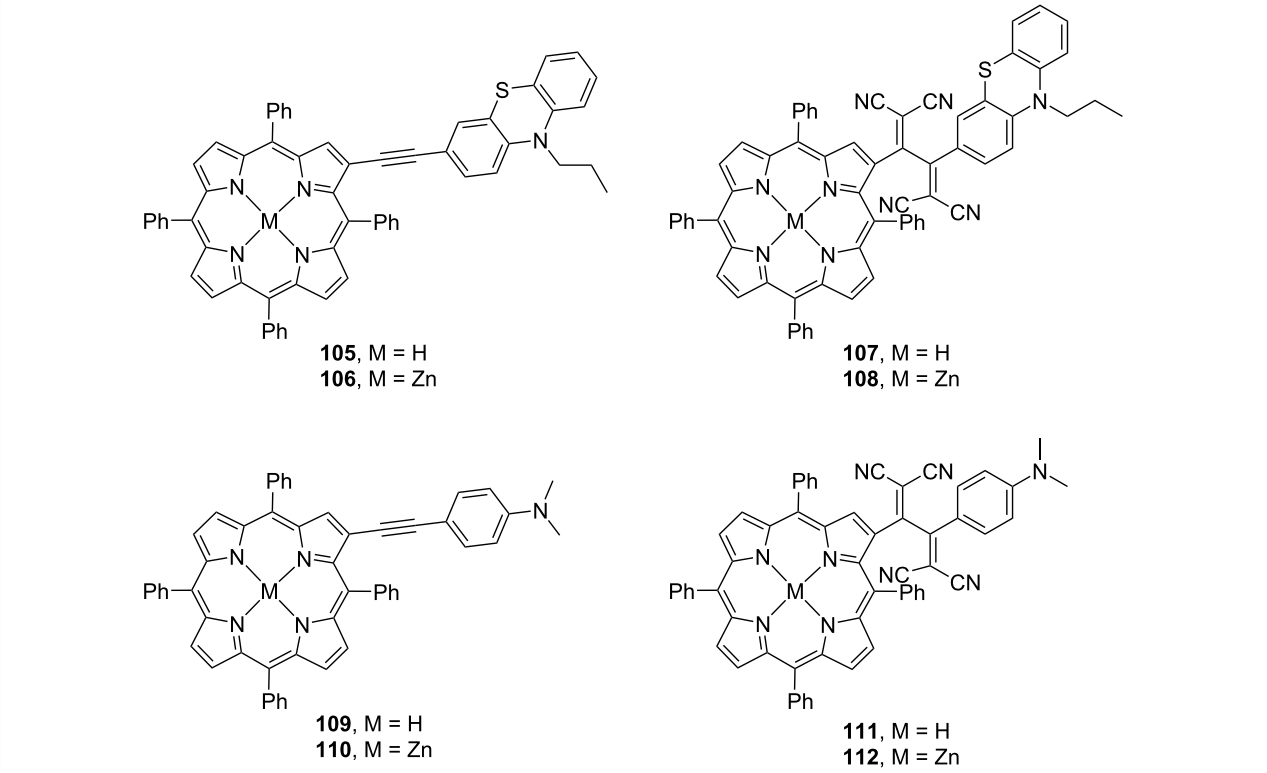

Figure 12: Structures of the porphyrin–PTZ or DMA conjugates **105**–**112**.

state, ^{3}MP* can partially emerge at the intersystem crossing from the S_1 state; a transition from the CS state to ^{3}MP* is also possible. In contrast, for molecules **107**, **108**, **111**, and **112** bearing the TCBD structure, the S_2 state emerges due to Soret-band excitation (426 nm) in benzonitrile. Further, after the transition from S_2 to S_1 by internal conversion, a CT state emerges: $MP^{\delta+}$–$TCBD^{\delta-}$–donor, where donor = phenothiazine (PTZ) or DMA. From this CT state, electron transfer occurs to form a CS state ($MP^{\bullet+}$–$TCBD^{\bullet-}$–donor), which returns to the ground state by charge recombination. These results indicate that MP functions as an electron acceptor in molecules without the TCBD structure, while the presence of the TCBD structure causes the porphyrin molecule to behave as an electron donor.

Misra et al. synthesized a series of TCBD and DCNQ derivatives with BF_2-chelated BODIPYs and reported their photophysical properties [1,151]. Notably, for the CS state to emerge, it must have energy lower than the excited triplet state of BODIPY. Conjugates **113** and **114** have molecular structures wherein the TCBD or DCNQ moieties are inserted between the BODIPY and triphenylamine (TPA) moieties, as shown in Figure 13. The energy-level diagrams estimated from the Rehm–Weller equation suggested that at least two CS states were possible in the conjugates (BODIPY$^{\bullet+}$–acceptor$^{\bullet-}$–TPA and BODIPY–acceptor$^{\bullet-}$–TPA$^{\bullet+}$ (acceptor = TCBD or DCNQ)). In fact, when the transient absorption spectra of **113** and **114** were obtained using an excitation wavelength of 400 nm (the wavelength at which BODIPY is mainly excited), transient corresponding to the BODIPY$^{\bullet+}$–acceptor$^{\bullet-}$–TPA and BODIPY–acceptor$^{\bullet-}$–TPA$^{\bullet+}$ states were observed, highlighting ultrafast CS and charge-recombination events. In compounds **115** and **116** containing TCBD or DCNQ structures incorporated between BODIPY and PTZ, CS states, namely BODIPY–TCBD$^{\bullet-}$–PTZ$^{\bullet+}$ and BODIPY-DCNQ$^{\bullet-}$–PTZ$^{\bullet+}$, with a time constant of approximately 4 ps were observed after the formation of the excited singlet state of BODIPY by excitation at 511–512 nm in benzonitrile.

Sankar et al. designed and synthesized a conjugate consisting of TCBD coupled with a metal corrole to develop a system that can achieve an efficient population of the triplet states through the excited CT state [64]. TCBD derivatives containing copper or silver corrole complexes, denoted as **117** and **118**, respectively, were synthesized in a single step from their corresponding alkynyl precursors (Figure 14). The corresponding DCNQ derivatives were not successfully synthesized because of degradation during column purification. For these systems, the computationally calculated energy of the CT state (E_{CT}) was lower than the excitation energies at the Soret (i.e., S_2) and visible

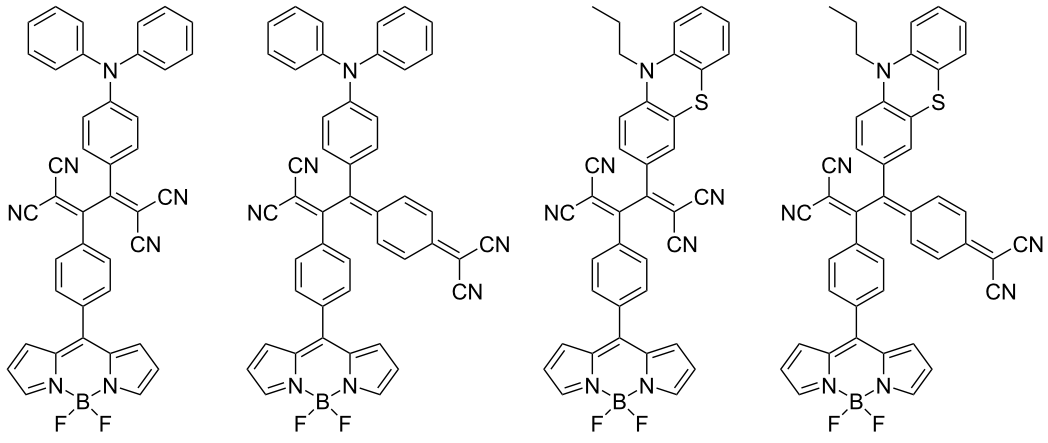

Figure 13: Structures of the BODIPY–Acceptor–TPA or PTZ conjugates **113–116**.

peak positions. Furthermore, the E_{CT} was higher than the triplet-state energies of the metal corroles. When **117** was subjected to the Soret-band (426 nm) excitation in benzonitrile, a short-lived, vibrationally hot S_1 state emerged, along with a broad absorption peak at ≈592 nm, which is characteristic of the triplet state; the decay time constant of this state was 4.98 ns. Although the expected spectral features of the CT state were not observed in the transient absorption spectra because they were overwhelmed by the absorption band of the hot S_1 state, the results suggested that the hot S1 state formed from the internal conversion of the initial S_2 state promoted the formation of the CT state. Conversely, no transient absorption corresponding to the triplet state was observed when **117** was subjected to the visible band excitation (S_1). In contrast, for **118**, a triplet state was observed for both S_2 and S_1 excitations, with time constants of 3.5 ns and 86 ps, respectively.

Material applications

Due to their high molecular conversion efficiency, [2 + 2] CA–RE reactions have been employed to develop dendritic systems [55,63,152-155]. He et al. reported the synthesis of **119,** which contains multiple dendritic TCBD motifs that form porous molecular crystals (Figure 15) [156]. The rotational freedom of the covalent linkage within **119** is postulated to be substantially restricted due to its pronounced steric hindrance. This tenacious microporous crystalline structure exhibited robust thermal stability (up to 200 °C), as confirmed by powder X-ray diffraction studies. Gas-sorption studies were also performed on the solid samples post activation at 120 °C, revealing CO_2 adsorption with pronounced hysteresis. This may be attributed to the presence of narrow, slit-like pores and voids, as seen in the crystal lattice of **119**. The Langmuir surface area of the compound was determined to be 317 m^2/g. Furthermore, the

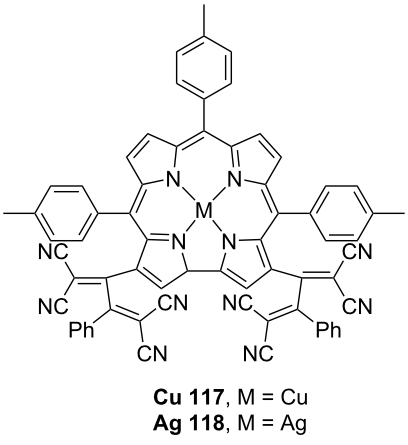

Figure 14: Structures of the corrole–TCBD conjugates **117** and **118**.

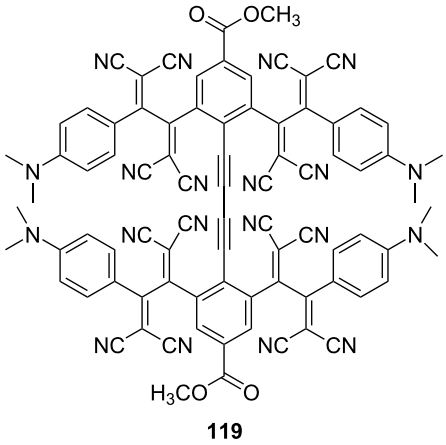

Figure 15: Structure of the dendritic TCBD **119**.

compound exhibits easy fabrication of its thin films due to exceptional crystalline integrity when deposited on glass plates, highlighting its good reproducibility in solution-based processes. Li et al. analyzed the aggregation tendencies of push–pull chromophores involving TCBD or DCNQ moieties in the benzothiazole framework. Their findings revealed potential for the generation of hollow microstructures characterized by spherical or tubular morphologies [157].

TCBDs and related push–pull chromophores have attracted attention as organic nonlinear optical (NLO) materials because of their highly polarizable π-electron systems [158]. Thus far, second- and third-order NLO responses of several TCBD compounds have been evaluated [16,61,82,89,135,159-163]. Yang and Si theoretically calculated the second-order polarizability values that relate the second-order NLO responses of TCBD derivatives with different substituents and showed that the NLO properties can be tuned by changing the substituents [164]. Furthermore, Biaggio conducted a detailed study of the third-order NLO properties of TCBD derivatives – an overview is reported in a recent paper [165]. They experimentally determined the orientational average of the off-resonant third-order polarizability value (γ_{rot}) of **120** (a benchmark compound) to be $12 \pm 2 \times 10^{-48}$ m^5 V^{-2} (Figure 16). Furthermore, the γ_{rot} values of a series of compounds containing acetylene spacers of different lengths between the anilino group and TCBD moiety (**121**–**126**) have been determined, and a correlation between the length of the acetylene spacer and the γ_{rot} value was established: longer linking distances of the acetylene spacer result in larger the γ_{rot} values [160]. The appeal of **120** is its ability to undergo sublimation without decomposition and produce high-density, high-quality homogeneous molecular assemblies via molecular beam deposition [166]. Freude et al. fabricated a silicon–organic-hybrid slot waveguide by depositing **120** between two silicon ribs via molecular beam deposition and successfully demonstrated the all-optical demultiplexing of a 170.8 Gb s^{-1} telecommunication signal to 42.7 Gb s^{-1} [167].

The two-photon absorption (2PA) properties of the TCBD derivatives have also been studied [135,168]. For example, the 2PA cross-section (σ_2) of **128** measured by the Z-scan method was estimated to be 390 GM (2PA wavelength = 1,050 nm) (Figure 17) [135]. Although this value is smaller than that of the precursor (**127**; 540 GM; 2PA wavelength = 700 nm), **128** is expected to be used as a two-photon absorber in the NIR region. The branched TCBD derivatives **129** and **130** bearing the triarylamino core have also been synthesized and their 2PA properties have been evaluated. The σ_2 values for **129** were 80 GM at 1,150 nm and 275 GM at 900 nm, and those of **130** were 90 GM at 1,150 nm and 350 GM at 900 nm, indicating that both compounds have relatively high 2PA cross-sections.

TCBDs and their related push–pull chromophores have also been studied as candidate materials for applications in photovoltaic devices because of their exceptional redox properties. Notably, push–pull chromophores, such as TCBD and DCNQ, exhibit flexible highest occupied molecular orbital/lowest unoccupied molecular orbital levels that can be tuned by the appropriate selection of electron donor and acceptor [41,44-46,169,170]. To date, various bulk heterojunction organic solar cells (BHJ OSCs) based on TCBD derivatives have been developed and their photoelectric conversion properties have been evaluated. A comprehensive overview of the advances in this regard can be found in the work of Butenschön et al. [8]. While fullerene derivatives, such as [6,6]-phenyl-C_{61}-butyric acid methyl ester ([60]PCBM) and [6,6]-phenyl-C_{71}-butyric acid methyl ester ([70]PCBM) [171], have been widely used as electron-acceptor materials in BHJ OSCs, TCBD derivatives are considered as promising nonfullerene electron acceptors [26,172-176]. The power conversion efficiency of the BHJ OSCs fabricated using the TCBD derivative containing carbazole and diketopyrrolopyrrole structures, denoted as **131**, as the electron acceptor reached 7.19% (Figure 18) [173]. Some researchers have also focused on the introduction of electron-donating substituents into the TCBD structure and studied the

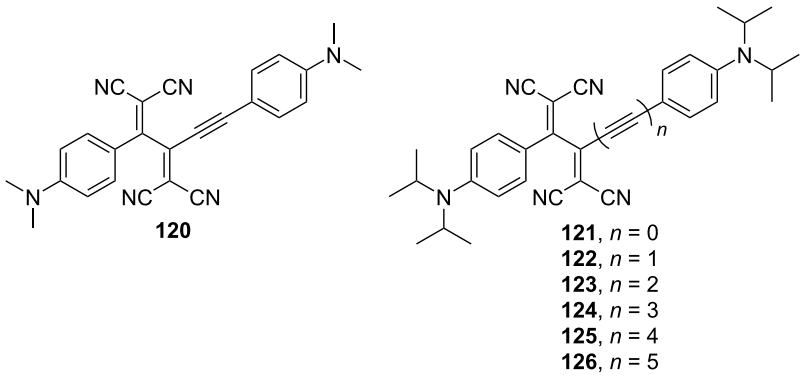

Figure 16: Structures of the TCBDs **120**–**126**.

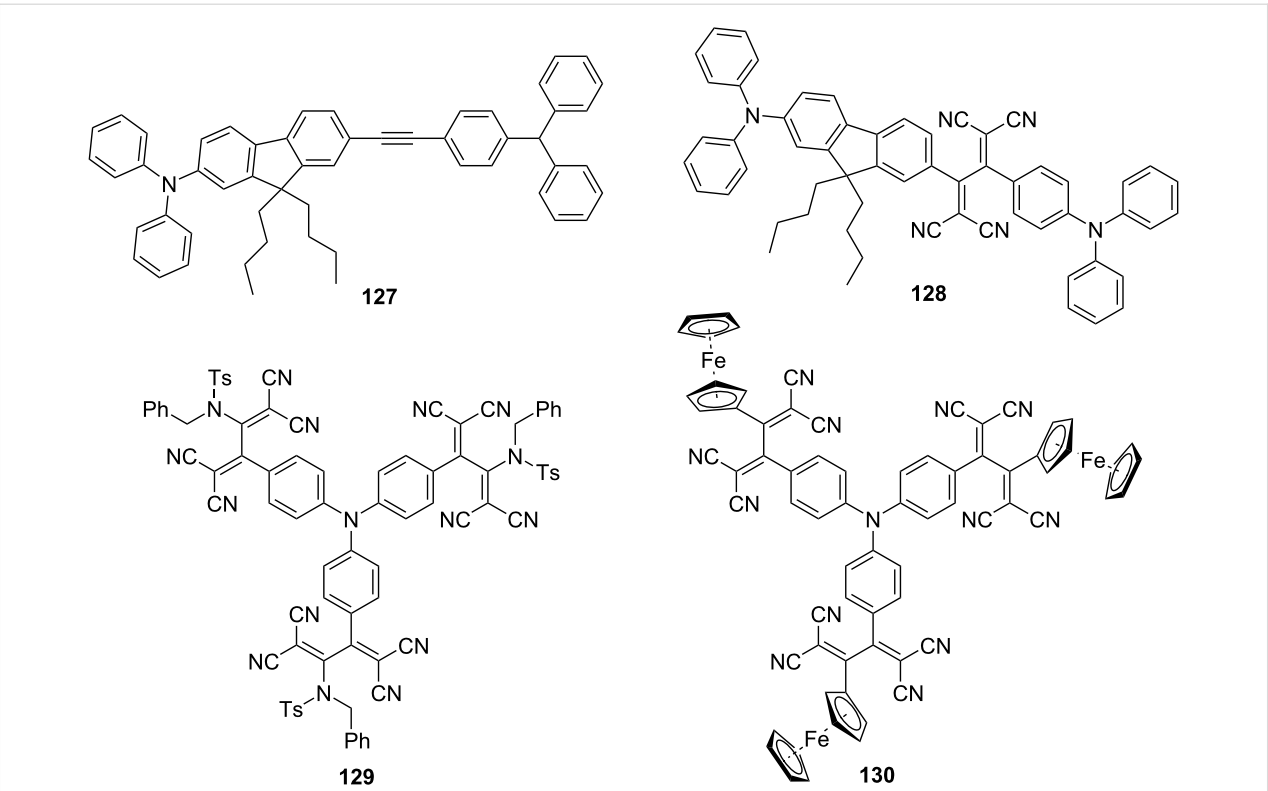

Figure 17: Structures of the precursor **127** and TCBDs **128**–**130**.

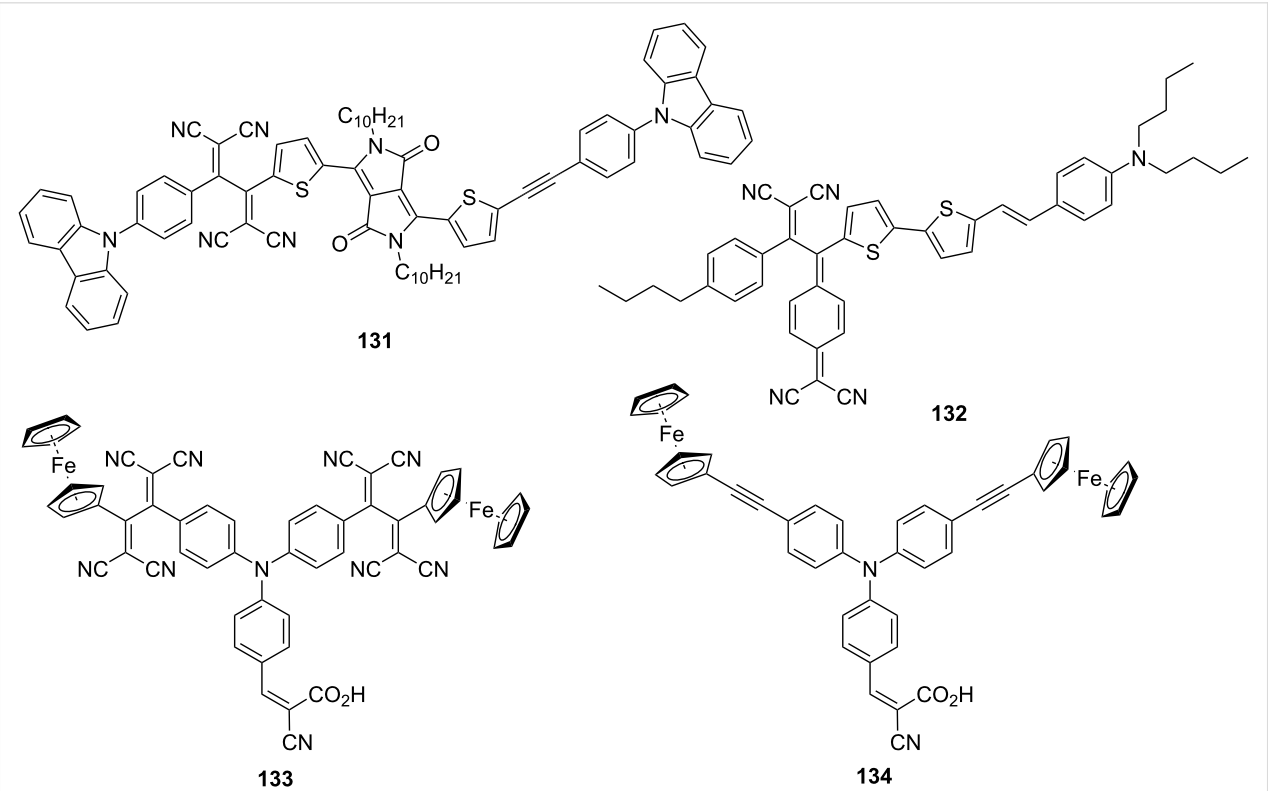

Figure 18: Structures of **131**–**134** utilized for BHJ OSCs.

use of TCBD as an electron donor in BHJ OSCs [24,25,177-181]. Praveen et al. fabricated BHJ OSCs with a 1:1 blending ratio of the DCNQ derivative **132** as an electron donor and [70]PCBM as an electron acceptor and reported that the power conversion efficiency reached 7.79% [25]. Dye-sensitized solar cells using **133**, a compound with two ferrocenyl TCBD structures introduced into the TPA structure, as a sensitizer have also been fabricated, achieving a power conversion efficiency of 4.96% [182]. Further, a power conversion efficiency was 3.65% was obtained when the precursor compound **134** was used. Therefore, the light-harvesting capability of the TCBD derivative is expected to contribute to the conversion efficiency.

Conclusion

In summary, recent research advancements have revealed that [2 + 2] CA–RE reactions can not only yield nonplanar push–pull chromophores characterized by TCBD and DCNQ structures but also an array of π-electron compounds featuring attractive electronic and optical properties. These push–pull chromophores have been integrated into various molecules, including CPP, rotaxane, and fullerenes. Furthermore, studies have elucidated the linear and nonlinear optical characteristics of these compounds along with the dynamics of their excited states. Substantial progress has been made in the research on their utilization in photoelectric conversion and NLO materials. Future studies on these compounds should focus on improving their physical properties and functions to surpass those of the existing molecules.

Funding

This work was supported by JSPS KAKENHI, Grant Numbers JP20K05472 and JP23K04704. It was also supported by the Shorai Foundation for Science and Technology.

ORCID® iDs

Michio Yamada - https://orcid.org/0000-0002-6715-4202

References

1. Bureš, F. *RSC Adv.* **2014,** *4,* 58826–58851. doi:10.1039/c4ra11264d
2. Levi, L.; Müller, T. J. J. *Chem. Soc. Rev.* **2016,** *45,* 2825–2846. doi:10.1039/c5cs00805k
3. Bruce, M. I.; Rodgers, J. R.; Snow, M. R.; Swincer, A. G. *J. Chem. Soc., Chem. Commun.* **1981,** 271–272. doi:10.1039/c39810000271
4. Kivala, M.; Diederich, F. *Acc. Chem. Res.* **2009,** *42,* 235–248. doi:10.1021/ar8001238
5. Kato, S.-i.; Diederich, F. *Chem. Commun.* **2010,** *46,* 1994–2006. doi:10.1039/b926601a
6. Bruce, M. I. *J. Organomet. Chem.* **2013,** *730,* 3–19. doi:10.1016/j.jorganchem.2012.11.004
7. Michinobu, T.; Diederich, F. *Angew. Chem., Int. Ed.* **2018,** *57,* 3552–3577. doi:10.1002/anie.201711605
8. Patil, Y.; Butenschön, H.; Misra, R. *Chem. Rec.* **2023,** *23,* e202200208. doi:10.1002/tcr.202200208
9. Michinobu, T. *Pure Appl. Chem.* **2010,** *82,* 1001–1009. doi:10.1351/pac-con-09-09-09
10. Michinobu, T. *Chem. Soc. Rev.* **2011,** *40,* 2306–2316. doi:10.1039/c0cs00205d
11. Kivala, M.; Stanoeva, T.; Michinobu, T.; Frank, B.; Gescheidt, G.; Diederich, F. *Chem. – Eur. J.* **2008,** *14,* 7638–7647. doi:10.1002/chem.200800716
12. Kivala, M.; Boudon, C.; Gisselbrecht, J.-P.; Seiler, P.; Gross, M.; Diederich, F. *Chem. Commun.* **2007,** 4731–4733. doi:10.1039/b713683h
13. Bruce, M. I.; Burgun, A.; Grelaud, G.; Lapinte, C.; Parker, C. R.; Roisnel, T.; Skelton, B. W.; Zaitseva, N. N. *Organometallics* **2012,** *31,* 6623–6634. doi:10.1021/om3006728
14. García, R.; Calbo, J.; Viruela, R.; Herranz, M. Á.; Ortí, E.; Martín, N. *ChemPlusChem* **2018,** *83,* 300–307. doi:10.1002/cplu.201700553
15. Michinobu, T.; Boudon, C.; Gisselbrecht, J.-P.; Seiler, P.; Frank, B.; Moonen, N. N. P.; Gross, M.; Diederich, F. *Chem. – Eur. J.* **2006,** *12,* 1889–1905. doi:10.1002/chem.200501113
16. Michinobu, T.; May, J. C.; Lim, J. H.; Boudon, C.; Gisselbrecht, J.-P.; Seiler, P.; Gross, M.; Biaggio, I.; Diederich, F. *Chem. Commun.* **2005,** 737–739. doi:10.1039/b417393g
17. Reutenauer, P.; Kivala, M.; Jarowski, P. D.; Boudon, C.; Gisselbrecht, J.-P.; Gross, M.; Diederich, F. *Chem. Commun.* **2007,** 4898–4900. doi:10.1039/b714731g
18. Dar, A. H.; Gowri, V.; Gopal, A.; Muthukrishnan, A.; Bajaj, A.; Sartaliya, S.; Selim, A.; Ali, M. E.; Jayamurugan, G. *J. Org. Chem.* **2019,** *84,* 8941–8947. doi:10.1021/acs.joc.9b00841
19. Gowri, V.; Jalwal, S.; Dar, A. H.; Gopal, A.; Muthukrishnan, A.; Bajaj, A.; Ali, M. E.; Jayamurugan, G. *J. Photochem. Photobiol., A* **2021,** *410,* 113163. doi:10.1016/j.jphotochem.2021.113163
20. Kato, S.-i.; Noguchi, H.; Jin, S.; Nakamura, Y. *Asian J. Org. Chem.* **2016,** *5,* 246–256. doi:10.1002/ajoc.201500431
21. Okuno, T.; Iwahashi, H. *Acta Crystallogr., Sect. E: Struct. Rep. Online* **2013,** *69,* o665. doi:10.1107/s1600536813008799
22. Yadav, I. S.; Misra, R. *New J. Chem.* **2022,** *46,* 15999–16006. doi:10.1039/d2nj03089f
23. Pappenfus, T. M.; Schneiderman, D. K.; Casado, J.; López Navarrete, J. T.; Ruiz Delgado, M. C.; Zotti, G.; Vercelli, B.; Lovander, M. D.; Hinkle, L. M.; Bohnsack, J. N.; Mann, K. R. *Chem. Mater.* **2011,** *23,* 823–831. doi:10.1021/cm102128g
24. Simón Marqués, P.; Castán, J. M. A.; Raul, B. A. L.; Londi, G.; Ramirez, I.; Pshenichnikov, M. S.; Beljonne, D.; Walzer, K.; Blais, M.; Allain, M.; Cabanetos, C.; Blanchard, P. *Chem. – Eur. J.* **2020,** *26,* 16422–16433. doi:10.1002/chem.202002810
25. Raheem, A. A.; Kumar, C.; Shanmugam, R.; Murugan, P.; Praveen, C. *J. Mater. Chem. C* **2021,** *9,* 4562–4575. doi:10.1039/d1tc00708d
26. Raheem, A. A.; Murugan, P.; Shanmugam, R.; Praveen, C. *ChemPlusChem* **2021,** *86,* 1451–1460. doi:10.1002/cplu.202100392
27. Kato, S.-i.; Kivala, M.; Schweizer, W. B.; Boudon, C.; Gisselbrecht, J.-P.; Diederich, F. *Chem. – Eur. J.* **2009,** *15,* 8687–8691. doi:10.1002/chem.200901630
28. García, R.; Herranz, M. Á.; Torres, M. R.; Bouit, P.-A.; Delgado, J. L.; Calbo, J.; Viruela, P. M.; Ortí, E.; Martín, N. *J. Org. Chem.* **2012,** *77,* 10707–10717. doi:10.1021/jo302047m
29. Mochida, T.; Yamazaki, S. *J. Chem. Soc., Dalton Trans.* **2002,** 3559–3564. doi:10.1039/b204168e

30. Jordan, M.; Kivala, M.; Boudon, C.; Gisselbrecht, J.-P.; Schweizer, W. B.; Seiler, P.; Diederich, F. *Chem. – Asian J.* **2011,** *6,* 396–401. doi:10.1002/asia.201000539
31. Shoji, T.; Ito, S.; Okujima, T.; Morita, N. *Eur. J. Org. Chem.* **2011,** 5134–5140. doi:10.1002/ejoc.201100650
32. Shoji, T.; Ito, S.; Okujima, T.; Morita, N. *Chem. – Eur. J.* **2013,** *19,* 5721–5730. doi:10.1002/chem.201202257
33. Misra, R.; Sharma, R.; Mobin, S. M. *Dalton Trans.* **2014,** *43,* 6891–6896. doi:10.1039/c4dt00210e
34. Gautam, P.; Maragani, R.; Misra, R. *Tetrahedron Lett.* **2014,** *55,* 6827–6830. doi:10.1016/j.tetlet.2014.10.094
35. Maragani, R.; Misra, R. *Tetrahedron* **2014,** *70,* 3390–3399. doi:10.1016/j.tet.2014.03.096
36. Shoji, T.; Maruyama, A.; Yaku, C.; Kamata, N.; Ito, S.; Okujima, T.; Toyota, K. *Chem. – Eur. J.* **2015,** *21,* 402–409. doi:10.1002/chem.201405004
37. Shoji, T.; Kamata, N.; Maruyama, A.; Ito, S.; Okujima, T. *Bull. Chem. Soc. Jpn.* **2015,** *88,* 1338–1346. doi:10.1246/bcsj.20150165
38. Misra, R.; Gautam, P.; Maragani, R. *Tetrahedron Lett.* **2015,** *56,* 1664–1666. doi:10.1016/j.tetlet.2015.02.031
39. Dhokale, B.; Jadhav, T.; Mobin, S. M.; Misra, R. *RSC Adv.* **2015,** *5,* 57692–57699. doi:10.1039/c5ra11433k
40. Kraße, N.; Kielmann, M.; Ma, J.; Butenschön, H. *Eur. J. Org. Chem.* **2015,** 2622–2631. doi:10.1002/ejoc.201500105
41. Dhokale, B.; Jadhav, T.; Mobin, S. M.; Misra, R. *Dalton Trans.* **2016,** *45,* 1476–1483. doi:10.1039/c5dt04037j
42. Patil, Y.; Jadhav, T.; Dhokale, B.; Misra, R. *Eur. J. Org. Chem.* **2016,** 733–738. doi:10.1002/ejoc.201501123
43. Patil, Y.; Misra, R. *J. Organomet. Chem.* **2017,** *840,* 23–29. doi:10.1016/j.jorganchem.2017.03.048
44. Patil, Y.; Popli, C.; Misra, R. *New J. Chem.* **2018,** *42,* 3892–3899. doi:10.1039/c7nj05162j
45. Rout, Y.; Mobin, S. M.; Misra, R. *New J. Chem.* **2019,** *43,* 12299–12307. doi:10.1039/c9nj01887e
46. Rout, Y.; Misra, R. *New J. Chem.* **2021,** *45,* 9838–9845. doi:10.1039/d1nj00919b
47. Shoji, T.; Ito, S.; Toyota, K.; Yasunami, M.; Morita, N. *Chem. – Eur. J.* **2008,** *14,* 8398–8408. doi:10.1002/chem.200701981
48. Shoji, T.; Ito, S.; Toyota, K.; Iwamoto, T.; Yasunami, M.; Morita, N. *Eur. J. Org. Chem.* **2009,** 4316–4324. doi:10.1002/ejoc.200900539
49. Shoji, T.; Maruyama, M.; Ito, S.; Morita, N. *Bull. Chem. Soc. Jpn.* **2012,** *85,* 761–773. doi:10.1246/bcsj.20120037
50. Shoji, T.; Maruyama, M.; Shimomura, E.; Maruyama, A.; Ito, S.; Okujima, T.; Toyota, K.; Morita, N. *J. Org. Chem.* **2013,** *78,* 12513–12524. doi:10.1021/jo402104n
51. Shoji, T.; Shimomura, E.; Maruyama, M.; Maruyama, A.; Ito, S.; Okujima, T.; Toyota, K.; Morita, N. *Eur. J. Org. Chem.* **2013,** 7785–7799. doi:10.1002/ejoc.201301006
52. Shoji, T.; Maruyama, M.; Maruyama, A.; Ito, S.; Okujima, T.; Toyota, K. *Chem. – Eur. J.* **2014,** *20,* 11903–11912. doi:10.1002/chem.201402939
53. Shoji, T.; Maruyama, A.; Shimomura, E.; Nagai, D.; Ito, S.; Okujima, T.; Toyota, K. *Eur. J. Org. Chem.* **2015,** 1979–1990. doi:10.1002/ejoc.201403556
54. Shoji, T.; Maruyama, A.; Tanaka, M.; Nagai, D.; Shimomura, E.; Fujimori, K.; Ito, S.; Okujima, T.; Toyota, K.; Yasunami, M. *ChemistrySelect* **2016,** *1,* 49–57. doi:10.1002/slct.201500036
55. Shoji, T.; Ito, S. *Chem. – Eur. J.* **2017,** *23,* 16696–16709. doi:10.1002/chem.201702806
56. Shoji, T.; Miura, K.; Araki, T.; Maruyama, A.; Ohta, A.; Sekiguchi, R.; Ito, S.; Okujima, T. *J. Org. Chem.* **2018,** *83,* 6690–6705. doi:10.1021/acs.joc.8b01067
57. Shoji, T.; Higashi, J.; Ito, S.; Okujima, T.; Yasunami, M.; Morita, N. *Chem. – Eur. J.* **2011,** *17,* 5116–5129. doi:10.1002/chem.201003628
58. Shoji, T.; Higashi, J.; Ito, S.; Okujima, T.; Yasunami, M.; Morita, N. *Org. Biomol. Chem.* **2012,** *10,* 2431–2438. doi:10.1039/c2ob06931h
59. Niu, S.; Ulrich, G.; Retailleau, P.; Ziessel, R. *Org. Lett.* **2011,** *13,* 4996–4999. doi:10.1021/ol201600s
60. Niu, S.; Ulrich, G.; Retailleau, P.; Ziessel, R. *Tetrahedron Lett.* **2011,** *52,* 4848–4853. doi:10.1016/j.tetlet.2011.07.028
61. Ulrich, G.; Barsella, A.; Boeglin, A.; Niu, S.; Ziessel, R. *ChemPhysChem* **2014,** *15,* 2693–2700. doi:10.1002/cphc.201402123
62. Koszelewski, D.; Nowak-Król, A.; Gryko, D. T. *Chem. – Asian J.* **2012,** *7,* 1887–1894. doi:10.1002/asia.201200179
63. Pengxia, L.; Du, Z.; Wang, D.; Yang, Z.; Sheng, H.; Liang, S.; Cao, H.; He, W.; Yang, H. *ChemPhysChem* **2014,** *15,* 3523–3529. doi:10.1002/cphc.201402401
64. Yadav, I.; Sharma, J. K.; Sankar, M.; D'Souza, F. *Chem. – Eur. J.* **2023,** *29,* e202301806. doi:10.1002/chem.202301806
65. Sasaki, S.-i.; Mizutani, K.; Kunieda, M.; Tamiaki, H. *Tetrahedron* **2013,** *69,* 9772–9778. doi:10.1016/j.tet.2013.09.007
66. Tamiaki, H.; Mizutani, K.; Sasaki, S.-i.; Tatebe, T. *Tetrahedron* **2016,** *72,* 6626–6633. doi:10.1016/j.tet.2016.08.079
67. Perrin, F. G.; Kiefer, G.; Jeanbourquin, L.; Racine, S.; Perrotta, D.; Waser, J.; Scopelliti, R.; Severin, K. *Angew. Chem., Int. Ed.* **2015,** *54,* 13393–13396. doi:10.1002/anie.201507033
68. Mammadova, F.; Ozsinan, S.; Okutan, M.; Dengiz, C. *J. Mol. Struct.* **2020,** *1220,* 128726. doi:10.1016/j.molstruc.2020.128726
69. Betou, M.; Kerisit, N.; Meledje, E.; Leroux, Y. R.; Katan, C.; Halet, J.-F.; Guillemin, J.-C.; Trolez, Y. *Chem. – Eur. J.* **2014,** *20,* 9553–9557. doi:10.1002/chem.201402653
70. Betou, M.; Durand, R. J.; Sallustrau, D. A.; Gousset, C.; Le Coz, E.; Leroux, Y. R.; Toupet, D. L.; Trzop, E.; Roisnel, T.; Trolez, Y. *Chem. – Asian J.* **2017,** *12,* 1338–1346. doi:10.1002/asia.201700353
71. Philippe, C.; Bui, A. T.; Batsongo-Boulingui, S.; Pokladek, Z.; Matczyszyn, K.; Mongin, O.; Lemiègre, L.; Paul, F.; Hamlin, T. A.; Trolez, Y. *Org. Lett.* **2021,** *23,* 2007–2012. doi:10.1021/acs.orglett.1c00136
72. Huang, S.; Ma, J.; Yi, Y.; Li, M.; Cai, P.; Wu, N. *Org. Biomol. Chem.* **2022,** *20,* 4081–4085. doi:10.1039/d2ob00677d
73. Erden, K.; Dengiz, C. *J. Org. Chem.* **2022,** *87,* 4385–4399. doi:10.1021/acs.joc.2c00067
74. Philippe, C.; Melan, J.; Barsella, A.; Vives, T.; Leroux, Y. R.; Robin-Le Guen, F.; Lemiègre, L.; Jacquemin, D.; Gauthier, S.; Trolez, Y. *Tetrahedron Chem* **2023,** *5,* 100036. doi:10.1016/j.tchem.2023.100036
75. Kivala, M.; Boudon, C.; Gisselbrecht, J.-P.; Enko, B.; Seiler, P.; Müller, I. B.; Langer, N.; Jarowski, P. D.; Gescheidt, G.; Diederich, F. *Chem. – Eur. J.* **2009,** *15,* 4111–4123. doi:10.1002/chem.200802563
76. Jarowski, P. D.; Wu, Y.-L.; Boudon, C.; Gisselbrecht, J.-P.; Gross, M.; Schweizer, W. B.; Diederich, F. *Org. Biomol. Chem.* **2009,** *7,* 1312–1322. doi:10.1039/b821230a
77. Wu, Y.-L.; Jarowski, P. D.; Schweizer, W. B.; Diederich, F. *Chem. – Eur. J.* **2010,** *16,* 202–211. doi:10.1002/chem.200902645
78. Rijkers, D. T. S.; de Prada López, F.; Liskamp, R. M. J.; Diederich, F. *Tetrahedron Lett.* **2011,** *52,* 6963–6967. doi:10.1016/j.tetlet.2011.10.084

79. Silvestri, F.; Jordan, M.; Howes, K.; Kivala, M.; Rivera-Fuentes, P.; Boudon, C.; Gisselbrecht, J.-P.; Schweizer, W. B.; Seiler, P.; Chiu, M.; Diederich, F. *Chem. – Eur. J.* **2011,** *17,* 6088–6097. doi:10.1002/chem.201003672
80. Tancini, F.; Wu, Y.-L.; Schweizer, W. B.; Gisselbrecht, J.-P.; Boudon, C.; Jarowski, P. D.; Beels, M. T.; Biaggio, I.; Diederich, F. *Eur. J. Org. Chem.* **2012,** 2756–2765. doi:10.1002/ejoc.201200111
81. Galán, E.; Andreu, R.; Garín, J.; Orduna, J.; Villacampa, B.; Diosdado, B. E. *Org. Biomol. Chem.* **2012,** *10,* 8684–8691. doi:10.1039/c2ob26515j
82. Chiu, M.; Jaun, B.; Beels, M. T. R.; Biaggio, I.; Gisselbrecht, J.-P.; Boudon, C.; Schweizer, W. B.; Kivala, M.; Diederich, F. *Org. Lett.* **2012,** *14,* 54–57. doi:10.1021/ol202815q
83. Finke, A. D.; Dumele, O.; Zalibera, M.; Confortin, D.; Cias, P.; Jayamurugan, G.; Gisselbrecht, J.-P.; Boudon, C.; Schweizer, W. B.; Gescheidt, G.; Diederich, F. *J. Am. Chem. Soc.* **2012,** *134,* 18139–18146. doi:10.1021/ja309141r
84. Finke, A. D.; Diederich, F. *Chem. Rec.* **2015,** *15,* 19–30. doi:10.1002/tcr.201402060
85. Fesser, P.; Iacovita, C.; Wäckerlin, C.; Vijayaraghavan, S.; Ballav, N.; Howes, K.; Gisselbrecht, J.-P.; Crobu, M.; Boudon, C.; Stöhr, M.; Jung, T. A.; Diederich, F. *Chem. – Eur. J.* **2011,** *17,* 5246–5250. doi:10.1002/chem.201100733
86. Lacy, A. R.; Vogt, A.; Boudon, C.; Gisselbrecht, J.-P.; Schweizer, W. B.; Diederich, F. *Eur. J. Org. Chem.* **2013,** 869–879. doi:10.1002/ejoc.201201371
87. Breiten, B.; Wu, Y.-L.; Jarowski, P. D.; Gisselbrecht, J.-P.; Boudon, C.; Griesser, M.; Onitsch, C.; Gescheidt, G.; Schweizer, W. B.; Langer, N.; Lennartz, C.; Diederich, F. *Chem. Sci.* **2011,** *2,* 88–93. doi:10.1039/c0sc00387e
88. Breiten, B.; Jordan, M.; Taura, D.; Zalibera, M.; Griesser, M.; Confortin, D.; Boudon, C.; Gisselbrecht, J.-P.; Schweizer, W. B.; Gescheidt, G.; Diederich, F. *J. Org. Chem.* **2013,** *78,* 1760–1767. doi:10.1021/jo301194y
89. Kato, S.-i.; Beels, M. T. R.; La Porta, P.; Schweizer, W. B.; Boudon, C.; Gisselbrecht, J.-P.; Biaggio, I.; Diederich, F. *Angew. Chem., Int. Ed.* **2010,** *49,* 6207–6211. doi:10.1002/anie.201002236
90. Dengiz, C.; Dumele, O.; Kato, S.-i.; Zalibera, M.; Cias, P.; Schweizer, W. B.; Boudon, C.; Gisselbrecht, J.-P.; Gescheidt, G.; Diederich, F. *Chem. – Eur. J.* **2014,** *20,* 1279–1286. doi:10.1002/chem.201303533
91. Shoji, T.; Higashi, J.; Ito, S.; Yasunami, M.; Moria, N. *Heterocycles* **2011,** *83,* 2271–2274. doi:10.3987/com-11-12303
92. Shoji, T.; Maruyama, M.; Shimomura, E.; Maruyama, A.; Ito, S.; Yasunami, M.; Higashi, J.; Toyota, K.; Morita, N. *Heterocycles* **2014,** *88,* 319–329. doi:10.3987/com-13-s(s)24
93. Dengiz, C.; Prange, C.; Gawel, P.; Trapp, N.; Ruhlmann, L.; Boudon, C.; Diederich, F. *Tetrahedron* **2016,** *72,* 1213–1224. doi:10.1016/j.tet.2016.01.017
94. Erden, K.; Savaş, İ.; Dengiz, C. *Tetrahedron Lett.* **2019,** *60,* 1982–1985. doi:10.1016/j.tetlet.2019.06.046
95. Reekie, T. A.; Donckele, E. J.; Ruhlmann, L.; Boudon, C.; Trapp, N.; Diederich, F. *Eur. J. Org. Chem.* **2015,** 7264–7275. doi:10.1002/ejoc.201501085
96. Januszewski, J. A.; Hampel, F.; Neiss, C.; Görling, A.; Tykwinski, R. R. *Angew. Chem., Int. Ed.* **2014,** *53,* 3743–3747. doi:10.1002/anie.201309355
97. Gawel, P.; Dengiz, C.; Finke, A. D.; Trapp, N.; Boudon, C.; Gisselbrecht, J.-P.; Diederich, F. *Angew. Chem., Int. Ed.* **2014,** *53,* 4341–4345. doi:10.1002/anie.201402299
98. Wu, Y.-L.; Tancini, F.; Schweizer, W. B.; Paunescu, D.; Boudon, C.; Gisselbrecht, J.-P.; Jarowski, P. D.; Dalcanale, E.; Diederich, F. *Chem. – Asian J.* **2012,** *7,* 1185–1190. doi:10.1002/asia.201100997
99. Gawel, P.; Wu, Y.-L.; Finke, A. D.; Trapp, N.; Zalibera, M.; Boudon, C.; Gisselbrecht, J.-P.; Schweizer, W. B.; Gescheidt, G.; Diederich, F. *Chem. – Eur. J.* **2015,** *21,* 6215–6225. doi:10.1002/chem.201406583
100. Dar, A. H.; Gowri, V.; Neethu, K. M.; Jayamurugan, G. *ChemistrySelect* **2020,** *5,* 12437–12441. doi:10.1002/slct.202003179
101. Jayamurugan, G.; Finke, A. D.; Gisselbrecht, J.-P.; Boudon, C.; Schweizer, W. B.; Diederich, F. *J. Org. Chem.* **2014,** *79,* 426–431. doi:10.1021/jo402440m
102. Jayamurugan, G.; Gisselbrecht, J.-P.; Boudon, C.; Schoenebeck, F.; Schweizer, W. B.; Bernet, B.; Diederich, F. *Chem. Commun.* **2011,** *47,* 4520–4522. doi:10.1039/c1cc10247h
103. Jayamurugan, G.; Dumele, O.; Gisselbrecht, J.-P.; Boudon, C.; Schweizer, W. B.; Bernet, B.; Diederich, F. *J. Am. Chem. Soc.* **2013,** *135,* 3599–3606. doi:10.1021/ja312084s
104. Hansen, J. K. S.; Tortzen, C. G.; Sørensen, P. G.; Brøndsted Nielsen, M. *Chem. – Eur. J.* **2023,** *29,* e202202833. doi:10.1002/chem.202202833
105. Nielsen, M. B. *ChemPhysChem* **2023,** *24,* e202300236. doi:10.1002/cphc.202300236
106. Lemiègre, L.; Trolez, Y. *Asian J. Org. Chem.* **2023,** *12,* e202300321. doi:10.1002/ajoc.202300321
107. Sletten, E. M.; Bertozzi, C. R. *Angew. Chem., Int. Ed.* **2009,** *48,* 6974–6998. doi:10.1002/anie.200900942
108. Sletten, E. M.; Bertozzi, C. R. *Acc. Chem. Res.* **2011,** *44,* 666–676. doi:10.1021/ar200148z
109. Debets, M. F.; van Berkel, S. S.; Dommerholt, J.; Dirks, A. T. J.; Rutjes, F. P. J. T.; van Delft, F. L. *Acc. Chem. Res.* **2011,** *44,* 805–815. doi:10.1021/ar200059z
110. Chiu, M.; Tchitchanov, B. H.; Zimmerli, D.; Sanhueza, I. A.; Schoenebeck, F.; Trapp, N.; Schweizer, W. B.; Diederich, F. *Angew. Chem., Int. Ed.* **2015,** *54,* 349–354. doi:10.1002/anie.201409289
111. Schaub, T. A.; Margraf, J. T.; Zakharov, L.; Reuter, K.; Jasti, R. *Angew. Chem., Int. Ed.* **2018,** *57,* 16348–16353. doi:10.1002/anie.201808611
112. Yamada, M.; Schweizer, W. B.; Schoenebeck, F.; Diederich, F. *Chem. Commun.* **2010,** *46,* 5334–5336. doi:10.1039/c0cc00881h
113. Reisinger, C. M.; Rivera-Fuentes, P.; Lampart, S.; Schweizer, W. B.; Diederich, F. *Chem. – Eur. J.* **2011,** *17,* 12906–12911. doi:10.1002/chem.201102852
114. Kerisit, N.; Finke, A. D.; Trapp, N.; Leroux, Y. R.; Guillemin, J.-C.; Trolez, Y.; Diederich, F. *Tetrahedron* **2015,** *71,* 4393–4399. doi:10.1016/j.tet.2015.03.081
115. Donckele, E. J.; Finke, A. D.; Ruhlmann, L.; Boudon, C.; Trapp, N.; Diederich, F. *Org. Lett.* **2015,** *17,* 3506–3509. doi:10.1021/acs.orglett.5b01598
116. Shoji, T.; Nagai, D.; Tanaka, M.; Araki, T.; Ohta, A.; Sekiguchi, R.; Ito, S.; Mori, S.; Okujima, T. *Chem. – Eur. J.* **2017,** *23,* 5126–5136. doi:10.1002/chem.201700121
117. Neethu, K. M.; Nag, K.; Dar, A. H.; Bajaj, A.; Gopal, S. A.; Gowri, V.; Nagpure, M.; Sartaliya, S.; Sharma, R.; Solanki, A. K.; Ehesan Ali, M.; Muthukrishnan, A.; Jayamurugan, G. *Org. Biomol. Chem.* **2023,** *21,* 2922–2929. doi:10.1039/d3ob00053b

118. Bruce, M. I.; Burgun, A.; Jevric, M.; Morris, J. C.; Nicholson, B. K.; Parker, C. R.; Scoleri, N.; Skelton, B. W.; Zaitseva, N. N. *J. Organomet. Chem.* **2014,** *756,* 68–78. doi:10.1016/j.jorganchem.2013.12.038
119. Mateo, L. M.; Sagresti, L.; Luo, Y.; Guldi, D. M.; Torres, T.; Brancato, G.; Bottari, G. *Chem. – Eur. J.* **2021,** *27,* 16049–16055. doi:10.1002/chem.202103079
120. Zhou, W.; Xu, J.; Zheng, H.; Liu, H.; Li, Y.; Zhu, D. *J. Org. Chem.* **2008,** *73,* 7702–7709. doi:10.1021/jo8014566
121. Zhou, W.; Xu, J.; Zheng, H.; Yin, X.; Zuo, Z.; Liu, H.; Li, Y. *Adv. Funct. Mater.* **2009,** *19,* 141–149. doi:10.1002/adfm.200801149
122. Li, Y.; Liu, T.; Liu, H.; Tian, M.-Z.; Li, Y. *Acc. Chem. Res.* **2014,** *47,* 1186–1198. doi:10.1021/ar400264e
123. Trolez, Y.; Finke, A. D.; Silvestri, F.; Monti, F.; Ventura, B.; Boudon, C.; Gisselbrecht, J.-P.; Schweizer, W. B.; Sauvage, J.-P.; Armaroli, N.; Diederich, F. *Chem. – Eur. J.* **2018,** *24,* 10422–10433. doi:10.1002/chem.201801161
124. Alonso-Gómez, J. L.; Schanen, P.; Rivera-Fuentes, P.; Seiler, P.; Diederich, F. *Chem. – Eur. J.* **2008,** *14,* 10564–10568. doi:10.1002/chem.200801456
125. Alonso-Gómez, J. L.; Petrovic, A. G.; Harada, N.; Rivera-Fuentes, P.; Berova, N.; Diederich, F. *Chem. – Eur. J.* **2009,** *15,* 8396–8400. doi:10.1002/chem.200900103
126. Frank, B. B.; Camafort Blanco, B.; Jakob, S.; Ferroni, F.; Pieraccini, S.; Ferrarini, A.; Boudon, C.; Gisselbrecht, J.-P.; Seiler, P.; Spada, G. P.; Diederich, F. *Chem. – Eur. J.* **2009,** *15,* 9005–9016. doi:10.1002/chem.200900913
127. Frank, B. B.; Kivala, M.; Camafort Blanco, B.; Breiten, B.; Schweizer, W. B.; Laporta, P. R.; Biaggio, I.; Jahnke, E.; Tykwinski, R. R.; Boudon, C.; Gisselbrecht, J.-P.; Diederich, F. *Eur. J. Org. Chem.* **2010,** 2487–2503. doi:10.1002/ejoc.201000030
128. Ozcelik, A.; Pereira-Cameselle, R.; Peña-Gallego, Á.; Alonso-Gómez, J. L. *Eur. J. Org. Chem.* **2022,** e202101333. doi:10.1002/ejoc.202101333
129. Bouvier, R.; Durand, R.; Favereau, L.; Srebro-Hooper, M.; Dorcet, V.; Roisnel, T.; Vanthuyne, N.; Vesga, Y.; Donnelly, J.; Hernandez, F.; Autschbach, J.; Trolez, Y.; Crassous, J. *Chem. – Eur. J.* **2018,** *24,* 14484–14494. doi:10.1002/chem.201802763
130. Yamada, M.; Rivera-Fuentes, P.; Schweizer, W. B.; Diederich, F. *Angew. Chem., Int. Ed.* **2010,** *49,* 3532–3535. doi:10.1002/anie.200906853
131. Winterfeld, K. A.; Lavarda, G.; Guilleme, J.; Sekita, M.; Guldi, D. M.; Torres, T.; Bottari, G. *J. Am. Chem. Soc.* **2017,** *139,* 5520–5529. doi:10.1021/jacs.7b01460
132. Lavarda, G.; Bhattacharjee, N.; Brancato, G.; Torres, T.; Bottari, G. *Angew. Chem., Int. Ed.* **2020,** *59,* 21224–21229. doi:10.1002/anie.202010133
133. Winterfeld, K. A.; Lavarda, G.; Yoshida, K.; Bayerlein, M. J.; Kise, K.; Tanaka, T.; Osuka, A.; Guldi, D. M.; Torres, T.; Bottari, G. *J. Am. Chem. Soc.* **2020,** *142,* 7920–7929. doi:10.1021/jacs.0c01646
134. Monti, F.; Venturini, A.; Nenov, A.; Tancini, F.; Finke, A. D.; Diederich, F.; Armaroli, N. *J. Phys. Chem. A* **2015,** *119,* 10677–10683. doi:10.1021/acs.jpca.5b09291
135. Pokladek, Z.; Ripoche, N.; Betou, M.; Trolez, Y.; Mongin, O.; Olesiak-Banska, J.; Matczyszyn, K.; Samoc, M.; Humphrey, M. G.; Blanchard-Desce, M.; Paul, F. *Chem. – Eur. J.* **2016,** *22,* 10155–10167. doi:10.1002/chem.201600897
136. Gautam, P.; Misra, R.; Thomas, M. B.; D'Souza, F. *Chem. – Eur. J.* **2017,** *23,* 9192–9200. doi:10.1002/chem.201701604
137. Xu, J.; Liu, X.; Lv, J.; Zhu, M.; Huang, C.; Zhou, W.; Yin, X.; Liu, H.; Li, Y.; Ye, J. *Langmuir* **2008,** *24,* 4231–4237. doi:10.1021/la703662w
138. Bui, A. T.; Philippe, C.; Beau, M.; Richy, N.; Cordier, M.; Roisnel, T.; Lemiègre, L.; Mongin, O.; Paul, F.; Trolez, Y. *Chem. Commun.* **2020,** *56,* 3571–3574. doi:10.1039/c9cc09560h
139. Philippe, C.; Bui, A. T.; Beau, M.; Bloux, H.; Riobé, F.; Mongin, O.; Roisnel, T.; Cordier, M.; Paul, F.; Lemiègre, L.; Trolez, Y. *Chem. – Eur. J.* **2022,** *28,* e202200025. doi:10.1002/chem.202200025
140. Philippe, C.; Coste, M.; Bretonnière, Y.; Lemiègre, L.; Ulrich, S.; Trolez, Y. *Eur. J. Org. Chem.* **2022,** 10.1002/ejoc.202200049. doi:10.1002/ejoc.202200049
141. Dar, A. H.; Gowri, V.; Mishra, R. K.; Khan, R.; Jayamurugan, G. *Langmuir* **2022,** *38,* 430–438. doi:10.1021/acs.langmuir.1c02797
142. Yamada, M.; Tancini, F.; Sekita, M.; Guldi, D. M.; Boudon, C.; Gisselbrecht, J.-P.; Alberti, M. N.; Schweizer, W. B.; Diederich, F. *Fullerenes, Nanotubes, Carbon Nanostruct.* **2014,** *22,* 99–127. doi:10.1080/1536383x.2013.794342
143. Marcus, R. A. *J. Chem. Phys.* **1956,** *24,* 966–978. doi:10.1063/1.1742723
144. Sekita, M.; Ballesteros, B.; Diederich, F.; Guldi, D. M.; Bottari, G.; Torres, T. *Angew. Chem., Int. Ed.* **2016,** *55,* 5560–5564. doi:10.1002/anie.201601258
145. Tancini, F.; Monti, F.; Howes, K.; Belbakra, A.; Listorti, A.; Schweizer, W. B.; Reutenauer, P.; Alonso-Gómez, J.-L.; Chiorboli, C.; Urner, L. M.; Gisselbrecht, J.-P.; Boudon, C.; Armaroli, N.; Diederich, F. *Chem. – Eur. J.* **2014,** *20,* 202–216. doi:10.1002/chem.201303284
146. Rehm, D.; Weller, A. *Isr. J. Chem.* **1970,** *8,* 259–271. doi:10.1002/ijch.197000029
147. Urner, L. M.; Sekita, M.; Trapp, N.; Schweizer, W. B.; Wörle, M.; Gisselbrecht, J.-P.; Boudon, C.; Guldi, D. M.; Diederich, F. *Eur. J. Org. Chem.* **2015,** 91–108. doi:10.1002/ejoc.201403252
148. Reekie, T. A.; Sekita, M.; Urner, L. M.; Bauroth, S.; Ruhlmann, L.; Gisselbrecht, J.-P.; Boudon, C.; Trapp, N.; Clark, T.; Guldi, D. M.; Diederich, F. *Chem. – Eur. J.* **2017,** *23,* 6357–6369. doi:10.1002/chem.201700043
149. Jayamurugan, G.; Gowri, V.; Hernández, D.; Martin, S.; González-Orive, A.; Dengiz, C.; Dumele, O.; Pérez-Murano, F.; Gisselbrecht, J.-P.; Boudon, C.; Schweizer, W. B.; Breiten, B.; Finke, A. D.; Jeschke, G.; Bernet, B.; Ruhlmann, L.; Cea, P.; Diederich, F. *Chem. – Eur. J.* **2016,** *22,* 10539–10547. doi:10.1002/chem.201505216
150. Sekaran, B.; Dawson, A.; Jang, Y.; MohanSingh, K. V.; Misra, R.; D'Souza, F. *Chem. – Eur. J.* **2021,** *27,* 14335–14344. doi:10.1002/chem.202102865
151. Poddar, M.; Jang, Y.; Misra, R.; D'Souza, F. *Chem. – Eur. J.* **2020,** *26,* 6869–6878. doi:10.1002/chem.202000346
152. Kivala, M.; Boudon, C.; Gisselbrecht, J.-P.; Seiler, P.; Gross, M.; Diederich, F. *Angew. Chem., Int. Ed.* **2007,** *46,* 6357–6360. doi:10.1002/anie.200701733
153. Wu, Y.-L.; Stuparu, M. C.; Boudon, C.; Gisselbrecht, J.-P.; Schweizer, W. B.; Baldridge, K. K.; Siegel, J. S.; Diederich, F. *J. Org. Chem.* **2012,** *77,* 11014–11026. doi:10.1021/jo302217n
154. Dengiz, C.; Breiten, B.; Gisselbrecht, J.-P.; Boudon, C.; Trapp, N.; Schweizer, W. B.; Diederich, F. *J. Org. Chem.* **2015,** *80,* 882–896. doi:10.1021/jo502367h
155. Sharma, R.; Maragani, R.; Misra, R. *New J. Chem.* **2018,** *42,* 882–890. doi:10.1039/c7nj03934d
156. Cheng, S.; Ma, X.; He, Y.; He, J.; Zeller, M.; Xu, Z. *Cryst. Growth Des.* **2019,** *19,* 7411–7419. doi:10.1021/acs.cgd.9b01488

157. Chen, S.; Li, Y.; Liu, C.; Yang, W.; Li, Y. *Eur. J. Org. Chem.* **2011,** 6445–6451. doi:10.1002/ejoc.201101009
158. Tykwinski, R. R.; Gubler, U.; Martin, R. E.; Diederich, F.; Bosshard, C.; Günter, P. *J. Phys. Chem. B* **1998,** *102,* 4451–4465. doi:10.1021/jp980829o
159. Frank, B. B.; Laporta, P. R.; Breiten, B.; Kuzyk, M. C.; Jarowski, P. D.; Schweizer, W. B.; Seiler, P.; Biaggio, I.; Boudon, C.; Gisselbrecht, J.-P.; Diederich, F. *Eur. J. Org. Chem.* **2011,** 4307–4317. doi:10.1002/ejoc.201100378
160. Štefko, M.; Tzirakis, M. D.; Breiten, B.; Ebert, M.-O.; Dumele, O.; Schweizer, W. B.; Gisselbrecht, J.-P.; Boudon, C.; Beels, M. T.; Biaggio, I.; Diederich, F. *Chem. – Eur. J.* **2013,** *19,* 12693–12704. doi:10.1002/chem.201301642
161. Han, P.; Yang, Z.; Cao, H.; He, W.; Wang, D.; Zhang, J.; Xing, Y.; Gao, H. *Tetrahedron* **2017,** *73,* 6210–6216. doi:10.1016/j.tet.2017.09.020
162. Reekie, T. A.; Gisselbrecht, J.-P.; Boudon, C.; Trapp, N.; Diederich, F. *Tetrahedron Lett.* **2017,** *58,* 2414–2416. doi:10.1016/j.tetlet.2017.05.009
163. Mammadova, F.; Inyurt, F. C.; Barsella, A.; Dengiz, C. *Dyes Pigm.* **2023,** *209,* 110894. doi:10.1016/j.dyepig.2022.110894
164. Si, Y.; Yang, G. *J. Phys. Chem. A* **2014,** *118,* 1094–1102. doi:10.1021/jp4099717
165. Biaggio, I. *Chem. – Eur. J.* **2022,** *28,* e202103168. doi:10.1002/chem.202103168
166. Esembeson, B.; Scimeca, M. L.; Michinobu, T.; Diederich, F.; Biaggio, I. *Adv. Mater. (Weinheim, Ger.)* **2008,** *20,* 4584–4587. doi:10.1002/adma.200801552
167. Koos, C.; Vorreau, P.; Vallaitis, T.; Dumon, P.; Bogaerts, W.; Baets, R.; Esembeson, B.; Biaggio, I.; Michinobu, T.; Diederich, F.; Freude, W.; Leuthold, J. *Nat. Photonics* **2009,** *3,* 216–219. doi:10.1038/nphoton.2009.25
168. Ripoche, N.; Betou, M.; Philippe, C.; Trolez, Y.; Mongin, O.; Dudek, M.; Pokladek, Z.; Matczyszyn, K.; Samoc, M.; Sahnoune, H.; Halet, J.-F.; Roisnel, T.; Toupet, L.; Cordier, M.; Moxey, G. J.; Humphrey, M. G.; Paul, F. *Phys. Chem. Chem. Phys.* **2021,** *23,* 22283–22297. doi:10.1039/d1cp03346h
169. Rout, Y.; Chauhan, V.; Misra, R. *J. Org. Chem.* **2020,** *85,* 4611–4618. doi:10.1021/acs.joc.9b03267
170. Banziger, S. D.; Clendening, R. A.; Oxley, B. M.; Ren, T. *J. Phys. Chem. B* **2020,** *124,* 11901–11909. doi:10.1021/acs.jpcb.0c09450
171. Yu, G.; Gao, J.; Hummelen, J. C.; Wudl, F.; Heeger, A. J. *Science* **1995,** *270,* 1789–1791. doi:10.1126/science.270.5243.1789
172. Patil, Y.; Misra, R.; Keshtov, M. L.; Sharma, G. D. *J. Phys. Chem. C* **2016,** *120,* 6324–6335. doi:10.1021/acs.jpcc.5b12307
173. Patil, Y.; Misra, R.; Keshtov, M. L.; Sharma, G. D. *J. Mater. Chem. A* **2017,** *5,* 3311–3319. doi:10.1039/c6ta09607g
174. Gautam, P.; Sharma, R.; Misra, R.; Keshtov, M. L.; Kuklin, S. A.; Sharma, G. D. *Chem. Sci.* **2017,** *8,* 2017–2024. doi:10.1039/c6sc04461a
175. Patil, Y.; Misra, R.; Singhal, R.; Sharma, G. D. *J. Mater. Chem. A* **2017,** *5,* 13625–13633. doi:10.1039/c7ta03322b
176. Raheem, A. A.; Kumar, C.; Murugan, P.; Praveen, C. *ACS Appl. Energy Mater.* **2021,** *4,* 11609–11623. doi:10.1021/acsaem.1c02353
177. Leliège, A.; Blanchard, P.; Rousseau, T.; Roncali, J. *Org. Lett.* **2011,** *13,* 3098–3101. doi:10.1021/ol201002j
178. Gautam, P.; Misra, R.; Koukaras, E. N.; Sharma, A.; Sharma, G. D. *Org. Electron.* **2015,** *27,* 72–83. doi:10.1016/j.orgel.2015.09.006
179. Gautam, P.; Misra, R.; Siddiqui, S. A.; Sharma, G. D. *ACS Appl. Mater. Interfaces* **2015,** *7,* 10283–10292. doi:10.1021/acsami.5b02250
180. Gautam, P.; Misra, R.; Sharma, G. D. *Phys. Chem. Chem. Phys.* **2016,** *18,* 7235–7241. doi:10.1039/c6cp00243a
181. Raheem, A. A.; Kamaraj, S.; Sannasi, V.; Praveen, C. *Org. Chem. Front.* **2018,** *5,* 777–787. doi:10.1039/c7qo00920h
182. Misra, R.; Maragani, R.; Patel, K. R.; Sharma, G. D. *RSC Adv.* **2014,** *4,* 34904–34911. doi:10.1039/c4ra03088e

License and Terms

BEILSTEIN JOURNAL OF ORGANIC CHEMISTRY

Unveiling the regioselectivity of rhodium(I)-catalyzed [2 + 2 + 2] cycloaddition reactions for open-cage C_{70} production

Cristina Castanyer, Anna Pla-Quintana, Anna Roglans, Albert Artigas* and Miquel Solà*

Full Research Paper

Open Access

Address:
Institut de Química Computacional i Catàlisi (IQCC) and Departament de Química, Universitat de Girona (UdG), Girona 17003 Catalunya, Spain

Email:
Albert Artigas* - albert.artigas@udg.edu; Miquel Solà* - miquel.sola@udg.edu

* Corresponding author

Keywords:
cycloadditions; DFT calculations; [70]fullerene; open-cage fullerenes; rhodium

Beilstein J. Org. Chem. **2024,** *20,* 272–279.
https://doi.org/10.3762/bjoc.20.28

Received: 07 November 2023
Accepted: 30 January 2024
Published: 13 February 2024

This article is part of the thematic issue "Carbon-rich materials: from polyaromatic molecules to fullerenes and other carbon allotropes".

Guest Editor: Y. Yamakoshi

Abstract

The regioselective functionalization of fullerenes holds significant promise for applications in the fields of medicinal chemistry, materials science, and photovoltaics. In this study, we investigate the regioselectivity of the rhodium(I)-catalyzed [2 + 2 + 2] cycloaddition reactions between diynes and C_{70} as a novel procedure for generating C_{70} bis(fulleroid) derivatives. The aim is to shed light on the regioselectivity of the process through both experimental and computational approaches. In addition, the photooxidation of one of the C–C double bonds in the synthesized bis(fulleroids) affords open-cage C_{70} derivatives having a 12-membered ring opening.

Introduction

The discovery of C_{60} (buckminsterfullerene) in 1985 [1] initiated the search for possible technological applications of fullerenes. Nowadays, applications for these carbon-based molecules have been proposed in different fields such as medicinal chemistry [2-6], materials science [7,8], energy production, storage, and delivery [9-13], and electronics and optoelectronics [14-16]. Despite fullerenes having immense promise in all of these areas, their practical applications are still in various stages of research and development.

The functionalization of fullerenes makes them versatile materials, broadening the range of potential applications [17,18]. It allows the properties of these carbon cages to be tuned, making them more soluble (especially in water for medical applications) and improving their stability, among other desirable properties. The most common reactions used to functionalize fullerenes are Diels–Alder and 1,3-dipolar cycloadditions and Bingel–Hirsch cyclopropanations [19,20].

In most cases, functionalization occurs while preserving the carbon cages. However, in other cases, some of the bonds between the C atoms of the cage are broken and the cage is opened. The first example of an open-cage fullerene was reported in 1995 by Hummelen, Prato, and Wudl [21] through the reaction of C_{60}

with azides followed by photooxygenation. Since then, many open-cage C_{60} derivatives have been reported. These open-cage fullerenes can act as molecular containers. Of special interest is the procedure called molecular surgery designed by Murata et al. [22-25] in which a hole in the fullerene is opened, an atom or small molecule is introduced and then the hole is closed restoring the original cage. Among the species that have been incarcerated with this procedure, we can find He, Ne, Ar, Kr, H_2, N_2, O_2, HF, CO, CO_2, H_2O, H_2O_2, CH_4, NH_3, HCOH, HCCH, and CH_3OH [26,27]. The encapsulation of atoms or small molecules inside the fullerene has been found to be able to produce meaningful changes in the reactivity of the cage [28-32].

In 2018, our group reported a catalytic process to transform C_{60} in bis(fulleroid) derivatives [33-35]. This transformation encompassed a partially intermolecular Rh-catalyzed [2 + 2 + 2] cycloaddition reaction between diynes and C_{60}, followed by a cage-opening through a Rh-catalyzed di-π-methane rearrangement (Scheme 1). It is well-known that [6,6]-bonds (the bonds at the junction between two six-membered rings, Figure 1, left) are more reactive than [5,6]-bonds in C_{60} [36-38], and, not unexpectedly, the [6,6]-bond in C_{60} was the one involved in this [2 + 2 + 2] cycloaddition.

Although there are several papers reporting the opening of a hole in C_{70} [39-45], this chemistry has been less explored than in C_{60}. The lower D_{5h} symmetry of C_{70} compared to the I_h of C_{60} increases the number of possible regioisomers. Indeed, C_{70} has eight different bonds, half of which are different types of [6,6]-bonds, namely the α-, β-, γ-, and δ-bonds (Figure 1, right) [46]. The α- and β-bonds of C_{70} are the most reactive ones [47].

With this in mind, the main goal of the present work is to explore, both experimentally and computationally, the Rh-catalyzed intermolecular [2 + 2 + 2] cycloaddition reaction between diynes and C_{70} as a new procedure to generate C_{70}

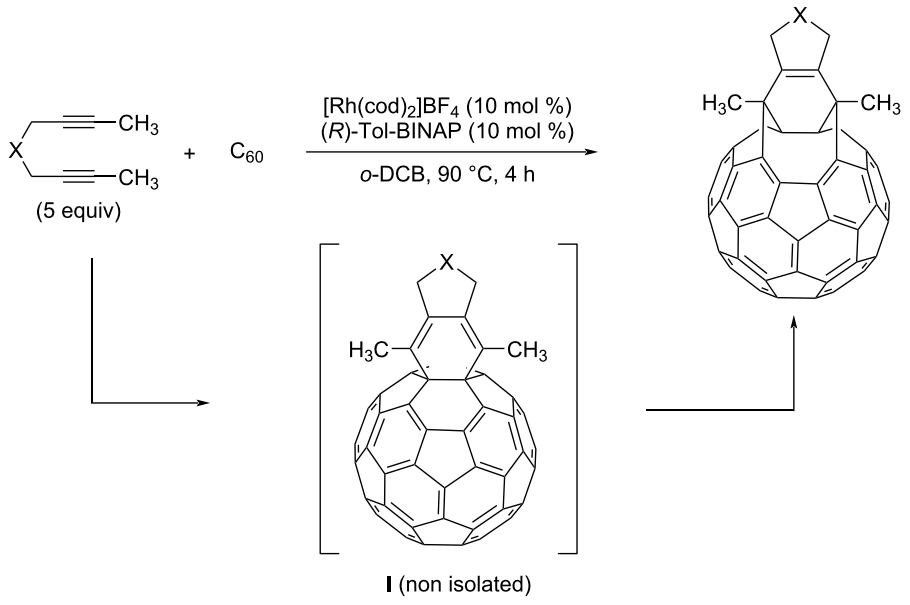

Scheme 1: Rhodium(I)-catalyzed cycloaddition of C_{60} with diynes to afford bis(fulleroid) derivatives [33].

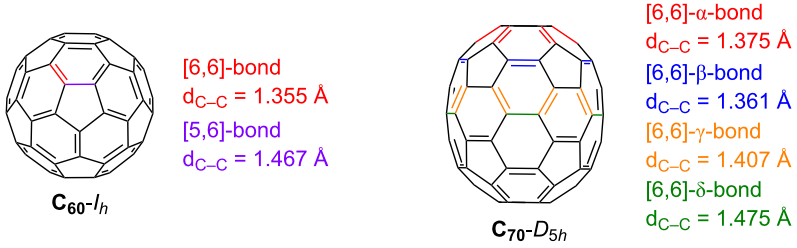

Figure 1: Types of [6,6]-bonds together with the [5,6]-bond of C_{60} with their C–C distances in pristine C_{60} and C_{70}.

bis(fulleroids). We are particularly interested in the analysis of the regioselectivity of this [2 + 2 + 2] cycloaddition.

Results and Discussion

We started our study by testing the cycloaddition of *N*-tosyl-tethered bisalkyne **1a** and C_{70} (Scheme 2) using our previously optimized reaction conditions for the C_{60} derivative [33]: that is, using 10 mol % of a mixture of $[Rh(cod)_2]BF_4$ and Tol-BINAP in *o*-dichlorobenzene (*o*-DCB) and heating at 90 °C for 4 hours. The crude reaction mass obtained with these conditions was then purified by column chromatography (toluene). After eluting unreacted pristine C_{70}, a dark reddish fraction was isolated and analyzed by HPLC. A major peak was observed at a retention time of 17.5 minutes, which we analyzed by UV–vis spectroscopy. This peak was assigned as a bis(fulleroid) compound by comparing the spectra with the UV–vis absorption pattern exhibited by previously characterized C_{70} bis(fulleroids) reported by Murata et al. [43,48]. In addition, a minor peak at a retention time of 20 minutes was also observed in the HPLC chromatogram, whose UV–vis has a pattern that is similar to a previously reported α-adduct [49]. We reasoned that this minor compound was the cyclohexadiene-fused C_{70} intermediate, analogous to cyclohexadiene-fused C_{60} **I** (see Scheme 1), which had not completely evolved into the corresponding bis(fulleroid) product after 4 h of reaction (Figure S1 in Supporting Information File 1). Importantly, the observation of this intermediate represents an experimental proof of the proposed reaction mechanism. Confirmation that only one unit of **1a** reacted with C_{70} in the reaction was obtained from HRMS, which gave a single peak at *m*/*z* 1138.0868 corresponding to [**2a** + Na]$^+$. Further optimization was then carried out to obtain the bis(fulleroid) derivative alone (Table S1 in Supporting Information File 1). On increasing the reaction temperature to 120 °C and 180 °C the results were found to be the same, showing that 90 °C is sufficient for the reaction to proceed. In contrast, on extending the reaction time to 24 hours, the minor peak in the HPLC disappeared and only the peak corresponding to the bis(fulleroid) remained. The yield of derivative **2a** was 45%. Other experiments were run using other solvents such as toluene and chlorobenzene, increasing the C_{70} concentration from 1.2 M to 2.4 M, and decreasing the catalytic load to 5 mol % (Table S1 in Supporting Information File 1). However, none of these trials improved the yield of bis(fulleroid) **2a**.

The same reaction was run starting with malonate-tethered diyne **1b**. In this case, the reaction was finished after 4 hours and bis(fulleroid) **2b** was obtained with a 34% yield (Scheme 2). The corresponding compound **2b** was analyzed by HPLC, giving only one peak. UV–vis experiments revealed the formation of a bis(fulleroid) derivative (Figure S2 in Supporting Information File 1). The lower yield of **2b** compared to **2a** is probably due to the [2 + 2 + 2] homocoupling cycloaddition of the corresponding starting diyne, which is more favorable when the tether is a malonate rather than an NTs-sulfonamide.

Among the four different [6,6]-bonds (α, β, γ, and δ) in pristine C_{70}, α and β junctions are pyracylenic bonds, which happen to be the most reactive due to their higher degree of pyramidalization. Between both the α- and β-bonds, the higher curvature strain in α-bonds compared to β-double bonds makes the first one more reactive, leading to β-site isomers as minor products. Taking this into account, we carefully analyzed the NMR spectra of compound **2a**. Analysis of ^{1}H NMR spectra of **2a** provided valuable information that confirmed the generation of two regioisomers in a 71:29 ratio (Figure 2). Comparable proportions of reactions at α- and β-bonds were systematically observed at different temperatures.

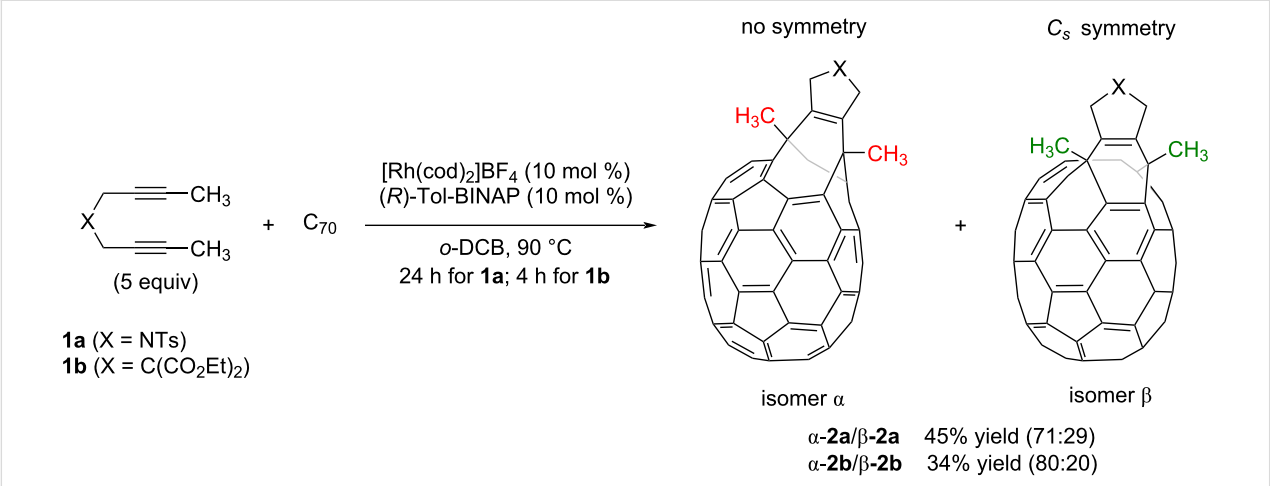

Scheme 2: Rhodium-catalyzed cycloaddition of C_{70} with diynes **1a** and **1b**.

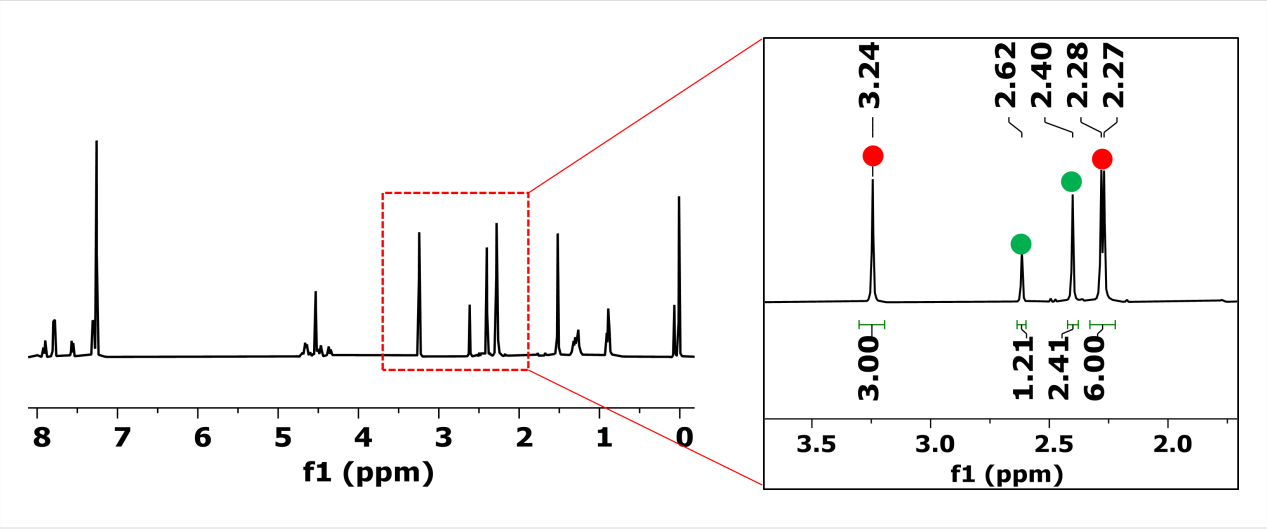

Figure 2: ^{1}H NMR (CS_2/$CDCl_3$, 400 MHz) spectrum of compound **2a** as a mixture of two isomers.

The protons of the two methyl groups around δ 2.30 ppm were used as diagnostic signals. For the major isomer (red dots, Figure 2), the spectrum exhibits two singlets at δ = 2.27 and 2.28 ppm, corresponding to the two different methyl groups in the six-membered ring formed in the cycloaddition and coming from the starting diyne **1a** (highlighted in red in Scheme 2). In contrast, for the minor isomer (green dots), which has C_s symmetry, the two methyl groups (highlighted in green in Scheme 2) appear as a single peak at δ = 2.40 ppm. A second signal that also helps us to determine the ratio between the two isomers is the methyl of the tosyl group. For the major isomer the methyl appears at δ = 3.24 ppm, whereas for the minor isomer the peak is observed at δ = 2.62 ppm. Considering that isomer α has no symmetry and isomer β has C_s symmetry [50], we can conclude that the major product formed was the α-isomer, as previously anticipated. All attempts to separate the two isomers by column chromatography and preparative TLC were unsuccessful. Malonate-tethered compound **2b** had the same spectroscopic behavior as **2a** though in this case the ratio in favor of the α-isomer was higher (80:20, Figure S6 in Supporting Information File 1).

To gain theoretical insight into the regioselectivity of the reaction, a density functional theory (DFT) investigation was carried out, as depicted in Figure 3. In the computations, the tosyl group was substituted by a mesyl substituent and BIPHEP was used as a model phosphine ligand instead of Tol-BINAP to reduce the computational cost. The calculations, conducted at the B3LYP-D3/cc-pVTZ-PP(SMD=o-DCB)//B3LYP-D3/cc-pVDZ-PP level (see full computational details in Supporting Information File 1), unveiled the following reaction mechanism: initially, an oxidative coupling of the two alkyne moieties of our model **1a** leads to the formation of **INT 1**, as previously reported [33]. This step, with a Gibbs energy barrier of 25.7 kcal·mol^{-1}, is the rate-determining step for this process. Next, **INT 1** readily coordinates with a C_{70} molecule to generate **INT 2**, with this step being exergonic by 16.7 kcal·mol^{-1}. From **INT 2**, the reaction can follow two distinct pathways, culminating in either an α-adduct or a β-adduct. In the α-adduct pathway (black line), a formal [2 + 2] cycloaddition occurs between the rhodacyclopentadiene moiety and a [6,6]-α-bond of C_{70}, yielding rhodabicyclo[3.2.0]heptadiene intermediate α-**INT 3**. This step has a cost of 9.5 kcal·mol^{-1}. Alternatively, a [6,6]-β-bond of C_{70} can be involved in this step (grey line) to produce β-**INT 3**, albeit with a slightly higher Gibbs energy barrier ($\Delta\Delta G$ = 0.9 kcal·mol^{-1}). The formation of intermediate α-**INT 3** and β-**INT 3** was found endergonic by 9.3 and 7.6 kcal·mol^{-1}, respectively. Subsequently, both site isomers of **INT 3** can undergo reductive elimination with barriers of 6.9 and 9.4 kcal·mol^{-1} to deliver the corresponding cyclohexadiene-fused adducts, denoted as α-**INT 4** and β-**INT 4**, which will ultimately evolve into the final bis(fulleroid) reaction products [33]. As the site-selectivity of the reaction depends on these two consecutive steps, it indicates a preference for the α-bonds over the β-bonds, consistent with the experimental findings discussed earlier. Once **INT 1** is formed, for the rest of the process, the TOF determining transition state (TDTS) of the process is α/β-**TS 2** and the TOF determining intermediate (TDI) is **INT 2** and the energetic span (δG) is 16.2 kcal·mol^{-1} for the α-attack and 17.0 kcal·mol^{-1} for the β-attack [51,52].

As previously described for our analogous C_{60} bis(fulleroids) [33], one of the double bonds of the eight-membered ring in **2a** can undergo oxidative cleavage affording open-cage C_{70} fullerenes that bear a twelve-membered orifice. There has been con-

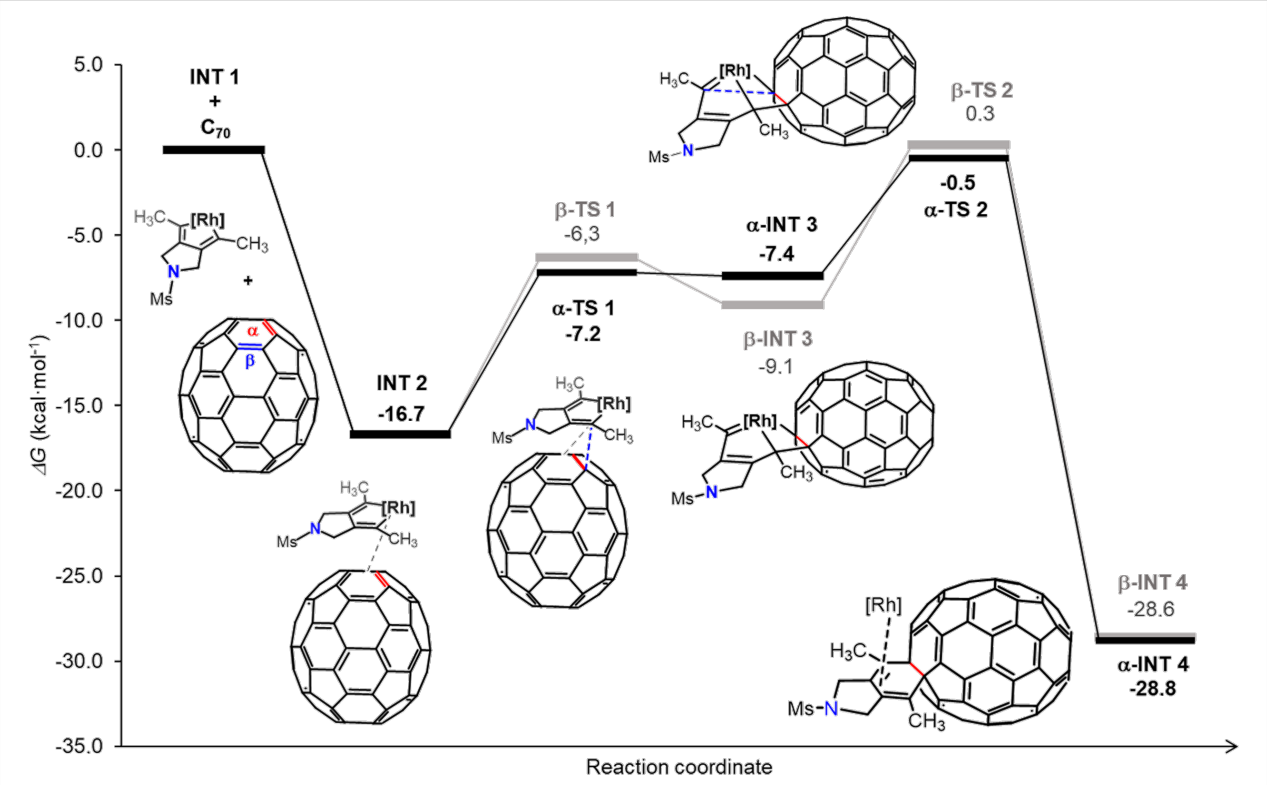

Figure 3: B3LYP-D3/cc-pVTZ-PP(SMD=o-DCB)//B3LYP-D3/CC-pVDZ-PP Gibbs energy profile of the [2 + 2 + 2] cycloaddition between our model diyne **1a** and C_{70}. Comparison between α- and β-reaction pathways. Black line: α-pathway. Grey line: β-pathway. Molecular structures correspond to the α-pathway. [Rh] = $[Rh(BIPHEP)]^+$.

siderable interest in the construction of larger orifices in C_{70} derivatives given that the larger cavity compared to its C_{60} counterpart can facilitate the encapsulation of multiple atoms and molecules [40,43,53,54]. To fulfil this objective, compound **2a** was subjected to oxidative cleavage by exposing it to light in the presence of air (Scheme 3).

Given the lower symmetry of C_{70} in comparison to C_{60}, the oxidative opening of the eight-membered ring of the mixture of α- and β-isomers **2** can result in more than two oxidized isomers, depending on which double bond is cleaved. After 5 hours of irradiation, the crude mixture was purified by column chromatography, giving an inseparable mixture of different isomers. The

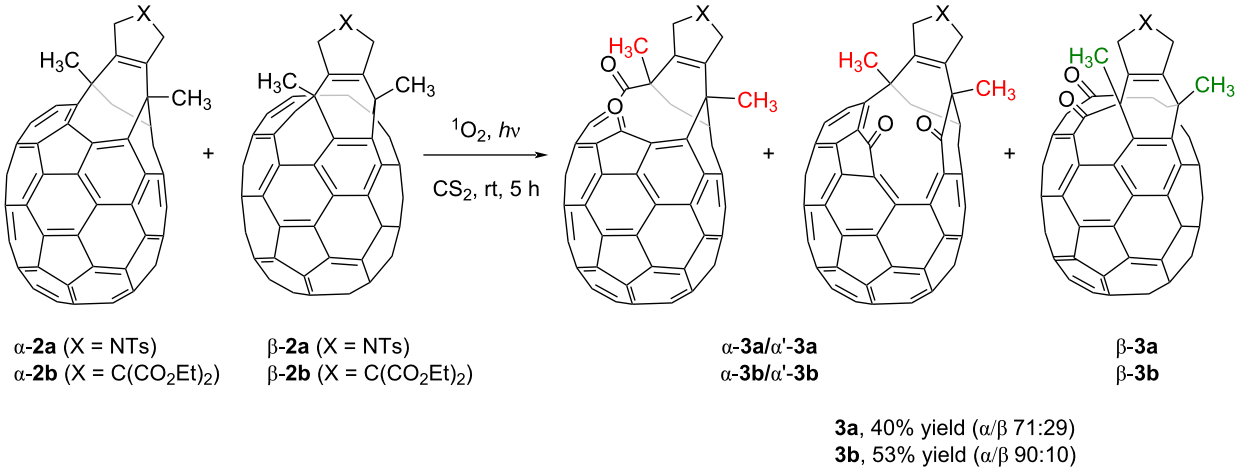

Scheme 3: Oxidative cleavage of bis(fulleroid) derivatives **2a** and **2b**.

oxygenation process was confirmed by HRMS, which gave a single peak at m/z = 1170.0756 corresponding to [**3a** + Na]$^+$. On analyzing carefully the mixture by ^{1}H NMR spectroscopy, we observed three different sets of three methyl groups corresponding to the two methyls derived from bisalkyne **1a** and the methyl in the tosyl group in the spectrum (Figure 4). These results indicate that there are three regioisomers found in a ratio of 56:29:15. Two of them result from the oxidation of α-**2a**, whose lack of symmetry results in two different bonds available for oxidative cleavage. Site-isomer β-**2a** displays C_s symmetry, and thus both bonds available for oxygenation are enantiotopic. Considering that starting **2a** consisted of a 71:29 mixture of α- and β-**2** isomers, we assumed that α- and α'-isomers (56% + 15% = 71%) correspond to the protons marked in red and the ones marked in green might be those of the β-isomer (29%). Unfortunately, NMR experiments did not allow to differentiate between α- and β-**3a** derivatives. The reaction was carried out also with bis(fulleroid) derivative **2b**, exhibiting the same behavior.

Conclusion

In this study, we have explored the regioselectivity of the rhodium(I)-catalyzed [2 + 2 + 2] cycloaddition reaction between two different diynes and C_{70} with the objective of producing C_{70} bis(fulleroids). Mixtures of α- and β-site isomers were obtained, with the α-adduct being the major product of the reaction in both cases. This preference was rationalized by means of DFT calculations. Moreover, the photooxidation of one of the C–C double bonds of the new bis(fulleroids) afford open-cage C_{70} derivatives having a 12-membered ring opening. It is noteworthy to mention that examples of open-cage C_{70} derivatives are relatively scarce, likely owing to the challenges associated with their synthesis and the characterization of asymmetric structures. The findings of this study contribute to the ongoing efforts in the field of fullerene chemistry and provide a foundation for further exploration of regioselective [2 + 2 + 2] cycloaddition reactions as a means to tailor the properties of fullerenes for specific applications.

Supporting Information

Supporting Information File 1

General materials and methods, experimental procedures and characterization of all new compounds.
[https://www.beilstein-journals.org/bjoc/content/supplementary/1860-5397-20-28-S1.pdf]

Acknowledgements

Dr. Carles Fuertes-Espinosa is acknowledged for assistance in HPLC and UV–vis experiments.

Funding

We are grateful for the financial support from the Ministerio de Ciencia e Innovación and EU (Project PID2020-113711GB-I00 MCIN/AEI/10.13039/501100001103, FPI predoctoral grant to C.C. and Margarita Salas grant (NextGenerationEU) to A.A.) and the Generalitat de Catalunya (Project 2021-SGR-623).

ORCID® iDs

Cristina Castanyer - https://orcid.org/0000-0002-8104-2012
Anna Pla-Quintana - https://orcid.org/0000-0003-2545-9048
Anna Roglans - https://orcid.org/0000-0002-7943-5706
Albert Artigas - https://orcid.org/0000-0002-7351-0066
Miquel Solà - https://orcid.org/0000-0002-1917-7450

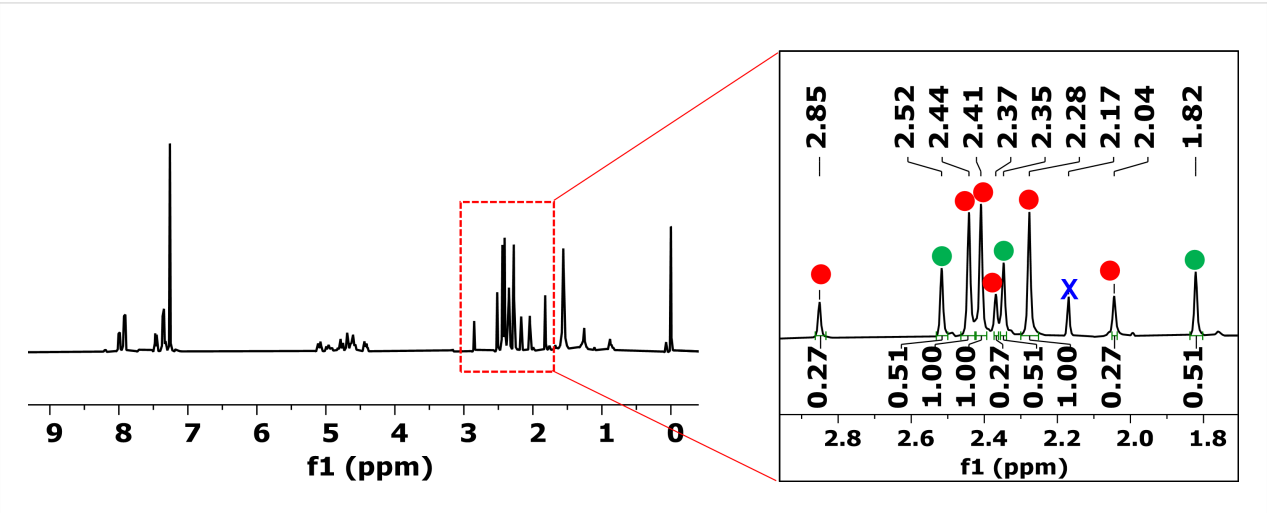

Figure 4: ^{1}H NMR (CS_2/$CDCl_3$, 400 MHz) spectrum of compound **3a** as a mixture of three isomers. X = residual toluene.

Data Availability Statement

All experimental data available in published article and/or supplementary material. All computational data are available through the ioChem-BD repository: https://www.iochem-bd.org/handle/10/356060, https://doi.org/10.19061/iochem-bd-4-67.

References

1. Kroto, H. W.; Heath, J. R.; O'Brien, S. C.; Curl, R. F.; Smalley, R. E. *Nature* **1985,** *318,* 162–163. doi:10.1038/318162a0
2. Bakry, R.; Vallant, R. M.; Najam-ul-Haq, M.; Rainer, M.; Szabo, Z.; Huck, C. W.; Bonn, G. K. *Int. J. Nanomed.* **2007,** *2,* 639–649.
3. Castro, E.; Hernandez Garcia, A.; Zavala, G.; Echegoyen, L. *J. Mater. Chem. B* **2017,** *5,* 6523–6535. doi:10.1039/c7tb00855d
4. Panwar, N.; Soehartono, A. M.; Chan, K. K.; Zeng, S.; Xu, G.; Qu, J.; Coquet, P.; Yong, K.-T.; Chen, X. *Chem. Rev.* **2019,** *119,* 9559–9656. doi:10.1021/acs.chemrev.9b00099
5. Ramos-Soriano, J.; Reina, J. J.; Illescas, B. M.; de la Cruz, N.; Rodríguez-Pérez, L.; Lasala, F.; Rojo, J.; Delgado, R.; Martín, N. *J. Am. Chem. Soc.* **2019,** *141,* 15403–15412. doi:10.1021/jacs.9b08003
6. Cataldo, F.; Da Ros, T., Eds. *Medicinal Chemistry and Pharmacological Potential of Fullerenes and Carbon Nanotubes;* Carbon Materials: Chemistry and Physics; Springer Netherlands: Dordrecht, Netherlands, 2008. doi:10.1007/978-1-4020-6845-4
7. Montellano López, A.; Mateo-Alonso, A.; Prato, M. *J. Mater. Chem.* **2011,** *21,* 1305–1318. doi:10.1039/c0jm02386h
8. Canevet, D.; Pérez, E. M.; Martín, N. *Angew. Chem., Int. Ed.* **2011,** *50,* 9248–9259. doi:10.1002/anie.201101297
9. Kim, Y.; Cook, S.; Tuladhar, S. M.; Choulis, S. A.; Nelson, J.; Durrant, J. R.; Bradley, D. D. C.; Giles, M.; McCulloch, I.; Ha, C.-S.; Ree, M. *Nat. Mater.* **2006,** *5,* 197–203. doi:10.1038/nmat1574
10. Collavini, S.; Delgado, J. L. *Sustainable Energy Fuels* **2018,** *2,* 2480–2493. doi:10.1039/c8se00254a
11. Jia, L.; Chen, M.; Yang, S. *Mater. Chem. Front.* **2020,** *4,* 2256–2282. doi:10.1039/d0qm00295j
12. Gopal, J.; Muthu, M.; Sivanesan, I. *Polymers (Basel, Switz.)* **2023,** *15,* 701. doi:10.3390/polym15030701
13. Kausar, A. *Polym.-Plast. Technol. Mater.* **2023,** *62,* 618–631. doi:10.1080/25740881.2022.2121223
14. Jariwala, D.; Sangwan, V. K.; Lauhon, L. J.; Marks, T. J.; Hersam, M. C. *Chem. Soc. Rev.* **2013,** *42,* 2824–2860. doi:10.1039/c2cs35335k
15. Babu, S. S.; Möhwald, H.; Nakanishi, T. *Chem. Soc. Rev.* **2010,** *39,* 4021–4035. doi:10.1039/c000680g
16. Scarselli, M.; Castrucci, P.; De Crescenzi, M. *J. Phys.: Condens. Matter* **2012,** *24,* 313202. doi:10.1088/0953-8984/24/31/313202
17. Ai, M.; Chen, M.; Yang, S. *Chin. J. Chem.* **2023,** *41,* 2337–2353. doi:10.1002/cjoc.202300105
18. Paukov, M.; Kramberger, C.; Begichev, I.; Kharlamova, M.; Burdanova, M. *Materials* **2023,** *16,* 1276. doi:10.3390/ma16031276
19. Hirsch, A. *Angew. Chem., Int. Ed. Engl.* **1993,** *32,* 1138–1141. doi:10.1002/anie.199311381
20. Taylor, R. *C. R. Chim.* **2006,** *9,* 982–1000. doi:10.1016/j.crci.2006.01.004
21. Hummelen, J. C.; Prato, M.; Wudl, F. *J. Am. Chem. Soc.* **1995,** *117,* 7003–7004. doi:10.1021/ja00131a024
22. Komatsu, K.; Murata, M.; Murata, Y. *Science* **2005,** *307,* 238–240. doi:10.1126/science.1106185
23. Murata, M.; Murata, Y.; Komatsu, K. *Chem. Commun.* **2008,** 6083–6094. doi:10.1039/b811738a
24. Hashikawa, Y.; Yasui, H.; Kurotobi, K.; Murata, Y. *Mater. Chem. Front.* **2018,** *2,* 206–213. doi:10.1039/c7qm00449d
25. Hashikawa, Y.; Murata, Y. *Bull. Chem. Soc. Jpn.* **2023,** *96,* 943–967. doi:10.1246/bcsj.20230135
26. Stanisky, C. M.; Cross, R. J.; Saunders, M. *J. Am. Chem. Soc.* **2009,** *131,* 3392–3395. doi:10.1021/ja809831a
27. Gao, R.; Liu, Z.; Liu, Z.; Liang, T.; Su, J.; Gan, L. *Angew. Chem., Int. Ed.* **2023,** *62,* e202300151. doi:10.1002/anie.202300151 and references cited therein.
28. Hashikawa, Y.; Murata, Y. *Chem. – Eur. J.* **2019,** *25,* 2482–2485. doi:10.1002/chem.201806030
29. Maroto, E. E.; Izquierdo, M.; Murata, M.; Filippone, S.; Komatsu, K.; Murata, Y.; Martín, N. *Chem. Commun.* **2014,** *50,* 740–742. doi:10.1039/c3cc46999a
30. Maroto, E. E.; Mateos, J.; Garcia-Borràs, M.; Osuna, S.; Filippone, S.; Herranz, M. Á.; Murata, Y.; Solà, M.; Martín, N. *J. Am. Chem. Soc.* **2015,** *137,* 1190–1197. doi:10.1021/ja5108854
31. Vidal, S.; Izquierdo, M.; Alom, S.; Garcia-Borràs, M.; Filippone, S.; Osuna, S.; Solà, M.; Whitby, R. J.; Martín, N. *Chem. Commun.* **2017,** *53,* 10993–10996. doi:10.1039/c7cc05987f
32. Hashikawa, Y.; Murata, M.; Wakamiya, A.; Murata, Y. *J. Am. Chem. Soc.* **2016,** *138,* 4096–4104. doi:10.1021/jacs.5b12795
33. Artigas, A.; Pla-Quintana, A.; Lledó, A.; Roglans, A.; Solà, M. *Chem. – Eur. J.* **2018,** *24,* 10653–10661. doi:10.1002/chem.201802298
34. Artigas, A.; Lledó, A.; Pla-Quintana, A.; Roglans, A.; Solà, M. *Chem. – Eur. J.* **2017,** *23,* 15067–15072. doi:10.1002/chem.201702494
35. Castro, E.; Artigas, A.; Pla-Quintana, A.; Roglans, A.; Liu, F.; Perez, F.; Lledó, A.; Zhu, X.-Y.; Echegoyen, L. *Materials* **2019,** *12,* 1314. doi:10.3390/ma12081314
36. Taylor, R.; Wasserman, E.; Haddon, R. C.; Kroto, H. W. The pattern of additions to fullerenes. *The Fullerenes;* Cambridge University Press: Cambridge, UK, 1993; pp 87–102. doi:10.1017/cbo9780511622946.009
37. Hirsch, A. *The Chemistry of the Fullerenes;* Thieme: Stuttgart, Germany, 1994.
38. Fernández, I.; Solà, M.; Bickelhaupt, F. M. *Chem. – Eur. J.* **2013,** *19,* 7416–7422. doi:10.1002/chem.201300648
39. Birkett, P. R.; Avent, A. G.; Darwish, A. D.; Kroto, H. W.; Taylor, R.; Walton, D. R. M. *J. Chem. Soc., Chem. Commun.* **1995,** 1869–1870. doi:10.1039/c39950001869
40. Hashikawa, Y.; Sadai, S.; Murata, Y. *Chem. Commun.* **2023,** *59,* 7387–7390. doi:10.1039/d3cc01717f
41. Lou, N.; Li, Y.; Gan, L. *Angew. Chem., Int. Ed.* **2017,** *56,* 2403–2407. doi:10.1002/anie.201612054
42. Sadai, S.; Hashikawa, Y.; Murata, Y. *Org. Lett.* **2023,** *25,* 2815–2819. doi:10.1021/acs.orglett.3c00726
43. Murata, Y.; Maeda, S.; Murata, M.; Komatsu, K. *J. Am. Chem. Soc.* **2008,** *130,* 6702–6703. doi:10.1021/ja801753m
44. Hashikawa, Y.; Shimizu, Y.; Murata, Y. *Org. Lett.* **2020,** *22,* 8624–8628. doi:10.1021/acs.orglett.0c03216
45. Cerón, M. R.; Izquierdo, M.; Aghabali, A.; Valdez, J. A.; Ghiassi, K. B.; Olmstead, M. M.; Balch, A. L.; Wudl, F.; Echegoyen, L. *J. Am. Chem. Soc.* **2015,** *137,* 7502–7508. doi:10.1021/jacs.5b03768
46. McKenzie, D. R.; Davis, C. A.; Cockayne, D. J. H.; Muller, D. A.; Vassallo, A. M. *Nature* **1992,** *355,* 622–624. doi:10.1038/355622a0

47. Mestres, J.; Duran, M.; Solà, M. *J. Phys. Chem.* **1996,** *100,* 7449–7454. doi:10.1021/jp960312h
48. Zhang, R.; Futagoishi, T.; Murata, M.; Wakamiya, A.; Murata, Y. *J. Am. Chem. Soc.* **2014,** *136,* 8193–8196. doi:10.1021/ja504054s
49. Castro, E.; Fernandez-Delgado, O.; Artigas, A.; Zavala, G.; Liu, F.; Moreno-Vicente, A.; Rodríguez-Fortea, A.; Velasquez, J. D.; Poblet, J. M.; Echegoyen, L. *J. Mater. Chem. C* **2020,** *8,* 6813–6819. doi:10.1039/d0tc01382j
50. Only the most stable of the two possible regioisomers of β-**2a** based on DFT calculations is depicted in Scheme 2 (see Figure S25 in Supporting Information File 1).
51. Kozuch, S.; Shaik, S. *J. Phys. Chem. A* **2008,** *112,* 6032–6041. doi:10.1021/jp8004772
52. Kozuch, S.; Shaik, S. *Acc. Chem. Res.* **2011,** *44,* 101–110. doi:10.1021/ar1000956
53. Murata, M.; Maeda, S.; Morinaka, Y.; Murata, Y.; Komatsu, K. *J. Am. Chem. Soc.* **2008,** *130,* 15800–15801. doi:10.1021/ja8076846
54. Morinaka, Y.; Tanabe, F.; Murata, M.; Murata, Y.; Komatsu, K. *Chem. Commun.* **2010,** *46,* 4532–4534. doi:10.1039/c0cc00113a

License and Terms

BEILSTEIN JOURNAL OF ORGANIC CHEMISTRY

Synthesis of π-conjugated polycyclic compounds by late-stage extrusion of chalcogen fragments

Aissam Okba[‡1,2], Pablo Simón Marqués[‡1], Kyohei Matsuo[3], Naoki Aratani[2], Hiroko Yamada[3], Gwénaël Rapenne[1,2] and Claire Kammerer[*1]

Review

Open Access

Address:
[1]CEMES, Université de Toulouse, CNRS, 29 rue Marvig, F-31055 Toulouse Cedex 4, France, [2]Division of Materials Science, Nara Institute of Science and Technology, NAIST, 8916-5 Takayama-cho, Ikoma, Nara 630-0192, Japan and [3]Institute for Chemical Research, Kyoto University, Gokasho, Uji, Kyoto 611-0011, Japan

Email:
Claire Kammerer[*] - claire.kammerer@cemes.fr

* Corresponding author ‡ Equal contributors

Keywords:
arenes; chalcogens; extrusion; fused-ring systems; precursor approach

Beilstein J. Org. Chem. **2024,** *20,* 287–305.
https://doi.org/10.3762/bjoc.20.30

Received: 30 November 2023
Accepted: 31 January 2024
Published: 15 February 2024

This article is part of the thematic issue "Carbon-rich materials: from polyaromatic molecules to fullerenes and other carbon allotropes".

Associate Editor: J. G. Hernández

Abstract

The "*precursor approach*" has proved particularly valuable for the preparation of insoluble and unstable π-conjugated polycyclic compounds (π-CPCs), which cannot be synthesized via in-solution organic chemistry, for their improved processing, as well as for their electronic investigation both at the material and single-molecule scales. This method relies on the synthesis and processing of soluble and stable direct precursors of the target π-CPCs, followed by their final conversion in situ, triggered by thermal activation, photoirradiation or redox control. Beside well-established reactions involving the elimination of carbon-based small molecules, i.e., retro-Diels–Alder and decarbonylation processes, the late-stage extrusion of chalcogen fragments has emerged as a highly promising synthetic tool to access a wider variety of π-conjugated polycyclic structures and thus to expand the potentialities of the "*precursor approach*" for further improvements of molecular materials' performances. This review gives an overview of synthetic strategies towards π-CPCs involving the ultimate elimination of chalcogen fragments upon thermal activation, photoirradiation and electron exchange.

Introduction

π-Conjugated polycyclic compounds (π-CPCs), including polycyclic aromatic hydrocarbons and their heteroatom-based counterparts, have attracted the attention of the scientific community for two centuries already. Initially, major interest resulted from their structural, optical and electronic properties at the molecular level, but the last decades witnessed the rise of molecular materials and π-conjugated polycyclic compounds appeared as particularly valuable in this field. Indeed, many of them

demonstrated excellent performances as active components of electronic devices such as organic field effect transistors (OFETs), organic photovoltaic cells (OPVs) and organic light-emitting diodes (OLEDs). This has prompted an ever-increasing number of research groups to design new synthetic routes towards π-CPCs, aiming at i) new organic structures for improved performances, ii) higher synthetic efficiency and modularity, and iii) better processability of target compounds to build opto-electronic devices [1-8]. In this regard, the planar character of most (non-substituted) π-CPCs represents a challenge, as it results in very low solubility in common organic solvents due to favorable intermolecular π–π stacking interactions. This inherently hampers the purification of the target compounds, thus limiting their final purity, and restricts the processing techniques to physical vapor deposition. In addition, some π-CPCs appear to be sensitive to oxidative and/or photolytic degradation, which hinders their use in devices under ambient conditions.

The case of acenes is representative of this situation. Acenes are a class of aromatic compounds composed of linearly fused benzene rings, which can be regarded as the narrowest graphene nanoribbons. They are highly promising p-type organic semiconductors, but suffer from insolubility and instability leading to dimerization and/or endoperoxide formation. To overcome these issues, the "*precursor approach*" was developed and relies on the synthesis, purification and characterization of soluble and stable precursors of the target active π-CPCs, followed by their (solution) processing and their final deprotection once assembled in thin-films or crystals, or adsorbed on metallic substrates [9-12]. Conversion of the non-planar soluble precursor into the flat π-conjugated target compound is triggered on demand by a stimulus such as thermal activation, irradiation with light or injection of electrons, leading to the elimination of small volatile molecules. Importantly, this ultimate synthetic step, performed in situ, should be quantitative and should not require the addition of chemical reagents, since any non-volatile byproduct would be trapped in the material and thus impact its performances. The "*precursor approach*" was introduced by Herwig and Müllen as early as in 1996 for pentacene, which was ultimately obtained in a thin-film by a thermally-activated retro-Diels–Alder reaction from a tailor-made tetrachlorobenzene-pentacene soluble adduct (Scheme 1, top left) [13,14]. Over the years, thermally-induced retrocycloadditions were further exploited from bridged bicyclo[2.2.2]octadiene solubilizing fragments to generate (hetero)acenes and larger bidimensional π-CPCs such as extended porphyrin derivatives with the concomitant release of ethylene (Scheme 1, bottom left) [9,11,15]. It is important to note here that in the "*precursor approach*", a synthetic strategy has to be devised according to a multi-step route to prepare the soluble precursor, in turn specifically designed to deliver the target π-CPC after activation in situ. This is thus fundamentally different from the approach consisting in reacting a pristine acene with a dienophile to transiently form a cycloadduct with increased solubility for processing purposes, and unmasking it afterwards via a retro-Diels–Alder reaction [16-19].

In parallel to retro-Diels–Alder reactions, another efficient strategy for the in situ aromatization of target π-CPCs relies on the extrusion of carbon monoxide (CO) from soluble precursors incorporating bridging ketone fragment(s). In contrast with the thermal activation required in retro-Diels–Alder reactions, photoirradiation of α-diketones triggers a Strating–Zwanenburg decarbonylation leading to the release of two CO molecules (Scheme 1, top right). After a proof of concept on pentacene

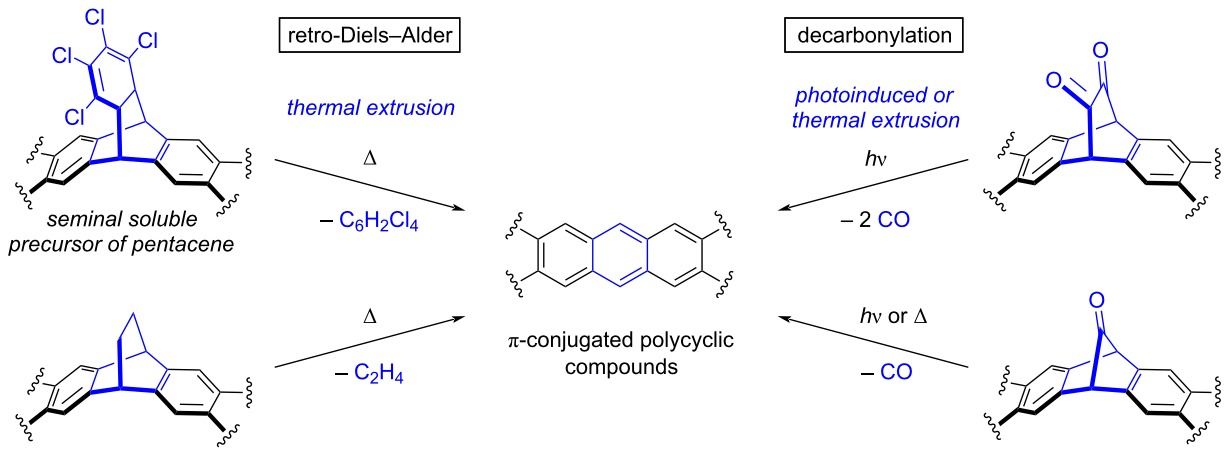

Scheme 1: "*Precursor approach*" for the synthesis of π-conjugated polycyclic compounds, with the thermally- or photoinduced late-stage extrusion of carbon-based fragments resulting from retro-Diels–Alder and decarbonylation reactions. The seminal design of pentacene's soluble precursor, as reported by Müllen and Herwig [14], is depicted in the top left.

with soluble precursors including a bicyclo[2.2.2]octane-2,3-dione framework [20,21], α-diketones were intensely exploited as soluble photoprecursors for the synthesis of acenes of increasing length up to undecacene, in matrices [22-25] or in a single crystal [26]. This strategy has also been extended to the synthesis of dyads involving an acene moiety combined with a chromophore [27]. Alternatively, when inserting a monoketone bridging fragment, i.e., a norbornadien-7-one moiety, in the soluble precursor, recovery of the target π-CPC is possible via a cheletropic decarbonylation step upon photolysis or thermolysis (Scheme 1, bottom right). This dual activation mode has led to the solid-state formation, on a preparative scale, of higher acenes up to nonacene [28-33] and bidimensional structures such as starphenes [34] from custom-made stable and soluble precursors. Interestingly, extrusion of CO from mono- or α-diketone precursors has also been achieved on metallic surfaces under ultra-high vacuum (UHV) conditions upon thermal annealing, photoirradiation or activation by the tip of a scanning tunneling microscope (STM) [11,34-36]. Owing to the subatomic resolution now available with scanning probe microscopy techniques (STM and non-contact atomic force microscopy, nc-AFM), the "*precursor approach*" has opened the way for in-depth structural and electronic investigations at the single molecule scale of π-CPCs, which could otherwise not be synthesized and/or deposited on surface.

As seen above, the "*precursor approach*" has proved particularly valuable i) for the preparation of insoluble and unstable π-CPCs which cannot be synthesized (and purified) via conventional in-solution organic chemistry techniques, ii) for their improved processing, as well as iii) for their in situ structural characterization and electronic investigation both at the material and single-molecule scales. Reactions involving the elimination of carbon-based small molecules, i.e., retro-Diels–Alder and decarbonylation processes, have been predominantly exploited as an ultimate step performed in situ to release the target compounds. However, the bridging character of the bicyclo[2.2.2]octadiene, bicyclo[2.2.2]octane-2,3-dione and norbornadien-7-one fragments in the appropriate soluble precursors inherently limits the applicability of these reactions to the synthesis of π-CPCs containing linearly-fused benzene rings in their core scaffold (i.e., at least an anthracene pattern), or to the deprotection of peripheral benzene rings. To reach a wider variety of structures, novel synthetic strategies in line with the "*precursor approach*" have been recently reported, in which chalcogen-containing precursors undergo a ring contraction combined with the extrusion of a chalcogen fragment in the ultimate step. In view of the diversity of π-conjugated polycyclic structures potentially accessible via this route, the extrusion of chalcogen fragments appears as a highly promising synthetic tool to complement the retro-Diels–Alder and decarbonylation reactions mostly exploited up to now, and thus to expand the potentialities of the "*precursor approach*" for further improvements of molecular materials performances.

Since the synthesis of π-CPCs involving as final step the elimination of C-based molecules, i.e., a retro-Diels–Alder reaction or a decarbonylation, has already been thoroughly reviewed in the past years [4,5,9-12], this review focuses on the late-stage extrusion of chalcogen fragments triggered by thermal activation, photoirradiation and electron exchange as a powerful synthetic strategy to prepare a variety of π-CPCs.

Review

Contraction of 7-membered rings: chalcogen extrusion from heteropines

The family of chalcogen heteropines, i.e., cycloheptatriene analogues incorporating one group-16 atom, have attracted attention from the chemists' community since the 1950s, when the first syntheses of oxepine [37] and thiepine [38] were reported (Scheme 2). Analogues containing heavier atoms such as Se [39] and Te [40] appeared later in the literature. In relationship with its structure, this class of compounds is prone to valence isomerization via 6π-electrocyclization leading to the formation of heteroatom-containing norcaradiene, and oxepine has been shown to exist in equilibrium with its valence isomer benzene oxide [37]. In contrast with the parent oxepine, which is isolable at room temperature, other group-16 heteropines suffer from thermal instability. Indeed, the low activation barrier for S, Se or Te cheletropic extrusion from the norcaradiene valence isomer, combined with the irreversibility of this process, shifts the tautomerization equilibrium and delivers benzene as the organic product along with inorganic species [41-44]. Over the years, many efforts were thus devoted to the synthesis of thiepine derivatives with increased thermal stability, with the aim to disfavor the formation of the transient thianorcaradiene intermediate as a way to prevent the sulfur extrusion [44]. It appeared that thiepines carrying sterically demanding substituents on the sulfur α-positions as well as annelated analogues

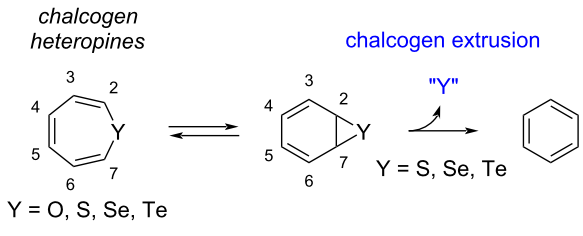

Scheme 2: Valence isomerization of chalcogen heteropines and subsequent cheletropic extrusion in the case of sulfur, selenium and tellurium derivatives.

show substantially increased lifetimes, owing to steric and electronic effects [45]. With these criteria in mind, a variety of thermally-stable annelated thiepines were progressively isolated as a result of very diverse synthetic strategies [46-49], which were further applied to the preparation of stable selenepines and tellurepines [50-53].

Extrusion reactions from sulfur-, selenium- and tellurium-containing compounds have long been recognized as valuable synthetic tools in organic chemistry [54], with the most famous S-extrusion process to generate new C–C bonds probably being the Ramberg–Bäcklund reaction [55]. In the case of heteropines, chalcogen extrusion leads to a six-membered ring via the intramolecular formation of a C–C bond, and this reactivity pattern was exploited as early as in the 1950s to generate in a controlled way polycyclic aromatic compounds from isolable heteropine precursors. By way of example, the phenanthrene derivative **2** was obtained by heating the dibenzo[*b*,*f*]thiepine precursor **1** in the presence of copper bronze in refluxing quinoline, thus triggering a S-extrusion along with a decarboxylation reaction (Scheme 3) [56]. From a retrosynthetic point of view, this example nicely illustrates the fact that polyannelated thiepines, and more generally S-, Se- and Te-based heteropines, are straightforward precursors of π-CPCs bearing non linearly-fused benzene rings. In addition, the non-planar geometry of such heteropines appears as an asset towards increased solubility, and the existence of several oxidation states for these heteroatoms expands the panel of reaction conditions applicable to trigger the extrusion process. In line with these considerations, chalcogen extrusion from heteropines has thus been explored in the frame of the "*precursor approach*" as a synthetic tool to complement retro-Diels–Alder and decarbonylation reactions and reach diversified π-conjugated polycyclic structures.

In 2020, Yamada, Fukui, Shinokubo and co-workers tackled the synthesis of perylene bisimide (PBI), a valuable n-type semiconductor, via a "*precursor approach*" based on the late-stage extrusion of S-based fragments [57]. Dinaphthothiepine bisimides **3a** and **3b**, bearing octyl- and butylimide substituents respectively, were synthesized as direct soluble precursors of PBIs **6a**,**b**, along with the corresponding oxides, namely sulfoxides **4a**,**b** and sulfone **5** (Scheme 4). An X-ray crystal structure of the extended thiepine **3b** confirmed its bent structure, with a protrusion of the sulfur atom out of the π-surface (Figure 1). As expected, the non-planar thiepine derivatives **3**–**5** exhibit substantially higher solubility in organic solvents compared with the parent PBI compounds, with a 150- to 1700-fold increase in dichloromethane depending on the sulfur oxidation state. Conversion of the dinaphthothiepine core into the corresponding perylene moiety was next tested upon different stimuli, such as electron injection, thermal activation and photoirradiation. Importantly, the dinaphthothiepine *S*,*S*-dioxide, i.e., the sulfone soluble precursor **5**, failed to deliver PBI whatever the activation mode (Scheme 4, bottom). For dinaphthothiepine **3** and the related sulfoxide **4**, it was first demonstrated that electron injection is able to trigger S- (or SO-) extrusion, electrochemically but also chemically, employing decamethylcobaltocene $CoCp^*_2$ as a reducing agent (Scheme 4, top). Under the latter conditions, the target PBI compound **6a** was obtained in 89% yield on a ≈10 mg scale from its sulfoxide precursor **4a**. In anticipation of device fabrication, activation methods which do not require the addition of chemical reagents were next tested. Thermally-induced S-extrusion was first investigated by means of thermogravimetric analysis: the thiepine precursor **3a** exhibited a mass decrease at 300 °C in agreement with the expected elimination of sulfur to yield almost quantitatively the corresponding PBI **6a**. Its sulfoxide analogue **4a** exhibited higher thermal reactivity, with the loss of SO identified at lower temperature (225 °C). As a proof of concept, a thin-film of the latter sulfoxide precursor, spin-coated onto a glass sample, yielded full conversion to PBI **6a** in only 2 min, confirming the potential application of this precursor in electronic devices. Light irradiation was next tested as an alternative activation method, since photoextrusion of S and SO_2 fragments are classical methods in organic synthesis [54,58,59], whereas photoextrusion of SO from bisaryl sulfoxide moieties has been evidenced more recently by Wolf et al. [60,61]. Solutions of dinaphthothiepine **3a** and its sulfoxide analogue **4a** in dichloromethane were irradiated using a high-pressure mercury lamp equipped with a sharp cut filter (λ > 380 nm), which resulted in a smooth conversion into the PBI product **6a** within 20 min. Interestingly, the sulfoxide derivative exhibited enhanced kinetics, as confirmed by UV–vis spectroscopy and NMR experiments. The latter was also reac-

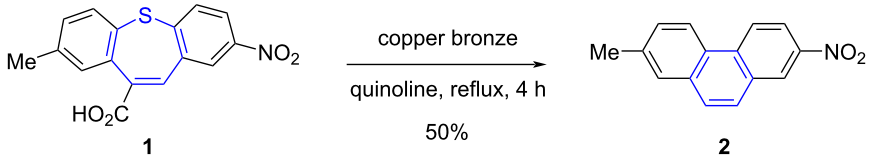

Scheme 3: Early example of phenanthrene synthesis via a chemically-induced S-extrusion (and concomitant decarboxylation) from a dibenzothiepine precursor [56].

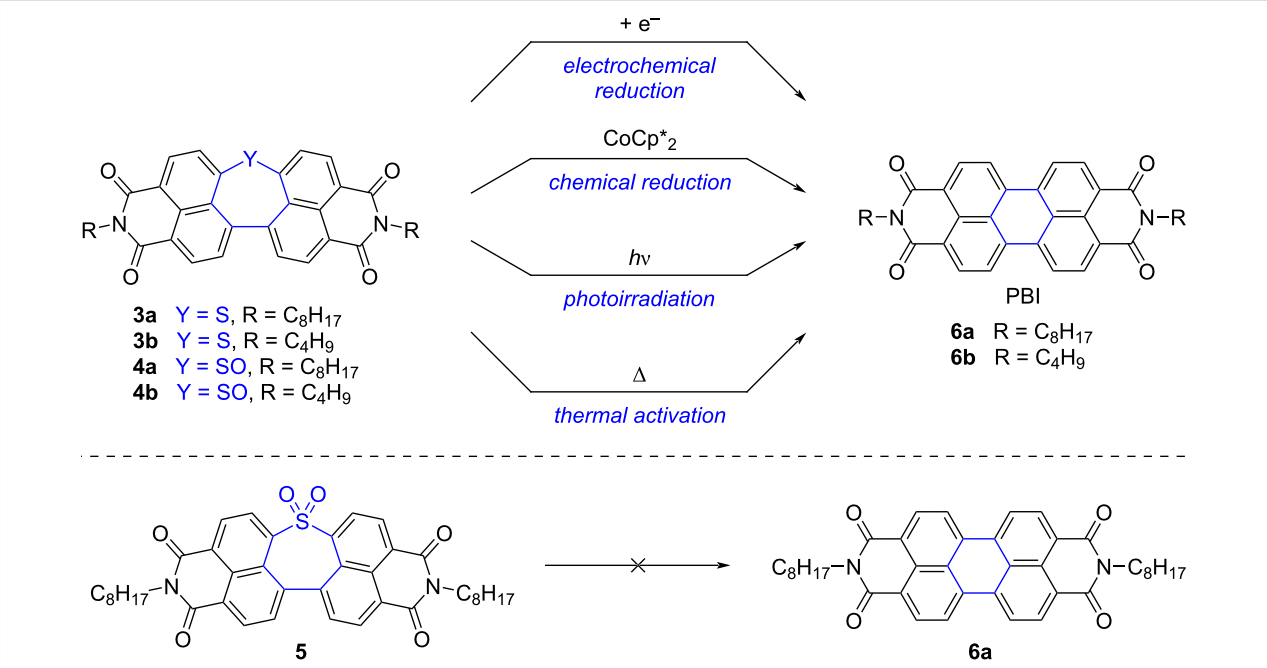

Scheme 4: Top: Conversion of dinaphthothiepine bisimides **3a**,**b** and their sulfoxide analogues **4a**,**b** into PBIs **6a**,**b** by S-extrusion triggered by electron injection, photo- and thermal activation. Bottom: Dinaphthothiepine *S*,*S*-dioxide **5** fails to deliver PBI **6a** whatever the activation mode [57].

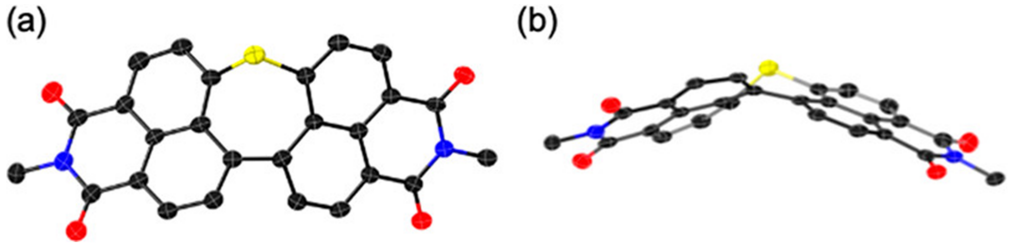

Figure 1: Top view (a) and side view (b) of the X-ray crystal structure of thiepine **3b** showing its bent conformation. Thermal ellipsoids are shown at the 50% probability level, and all hydrogen atoms as well as propyl groups on imide substituents have been omitted for clarity. Reprinted with permission from [57]. Copyright 2020 American Chemical Society. This content is not subject to CC BY 4.0.

tive as a thin-film on a glass substrate, with the generation of the desired perylene upon photoirradiation with a blue LED (λ = 470 nm) [62]. Finally, cooperativity of light and heat was demonstrated on a crystalline sample of sulfoxide **4a**, where photoirradiation enhanced the SO-extrusion process at lower temperature (140 °C) than previously.

These preliminary studies thus validated the suitability of the dinaphthothiepine core and particularly its *S*-oxide as soluble precursors for perylene, with three different activation modes to generate the target PBI semiconductor. This "*precursor approach*" was next tested at the device fabrication stage in the case of OFETs. An Al_2O_3/SiO_2 dielectric layer with a self-assembled monolayer of 12-cyclohexyldodecylphosphonic acid was chosen as substrate and thin-films of sulfoxide **4a** were formed by spin-coating from a chloroform solution. After thermal annealing at 230 °C for 5 min to induce SO-extrusion and subsequent vacuum deposition of the source and drain gold electrodes, the resulting OFET exhibited a typical n-type behavior with an electron mobility up to 0.41 $cm^2\ V^{-1}\ s^{-1}$, comparable to vacuum deposited films of pristine PBI. When repeating the same protocol with a photoconversion of **4a** thin-film instead of thermal conversion, a decrease of the charge transport efficiency was observed, with electron mobilities of $8.4 \times 10^{-2}\ cm^2\ V^{-1}\ s^{-1}$, which can be ascribed to the lower quality of the PBI thin-film generated upon photoextrusion due to the absence of thermal solid-state reorganization [62].

This work thus unequivocally revealed the potential of thiepines and thiepine *S*-oxides as direct soluble precursors of polycyclic

aromatic compounds with dual stimuli-responsiveness, thus opening the way to solution-based processing for the fabrication of devices and in situ generation of the active material by late stage S-extrusion. Nevertheless, the synthetic route towards dinaphthothiepine bisimides initially reported suffered from several drawbacks: it had limited efficiency (1.2% overall yield over 8 steps for the synthesis of thiepine **3a**), it was non-scalable and displayed low modularity. Indeed, the imide groups along with their substituents were introduced at a rather early stage of the synthesis, with the ultimate synthetic step being the formation of the thiepine ring via a two-fold nucleophilic aromatic substitution by sodium sulfide (Na_2S). Since the nature of the imide substituents is very important to control the solid state molecular arrangement, the same authors revised their initial synthetic route to allow for a late stage introduction of the imide groups, thus leading to the preparation of a series of variously-substituted soluble precursors **3a–f** owing to increased modularity (Scheme 5) [62]. To this aim, acenaphthene was selected as key building block and it underwent two successive regioselective halogenations to give bromochloroacenaphthene **8** in 64% overall yield. The latter was next converted into the corresponding boronic acid **9** and a Suzuki–Miyaura cross-coupling between **8** and **9** gave rise to dimer **10**, followed by the oxidation of both acenaphthene units into 1,8-naphthalic anhydrides. Installation of the thiepine ring was achieved by a double nucleophilic aromatic substitution induced by sodium sulfide (Na_2S) to afford dinaphthothiepinetetracarboxylic anhydride **12** as key precursor of a series of thiepine bisimides bearing diverse substituents. Due to its very low solubility, the tetracarboxylic anhydride **12** was not isolated and was directly reacted with a variety of amines to yield the target soluble precursors **3a–f**. Diverse primary alkylamines were well tolerated, also when an electron-withdrawing polyfluoroalkyl group (**3d**) was included, and bulkier amines, such as 3-pentylamine (**3e**) or trimethylaniline (**3f**), could also be inserted. As a matter of fact, the choice of amines was limited by the temperature required for the imide formation, as high temperature (>130 °C) induced undesired thermally-activated S-extrusion as side-reaction. According to this new synthetic route, compound **3a** carrying octyl substituents was obtained on a gram-scale in 7 steps from acenaphthene, in 14% overall yield. The series of thiepines **3a–d** could finally be smoothly oxidized to give the corresponding sulfoxides **4a–d** in high yields. Thermogravimetric analysis of these thiepine *S*-oxides interestingly revealed that the temperature required for SO-extrusion is almost independent of the nature of the imide substituents, and the dinaphthothiepine

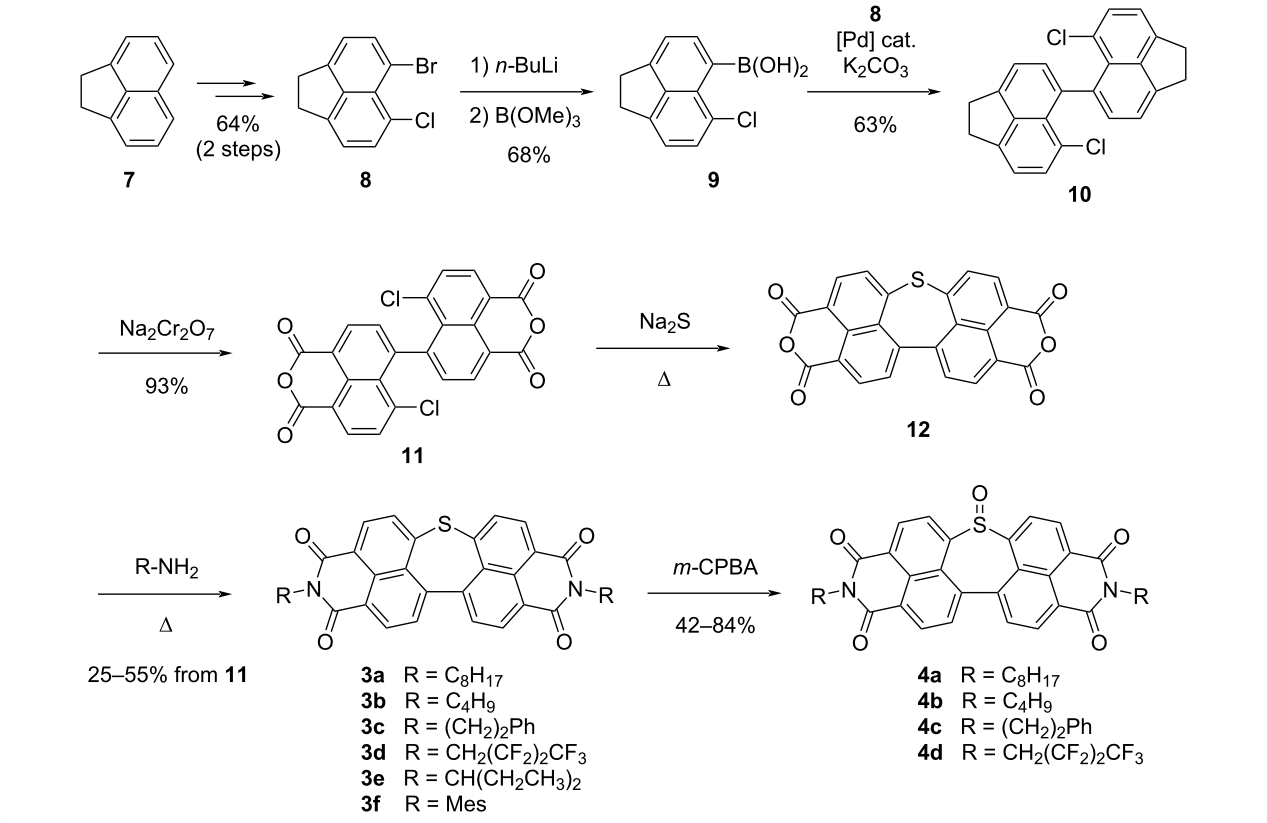

Scheme 5: Modular synthetic route towards dinaphthothiepines **3a–f** and the corresponding *S*-oxides **4a–d**, incorporating a variety of imide substituents [62].

S-oxides bearing long alkyl chains are thus very promising soluble precursors to afford n-type semiconducting layers by in situ SO-extrusion.

As part of their work dedicated to mechanically-responsive materials controlled by an electrochemical stimulus, Song and Swager synthesized thiepine-containing polymers designed to undergo redox-driven bent-to-planar conformational changes [63]. However, upon electrochemical oxidation of the drop-cast film of polymer **13**, the authors observed the conversion of the dithienobenzothiepine monomeric units into dithienonaphthalenes, which can be ascribed to a redox-driven S-extrusion (Scheme 6). This behavior of extended thiepines upon oxidation was further confirmed by investigating the corresponding sulfoxide, which appeared labile and readily underwent ring contraction. Since thiepine precursors (such as **15**) and the corresponding dithienonaphthalene products (e.g., **16**) exhibit very different fluorescence properties, S-extrusion from thiophene-annelated thiepines was consequently exploited for peroxide sensing.

Very recently, Zhou et al. reported the synthesis of S-doped phenanthrene and triphenylene derivatives via the thermally-induced ring contraction of thiepine scaffolds, fused with two or three thiophene, thiopyran or polycyclic hydrocarbon moieties [64]. Indeed, a series of polyannelated thiepine derivatives were prepared according to an original approach, consisting in the introduction of the bridging sulfur atom from the outset of the synthesis and a final closure of the 7-membered ring by C–C bond formation. This is in sharp contrast with the widely adopted strategy relying on the late-stage insertion of the sulfur atom with concomitant ring closure, using either electrophilic or nucleophilic sulfur reagents. By way of example, thiepine derivative **21** was synthesized in six steps in 14% overall yield from 3-bromothiophene (**17**, Scheme 7). In the first step, the sulfur atom embedded in the final thiepine ring was introduced via a palladium-catalyzed *S*-arylation of 3-bromothiophene in the presence of potassium thioacetate, to afford the corresponding bis(thiophenyl) thioether, which then underwent successive bromination and iodination to give intermediate **18**. Next, a two-fold Suzuki–Miyaura cross-coupling occurring chemoselectively on the iodinated positions allowed the symmetric extension of the hydrocarbon scaffold, with the insertion of two naphthyl substituents carrying each an alkyne moiety on the *ortho* position. Ring expansion of both thiophene units in **19** was then triggered by platinum catalysis to generate the corresponding thiopyrans, and finally the bromine atoms located on the latter rings were exploited for the ring closure of the thiepine via a two-fold Suzuki–Miyaura cross-coupling with 1,2-phenylenediboronic pinacol ester. The resulting S-doped extended tribenzothiepine **21** proved stable under ambient conditions for several months and exhibited good solubility in common organic solvents, which is ascribed to the boat-shape conformation of the thiepine ring, thus weakening the π–π stacking intermolecular interactions. Finally, solid-state S-extrusion could be triggered in a controlled way upon thermal activation of **21**, as observed in thermogravimetric analysis, with the loss of sulfur detected at 223 °C to yield the planar S-doped triphenylene derivative **22**.

In the same year, An et al. reported their investigations regarding chalcogen-doped hexa-*peri*-benzocoronene (HBC)

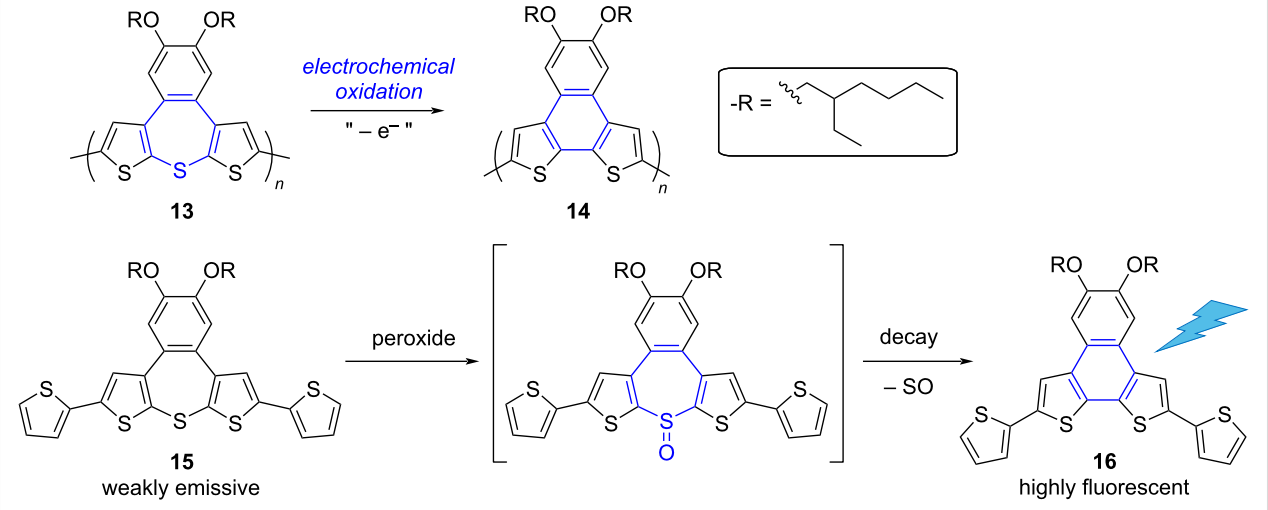

Scheme 6: Top: Conversion of dithienobenzothiepine monomeric units into dithienonaphthalenes, upon S-extrusion triggered by electrochemical oxidation. Bottom: Exploitation of the S-extrusion process for peroxide sensing, taking advantage of the lability of oxidized dithienobenzothiepine to generate highly fluorescent dithienonaphthalene [63].

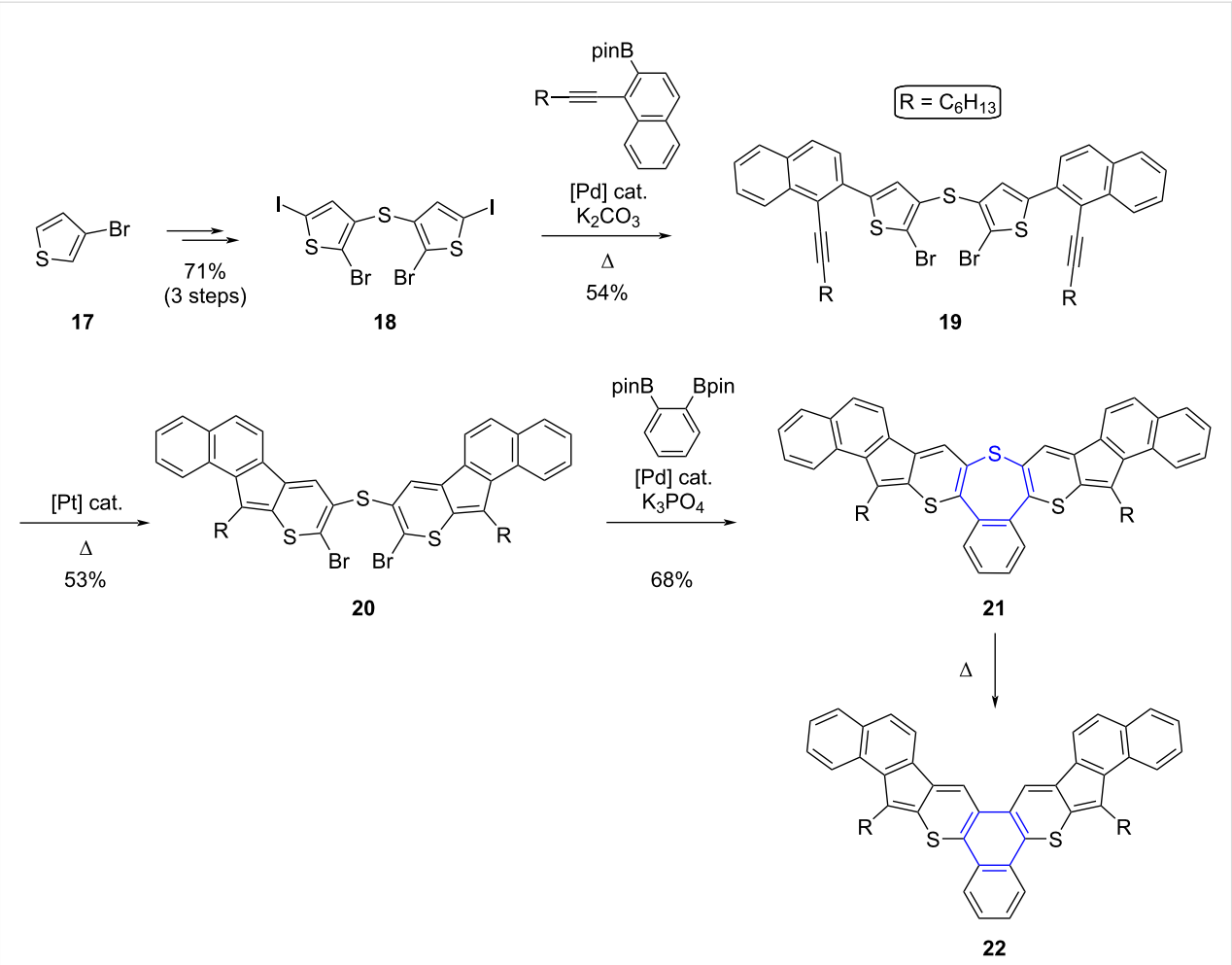

Scheme 7: Synthesis of S-doped extended triphenylene derivative **22** from 3-bromothiophene (**17**) with the thermally-induced ring contraction of thiepine **21** as key step [64].

derivatives and their controllable conversion into hydrocarbon nanographenes by ring contraction of the heteropine moiety [65]. The authors first tackled the synthesis of a series of HBC precursors incorporating a group-16 heteroatom embedded in a seven-membered ring. In the case of oxygen, the fully cyclized HBC **26a** containing an oxepine ring and exhibiting a saddle-shape tridimensional structure was successfully prepared (Scheme 8, top). Conversely, with heavier chalcogens, only partially cyclized backbones, namely *seco*-HBCs **28**, were obtained (Scheme 8, bottom). The synthesis of these helical compounds was based on S-, Se- or Te-dibenzo[*b*,*f*]heteropines **23b–d** as key intermediates, which were engaged in a Diels–Alder reaction with tetrabromothiophene *S*,*S*-dioxide **24** at 120–140 °C to yield the corresponding *S*- and *Se*-tribenzo[*b*,*d*,*f*]heteropines, **25b** and **25c** respectively, after oxidative aromatization mediated by DDQ. In the case of tellurepine **23d**, attempts of thermally-activated Diels–Alder reaction resulted in Te-extrusion to afford phenanthrene as the main product. This result highlights the higher sensitivity of the Te-heteropines compared to S- and Se-counterparts towards thermal chalcogen extrusion. Next, four-fold Suzuki–Miyaura coupling of the tetrabrominated tribenzoheteropines **25b** and **25c** delivered compounds **27b** and **27c** as direct precursors of S- and Se-inserted HBCs. The subsequent Scholl reaction allowed the formation of four new C–C bonds, but failed to afford the fully cyclized chalcogen-embedded HBC whatever the conditions tested, presumably due to large strain in line with the size of S and Se atoms as compared with O. The helical S- and Se-doped *seco*-HBCs **28b** and **28c** were thus obtained as racemic mixtures in three steps from dibenzoheteropines **23b** and **23c** in 45% and 18% overall yield, respectively. To evaluate the impact of the heteroatom oxidation state on reactivity, the sulfur and selenium oxides were next prepared via selective oxidation of thiepine and selenepine to give rise to the corresponding sulfoxide **29b**, selenoxide **29c** and sulfone **30b** in excellent yields.

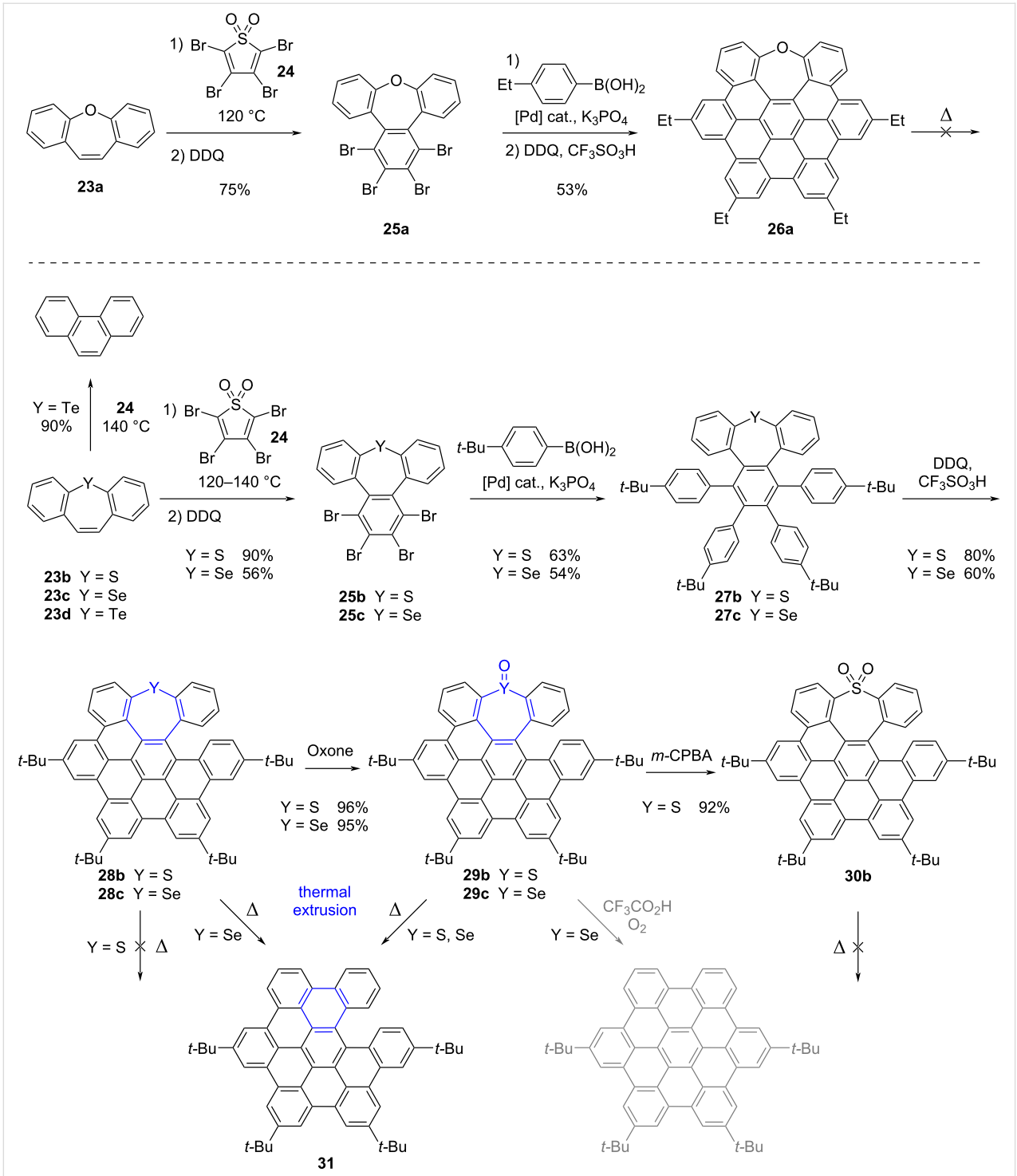

Scheme 8: Top: Synthesis of thermally-stable O-doped HBC **26a**. Bottom: Synthesis of S- and Se-based soluble precursors of *seco*-HBC **31** and their conversion by chalcogen extrusion upon thermal activation [65].

All the prepared chalcogen-doped HBC derivatives exhibit good solubility in organic solvents, in line with their highly distorted saddle-shaped or helical structure induced by the embedded heteropine ring. By way of example, the solubility of SeO-doped *seco*-HBC **29c** is more than 100-fold higher than pristine HBC carrying four *tert*-butyl groups in both dichloromethane and ethanol.

Ring contraction was next attempted on the series of heteropines synthesized previously. Importantly, photoirradia-

tion at 254 nm or 365 nm failed to induce any chalcogen extrusion. When thermal activation was tested on solid samples, oxepine **26a**, thiepine **28b** and thiepine *S*,*S*-dioxide **30b** were not converted upon heating at 250 °C for 2 hours, thus highlighting their high thermal stability. Conversely, selenepine **28c** and selenepine *Se*-oxide **29c** were quantitatively converted into the *seco*-HBC **31** by thermal activation at 200 °C for 5 min, as evidenced by UV–visible absorption and HPLC monitoring. SO-extrusion from thiepine *S*-oxide **29b** was also successfully triggered in the solid state, but it required prolonged heating at higher temperature (250 °C). In this work, *seco*-HBC **31** was thus successfully obtained via thermally-induced ring contraction of certain heteropines with the concomitant cheletropic elimination of chalcogen fragments. These results nicely illustrate how the nature, as well as the oxidation state of the embedded chalcogen atom, allows controlling the stability of the heteropine, and thus its propensity to undergo thermal extrusion. Although beyond the scope of this review, it is noteworthy that the authors successfully converted the selenepine *Se*-oxide **29c** into the corresponding planar HBC at room temperature upon acidic treatment under air, thus triggering SeO-elimination as well as cyclodehydrogenation in a single step.

As mentioned above, oxepine derivatives display higher stability compared to other chalcogen heteropines and direct oxygen extrusion from oxepines under photo- or thermal activation has not been reported. Oxygen thus appears as the chalcogen element of choice to obtain stable heteropines embedded in π-CPCs and study the properties of such non-planar compounds.

Very recently, Fukui, Shinokubo and co-worker reported the synthesis of dinaphthooxepine bisimides [66], which are analogues of the dinaphthothiepine bisimides presented above with an oxygen atom substituting the sulfur atom (Scheme 9). Their synthesis was successfully achieved in two steps from the known intermediate 5,5'-linked 4-chloro-1,8-naphthalic anhydride dimer **11**, already exploited in the previous thiepine synthesis (see Scheme 5). Installation of the imide groups was performed first and dianhydride **11** was thus treated with 2,4,6-trimethylaniline to afford the corresponding bisimide **32** in good yield. Subsequently, reaction with α-benzaldoxime in the presence of sodium hydride resulted in the formation of the oxepine ring by a double substitution reaction, to yield the desired dinaphthooxepine **33**.

The non-planar character of dinaphthooxepine bisimides was confirmed by X-ray crystal structure, and stability towards thermal or photoactivation was also established. Cyclic voltammetry studies revealed that reduction of dinaphthooxepine **33** proceeds irreversibly, giving rise to a new chemical species (Figure 2), and this was further confirmed by chemical reduction in the presence of decamethylcobaltocene $CoCp^*_2$ at room temperature. Using two equivalents of this 1-electron reducing agent, O-extrusion takes place with concomitant ring contraction to give the corresponding PBI **6f**, isolated in 63% yield after oxidative quenching and work-up. Contrary to photo- or thermal activation, it is important to note that the mechanism for O-extrusion involves in this case the dianion of dinaphthooxanorcaradiene bisimide valence isomer obtained upon electron injection and not its neutral form, as shown by UV–vis absorption and DFT studies. The mechanism of the final release of oxygen still remains unclear.

This example shows that a careful molecular design allows endowing chalcogen heteropines with thermal- and photosta-

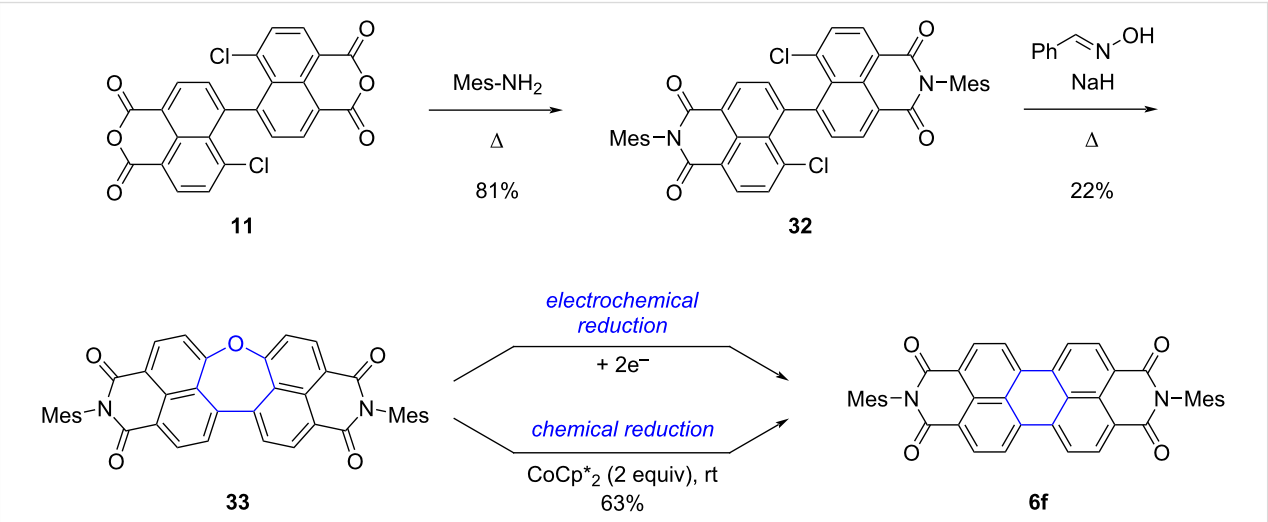

Scheme 9: Synthesis of dinaphthooxepine bisimide **33** and conversion into PBI **6f** by O-extrusion triggered by electron injection [66].

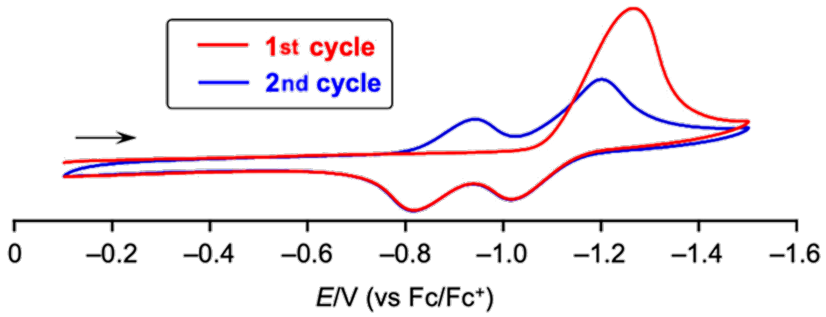

Figure 2: Cyclic voltammogram of dinaphthooxepine **33**, evidencing the irreversibility of the reduction process during the first cycle, leading to the formation of PBI **6f** upon redox-triggered O-extrusion. Reprinted with permission from [66]. Copyright 2023 American Chemical Society. This content is not subject to CC BY 4.0.

bility by the choice of oxygen as heteroatom, while keeping the possibility to trigger chalcogen extrusion via a radically different mechanistic route, as a result of the injection of electrons. Here, the presence of the imide functions appended to the naphthyl scaffold is crucial, since previously reported bare and aryl-substituted dinaphthooxepines exhibited reversible reduction [67].

In summary, owing to the heteroatom-dependent behavior of heteropines, it is possible to control the structure of the target compound: on the one hand, thermally stable chalcogen-doped π-CPCs with distorted structures can be obtained and their intrinsic properties investigated, and on the other hand, with a subtle choice of the chalcogen element and its oxidation state, controlled extrusion coupled to 7-membered ring contraction will lead to planar benzenoid π-CPCs in situ, in response to diverse stimuli.

In the next section, chalcogen extrusion resulting from the contraction of 6-membered rings upon photo- and thermal activation will be detailed.

Contraction of 6-membered rings coupled to chalcogen extrusion

Ring contraction of 6-membered heterocycles containing chalcogen atoms has been employed as a strategy to synthesize π-CPCs containing 5-membered rings. The controlled extrusion of sulfur from 1,2-dithia-3,5-cyclohexadienes (1,2-dithiins) was exploited as early as in the 1950s to prepare extended thiophene derivatives, such as dibenzo- and dinaphthothiophene (Scheme 10, top) [68,69]. Similarly to the early transformations of thiepines, sulfur elimination was triggered by copper bronze at high temperature, thus leading to the conversion of the 6-membered cyclic disulfide into the corresponding thiophene.

The 1,2-dithiin scaffold is found in natural products such as thiarubrines A and B, which have been shown to be particularly sensitive to light [70]. Upon exposure to UV or visible light, thiarubrine A (**36**) undergoes a desulfurization process to give rise to the corresponding thiophene **37**, exhibiting enhanced antibiotic activity (Scheme 10, bottom). This naturally-occurring S-extrusion under light activation thus prompted the inves-

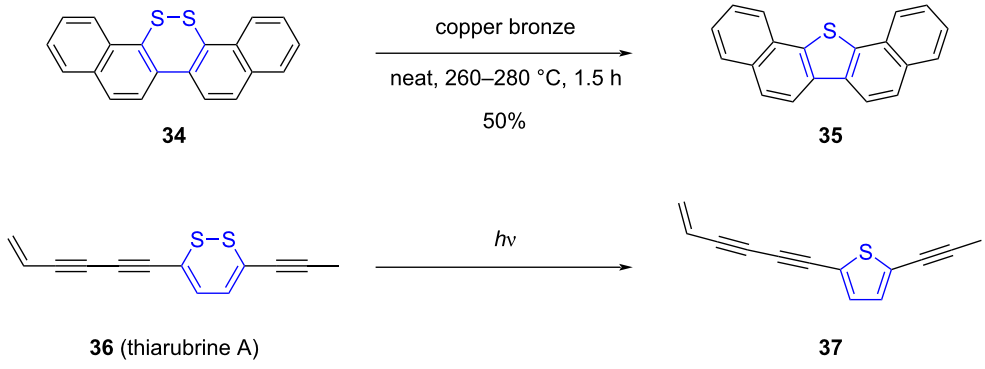

Scheme 10: Top: Early example of 6-membered ring contraction with concomitant S-extrusion leading to dinaphthothiophene [69]. Bottom: Photoactivated S-extrusion occurring in natural product thiarubrine A [70].

tigation of 1,2-dithia-3,5-cyclohexadienes as synthetic photoprecursors of thiophene-based π-CPCs.

In this sense, Schroth et al. reported the synthesis of thienothiophene and benzothienothiophene **40** from dithiin key intermediates (Scheme 11, top) [71]. Benzo[4,5]thieno[3,2-*c*][1,2]dithiin (**39**) was prepared by intramolecular oxidative coupling of a dithiolate generated in situ from dithioacetate **38**, and subsequent exposition to daylight of a solution of **39** triggered ring contraction with concomitant elimination of sulfur to yield target benzothienothiophene **40**. Importantly, light-induced S-extrusion from 1,2-dithiins appears to be structure-dependent, as di-annelated dithieno[1,2]dithiin analogues (i.e., 1,2-dithiins fused with two thiophene moieties) proved stable upon light exposure.

In their work aiming at deciphering the electronic interactions between carboranes and chalcogen-doped π-conjugated heterocycles, Yang and co-workers devised a two-step strategy for the synthesis of carborane-fused thiophene **43** (Scheme 11, bottom) [72]. Double lithiation of carboranyl indole **41** was followed by trapping with disulfur dichloride as chalcogen source to afford 1,2-dithiin **42**. At room temperature, the latter then spontaneously evolved via a S-extrusion to yield the desired carborane-fused thiophene **43**. The same method was further employed to prepare other analogues incorporating a group-16 heteroatom.

The strategy involving 6-membered ring contraction by chalcogen extrusion thus appears as highly promising for the synthesis of conjugated materials containing thiophene or selenophene moieties. However, 1,2-dichalcogenin cycles stabilized in highly conjugated scaffolds are not easily converted by light or thermal activation, as mentioned above, and their reactivity in the absence of external reagent (i.e., their photo- and thermal reactivity) has been far less explored than for heteropines. Nowadays, the most common protocol to trigger extrusion from 1,2-dichalcogenins and generate S- and Se-doped π-CPCs still relies on copper (as nanopowder) at high temperature under neat conditions [73-77].

In order to promote light-induced ring contraction of 1,2-dithiin scaffolds, Furukuwa et al. explored the reactivity of precursors bearing one sulfur atom in a higher oxidation state [78]. In their synthesis of dibenzo[1,4]dithiapentalene **46**, the 1,2-dithiin precursor **44** was first oxidized by means of *m*-CPBA into thiosulfonate **45**, which was subsequently irradiated with light in benzene to give dithiapentalene **46** in 61% yield upon SO_2-extrusion (Scheme 12).

In the same context, the thermal and photochemical extrusion of SO has been exploited as well in 6-membered rings containing a sulfoxide moiety. For instance, Grainger and co-workers designed a series of naphthotrithiin-2-oxides, such as **47**, to act as SO transfer reagents (Scheme 13) [79]. These triplet SO precursors were prepared by treatment of 1,8-naphthalene dithiols with thionyl chloride to generate the trisulfide-2-oxide moiety. Thermal activation of **47** in refluxing chlorobenzene triggered the elimination of SO, which was subsequently trapped by a variety of conjugated dienes such as 2,3-dimethylbutadiene (**48**), to afford in good to excellent yields 2,5-dihydrothiophene *S*-oxides, along with the 5-membered 1,8-naphthalene disulfide **49** resulting from the ring contraction of precursor **47**. Such SO transfer process, favoured by the *peri*-interaction existing in the trisulfide-2-oxide substrate, was also successfully promoted by light and the cyclic sulfoxide **50** was obtained under milder

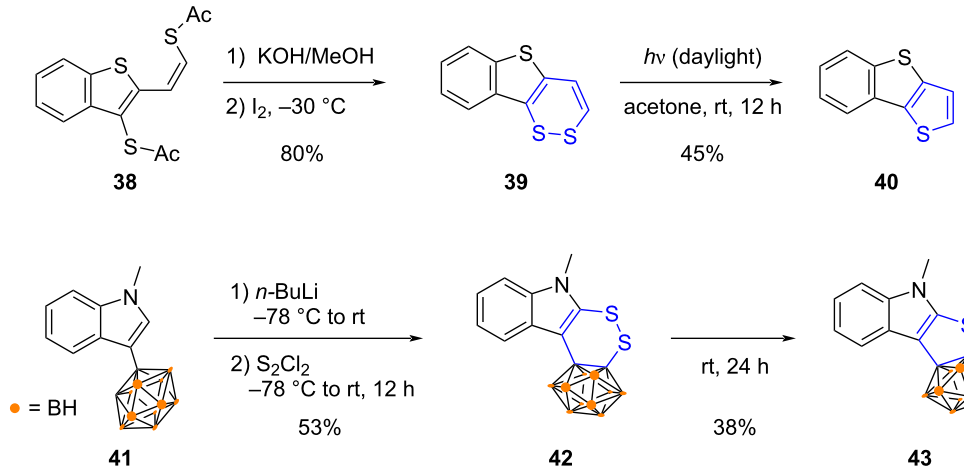

Scheme 11: Examples of S-extrusion from annelated 1,2-dithiins under photoactivation (top) or thermal activation (bottom) [71,72].

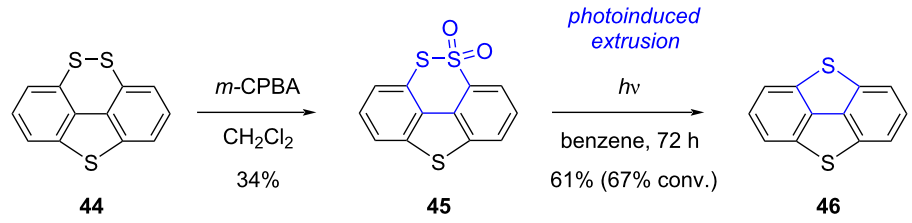

Scheme 12: Synthesis of dibenzo[1,4]dithiapentalene upon photoextrusion of SO_2 [78].

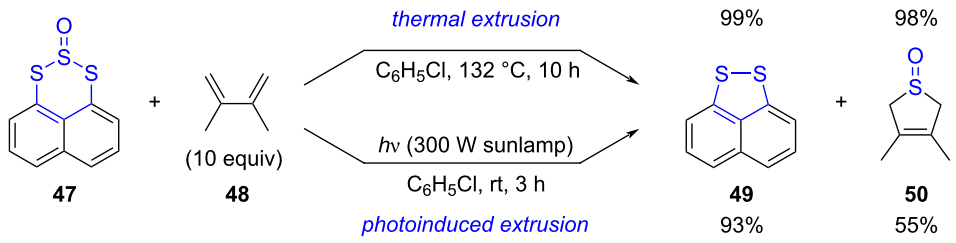

Scheme 13: Extrusion of SO in naphthotrithiin-2-oxides for the synthesis of 2,5-dihydrothiophene 1-oxides [79].

conditions in 55% yield. For increased synthetic utility, the latter could be converted in a straightforward manner into the corresponding thiophene under Pummerer conditions.

A 6-membered ring contraction through SO-extrusion was also introduced as key step in a molecular "surgical" method developed by Murata, Komatsu et al. [80]. In this approach, C_{60} or C_{70} fullerenes are modified stepwise towards an open-cage derivative in order to encapsulate small molecules such as H_2 [81,82]. Eventually, the chemical modifications are reversed to close the hole and give an endohedral fullerene. As depicted in Scheme 14, the 12-membered ring orifice of fullerene **51** was first enlarged by electrophilic addition of sulfur. After encapsulation of H_2 molecule(s) (n = 1 or 2), four synthetic steps were

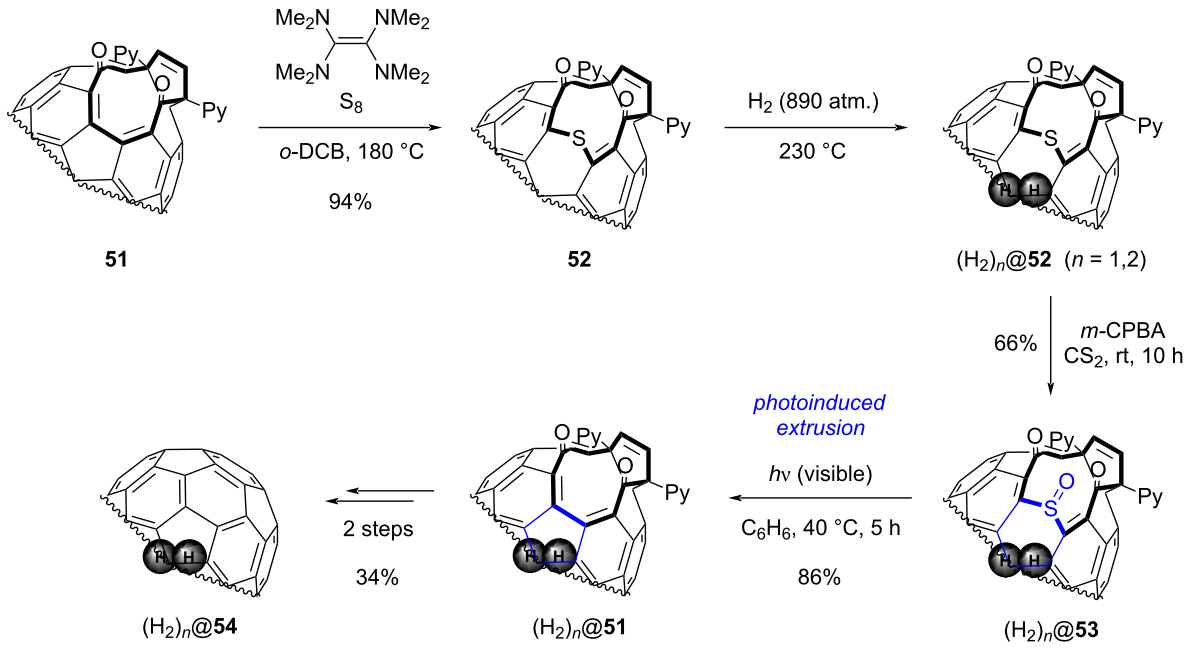

Scheme 14: SO-extrusion as a key step in the synthesis of fullerenes (C_{60} and C_{70}) encapsulating H_2 molecules [80,82].

required to reduce the hole size and ultimately obtain cage-closed compound $(H_2)_n$@**54**. In order to remove sulfur and regenerate the initial 5-membered carbocycle, the thiopyran scaffold in $(H_2)_n$@**52** was first oxidized with *m*-CPBA to yield the corresponding sulfoxide $(H_2)_n$@**53**. As a key step, the latter was next subjected to photoinduced SO-extrusion under visible light, leading to a ring contraction in 86% yield. At that stage, the initial ring size of precursor **51** was recovered, and two further steps including a McMurry reaction and a thermolysis were then necessary to obtain endohedral fullerene $(H_2)_n$@**54**.

As seen in the two first parts of this review, synthetic strategies involving a late-stage ring contraction, accompanied with the extrusion of a chalcogen fragment, have led to the preparation of a variety of π-CPCs, displaying a wide range of 2D or 3D structures. While contraction of 6-membered rings has not been exploited yet for the in situ generation of molecular materials, chalcogen extrusion from group-16 heteropines was successfully implemented as a key step in the fabrication of devices with highly promising properties. Elimination of chalcogen fragments coupled to ring contraction thus appears as a powerful synthetic tool to complement retro-Diels–Alder reactions and decarbonylations widely used in the frame of the "*precursor approach*", and further contributions to this field will most probably widely expand the range of π-conjugated polycyclic structures to be investigated as active materials in opto-electronic devices.

In contrast with the two previous sections, the last part of this review focuses on extrusion of chalcogen fragments which does not involve ring contraction. In such case, the soluble precursors display a bridged structure, reminiscent of the bicyclo[2.2.2]octadiene, bicyclo[2.2.2]octane-2,3-dione and norbornadien-7-one exploited as photo- and thermal precursors of acenes, as described in the introduction.

Chalcogen extrusion from bridged precursors: access to acenes

Deoxygenation of endoxides belongs to the classical methods used in organic chemistry to generate polycylic aromatic hydrocarbons, through a reductive aromatization relying on a variety of chemical reagents [4]. The non-planar character of the bridging epoxide moieties endows the precursors with increased solubility, and endoxides have thus been envisioned as soluble precursors of acenes. Since the addition of chemical reagents is not desirable in this context, thermal activation and electron injection were investigated as stimuli to trigger O-extrusion.

Moresco, Peña and co-workers thus designed diepoxytetracene precursor **56**, displaying an oxabicyclo moiety at each extremity (Scheme 15) [83]. The latter was prepared in one step via a double Diels–Alder reaction between furan and 2,6-naphthodiyne, generated in situ from bistriflate **55** in the presence of cesium fluoride. Diepoxide **56** was obtained in 40% yield as a *syn*/*anti* mixture in a 1:1.7 ratio.

Diepoxide **56** (as a diastereoisomeric mixture) was deposited on a Cu(111) surface by sublimation under UHV conditions and the molecular species adsorbed on the metallic surface were characterized by combined STM and nc-AFM at low temperature (5 K), thus evidencing the presence of the two bridging oxygens. Next, the STM tip-induced extrusion of oxygen was investigated: application of a bias voltage of ≈2.2 V on top of one 1,4-epoxide bridge led to a planarization of the carbon-based scaffold along with the elimination of one oxygen atom to give a monoepoxide species. When the latter was submitted to a second voltage pulse, a fully planar and aromatic backbone made of four linearly-fused benzene rings was observed on STM and AFM images, thus unambiguously proving the formation of tetracene **57**. Importantly, the oxygen atoms extruded

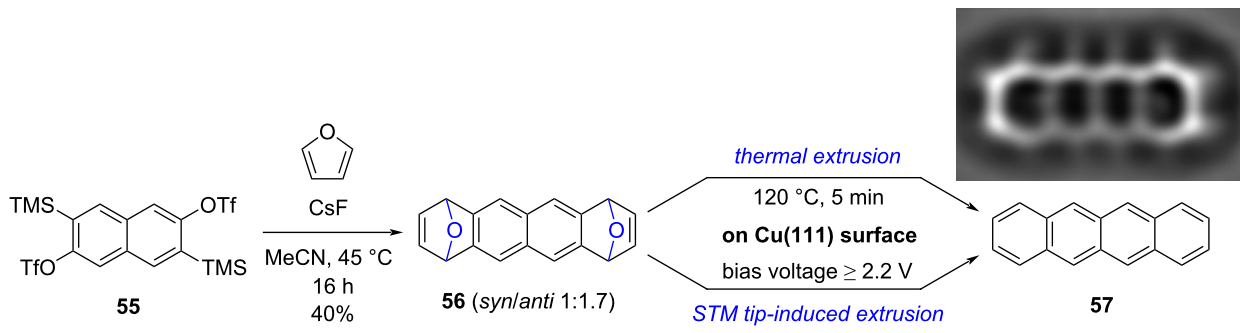

Scheme 15: Synthesis of diepoxytetracene precursor **56** and its on-surface conversion into tetracene upon O-extrusion. Inset in the top right shows a Laplace-filtered AFM image of a tetracene molecule produced on a Cu(111) surface. Inset adapted with permission from [83]. Copyright 2016 American Chemical Society. This content is not subject to CC BY 4.0.

from precursor **56** were observed on the copper surface in close proximity to the converted molecule.

In contrast with this tip-induced conversion of soluble precursor **56**, which occurs stepwise and gives rise to one single target molecule after each manipulation cycle, thermal activation of the population of adsorbed diepoxides **56** was next attempted. Annealing at 120 °C for 5 min successfully promoted the O-extrusion to yield the corresponding tetracene molecules, without any trace of partially-converted monoepoxide intermediate.

As mentioned in the introduction section, the quest for longer unsubstituted acenes has captivated chemists and physicists for almost two decades now, with the aim to explore their electronic properties. In this context, on-surface synthesis of higher acenes according to the *"precursor approach"* is particularly interesting, since the as-prepared π-extended structures can undergo in-depth structural characterization and electronic investigations in situ at the single molecule scale, thanks to scanning probe microscopy and spectroscopy. The synthetic route relying on O-extrusion was thus transposed to the synthesis of hexacene [84], decacene [85] and ultimately dodecacene [86], which is the longest acene prepared to date. The related soluble precursors **58**–**60** incorporate 3 to 5 oxabicyclo moieties in their hydrocarbon scaffold (Scheme 16), and are sufficiently stable and soluble to undergo purification by column chromatography prior to their on-surface deposition.

By way of example, the synthesis of decacene precursor **59** was achieved in three synthetic steps by iterative [4 + 2] cycloadditions with an overall yield of 4.7% (Scheme 17). The synthesis of epoxyacene **59** started with the mono-Diels–Alder reaction of naphthodiyne precursor **55** with isobenzofuran **61** to give monoepoxide **62** as a mixture of regioisomers. Further treatment of the latter with one equivalent of cesium fluoride allowed the regioselective Diels–Alder with the previous diene **61**, to afford **63** as another mixture of position isomers. Finally,

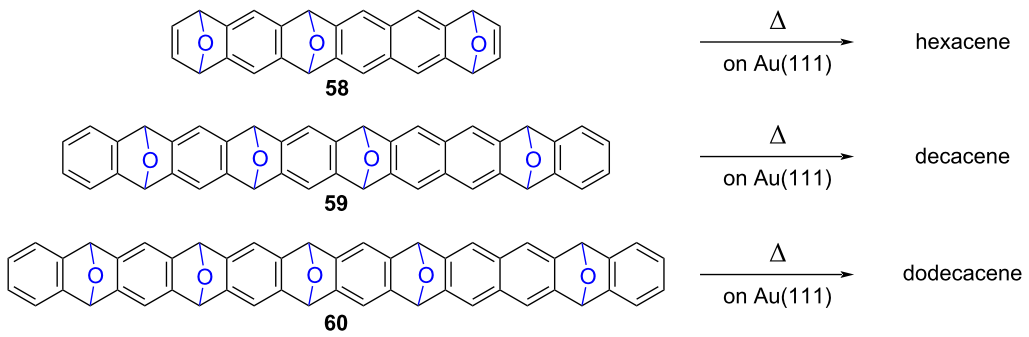

Scheme 16: Soluble precursors of hexacene, decacene and dodecacene incorporating 1,4-epoxides in their hydrocarbon scaffold, and on-surface conversion into higher acenes by thermally-activated O-extrusion [84-86].

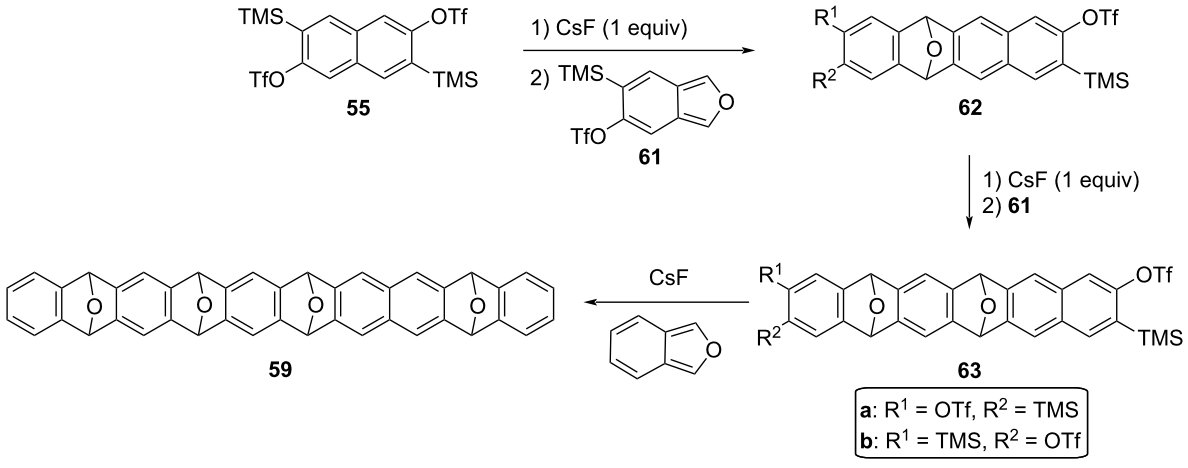

Scheme 17: Synthesis of tetraepoxide **59** as soluble precursor of decacene [85].

reaction of this bisaryne precursor with an excess cesium fluoride and bare isobenzofuran gave rise to the end-capped soluble precursor **59** via a double cycloaddition process.

All polyepoxides **58**–**60** were deposited by sublimation on a Au(111) surface, triggering in some cases partial deoxygenation during this physical vapor deposition. Subsequent annealing in the 150–220 °C range led to the thermally-induced surface-assisted cleavage of oxygen to give rise to the corresponding acenes, namely hexacene, decacene and dodecacene. Their structure was unambiguously assigned thanks to high-resolution STM and AFM images, revealing the linear fusion of benzene rings with a zigzag edge (Figure 3), and their electronic properties were investigated at the single-molecule scale, with a particular attention devoted to the evolution of the HOMO–LUMO gap along the incremental series of acenes.

Conclusion

Over the last decades, the "*precursor approach*" has proved particularly valuable for the preparation of insoluble and unstable π-CPCs, which cannot be synthesized via in-solution organic chemistry, for their improved processing, as well as for their structural characterization and electronic investigation both at the material and single-molecule scales. Beside reactions involving the elimination of carbon-based small molecules, i.e. retro-Diels–Alder and decarbonylation processes, the late-stage extrusion of chalcogen fragments has emerged as a highly promising synthetic tool to access a wider variety of π-conjugated polycyclic structures upon thermal activation, photoirradiation and redox control.

While contraction of 6-membered rings has not been exploited yet for the in situ generation of molecular materials, chalcogen extrusion from group-16 heteropines was successfully implemented as a key step in the fabrication of devices. Notably, the use of heteropines as soluble precursors allowed to expand the "*precursor approach*" to new families of organic semiconductors, such as PBIs and triphenylenes. It is important to mention here that, depending on the nature of the soluble heteropine precursor, the extrusion process may lead to volatile and/or non-volatile chalcogen species. In the latter case, the target π-CPCs may be contaminated by inorganic impurities, especially when extrusion reactions are performed in the solid state, which may in turn alter the properties of the resulting molecular materials. Further investigations regarding the fate of the extruded chalcogen fragments and their impact on device performances are thus desirable and will surely drive the design of future chalcogen-based soluble precursors.

Chalcogen extrusion has also been investigated in the absence of concomitant ring contraction, and in this context, endoxides have been envisioned as soluble precursors of higher acenes.

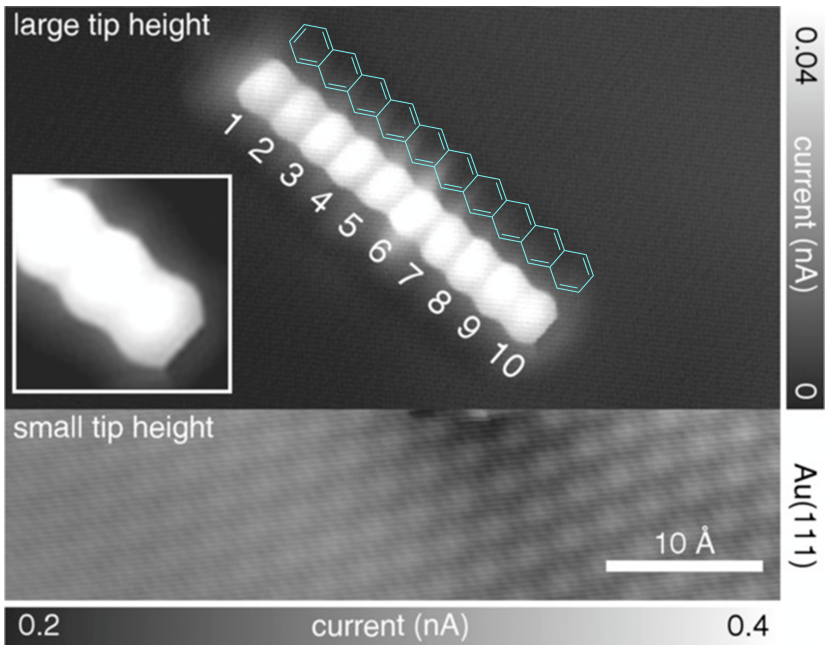

Figure 3: Constant-height STM measurement of decacene on Au(111) using a CO-functionalized tip (sample voltage V = 20 mV), with the chemical structure of decacene superimposed in blue as a guide to the eye. Two different tip height domains were employed to resolve the Au(111) lattice as well as the adsorbed molecule with atomic resolution. Adapted with permission from [85], J. Krüger et al., "Decacene: On-Surface Generation", *Angew. Chem., Int. Ed.*, with permission from John Wiley and Sons.

Conversion of polyepoxide precursors was successfully achieved on metallic surfaces, at the single-molecule scale, upon STM tip-induced or thermally-activated O-extrusion to yield acenes of increasing lengths, up to the long-sought dodecacene.

Following the pioneering works detailed in this review, further contributions to this field will most probably widely expand the range of π-conjugated polycyclic structures accessible via chalcogen extrusion in the upcoming years.

Funding

This work was supported by the University Paul Sabatier (Toulouse), CNRS, Nara Institute of Science and Technology, and Kyoto University. It has received funding from the French National Research Agency (ANR) under the project CROSS (n° ANR-21-CE09-0002) and it has been partially supported through the EUR grant NanoX (n° ANR-17-EURE-0009) in the framework of the "Programme des Investissements d'Avenir", Japan Society for the Promotion of Science (JSPS) KAKENHI Grant Numbers JP22K05255 (K. M.), JP22K19067 (N. A.), JP23H01787 (N. A.), JP20H00379 (H. Y.), and JP20H05833 (Transformative Research Areas "Dynamic Exciton") (H. Y.). This work was partially supported by ISHIZUE 2023 of Kyoto University.

ORCID® iDs

Aissam Okba - https://orcid.org/0009-0000-6615-4270
Pablo Simón Marqués - https://orcid.org/0000-0001-7421-8473
Kyohei Matsuo - https://orcid.org/0000-0002-2472-9459
Hiroko Yamada - https://orcid.org/0000-0002-2138-5902
Gwénaël Rapenne - https://orcid.org/0000-0002-4993-4213
Claire Kammerer - https://orcid.org/0000-0002-5292-5975

Data Availability Statement

Data sharing is not applicable as no new data was generated or analyzed in this study.

References

1. Anthony, J. E. *Chem. Rev.* **2006,** *106,* 5028–5048. doi:10.1021/cr050966z
2. Wang, C.; Dong, H.; Hu, W.; Liu, Y.; Zhu, D. *Chem. Rev.* **2012,** *112,* 2208–2267. doi:10.1021/cr100380z
3. Narita, A.; Wang, X.-Y.; Feng, X.; Müllen, K. *Chem. Soc. Rev.* **2015,** *44,* 6616–6643. doi:10.1039/c5cs00183h
4. Marshall, J. L.; Lehnherr, D.; Lindner, B. D.; Tykwinski, R. R. *ChemPlusChem* **2017,** *82,* 967–1001. doi:10.1002/cplu.201700168
5. Dorel, R.; Echavarren, A. M. *Eur. J. Org. Chem.* **2017,** 14–24. doi:10.1002/ejoc.201601129
6. Stępień, M.; Gońka, E.; Żyła, M.; Sprutta, N. *Chem. Rev.* **2017,** *117,* 3479–3716. doi:10.1021/acs.chemrev.6b00076
7. Wang, X.-Y.; Yao, X.; Narita, A.; Müllen, K. *Acc. Chem. Res.* **2019,** *52,* 2491–2505. doi:10.1021/acs.accounts.9b00322
8. Borissov, A.; Maurya, Y. K.; Moshniaha, L.; Wong, W.-S.; Żyła-Karwowska, M.; Stępień, M. *Chem. Rev.* **2022,** *122,* 565–788. doi:10.1021/acs.chemrev.1c00449
9. Yamada, H.; Okujima, T.; Ono, N. *Chem. Commun.* **2008,** 2957–2974. doi:10.1039/b719964c
10. Watanabe, M.; Chen, K.-Y.; Chang, Y. J.; Chow, T. J. *Acc. Chem. Res.* **2013,** *46,* 1606–1615. doi:10.1021/ar400002y
11. Yamada, H.; Kuzuhara, D.; Suzuki, M.; Hayashi, H.; Aratani, N. *Bull. Chem. Soc. Jpn.* **2020,** *93,* 1234–1267. doi:10.1246/bcsj.20200130
12. Yamada, H.; Hayashi, H. *Photochem. Photobiol. Sci.* **2022,** *21,* 1511–1532. doi:10.1007/s43630-022-00235-x
13. Brown, A. R.; Pomp, A.; de Leeuw, D. M.; Klaassen, D. B. M.; Havinga, E. E.; Herwig, P.; Müllen, K. *J. Appl. Phys.* **1996,** *79,* 2136–2138. doi:10.1063/1.361071
14. Herwig, P. T.; Müllen, K. *Adv. Mater. (Weinheim, Ger.)* **1999,** *11,* 480–483. doi:10.1002/(sici)1521-4095(199904)11:6<480::aid-adma480>3.0.co;2-u
15. Chan, Y. S.; Hayashi, H.; Sato, S.; Kasahara, S.; Matsuo, K.; Aratani, N.; Yamada, H. *Eur. J. Org. Chem.* **2022,** e202200621. doi:10.1002/ejoc.202200621
16. Afzali, A.; Dimitrakopoulos, C. D.; Breen, T. L. *J. Am. Chem. Soc.* **2002,** *124,* 8812–8813. doi:10.1021/ja0266621
17. Joung, M.-J.; Ahn, J.-H.; Kang, S.-Y.; Baek, K.-H.; Ahn, S.-D.; Do, L.-M.; Kim, C.-A.; Kim, G.-H.; You, I.-K.; Yoon, S.-M.; Suh, K.-S. *Bull. Korean Chem. Soc.* **2003,** *24,* 1862–1864.
18. Vets, N.; Smet, M.; Dehaen, W. *Tetrahedron Lett.* **2004,** *45,* 7287–7289. doi:10.1016/j.tetlet.2004.08.011
19. Chao, T.-H.; Chang, M.-J.; Watanabe, M.; Luo, M.-H.; Chang, Y. J.; Fang, T.-C.; Chen, K.-Y.; Chow, T. J. *Chem. Commun.* **2012,** *48,* 6148–6150. doi:10.1039/c2cc31754k
20. Uno, H.; Yamashita, Y.; Kikuchi, M.; Watanabe, H.; Yamada, H.; Okujima, T.; Ogawa, T.; Ono, N. *Tetrahedron Lett.* **2005,** *46,* 1981–1983. doi:10.1016/j.tetlet.2005.01.157
21. Yamada, H.; Yamashita, Y.; Kikuchi, M.; Watanabe, H.; Okujima, T.; Uno, H.; Ogawa, T.; Ohara, K.; Ono, N. *Chem. – Eur. J.* **2005,** *11,* 6212–6220. doi:10.1002/chem.200500564
22. Mondal, R.; Shah, B. K.; Neckers, D. C. *J. Am. Chem. Soc.* **2006,** *128,* 9612–9613. doi:10.1021/ja063823i
23. Mondal, R.; Adhikari, R. M.; Shah, B. K.; Neckers, D. C. *Org. Lett.* **2007,** *9,* 2505–2508. doi:10.1021/ol0709376
24. Tönshoff, C.; Bettinger, H. F. *Angew. Chem., Int. Ed.* **2010,** *49,* 4125–4128. doi:10.1002/anie.200906355
25. Shen, B.; Tatchen, J.; Sanchez-Garcia, E.; Bettinger, H. F. *Angew. Chem., Int. Ed.* **2018,** *57,* 10506–10509. doi:10.1002/anie.201802197
26. Hayashi, H.; Hieda, N.; Yamauchi, M.; Chan, Y. S.; Aratani, N.; Masuo, S.; Yamada, H. *Chem. – Eur. J.* **2020,** *26,* 15079–15083. doi:10.1002/chem.202002155
27. Suzuki, M.; Aotake, T.; Yamaguchi, Y.; Noguchi, N.; Nakano, H.; Nakayama, K.-i.; Yamada, H. *J. Photochem. Photobiol., C* **2014,** *18,* 50–70. doi:10.1016/j.jphotochemrev.2013.10.003
28. Chen, K.-Y.; Hsieh, H.-H.; Wu, C.-C.; Hwang, J.-J.; Chow, T. J. *Chem. Commun.* **2007,** 1065–1067. doi:10.1039/b616511g
29. Watanabe, M.; Chang, Y. J.; Liu, S.-W.; Chao, T.-H.; Goto, K.; Islam, M. M.; Yuan, C.-H.; Tao, Y.-T.; Shinmyozu, T.; Chow, T. J. *Nat. Chem.* **2012,** *4,* 574–578. doi:10.1038/nchem.1381

30. Miyazaki, T.; Watanabe, M.; Matsushima, T.; Chien, C.-T.; Adachi, C.; Sun, S.-S.; Furuta, H.; Chow, T. J. *Chem. – Eur. J.* **2021,** *27,* 10677–10684. doi:10.1002/chem.202100936
31. Jančařík, A.; Levet, G.; Gourdon, A. *Chem. – Eur. J.* **2019,** *25,* 2366–2374. doi:10.1002/chem.201805975
32. Bedel Pereira, E.; Bassaler, J.; Laval, H.; Holec, J.; Monflier, R.; Mesnilgrente, F.; Salvagnac, L.; Daran, E.; Duployer, B.; Tenailleau, C.; Gourdon, A.; Jančařík, A.; Séguy, I. *RSC Adv.* **2022,** *12,* 671–680. doi:10.1039/d1ra07808a
33. Jančařík, A.; Holec, J.; Nagata, Y.; Šámal, M.; Gourdon, A. *Nat. Commun.* **2022,** *13,* 223. doi:10.1038/s41467-021-27809-0
34. Holec, J.; Cogliati, B.; Lawrence, J.; Berdonces-Layunta, A.; Herrero, P.; Nagata, Y.; Banasiewicz, M.; Kozankiewicz, B.; Corso, M.; de Oteyza, D. G.; Jancarik, A.; Gourdon, A. *Angew. Chem., Int. Ed.* **2021,** *60,* 7752–7758. doi:10.1002/anie.202016163
35. Zugermeier, M.; Gruber, M.; Schmid, M.; Klein, B. P.; Ruppenthal, L.; Müller, P.; Einholz, R.; Hieringer, W.; Berndt, R.; Bettinger, H. F.; Gottfried, J. M. *Nanoscale* **2017,** *9,* 12461–12469. doi:10.1039/c7nr04157h
36. Urgel, J. I.; Mishra, S.; Hayashi, H.; Wilhelm, J.; Pignedoli, C. A.; Di Giovannantonio, M.; Widmer, R.; Yamashita, M.; Hieda, N.; Ruffieux, P.; Yamada, H.; Fasel, R. *Nat. Commun.* **2019,** *10,* 861. doi:10.1038/s41467-019-08650-y
37. Vogel, E.; Schubart, R.; Böll, W. A. *Angew. Chem., Int. Ed. Engl.* **1964,** *3,* 510. doi:10.1002/anie.196405101
38. Scott, G. P. *J. Am. Chem. Soc.* **1953,** *75,* 6332–6333. doi:10.1021/ja01120a531
39. Šindelář, K.; Metyšová, J.; Protiva, M. *Collect. Czech. Chem. Commun.* **1969,** *34,* 3801–3810. doi:10.1135/cccc19693801
40. Sashida, H.; Kurahashi, H.; Tsuchiya, T. *J. Chem. Soc., Chem. Commun.* **1991,** 802. doi:10.1039/c39910000802
41. Jansen, H.; Slootweg, J. C.; Lammertsma, K. *Beilstein J. Org. Chem.* **2011,** *7,* 1713–1721. doi:10.3762/bjoc.7.201
42. Kassaee, M. Z.; Musavi, S. M.; Majdi, M.; Cheshmehkani, A.; Motamedi, E.; Aghaee, A. *J. Mol. Struct.: THEOCHEM* **2008,** *848,* 67–73. doi:10.1016/j.theochem.2007.09.012
43. Kassaee, M. Z.; Musavi, S. M.; Majdi, M. *Struct. Chem.* **2009,** *20,* 369–376. doi:10.1007/s11224-008-9396-6
44. Murata, I.; Nakasuji, K. Recent Advances in Thiepin Chemistry. *Organic Chemistry; Topics in Current Chemistry*; Springer: Berlin, Heidelberg, 1981; pp 33–70. doi:10.1007/bfb0037040
45. Gleiter, R.; Krennrich, G.; Cremer, D.; Yamamoto, K.; Murata, I. *J. Am. Chem. Soc.* **1985,** *107,* 6874–6879. doi:10.1021/ja00310a022
46. Shirani, H.; Janosik, T. *J. Org. Chem.* **2007,** *72,* 8984–8986. doi:10.1021/jo701627g
47. Cai, Z.; Zhang, H.; Geng, H.; Liu, Z.; Yang, S.; Luo, H.; Jiang, L.; Peng, Q.; Zhang, G.; Chen, J.; Yi, Y.; Hu, W.; Zhang, D. *Chem. – Eur. J.* **2013,** *19,* 14573–14580. doi:10.1002/chem.201302114
48. Inami, T.; Takahashi, T.; Kurahashi, T.; Matsubara, S. *J. Am. Chem. Soc.* **2019,** *141,* 12541–12544. doi:10.1021/jacs.9b07948
49. Wang, W.; Hanindita, F.; Tanaka, Y.; Ochiai, K.; Sato, H.; Li, Y.; Yasuda, T.; Ito, S. *Angew. Chem., Int. Ed.* **2023,** *62,* e202218176. doi:10.1002/anie.202218176
50. Sashida, H.; Ito, K.; Tsuchiya, T. *Chem. Pharm. Bull.* **1995,** *43,* 19–25. doi:10.1248/cpb.43.19
51. Yasuike, S.; Kiharada, T.; Tsuchiya, T.; Kurita, J. *Chem. Pharm. Bull.* **2003,** *51,* 1283–1288. doi:10.1248/cpb.51.1283
52. Shirani, H.; Janosik, T. *Organometallics* **2008,** *27,* 3960–3963. doi:10.1021/om8003114
53. Maier, D. I. H.; Bezuidenhoudt, B. C. B.; Marais, C. *Beilstein J. Org. Chem.* **2023,** *19,* 700–718. doi:10.3762/bjoc.19.51
54. Guziec, F. S., Jr.; Sanfilippo, L. J. *Tetrahedron* **1988,** *44,* 6241–6285. doi:10.1016/s0040-4020(01)89815-x
55. Taylor, R. J. K. *Chem. Commun.* **1999,** 217–227. doi:10.1039/a806615i
56. Loudon, J. D.; Sloan, A. D. B.; Summers, L. A. *J. Chem. Soc.* **1957,** 3814–3818. doi:10.1039/jr9570003814
57. Hayakawa, S.; Matsuo, K.; Yamada, H.; Fukui, N.; Shinokubo, H. *J. Am. Chem. Soc.* **2020,** *142,* 11663–11668. doi:10.1021/jacs.0c04096
58. Boekelheide, V.; Reingold, I. D.; Tuttle, M. *J. Chem. Soc., Chem. Commun.* **1973,** 406–407. doi:10.1039/c39730000406
59. Givens, R. S.; Olsen, R. J.; Wylie, P. L. *J. Org. Chem.* **1979,** *44,* 1608–1613. doi:10.1021/jo01324a005
60. Christensen, P. R.; Patrick, B. O.; Caron, É.; Wolf, M. O. *Angew. Chem., Int. Ed.* **2013,** *52,* 12946–12950. doi:10.1002/anie.201306236
61. Yuan, J.; Xu, Z.; Wolf, M. O. *Chem. Sci.* **2022,** *13,* 5447–5464. doi:10.1039/d2sc01128j
62. Tanaka, Y.; Matsuo, K.; Yamada, H.; Fukui, N.; Shinokubo, H. *Eur. J. Org. Chem.* **2022,** e202200770. doi:10.1002/ejoc.202200770
63. Song, C.; Swager, T. M. *J. Org. Chem.* **2010,** *75,* 999–1005. doi:10.1021/jo902079j
64. Ming, B.; Yan, C.; Xie, S.; Liu, S.; Ren, Y.; Zong, H.; Chen, W.; Zhou, G. *Chin. J. Chem.* **2023,** *41,* 13–20. doi:10.1002/cjoc.202200518
65. Li, R.; Ma, B.; Li, S.; Lu, C.; An, P. *Chem. Sci.* **2023,** *14,* 8905–8913. doi:10.1039/d3sc02595k
66. Odajima, M.; Fukui, N.; Shinokubo, H. *Org. Lett.* **2023,** *25,* 282–287. doi:10.1021/acs.orglett.2c04173
67. Dobelmann, L.; Parham, A. H.; Büsing, A.; Buchholz, H.; König, B. *RSC Adv.* **2014,** *4,* 60473–60477. doi:10.1039/c4ra10652k
68. Armarego, W. L. F.; Turner, E. E. *J. Chem. Soc.* **1956,** 1665–1670. doi:10.1039/jr9560001665
69. Armarego, W. L. F. *J. Chem. Soc.* **1960,** 433–436. doi:10.1039/jr9600000433
70. Block, E.; Page, J.; Toscano, J. P.; Wang, C.-X.; Zhang, X.; DeOrazio, R.; Guo, C.; Sheridan, R. S.; Towers, G. H. N. *J. Am. Chem. Soc.* **1996,** *118,* 4719–4720. doi:10.1021/ja960589v
71. Schroth, W.; Hintzsche, E.; Jordan, H.; Jende, T.; Spitzner, R.; Thondorf, I. *Tetrahedron* **1997,** *53,* 7509–7528. doi:10.1016/s0040-4020(97)00439-0
72. Yang, X.; Zhang, B.; Zhang, S.; Li, G.; Xu, L.; Wang, Z.; Li, P.; Zhang, Y.; Liu, Z.; He, G. *Org. Lett.* **2019,** *21,* 8285–8289. doi:10.1021/acs.orglett.9b03047
73. Schroth, W.; Hintzsche, E.; Viola, H.; Winkler, R.; Klose, H.; Boese, R.; Kempe, R.; Sieler, J. *Chem. Ber.* **1994,** *127,* 401–408. doi:10.1002/cber.19941270217
74. Okamoto, T.; Kudoh, K.; Wakamiya, A.; Yamaguchi, S. *Org. Lett.* **2005,** *7,* 5301–5304. doi:10.1021/ol0523650
75. Jiang, W.; Zhou, Y.; Geng, H.; Jiang, S.; Yan, S.; Hu, W.; Wang, Z.; Shuai, Z.; Pei, J. *J. Am. Chem. Soc.* **2011,** *133,* 1–3. doi:10.1021/ja107599r
76. Li, X.; Zhu, Y.; Shao, J.; Wang, B.; Zhang, S.; Shao, Y.; Jin, X.; Yao, X.; Fang, R.; Shao, X. *Angew. Chem., Int. Ed.* **2014,** *53,* 535–538. doi:10.1002/anie.201308781
77. Xu, W.; Wang, M.; Ma, Z.; Shan, Z.; Li, C.; Wang, H. *J. Org. Chem.* **2018,** *83,* 12154–12163. doi:10.1021/acs.joc.8b02107

78. Kimura, T.; Ishikawa, Y.; Ogawa, S.; Nishio, T.; Iida, I.; Furukawa, N. *Tetrahedron Lett.* **1992,** *33,* 6355–6358. doi:10.1016/s0040-4039(00)60972-3
79. Grainger, R. S.; Patel, B.; Kariuki, B. M.; Male, L.; Spencer, N. *J. Am. Chem. Soc.* **2011,** *133,* 5843–5852. doi:10.1021/ja108865w
80. Murata, M.; Maeda, S.; Morinaka, Y.; Murata, Y.; Komatsu, K. *J. Am. Chem. Soc.* **2008,** *130,* 15800–15801. doi:10.1021/ja8076846
81. Murata, Y.; Murata, M.; Komatsu, K. *Chem. – Eur. J.* **2003,** *9,* 1600–1609. doi:10.1002/chem.200390184
82. Murata, Y.; Maeda, S.; Murata, M.; Komatsu, K. *J. Am. Chem. Soc.* **2008,** *130,* 6702–6703. doi:10.1021/ja801753m
83. Krüger, J.; Pavliček, N.; Alonso, J. M.; Pérez, D.; Guitián, E.; Lehmann, T.; Cuniberti, G.; Gourdon, A.; Meyer, G.; Gross, L.; Moresco, F.; Peña, D. *ACS Nano* **2016,** *10,* 4538–4542. doi:10.1021/acsnano.6b00505
84. Krüger, J.; Eisenhut, F.; Alonso, J. M.; Lehmann, T.; Guitián, E.; Pérez, D.; Skidin, D.; Gamaleja, F.; Ryndyk, D. A.; Joachim, C.; Peña, D.; Moresco, F.; Cuniberti, G. *Chem. Commun.* **2017,** *53,* 1583–1586. doi:10.1039/c6cc09327b
85. Krüger, J.; García, F.; Eisenhut, F.; Skidin, D.; Alonso, J. M.; Guitián, E.; Pérez, D.; Cuniberti, G.; Moresco, F.; Peña, D. *Angew. Chem., Int. Ed.* **2017,** *56,* 11945–11948. doi:10.1002/anie.201706156
86. Eisenhut, F.; Kühne, T.; García, F.; Fernández, S.; Guitián, E.; Pérez, D.; Trinquier, G.; Cuniberti, G.; Joachim, C.; Peña, D.; Moresco, F. *ACS Nano* **2020,** *14,* 1011–1017. doi:10.1021/acsnano.9b08456

License and Terms

BEILSTEIN JOURNAL OF ORGANIC CHEMISTRY

Enhanced host–guest interaction between [10]cycloparaphenylene ([10]CPP) and [5]CPP by cationic charges

Eiichi Kayahara*, Yoshiyuki Mizuhata and Shigeru Yamago*

Letter

Open Access

Address:
Institute for Chemical Research, Kyoto University, Uji 611-0011, Japan

Email:
Eiichi Kayahara* - kayahara@scl.kyoto-u.ac.jp; Shigeru Yamago* - yamago@scl.kyoto-u.ac.jp

* Corresponding author

Keywords:
charge-transfer; cycloparaphenylene; dication; host–guest chemistry

Beilstein J. Org. Chem. **2024,** *20,* 436–444.
https://doi.org/10.3762/bjoc.20.38

Received: 25 December 2023
Accepted: 14 February 2024
Published: 23 February 2024

This article is part of the thematic issue "Carbon-rich materials: from polyaromatic molecules to fullerenes and other carbon allotropes".

Guest Editor: Y. Yamakoshi

Abstract

A dication of [5]cycloparaphenylene ([5]CPP^{2+}) was selectively encapsulated by neutral [10]CPP to form the shortest double-layer carbon nanotube, [10]CPP⊃[5]CPP^{2+}. While the same host–guest complex consisted of neutral CPPs, [10]CPP⊃[5]CPP, was already reported, the cationic complex showed an about 20 times higher association constant in $(CDCl_2)_2$ at 25 °C (10^3 mol L^{-1}). Electrochemical and photophysical analyses and theoretical calculations suggested the partial electron transfer from [10]CPP to [5]CPP^{2+} in the complex, and this charge-transfer (CT) interaction is most likely the origin of the higher association constant of the dicationic complex than the neutral one.

Introduction

Since the first bottom-up organic synthesis of cycloparaphenylenes (CPPs) [1-7], which are the carbon nanorings with the shortest possible structural constituent of armchair carbon nanotubes (CNTs), a new science of cyclic nanocarbons has emerged through synthesizing new CPP analogs [4-8] and unveiling their unique physical properties, such as size-dependent photophysical [9-15] and redox properties [16-21]. The other, and one of the most exciting, functions of CPPs derived from the ring structure is their host function. After our first report on the selective encapsulation of C_{60} by [10]CPP (the number in the brackets is the number of paraphenylene units in the CPP) (Figure 1a) [22], the concave inner surface of CPPs was found to interact with a variety of molecules with convex surfaces through π–π interactions [23-26] and CH–π interactions [27-30], forming the corresponding host–guest complexes. In addition, the concave outer surface of the CPP also interacts with the convex surface of the CPP (Figure 1b) [31-33], resulting in the formation of the shortest possible double-layer CNTs. Furthermore, Isobe and co-workers also showed that the carbon nanorings with the simplest structural unit of chiral CNTs, such as cyclochrysenylene [34], cyclonaphthylenes [35], and cycloanthanthrenylene [36], are also excellent hosts of fuller-

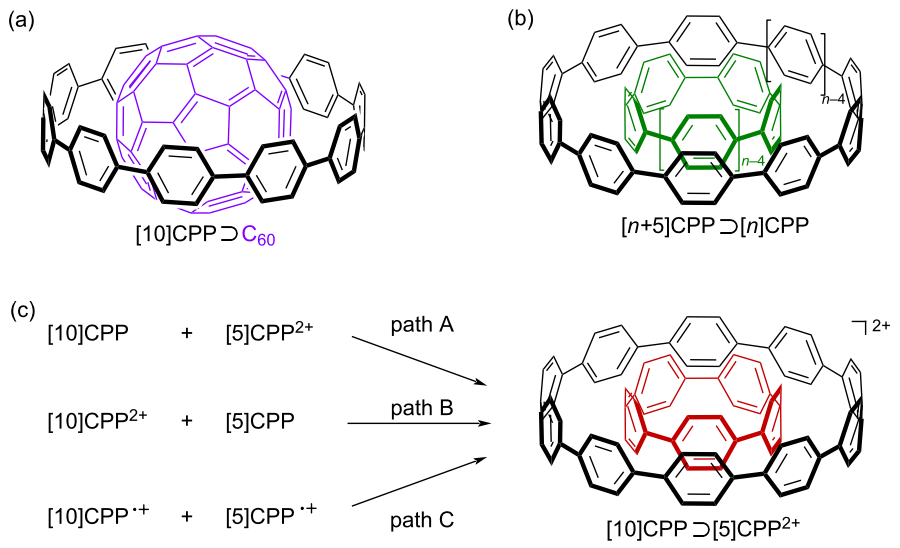

Figure 1: Structures of a) [10]CPP⊃C_{60}, (b) [*n*+5]CPP⊃[*n*]CPP, and (c) [10]CPP⊃[5]CPP^{2+} (this work).

enes with exceptionally high binding constants. These results open up new possibilities for the fabrication of supramolecular structures based on the non-covalent interactions using carbon nanorings [37,38].

Despite the unique structure of the host–guest complexes, however, their electronic structures are not very attractive. This is because the complex formation is driven by van der Waals interactions, and no new electronic states are created by electronic perturbations between the host and the guest, except for a few examples using special fullerenes as guest molecules, i.e. [11]CPP⊃La@C_{82} [39], and [10]CPP⊃Li^+@C_{60} [40], and [10]CPP⊃$(C_{59}N)_2$ [41], or applying high pressure (6 GPa) in the complexation between [9]CPP and C_{60} [42]. In these examples, partial charge transfer (CT) from the CPP host to the guest was observed, but the degree of CT was limited. Furthermore, no clear effects of CT on the physical properties have been reported.

We have already reported that two-electron oxidation of [*n*]CPPs yields dications, [*n*]$CPPs^{2+}$ [17,21,43], which are unusually stable due to the presence of in-plane aromaticity derived from the ring structure [19]. Therefore, we speculated that the CPP dication could be used as a host or a guest to alter the electronic state of the corresponding host–guest complex. Here, we report on the size complementary formation of the host–guest complex between [10]CPP and the dication of [5]CPP, [10]CPP⊃[5]CPP^{2+} (Figure 1c). The association constant, K_a, determined by ^{1}H NMR titration, was about 20 times higher than that of the host–guest complex consisting of neutral [10]CPP and [5]CPP, [10]CPP⊃[5]CPP [31]. While the ^{1}H NMR analysis also supported the closed-shell electronic structure of both the host and the guest, neutral [10]CPP and [5]CPP^{2+}, respectively, a partial CT from the host to the guest was suggested by the photophysical and electrochemical analyses and DFT calculations. Therefore, this CT is most likely the origin of the increased K_a value. We also discuss the charged double-layer structure, as determined by X-ray crystallographic analysis.

Results and Discussion

The size-complementary interaction between CPP^{2+} and neutral CPP was first examined by adding a solution of [5]$CPP^{2+}[B(C_6F_5)_4^-]_2$ in CD_2Cl_2 to a mixture of [8]-, [9]-, [10]-, [11]-, and [12]CPPs in CD_2Cl_2 at 25 °C (Figure 2a). In the ^{1}H NMR spectrum of the resulting mixture, only the signals of [10]CPP and [5]CPP^{2+} shifted downfield by about 0.44 ppm and upfield by about 0.23 ppm, respectively, with peak broadening. The other spectra derived from [8]-, [9]-, [11]-, and [12]CPPs did not change at all. A separate experiment mixing an equimolar amount of [10]CPP and [5]$CPP^{2+}[B(C_6F_5)_4^-]_2$ gave the same result (Figure 2b), indicating a size-complementary interaction between [5]CPP^{2+} and [10]CPP. The same size selectivity was observed for the complex formation between neutral CPPs [31]. As the protons in the ^{1}H NMR of [10]CPP^{2+} and neutral [5]CPP resonate at 4.72 and 7.84 ppm, respectively [21], the observed chemical shifts of the complex indicate that the complex formation occurs between neutral [10]CPP and [5]CPP^{2+} forming [10]CPP⊃[5]CPP^{2+} (Figure 1c, path A) [21]. The absence of signals in the ESR measurements at room temperature also suggests the formation of complexes with a closed-shell electronic structure.

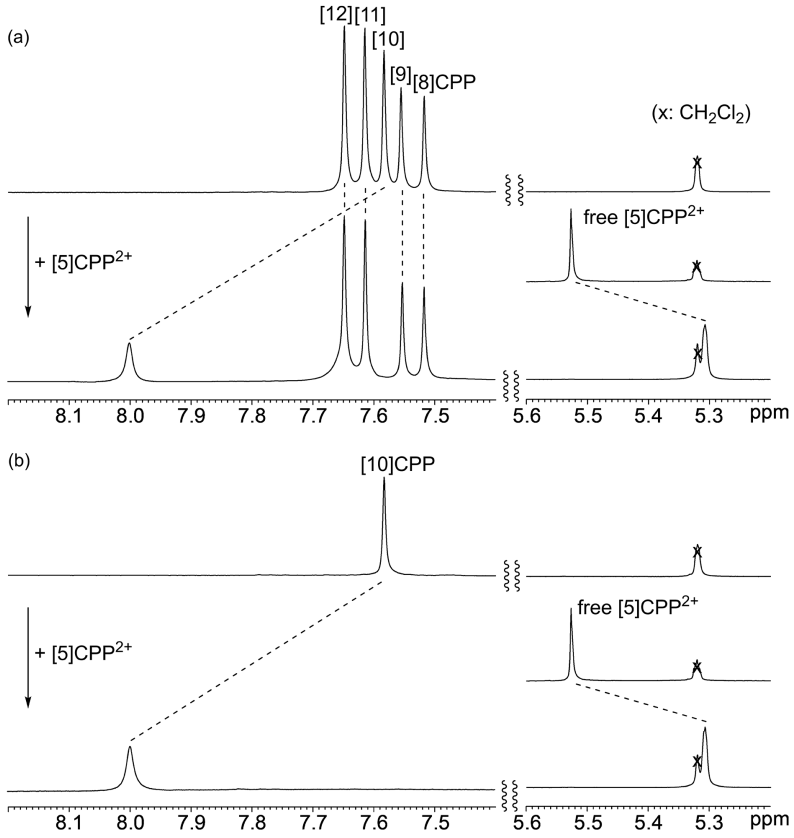

Figure 2: ^{1}H NMR spectra (CD_2Cl_2, 25 °C) of a) a mixture of [8]–[12]CPPs and [5]CPP^{2+}[B(C_6F_5)$_4^-$]$_2$ before and after the addition of [5]CPP^{2+}[B(C_6F_5)$_4^-$]$_2$, and b) [10]CPP and [5]CPP^{2+}[B(C_6F_5)$_4^-$]$_2$ before and after the addition of [5]CPP^{2+}[B(C_6F_5)$_4^-$]$_2$.

The same complex was formed regardless of the oxidation state of the starting CPPs. Thus, when neutral [5]CPP was mixed with [10]CPP^{2+} ($SbCl_6^-$)$_2$, only the signals at 8.0 and 5.3 ppm corresponding to [10]CPP⊃[5]CPP^{2+} were observed (Figure 1c, path B), suggesting a quick electron transfer from [5]CPP to [10]CPP^{2+} has occurred. The same complex was also formed by mixing a 1:1 mixture of radical cations of [5]- and [10]CPP, [5]CPP$^{•+}$ ($SbCl_6^-$) and [10]CPP$^{•+}$ ($SbCl_6^-$), respectively (Figure 1c, path C). The observed results can be explained by two reasons; one is the oxidation potentials of [10]- and [5]CPPs. In sharp contrast to linear π-conjugated molecules, CPPs with shorter conjugations have lower oxidation potentials than larger CPPs, and the first and the second oxidation potentials of [5]CPP are by 0.69 and 0.51 V lower than those of [10]CPP, respectively [43]. The other is the stability of the CPP dications. Since the dications are stabilized by in-plane aromaticity, the single-electron transfer from [10]CPP to [5]CPP^{2+} to form [10]CPP$^{•+}$⊃[5]CPP$^{•+}$ is energetically unfavorable.

The association constant (K_a) between [10]CPP⊃[5]CPP^{2+}[B(C_6F_5)$_4^-$]$_2$ in 1,1,2,2-tetrachloroethane-d_2 (TCE-d_2) at 50 °C was determined to be 1.07×10^3 L·mol^{-1} by ^{1}H NMR titration experiments (see Supporting Information File 1, Figure S1), indicating that the complexation was exergonic with a ΔG = −19 kJ mol^{-1}. This value is about 20 times higher than that of the neutral complex, [10]CPP⊃[5]CPP (K_a = 0.053 × 10^3 L·mol^{-1} in TCE-d_2 at 50 °C, ΔG = −11 kJ mol^{-1}) [31]. The increased K_a is most likely attributed to the ionic interaction caused by the presence of the cationic species, as will be discussed below. To clarify the effect of the polar interaction, the host–guest complexation was studied in a polar solvent, such as nitrobenzene and acetonitrile. However, the low solubility and stability of the dication in polar solvents prevented confirmation of the solvent effect.

To clarify the additional interaction in the complex, the electrochemical analysis of the [10]CPP⊃[5]CPP^{2+}[B(C_6F_5)$_4^-$]$_2$ was examined by using cyclic voltammetry, which was performed in a 1,2-dichloroethane solution of a sample containing 0.10 mol L^{-1} Bu_4N^+ B(C_6F_5)$_4^-$. The cyclic voltammogram of the complex showed one reversible oxidation wave of [10]CPP at 0.92 V versus (vs) ferrocene/ferrocenium couple (Fc/Fc$^+$) (Figure 3a), which was positively shifted by 0.13 V from that of

neutral, free [10]CPP. Upon scanning into the negative direction, two pseudo reversible reduction waves of [5]CPP^{2+} were observed at 0.22 and 0.17 V vs Fc/Fc^{+} (Figure 3b), which were negatively shifted by 0.11 and 0.10 V from that of free [5]CPP^{2+}[B(C$_6$F$_5$)$_4^-$]$_2$. These results suggest the electron density of [10]CPP and [5]CPP^{2+} decreased and increased, respectively, upon complex formation and clearly indicate the partial electron transfer from [10]CPP to [5]CPP^{2+} in the complex.

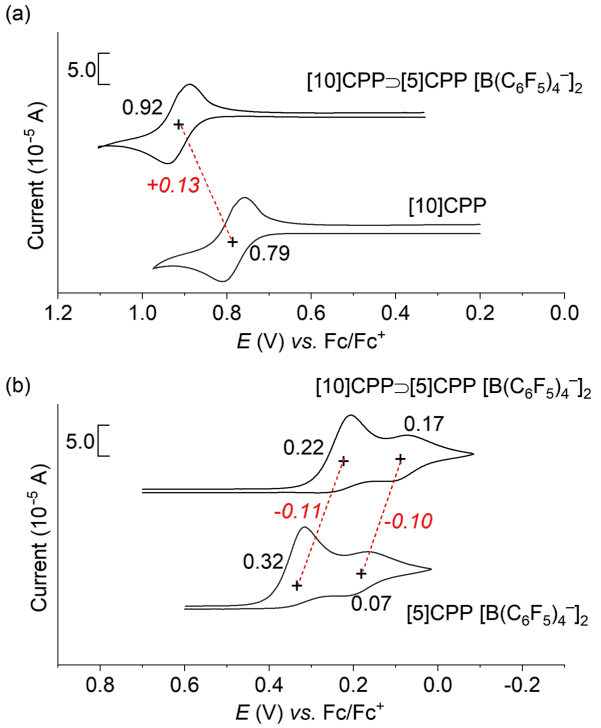

Figure 3: Cyclic voltammograms of [10]CPP⊃[5]CPP^{2+}[B(C$_6$F$_5$)$_4^-$]$_2$, [10]CPP, and [5]CPP^{2+}[B(C$_6$F$_5$)$_4^-$]$_2$ in Bu$_4$N$^+$ B(C$_6$F$_5$)$_4^-$/1,2-dichloroethane upon scanning in (a) positive and (b) negative directions.

The involvement of a CT in the complex was further supported by the UV–vis–NIR absorption spectra. The complex showed several absorption bands in the visible region and characteristic broad absorption bands extending to the NIR region (≈2000 nm) (Figure 4, black line). According to time-dependent density functional theory (DFT) calculations at the ωB97-XD/6-31G* level of theory, the NIR absorption of the most thermodynamically stable complex (see below) can be ascribed to the transition from the HOMO (highest occupied molecular orbital) to the LUMO (lowest unoccupied molecular orbital) with oscillator strengths (f) = 0.0001. As the HOMO and LUMO are selectively localized to [10]CPP and [5]CPP^{2+}, respectively (see below), this transition corresponds to the CT band.

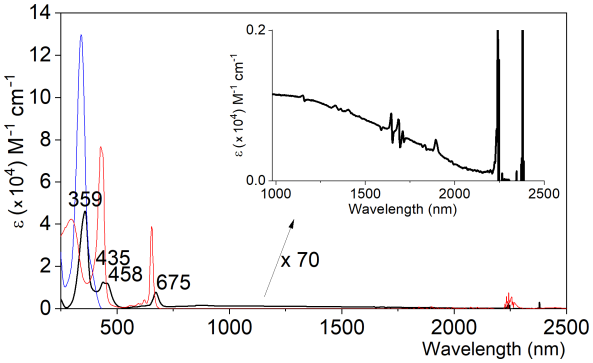

Figure 4: UV–vis–NIR spectra of [10]CPP⊃[5]CPP^{2+}[B(C$_6$F$_5$)$_4^-$]$_2$ (black), [10]CPP (blue), and [5]CPP^{2+}[B(C$_6$F$_5$)$_4^-$]$_2$ (red) in CH$_2$Cl$_2$.

The structure and stability of [10]CPP⊃[5]CPP^{2+} were estimated by DFT calculations at the ωB97-XD/6-31G* level of theory. Three isomeric structures were optimized, of which complex **1**, with two CPPs aligned in parallel, is the most thermodynamically stable (Figure 5a). The other two isomers, **2** and **3** (Figure 5b,c), with two CPPs tilted at 15.6° and 45.5°, are 2.5 and 4.2 kJ mol^{-1} less stable than complex **1**, respectively. The stability among the isomers is low, and the activation energy for isomerization should be very low. Therefore, all isomers are expected to be present in solution when the solvent effect is negligible.

Formation of complex **1** in the gas phase was highly exothermic with ΔG = −222 kJ mol^{-1} at 298.15 K and 1.00 atm, and this value is about two times higher than that of the complex formation of neutral [10]CPP⊃[5]CPP (ΔG = −114 kJ mol^{-1}). Therefore, the same trend of the relative stability between [10]CPP⊃[5]CPP^{2+} and [10]CPP⊃[5]CPP was also observed in the gas phase. The significant increase in relative stability in the gas phase compared to the solution state is likely due to the overestimation of electronic interactions due to CT in the absence of a solvent.

Complex **1** possesses a 5-fold rotational axis through the focal point of the complex, and each paraphenylene unit of [5]CPP^{2+} interacts with that of [10]CPP every other unit (Figure 5a). The interfacial distance between the nearest neighbor centroid of a paraphenylene unit of [5]CPP^{2+} and [10]CPP is 0.365 nm, which is very close to the sum of the van der Waals radii of an sp^2 carbon (0.340 nm) [44]. This mode of interaction is similar to that observed in the complex formed from [10]CPP and C$_{70}$ [24]. In contrast, complex **2** has a less ordered interaction compared to **1**; while each paraphenylene unit of [5]CPP^{2+} interacts with that of [10]CPP every other unit like in **1**, the interfacial distance between the nearest neighbor centroid of a paraphenylene unit is in the range of 0.356–0.379 nm due to the inclina-

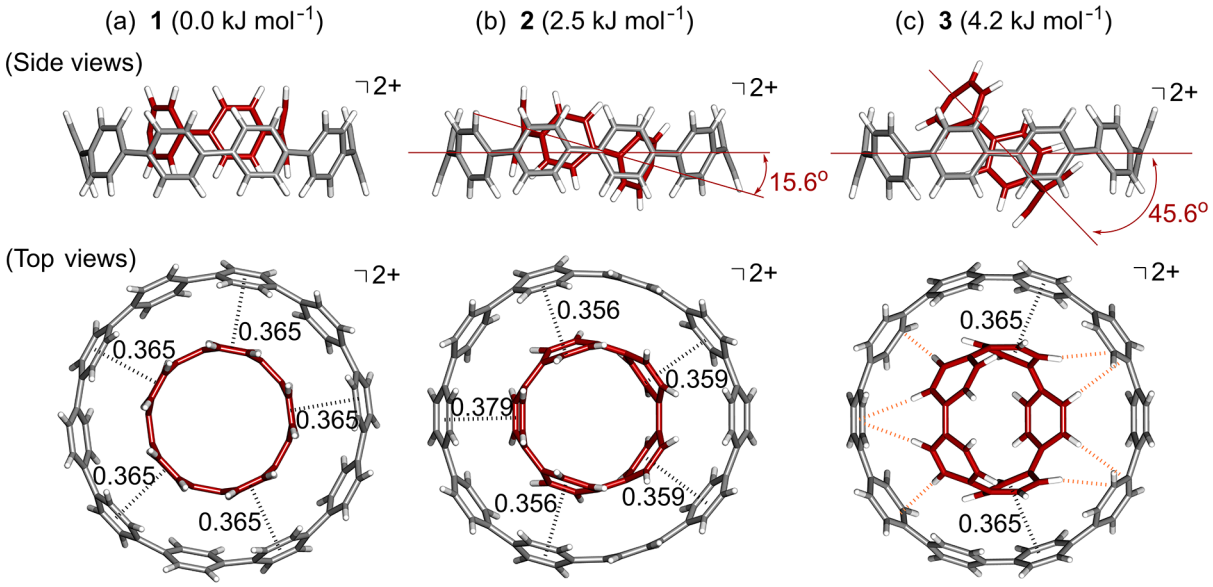

Figure 5: Top and side view of [10]CPP⊃[5]CPP^{2+} complexes a) **1**, b) **2**, and c) **3** obtained by DFT calculation at the ωB97-XD/6-31G(d) level of theory. The distances (nm) between the nearest centroids of a paraphenylene unit of [10]CPP and [5]CPP are shown by the black dotted lines in the top view. The orange dotted lines in the top view of c) show the CH–π interactions between the hydrogen of [5]CPP and the nearest sp^2 carbon of [10]CPP within 0.30 nm.

tion (Figure 5b). Despite the slight structural differences between complexes **1** and **2**, the observed interlayer distances indicate the importance of the π–π interactions in complex formation. In contrast, complex **3** has fewer π–π interactions between [10]CPP and [5]CPP^{2+} than complexes **1** and **2** have. However, several CH–π interactions are observed, as indicated by an orange dotted line (Figure 5c), significantly stabilizing the complex formation. These results confirm the importance of van der Waals interactions for the formation of [10]CPP⊃[5]CPP^{2+}.

Mulliken population analysis indicates 10 to ≈15% electron transfer from the host [10]CPP to the guest [5]CPP^{2+} in complexes **1**, **2**, and **3**. While the extent of the CT in the current complexes is slightly greater than that in [11]CPP⊃La@C_{82} (7%) [39], the results are still far from being sufficient for the formation of a radical ion complex, [10]CPP$^{\bullet+}$⊃[5]CPP$^{\bullet+}$. Indeed, the structural properties, as seen from the bond length alternation, showed that the [10]CPP host and [5]CPP guest of the complex were in good agreement with the neutral [10]CPP and [5]CPP^{2+} (see Supporting Information File 1, Table S3). All these theoretical results agree well with the experimental results.

In the molecular orbital analysis, the HOMO and HOMO−1s are exclusively localized on the [10]CPP host, while the LUMO and LUMO+1 are solely localized on the [5]CPP^{2+} guest (Figure 6). No orbital mixing was observed between [10]CPP and [5]CPP. However, the complex formation significantly lowered the HOMO and HOMO−1 energies derived from [10]CPP and increased the LUMO and LUMO+1 energies derived from [5]CPP^{2+}. Similar changes in orbital energies are also observed for complexes **2** and **3** (see Supporting Information File 1, Figure S2), and the results are attributed to the partial electron transfer from [10]CPP to [5]CPP^{2+} in the complex. These observations also agree well with the change in oxidation and reduction potentials upon complex formation observed in the electrochemical analysis.

The double-layered structure of the complex was unambiguously determined by single-crystal X-ray analysis (Figure 7), which was performed on a crystal obtained by slow evaporation of a solution of [10]CPP⊃[5]CPP^{2+}[$B(C_6F_5)_4^-$]$_2$ in CH_2Cl_2 at −20 °C. In the crystal, [10]CPP encapsulated [5]CPP with an inclination angle of 20.2° (Figure 7a), and the observed structure was similar to the second most stable complex **2** obtained by the calculations. The discrepancy between the most stable calculated structure **1** and the crystalline structure is likely due to crystal packing forces, the presence of the counterion, and the inclusion of solvent molecules. The interfacial distances between the nearest neighbor centroid of a paraphenylene unit of [10]CPP and [5]CPP were in the range of 0.35–0.39 nm (Figure 7b), illustrating the importance of π–π interactions. The Hirshfeld surface of the [5]CPP guest in the complex has a cylindrical structure and is confined to the interior of [10]CPP (Figure 7c) [45,46]. In the d_e mapping (Figure 7d), which shows the distance between the Hirshfeld surface and the contacting

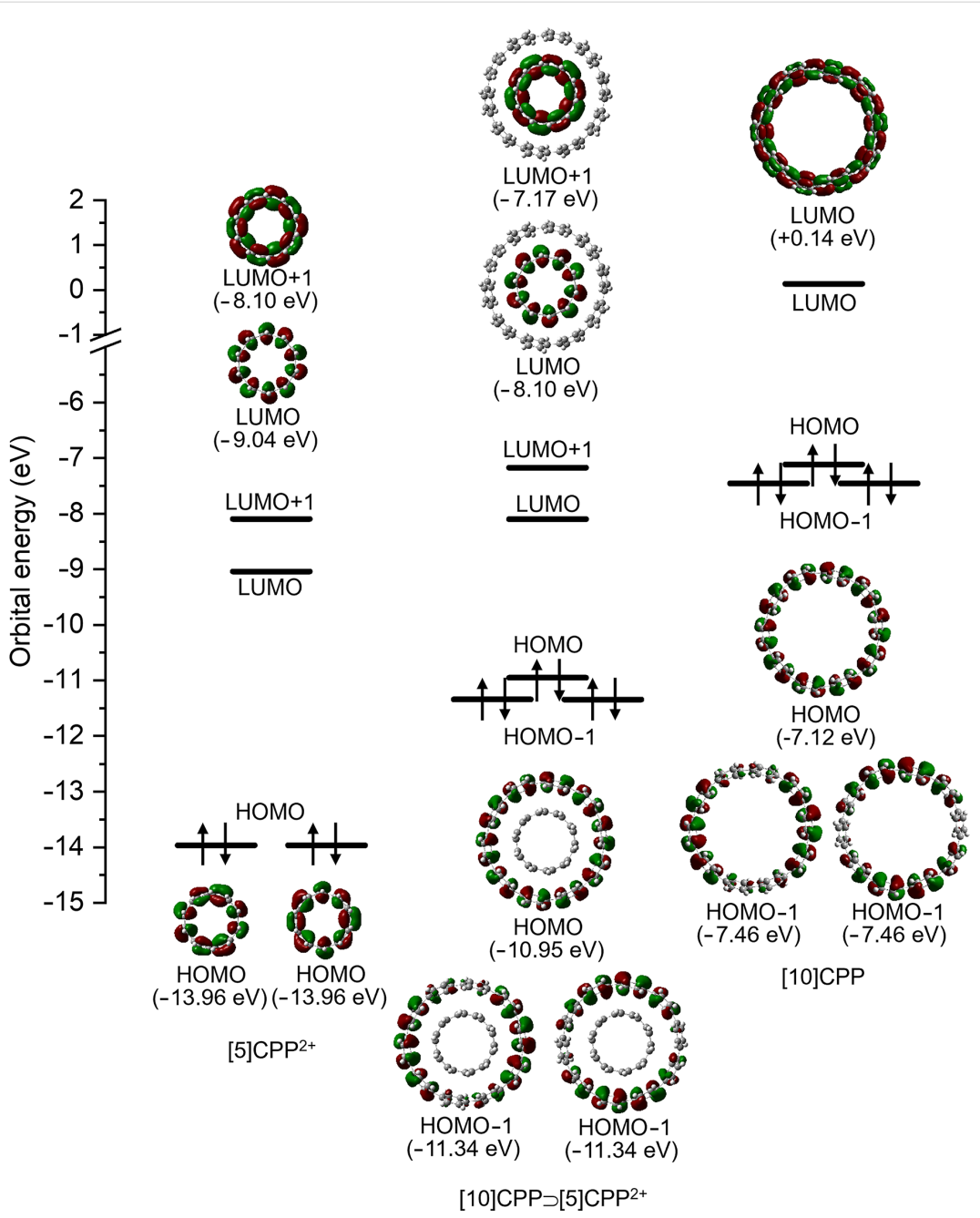

Figure 6: HOMO−1, HOMO, LUMO, and LUMO+1 orbitals of [10]CPP⊃[5]CPP^{2+} (**1**), [5]CPP^{2+}, and [10]CPP.

atoms, most sp^2-hybridzed carbon atoms of the [10]CPP host have short contact with the Hirshfeld surface, as shown in green, despite the tilting of [10]CPP and [5]CPP.

In the crystal packing, there were two orientations, as highlighted in blue and red in Figure 7e. In the packing shown in red, the host–guest complex is alternately stacked with two counterions to forms a one-dimensional (1D) columnar structure in which the complex is tilted at approximately 45° relative to the short axis (Figure 7f and Supporting Information File 1, Figure S3). Furthermore, the tilting of the complex in adjacent columnar structures with respect to the short axis is opposite to each other, as in a herringbone structure, and such columnar structures are parallel to each other through a columnar structure consisting of a host–guest complex in blue and its counterions. On the other hand, the complex in blue forms a 1D columnar structure with alternating counterions (Figure 7g), and each column is parallel to the others. Further-

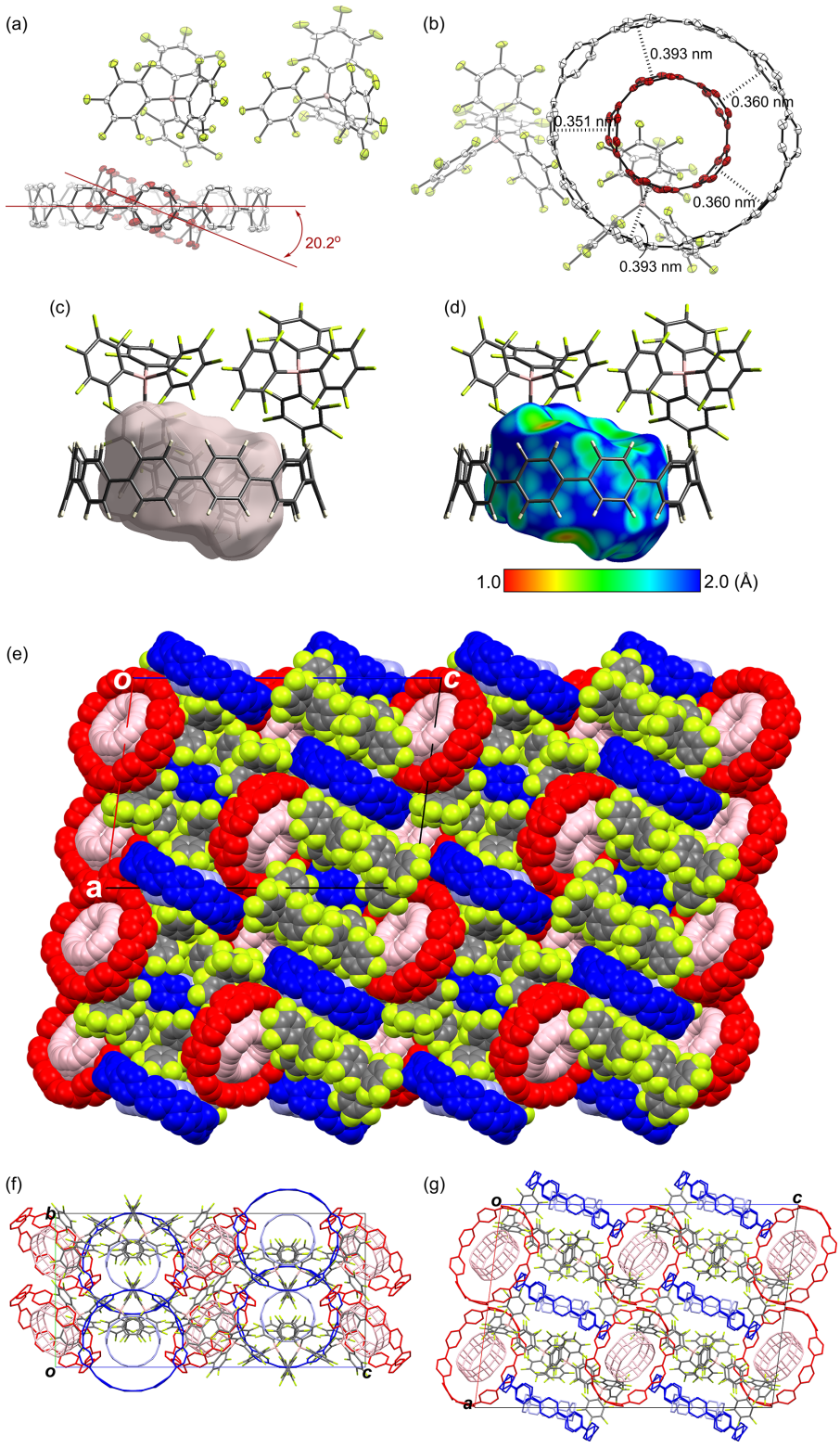

Figure 7: X-ray crystal structure of [10]CPP⊃[5]CPP^{2+}[B(C_6F_5)$_4$]$_2$. a) Side and b) top views of ORTEP drawings. The thermal ellipsoids are scaled at the 50% probability level. All hydrogen atoms and solvent molecules are omitted for clarity. c) Hirshfeld surfaces of [5]CPP in the complex (side images). d) The Hirshfeld surfaces are colored according to the local value of d_e (distance from the surface to the nearest external atomic nuclei), and the colors range from cool (blue, 2.0 Å) to hot (red, 1.0 Å) as d_e decreases. e) Space-filling view of packing structure containing four crystalline unit lattices viewed from the *b*-axis. Wire-flame view of the packing structure of crystalline unit lattices viewed from f) the *a*-axis and g) the *b*-axis.

more, the complex is tilted at approximately 30° relative to the long axis of the unit lattice.

Conclusion

[10]CPP encapsulates [5]CPP^{2+} in a highly size-complementary manner, forming the corresponding host–guest complex. While several electronic structures are possible, such as [10]CPP⊃[5]CPP^{2+}, [10]CPP^{2+}⊃[5]CPP, and [10]CPP$^{•+}$⊃[5]CPP$^{•+}$, experimental and theoretical results reveal the formation of [10]CPP⊃[5]CPP^{2+} with ca. 10% CT from [10]CPP to [5]CPP^{2+}. The association constant of the complex formation is about 20 times higher than that of the complex consisting of neutral [10] and [5]CPPs, and the increased association constant is ascribed to the increase of electronic interactions between the host and the guest. These findings will help tune the electronic properties of the host–guest complexes and design novel materials based on hierarchical supramolecular structures involving cyclic nanocarbons.

Supporting Information

Supporting Information File 1

Experimental procedures and computation data.
[https://www.beilstein-journals.org/bjoc/content/supplementary/1860-5397-20-38-S1.pdf]

Supporting Information File 2

Crystallographic information file for [10]CPP⊃[5]CPP^{2+}[B(C_6F_5)$_4$]$_2$.
[https://www.beilstein-journals.org/bjoc/content/supplementary/1860-5397-20-38-S2.cif]

Acknowledgements

The calculation was supported by the Super Computer Laboratory, Institute for Chemical Research, Kyoto University.

Funding

This work was partly supported by the Japan Society for the Promotion of Science (JSPS) KAKENHI Grant No. 21H05481 (EK), No. 21H05027 (SY), JST FOREST Program Grant No. JPMJFR211M (EK).

Author Contributions

Eiichi Kayahara: conceptualization; formal analysis; funding acquisition; investigation; validation; visualization; writing – original draft. Yoshiyuki Mizuhata: investigation; visualization. Shigeru Yamago: conceptualization; data curation; funding acquisition; project administration; supervision; validation; writing – original draft.

ORCID® iDs

Eiichi Kayahara - https://orcid.org/0000-0003-1663-5273
Yoshiyuki Mizuhata - https://orcid.org/0000-0001-5301-0024
Shigeru Yamago - https://orcid.org/0000-0002-4112-7249

Data Availability Statement

All data that supports the findings of this study is available in the published article and/or the supporting information to this article. The crystal data generated and analyzed during this study is openly available in the Cambridge Crystallographic Data Centre with deposition number 2314282.

References

1. Jasti, R.; Bhattacharjee, J.; Neaton, J. B.; Bertozzi, C. R. *J. Am. Chem. Soc.* **2008,** *130,* 17646–17647. doi:10.1021/ja807126u
2. Takaba, H.; Omachi, H.; Yamamoto, Y.; Bouffard, J.; Itami, K. *Angew. Chem., Int. Ed.* **2009,** *48,* 6112–6116. doi:10.1002/anie.200902617
3. Yamago, S.; Watanabe, Y.; Iwamoto, T. *Angew. Chem., Int. Ed.* **2010,** *49,* 757–759. doi:10.1002/anie.200905659
4. Omachi, H.; Segawa, Y.; Itami, K. *Acc. Chem. Res.* **2012,** *45,* 1378–1389. doi:10.1021/ar300055x
5. Yamago, S.; Kayahara, E.; Iwamoto, T. *Chem. Rec.* **2014,** *14,* 84–100. doi:10.1002/tcr.201300035
6. Golder, M. R.; Jasti, R. *Acc. Chem. Res.* **2015,** *48,* 557–566. doi:10.1021/ar5004253
7. Segawa, Y.; Yagi, A.; Matsui, K.; Itami, K. *Angew. Chem., Int. Ed.* **2016,** *55,* 5136–5158. doi:10.1002/anie.201508384
8. Leonhardt, E. J.; Jasti, R. *Nat. Rev. Chem.* **2019,** *3,* 672–686. doi:10.1038/s41570-019-0140-0
9. Fujitsuka, M.; Cho, D. W.; Iwamoto, T.; Yamago, S.; Majima, T. *Phys. Chem. Chem. Phys.* **2012,** *14,* 14585–14588. doi:10.1039/c2cp42712e
10. Segawa, Y.; Fukazawa, A.; Matsuura, S.; Omachi, H.; Yamaguchi, S.; Irle, S.; Itami, K. *Org. Biomol. Chem.* **2012,** *10,* 5979–5984. doi:10.1039/c2ob25199j
11. Nishihara, T.; Segawa, Y.; Itami, K.; Kanemitsu, Y. *J. Phys. Chem. Lett.* **2012,** *3,* 3125–3128. doi:10.1021/jz3014826
12. Fujitsuka, M.; Iwamoto, T.; Kayahara, E.; Yamago, S.; Majima, T. *ChemPhysChem* **2013,** *14,* 1570–1572. doi:10.1002/cphc.201300144
13. Fujitsuka, M.; Lu, C.; Iwamoto, T.; Kayahara, E.; Yamago, S.; Majima, T. *J. Phys. Chem. A* **2014,** *118,* 4527–4532. doi:10.1021/jp504689q
14. Peña Alvarez, M.; Mayorga Burrezo, P.; Iwamoto, T.; Qiu, L.; Kertesz, M.; Taravillo, M.; Baonza, V. G.; López Navarrete, J. T.; Yamago, S.; Casado, J. *Faraday Discuss.* **2014,** *173,* 157–171. doi:10.1039/c4fd00103f
15. Hines, D. A.; Darzi, E. R.; Jasti, R.; Kamat, P. V. *J. Phys. Chem. A* **2014,** *118,* 1595–1600. doi:10.1021/jp4123562
16. Iwamoto, T.; Watanabe, Y.; Sakamoto, Y.; Suzuki, T.; Yamago, S. *J. Am. Chem. Soc.* **2011,** *133,* 8354–8361. doi:10.1021/ja2020668
17. Kayahara, E.; Kouyama, T.; Kato, T.; Takaya, H.; Yasuda, N.; Yamago, S. *Angew. Chem., Int. Ed.* **2013,** *52,* 13722–13726. doi:10.1002/anie.201306881
18. Fujitsuka, M.; Tojo, S.; Iwamoto, T.; Kayahara, E.; Yamago, S.; Majima, T. *J. Phys. Chem. Lett.* **2014,** *5,* 2302–2305. doi:10.1021/jz5009054

19. Toriumi, N.; Muranaka, A.; Kayahara, E.; Yamago, S.; Uchiyama, M. *J. Am. Chem. Soc.* **2015,** *137,* 82–85. doi:10.1021/ja511320f
20. Talipov, M. R.; Jasti, R.; Rathore, R. *J. Am. Chem. Soc.* **2015,** *137,* 14999–15006. doi:10.1021/jacs.5b09596
21. Kayahara, E.; Kouyama, T.; Kato, T.; Yamago, S. *J. Am. Chem. Soc.* **2016,** *138,* 338–344. doi:10.1021/jacs.5b10855
22. Iwamoto, T.; Watanabe, Y.; Sadahiro, T.; Haino, T.; Yamago, S. *Angew. Chem., Int. Ed.* **2011,** *50,* 8342–8344. doi:10.1002/anie.201102302
23. Xia, J.; Bacon, J. W.; Jasti, R. *Chem. Sci.* **2012,** *3,* 3018–3021. doi:10.1039/c2sc20719b
24. Iwamoto, T.; Watanabe, Y.; Takaya, H.; Haino, T.; Yasuda, N.; Yamago, S. *Chem. – Eur. J.* **2013,** *19,* 14061–14068. doi:10.1002/chem.201302694
25. Xu, Y.; Kaur, R.; Wang, B.; Minameyer, M. B.; Gsänger, S.; Meyer, B.; Drewello, T.; Guldi, D. M.; von Delius, M. *J. Am. Chem. Soc.* **2018,** *140,* 13413–13420. doi:10.1021/jacs.8b08244
26. Huang, Q.; Zhuang, G.; Jia, H.; Qian, M.; Cui, S.; Yang, S.; Du, P. *Angew. Chem., Int. Ed.* **2019,** *58,* 6244–6249. doi:10.1002/anie.201900084
27. Matsuki, H.; Okubo, K.; Takaki, Y.; Niihori, Y.; Mitsui, M.; Kayahara, E.; Yamago, S.; Kobayashi, K. *Angew. Chem., Int. Ed.* **2021,** *60,* 998–1003. doi:10.1002/anie.202012120
28. Adachi, S.; Shibasaki, M.; Kumagai, N. *Nat. Commun.* **2019,** *10,* 3820. doi:10.1038/s41467-019-11818-1
29. Kwon, H.; Newell, B. S.; Bruns, C. J. *Nanoscale* **2022,** *14,* 14276–14285. doi:10.1039/d2nr03852h
30. Kwon, H.; Bruns, C. J. *Nano Res.* **2022,** *15,* 5545–5555. doi:10.1007/s12274-022-4145-5
31. Hashimoto, S.; Iwamoto, T.; Kurachi, D.; Kayahara, E.; Yamago, S. *ChemPlusChem* **2017,** *82,* 1015–1020. doi:10.1002/cplu.201700097
32. Hashimoto, S.; Kayahara, E.; Mizuhata, Y.; Tokitoh, N.; Takeuchi, K.; Ozawa, F.; Yamago, S. *Org. Lett.* **2018,** *20,* 5973–5976. doi:10.1021/acs.orglett.8b02715
33. Zhao, C.; Liu, F.; Feng, L.; Nie, M.; Lu, Y.; Zhang, J.; Wang, C.; Wang, T. *Nanoscale* **2021,** *13,* 4880–4886. doi:10.1039/d0nr08931a
34. Isobe, H.; Hitosugi, S.; Yamasaki, T.; Iizuka, R. *Chem. Sci.* **2013,** *4,* 1293–1297. doi:10.1039/c3sc22181d
35. Sun, Z.; Mio, T.; Okada, T.; Matsuno, T.; Sato, S.; Kono, H.; Isobe, H. *Angew. Chem., Int. Ed.* **2019,** *58,* 2040–2044. doi:10.1002/anie.201812771
36. Matsuno, T.; Sato, S.; Iizuka, R.; Isobe, H. *Chem. Sci.* **2015,** *6,* 909–916. doi:10.1039/c4sc02812k
37. Xu, Y.; von Delius, M. *Angew. Chem., Int. Ed.* **2020,** *59,* 559–573. doi:10.1002/anie.201906069
38. Matsuno, T.; Isobe, H. *Bull. Chem. Soc. Jpn.* **2023,** *96,* 406–419. doi:10.1246/bcsj.20230052
39. Iwamoto, T.; Slanina, Z.; Mizorogi, N.; Guo, J.; Akasaka, T.; Nagase, S.; Takaya, H.; Yasuda, N.; Kato, T.; Yamago, S. *Chem. – Eur. J.* **2014,** *20,* 14403–14409. doi:10.1002/chem.201403879
40. Nakanishi, Y.; Omachi, H.; Matsuura, S.; Miyata, Y.; Kitaura, R.; Segawa, Y.; Itami, K.; Shinohara, H. *Angew. Chem., Int. Ed.* **2014,** *53,* 3102–3106. doi:10.1002/anie.201311268
41. Rio, J.; Beeck, S.; Rotas, G.; Ahles, S.; Jacquemin, D.; Tagmatarchis, N.; Ewels, C.; Wegner, H. A. *Angew. Chem., Int. Ed.* **2018,** *57,* 6930–6934. doi:10.1002/anie.201713197
42. Alvarez, M. P.; Burrezo, P. M.; Kertesz, M.; Iwamoto, T.; Yamago, S.; Xia, J.; Jasti, R.; Navarrete, J. T. L.; Taravillo, M.; Baonza, V. G.; Casado, J. *Angew. Chem., Int. Ed.* **2014,** *53,* 7033–7037. doi:10.1002/anie.201400719
43. Kayahara, E.; Fukayama, K.; Nishinaga, T.; Yamago, S. *Chem. – Asian J.* **2016,** *11,* 1793–1797. doi:10.1002/asia.201600582
44. Bondi, A. *J. Phys. Chem.* **1964,** *68,* 441–451. doi:10.1021/j100785a001
45. Spackman, M. A.; Jayatilaka, D. *CrystEngComm* **2009,** *11,* 19–32. doi:10.1039/b818330a
46. Spackman, P. R.; Turner, M. J.; McKinnon, J. J.; Wolff, S. K.; Grimwood, D. J.; Jayatilaka, D.; Spackman, M. A. *J. Appl. Crystallogr.* **2021,** *54,* 1006–1011. doi:10.1107/s1600576721002910

License and Terms

BEILSTEIN JOURNAL OF ORGANIC CHEMISTRY

Possible bi-stable structures of pyrenebutanoic acid-linked protein molecules adsorbed on graphene: theoretical study

Yasuhiro Oishi, Motoharu Kitatani and Koichi Kusakabe*

Full Research Paper

Open Access

Address:
Graduate School of Science, University of Hyogo, Kamigori, Hyogo 678-1297, Japan

Email:
Koichi Kusakabe* - kusakabe@sci.u-hyogo.ac.jp

* Corresponding author

Keywords:
biosensor; DFT; PASE; protein; surface adsorption

Beilstein J. Org. Chem. **2024,** *20,* 570–577.
https://doi.org/10.3762/bjoc.20.49

Received: 09 December 2023
Accepted: 19 February 2024
Published: 11 March 2024

This article is part of the thematic issue "Carbon-rich materials: from polyaromatic molecules to fullerenes and other carbon allotropes".

Guest Editor: Y. Yamakoshi

Abstract

We theoretically analyze possible multiple conformations of protein molecules immobilized by 1-pyrenebutanoic acid succinimidyl ester (PASE) linkers on graphene. The activation barrier between two bi-stable conformations exhibited by PASE is confirmed to be based on the steric hindrance effect between a hydrogen on the pyrene group and a hydrogen on the alkyl group of this molecule. Even after the protein is supplemented, this steric hindrance effect remains if the local structure of the linker consisting of an alkyl group and a pyrene group is maintained. Therefore, it is likely that the kinetic behavior of a protein immobilized with a single PASE linker exhibits an activation barrier-type energy surface between the bi-stable conformations on graphene. We discuss the expected protein sensors when this type of energy surface appears and provide a guideline for improving the sensitivity, especially as an oscillator-type biosensor.

Introduction

Consideration of the atomic-scale motion of molecules based on nanoscience can lead to a better understanding of the behavior of target biomaterials and improve the sensitivity of specific dynamical systems, such as biosensors. In this study, we investigate the behavior of proteins immobilized with linker molecules on graphene substrates. It is known that graphene may not easily adsorb proteins [1]. On the other hand, proteins can be immobilized on graphene by using appropriate linker molecules, such as 1-pyrenebutanoic acid succinimidyl ester (PASE). Actually, pyrene and its derivatives have been demonstrated to form stable bindings to carbon materials [2,3]. The properties and characteristics of these linker molecules are keys

not only to the purpose of protein immobilization, but also to the behavior of the entire biosensor system.

In oscillator-based biosensors, further adsorption on the sensor, such as viruses using antigen/antibody reactions, may be detected via elastic-wave measurements. For this purpose, the antibody protein must first be immobilized on graphene. The antibody that specifically reacts with the target antigen is immobilized onto a graphene surface via the PASE linker. After that, the antigen is injected on sensor chips and specifically binds to the antibody. The antigen is then detected by observing the change in the vibrational frequency before and after the injection of the antigen.

The immobilization of a protein using a PASE linker on carbon nanotube [1], graphite [4], and graphene [5] has been reported. The adsorption of PASE has been considered to mainly come from the pyrene fragment, which forms π–π stacking on these graphitic carbon materials [6-8].

The sensitivity of the oscillator-based sensor depends on the structure of the linker molecule. Therefore, understanding the adsorption mechanism of the PASE linker on graphene and identifying characteristic conformations of the adsorbed molecules are of great importance. Recently, a research group including two of the present authors theoretically investigated the adsorption structure of PASE [9], revealing that PASE on graphene has a stable configuration (conformation 1) in a straight form on graphene. There is at least one metastable bent configuration (conformation 2) on the potential energy surface. Besides, the reaction barrier of the conformational change of the PASE was determined.

In this paper, we further examine a reaction pathway on the adiabatic potential energy surface that connects these conformations caused by the deformation of the PASE linker. The reaction pathway for the conformational change of the PASE itself was found to have a reaction activation barrier [9]. First, we identify that the origin of the barrier is the steric hindrance effect between two hydrogen atoms in the molecule.

A discussion on how the activation barrier between possible conformations of a protein immobilized on graphene by linkers appears is also provided. We consider the adsorption of the linker molecule forming a bond with a protein, and derive the sufficient conditions for the adiabatic potential energy surface to have an activation barrier.

The reaction pathway having an activation barrier has an advantage in the detection of adsorbed molecules using elastic wave measurements. We explore the conditions under which this advantage can be expected for proteins immobilized on graphene. As a result, we propose a strategy for improving the accuracy of the sensing process in elastic wave measurement sensors through antigen/antibody reactions.

Results and Discussion

PASE and PASE-derivatives on graphene

Among pyrene derivatives, PASE is widely used as a linker to connect carbon materials and proteins (Figure 1a) [1,4,5]. The PASE linker and a certain protein can be connected through a dehydration condensation reaction so that the succinimidyl ester group is replaced by an amido group with a protein (Figure 1b). This dehydration-condensed linker with the protein may be used to immobilize proteins onto graphene. Since the connecting linker becomes a pyrenebutanoic acid derivative (PBA), we will call them PBA-linked molecules. The adsorption of such molecules on graphene is known to happen by a mechanism similar to the adsorption of PASE on graphene [3,4].

The protein and pyrene are connected via an alkyl chain. The atomic configuration of this alkyl chain is believed not to be largely affected by the substitution of the succinimidyl group with an amino group. On the other hand, proteins alone do not readily form adsorbed structures on graphene [1]. Therefore, the pyrene moiety is bound to graphene, and at the same time, the protein is supplemented by a dehydration-condensed linker with the protein.

As introduced, on graphene, PASE is found to be straight as the most stable conformation (conformation1 in Figure 1c) [9]. On the potential energy surface, a curved conformation (conformation 2 in Figure 1d) exists. Our previous results suggested that conformation 2 is a metastable state. The relative stability of these conformations is known to vary depending on the surrounding environment, e.g., solvents and solutes [9].

Actually, the presence of solutes consisting of water and proteins improves the stability of conformation 2. This stabilization is explained partly by the formation of hydrogen bonds between water molecules and PASE. Conformation 2 increases the number of sites where hydrogen bonds can form with water molecules because the chain portion of PASE turns upward. Therefore, the stabilization energy of hydrogen-bond formation is greater in conformation 2 than in conformation 1.

To improve the stability of conformation 2, hydration effects by electrostatic interactions between PASE and the solvent are also important. A selective hydration of the polar moiety while keeping the pyrene moiety stable can relatively strengthen the stability of conformation 2. Thus, as the polarity of the solvent

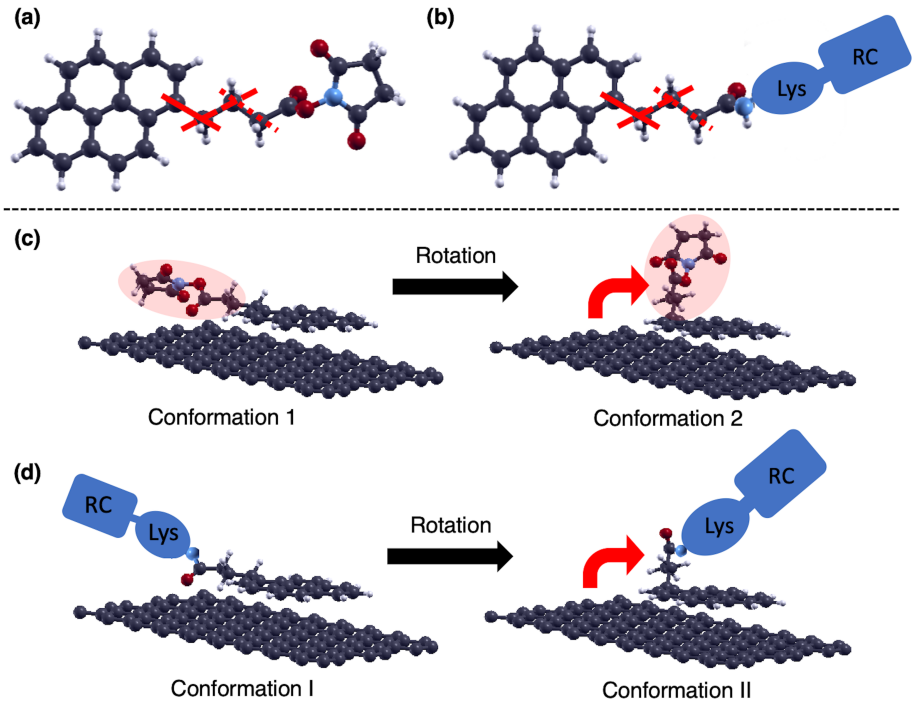

Figure 1: (a) Molecular structure of 1-pyrenebutanoic acid succinimidyl ester (PASE). The black, white, red, and blue balls represent C, H, O, and N atoms, respectively. The solid, broken, and dotted red lines represent the rotation axis. Atomic geometry is visualized by Xcrysden [10] throughout this paper. (b) Schematic diagram of the dehydration-condensation structure of a hypothetical protein and PASE. Lys indicates lysine, and RC is the active center of the antigen/antibody reaction. (c) Structures of PASE linker on graphene for conformation 1 and 2, respectively [9]. (d) Schematic PBA-linked molecular structures on graphene for conformation I and II, respectively.

increases, the probability of conformation 2 appearance is expected to increase.

Mechanism of bi-stability in PASE on graphene

Conformations of PASE are interconverted by mutual transition when the molecule is twisted around one of the carbon–carbon single bonds in the alkyl chain. The rotational motion connecting conformation 1 and conformation 2 happens around the single bond indicated by the solid red line in Figure 1a. The results of the nudged elastic band calculations show that the energy difference between the conformations is about 0.35 eV and the activation barrier on the path is about 0.55 eV (Figure 2) [9]. We will refer to the pathway on the potential energy surface with such an activation barrier as an activation barrier-type pathway.

The pathway connecting conformations 1 and 2 appears as a torsion of the alkyl chain around the carbon–carbon single bond, as indicated by the solid red line in Figure 1a. This is a kind of rotational motion. We determined the dihedral angles formed by the four carbon atoms connected by the red line in Figure 3, and the values of dihedral angles for conformations 1, 2, and the conformation at the activation barrier top are collected in Table 1. From these values, we can interpret the torsion as an approximate rotation. We call the rotations 0, $\pi/3$, and $2\pi/3$ as an approximation, where conformation 1 corresponds to a 0 rotation, conformation 2 a $2\pi/3$ rotation, and the conformation at the activation barrier top a $\pi/3$ rotation, respectively.

To confirm the origin of the activation barrier that appears between conformation 1 and 2, we discuss the structural features of the activation barrier in detail. Figure 3 shows the structure at the activation barrier top. Two hydrogen atoms connected by the green line are characteristically close to each other. One hydrogen is on the pyrene skeleton and the other is on the alkyl chain. The distance between these hydrogens is close, with about 1.8 Å (Table 1). If we compare this distance with the distance between the same hydrogen pairs in conformation 1 and conformation 2, we can see that 1.8 Å is indeed very short compared with that for the others (about 2.2 Å). Therefore, we conclude that a local steric hindrance occurs at the activation barrier.

This steric hindrance effect is analogous to the well-known steric hindrance effect of the rotation around the C–C bond in ethane. Indeed, on the graphene surface, the possible conforma-

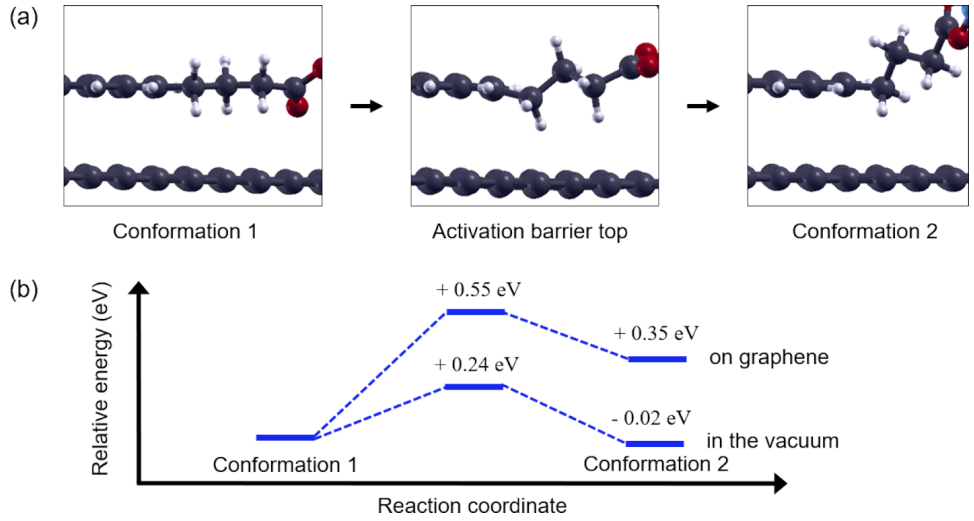

Figure 2: (a) Local structures around the butyl chain in conformation 1, the structure at activation barrier top, and conformation 2 of PASE. (b) Relative energies of PASE in a vacuum are compared to those of reported values for PASE on graphene for each conformation [9]. The energy of conformation 1 is taken as an origin.

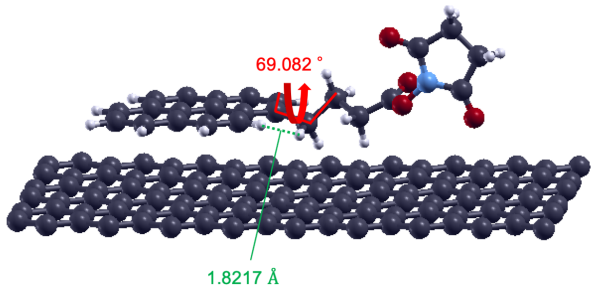

Figure 3: Structure of PASE on graphene at the activation barrier top [9]. Detailed values of the torsion angle and the distance between hydrogen atoms reveal appearance of a steric hindrance effect.

Table 1: The dihedral angles formed by the four carbon atoms connected by the red line in Figure 3, and the distance between hydrogen atoms connected by the green line in Figure 3, for conformation 1, 2, and the conformation at the activation barrier top, respectively.

Conformation	Dihedral angle [degree]	Distance between H atoms [Å]
conformation 1	3.244	2.2443
activation barrier top	69.082	1.8217
conformation 2	107.601	2.1785

tions resulting from the rotation are effectively limited to conformation 2, due, in part, to the restricted direction of rotation. In this case, the activation barrier is created by the proximity of two hydrogen atoms.

Interpretation of the steric hindrance in the molecule is certified by looking at an activation barrier caused by the rotational motion of isolated PASE. In Figure 2b, we added an estimation of the energy pathway of isolated PASE. The barrier height is around 0.2 eV. At the top of the barrier, the proximity of corresponding two hydrogen atoms happens. A reason for a higher barrier of PASE on graphene than for the isolated one is a larger exothermic adsorption energy of conformation 1 (1.63 eV), than that of conformation 2, which is about 1.28 eV. The stabilization of conformation 1 partly comes from interaction between the succinimidyl ester part and graphene.

There are other C–C single bonds in the alkyl chain, such as those shown by the dashed and dotted lines in Figure 1a. Rotations around each bond can also happen and we expect similar steric hindrance effects to appear.

Mechanical properties of PBA-linked molecular structure on graphene

Here, we discuss possible conformations of the PBA-linked molecule. Would a similar activation barrier-type potential energy surface be expected to appear in the case of succinimide substitutions by proteins? To answer this question, we consider imide substitutions extensively. In principle, if the effect of substitution only provides a weak perturbation, the potential energy surface is only slightly changed and the barrier is maintained.

A substitution effect that does not effectively change the potential energy surface is isotopic substitution. In fact, the adiabatic

potential surface defined for a hypothetical motion at the absolute zero is not changed by a change in nuclear mass. Even in density functional theory calculations, for example, the adiabatic potential energy surface, defined as the Born–Oppenheimer surface, is invariant for substitution between isotopes of carbon. This is an example of the weak perturbation.

In substitutions where the mass effect can be regarded as the predominant effect, it is safe to assume that similar steric hindrance effects appear when rotation around the alkyl chain occurs. Such an assumption may not be valid when substitutional binding of the linker to the protein causes some effects to the extent which rotation is not defined, such as a strong chemical bond change, a conformational change around the alkyl chain, or a distortion effect appearing in the adsorption structure of the linker itself. Those effects are not represented by mass substitution.

Thus, we suppose that a substitution occurs to the extent which rotational motion around a C–C single bond in the alkyl chain is defined. We assume that this is a case that can be treated as a weak perturbation that manifests itself as a mass effect. Then, two (meta-)stable conformations would appear, one with the protein-containing part linearly lying on graphene (conformation I), and the other with the conformation resulting from rotation at the alkyl chain (conformation II), as shown in Figure 1d. Rotational motion at the alkyl chain inevitably involves steric hindrance effects around the C–C bond. In particular, for motions corresponding to rotations around the C–C bond in PASE represented by the solid red line in Figure 1a and b, the magnitude of the activation barrier is expected to be close to that in PASE. This is expected to be the case since a protein weakly bound to the carbon graphitic network can be supplemented onto graphene only by linkers as PASE, which has often been observed experimentally [1]. This type of proteins is weakly coupled to graphene. It can be concluded that except for bulky structures that allow multiple binding on graphene by several linkers, the above cases will be of a weakly perturbed nature when making a single link for protein capture.

Discussion on strategy for improving biosensors

The vibrational properties of elastic waves, such as phase and amplitude, are known to be highly sensitive to the mass of adsorbed materials on multilayered graphene. Recently, a biosensor that detects target antigens by elastic wave measurement has been developed [11,12], using the method of immobilizing an antibody protein on graphitic material by a linker. The target antigen is introduced onto the sensor chips through antibody/antigen reaction. The present study is concerned with the mechanical deformation of the linker molecule. The mechanical properties of the rotational motion are almost the same whether modelled in single-layer graphene or in multilayer graphene.

Graphene has been considered as an ideal material for the platform of biosensors [13-23], benefiting from its excellent properties such as large detection area and high thermal conductivity [14,24,25]. Various biosensors have already been developed, many of which require immobilization of antibody proteins on graphene surface. Therefore, protein capture by linkers is used in a relatively large number of sensors.

In the elastic wave measurement system, elastic waves are generated by laser irradiation and their responses are observed. The elastic wave is excited by a pump light, and the response of the substrate is observed via the probe light. The refractive index of metallic substrates such as graphene may change due to the arrival of elastic waves, and this change can be observed by detecting the reflected light of the probe light. For such laser-based biosensors, graphene's conductivity can provide a unique advantage. In fact, the conductivity of multilayered graphene is highly anisotropic. Therefore, the use of multilayer graphene avoids the burning of biomaterials by lasers irradiated from the backside of the substrate.

Here, we will see how the sensitivity of this sensor can be improved when there is such rotational motion of the linked molecules adsorbed on graphene. There are two steps improved effectively by our strategy, i.e., i) creation of PBA-linked molecular structures densely on graphene, and ii) enhancement of the antigen/antibody reaction.

As already mentioned, the stability of conformation 2 of PASE is improved in solution. When the energies of two conformations come close, the activation barrier is expected to be lowered. This tendency holds in the result of Figure 2b. When a PBA-linked molecule is used, the relative energy of conformation II to that of conformation I can be better suited using our strategy.

This stabilization is explained partly by the formation of hydrogen bonds between water molecules and PASE. As in the case of PASE, the chain portion of the PBA-linked molecule turns upward, increasing the number of sites that can form hydrogen bonds with water molecules in conformation II. Therefore, the formation of hydrogen bonds can stabilize conformation II relatively more strongly than conformation I. The hydration effect also improves the stability of conformation II. Thus, as the polarity of the solvent increases, the probability of the appearance of conformation II is expected to increase. Then, conditions of the temperature and the external pressure of gases have to be chosen properly, too. We need to keep the pyrene part

stable in the whole procedures while activating the rotational motion.

Antigen/antibody reactions occur at the active center in the protein portion. Therefore, the reaction at this active center should be more activated at the stage of contact with the antigen. In a relatively large number of cases, specimens such as viruses are collected in a captured state in a solvent. The specimen is introduced onto a graphene substrate linked with a protein prepared as a sensor.

Therefore, the rotational motion at the linker portion should be more active in a solution consisting of a solvent having higher polarity, and this will lead to an increase in the probability that the active center of the antigen/antibody reaction reacts with the antigen. To realize a good temperature condition, the barrier height should be close to or even less than 0.3 eV. Reducing the barrier height may be achieved by optimizing the solution to achieve nearly equal stability in between two conformations. Selection of a solute with a solvent, e.g., those considered in reference [9] can be a solution. Therefore, it is desirable to select the solvent and temperature conditions so that the probability of appearance of conformation II increases as well as conformation 2 in the protein capture step.

On the other hand, at the time of sensing, the proteins and sample antigens bound by the linker should be strongly bound on the graphene surface. This makes it easier to observe the increased mass by generating a reflected wave with a strong amplitude relative to the incident elastic wave. Therefore, it is advisable to adjust the protein portion containing the supplemented antibody to be on the graphene surface corresponding to conformation I by evaporating the solvent or by changing the temperature and gas pressure conditions. To convert all reacted sites in the planer conformation I at the detection stage, we may dry the sensor system by controlling the external gas pressure.

Here, we mention another merit that a pyrene derivative has for another type of biosensor. In immobilizing proteins on graphene, a pyrene derivative has another merit: non-covalent functionalization, i.e., weaker in bonding with graphene than covalent one for functionalization. Actually, widely employed covalent functionalization may not be suitable for a special purpose [26]. This approach is known to have an undesirable effect of disturbing the electronic properties of graphene [15]. On the other hand, in non-covalent functionalization, the electronic properties of graphene can be preserved [27-29]. Therefore, the PASE linker and its properties may be relevant for another type of the electronic sensing strategy, such as field effect transistor-based biosensors.

Conclusion

We discussed how an activation barrier appears on the potential energy surface in PASE adsorbed on graphene. The conformational change between two bi-stable PASE structures can be regarded as rotational motion around a C–C bond in the alkyl chain. An origin of an activation barrier is the steric hindrance coming from the proximity of a hydrogen on the pyrene to that on the alkyl group.

We also considered the state after a protein is supplemented, and discussed how a similar potential energy surface to that in PASE is expected. If the supplementation of protein can be regarded as a weak perturbation, the rotational motion is expected to remain and the activation barrier is maintained. Then, the probability of the appearance of conformation 2 relative to conformation 1 and vice versa can be adjusted by arranging the environment such as temperature and solvent.

We provided a guideline for an improvement of a biosensing device. In oscillator-type biosensors, by arranging an appropriate surrounding environment, an improvement of the sensitivity is expected.

Computational Method

The density functional theory (DFT) calculation determined stable atomic configurations of conformation 1 and 2 of PASE on graphene. In the DFT calculation realized by the PWscf code of Quantum ESPRESSO [30-32], the DFT-D3 correlation [33] together with PBEsol functional [34] for the exchange-correlation functional described van der Waals interaction between graphene and pyrene fragment in PASE. Ultrasoft pseudopotentials [35] with the energy cutoff of 35 (350) Ry for the expansion of wavefunction (charge density) described the electron-nuclear interaction. Using the $2 \times 4 \times 1$ k-point mesh of Monkhorst–Pack [36], the Brillouin zone sampling was safely performed. Additional details of calculation conditions may be found in a previous paper [9].

After the structural optimization calculation of the (meta)stable conformations until the Hellman–Feynman force acting on each atom was less than 10^{-6} Ry/Bohr, the nudged elastic band method determined the minimum energy pathway. Intermediate images created by linear interpolation between conformation 1 and 2 were optimized so that each image had lower energy while adequate spaces between neighboring images on the energy surface were kept.

To explore the origin of the activation barrier, we analyzed the structure of the saddle point on the minimum energy pathway. Having conformation 1, 2, and the conformation at the saddle

point, we measured the dihedral angles and the distance between two hydrogen atoms using Xcrysden [10].

Acknowledgements

We are grateful to Prof. H. Ogi, Prof. M. Ohtani, Prof. N. Nakamura, Prof. K. Tanigaki, Prof. S. Hagiwara, and Prof. K. Nakajima for fruitful discussions. The calculations were done at the computer centers of Kyushu University and ISSP, University of Tokyo.

Funding

This work is partly supported by JSPS KAKENHI Grant No. JP22K04864.

Author Contributions

Yasuhiro Oishi: formal analysis; investigation; visualization; writing – original draft. Motoharu Kitatani: investigation; software; validation; writing – review & editing. Koichi Kusakabe: conceptualization; methodology; project administration; supervision; writing – original draft.

ORCID® iDs

Koichi Kusakabe - https://orcid.org/0000-0002-0206-8864

Data Availability Statement

The data that supports the findings of this study is available from the corresponding author upon reasonable request.

Preprint

A non-peer-reviewed version of this article has been previously published as a preprint: https://doi.org/10.3762/bxiv.2023.59.v1

References

1. Chen, R. J.; Zhang, Y.; Wang, D.; Dai, H. *J. Am. Chem. Soc.* **2001,** *123,* 3838–3839. doi:10.1021/ja010172b
2. Parviz, D.; Das, S.; Ahmed, H. S. T.; Irin, F.; Bhattacharia, S.; Green, M. J. *ACS Nano* **2012,** *6,* 8857–8867. doi:10.1021/nn302784m
3. Jaegfeldt, H.; Kuwana, T.; Johansson, G. *J. Am. Chem. Soc.* **1983,** *105,* 1805–1814. doi:10.1021/ja00345a021
4. Katz, E. *J. Electroanal. Chem.* **1994,** *365,* 157–164. doi:10.1016/0022-0728(93)02975-n
5. Kodali, V. K.; Scrimgeour, J.; Kim, S.; Hankinson, J. H.; Carroll, K. M.; de Heer, W. A.; Berger, C.; Curtis, J. E. *Langmuir* **2011,** *27,* 863–865. doi:10.1021/la1033178
6. Fan, W.; Zhang, R. *Sci. China, Ser. B: Chem.* **2008,** *51,* 1203–1210. doi:10.1007/s11426-008-0140-2
7. Karachevtsev, V. A.; Stepanian, S. G.; Glamazda, A. Y.; Karachevtsev, M. V.; Eremenko, V. V.; Lytvyn, O. S.; Adamowicz, L. *J. Phys. Chem. C* **2011,** *115,* 21072–21082. doi:10.1021/jp207916d
8. Wu, G.; Tang, X.; Meyyappan, M.; Lai, K. W. C. Chemical functionalization of graphene with aromatic molecule. In *Proceedings of the 2015 IEEE 15th International Conference on Nanotechnology IEEE-NANO,* Rome, July 27–30, 2015; IEEE, 2016; pp 1324–1327. doi:10.1109/nano.2015.7388878
9. Oishi, Y.; Ogi, H.; Hagiwara, S.; Otani, M.; Kusakabe, K. *ACS Omega* **2022,** *7,* 31120–31125. doi:10.1021/acsomega.2c03257
10. Kokalj, A. *J. Mol. Graphics Modell.* **1999,** *17,* 176–179. doi:10.1016/s1093-3263(99)00028-5
11. Murashima, K.; Murakami, M.; Ogi, H.; Kusakabe, K. Carbon-based material vibrator. A sensor element having the same and a biological-substance detection device having the same. U.S. Patent Application US 2021/0223212 A1, July 22, 2021.
12. Haraguchi, T.; Nagakubo, A.; Murashima, K.; Murakami, M.; Ogi, H. 3Pa2-2 Development of 30-GHz phonon biosensor using graphite thin-film resonator. In *Proceedings of Symposium on Ultrasonic Electronics, Vol. 42,* J-Stage: Japan, 2021. doi:10.24492/use.42.0_3pa2-2
13. Mohanty, N.; Berry, V. *Nano Lett.* **2008,** *8,* 4469–4476. doi:10.1021/nl802412n
14. Castro Neto, A. H.; Guinea, F.; Peres, N. M. R.; Novoselov, K. S.; Geim, A. K. *Rev. Mod. Phys.* **2009,** *81,* 109–162. doi:10.1103/revmodphys.81.109
15. Georgakilas, V.; Otyepka, M.; Bourlinos, A. B.; Chandra, V.; Kim, N.; Kemp, K. C.; Hobza, P.; Zboril, R.; Kim, K. S. *Chem. Rev.* **2012,** *112,* 6156–6214. doi:10.1021/cr3000412
16. Wang, Y.; Li, Z.; Wang, J.; Li, J.; Lin, Y. *Trends Biotechnol.* **2011,** *29,* 205–212. doi:10.1016/j.tibtech.2011.01.008
17. Myung, S.; Solanki, A.; Kim, C.; Park, J.; Kim, K. S.; Lee, K.-B. *Adv. Mater. (Weinheim, Ger.)* **2011,** *23,* 2221–2225. doi:10.1002/adma.201100014
18. Yang, W.; Ratinac, K. R.; Ringer, S. P.; Thordarson, P.; Gooding, J. J.; Braet, F. *Angew. Chem., Int. Ed.* **2010,** *49,* 2114–2138. doi:10.1002/anie.200903463
19. Peña-Bahamonde, J.; Nguyen, H. N.; Fanourakis, S. K.; Rodrigues, D. F. *J. Nanobiotechnol.* **2018,** *16,* No. 75. doi:10.1186/s12951-018-0400-z
20. Szunerits, S.; Boukherroub, R. *Interface Focus* **2018,** *8,* 20160132. doi:10.1098/rsfs.2016.0132
21. Kuila, T.; Bose, S.; Khanra, P.; Mishra, A. K.; Kim, N. H.; Lee, J. H. *Biosens. Bioelectron.* **2011,** *26,* 4637–4648. doi:10.1016/j.bios.2011.05.039
22. Chen, S.; Zhang, Z.-B.; Ma, L.; Ahlberg, P.; Gao, X.; Qiu, Z.; Wu, D.; Ren, W.; Cheng, H.-M.; Zhang, S.-L. *Appl. Phys. Lett.* **2012,** *101,* 154106. doi:10.1063/1.4759147
23. Ohno, Y.; Maehashi, K.; Yamashiro, Y.; Matsumoto, K. *Nano Lett.* **2009,** *9,* 3318–3322. doi:10.1021/nl901596m
24. Geim, A. K.; Novoselov, K. S. *Nat. Mater.* **2007,** *6,* 183–191. doi:10.1038/nmat1849
25. Novoselov, K. S.; Geim, A. K.; Morozov, S. V.; Jiang, D.; Zhang, Y.; Dubonos, S. V.; Grigorieva, I. V.; Firsov, A. A. *Science* **2004,** *306,* 666–669. doi:10.1126/science.1102896
26. Loh, K. P.; Bao, Q.; Ang, P. K.; Yang, J. *J. Mater. Chem.* **2010,** *20,* 2277–2289. doi:10.1039/b920539j
27. Liu, J.; Bibari, O.; Mailley, P.; Dijon, J.; Rouvière, E.; Sauter-Starace, F.; Caillat, P.; Vinet, F.; Marchand, G. *New J. Chem.* **2009,** *33,* 1017–1024. doi:10.1039/b813085j
28. Tournus, F.; Latil, S.; Heggie, M. I.; Charlier, J.-C. *Phys. Rev. B* **2005,** *72,* 075431. doi:10.1103/physrevb.72.075431
29. Zhou, L.; Mao, H.; Wu, C.; Tang, L.; Wu, Z.; Sun, H.; Zhang, H.; Zhou, H.; Jia, C.; Jin, Q.; Chen, X.; Zhao, J. *Biosens. Bioelectron.* **2017,** *87,* 701–707. doi:10.1016/j.bios.2016.09.025

30. Giannozzi, P.; Baroni, S.; Bonini, N.; Calandra, M.; Car, R.; Cavazzoni, C.; Ceresoli, D.; Chiarotti, G. L.; Cococcioni, M.; Dabo, I.; Dal Corso, A.; de Gironcoli, S.; Fabris, S.; Fratesi, G.; Gebauer, R.; Gerstmann, U.; Gougoussis, C.; Kokalj, A.; Lazzeri, M.; Martin-Samos, L.; Marzari, N.; Mauri, F.; Mazzarello, R.; Paolini, S.; Pasquarello, A.; Paulatto, L.; Sbraccia, C.; Scandolo, S.; Sclauzero, G.; Seitsonen, A. P.; Smogunov, A.; Umari, P.; Wentzcovitch, R. M. *J. Phys.: Condens. Matter* **2009,** *21,* 395502. doi:10.1088/0953-8984/21/39/395502
31. Giannozzi, P.; Andreussi, O.; Brumme, T.; Bunau, O.; Buongiorno Nardelli, M.; Calandra, M.; Car, R.; Cavazzoni, C.; Ceresoli, D.; Cococcioni, M.; Colonna, N.; Carnimeo, I.; Dal Corso, A.; de Gironcoli, S.; Delugas, P.; DiStasio, R. A., Jr.; Ferretti, A.; Floris, A.; Fratesi, G.; Fugallo, G.; Gebauer, R.; Gerstmann, U.; Giustino, F.; Gorni, T.; Jia, J.; Kawamura, M.; Ko, H.-Y.; Kokalj, A.; Küçükbenli, E.; Lazzeri, M.; Marsili, M.; Marzari, N.; Mauri, F.; Nguyen, N. L.; Nguyen, H.-V.; Otero-de-la-Roza, A.; Paulatto, L.; Poncé, S.; Rocca, D.; Sabatini, R.; Santra, B.; Schlipf, M.; Seitsonen, A. P.; Smogunov, A.; Timrov, I.; Thonhauser, T.; Umari, P.; Vast, N.; Wu, X.; Baroni, S. *J. Phys.: Condens. Matter* **2017,** *29,* 465901. doi:10.1088/1361-648x/aa8f79
32. Giannozzi, P.; Baseggio, O.; Bonfà, P.; Brunato, D.; Car, R.; Carnimeo, I.; Cavazzoni, C.; de Gironcoli, S.; Delugas, P.; Ferrari Ruffino, F.; Ferretti, A.; Marzari, N.; Timrov, I.; Urru, A.; Baroni, S. *J. Chem. Phys.* **2020,** *152,* 154105. doi:10.1063/5.0005082
33. Grimme, S.; Antony, J.; Ehrlich, S.; Krieg, H. *J. Chem. Phys.* **2010,** *132,* 154104. doi:10.1063/1.3382344
34. Perdew, J. P.; Ruzsinszky, A.; Csonka, G. I.; Vydrov, O. A.; Scuseria, G. E.; Constantin, L. A.; Zhou, X.; Burke, K. *Phys. Rev. Lett.* **2008,** *100,* 136406. doi:10.1103/physrevlett.100.136406
35. Vanderbilt, D. *Phys. Rev. B* **1990,** *41,* 7892–7895. doi:10.1103/physrevb.41.7892
36. Monkhorst, H. J.; Pack, J. D. *Phys. Rev. B* **1976,** *13,* 5188–5192. doi:10.1103/physrevb.13.5188

License and Terms

BEILSTEIN JOURNAL OF ORGANIC CHEMISTRY

Enhanced reactivity of $Li^+@C_{60}$ toward thermal [2 + 2] cycloaddition by encapsulated Li^+ Lewis acid

Hiroshi Ueno*[1,2,3], Yu Yamazaki[3], Hiroshi Okada[2], Fuminori Misaizu[2], Ken Kokubo[3,§] and Hidehiro Sakurai[3]

Full Research Paper

Open Access

Address:
[1]Creative Interdisciplinary Research Division, Frontier Research Institute for Interdisciplinary Sciences (FRIS), Tohoku University, 6-3 Aoba, Aramaki, Aoba-ku, Sendai 980-8578, Japan, [2]Department of Chemistry, Graduate School of Science, Tohoku University, 6-3 Aoba, Aramaki, Aoba-ku, Sendai 980-8578, Japan and [3]Division of Applied Chemistry, Graduate School of Engineering, Osaka University, 2-1 Yamadaoka, Suita, Osaka 565-0871, Japan

Email:
Hiroshi Ueno* - hiroshi.ueno.d5@tohoku.ac.jp

* Corresponding author
§ Present address: Nano Carbon Device Research Center, National Institute of Advanced Industrial Science and Technology (AIST), Tsukuba Central 5, 1-1-1 Higashi, Ibaraki, Tsukuba, 305-8565, Japan

Keywords:
electron transfer; fullerene; ion-endohedral fullerene; Lewis acid catalyst; thermal [2 + 2] cycloaddition

Beilstein J. Org. Chem. **2024,** *20,* 653–660.
https://doi.org/10.3762/bjoc.20.58

Received: 01 December 2023
Accepted: 14 March 2024
Published: 25 March 2024

This article is part of the thematic issue "Carbon-rich materials: from polyaromatic molecules to fullerenes and other carbon allotropes".

Guest Editor: Y. Yamakoshi

Abstract

Lithium ion-endohedral fullerene ($Li^+@C_{60}$), a member of the burgeoning family of ion-endohedral fullerenes, holds substantial promise for diverse applications owing to its distinctive ionic properties. Despite the high demand for precise property tuning through chemical modification, there have been only a few reports detailing synthetic protocols for the derivatization of this novel material. In this study, we report the synthesis of $Li^+@C_{60}$ derivatives via the thermal [2 + 2] cycloaddition reaction of styrene derivatives, achieving significantly higher yields of monofunctionalized $Li^+@C_{60}$ compared to previously reported reactions. Furthermore, by combining experimental and theoretical approaches, we clarified the range of applicable substrates for the thermal [2 + 2] cycloaddition of $Li^+@C_{60}$, highlighting the expanded scope of this straightforward and selective functionalization method.

Introduction

Chemical functionalization of fullerenes is a fascinating and extensively studied approach, playing a pivotal role in fullerene-based materials science to introduce various characteristic functionalities [1-7]. Significant progress in synthetic procedures has contributed to diversifying their properties, enabling widespread and interdisciplinary applications in various research fields, such as biomedicine, photovoltaic devices, and materials chemistry.

Meanwhile, lithium ion-endohedral fullerenes ($Li^+@C_{60}$) [8], the first member of the emerging ion-endohedral fullerene family, have attracted significant attention owing to the distinctive ionic properties originating from the ion pair structure consisting of a cationic endohedral fullerene core and an external counter anion. Despite being a relatively recent addition, $Li^+@C_{60}$ has been the focus of intensive studies in chemistry, physics, and related interdisciplinary fields over the past 13 years [9]. A noteworthy discovery during these investigations is the significant enhancement of reactivity arising from the encapsulated Li^+. Both experimental and theoretical approaches have diligently explored the details of reaction kinetics, quantitatively elucidating the impact of encapsulated Li^+ on the reactivity of the outer fullerene cage as a specialized "encapsulated" Lewis acid catalyst [10,11]. While previous studies have revealed valuable insights, such as accelerated 1,3-dipolar and Diels–Alder reactions [12,13], it is noteworthy that the anticipated diverse properties resulting from the derivatization of $Li^+@C_{60}$ have not yet been fully realized. To further leverage the unique properties of the novel ion-endohedral fullerene, achieving diverse property tuning through chemical modification has been in high demand for its further applications, which is similar to what has been developed during the recent empty fullerene sciences.

As a continuation of our studies on the synthesis of $Li^+@C_{60}$ derivatives, we herein focus on the modification of $Li^+@C_{60}$ through thermal [2 + 2] cycloaddition. The [2 + 2] cycloaddition reactions of empty C_{60} have been known to proceed with unsaturated substrates having HOMO levels suitable for the thermal or photoinduced single-electron-transfer (SET) process (Scheme 1) [14-23]. Although the thermal [2 + 2] reactions are generally simple and scalable, the reactions are scarcely applied for the derivatization of fullerenes due to the limitation in the variety of possible substrates. Considering the electronic effect of the encapsulated Li^+ on the outer C_{60} cage, $Li^+@C_{60}$ can react with a wider range of unsaturated substrates having a relatively lower HOMO level.

With the previously uncovered reactivity of $Li^+@C_{60}$ in hand, we synthesized $Li^+@C_{60}$ derivatives in this study through the thermal [2 + 2] cycloaddition of styrene derivatives, which do not react with empty C_{60} through the same reaction pathway. Although a major issue in the derivatization of $Li^+@C_{60}$ is the formation of multifunctionalized byproducts, it was significantly prevented in the reaction, leading to a much better yield of the target monofunctionalized $Li^+@C_{60}$ derivatives [24]. Additionally, we investigated the range of the HOMO level of the reactants suitable for the thermal [2 + 2] cycloaddition of $Li^+@C_{60}$ using both experimental and theoretical approaches. This study clearly demonstrated the significantly improved reactivity of $Li^+@C_{60}$ in the thermal [2 + 2] cycloaddition reaction, highlighting the expanded scope of this straightforward and selective reaction for $Li^+@C_{60}$.

Results and Discussion

We began by performing density functional theory (DFT) calculations to screen the substrates with suitable HOMO levels for the thermal [2 + 2] cycloaddition with $Li^+@C_{60}$. The structures of several kinds of possible reactants were optimized at the B3LYP/6-31G(d) level of theory. The calculated HOMO levels are summarized in Figure 1 along with the LUMO levels of $Li^+@C_{60}$ and empty C_{60} computed at the same level of theory. Among the computed substrates having a carbon–carbon unsaturated bond, thermal [2 + 2] cycloaddition of *N*,*N*,*N*′,*N*′-tetraethylethynediamine and 1-morpholino-1-cyclopentene with empty C_{60} has been reported [17,23], while electron-rich styrene derivatives **1** and **2** can react with empty C_{60} only through a photoinduced SET pathway [19,22]. From these results, the energy gap between the HOMO of the alkene sub-

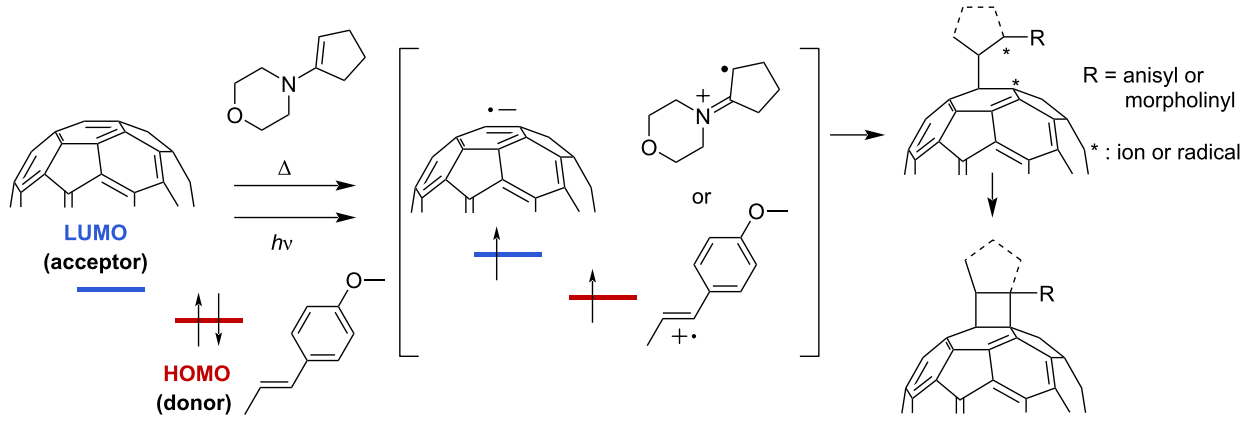

Scheme 1: Reaction mechanisms of thermal and photoinduced [2 + 2] cycloaddition on C_{60} [19,22,23].

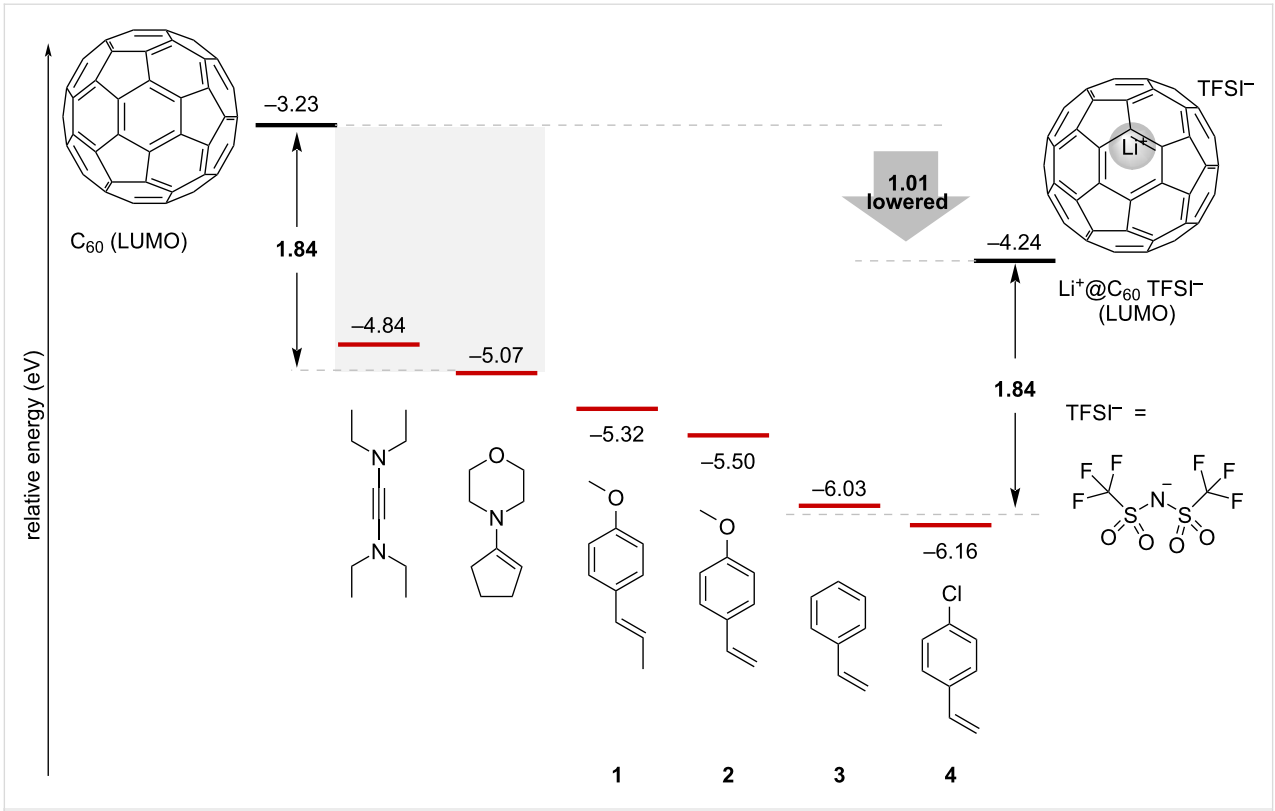

Figure 1: HOMO levels of unsaturated substrates and LUMO levels of fullerenes computed at the B3LYP/6-31G(d) level of theory.

strate and the LUMO of the fullerene acceptor, where the thermal SET reaction is presumed to occur, is estimated to be approximately less than 1.84 eV. Taking these results into consideration, $Li^+@C_{60}$ with a LUMO level of −4.24 eV is expected to undergo thermal [2 + 2] cycloaddition with reactants having a HOMO level of −6.08 eV or higher, such as styrene derivatives **1**, **2**, and **3**.

Based on the results of theoretical calculations, styrene derivatives **1**, **2**, and **3** were selected as the reactants for the thermal [2 + 2] cycloaddition with $Li^+@C_{60}$. For comparison, we also investigated the reaction of reactant **4**, which has a larger energy gap between its HOMO and LUMO of $Li^+@C_{60}$ (1.92 eV). All reactions were conducted in the dark to avoid photoinduced SET reactions (Scheme 2). First, the reactivity was assessed by monitoring the reaction progress using a previously developed electrolyte-added HPLC technique [25]. As expected, both substrates **1** and **2** reacted with $Li^+@C_{60}$ at room temperature and exhibited HPLC signals assignable to the desirable monoadducts **5a** and **5b** (Figure 2). It is noteworthy that the reaction of **2** proceeded faster than that of **1**, although **2** has a lower HOMO level than **1**. This is likely due to the steric effect caused by the methyl group directly connected to the alkenyl C=C bond in reactant **1**. After optimizing the reaction conditions, compounds **5a** and **5b** were isolated in 71% and 53% yields, respectively. Importantly, the generation of multiadducts in the thermal [2 + 2] cycloaddition was significantly prevented, even under conditions with an excess amount of reactant, resulting in much better yields of the target products compared to other reported reactions of $Li^+@C_{60}$. It should also be mentioned that while these products were stable at ambient temperature in the dark, photoirradiation triggered the elimination of the addends, reforming the starting $Li^+@C_{60}$ (Figure 3). No other insoluble or undetectable products by HPLC were identified during the study. On the other hand, the reactions of **3** and **4** with $Li^+@C_{60}$ did not proceed significantly even under higher temperature reaction conditions (**5c**: 1.6% and **5d**: 0.5% in HPLC yields, Figures S1 and S2 in Supporting Information File 1). This result indicates that the HOMO levels of compounds **3** and **4** are around the threshold HOMO level for the thermal reaction with $Li^+@C_{60}$. The slightly higher reactivity of **3** than **4** can be simply explained by the higher HOMO level of **3** compared to that of **4**.

The products were characterized by spectroscopic and spectrometric analyses (Figures S3–S11 in Supporting Information File 1). ^1H, and ^{13}C NMR spectra clearly indicated the formation of [2 + 2] monoadducts. ^7Li NMR spectra showed a sharp singlet signal at −12.4 (**5a**) and −13.5 ppm (**5b**), which clearly indicated that the Li^+ was encapsulated in the highly shielded

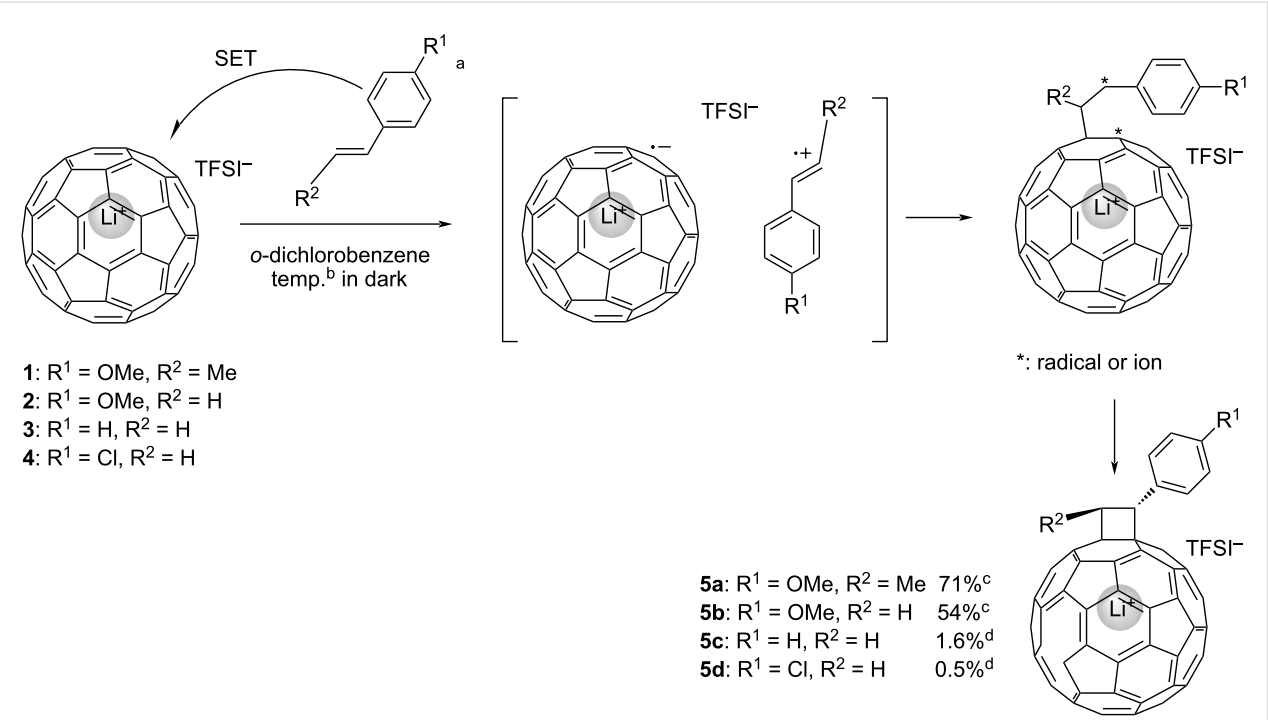

Scheme 2: Thermal [2 + 2] reaction of $Li^+@C_{60}$ $TFSI^-$ with substrates **1**–**4**. [a]100 equiv for the reaction screening, 20 equiv for the synthesis of **5a**, and 40 equiv for the synthesis of **5b**. [b]Room temperature for the reaction screening, 50 °C for the synthesis. [c]Isolated yield. [d]HPLC yield.

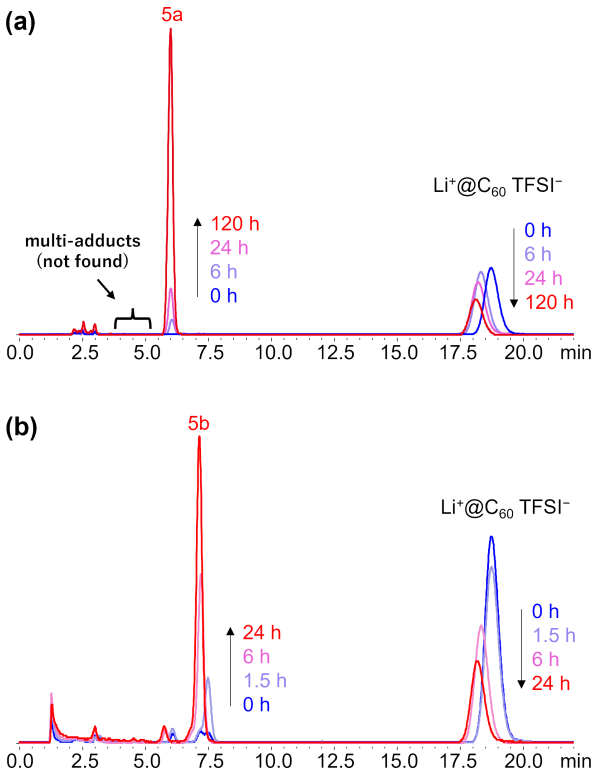

Figure 2: HPLC profiles of themal [2 + 2]reaction of $Li^+@C_{60}$ with substrate **1** (a) and **2** (b) in *o*-dichlorobenzene at room temperature.

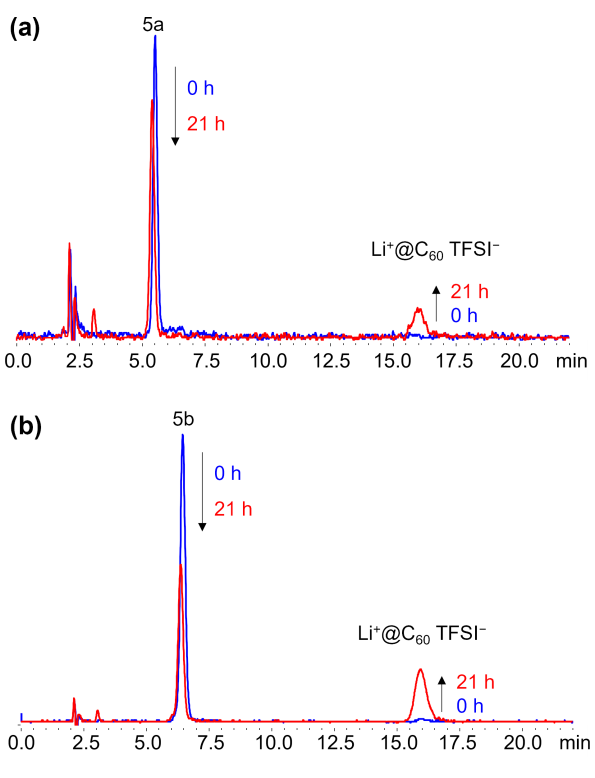

Figure 3: HPLC profiles of **5a** (a) and **5b** (b) before and after photoirradiation at room temperature.

inner space of the fullerene cage. The observed chemical shift was almost identical to that of reported $Li^+@C_{60}$ derivatives [10,12,24]. Although the product **5a** may have stereoisomers, only the *E*-isomer was observed, as confirmed by ^{1}H-^{1}H 2D-NOESY NMR spectrum (Figure 4). This is not surprising because similar stereoselectivity has been reported in the photoinduced [2 + 2] cycloaddition reaction of empty C_{60}, where the *E*-isomer is most thermodynamically stable [19,22]. The positive mode high-resolution matrix-assisted laser desorption ionization mass spectra showed the formation of the monoadducts at *m*/*z* 875.10431 (**5a**) and 861.08866 (**5b**), which were assigned to each molecular ion ([M]$^+$ calcd for $C_{70}H_{12}OLi$ (**5a**): 875.10427 and $C_{69}H_{10}OLi$ (**5b**): 861.08862, respectively). The UV–vis absorption spectra showed broad absorption in the visible region with an absorption maximum at 711 nm, which was known to show a characteristic pattern of functionalized fullerene having an addend on a [6,6] bond [26].

As mentioned above, a distinctive feature of this reaction is the significantly lower yield of multiadducts compared to previously reported functionalizations of $Li^+@C_{60}$. The reason can be explained by the difference in electron-accepting ability between the monoadduct and pristine $Li^+@C_{60}$ investigated by cyclic voltammetry (Figure 5). Both products exhibited reversible first and second redox waves, with subsequent reduction resulting in an irreversible electrochemical response. The first reduction potentials of **5a** and **5b** were measured at −0.51 V and −0.52 V (vs Fc/Fc$^+$), respectively, which were more negative than that of pristine $Li^+@C_{60}$ ($E_{1/2}^{red1}$ = −0.39 V). While the detailed reasons for the irreversible redox properties after the second reduction process have not been thoroughly investigated, the observed phenomena could potentially be attributed to ring opening or simple decomposition under the conditions. From these results, the LUMO levels of the compounds were estimated according to the following equation [27]: E_{LUMO} (eV) = −[4.80 + $E_{1/2}^{red1}$ (V vs Fc/Fc$^+$)], and the results were summarized in Table 1. The monoadducts with a higher LUMO level are expected to have lower reactivity in the thermal [2 + 2] cycloaddition than pristine $Li^+@C_{60}$. Moreover, it is plausible that unreacted $Li^+@C_{60}$ serves as an oxidant for the reduced monoadducts potentially generated by SET from reactants to monoadducts. These factors contribute to the suppression of multiadduct formation, resulting in the selective generation of the target monoadducts. Specifically, $Li^+@C_{60}$, influ-

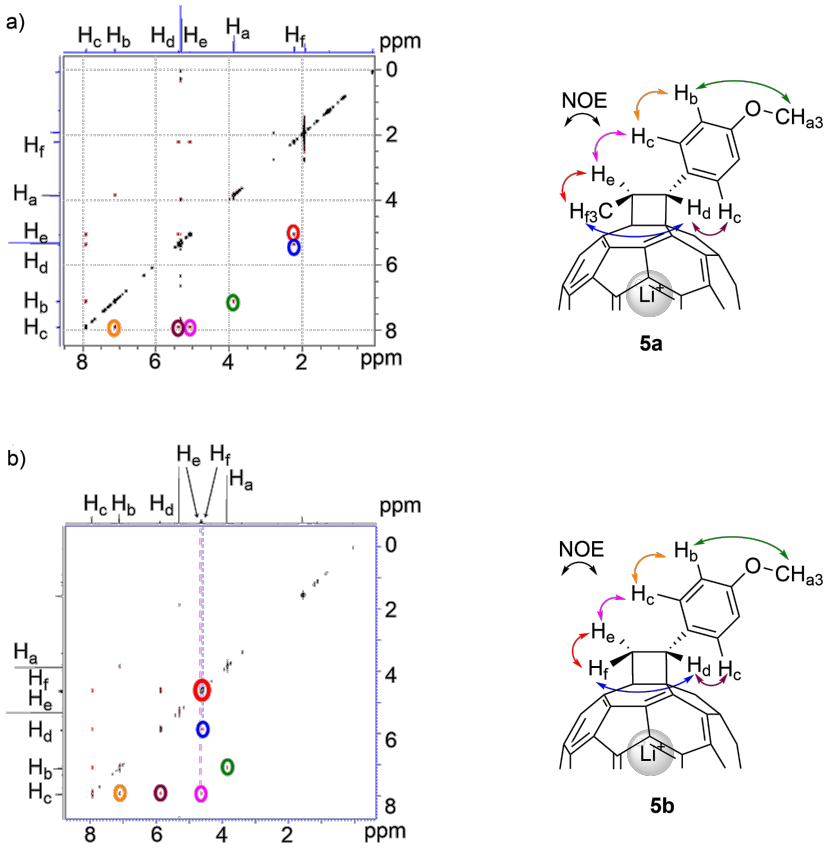

Figure 4: ^{1}H-^{1}H 2D-NOESY NMR spectrum (600 MHz, CD_2Cl_2) of **5a** (a) and NOE correlations between two protons. The spectrum (700 MHz, CD_2Cl_2) of **5b** is shown in (b).

enced by the electronic effects of the encapsulated Li^+ Lewis acid, commonly exhibits significantly higher reactivity compared to empty C_{60}. The much-enhanced reactivity often leads to the formation of multiadducts more notably than in the case of empty fullerenes, and hence, achieving the selective monofunctionalization of $Li^+@C_{60}$ has been a major challenge. The approach we developed in this study proves highly advantageous for the selective formation of monofunctionalized $Li^+@C_{60}$ derivatives, holding great promise for the design, properties tuning, and synthesis of $Li^+@C_{60}$-based materials for future applications.

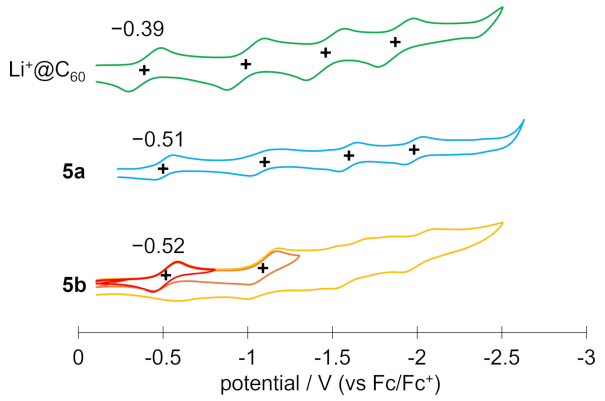

Figure 5: Cyclic voltammograms of **5a**, **5b**, and $Li^+@C_{60}$ $TFSI^-$ with the potentials relative to the ferrocene/ferrocenium (Fc/Fc^+) reference couple. Working electrode: Pt, counter electrode: Pt, reference electrode: Ag/Ag^+ in acetonitrile, solvent: *o*-dichlorobenzene, supporting electrolyte: 50 mM $TBAPF_6$.

Table 1: First reduction potential and estimated LUMO level of **5a** and **5b**. The values of $Li^+@C_{60}$ are also listed as a reference.

	$E_{1/2}^{red1}$ (V, vs Fc/Fc^+)	LUMO level (eV)
5a	−0.51	−4.29
5b	−0.52	−4.28
$Li^+@C_{60}$ $TFSI^-$	−0.39	−4.41

Conclusion

In summary, we successfully synthesized $Li^+@C_{60}$ derivatives through the thermal [2 + 2] cycloaddition of styrene derivatives. Due to the lower-lying LUMO of $Li^+@C_{60}$, the styrene reactant, which did not react with empty C_{60} through the same pathway, underwent a reaction with $Li^+@C_{60}$, yielding the target monofunctionalized products. The results underscore the significantly enhanced reactivity of $Li^+@C_{60}$ in the thermal [2 + 2] cycloaddition reaction due to the electronic effect of the encapsulated Li^+ Lewis acid. Moreover, the formation of undesirable bis- and multiadducts was notably suppressed, resulting in much better yields of the target monoadducts. Electrochemical measurements revealed that the functionalization raised the LUMO level of $Li^+@C_{60}$, leading to lower reactivity for the second addition. With this facile, selective, and high-yield approach for the derivatization of ion-endohedral fullerene, the design and synthesis of novel $Li^+@C_{60}$ derivatives for further application in various research fields are currently underway.

Experimental

General procedure

Unless otherwise noted, all chemicals, including anhydrous solvents, were obtained from commercial suppliers (FUJIFILM Wako Pure Chemical Corp., TCI, Sigma-Aldrich) and used as received without further purification. $Li^+@C_{60}TFSI^-$ was purchased as PF_6^- salt from Idea International Corp., and then its counter anion was exchanged to $TFSI^-$ according to reported procedures [9].

NMR spectra were recorded on a JEOL JNM-ECZ400S (^1H: 400 MHz, ^7Li: 155 MHz, ^{13}C: 100 MHz), a Bruker ADVANCE III (^1H: 600 MHz) and a Bruker ADVANCE III 700 (^1H: 700 MHz, ^7Li: 272 MHz, ^{13}C: 176 MHz) spectrometer. Chemical shifts (δ) were reported in parts per million (ppm) relative to residual proton of solvent for ^1H (5.32 ppm, $CDHCl_2$), LiCl in D_2O for ^7Li (0 ppm, external standard), and carbon of the solvent for ^{13}C (53.84 ppm, CD_2Cl_2). High-resolution matrix-assisted laser desorption ionization (HR-MALDI) mass spectra were obtained on a Bruker solariX 12T mass spectrometer with dithranol as a matrix. UV–vis absorption spectra were measured on a JASCO V-670 and a Shimadzu UV-1800 spectrophotometer. Cyclic voltammograms were recorded on a BAS ALS 600A and a BAS ALS 620D apparatus with a three-electrode system.

Reactivitiy comparison of $Li^+@C_{60}$ $TFSI^-$ and styrenes

In an Ar-filled glove box, $Li^+@C_{60}$ $TFSI^-$ and styrenes **1**–**4** were dissolved in anhydrous chlorobenzene. 100 µL of $Li^+@C_{60}$ $TFSI^-$ solution (2.0 mM) and 100 µL of each styrene solution (200 mM) were mixed, respectively. The solutions were stirred in glove box for the indicated reaction time. At the time, 20 µL of solution was divided, taken out from glove box, frozen by liq. N_2, and stored in a freezer until HPLC measurement.

The solutions were subjected to analytical HPLC. HPLC profiles are shown in Supporting Information File 1. HPLC conditions: column: Buckyprep ø 4.6 × (10 + 250) mm; mobile phase: chlorobenzene/acetonitrile 95:5 containing 30 mM LiTFSI; flow rate: 1.5 mL/min; temperature: 50 °C; detector: UV 337 nm; injection sample volume: 5 µL.

Synthesis of $Li^+@C_{60}$\{(4-$MeOC_6H_4$)CH=CHMe\} $TFSI^-$ (**5a**)

To 2.5 mL of a chlorobenzene/acetonitrile 1:1 (v/v) solution containing $Li^+@C_{60}$ $TFSI^-$ (8.5 mg, 8.4 μmol) was added *trans*-anethole (25 μL, 24.7 mg, 0.17 mmol). The solution was stirred at 50 °C for 15 hours. The resulted solution was subjected to preparative HPLC. Condition: solvent: chlorobenzene/acetonitrile 4:11 (v/v) containing 2 mM LiTFSI; column: Inertsil CX (GL Sciences), ø 4.6 × 250 mm. The fraction containing $Li^+@C_{60}$\{(4-$MeOC_6H_4$)CH=CHMe\} was collected and evaporated under reduced pressure. The resulting solid was washed with diethyl ether and dissolved in dichloromethane. The desired monoadduct $Li^+@C_{60}$\{(4-$MeOC_6H_4$)CH=CHMe\} $TFSI^-$ (**5a**, 6.9 mg, 6.0 μmol, 71%) was afforded from the solution by vapor-diffusion recrystallization with diethyl ether.

^{1}H NMR (400 MHz, CD_2Cl_2) δ 2.23 (d, J = 6.9 Hz, 3H), 3.88 (s, 3H), 5.07 (qd, J = 6.9 8.7 Hz, 1H), 5.38 (d, J = 8.7 Hz, 1H), 7.12 (d, J = 8.7 Hz, 2H), 7.92 (d, J = 8.8 Hz, 2H); ^{13}C NMR (100 MHz, CD_2Cl_2) δ 19.83, 47.39, 55.80, 58.72, 70.58, 73.03, 115.10, 119.84 (q, J_{CF} = 320 Hz, CF_3), 129.96, 130.56, 136.89, 136.93, 139.24, 139.66, 140.23, 140.50, 141.45, 141.62, 141.70, 141.79, 141.82, 141.85, 142.02, 142.34, 142.50, 142.53, 142.76, 142.84, 142.85, 142.92, 142.96, 143.00, 143.19, 144.04, 144.24, 144.32, 144.80, 144.89, 144.93, 145.02, 145.20, 145.23, 145.35, 145.39, 145.50, 145.57, 145.62, 145.79, 145.82, 145.91, 145.96, 145.99, 146.05, 146.12, 146.66, 146.72, 147.48, 147.85, 153.12, 153.33, 156.27, 156.48, 160.24; ^{7}Li NMR (155 MHz, CD_2Cl_2) δ −12.4; HRMS–MALDI–TOF, positive ion mode, dithranol (m/z): $[M]^+$ calcd for $C_{70}H_{12}OLi$, 875.10427; found, 875.10431.

Synthesis of $Li^+@C_{60}$\{(4-$MeOC_6H_4$)CH=CH_2\} $TFSI^-$ (**5b**)

To 2.5 mL of a chlorobenzene/acetonitrile 1:1 (v/v) solution containing $Li^+@C_{60}$ $TFSI^-$ (9.4 mg, 9.3 μmol) was added 4-methoxystyrene (50.1 μL, 50.1 mg, 0.37 mmol). The solution was stirred at 50 °C for 45 min. The resulted solution was subjected to preparative HPLC. Conditions: solvent: chlorobenzene/acetonitrile 95:5 (v/v) containing 30 mM LiTFSI; column: Buckyprep (Nacalai tesque), ø 10 × (20 + 250) mm. The fraction containing $Li^+@C_{60}$\{(4-$MeOC_6H_4$)CH=CH_2\} was concentrated under reduced pressure. The desired monoadduct $Li^+@C_{60}$\{(4-$MeOC_6H_4$)CH=CH_2\} $TFSI^-$ (**5b**, 5.6 mg, 4.9 μmol, 53%) was afforded by precipitation with diethyl ether and filtration.

^{1}H NMR (700 MHz, CD_2Cl_2) δ 3.87 (s, 3H), 4.59 (dd, J = 10.8 Hz, 13.8 Hz, 1H), 4.69 (dd, J = 8.6 Hz, 13.8 Hz, 1H), 5.89 (dd, J = 8.6, 10.7 Hz, 1H), 7.12 (d, J = 8.8 Hz, 2H), 7.95 (d, J = 8.7 Hz, 2H); ^{13}C NMR (176 MHz, CD_2Cl_2) δ 37.94, 49.75, 55.65, 64.70, 74.90, 114.85, 120.07 (q, J_{CF} = 321 Hz, CF_3), 129.69, 131.42, 136.98, 137.32, 137.89 ,138.88, 139.99, 140.14, 140.24, 140.27, 141.24, 141.34, 141.55, 141.57, 141.60, 141.66, 141.68, 141.71, 142.18, 142.23, 142.35, 142.37, 142.61, 142.65, 142.66, 142.73, 142.76, 142.80, 143.01, 143.90, 144.02, 144.06, 144.09, 144.73, 144.83, 144.90, 144.94, 145.02, 145.14, 145.22, 145.29, 145.43, 145.57, 145.61, 145.63, 145.67, 145.72, 145.77, 145.82, 145.90, 146.51, 146.69, 146.85, 153.12, 155.45, 155.75, 155.85, 159.84; ^{7}Li NMR (272 MHz, CD_2Cl_2) δ −13.3; HRMS–MALDI–TOF, positive ion mode, dithranol (m/z): $[M]^+$ calcd for $C_{69}H_{10}OLi$, 861.08862; found, 861.08866.

Supporting Information

Supporting Information File 1

HPLC profiles, NMR, HRMS, UV–vis absorption spectra, and computational details.
[https://www.beilstein-journals.org/bjoc/content/supplementary/1860-5397-20-58-S1.pdf]

Acknowledgements

We thank to Dr. N. Ikuma for a fruitful discussion. Generous support from the FRIS CoRE, Tohoku University, which is a shared research environment, is also acknowledged.

Funding

This work was partly supported by Grants-in-Aid for Scientific Research (21H01737 to H. U.) from JSPS, Japan, and financial supports from Fukamatsugumi Co., Ltd., Sendai, Japan (to Endowed Research Laboratory of Dimensional Integrated Nanomaterials, Graduate school of Science, Tohoku University).

ORCID® iDs

Hiroshi Ueno - https://orcid.org/0000-0003-3991-0610
Hiroshi Okada - https://orcid.org/0000-0002-0809-8167
Ken Kokubo - https://orcid.org/0000-0002-8776-7102
Hidehiro Sakurai - https://orcid.org/0000-0001-5783-4151

Data Availability Statement

The data that supports the findings of this study is available from the corresponding author upon reasonable request.

References

1. Taylor, R. *Lecture notes on fullerene chemistry. A handbook for chemists;* Imperial College Press: London, UK, 1999. doi:10.1142/9781848160675
2. Hirsch, A.; Brettreich, M. *Fullerenes: Chemistry and Reactions;* Wiley-VCH: Weinheim, Germany, 2005. doi:10.1002/3527603492

3. Nakamura, E.; Isobe, H. *Acc. Chem. Res.* **2003,** *36,* 807–815. doi:10.1021/ar030027y
4. Matsuo, Y. *Chem. Lett.* **2012,** *41,* 754–759. doi:10.1246/cl.2012.754
5. Li, C.-Z.; Yip, H.-L.; Jen, A. K.-Y. *J. Mater. Chem.* **2012,** *22,* 4161–4177. doi:10.1039/c2jm15126j
6. Li, Y. *Chem. – Asian J.* **2013,** *8,* 2316–2328. doi:10.1002/asia.201300600
7. Liu, J.; Qiu, L.; Shao, S. *J. Mater. Chem. C* **2021,** *9,* 16143–16163. doi:10.1039/d1tc04038c
8. Aoyagi, S.; Nishibori, E.; Sawa, H.; Sugimoto, K.; Takata, M.; Miyata, Y.; Kitaura, R.; Shinohara, H.; Okada, H.; Sakai, T.; Ono, Y.; Kawachi, K.; Yokoo, K.; Ono, S.; Omote, K.; Kasama, Y.; Ishikawa, S.; Komuro, T.; Tobita, H. *Nat. Chem.* **2010,** *2,* 678–683. doi:10.1038/nchem.698
9. Matsuo, Y.; Okada, H.; Ueno, H. *Endohedral Lithium-containing Fullerenes: Preparation, Derivatization, and Application;* Springer: Berlin, Germany, 2017. doi:10.1007/978-981-10-5004-6
10. Ueno, H.; Kawakami, H.; Nakagawa, K.; Okada, H.; Ikuma, N.; Aoyagi, S.; Kokubo, K.; Matsuo, Y.; Oshima, T. *J. Am. Chem. Soc.* **2014,** *136,* 11162–11167. doi:10.1021/ja505952y
11. Ma, Y.; Ueno, H.; Okada, H.; Manzhos, S.; Matsuo, Y. *Org. Lett.* **2020,** *22,* 7239–7243. doi:10.1021/acs.orglett.0c02570
12. Matsuo, Y.; Okada, H.; Maruyama, M.; Sato, H.; Tobita, H.; Ono, Y.; Omote, K.; Kawachi, K.; Kasama, Y. *Org. Lett.* **2012,** *14,* 3784–3787. doi:10.1021/ol301671n
13. Fujiki, S.; Takada, T.; Nagasawa, S.; Okada, H.; Sasano, Y.; Kwon, E.; Matsuo, Y.; Iwabuchi, Y. *Chem. Commun.* **2023,** *59,* 1237–1240. doi:10.1039/d2cc06301h
14. Wilson, S. R.; Kaprinidis, N.; Wu, Y.; Schuster, D. I. *J. Am. Chem. Soc.* **1993,** *115,* 8495–8496. doi:10.1021/ja00071a088
15. Zhang, X.; Romero, A.; Foote, C. S. *J. Am. Chem. Soc.* **1993,** *115,* 11024–11025. doi:10.1021/ja00076a084
16. Wilson, S. R.; Wu, Y.; Kaprinidis, N. A.; Schuster, D. I.; Welch, C. J. *J. Org. Chem.* **1993,** *58,* 6548–6549. doi:10.1021/jo00076a007
17. Zhang, X.; Foote, C. S. *J. Am. Chem. Soc.* **1995,** *117,* 4271–4275. doi:10.1021/ja00120a007
18. Zhang, X.; Fan, A.; Foote, C. S. *J. Org. Chem.* **1996,** *61,* 5456–5461. doi:10.1021/jo9602231
19. Vassilikogiannakis, G.; Orfanopoulos, M. *Tetrahedron Lett.* **1997,** *38,* 4323–4326. doi:10.1016/s0040-4039(97)00891-5
20. Vassilikogiannakis, G.; Chronakis, N.; Orfanopoulos, M. *J. Am. Chem. Soc.* **1998,** *120,* 9911–9920. doi:10.1021/ja981377w
21. Vassilikogiannakis, G.; Orfanopoulos, M. *J. Org. Chem.* **1999,** *64,* 3392–3393. doi:10.1021/jo982486w
22. Vassilikogiannakis, G.; Hatzimarinaki, M.; Orfanopoulos, M. *J. Org. Chem.* **2000,** *65,* 8180–8187. doi:10.1021/jo0006223
23. Mikie, T.; Asahara, H.; Nagao, K.; Ikuma, N.; Kokubo, K.; Oshima, T. *Org. Lett.* **2011,** *13,* 4244–4247. doi:10.1021/ol201590a
24. Ueno, H.; Okada, H.; Aoyagi, S.; Matsuo, Y. *J. Org. Chem.* **2017,** *82,* 11631–11635. doi:10.1021/acs.joc.7b01893
25. For the details of electrolyte-added HPLC techniques, see refences [9-11,24].
26. Smith, A. B., III; Strongin, R. M.; Brard, L.; Furst, G. T.; Romanow, W. J.; Owens, K. G.; King, R. C. *J. Am. Chem. Soc.* **1993,** *115,* 5829–5830. doi:10.1021/ja00066a063
27. Wong, W.-Y.; Wang, X.-Z.; He, Z.; Djurišić, A. B.; Yip, C.-T.; Cheung, K.-Y.; Wang, H.; Mak, C. S. K.; Chan, W.-K. *Nat. Mater.* **2007,** *6,* 521–527. doi:10.1038/nmat1909

License and Terms

BEILSTEIN JOURNAL OF ORGANIC CHEMISTRY

Synthesis and characterization of water-soluble C_{60}–peptide conjugates

Yue Ma, Lorenzo Persi and Yoko Yamakoshi*

Full Research Paper

Open Access

Address:
Department of Chemistry and Applied Biosciences, ETH Zürich, Vladimir-Prelog-Weg 3, 8093 Zürich, Switzerland

Email:
Yoko Yamakoshi* - yamakoshi@org.chem.ethz.ch

* Corresponding author

Keywords:
biomaterial; fullerene; peptide; water-soluble

Beilstein J. Org. Chem. **2024,** *20,* 777–786.
https://doi.org/10.3762/bjoc.20.71

Received: 28 December 2023
Accepted: 27 March 2024
Published: 12 April 2024

This article is part of the thematic issue "Carbon-rich materials: from polyaromatic molecules to fullerenes and other carbon allotropes".

Associate Editor: N. Sewald

Abstract

With the aim of developing biocompatible and water-soluble C_{60} derivatives, three types of C_{60}–peptide conjugates consisting of hydrophilic oligopeptide anchors (oligo-Lys, oligo-Glu, and oligo-Arg) were synthesized. A previously reported Prato reaction adduct of a biscarboxylic acid-substituted C_{60} derivative was subjected to a solid phase synthesis for amide formation with N-terminal amines of peptides on resin to successfully provide C_{60}–peptide conjugates with one C_{60} and two peptide anchors as water-soluble moieties. Among three C_{60}–peptide conjugates prepared, C_{60}–oligo-Lys was soluble in water at neutral pH, and C_{60}–oligo-Glu was soluble in buffer with a higher pH value, but C_{60}–oligo-Arg was insoluble in water and most other solvents. C_{60}–oligo-Lys and C_{60}–oligo-Glu were characterized by ^{1}H and ^{13}C NMR. Photoinduced $^{1}O_2$ generation was observed in the most soluble C_{60}–oligo-Lys conjugate under visible light irradiation (527 nm) to show the potential of this highly water-soluble molecule in biological systems, for example, as a photosensitizer in photodynamic therapy.

Introduction

Since the seminal discovery in 1985 by Kroto, Smalley, Curl, and co-workers [1], fullerenes, specifically buckminsterfullerene C_{60}, have intrigued the scientific community. The unique structure of fullerenes, characterized by a fully conjugated closed-cage structure, containing a mixture of hexagonal and pentagonal rings, have been recognized for the unique electronic [2-4], optical [5,6], and mechanical properties [7,8]. Despite the notable achievements in fullerene research and the potential applications in diverse fields, a significant obstacle remained for the use in biological studies: fullerenes are poorly soluble in polar solvents, including water and other water-miscible solvents [9]. This challenge consequently restricted the studies of fullerenes as biomaterials since related in vitro bioassay systems require water solubility of the chemicals for

testing. To overcome this important obstacle, over the past decades, a variety of water-soluble fullerenes have been reported [10].

General approaches towards enhancing the water solubility of fullerenes involve either 1) covalent functionalization of the fullerene surface with polar moieties or 2) complexation with water-soluble host molecules or polymers. Related to the former approach, the Nakamura group [11], Wudl group [12], and Hirsch group [13] reported initial work in the early 1990s on water-soluble C_{60} derivatives by covalently attaching water-soluble moieties to the fullerene core. Subsequently, Nakamura and co-workers further developed reactions between C_{60} and organocopper reagents, enabling the sequential addition of functional groups to obtain penta- and decaadducts, which largely enhanced the water solubility [14,15]. As early examples of the latter approach in the 1990s, Wennerström and co-workers reported the study of supramolecular BiCAP complexation of C_{60} with γ-cyclodextrin (γ-CD) [16]. Shinkai and co-workers synthesized water-soluble calixarene derivatives to form water-soluble complexes with C_{60} [17,18]. By either chemical functionalization or complexation of the fullerene core, a number of biocompatible fullerene materials with interesting biological activities were recently prepared and reported [19-24].

We have reported water-soluble complexes of C_{60} with a nontoxic and nonionic polymer, poly(vinylpyrrolidone) (PVP) [25] and applied these to several in vitro biological assays to report DNA photocleavage [26] and related ROS generation [27,28], antimicrobial photoactivity [29], chondrogenesis-promoting activity [30,31], photocytotoxicity [32,33], and GST enzyme inhibition [34]. For the covalent functionalization, we have previously developed a versatile and convenient biscarboxylic acid-substituted C_{60} derivative (**3**, Figure 1) [35], which was prepared via the Prato reaction [36]. We used this derivative **3** as a starting material and synthesized a series of water-soluble C_{60} and C_{70} derivatives by covalently attaching biocompatible water-soluble polymers, such as polyethylene glycol (PEG) [37,38] and PVP [39]. Although these C_{60}– and C_{70}–polymer conjugates revealed high water-solubility, it was found that they, especially the PEG conjugates, formed micelle-like aggregations in aqueous solution, as observed by dynamic light scattering (DLS), cryoTEM, and concentration-dependent surface tension measurements [40]. Despite the small size (≈10 nm in hydrodynamic diameter), the aggregation of these fullerene moieties was not ideal for biological applications as photodynamic therapy photosensitizers (PDT PSs) [41] and magnetic resonance imaging contrast agents (MRI CAs) [42], which are the most relevant topics in fullerene biological studies. Aggregated fullerenes in the micelle structure may cause self-quenching of the excited state of PS fullerenes or may inhibit the approach of bulk water molecules to the fullerene core and hamper water exchange – an important factor for enhancement in MRI. Well-dispersed water-soluble C_{60} derivatives exhibiting less aggregation are in high demand.

To address the challenge mentioned above, we developed highly water-soluble C_{60}–peptide conjugates in this study. In addition to the water solubility introduced by the peptides, these conjugates have a superior biocompatibility compared to those with synthetic polymers, such as PEG and PVP. We utilized the previously reported biscarboxylic acid derivative **3**, which was suitable for the coupling to peptides on resin, prepared by solid-phase peptide synthesis (SPPS) [35]. The detailed conditions for the amide-forming reaction were optimized using biscarboxylic acid-substituted C_{60} derivative **3** and a similar peptide with a primary amine derived from γ-aminobutyric acid (GABA) at the N-terminus of the Lys pentamer peptide on resin. Using the optimal reaction conditions, three types of hydrophilic peptide pentamers on resin, oligo-Lys (**2a**), oligo-Glu (**2b**), and oligo-Arg (**2c**), were subjected to the reaction with **3** for the synthesis of C_{60}–peptide conjugates **5a**–**c** (Figure 1).

Results and Discussion

Syntheses of C_{60}–oligopeptides **5a–c**

The oligopeptides **2a**–**c** were synthesized on resin using Fmoc-protected amino acids with a standard SPPS method (Figure 1a) [43]. A moderate loading (0.4 mmol·g^{-1}) of the initial amino acid was used. After synthesizing the pentamer of Lys on resin, a GABA residue was attached to the N-terminus of the peptide in order to provide a less-hindered primary amine, enabling an efficient amide conjugation reaction with biscarboxylic acid-substituted C_{60} derivative **3**.

Compound **3** was prepared by Prato reaction of C_{60} and an *N*-glycine derivative and subsequent deprotection of the *t*-Bu group under acidic conditions, without affecting the C_{60} cage (Figure 1b). Challenges in this step included finding suitable conditions to conjugate one C_{60} moiety and two peptide anchors on the resin. Preliminarily, the reaction conditions were optimized using a similar peptide (GABA-$(Lys)_5$-peptide-PEG) on resin for the reaction with compound **3**. Initial trials, using 2-(1*H*-7-azabenzotriazol-1-yl)-1,1,3,3-tetramethyluronium hexafluorophosphate (HATU) and *N*-methylmorpholine (NMM), respectively, as a coupling reagent and a base, and 5 equiv of peptide on resin (rink amide MBHA) relative to **3**, provided a rather low yield (13%, isolated by HPLC), which was increased to 24% by changing the solid phase to 2-chlorotrityl chloride resin. By replacing the base with *N*,*N*-diisopropylethylamine (DIPEA), the yield was slightly increased to 28%, which became higher (32%) when HBTU was used as a coupling

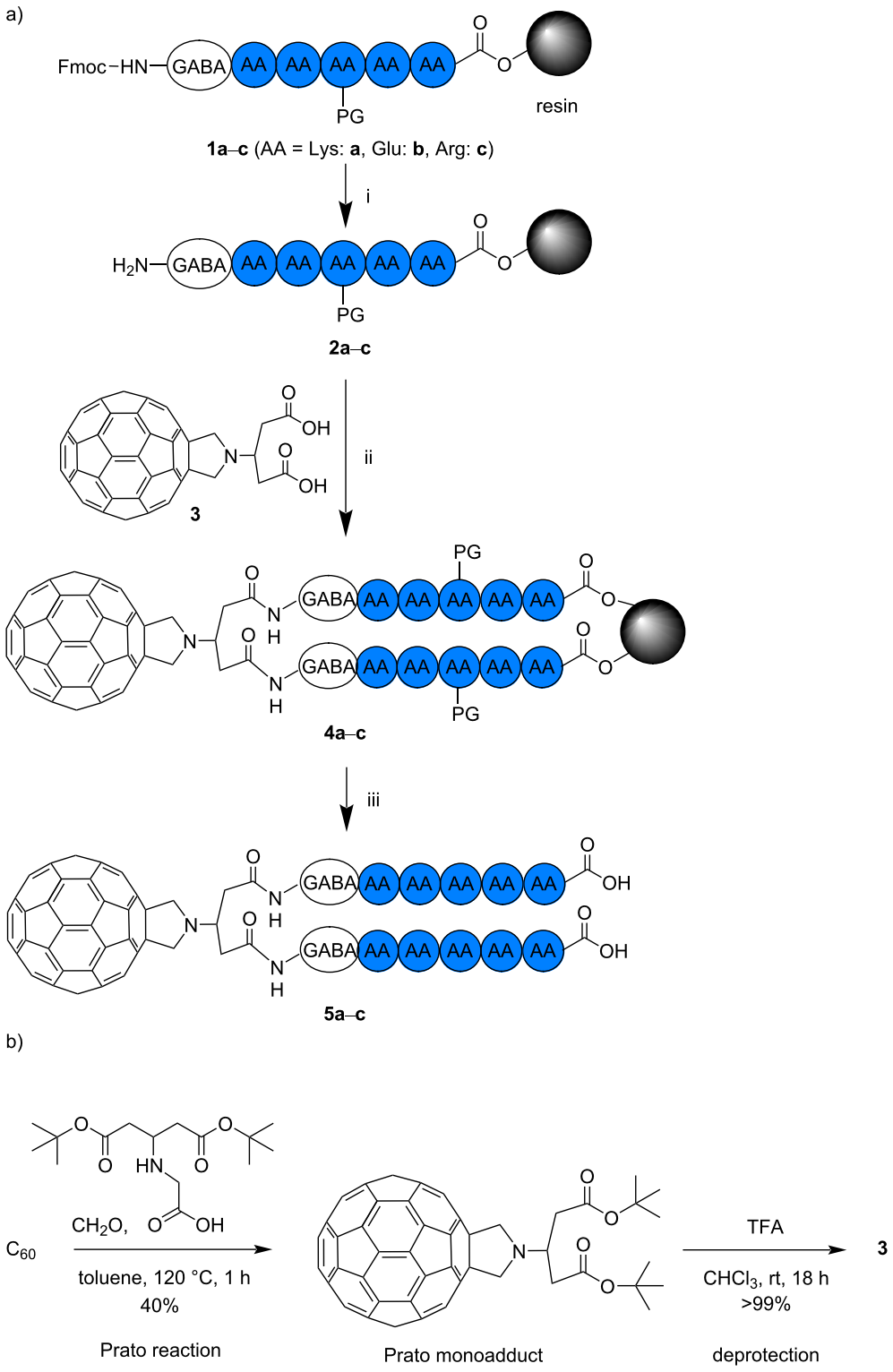

Figure 1: a) Synthesis of C_{60}–oligopeptide conjugates **5a–c** and b) synthesis of compound **3**. Fulleropyrrolidine-based biscarboxylic acid derivative **3** was prepared by Prato reaction and subsequent deprotection. Compound **3** was subjected to SPPS with the peptides on trityl resin (i.e., **2a–c**) to provide **4a–c**. By simultaneous deprotection of peptide side chains and cleavage from resin, C_{60}–oligo-Lys (**5a**), C_{60}–oligo-Glu (**5b**), and C_{60}–oligo-Arg (**5c**) were obtained. Reagents and conditions: i) 20% piperidine, rt, 2 × 10 min, ii) HBTU, DIPEA, in DMF, rt, overnight, and iii) trifluoroacetic acid (TFA)/triisopropylsilane (TIPS)/H_2O, rt, 1.5–2 h. AA and PG stand for amino acid and protecting group, respectively. All AAs in **1a–c**, **2a–c**, and **4a–c** were protected.

reagent. Finally, use of a greater excess (6.0 equiv) of peptide on resin relative to **3**, and a combination of HBTU and DIPEA as the coupling reagent and base, provided the C_{60}–peptide conjugate in an isolated yield of 41% (based on the used compound **3**). The yield of C_{60}–peptide conjugate formation decreased when using fewer equivalents of peptide on resin relative to compound **3**, providing as a byproduct the C_{60}–peptide conjugate connected to only one peptide anchor.

Based on the optimized reaction conditions outlined above, the conjugation of biscarboxylic acid-substituted C_{60} derivative **3** and the peptides on resin **2a–c** were performed by SPPS to provide the C_{60}–oligopeptides on resin **4a–c** (Figure 1a). Subsequently, the last step of the reaction – the cleavage of the C_{60}–peptide conjugate from the resin and the simultaneous deprotection of the amino acid residues – provided C_{60}–peptide conjugates **5a–c** with fully deprotected peptides.

The syntheses of C_{60}–oligo-Lys (**5a**), C_{60}–oligo-Glu (**5b**), and C_{60}–oligo-Arg (**5c**) were confirmed by HRMS (Figures S2, S11, and S18, Supporting Information File 1). While C_{60}–oligo-Lys (**5a**) was successfully observed by HRESIMS in a charged state of 3+ (Figure S2, Supporting Information File 1), C_{60}–oligo-Glu (**5b**) was confirmed by HRMS–MALDI (Figure S11, Supporting Information File 1) due to insolubility in the acidic eluent generally used for HRESIMS (a mixture of MeOH and water containing 0.1% formic acid). C_{60}–oligo-Arg (**5c**), which was not sufficiently soluble in most of the solvents, was slightly soluble in the acidic eluent, so that HRESIMS analysis provide HRMS data for a charged state of 4+ (Figure S18, Supporting Information File 1).

C_{60}–oligo-Lys (**5a**), with sufficient solubility in polar solvents, was isolated by reversed-phase HPLC. C_{60}–oligo-Glu (**5b**), which was soluble only in basic aqueous solution, could not be isolated by HPLC, especially in the presence of an oligo-Glu impurity, and was purified only after spin filtration. C_{60}–oligo-Arg (**5c**) was not soluble in any solvent and could not be further purified.

Solubility in water

The water solubility of C_{60}–peptide conjugates **5a–c** was tested after the removal of any remaining solvent traces by lyophilization. Upon addition of Milli-Q® water (pH 7.0), C_{60}–oligo-Lys (**5a**) was immediately and thoroughly solubilized. In contrast, the other conjugates, C_{60}–oligo-Glu (**5b**, purified) and C_{60}–oligo-Arg (**5c**, crude), did not produce transparent solutions in water at neutral pH value even by sonication (Figure 2). While C_{60}–oligo-Glu (**5b**) was soluble in buffer with a higher pH value (>8.3), C_{60}–oligo-Arg (**5c**) was not soluble in most

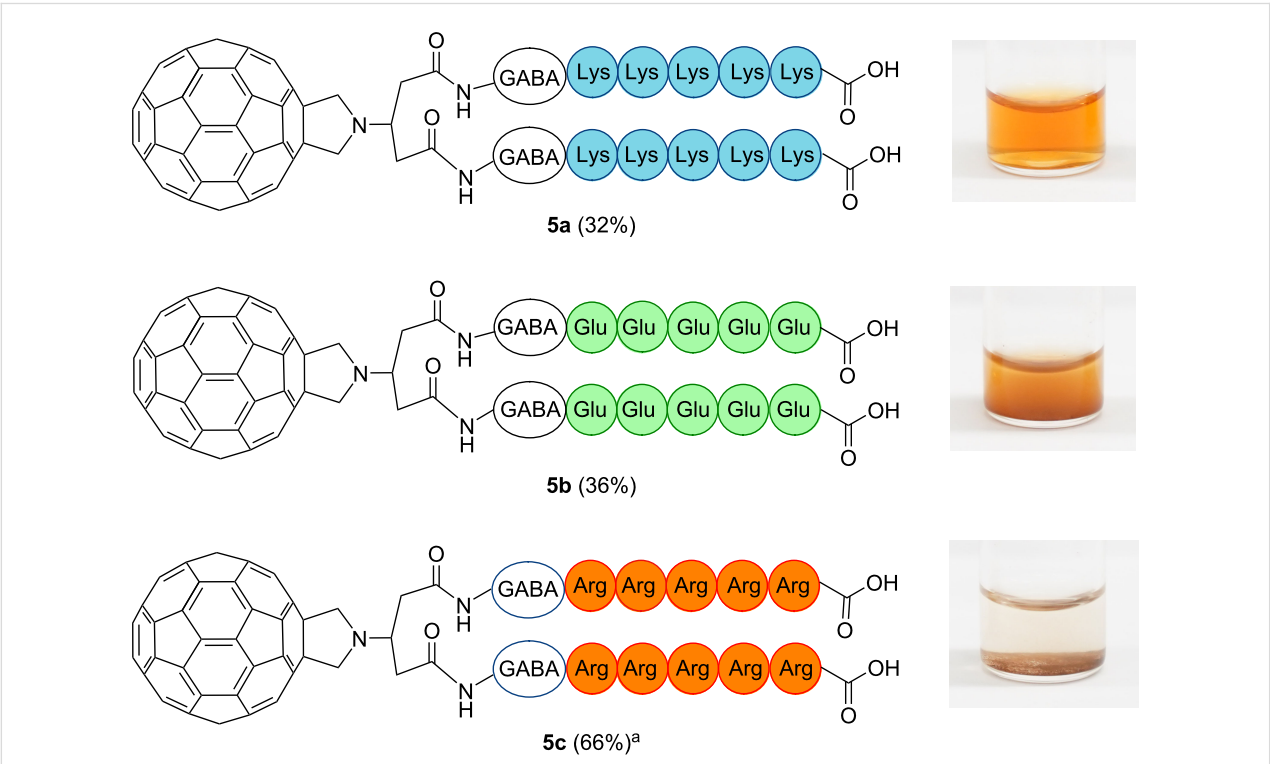

Figure 2: Structure of C_{60}–oligo-Lys (**5a**), C_{60}–oligo-Glu (**5b**), and C_{60}–oligo-Arg (**5c**) and images of dissolved or dispensed compounds in Milli-Q® water (pH 7.0). [a]Crude yield.

polar and nonpolar solvents. In addition, **5a** was not highly soluble in most nonpolar solvents, including toluene and CH_2Cl_2, but slightly soluble in other polar solvents, including MeOH and DMSO.

The solubility of C_{60}–peptide conjugates **5a–c** was in line with DLS data of the aqueous solutions or dispersions. While **5a** (blue line) revealed an extremely small hydrodynamic diameter (<10 nm) by DLS, **5b** (green line) and **5c** (purple line) revealed the presence of larger aggregates in water (pH 7.0), with a hydrodynamic diameters larger than 1 μm (Figure 3). In buffer at a higher pH value (e.g., pH 9, TRIS buffer), C_{60}–oligo-Glu (**5b**) showed much smaller aggregation (dotted green line, ≈12 nm), providing a transparent solution, while C_{60}–oligo-Arg (**5c**) remained insoluble over the tested pH value range (4.0–9.2). This was presumably due to the strong cation–π interactions between the cationic Arg moieties and the aromatic C_{60}, which is generally enhanced in polar environments [44-46]. The list of the solvents used to solubilize the molecules is summarized in Table S1, Supporting Information File 1.

Spectral characterizations of **5a** and **5b**

The absorption spectra of C_{60}–oligo-Lys (**5a**) and C_{60}–oligo-Glu (**5b**) were recorded in Milli-Q® water (pH 7.0) and in TRIS buffer (pH 9.0), respectively (Figure 4). The spectrum of C_{60}–oligo-Lys (**5a**) was in good agreement with that typically observed for C_{60} monoadduct derivatives [47]. The electronic spectra of the fulleropyrrolidines were characterized by notable π–π* absorption in the UV region. Additionally, **5a** exhibited broad absorption in the visible region with relatively low intensity as well as a distinctive sharp peak at around 430 nm [48]. However, those features were not observed in the spectrum of C_{60}–oligo-Glu (**5b**), presumably due to the aggregation [32].

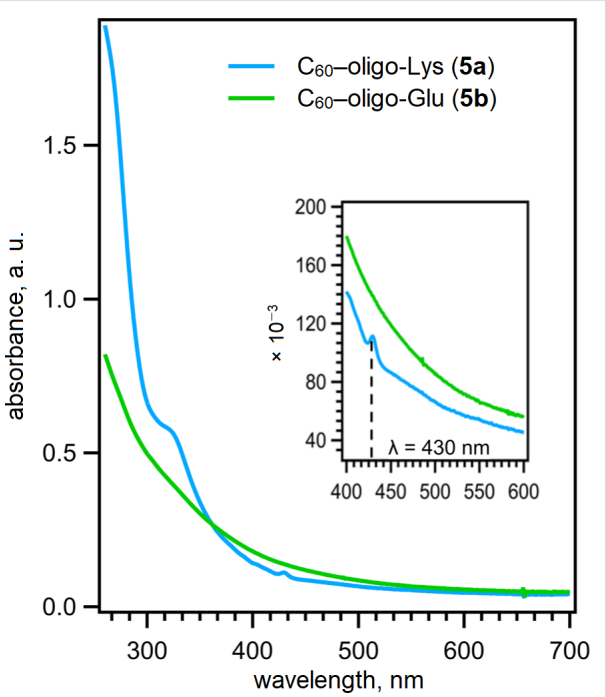

Figure 4: UV–vis spectra of C_{60}–peptide conjugates **5a** and **5b** (20 μM in Milli-Q® water for **5a** and in pH 9.0 TRIS buffer for **5b**).

The ^{1}H NMR spectrum of C_{60}–oligo-Lys (**5a**) was recorded in D_2O. As shown in Figure 5, the spectrum of **5a** (upper spec-

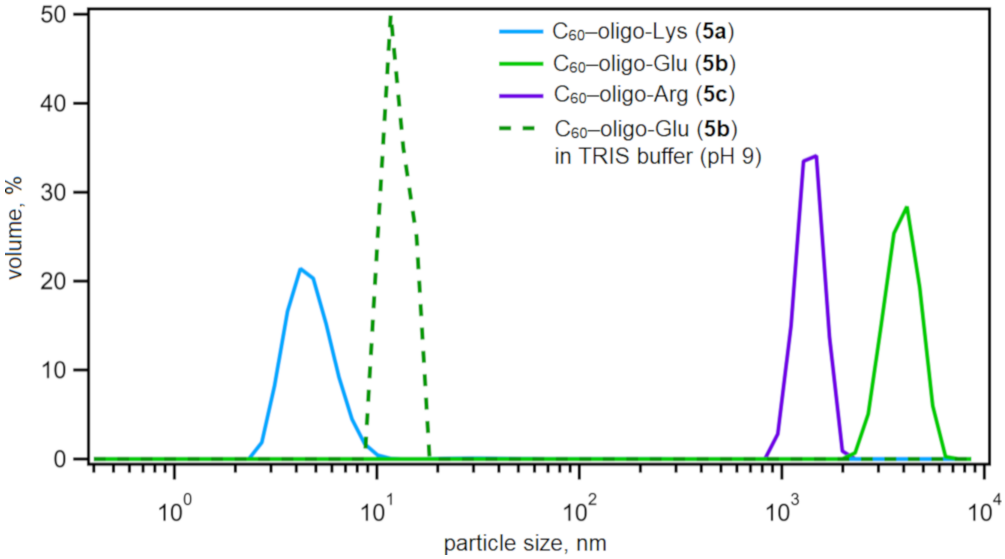

Figure 3: DLS diagrams of C_{60}–peptide conjugates **5a** (1 mM, in Milli-Q® water), **5b** (1 mM, in Milli-Q® water or in pH 9.0 TRIS buffer), and **5c** (1 mM, in Milli-Q® water). Particle size: mean, nm (polydispersity index, PDI): **5a**: 4.8 (0.757), **5b**: 3974 (0.906), **5c** (crude): 1382 (0.115) in Milli-Q® water and **5b**: 11.8 (1.000) in pH 9.0 TRIS buffer. Milli-Q® water was pH 7.0.

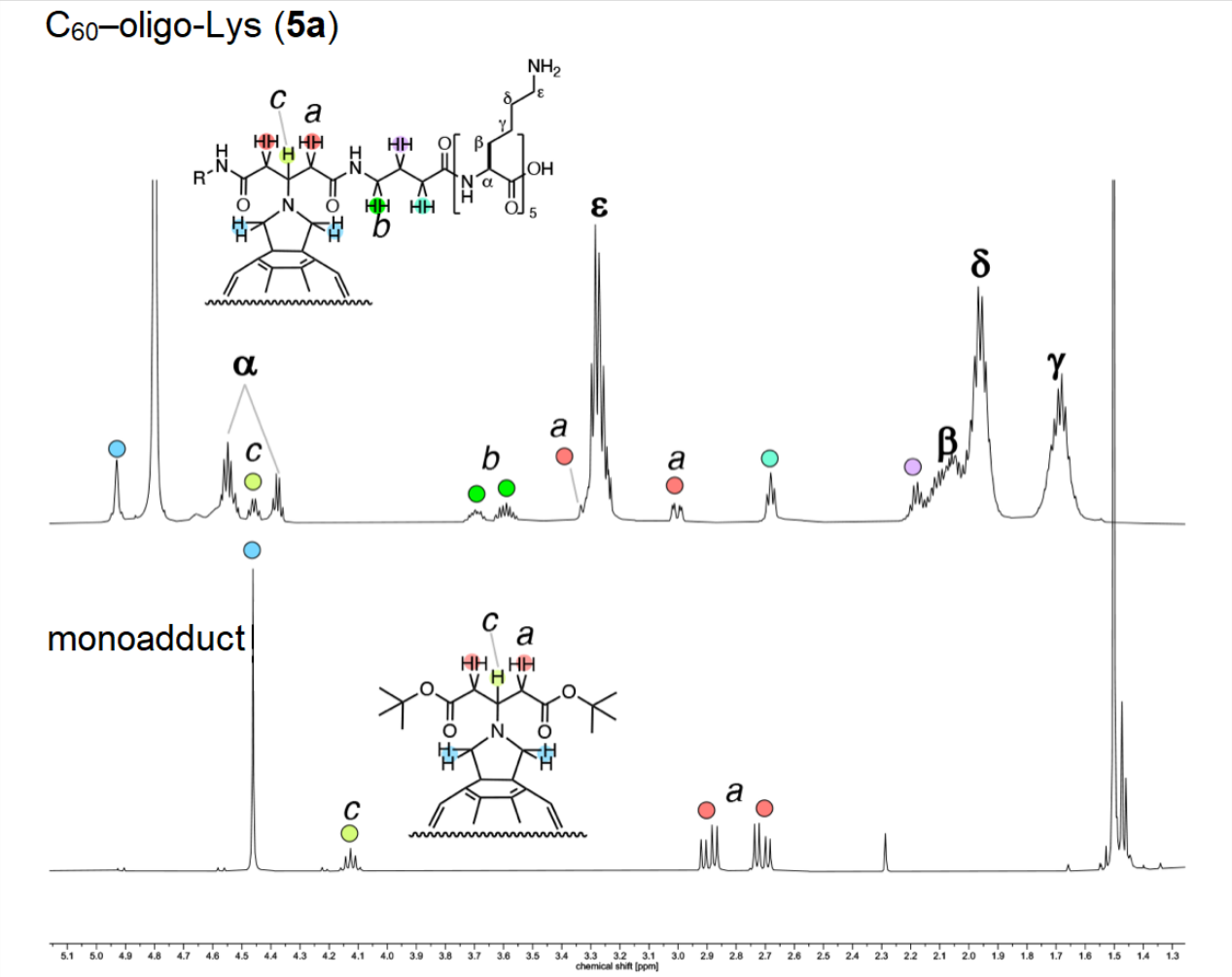

Figure 5: ^{1}H NMR spectrum of C_{60}–peptide conjugate **5a** in D_2O (above) and of the precursor monoadduct in $CDCl_3$ (bottom) at 600 MHz.

trum) clearly shows peaks for protons corresponding to the fulleropyrrolidine part, which are in line with the peaks in the spectrum of the C60 Prato monoadduct (lower spectrum), linker part, and oligo-Lys side chain part (α, β, γ, δ, and ε). The observed splitting of the protons a and b was presumably due to a diastereotopic effect of the methine proton c, similar to the spectrum of the monoadduct.

Figure 6a shows the ^{13}C NMR spectra of **5a** in D_2O and of the monoadduct in $CDCl_3$. Together with the ^{1}H NMR, COSY, HSQC, and HMBC spectra (Figures S3–S9, Supporting Information File 1), all peaks corresponding to the pyrrolidine part, linker part, and oligo-Lys part were assigned as shown in the chemical structure. In the sp^2 region of **5a** (Figure 6a, top), 17 signals (1C × 3 + 2C × 13) were observed similarly to the monoadduct (Figure 6a, bottom), which corresponds to the fullerene core in a characteristic manner for a C_{2v}-symmetric structure with a [6,6]-addition pattern. In the expanded spectrum of **5a** in the aromatic region (Figure 6b, top), several intense signals (corresponding to 2C) were observed as split peaks (highlighted by purple arrows). A similar situation was observed in the expanded spectrum of **5b** (Figure 6b, middle, measured in pyridine). This phenomenon suggests a symmetry break in the carbon cage moiety of the C_{60}–peptide conjugate upon the addition of chiral peptide anchors to the C_{60} core. Together with the HRESIMS results (Figure S2, Supporting Information File 1), it was confirmed that the highly water-soluble compound **5a** was successfully synthesized.

$^{1}O_2$ generation under visible light irradiation

To preliminarily evaluate the synthesized C_{60}–oligo-Lys (**5a**) as a PS, generation of singlet oxygen was measured by the ESR spin trapping method under irradiation of visible light (527 nm green LED). 4-Oxo-TEMP was used as a spin trapping reagent to form an adduct with $^{1}O_2$, i.e., 4-oxo-TEMPO, which was observed by ESR (Figure 7b). As shown in Figure 7a, upon visible light irradiation, three peaks corresponding to 4-oxo-TEMPO were observed in the solution of C_{60}–oligo-Lys (**5a**), similar to

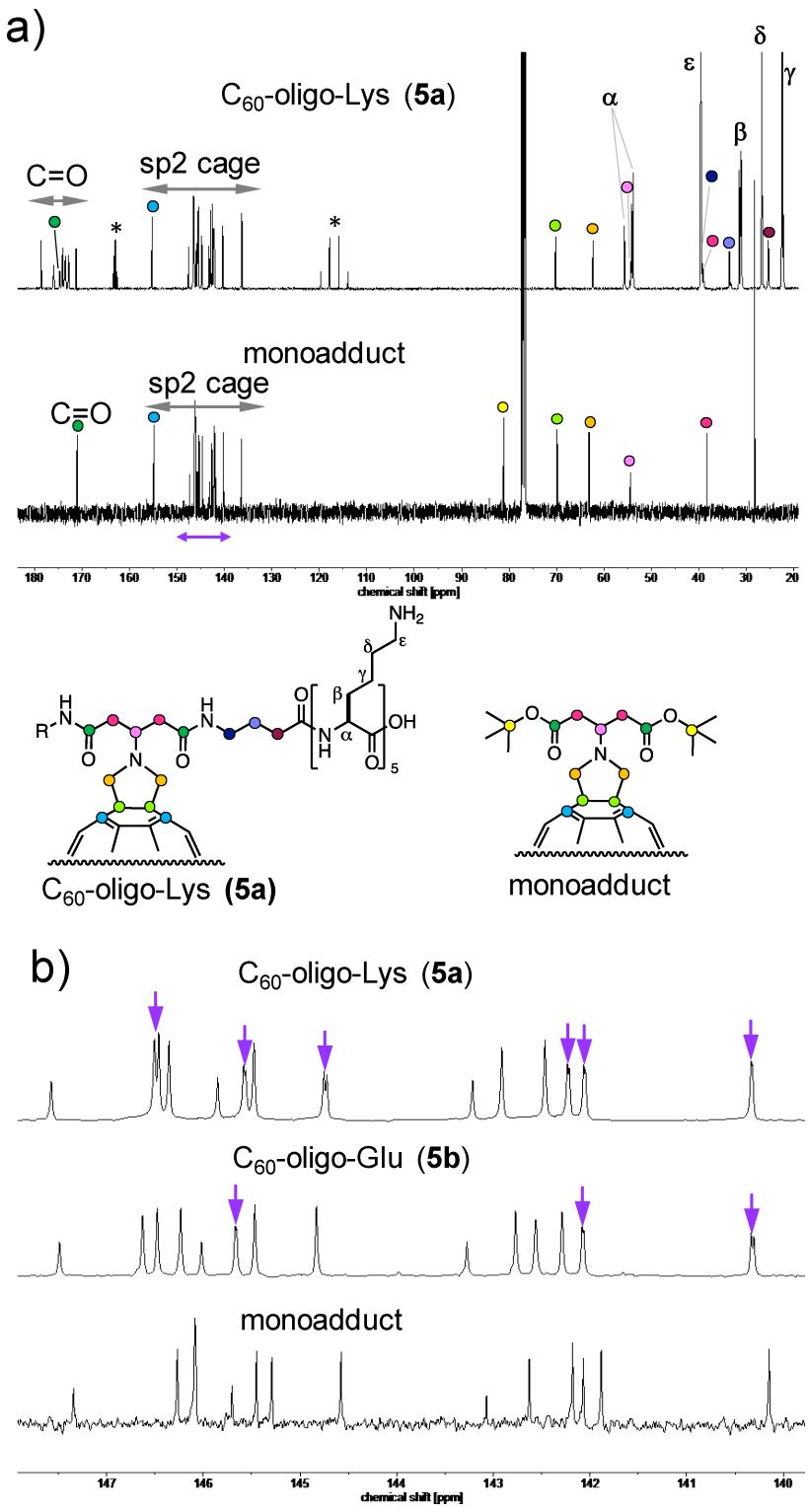

Figure 6: ^{13}C NMR spectrum of C_{60}–peptide conjugate **5a** in D_2O and of the precursor monoadduct in $CDCl_3$ at 150 MHz (a) and expansion of the sp^2 carbon region (b). The asterisks in (a) correspond to a TFA impurity. Purple arrows in (b) indicate the split peaks. The ^1H NMR spectrum of purified **5b** was measured in D_2O with 2% NaOD (Figure S12, Supporting Information File 1). ^{13}C NMR analysis of the same sample was not possible due to the high ionic strength of the solution. NMR characterization was performed using a crude sample of **5b**, with the penta-Glu impurity being soluble in pyridine-d_5 (Figures S13–S17, Supporting Information File 1).

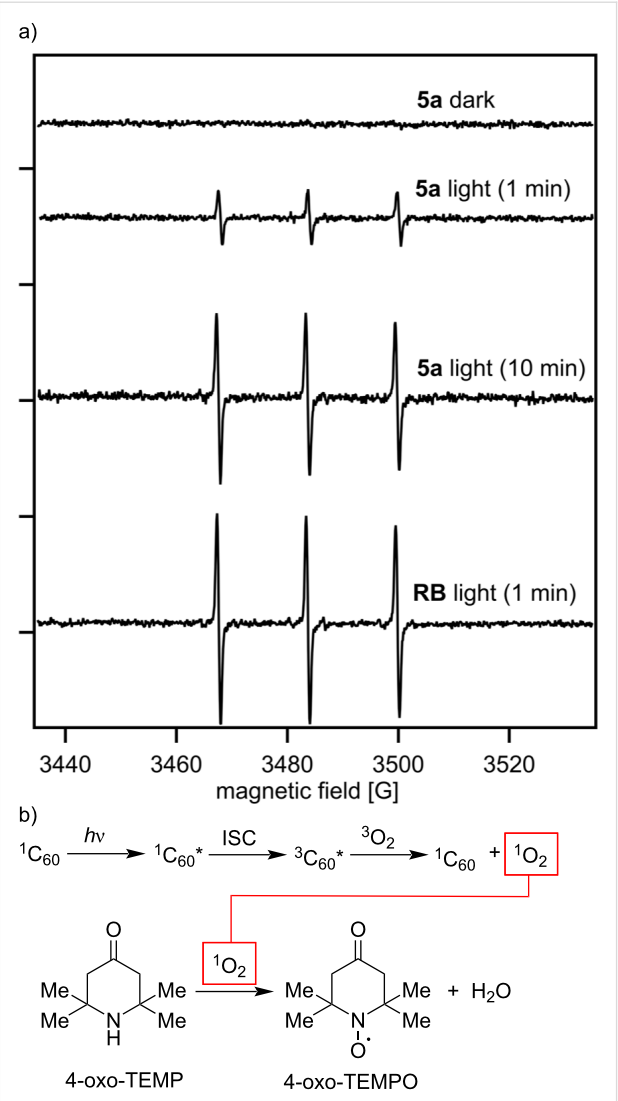

Figure 7: a) X-band ESR spectra of the 4-oxo-TEMP adduct with $^1O_2$ generated by C_{60}–oligo-Lys (**5a**) and rose bengal (RB), respectively, in aqueous solutions under irradiation with a green LED lamp (527 nm) for 1 min or 10 min. PS: 40 μM, 4-oxo-TEMP: 80 mM, in 60 mM phosphate buffer (pH 7.0). Measurement conditions: temperature 296 K, microwave frequency 10.03 GHz, microwave power 10 mW, receiver gain 5.0 × 10^4, modulation amplitude 1.00 G, modulation frequency 100 KHz, sweep time 83.89 s, number of scans: 1. b) Scheme for the photoinduced $^1O_2$ generation by C_{60} and reaction with spin trapping reagent 4-oxo-TEMP to form 4-oxo-TEMPO.

the results with rose bengal, a standard compound for $^1O_2$ generation. By taking into account that the absorption intensity of **5a** at 527 nm used for the photoirradiation was ≈10 times smaller than that of rose bengal, it was suggested that $^1O_2$ was sufficiently present in the solution of **5a**.

Conclusion

Starting from biscarboxylic acid-substituted fulleropyrrolidine derivative **3**, the three C_{60}–oligopeptides **5a–c** were synthesized through SPPS. Between these conjugates, C_{60}–oligo-Lys (**5a**) had sufficient solubility and a very small hydrodynamic diameter in a neutral aqueous medium, as shown by DLS analysis. Visible-light-induced $^1O_2$ generation by C_{60}–oligo-Lys (**5a**) was confirmed by ESR spin trapping. This suggests the high potential of **5a** as a basis for a fullerene-derived PS in biological applications.

Experimental

Synthesis of oligopeptides on resin **1a–c**

The oligopeptides on resin **1a–c** were synthesized via a general SPPS protocol. The first addition of Fmoc-AA(PG)-OH to the 2-chlorotrityl resin was performed in the presence of DIPEA (2 equiv) in CH_2Cl_2, followed by capping with a CH_2Cl_2/MeOH/DIPEA (18:2:1, v/v) mixture to quench any remaining unreacted chlorotrityl moieties on the resin surface. Subsequently, four additional Fmoc-AA(PG)-OH residues and one Fmoc-GABA-OH residue were added to the resin to provide the peptides on resin **1a–c**. Each coupling step was carried out in the presence of HCTU (4 equiv) and NMM (8 equiv) in DMF. Each Fmoc deprotection step of the peptide N-terminus was conducted by the repeated treatment of the peptide on resin with 20% piperidine in DMF (2 × 10 min). After each coupling reaction, the resin was washed with DMF.

Synthesis of C_{60}–peptide conjugates **5a–c**

The synthetic details and corresponding spectra for the C_{60}–peptide conjugates **5a–c** are shown in Supporting Information File 1. The optimization of the conditions for the reaction between the peptides on resin and fulleropyrrolidine **3** are described in the Results and Discussion section above. These were used to prepare the C_{60}–peptide conjugates on resin **4a–c** from **2a–c**. The C_{60}–oligopeptides **5a–c** were obtained by cleavage from resin and simultaneous deprotection of the PGs on the amino acid side chains through the addition of by the addition of a mixture of TFA and TIPS in water. The most soluble conjugate, C_{60}–oligo-Lys (**5a**), was purified by reversed-phase HPLC, while C_{60}–oligo-Glu (**5b**) was purified by spin filtration.

C_{60}–oligo-Lys (**5a**) was obtained in a yield of 32% for the total peptide synthesis and characterized by HRESIMS. HRESIMS (*m*/*z*): $[M + 3H]^{3+}$ calcd for $C_{135}H_{148}N_{23}O_{16}$, 782.3819; found, 782.3821.

C_{60}–oligo-Glu (**5b**) was obtained in a yield of 36% for the total peptide synthesis and characterized by HRMS–MALDI. HRMS–MALDI (*m*/*z*): $[M + H]^+$ calcd for $C_{125}H_{96}N_{13}O_{36}$, 2354.6075; found, 2354.6008.

C_{60}–oligo-Arg (**5c**) was obtained in a crude yield of 66% for the total peptide synthesis and characterized by HRESIMS.

HRESIMS (m/z): $[M + 4H]^{4+}$ calcd for $C_{135}H_{149}N_{43}O_{16}$, 657.0536; found, 657.0540.

Supporting Information

Supporting Information File 1

Details for the synthesis of **5a–c** and intermediates as well as spectral data.
[https://www.beilstein-journals.org/bjoc/content/supplementary/1860-5397-20-71-S1.pdf]

Acknowledgements

The authors thank Prof. Jean-Christophe Leroux at ETH Zürich for his help with DLS measurements. The authors thank Dr. Marc-Olivier Ebert at ETH Zürich for his help with NMR measurements and discussions. The authors thank the Molecular and Biomolecular Analytical Service (MoBiAS) at ETH Zürich for their support with HRMS measurements.

Funding

This study was supported in part by SNF project funding (200021_156097, 205321_173018, IZLJZ2_183660, and 200020_215397) and ETH Grants (ETH-45_19-1 and ETH-36_20-2).

Author Contributions

Yue Ma: investigation; writing – original draft. Lorenzo Persi: investigation; writing – review & editing. Yoko Yamakoshi: conceptualization; funding acquisition; methodology; project administration; resources; supervision; writing – original draft; writing – review & editing.

ORCID® iDs

Yue Ma - https://orcid.org/0000-0002-6476-3715
Lorenzo Persi - https://orcid.org/0009-0007-5312-4209
Yoko Yamakoshi - https://orcid.org/0000-0001-8466-0118

Data Availability Statement

All data that supports the findings of this study is available in the published article and/or the supporting information to this article.

References

1. Kroto, H. W.; Heath, J. R.; O'Brien, S. C.; Curl, R. F.; Smalley, R. E. *Nature* **1985,** *318,* 162–163. doi:10.1038/318162a0
2. Xu, J.; Buin, A.; Ip, A. H.; Li, W.; Voznyy, O.; Comin, R.; Yuan, M.; Jeon, S.; Ning, Z.; McDowell, J. J.; Kanjanaboos, P.; Sun, J.-P.; Lan, X.; Quan, L. N.; Kim, D. H.; Hill, I. G.; Maksymovych, P.; Sargent, E. H. *Nat. Commun.* **2015,** *6,* 7081. doi:10.1038/ncomms8081
3. Chiang, C.-H.; Wu, C.-G. *Nat. Photonics* **2016,** *10,* 196–200. doi:10.1038/nphoton.2016.3
4. Chai, Y.; Liu, L.; Xu, Y.; Liu, X.; Wang, C.; Bo, Y.; Zhang, Y.; Wang, Z.; Weng, Y.; Guldi, D. M.; Wu, B.; Wang, C. *J. Am. Chem. Soc.* **2023,** *145,* 14190–14195. doi:10.1021/jacs.3c03486
5. Yu, L.; Xu, J.; Peng, B.; Qin, G.; Su, G. *J. Phys. Chem. Lett.* **2022,** *13,* 11622–11629. doi:10.1021/acs.jpclett.2c02702
6. Eklund, P. C.; Rao, A. M.; Wang, Y.; Zhou, P.; Wang, K.-A.; Holden, J. M.; Dresselhaus, M. S.; Dresselhaus, G. *Thin Solid Films* **1995,** *257,* 211–232. doi:10.1016/0040-6090(94)05706-0
7. Pawlak, R.; Kawai, S.; Fremy, S.; Glatzel, T.; Meyer, E. *ACS Nano* **2011,** *5,* 6349–6354. doi:10.1021/nn201462g
8. David, W. I. F.; Ibberson, R. M.; Matthewman, J. C.; Prassides, K.; Dennis, T. J. S.; Hare, J. P.; Kroto, H. W.; Taylor, R.; Walton, D. R. M. *Nature* **1991,** *353,* 147–149. doi:10.1038/353147a0
9. Ruoff, R. S.; Tse, D. S.; Malhotra, R.; Lorents, D. C. *J. Phys. Chem.* **1993,** *97,* 3379–3383. doi:10.1021/j100115a049
10. Nakamura, E.; Isobe, H. *Acc. Chem. Res.* **2003,** *36,* 807–815. doi:10.1021/ar030027y
11. Tokuyama, H.; Yamago, S.; Nakamura, E.; Shiraki, T.; Sugiura, Y. *J. Am. Chem. Soc.* **1993,** *115,* 7918–7919. doi:10.1021/ja00070a064
12. Sijbesma, R.; Srdanov, G.; Wudl, F.; Castoro, J. A.; Wilkins, C.; Friedman, S. H.; DeCamp, D. L.; Kenyon, G. L. *J. Am. Chem. Soc.* **1993,** *115,* 6510–6512. doi:10.1021/ja00068a006
13. Lamparth, I.; Hirsch, A. *J. Chem. Soc., Chem. Commun.* **1994,** 1727–1728. doi:10.1039/c39940001727
14. Sawamura, M.; Iikura, H.; Nakamura, E. *J. Am. Chem. Soc.* **1996,** *118,* 12850–12851. doi:10.1021/ja962681x
15. Matsuo, Y.; Nakamura, E. *Chem. Rev.* **2008,** *108,* 3016–3028. doi:10.1021/cr0684218
16. Andersson, T.; Nilsson, K.; Sundahl, M.; Westman, G.; Wennerström, O. *J. Chem. Soc., Chem. Commun.* **1992,** 604–606. doi:10.1039/c39920000604
17. Ikeda, A.; Nobukuni, S.; Udzu, H.; Zhong, Z.; Shinkai, S. *Eur. J. Org. Chem.* **2000,** 3287–3293. doi:10.1002/1099-0690(200010)2000:19<3287::aid-ejoc3287>3.0.co;2-r
18. Ikeda, A.; Shinkai, S. *Chem. Rev.* **1997,** *97,* 1713–1734. doi:10.1021/cr960385x
19. Garbuio, L.; Antonello, S.; Guryanov, I.; Li, Y.; Ruzzi, M.; Turro, N. J.; Maran, F. *J. Am. Chem. Soc.* **2012,** *134,* 10628–10637. doi:10.1021/ja303696s
20. Jennepalli, S.; Hammer, K. A.; Riley, T. V.; Pyne, S. G.; Keller, P. A. *Eur. J. Org. Chem.* **2015,** 195–201. doi:10.1002/ejoc.201403046
21. Ousaka, N.; Mamiya, F.; Iwata, Y.; Nishimura, K.; Yashima, E. *Angew. Chem., Int. Ed.* **2017,** *56,* 791–795. doi:10.1002/anie.201611349
22. Dostalova, S.; Moulick, A.; Milosavljevic, V.; Guran, R.; Kominkova, M.; Cihalova, K.; Heger, Z.; Blazkova, L.; Kopel, P.; Hynek, D.; Vaculovicova, M.; Adam, V.; Kizek, R. *Monatsh. Chem.* **2016,** *147,* 905–918. doi:10.1007/s00706-016-1675-0
23. Liu, J.-H.; Cao, L.; Luo, P. G.; Yang, S.-T.; Lu, F.; Wang, H.; Meziani, M. J.; Haque, S. A.; Liu, Y.; Lacher, S.; Sun, Y.-P. *ACS Appl. Mater. Interfaces* **2010,** *2,* 1384–1389. doi:10.1021/am100037y
24. Li, Y.; Biswas, R.; Kopcha, W. P.; Dubroca, T.; Abella, L.; Sun, Y.; Crichton, R. A.; Rathnam, C.; Yang, L.; Yeh, Y.-W.; Kundu, K.; Rodríguez-Fortea, A.; Poblet, J. M.; Lee, K.-B.; Hill, S.; Zhang, J. *Angew. Chem., Int. Ed.* **2023,** *62,* e202380362. doi:10.1002/anie.202380362

25. Yamakoshi, Y. N.; Yagami, T.; Fukuhara, K.; Sueyoshi, S.; Miyata, N. *J. Chem. Soc., Chem. Commun.* **1994,** 517–518. doi:10.1039/c39940000517
26. Yamakoshi, Y. N.; Yagami, T.; Sueyoshi, S.; Miyata, N. *J. Org. Chem.* **1996,** *61,* 7236–7237. doi:10.1021/jo961210q
27. Yamakoshi, Y.; Sueyoshi, S.; Fukuhara, K.; Miyata, N.; Masumizu, T.; Kohno, M. *J. Am. Chem. Soc.* **1998,** *120,* 12363–12364. doi:10.1021/ja9823969
28. Yamakoshi, Y.; Umezawa, N.; Ryu, A.; Arakane, K.; Miyata, N.; Goda, Y.; Masumizu, T.; Nagano, T. *J. Am. Chem. Soc.* **2003,** *125,* 12803–12809. doi:10.1021/ja0355574
29. Kai, Y.; Komazawa, Y.; Miyajima, A.; Miyata, N.; Yamakoshi, Y. *Fullerenes, Nanotubes, Carbon Nanostruct.* **2003,** *11,* 79–87. doi:10.1081/fst-120018664
30. Tsuchiya, T.; Yamakoshi, Y. N.; Miyata, N. *Biochem. Biophys. Res. Commun.* **1995,** *206,* 885–894. doi:10.1006/bbrc.1995.1126
31. Tsuchiya, T.; Oguri, I.; Nakajima Yamakoshi, Y.; Miyata, N. *Fullerene Sci. Technol.* **1996,** *4,* 989–999. doi:10.1080/10641229608001157
32. Sakai, A.; Yamakoshi, Y. N.; Miyata, N. *Fullerene Sci. Technol.* **1995,** *3,* 377–388. doi:10.1080/153638x9508543792
33. Sakai, A.; Yamakoshi, Y.; Miyata, N. *Fullerene Sci. Technol.* **1999,** *7,* 743–756. doi:10.1080/10641229909351375
34. Iwata, N.; Mukai, T.; Yamakoshi, Y. N.; Haraa, S.; Yanase, T.; Shoji, M.; Endo, T.; Miyata, N. *Fullerene Sci. Technol.* **1998,** *6,* 213–226. doi:10.1080/10641229809350196
35. Aroua, S.; Schweizer, W. B.; Yamakoshi, Y. *Org. Lett.* **2014,** *16,* 1688–1691. doi:10.1021/ol500363r
36. Maggini, M.; Scorrano, G.; Prato, M. *J. Am. Chem. Soc.* **1993,** *115,* 9798–9799. doi:10.1021/ja00074a056
37. Aroua, S.; Tiu, E. G. V.; Ishikawa, T.; Yamakoshi, Y. *Helv. Chim. Acta* **2016,** *99,* 805–813. doi:10.1002/hlca.201600171
38. Liosi, K.; Stasyuk, A. J.; Masero, F.; Voityuk, A. A.; Nauser, T.; Mougel, V.; Solà, M.; Yamakoshi, Y. *JACS Au* **2021,** *1,* 1601–1611. doi:10.1021/jacsau.1c00239
39. Aroua, S.; Tiu, E. G. V.; Ayer, M.; Ishikawa, T.; Yamakoshi, Y. *Polym. Chem.* **2015,** *6,* 2616–2619. doi:10.1039/c4py01333f
40. Tiu, E. G. V.; Liosi, K.; Aroua, S.; Yamakoshi, Y. *J. Mater. Chem. B* **2017,** *5,* 6676–6680. doi:10.1039/c7tb00829e
41. Hamblin, M. R. *Photochem. Photobiol. Sci.* **2018,** *17,* 1515–1533. doi:10.1039/c8pp00195b
42. Shu, C.; Corwin, F. D.; Zhang, J.; Chen, Z.; Reid, J. E.; Sun, M.; Xu, W.; Sim, J. H.; Wang, C.; Fatouros, P. P.; Esker, A. R.; Gibson, H. W.; Dorn, H. C. *Bioconjugate Chem.* **2009,** *20,* 1186–1193. doi:10.1021/bc900051d
43. Amblard, M.; Fehrentz, J.-A.; Martinez, J.; Subra, G. *Mol. Biotechnol.* **2006,** *33,* 239–254. doi:10.1385/mb:33:3:239
44. Gromiha, M. M.; Santhosh, C.; Ahmad, S. *Int. J. Biol. Macromol.* **2004,** *34,* 203–211. doi:10.1016/j.ijbiomac.2004.04.003
45. Pletneva, E. V.; Laederach, A. T.; Fulton, D. B.; Kostić, N. M. *J. Am. Chem. Soc.* **2001,** *123,* 6232–6245. doi:10.1021/ja010401u
46. Marforio, T. D.; Calza, A.; Mattioli, E. J.; Zerbetto, F.; Calvaresi, M. *Int. J. Mol. Sci.* **2021,** *22,* 11567. doi:10.3390/ijms222111567
47. Guldi, D. M. *J. Phys. Chem. A* **1997,** *101,* 3895–3900. doi:10.1021/jp9702863
48. Guldi, D. M.; Prato, M. *Acc. Chem. Res.* **2000,** *33,* 695–703. doi:10.1021/ar990144m

License and Terms

BEILSTEIN JOURNAL OF ORGANIC CHEMISTRY

Spin and charge interactions between nanographene host and ferrocene

Akira Suzuki[1], Yuya Miyake[2], Ryoga Shibata[1] and Kazuyuki Takai[*1,2]

Letter

Open Access

Address:
[1]Graduated School of Science and Engineering, Hosei University, Tokyo 184-8584, Japan and [2]Department of Chemical Science and Technology, Hosei University, Tokyo 184-8584, Japan

Email:
Kazuyuki Takai[*] - takai@hosei.ac.jp

* Corresponding author

Keywords:
charge transfer; ferrocene; graphene; host–guest; spin interaction

Beilstein J. Org. Chem. **2024,** *20,* 1011–1019.
https://doi.org/10.3762/bjoc.20.89

Received: 01 December 2023
Accepted: 17 April 2024
Published: 02 May 2024

This article is part of the thematic issue "Carbon-rich materials: from polyaromatic molecules to fullerenes and other carbon allotropes".

Guest Editor: Y. Yamakoshi

Abstract

Ferrocene ($FeCp_2$) was introduced as a non-magnetic guest molecule to activated carbon fibers (ACFs) as a nanographene-based host having localized spins originating from zigzag edges of graphene. The introduction of the guest molecule was confirmed by FTIR for ACFs-$FeCp_2$ introduced at 55 (150) °C ($FeCp_2$-ACFs-55(150)). The appearance of satellite Fe_{2p} peaks and the increase in shake-up peak intensity of the C_{1s} in the XPS spectrum proved the emergence of charge-transfer host–guest interaction in $FeCp_2$-ACFs-150, supported by the red-shift of the G-band in the Raman spectrum. The six-times enhancement in the spin concentration in $FeCp_2$-ACFs-150 compared with ACFs indicates the spin magnetism of the non-magnetic guest $FeCp_2^+$ molecule induced by a charge-transfer host–guest interaction in the nanographene host. The larger ESR linewidth than that expected from the dipolar interaction estimated by the localized spin concentration suggests the exchange interaction between the nanographene and $FeCp_2$ spins. The narrowing of the ESR linewidth of $FeCp_2$-ACFs-55 upon higher excitation microwave power suggests the inhomogeneity of the environment for $FeCp_2^+$ molecules in the nanographene host. The observed induction of spin magnetism by the interfacial interactions between the nanographene host and the guest molecules will be a promising strategy for developing a new class of molecular magnets.

Introduction

Nanocarbon host material, which is based on elements free from resource depletion, is attracting much attention due to its potential for creating a new class of functional materials with various guest molecules [1]. In particular, nanosized graphene called nanographene, the macroscopic limit of polycyclic aromatic hydrocarbon molecules, is a magnetic host material with spins localized at edges [2]. The presence of edges greatly modifies the electronic structure of nanographene, which strongly depends on the geometry of the edges [3-5]. Edges at the periphery of nanographene sheets consist of two kinds of geom-

etry: zigzag edges and armchair edges. The presence of the zigzag part in the arbitrarily shaped edges results in the emergence of radical π-electron states called "edge states", which are spatially localized at the edge site. The edge states appear at the Dirac point at which two linear conduction (anti-bonding) π*- and valence (bonding) π-bands touch each other in the electronic energy bands of graphene. Since the Fermi level is located at the Dirac point for neutral nanographene, edge states are half-filled like singly occupied molecular orbitals (SOMO) of radical states. Namely, nanographene sheets become magnetic and chemically active due to the edge states with localized spins of unpaired electrons [6]. Thus, it is interesting to introduce a magnetic guest molecule into a magnetic nanographene host regarding the development of a new class of magnetic materials.

Oxygen [7-11], nitrogen monoxide molecules [12,13], and potassium clusters having unpaired spins [14,15] have been introduced to nanographene hosts as magnetic guest molecules so far. However, the decomposition of molecules, the vanishment of guest magnetism, etc., after accommodation by the host material prevent magnetic interactions between the host and guest in these systems. The material design should be important in this viewpoint, especially in choosing appropriate guest molecules. Since π electrons extend to in-plane directions in nanographene, a guest molecule with an aromatic ring is promising for significant interaction with the nanographene host through π–π stacking.

Ferrocene ($FeCp_2$) is a "sandwich" compound where the two cyclopentadienyl (Cp or C_5H_5-) rings sit above and below the Fe^{2+} ion [16]. The electronic structure of $FeCp_2$ satisfies the 18-electron rule, so this compound is stable due to a closed L-shell structure in view of the atomic orbitals of Fe and it is a diamagnetic molecule (S = 0, no spin magnetism) compared with other metallocenes [17]. However, $FeCp_2$ is easily oxidized to a monovalent cation, the electronic structure of which is magnetic (S = 1/2). Electron spin resonance (ESR) spectroscopy revealed the spin magnetism of cationic $FeCp_2$ accommodated in mesoporous silica (MCM-41) [18]. So, ferrocene is expected to exhibit strong host–guest interactions with a nanographene host through π–π stacking.

Regarding ferrocene as a guest molecule for nanocarbon hosts, carbon nanotubes (CNTs) have been used to accommodate guest ferrocene molecules, where the amount of the charge transfer from ferrocene to CNTs was estimated from the shift of peaks for van Hove singularities in the valence-band photoemission spectrum [19,20]. The magnetic properties of ferrocene encapsulated into CNTs have also been investigated by superconducting quantum interference devices (SQUID) [21,22] and X-ray magnetic circular dichroism (XMCD) spectroscopy [23]. However, only a tiny paramagnetic behavior of encapsulated ferrocene was observed, and no magnetic host–guest interactions were reported due to the diamagnetic nature of CNTs.

Activated carbon fibers (ACFs) consist of a three-dimensional disordered network of nanographite domains, each of which is a loose stack of 3–4 nanographene sheets with a mean in-plane size of 2–3 nm. ACFs have huge specific surface areas (about 2000 m^2/g [24,25]) due to the presence of nanopores of ca. 1 nm in diameter between the nanographite domains, where various guest chemical species can be accommodated [2]. Thus, ACFs are widely used as nanographene host materials. Interestingly, a ferromagnetic behavior below 120 K was once mentioned for $FeCp_2$-adsorbed ACFs, even though no data was shown in the report [26]. It is necessary to clarify the magnetic interactions between the nanographene host and $FeCp_2$ guest molecules to achieve a ferromagnet using nanographene host–guest systems.

In this study, we introduced ferrocene to ACFs and investigated the magnetic interaction between the host ACFs and ferrocene as magnetic guest molecule using X-ray photoelectron spectroscopy (XPS), Raman spectroscopy, Fourier-transform infrared (FTIR) spectroscopy, magnetic susceptibility, and electron-spin resonance (ESR).

Experimental

Commercially available ACFs (Kuraray, FR-20), of which the precursor was a phenol-resin, were pre-heat-treated in a glass tube at 200 °C for 24 hours under 2×10^{-4} Pa before the introduction of $FeCp_2$ in order to eliminate ambient gas molecules adsorbed in ACFs. The introduction of $FeCp_2$ was carried out by exposing ACFs to the vapor phase of $FeCp_2$ in the evacuated glass without exposing samples to air after the pre-heat-treatment at temperatures 55 °C and 150 °C ($FeCp_2$-ACFs-55, $FeCp_2$-ACFs-150), for 18 to 24 hours. The vapor pressure of ferrocene corresponding to each temperature was previously reported (15 Pa for 55 °C, 5.7×10^3 Pa for 150 °C) [27]. In the case of introduction at 150 °C, excessive $FeCp_2$ precipitated as crystals on the surface of ACFs, which were removed by heating the $FeCp_2$-treated ACFs at 150 °C for 3 hours without $FeCp_2$ vapor.

XPS spectra were recorded using a PHI-5600 (ULVAC-PHI) with an Al Kα X-ray source (1486.7 eV) for samples mounted on an indium film. Raman spectroscopy measurements were performed by LabRAM HR Evolution instruments (Horiba) with an excitation laser operated at 532 nm in the wavenumber range from 1000 to 2000 cm^{-1}. FTIR spectra were obtained using an FT/IR-6600 (JASCO) in ATR method with a diamond prism. Magnetic susceptibility measurements were carried out

by a superconducting quantum interference device (SQUID) magnetometer (Quantum Design, MPMS-XL) in the field of 1 T between 2 K and 300 K, where ca. 30 mg of the samples vacuum-sealed in glass tubes (for ACFs and $FeCp_2$-ACFs-150), mounted inside a plastic straw ($FeCp_2$) were used. The Weiss temperature Θ and the temperature-independent term of the magnetic susceptibility were obtained by least-square fitting the data of the temperature-dependence of the observed susceptibility χ with the following equation based on a model of the summation of the Curie–Weiss localized magnetism and temperature contribution,

$$\chi = \frac{C}{T-\Theta} + \chi_{const.},$$

where C denotes the Curie constant. The spin concentration N_{spin} for each sample was calculated from the Curie constant.

ESR measurements were performed using a conventional ESR X-band spectrometer (JEOL, JES-FA300) at room temperature, where ca 1 mg of samples vacuum-sealed in glass tubes were used. In order to prevent the skin effect, ACFs were ground in a mortar before the measurement.

Results and Discussion

XPS spectra acquired in a wide binding energy region for ACFs and $FeCp_2$-ACFs-150 are shown in Figure 1. Peaks of C_{1s} and O_{1s} were observed in ACFs, while C_{1s}, O_{1s}, and Fe_{2p} peaks appeared in the spectrum for $FeCp_2$-ACFs-150.

Figure 2 shows the Fe_{2p} spectrum for $FeCp_2$-ACFs-150 in a narrow binding energy region. The binding energies of the Fe_{2p} peaks are similar to the reported value for $FeCp_2$ [16]. So, the Fe_{2p} peaks observed in $FeCp_2$-ACFs-150 indicate the successful introduction of the $FeCp_2$ molecule into ACFs as nanographene host. In addition to the main peaks, satellite peaks clearly appear at the higher energy side (ca. +3 eV), which indicates that the $FeCp_2$ molecules partially become cationized (positively charged) in $FeCp_2$-ACFs-150.

Figure 3a and b show the C_{1s} spectra for $FeCp_2$-ACFs-150 and ACFs in a narrow binding energy region, respectively.

Table 1 shows peak positions for XPS C_{1s}, O_{1s}, and Fe_{2p} peaks for ACFs and $FeCp_2$-ACFs-150, where elemental abundances are obtained from the peak intensity. The amount of $FeCp_2$ is calculated as 0.39 mmol in 1 g of $FeCp_2$-ACFs-150 from the total intensity ratio of Fe_{2p}. The amount of the cationized $FeCp_2$ ($FeCp_2^+$) is obtained as 0.15 mmol/g of $FeCp_2$-ACFs-150 according to the intensity ratio of satellite peaks to the main peaks. The O_{1s} peaks mainly come from oxygen-containing functional groups bonded to nanographene because of oxidization by ambient gaseous species. The elemental abundance ratio O/C of 0.07 is the same for ACFs and $FeCp_2$-ACFs-150, similar to the carbon atoms ratio at the nanographene's edge part with the in-plane size of 2–3 nm, where the ratio of edge atoms

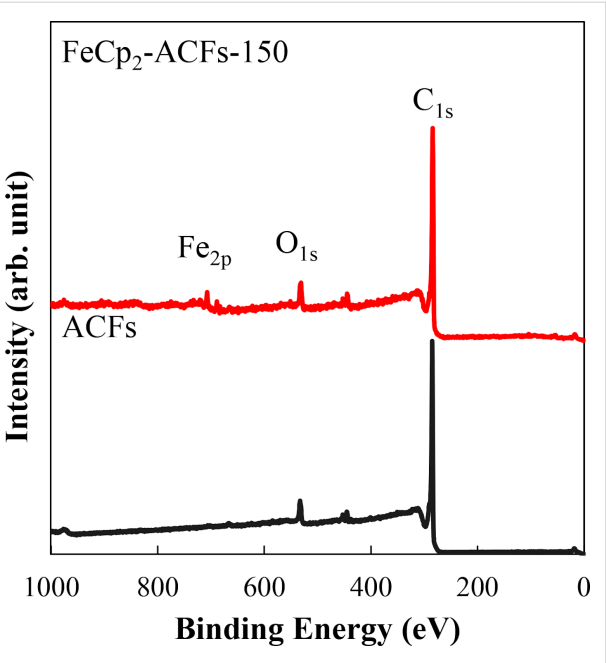

Figure 1: XPS spectra for ACFs and $FeCp_2$-ACFs-150. Peaks without labels originate from the indium substrate used for mounting the samples. The base lines of the spectra are shifted vertically from each other for clarification.

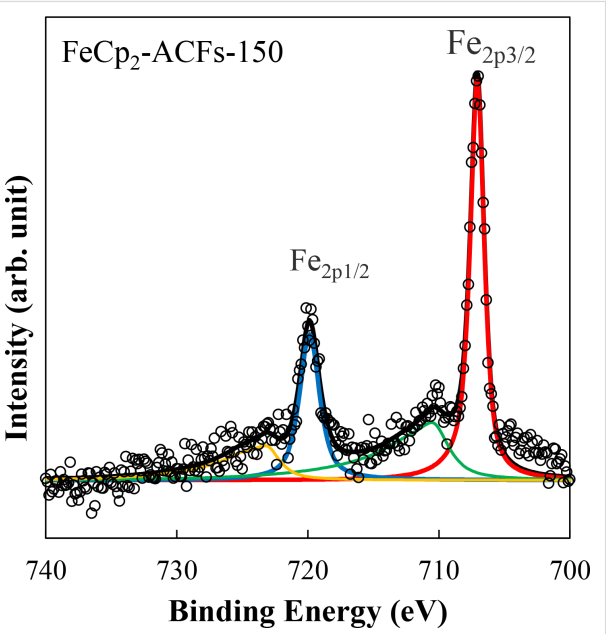

Figure 2: XPS spectrum for $FeCp_2$-ACFs-150 in the Fe_{2p} region shown with fitting curves.

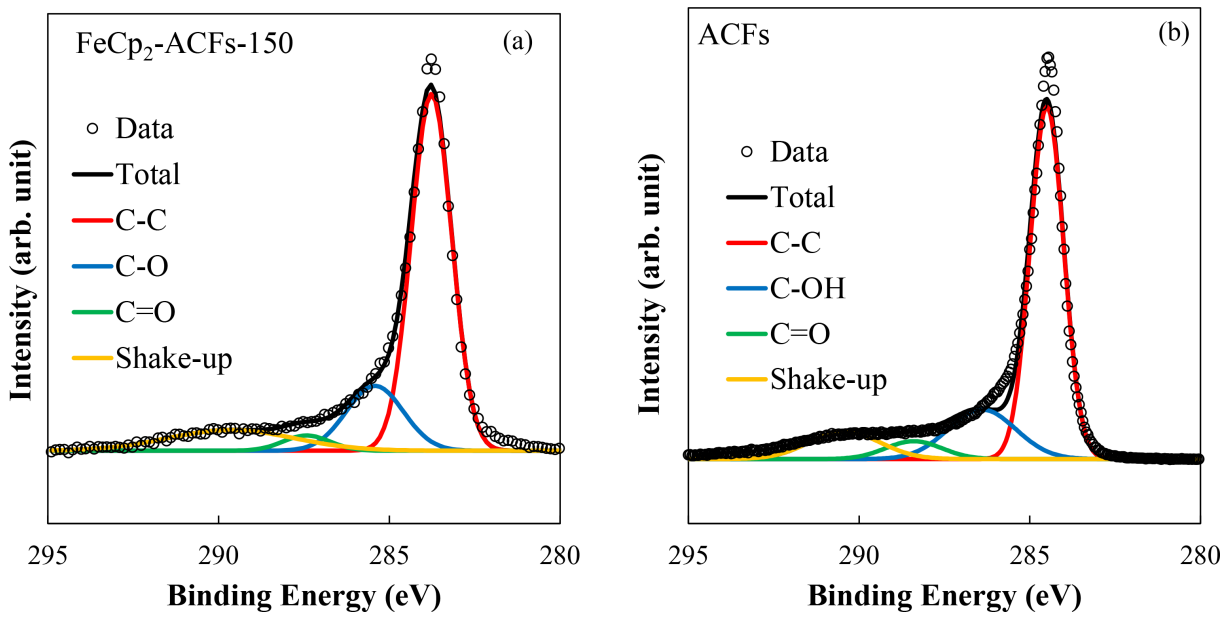

Figure 3: XPS spectra of (left) $FeCp_2$-ACFs-150 and (right) ACFs in the C_{1s} region with fitting curves.

Table 1: The peak positions for XPS C_{1s}, O_{1s}, and Fe_{2p} spectra and abundances of the peak components for $FeCp_2$-ACFs-150 and ACFs.

XPS peak	Sample	Binding energy (eV)	Abundance (atom %)
C_{1s} (C=C)	ACFs	284.6	64
	$FeCp_2$-ACFs-150	283.7	61
C_{1s} (C-O)	ACFs	286.4	16
	$FeCp_2$-ACFs-150	285.4	16
C_{1s} (C=O)	ACFs	288.4	3.8
	$FeCp_2$-ACFs-150	287.4	3.0
C_{1s} (shake-up)	ACFs	290.4	9.3
	$FeCp_2$-ACFs-150	289.6	12
O_{1s}	ACFs	532.9	6.8
	$FeCp_2$-ACFs-150	531.4	6.6
N_{1s}	ACFs	400.3	0.4
	$FeCp_2$-ACFs-150	–	–
Fe_{2p}	ACFs	–	–
	$FeCp_2$-ACFs-150	707.1, 719.9 710.5, 723.2	0.8 0.5

to total carbon atoms is ca. 0.1 with the assumption of a model circular nanographene $C_{324}H_{36}$. Thus, oxygen-containing functional groups in ACFs are mainly attached to the edge part of nanographene, being consistent with the higher chemical activity of the edges of graphene [2,6]. Furthermore, the almost same elemental abundance ratio O/C between ACFs and $FeCp_2$-ACFs-150 indicates no additional oxidization occurred in the process of $FeCp_2$ introduction to ACFs due to contaminated oxygen from ambient gaseous species.

Peaks of C_{1s} are assigned to sp^2 carbon atoms (C=C) of nanographene sheets, carbon atoms in/near oxygen-containing functional groups bounded to edges of nanographene sheets (C–O, C=O), shake-up peak by π–π^* transition of conduction π electrons (Shake-up) [28]. A more considerable contribution of the plasmon peak in C_{1s} indicates an increase in π-electron carriers for $FeCp_2$-ACFs-150. Indeed, the shift of the C=C peak of $FeCp_2$-ACFs-150 to the lower energy side indicates an increment of screening effect on photoemission hole by increasing in

conduction electrons. Increasing in conduction π electron of nanographene in $FeCp_2$-ACFs-150 suggests the charge transfer from $FeCp_2$ to ACFs. In this connection, the observed partial ionization of $FeCp_2$ is well understood by the structure of ACFs. Nanopores between nanographene domains provide huge spaces for the adsorption of guest molecules inside ACFs [2,6], where only a part of introduced molecules directly face the nanographene with the interfacial host–guest interactions, and the rest is accommodated into the nanopores without significant influences by nanographene domains.

The Raman spectra for both ACFs and $FeCp_2$–ACFs-150 shown in Figure 4 exhibit two broad peaks near 1350 and 1600 cm^{-1}. The peak around 1600 cm^{-1} corresponds to the Raman-allowed E_{2g} mode (G-band) in graphene. The D-band peak around 1350 cm^{-1} is forbidden in ideal graphene crystals but becomes Raman-active by an electron-scattering process due to impurities and edges in crystallites [29]. The G and D-bands were fitted with two Lorentzian curves, as shown in Figure 4. Although characteristic peaks of $FeCp_2$ molecules around 1100 cm^{-1} are not obtained in the spectrum for $FeCp_2$-ACFs-150 due to their tiny abundance, the G-band for $FeCp_2$-ACFs-150 shifts by 3 cm^{-1} to the lower wavenumber side compared to ACFs. The red shift indicates the weakening of C=C bonding in nanographene caused by filling anti-bonding states (π* states) due to electron injection into nanographene. This is consistent with the increment of shake-up peak for C_{1s} in XPS.

The Raman D-band also supports charge transfer from $FeCp_2$ to nanographene in $FeCp_2$-ACFs-150. The intensity ratio of the D-peak to G-peak I_D/I_G increases from 2.3 for ACFs to 2.4 for $FeCp_2$-ACFs-150. The larger I_D/I_G corresponds to the more significant carrier scattering by introducing $FeCp_2$ as a positively charged impurity caused by charge transfer with nanographene in $FeCp_2$-ACFs-150. This is also supported by the increase in the linewidth of the G-band from 28 cm^{-1} (ACFs) to 31 cm^{-1} ($FeCp_2$-ACFs-150).

Figure 5 shows IR spectra for $FeCp_2$, and the infrared spectra differences from that of ACFs for $FeCp_2$-ACFs-150 (Δ([$FeCp_2$-ACFs-150]-ACFs) and $FeCp_2$-ACFs-55 (Δ([$FeCp_2$-ACFs-55]-ACFs). The difference spectra exhibit peaks for vibration modes of Cp–Fe (ν), C–C (ν), C–H (γ), C–H (δ), Cp-breathing (ν) typical for $FeCp_2$ molecular vibration [30]. These spectra also indicate the successful introduction of $FeCp_2$ to ACFs and that most $FeCp_2$ maintains its molecular structure inside the nanographene host in both of $FeCp_2$-ACFs-55 and $FeCp_2$-ACFs-150. Moreover, the higher peak intensities of $FeCp_2$ molecular vibrations in the spectrum for $FeCp_2$-ACFs-150 than $FeCp_2$-ACFs-55 suggests that more guest molecules are introduced in $FeCp_2$-ACFs-150. This is quite reasonable, taking the much higher vapor pressure of $FeCp_2$ (5.7×10^3 Pa) into account in the process of guest molecular adsorption into ACFs for $FeCp_2$-ACFs-150 than $FeCp_2$-ACFs-55 (15 Pa). Here, it should be noted that the vibrational spectra are more distorted

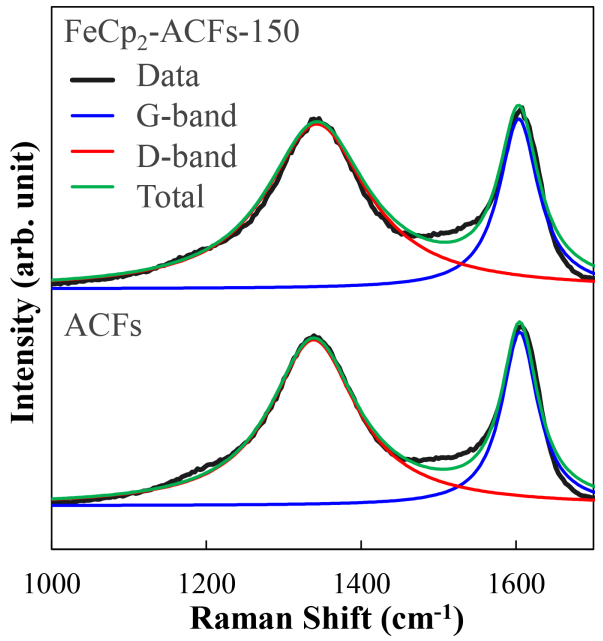

Figure 4: Raman spectra for ACFs and $FeCp_2$-ACFs-150. Each raw data (black) was fitted to the G-band (blue) and D-band (red) components, resulting in the total curve (green). The base lines of the spectra are shifted vertically from each other for clarify.

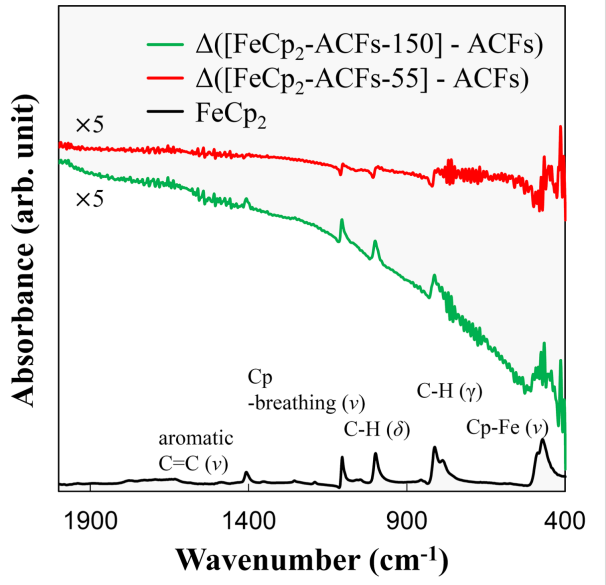

Figure 5: The raw infrared spectrum for $FeCp_2$ (black) and differential absorbance spectra for $FeCp_2$-ACFs-55 (red) and $FeCp_2$-ACFs-150 (green) after subtracting the ACFs spectrum as a background signal. The subtracted spectra are magnified five times, where the base lines are shifted vertically from each other for clarity. Raw spectra for $FeCp_2$-ACFs-55 and $FeCp_2$-ACFs-150 are shown in Figure S1 in Supporting Information File 1.

due to electromagnetic shielding effects by the conductive nature of graphene-based materials upon IR excitation. Thus, the "apparent" negative absorption peak in the spectrum of $FeCp_2$-ACFs-55 is caused by the phase shift of the IR electromagnetic wave by shielding effects of the conductive nanographene assembly. Interestingly, the $FeCp_2$ molecular vibrational peaks appear as typical positive peaks for $FeCp_2$-ACFs-150, indicating that most molecules are present inside the nanopores of ACFs without significant interactions such as charge transfer and electromagnetic shielding. This is well consistent with the observed partial cationization of the guest molecules for $FeCp_2$-ACFs-150 in XPS due to nanopore structure of the nanographene network in ACFs.

The host–guest interaction between guest $FeCp_2$ and host ACFs is most pronounced in the magnetic susceptibility measurements. The magnetic susceptibility for each sample shows the Curie–Weiss-type temperature dependence with temperature-independence susceptibility χ_{const}, mainly composed of the orbital diamagnetism by core and π electrons. Regarding $FeCp_2$-doped ACFs, ferromagnetism has been reported [26], but all of our samples showed only paramagnetism, and no ferromagnetism was observed in the present study.

The temperature-independent term of the magnetic susceptibility χ_{const} for ACFs and $FeCp_2$-ACFs-150 were obtained as -10×10^{-6} and -0.8×10^{-6} emu g^{-1}, respectively. The reduction in the absolute value of χ_{const} suggests the upshift of the Fermi energy from the Dirac point in the electronic band of nanographene in ACFs, being consistent with charge transfer from $FeCp_2$ observed in XPS. The decrease in the absolute value of the Weiss temperature Θ from −6.4 K for ACFs to −0.1 K for ACFs-$FeCp_2$-150 indicates the change in the character of the observed spins. The temperature dependences of the magnetic susceptibility χ multiplied by temperature T for $FeCp_2$-ACFs-150, ACFs, and plain $FeCp_2$ are shown in Figure 6, where χ_{const} was subtracted. The quantity χT tells us an estimation for the effective spin concentration modified by spin-exchange interactions at each temperature. The χT for ACFs remains constant in the temperature region above 50 K. However, it becomes decreasing below 10 K as temperature decreases. This is featured as the localized spin paramagnetism with antiferromagnetic interaction. ACFs exhibit the localized spin paramagnetism by edge-states of nanographene, as reported [2]. As expected from the diamagnetic (no spin magnetism) electronic structure of $FeCp_2$, plain $FeCp_2$ shows only tiny paramagnetism caused by impurities. On the other hand, after $FeCp_2$-introduction to ACFs, the χT remarkably increases for $FeCp_2$-ACFs-150, as shown in Figure 6. Indeed, N_{spin} for $FeCp_2$-ACFs-150 is about six times larger than that for non-doped ACFs (0.39×10^{20} g^{-1} for ACFs and 2.2×10^{20} g^{-1} for $FeCp_2$-ACFs-150). The results indicate that $FeCp_2$ in $FeCp_2$-ACFs-150 becomes cationized ($FeCp_2^+$) and magnetic (S = 1/2) by the charge-transfer interaction with nanographene.

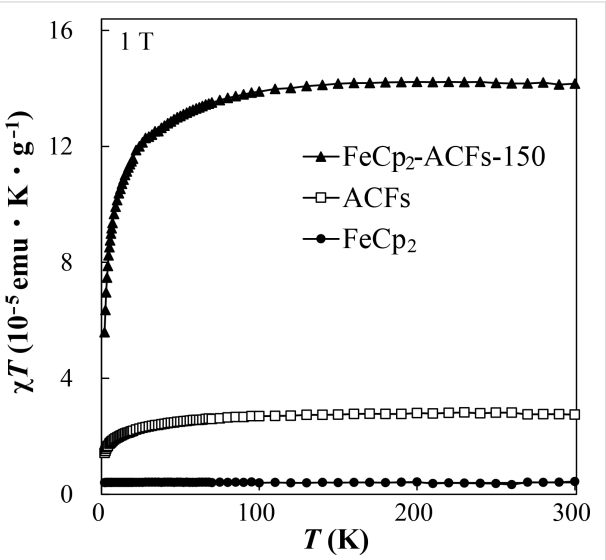

Figure 6: The temperature (T) dependence of the magnetic susceptibility χ for $FeCp_2$-ACFs-150, ACFs, and $FeCp_2$ measured at 1 T, where the vertical axis denotes the χ multiplied by T. The temperature-independent diamagnetic contribution to the magnetic susceptibility is subtracted.

Here, we quantitatively discuss the observed spin magnetism induced by charge-transfer interactions between host and guest with the results of XPS. The additional spin concentration by $FeCp_2$ introduction into ACFs is 1.8×10^{20} g^{-1} for $FeCp_2$-ACFs-150, being equivalent to 0.30 mmol for 1 g of $FeCp_2$-ACFs-150. The ratio of the satellite peak to the main peak of the XPS Fe_{2p} spectrum tells us 0.15 mmol of $FeCp_2^+$ for 1 g of $FeCp_2$-ACFs-150, which is in the same order as the observed spins induced by charge-transfer host–guest interactions. Considering the accuracy of elemental abundance by XPS (≈0.2 atom %), this is enough reasonable coincidence.

The Weiss temperature also supports the emergence of $FeCp_2^+$ spin magnetism. The absolute value of Θ decreases from −6 K to −0.09 K after $FeCp_2$ introduction to ACFs. The wavefunction of the edge-state is coupled to each other through the π-electron systems in the nanographene sheet, resulting in antiferromagnetic interactions. In contrast, the wavefunction (molecular orbital) of $FeCp_2^+$ has a more isolated nature, and the exchange interactions between cation spins are less than those for edge-state spins. The apparent reduction in Θ for $FeCp_2$-ACFs-150 is attributed to the contribution of $FeCp_2^+$ spins having less exchange interaction in the observed magnetic susceptibility. So, the spin magnetism of the guest molecule is induced by host–guest interactions in the nanographene host.

Despite the less interacting nature of $FeCp_2^+$ spins than that of edge-state spins, the ESR measurement proves the presence of the magnetic interaction between spins of the ACFs host and the guest $FeCp_2$ molecule. Figure 7a shows the ESR spectra for ACFs and $FeCp_2$-ACFs-55 at the excitation microwave powers of 1, 9, and 100 mW. The ESR linewidth of the spectrum for $FeCp_2$-ACFs-150 was extremely broad to analyze the spectra, such as estimation of the linewidths and intensities, where the spectra are merged with the baseline contribution on the wider field range, being hard to distinguish from each other (Figure S2 in Supporting Information File 1).

ESR for ACFs and $FeCp_2$–ACFs-55 gives a g-value of 2.0019 for ACFs and a g-value of 2.003 for $FeCp_2$-ACFs-55, being in good agreement with the reported value for edge-state spins of nanographene in ACFs (g = 2.002) [26]. These g-values are almost constant within the error bar in the excitation microwave power-dependence measurement. Figure 7b shows the excitation microwave power dependence of the ESR linewidth ΔH_{pp} for ACFs and $FeCp_2$-ACFs-55. If we only consider the magnetic dipole interaction, ΔH_{pp} is proportional to N_{spin} [26], so ΔH_{pp} for $FeCp_2$-ACFs-150 should be six times larger than that for ACFs, according to the magnetic susceptibility results. However, the ESR of $FeCp_2$-ACFs-150 results in a broad linewidth undistinguishable from the baseline (Figure S2 in Supporting Information File 1). Even ACFs-$FeCp_2$-55 shown in Figure 7a, where $FeCp_2$ was introduced at 1/300 lower pressure gives ΔH_{pp} about seven times larger than ACFs in ESR. The observed "excess" broadening factor for $FeCp_2$-ACFs-150 and $FeCp_2$-ACFs-55 in ESR is attributed to the exchange interaction between spins. Generally, the exchange interaction between identical spins results in the narrowing of the ESR peak (exchange narrowing). However, the exchange between non-identical spins broadens the ESR spectrum. In $FeCp_2$-ACFs-55 and $FeCp_2$-ACFs-150, the exchange interaction between nanographene spin and $FeCp_2^+$ spin (non-identical spins) contributes in addition to the magnetic dipolar interaction.

Figure 8 shows the square root of excitation microwave power dependence of relative intensities for ACFs and $FeCp_2$-ACFs-55. At higher excitation power conditions, the relative intensities of ESR decrease because of a larger excitation rate than the spin relaxation rate (saturation), accompanied by linewidth broadening (saturation broadening). ACFs show moderate saturation phenomena with simple saturation broadening as the excitation power increases, where the coupling with conduction electrons in nanographene sheets is the primary path for spin energy relaxation. In Figure 8, the relative intensity for $FeCp_2$-ACFs-55 suddenly decreases in the lower excitation power region. It shows a more saturated nature than ACFs at the same power region despite the larger conduction carrier than ACFs. The more saturating nature for $FeCp_2$-ACFs-55 is well explained by the contribution of $FeCp_2^+$ spin having a more isolated nature than edge-state spins, consistent with the magnetic susceptibility results. However, the ΔH_{pp} of $FeCp_2$-ACFs-55 suddenly decreases even at the lower excitation power similar to the relative intensity and remains a decreasing trend despite its easily saturated nature. These behaviors suggest that spins

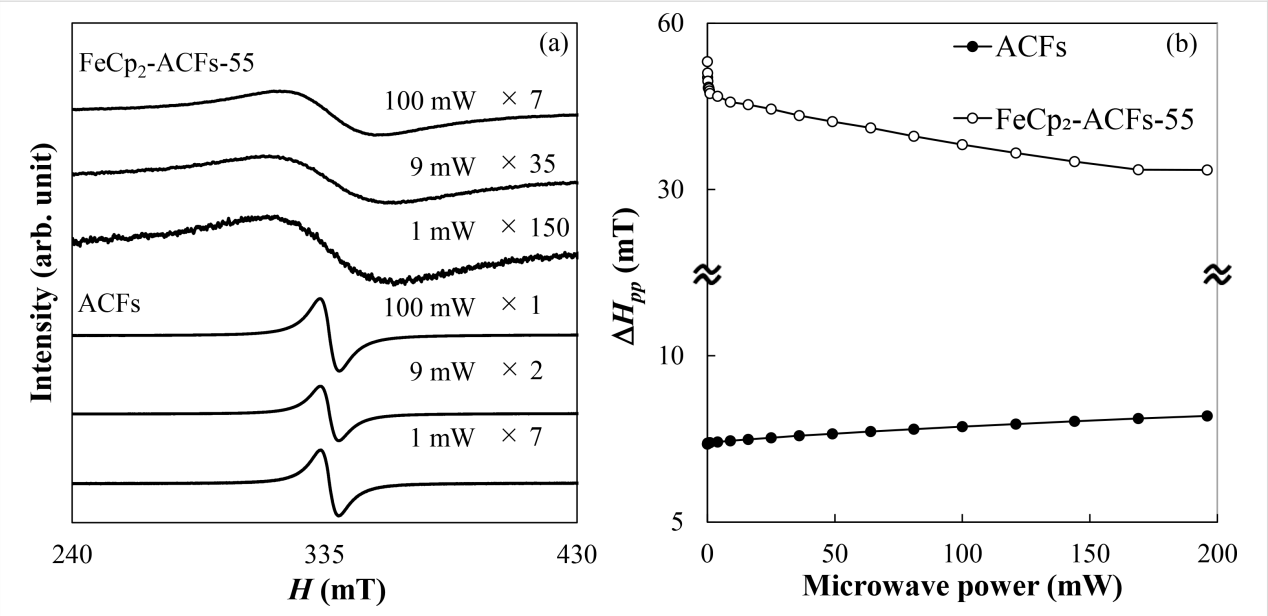

Figure 7: a) ESR spectra of ACFs and $FeCp_2$-ACFs-55 with different excitation microwave power. Each spectrum was magnified for clarity, where the base lines are shifted vertically from each other for clarity. b) The excitation microwave power dependence of ESR linewidth (ΔH_{pp}) for ACFs and $FeCp_2$-ACFs-55.

have an inhomogeneous environment for spin relaxation. In $FeCp_2$-ACFs-55, the adsorption site of $FeCp_2$ is not unique, and each $FeCp_2$ interacts with edge-state spins at the edges and π-electron carriers on nanographene sheets in different manners in ACFs as illustratively shown as the inset of Figure 8.

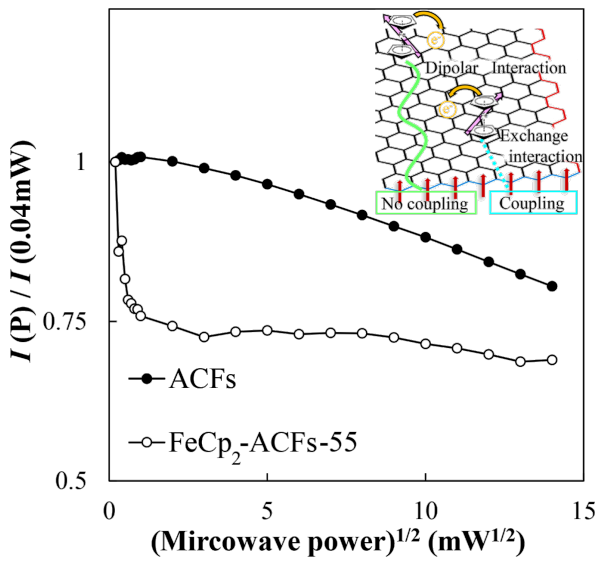

Figure 8: The square root of the excitation microwave power dependence of the relative ESR intensities for ACFs and $FeCp_2$-ACFs-55. Each intensity is normalized by that at microwave power of 0.04 mW. The insert is an illustrative sketch to explain spin and charge interactions between the nanographene host and $FeCp_2$ guest molecules.

Conclusion

Non-magnetic guest molecules with aromatic moiety were successfully introduced into the nanographene host. The charge-transfer interaction with the nanographene host in $FeCp_2$-ACFs induces the localized spin magnetism of the guest molecule (cationized $FeCp_2$). The presence of the exchange interaction by hybridization between $FeCp_2^+$ orbitals and edge-state orbitals is suggested in addition to the magnetic dipolar interaction. The observed induction and modulation of the spin magnetism by the interfacial interactions between magnetic nanographene host and guest molecules will give insight into a new class of developing methods of molecular magnets.

Supporting Information

Supporting Information File 1

Supporting figures.
[https://www.beilstein-journals.org/bjoc/content/supplementary/1860-5397-20-89-S1.pdf]

Funding

This work was partially supported by JSPS KAKENHI Grant Nos. 19K05410, 22K05056, 23K19256 and 26107532. This work was partially supported by the Research Center for Micro-nano Technology, the Research Center of Ion Beam Technology, and the Center for Instrumental analysis in Hosei University.

Author Contributions

Akira Suzuki: investigation; writing – original draft. Yuya Miyake: data curation; formal analysis; funding acquisition; resources; validation; visualization; writing – review & editing. Ryoga Shibata: data curation; formal analysis; resources; validation; writing – review & editing. Kazuyuki Takai: conceptualization; data curation; formal analysis; funding acquisition; investigation; project administration; supervision; writing – review & editing.

ORCID® iDs

Yuya Miyake - https://orcid.org/0000-0003-1956-209X
Ryoga Shibata - https://orcid.org/0009-0003-1495-4382
Kazuyuki Takai - https://orcid.org/0000-0002-3748-7911

Data Availability Statement

The data that supports the findings of this study is available from the corresponding author upon reasonable request.

References

1. Hebard, A. F.; Rosseinsky, M. J.; Haddon, R. C.; Murphy, D. W.; Glarum, S. H.; Palstra, T. T. M.; Ramirez, A. P.; Kortan, A. R. *Nature* **1991,** *350,* 600–601. doi:10.1038/350600a0
2. Takai, K.; Tsujimura, S.; Kang, F.; Inagaki, M. *Graphene: Preparations, Properties, Applications, and Prospects;* Elsevier: Amsterdam, Netherlands, 2019. doi:10.1016/c2019-0-00212-9
3. Fujita, M.; Wakabayashi, K.; Nakada, K.; Kusakabe, K. *J. Phys. Soc. Jpn.* **1996,** *65,* 1920–1923. doi:10.1143/jpsj.65.1920
4. Kobayashi, Y.; Fukui, K.-i.; Enoki, T.; Kusakabe, K.; Kaburagi, Y. *Phys. Rev. B* **2005,** *71,* 193406. doi:10.1103/physrevb.71.193406
5. Sakai, K.-i.; Takai, K.; Fukui, K.-i.; Nakanishi, T.; Enoki, T. *Phys. Rev. B* **2010,** *81,* 235417. doi:10.1103/physrevb.81.235417
6. Enoki, T.; Takai, K. *Solid State Commun.* **2009,** *149,* 1144–1150. doi:10.1016/j.ssc.2009.02.054
7. Kobayashi, N.; Enoki, T.; Ishii, C.; Kaneko, K.; Endo, M. *J. Chem. Phys.* **1998,** *109,* 1983–1990. doi:10.1063/1.476774
8. Takahara, K.; Takai, K.; Enoki, T.; Sugihara, K. *Phys. Rev. B* **2007,** *76,* 035442. doi:10.1103/physrevb.76.035442
9. Sevinçli, H.; Cuniberti, G. *Phys. Rev. B* **2010,** *81,* 113401. doi:10.1103/physrevb.81.113401
10. Osipov, V. Y.; Shames, A. I.; Enoki, T.; Takai, K.; Endo, M.; Kaburagi, Y.; Vul', A. Y. *Diamond Relat. Mater.* **2010,** *19,* 492–495. doi:10.1016/j.diamond.2010.01.027
11. Sumanasekera, G. U.; Chen, G.; Takai, K.; Joly, J.; Kobayashi, N.; Enoki, T.; Eklund, P. C. *J. Phys.: Condens. Matter* **2010,** *22,* 334208. doi:10.1088/0953-8984/22/33/334208

12. Hao, S.-J.; Takai, K.; Joly, V. L. J.; Yokota, K.; Kiguchi, M.; Enoki, T. *Bull. Chem. Soc. Jpn.* **2012,** *85,* 376–388. doi:10.1246/bcsj.20110300
13. Hao, S.; Takai, K.; Kang, F.; Enoki, T. *Carbon* **2008,** *46,* 110–116. doi:10.1016/j.carbon.2007.10.037
14. Takai, K.; Eto, S.; Inaguma, M.; Enoki, T.; Ogata, H.; Tokita, M.; Watanabe, J. *Phys. Rev. Lett.* **2007,** *98,* 017203. doi:10.1103/physrevlett.98.017203
15. Takai, K.; Suzuki, T.; Enoki, T.; Nishihara, H.; Kyotani, T. *Phys. Rev. B* **2010,** *81,* 205420. doi:10.1103/physrevb.81.205420
16. Woodbridge, C. M.; Pugmire, D. L.; Johnson, R. C.; Boag, N. M.; Langell, M. A. *J. Phys. Chem. B* **2000,** *104,* 3085–3093. doi:10.1021/jp993235+
17. Barber, M.; Connor, J. A.; Derrick, L. M. R.; Hall, M. B.; Hillier, I. H. *J. Chem. Soc., Faraday Trans. 2* **1973,** *69,* 559–562. doi:10.1039/f29736900559
18. Toda, Y.; Ishimaru, S.; Ikeda, R.; Mitani, T.; Kitao, S.; Seto, M. *J. Phys. Chem. Solids* **2004,** *65,* 471–473. doi:10.1016/j.jpcs.2003.09.018
19. Shiozawa, H.; Pichler, T.; Grüneis, A.; Pfeiffer, R.; Kuzmany, H.; Liu, Z.; Suenaga, K.; Kataura, H. *Adv. Mater. (Weinheim, Ger.)* **2008,** *20,* 1443–1449. doi:10.1002/adma.200701466
20. Sauer, M.; Shiozawa, H.; Ayala, P.; Ruiz-Soria, G.; Liu, X.; Chernov, A.; Krause, S.; Yanagi, K.; Kataura, H.; Pichler, T. *Carbon* **2013,** *59,* 237–245. doi:10.1016/j.carbon.2013.03.014
21. Li, Y.; Kaneko, T.; Ogawa, T.; Takahashi, M.; Hatakeyama, R. *Jpn. J. Appl. Phys.* **2008,** *47,* 2048–2055. doi:10.1143/jjap.47.2048
22. Li, Y.; Kaneko, T.; Ogawa, T.; Takahashi, M.; Hatakeyama, R. *Chem. Commun.* **2007,** 254–256. doi:10.1039/b611256k
23. Briones-Leon, A.; Liu, X.; Ayala, P.; Kataura, H.; Yanagi, K.; Weschke, E.; Pichler, T.; Shiozawa, H. *Phys. Status Solidi B* **2012,** *249,* 2424–2427. doi:10.1002/pssb.201200165
24. Oshida, K.; Kogiso, K.; Matsubayashi, K.; Takeuchi, K.; Kobayashi, S.; Endo, M.; Dresselhaus, M. S.; Dresselhaus, G. *J. Mater. Res.* **1995,** *10,* 2507–2517. doi:10.1557/jmr.1995.2507
25. El-Merraoui, M.; Tamai, H.; Yasuda, H.; Kanata, T.; Mondori, J.; Nadai, K.; Kaneko, K. *Carbon* **1998,** *36,* 1769–1776. doi:10.1016/s0008-6223(98)00122-5
26. Nakayama, A.; Ishii, C.; Takayama, T.; Watanabe, M.; Zanma, A.; Kaneko, K.; Sugihara, K. *Synth. Met.* **1997,** *86,* 2335–2336. doi:10.1016/s0379-6779(97)81149-6
27. Fulem, M.; Růžička, K.; Červinka, C.; Rocha, M. A. A.; Santos, L. M. N. B. F.; Berg, R. F. *J. Chem. Thermodyn.* **2013,** *57,* 530–540. doi:10.1016/j.jct.2012.07.023
28. Chiang, Y.-C.; Lee, C.-Y.; Lee, H.-C. *Mater. Chem. Phys.* **2007,** *101,* 199–210. doi:10.1016/j.matchemphys.2006.03.007
29. Cançado, L. G.; Takai, K.; Enoki, T.; Endo, M.; Kim, Y. A.; Mizusaki, H.; Jorio, A.; Coelho, L. N.; Magalhães-Paniago, R.; Pimenta, M. A. *Appl. Phys. Lett.* **2006,** *88,* 163106. doi:10.1063/1.2196057
30. Lippincott, E. R.; Nelson, R. D. *Spectrochim. Acta* **1958,** *10,* 307–329. doi:10.1016/0371-1951(58)80097-1

License and Terms

BEILSTEIN JOURNAL OF ORGANIC CHEMISTRY

Structure–property relationships in dicyanopyrazinoquinoxalines and their hydrogen-bonding-capable dihydropyrazinoquinoxalinedione derivatives

Tural N. Akhmedov[1], Ajeet Kumar[1], Daken J. Starkenburg[2], Kyle J. Chesney[1], Khalil A. Abboud[1], Novruz G. Akhmedov[3,4], Jiangeng Xue[2] and Ronald K. Castellano[*1]

Full Research Paper

Open Access

Address:
[1]Department of Chemistry, University of Florida, PO Box 117200, Gainesville, FL, 32611, United States, [2]Department of Materials Science and Engineering, University of Florida, PO Box 116400, Gainesville, Florida 32611, United States, [3]C. Eugene Bennett Department of Chemistry, West Virginia University, 100 Prospect Street, Morgantown, WV 26506, United States and [4]Department of Chemistry and Biochemistry, The University of Oklahoma, 101 Stephenson Parkway, Norman, OK 73019, United States

Email:
Ronald K. Castellano[*] - castellano@chem.ufl.edu

* Corresponding author

Keywords:
conjugated molecules; *N*-heteroacenes; hydrogen bonding; optoelectronic properties; organic field-effect transistors; organic semiconductors

Beilstein J. Org. Chem. **2024,** *20,* 1037–1052.
https://doi.org/10.3762/bjoc.20.92

Received: 22 January 2024
Accepted: 26 April 2024
Published: 08 May 2024

This article is part of the thematic issue "Carbon-rich materials: from polyaromatic molecules to fullerenes and other carbon allotropes".

Guest Editor: Y. Yamakoshi

Abstract

Presented here is the design, synthesis, and study of a variety of novel hydrogen-bonding-capable π-conjugated *N*-heteroacenes, 1,4-dihydropyrazino[2,3-*b*]quinoxaline-2,3-diones (DPQDs). The DPQDs were accessed from the corresponding weakly hydrogen-bonding dicyanopyrazinoquinoxaline (DCPQ) suspensions with excess potassium hydroxide, resulting in moderate to good yields. Both families of compounds were analyzed by UV–vis and NMR spectroscopy, where the consequences of hydrogen bonding capability could be assessed through the structure–property studies. Conversion of the DCPQs into hydrogen-bonding capable DPQDs results in modulation of frontier MO energies, higher molar extinction coefficients, enhanced crystallinity, and on-average higher thermal stability (where in some cases the 5% weight loss temperature is increased by up to 100 °C). Single crystal X-ray diffraction data could be obtained for three DPQDs. One reveals pairwise hydrogen bonding in the solid state as well as a herringbone packing arrangement rendering it a promising candidate for additional studies in the context of organic optoelectronic devices.

Introduction

The role of weak intermolecular interactions in tuning the properties of organic semiconductors has garnered significant attention in the past two decades, owing to their profound implications on device performance [1]. Among these interactions, hydrogen bonding (H-bonding, HB) as a highly directional noncovalent interaction can influence the structural, electronic,

and optoelectronic properties of bulk materials [2,3]. Hydrogen bonding plays a crucial role in molecular ordering in solid-state organic semiconductors, thereby dictating charge transport pathways as well as carrier mobilities of both electrons and holes [4-6]. Furthermore, strong hydrogen bonding interactions effectively modulate energy levels of semiconducting materials, affecting the bandgap and charge injection/extraction processes [7]. The additional merits of H-bonding designs in organic optoelectronic materials include higher thermal stability, synergistic stabilizing effects with π-stacking interactions, etc. [8].

Acenes and *N*-heteroacenes are two prominent π-conjugated scaffolds for both *n*- and *p*-type organic semiconductors [9-12]. The Würthner and Meijer groups presented an early example of the utility of hydrogen bonding in the fabrication of organic semiconductor devices. A thin-film device architecture was developed consisting of oligo(*p*-phenylenevinylene) (OPV) and perylenebisimide (PBI) components connected laterally through H-bonding and self-assembled orthogonally through π–π interactions [13]. Mixtures of PBI and OPV successfully exhibited ambipolar charge transport depending on processing conditions as a result of the co-assembled morphology.

Our group utilized a supramolecular approach in the solar cell arena. π-Conjugated linear and branched oligothiophenes appended to H-bonding capable phthalhydrazide (PH) were prepared [14,15]. These compounds demonstrated a power conversion efficiency (PCE) twice as high as that of non-hydrogen bonding controls upon photovoltaic device fabrication with the electron acceptor C_{60}. Subsequently, the design was extended to "ditopic" systems with diverse HB-capable units such as PH, 2,4-diamino-1,3,5-triazine (DAT), and barbiturate (B) that can form trimeric and hexameric "rosettes", respectively [16].

The Sokolowski and Głowacki groups have extensively developed H-bonded systems including dyes and pigments utilized in organic field-effect transistor (OFET) devices [17-20]. In two different studies, Głowacki reported H-bonding capable quinacridone and epindolidione-based semiconductors within OFET devices that offer moderate to excellent hole transport mobilities (1.5×10^{-3} and 1.5 cm^2/Vs, respectively) [21]. In 2012, Miao et al. reported an H-bonding capable 1,4-dihydropyrazinopyrazine fragment within *N*-heteroacenes [22]. The X-ray analysis of single crystals revealed the formation of highly-ordered ribbons constructed via intermolecular N–H···N interactions. However, vacuum-deposited films afforded poor hole transport. In separate work, Bunz et al. reported the serendipitous and understated synthesis of an H-bonding capable 1,4-dihydropyrazino[2,3-*b*]quinoxaline-2,3-dione (Figure 1a) [23]. In 2018, Takeda et al. reported the synthesis, electronic characteristics, and liquid-crystalline properties of several electron-accepting acenes, including 1,4-dihydropyrazinoquinoxalinediones (Figure 1b). The incorporation of strong hydrogen-bonding interactions facilitated the formation of a highly ordered liquid-crystalline phase within these systems [24]. These molecules are particularly intriguing as they bear resemblance to Głowacki's compounds discussed above. Reported here is a robust structure–property relationship study of these types of molecules with a particular interest in their optoelectronic properties.

Primary motivation for our effort comes from the work of Yamashita et al. who explored the OFET behavior of a library of electron-deficient dicyanopyrazinoquinoxaline (DCPQ) compounds [25]. The computations predicted low-lying LUMO levels, around −4.0 eV. However, the molecules exhibited poor *n*-type FET behavior and electron transport characteristics ($\mu_e = 1 \times 10^{-8}$ to 3.6×10^{-6} cm^2/Vs). Structurally, the combination of cyano groups and an electron-deficient pyrazinoquinoxaline creates an extremely electron poor π-system. Given our previous work and that of others, in 2013 we reasoned [26] that DCPQs could be efficiently transformed to tautomerically active, H-bonding capable 1,4-dihydropyrazino[2,3-*b*]quinoxaline-2,3-diones (Figure 1b, DPQDs) via nucleophilic aromatic substitution (S_NAr) at the *ipso*-CN positions. Here, the lactim–lactam tautomerization of DPQDs to arrive at the more stable 2,3-dione lactam form would mirror our prior work with phthalhydrazide (PH) and is also consistent with the work later reported by Takeda et al. We additionally envisioned that the DCPQs would serve as valuable comparators as the H-bonding capable DPQDs were studied.

Reported here is the synthesis of a library of dicyanopyrazinoquinoxalines (DCPQs) **1a**–**7a** and subsequent mild one-step synthesis of hydrogen-bonding dihydropyrazinoquinoxalinedione (DPQDs) **1b**–**7b**. The structure–property relationships have been established within and between the two families using optical measurements. Moreover, the incorporation of H-bonding functionality exhibits a noteworthy impact on the thermal stabilities (analyzed by TGA) of the compounds. The single-crystal X-ray diffraction of DPQD **2b** exhibits a desirable herringbone solid-state arrangement for a potential OFET application. Complementary gas-phase computational analysis has provided insight into the electronic structures of both families which is related to the optical properties studied in solution.

Results and Discussion

Synthesis of DCPQs and DPQDs

Compounds **12** and **13** are two major building blocks to obtain dicyanopyrazinoquinoxalines (DCPQs) **1a**–**7a**. The synthesis proceeded through highly scalable reactions (over 10-gram

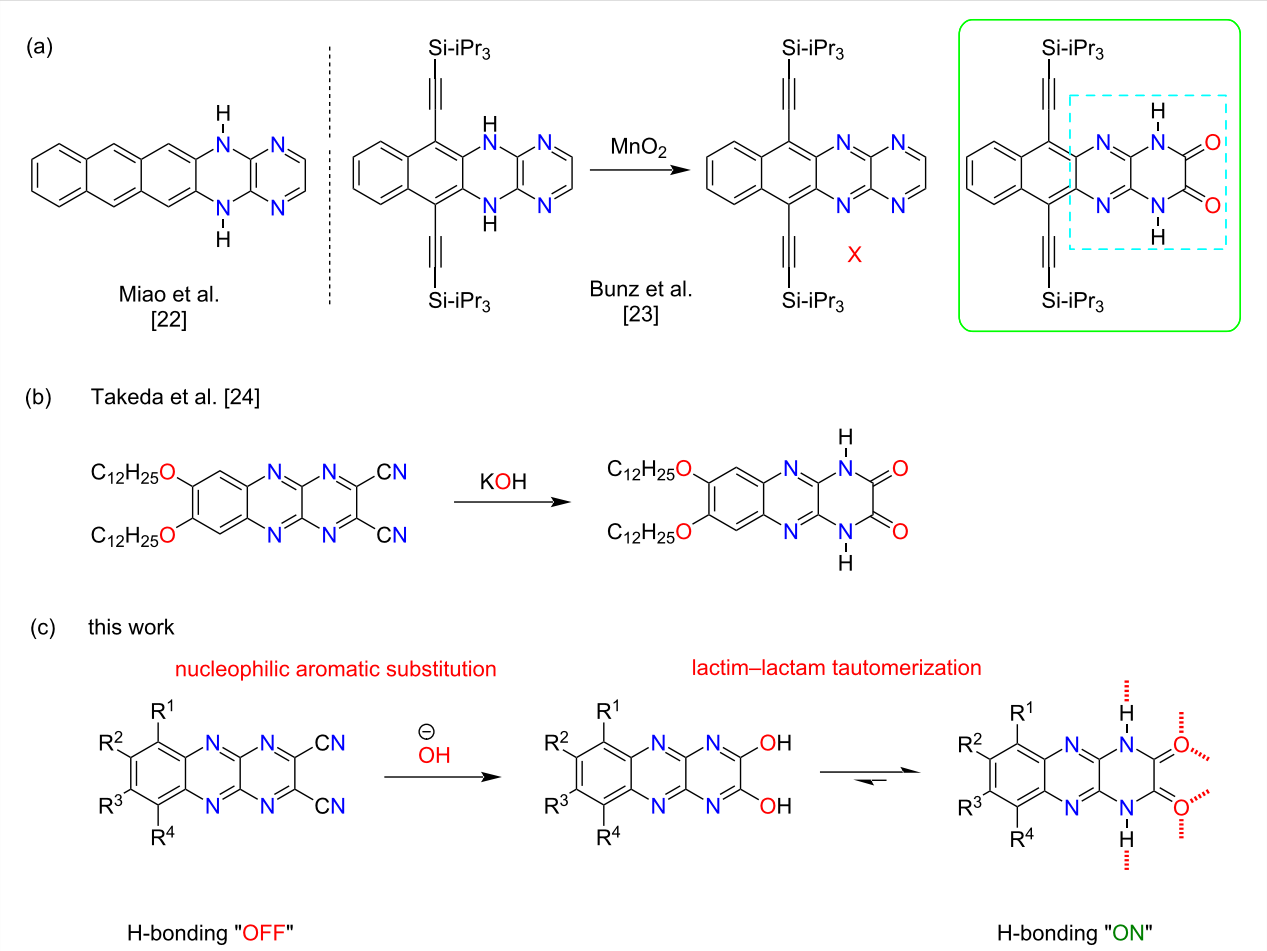

Figure 1: Chemical structures of H-bonding *N*-heteroacenes synthesized by Miao et al. and Bunz et al. (a) [22,23]. Preparation of electron-accepting azaacene derivatives as liquid-crystalline materials by Takeda et al. (b) [24]. Transformation of Yamashita's DCPQs to H-bonding capable DPQD derivatives discussed in this work (c) [25].

scale) using diaminomaleonitrile (**15**) as a starting material in accordance with the procedure in the literature (Scheme 1) [27]. The first step is the acylation with oxalyl chloride to yield **14** followed by a reaction with $SOCl_2$ in the presence of cat. DMF to obtain dichloropyrazine **13**. The solvent 1,4-dioxane is crucial to the synthesis and purification in the initial two steps as other solvents such as THF make the purification process more intricate. This sequence is followed by S_NAr with ammonia (29% v/v) to obtain building block diaminopyrazine **12**.

The synthesis of Yamashita's DCPQs **1a** (BenzCN) and **2a** (XyICN) began via S_NAr reaction of commercially available *o*-phenylenediamines **11a** and **11b** with building block **13** to afford dihydropyrazine derivatives **8** and **9**, respectively, as precipitates in 1,4-dioxane solution. The reaction generates two equivalents of HCl, adding a slight excess of diamines to sequester released HCl proved to be pivotal in achieving better yields. Oxidation with two equivalents of DDQ provided the comparator DCPQs **1a** and **2a** in 89% and 87% yield, respectively.

The synthesis of DCPQ **3a** was attempted rigorously under different conditions using building blocks 1,2-aceanthrylenedione and **12**, as detailed in Table S1 (Supporting Information File 1). However, an inseparable unknown impurity was observed along with the desired product **3a** in all cases when analyzed by ^{1}H NMR. Under strict temperature and time control (80 °C for 72 hours) using 2.5 equiv of 1,2-aceanthrylenedione, the reaction provided pure **3a** product in moderate yield (41%). Subsequent recrystallization with boiling DMSO provided pristine red-brown crystals of **3a**. The synthesis of DCPQ **4a** was simple and proceeded with the condensation of a 1:1 mixture of acenaphthenequinone and **12** under standard boiling acetic acid conditions, as reported in Scheme 1. The crude product could be collected via vacuum filtration, followed by additional purification via recrystallization from boiling DMF to afford golden crystals of **4a** in moderate yields.

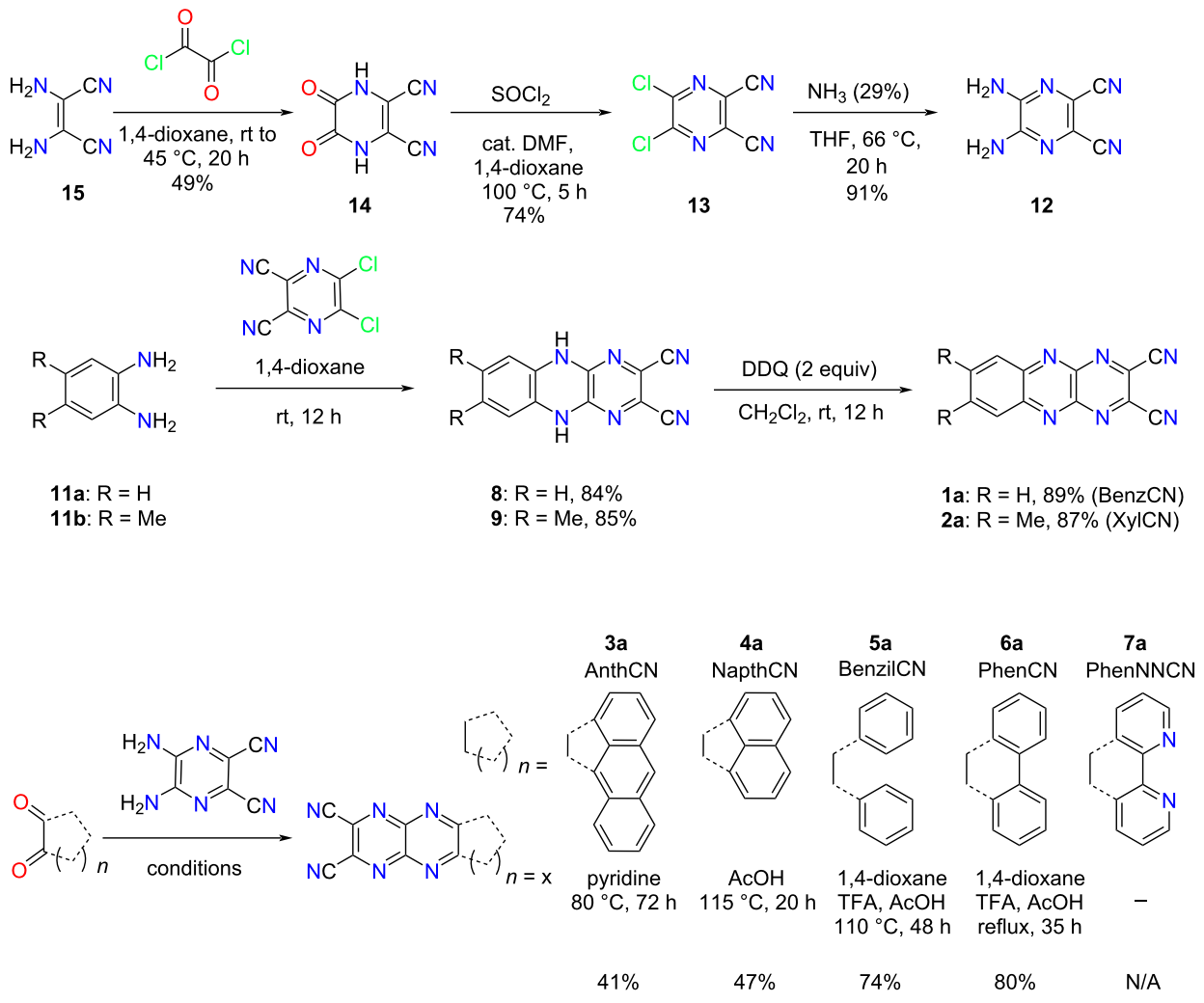

Scheme 1: Synthesis of dicyanopyrazinoquinoxaline derivatives **1a**–**7a**.

In order to access **5a** and **6a**, a modified procedure from the literature was implemented [28]. To synthesize **6a**, the condensation was performed with 9,10-phenanthrenequinone, building block **12** in the presence of glacial CH_3COOH, trifluoracetic acid, and 1,4-dioxane at reflux. Then, recrystallization from DMF and sublimation under ambient pressure worked well for the purification step to achieve an excellent 80% yield. To our delight, **5a** did not require any additional purification under the same reaction conditions.

Next, several unsuccessful synthetic efforts were made to access **7a** using starting material **7e** and building block **12**, listed in Table S2 (Supporting Information File 1). First, the starting material **7e** was obtained using 1,10-phenanthroline under harsh conditions as shown in Scheme 3 [29]. The same condensation reaction that worked for structurally similar **6a**, produced a poorly separable mixture in the case of **7a**. In the course of optimizing this reaction under different conditions, additional novel products were isolated in moderate yields (Scheme 2, Table S2, Supporting Information File 1). A variety of bis-alkoxylated products **16a**–**d** was obtained in moderate yields upon using different polar solvents such as methanol, ethanol, ethylene glycol, and diethylene glycol in the presence of excess triethylamine (Scheme 2). These products provide evidence for the in situ formation of DCPQ **7a** and demonstrate its ability to undergo trapping with various nucleophiles through an S_NAr mechanism.

An alternate strategy was employed to access **7a** as depicted in Scheme 3. The synthetic strategy first involved the access of dihydropyrazine precursor **10** which then underwent oxidation in the final step. Next, **7e** was easily converted to (*Z*,*E*)-bis-oxime derivative **7d** in satisfactory yield. The oxime stereochemistry shown is presumably secured due to the favorable

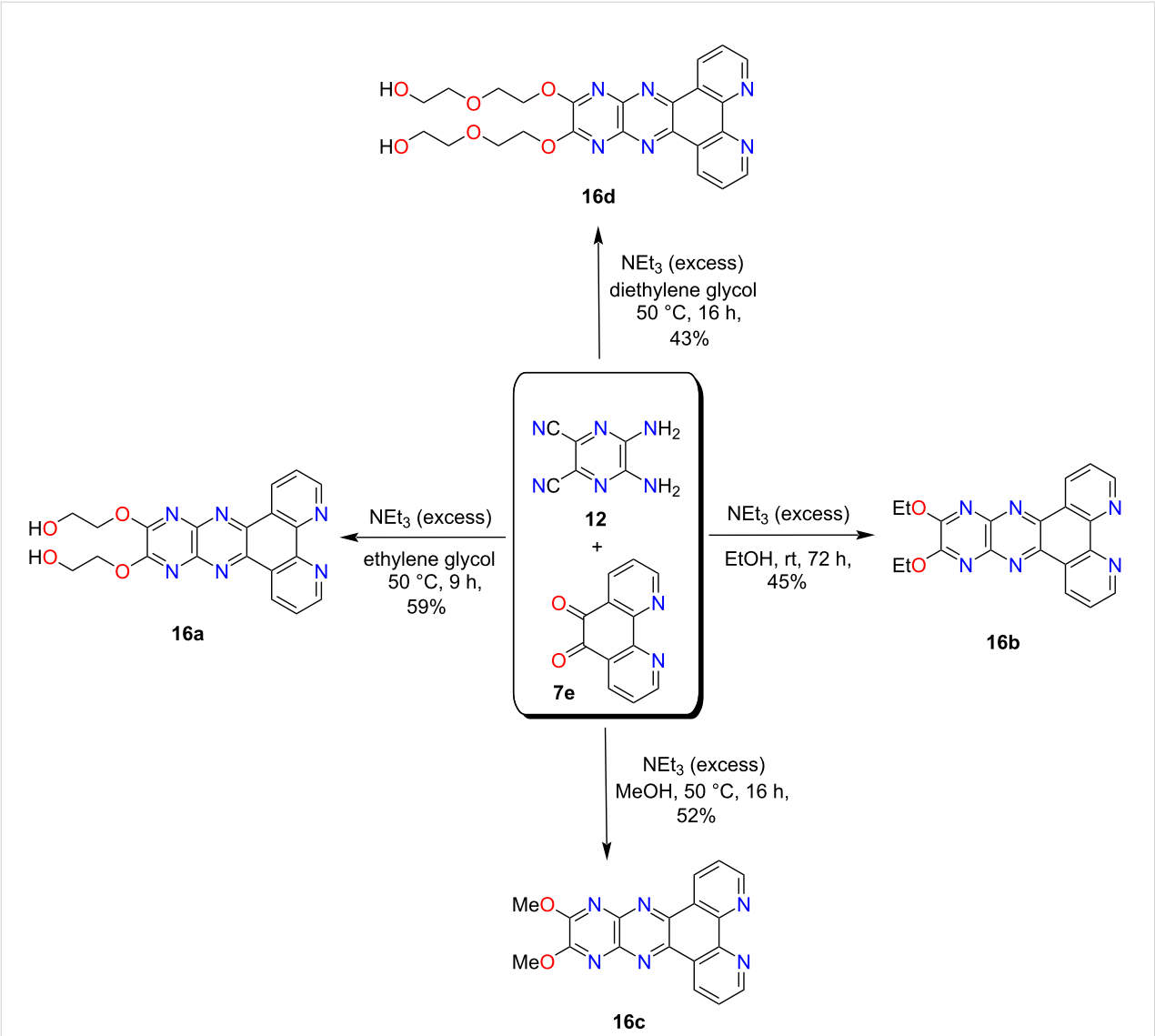

Scheme 2: Synthesis of bis-alkoxy-substituted π-conjugated phenanthrolines **16a**, **16b**, **16c**, and **16d**.

hydrogen bonding (O–H···N) between the oxime units; this idea is supported by ^{1}H NMR spectroscopy which shows the presence of two distinct hydroxyl proton signals. The reduction of **7d** in the presence of Pd/C and hydrazine monohydrate afforded 1,10-phenanthroline-5,6-diamine (**7c**) in moderate yield. The condensation of **7c** with **13** in the presence of 1,4-dioxane yielded poorly soluble **10**. Unfortunately, several oxidation attempts to access target **7a** failed presumably due to the insolubility of **10** even in high polarity solvents, listed in Table S3 (Supporting Information File 1).

The H-bonding capable dihydropyrazinoquinoxaline diones (DPQDs) were obtained by a S_NAr mechanism involving the corresponding DCPQ derivatives. Based on numerous examples in the literature, it has been established that for electron-deficient π-systems containing cyano groups, the addition–elimination pathway will dominate over hydrolysis. This preference was crucial to prevent the formation of undesired carboxylic acid products [28,30,31]. These results also align with the observations previously reported by Takeda and co-workers [24]. The reaction was carried out using a large excess (10 equiv) of KOH in a 1:1 THF/H_2O mixture to improve the solubility of the corresponding DCPQs (Scheme 4) at room temperature. A small amount of 1,4-dioxane (THF/H_2O/1,4-dioxane 4:5:1) was also added to improve the solubility of **3a**. The solution was rendered neutral by the addition of conc. HCl until precipitation occurred and precipitates were subsequently collected via vacuum filtration with no exception for any DPQDs **1b**–**6b**. The

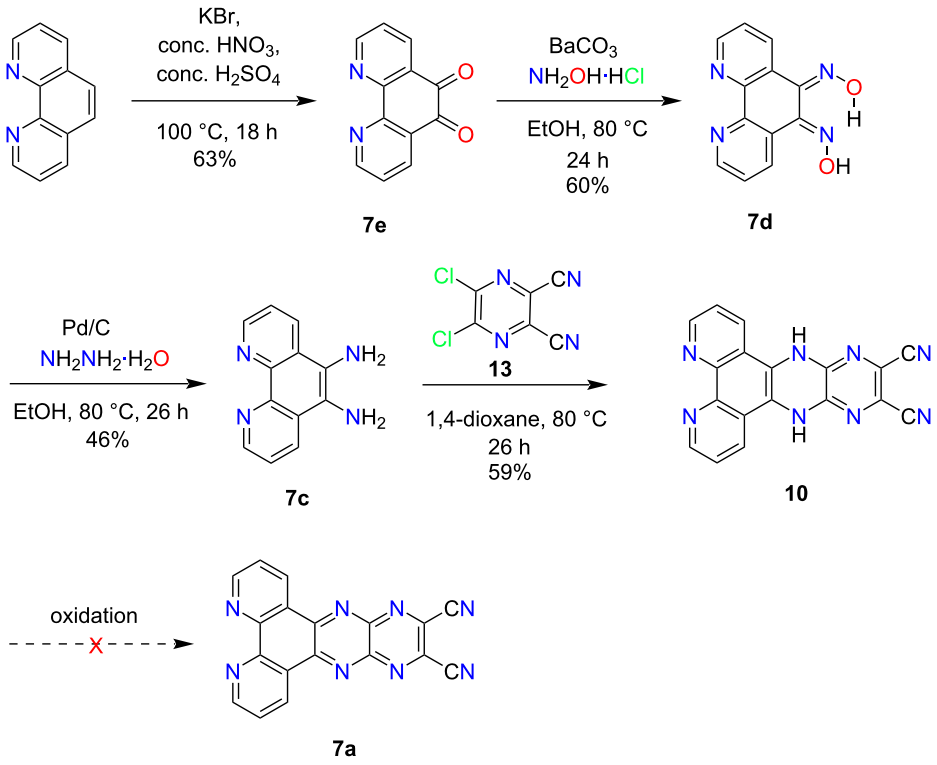

Scheme 3: An alternative synthetic route to access **7a**.

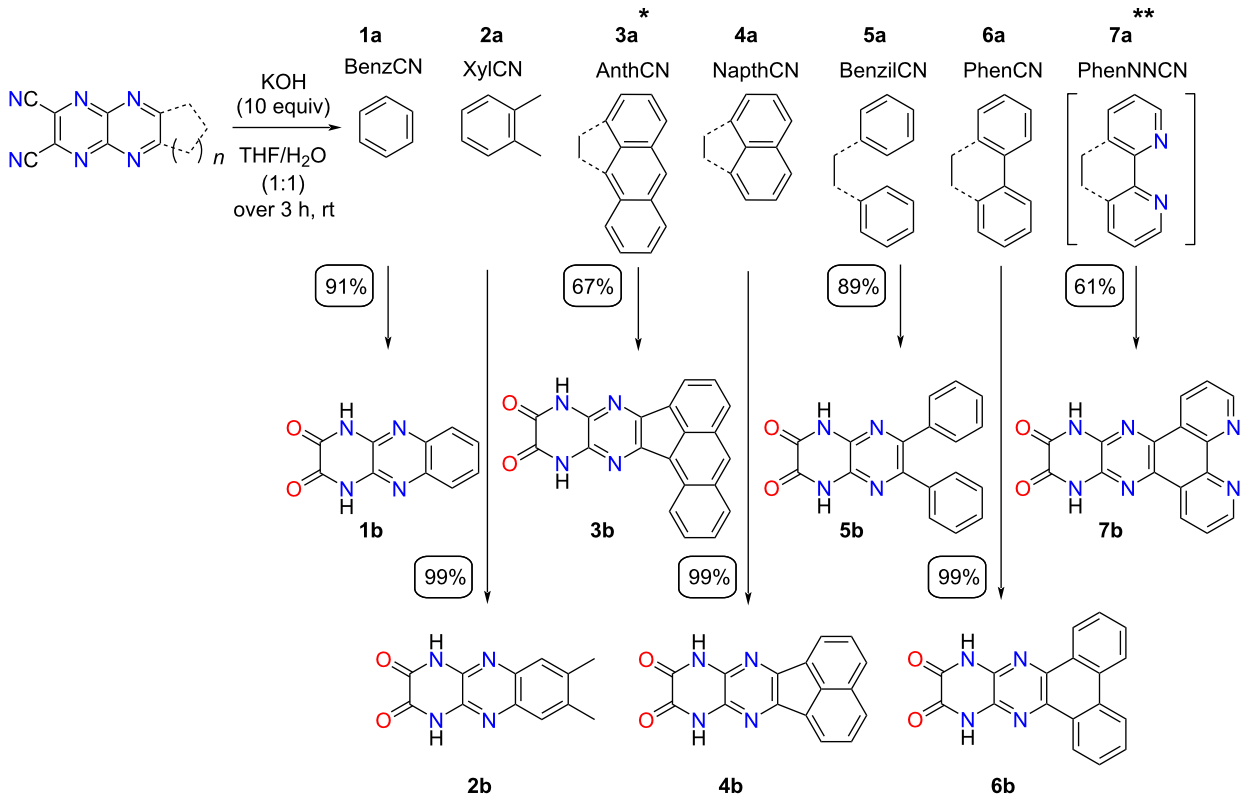

Scheme 4: Synthesis of DPQDs **1b–7b** from their corresponding DCPQs **1a–7a**. *THF/H_2O/1,4-dioxane (4:5:1). **in situ formation.

yields obtained in this step were moderate to excellent (61–99%). Target **7b** was synthesized from **12** and **7e** via the in situ generation of **7a** and subsequent S_NAr with KOH given the high reactivity of intermediate **7a** (Scheme 4).

After optimizing the successful synthesis of alkoxylated and diketone derivatives of **7a**, we were intrigued to investigate whether other dicyanopyrazinoquinoxaline derivatives could undergo a similar transformation. To assess the efficacy of the reaction, we subjected **6a** to the conditions outlined in Scheme 2. Remarkably, under the same conditions, an isostructural bis-ethoxy derivative, **16e**, was obtained in an excellent yield (87%). In addition, 10 equivalents of ammonium hydroxide yielded mono-aminated derivative **16f** (Scheme S4, Supporting Information File 1). The double substitution did not proceed presumably due to the strong electron-donating effect of -NH_2, diminishing the electrophilicity of the π-system. However, the mono-aminated product **16f** has the potential to serve as a useful building block for condensation with carbonyl functionality as well as Buchwald–Hartwig amination involving aryl halides.

Thermal studies

Thermal stabilities of DCPQs **1a**–**6a** and DPQDs **1b**–**7b** were evaluated using thermogravimetric analysis (TGA; Figure 2 and Table S4 in Supporting Information File 1). The thermal stability of the DCPQs is attributed to their favorable π–π stacking in the solid state. The 5% weight loss values range from 232 °C to 353 °C. Compounds with larger π-surfaces exhibited greater thermal stability (353 °C for **3a**, 304 °C for **4a**, 312 °C for **6a**) while others displayed 5% weight loss values under 250 °C (232 °C for **1a**, 244 °C for **2a** and 238 °C for **5a**). It was interesting to observe that there was a large difference in the thermal stabilities of non-planar **5a** and fully planar **6a** (5% weight loss of 238 °C vs 312 °C).

The TGA data for H-bonding DPQDs showed thermal stability with a 5% weight loss ranging between 288 °C and 361 °C. The 5% weight loss value is increased by about 100 °C, particularly in the case of **1b** as compared to the corresponding DCPQ **1a.** This enhancement can be attributed to the synergistic effect of π–π and H-bonding interactions on solid-state cohesive energy. However, **3b** and **7b** exhibited a decrease in 5% weight loss temperatures of 21 and 7 °C, respectively, from their corresponding DCPQ comparators.

To complement the TGA studies, the thermal stability of compound **4b** was evaluated through its exposure to air inside a 200 °C oven for one week. Structural evaluation by 2D NMR and mass spectrometry confirmed no decomposition and its high thermal stability.

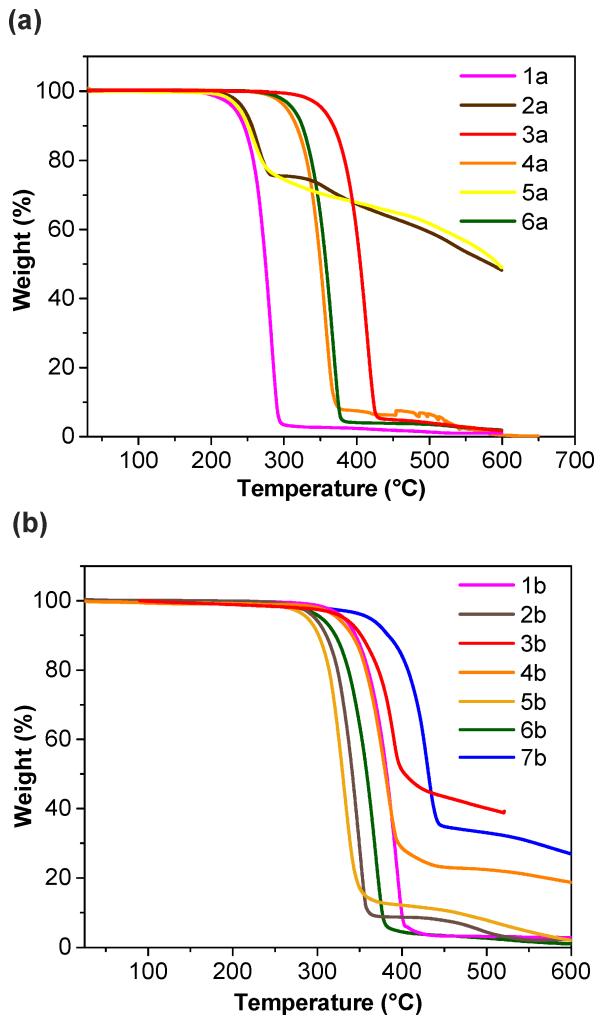

Figure 2: TGA of **1a**–**6a** (a) and **1b**–**7b** (b) obtained at 10 °C/min under nitrogen.

Optical properties

The electronic properties of the DCPQs **1a**–**6a** and DPQDs **1b**–**7b** were explored by UV–vis absorption spectroscopy in dimethyl sulfoxide (DMSO) at 25 °C (Figure 3). The electronic absorption spectra of DCPQs exhibited structureless bands with λ_{max} values from 388 to 423 nm, indicative of π–π* transitions. On the contrary, DPQDs exhibited more structured, blue-shifted bands with λ_{max} from 357–400 nm. At the same time, DCPQs exhibit intramolecular charge transfer (ICT) bands at lower energy due to the dicyanopyrazinopyrazine moiety as a strong acceptor and aromatic groups as strong donors in the backbone; the dione groups in the case of DPQDs diminish the acceptor properties of the aza π-system. It is worth mentioning that ICT is significantly influenced by solvent polarity and the comprehensive study of solvent effects is not within the scope of this investigation [32].

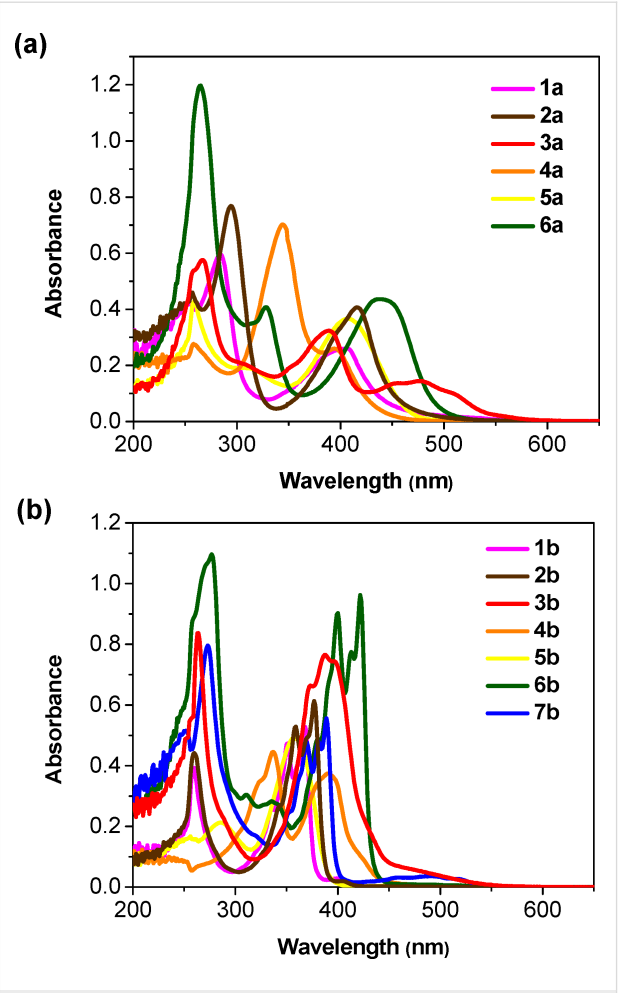

Figure 3: Absorption spectra (20 μM) for a) DCPQs **1a**–**6a** and b) DPQDs **1b**–**7b** in dimethyl sulfoxide.

Also, DPQDs displayed higher molar extinction coefficients (ε) than the corresponding DCPQs by a factor of approximately 1.4 to 5.3 in DMSO (Table 1). Furthermore, in all cases, the compounds from both families adhere to the Beer–Lambert law at the observed concentrations, as illustrated in Figures S37–S41 (Supporting Information File 1). This serves as good evidence that the synthesized compounds exhibit no signs of aggregation in DMSO within the assessed concentration range (i.e., 2.5–45 μM).

Electronic structure calculations

Gas-phase computational investigations were conducted to estimate energies of the frontier molecular orbitals (FMOs), specifically the highest occupied molecular orbital (HOMO) and the lowest unoccupied molecular orbital (LUMO), for DCPQs **1a**–**7a** as well as **1b**–**7b**. The density functional theory (DFT) calculations were performed using the B3LYP/6-31+G* level of theory (depicted in Figure 4 and Figure 5). Figure 4 reveals that the HOMOs of **1a**–**7a** are predominantly localized on the π-donor units, such as benzene and naphthalene, with an illustration in the case of **6a**. On the contrary, the LUMOs are delocalized across the entire π-systems, while also displaying some localization on the dicyanopyrazinopyrazine acceptor. Notably, compound **3a** displays the highest orbital density separation between donors and acceptors – an attribute relevant to efficient intramolecular charge transfer processes. This aligns with the observed lower optical HOMO–LUMO gap for **3a** in comparison to other compounds within the DCPQ family of compounds. As shown in Figure 5 and Table 1, the donor–acceptor character of the H-bonding counterparts is considerably muted and the HOMO and LUMO in these cases are both relatively delocalized. The HOMO energies of DPQD **1b**–**7b** are also deep (<−6.0 eV).

FMO energies are of great importance not only for the stability but also for device optimization. Raising the HOMO energy level can facilitate hole injection when using Pt electrodes [33], consequently enabling the fabrication of ambipolar devices supporting both hole and electron transport. On the other hand, unipolar electron transport could be facilitated in the case of DCPQs **1a**–**6a** given their extremely deep HOMO energy levels. Deep HOMO levels are important for optimal device performance and resistance to oxidation [34]. Compounds with deep LUMO energy levels are essential for efficient electron transport. However, compounds with LUMO levels ≈−4.0 eV are prone to undergo oxidation with O_2 or reduction with H_2O [35]. This could be the reason why electron transport properties in the OFETs previously reported by Yamashita are not very good [25]. Therefore, in the case of DPQD derivatives **1b**–**7b**, a balance is achieved, characterized by a HOMO with an energy level below –6.0 eV and moderately low LUMO with an energy level below −2.7 eV. The notable computed HOMO–LUMO difference between DCPQs and DPQDs amounting to more than 1.0 eV in certain cases, correlates well with optical gaps obtained from absorbance spectra, taken as the photon energy corresponding to the cut-off wavelength (Table 1). Subsequently, preliminary electrochemical studies were performed with selected DCPQs and corresponding DPQD counterparts using cyclic voltammetry (Figure S1, Supporting Information File 1). Cyclic voltammetric measurements of DCPQs, specifically **4a** and **6a**, and DPQDs **4b** and **6b**, support the overall trends observed through the electronic structure calculations.

X-ray crystallography

Single crystal X-ray diffraction data could be obtained for **2b**, **5b**, and **6b**. Figure 6 illustrates the single-crystal X-ray analysis of **2b**, and its important structural parameters were compared with that of **2a** (#CCDC 227464) reported in the literature [25]. An improved 2D nanostructure through highly ordered organization facilitated by H-bonding is revealed. Notably, the C–C

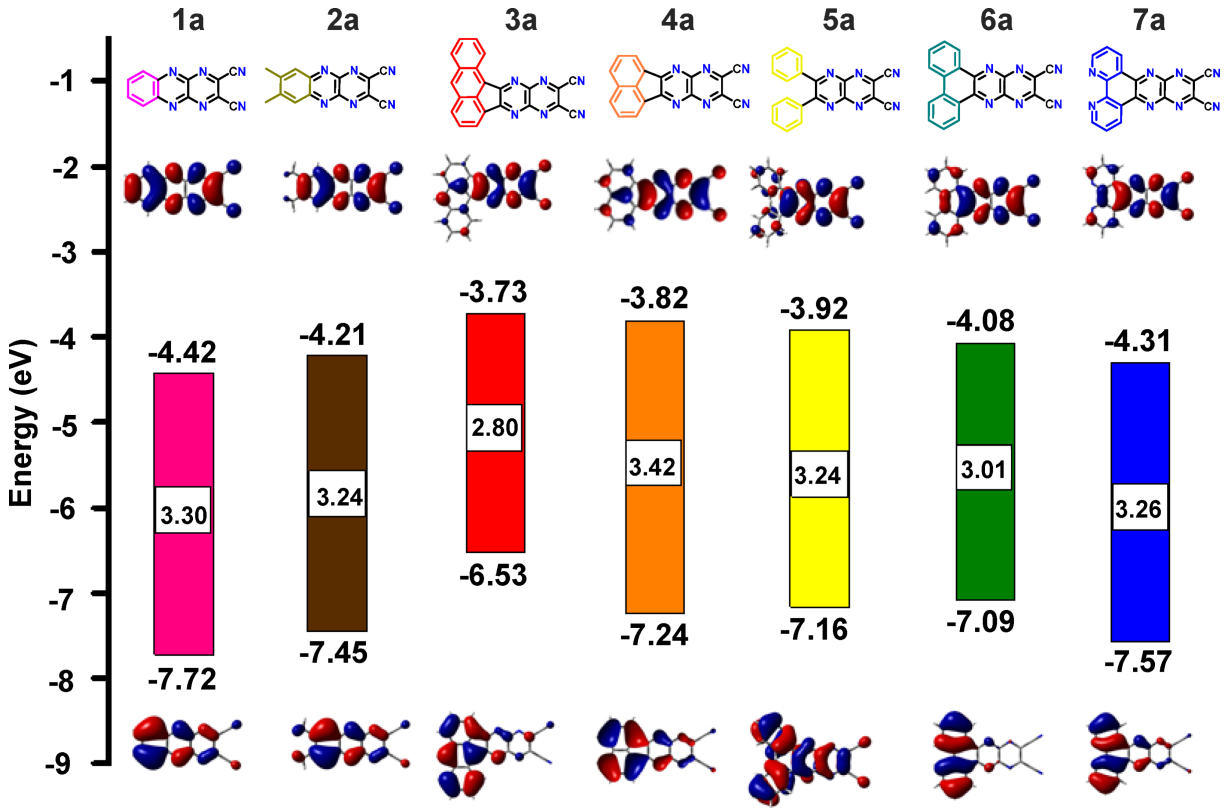

Figure 4: Calculated HOMO (below) and LUMO (above) energies by DFT analysis (B3LYP/6-31+G* level of theory), and corresponding molecular orbital plots for **1a**–**7a**.

distance between two carbonyl groups measures 1.531 Å, comparatively larger than that of aromatic systems and on the order of C_{sp^3}–C_{sp^3} bonds (Figure 6a). This represents the first evidence that the keto form is largely favored. Next, the molecule does not adopt a fully planar conformation, instead exhibiting a torsional angle of 4.33° with respect to the carbonyl groups (Figure 6b) and 5.25° concerning peripheral rings 1 and 3 (Figure 6c). The unit cell is composed of a dimer of **2b** held together by intermolecular N–H···N and C–H···O=C H-bonds with average distances of 2.30 Å and 2.28 Å, respectively (Figure 6d and 6e). The herringbone packing of **2b** is expected to be favorable for charge mobility within stacked arrangements [36,37]. Additionally, the intermolecular π–π stacking distance is reduced to 3.285 Å in the staggered form (Figure 6f and 6g), 0.27 Å shorter than its non-hydrogen bonding dicyano comparator **2a**. The single-crystal X-ray analysis of other DPQDs **5b** and **6b** did not reveal a herringbone lattice pattern, as shown in Tables S5 and S6 and Figures S42–S45 (Supporting Information File 1). In the case of **5b**, this is presumably due to the twisted phenyl rings that dictate the packing arrangement. Nonetheless, close π-stacking distances (≈3.2 Å) are observed between the **5b** units. For **6b**, this is likely due to the included solvent (ethylene glycol) that hydrogen bonds to the quinoxalinedione. Moving forward, **2b** stands out as a promising candidate for future solid-state characterization and device fabrication studies.

Conclusion

To conclude, we have used an efficient synthetic method to produce a structurally diverse class of H-bonding capable electron-deficient *N*-heteroacenes DPQDs **1b**–**7b**. The DPQDs were accessed from their respective *N*-heteroacenes DCPQs **1a**–**7a** in one step. Structure–property relationships for the DCPQs and DPQDs were established using gas-phase computational DFT analysis (B3LYP/6-31+G* level of theory), UV–visible spectroscopy, thermal analysis, and X-ray analysis in the solid state for **2b**, **5b**, and **6b**.

The primary takeaways from the work concern the attractive functional consequences of efficiently converting the DCPQs into hydrogen-bonding capable DPQDs. These include modulation of frontier MO energies, higher molar extinction coefficients, and on-average higher thermal stability (where in some cases the 5% weight loss temperature increased by up to

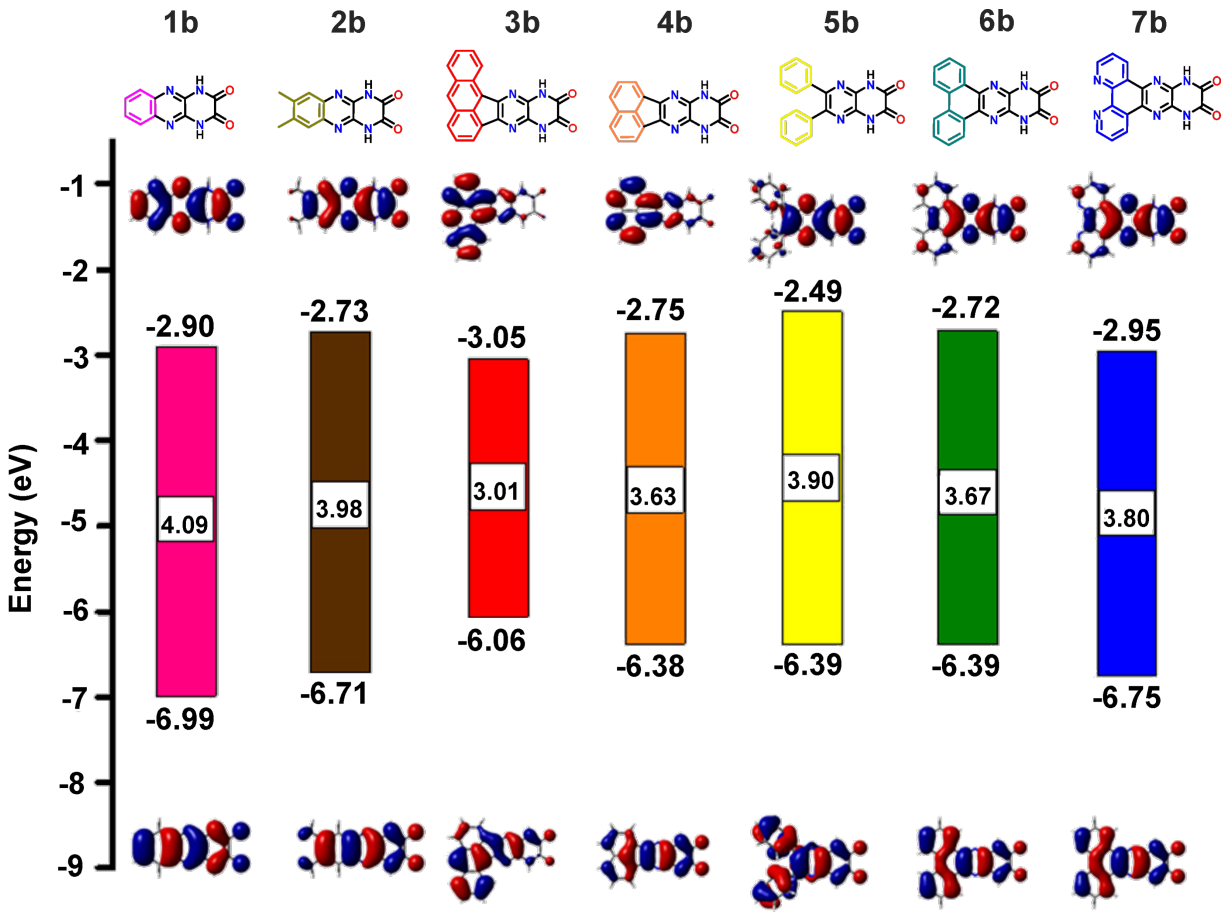

Figure 5: Calculated HOMO (below) and LUMO (above) energies by DFT analysis (B3LYP/6-31+G* level of theory), and corresponding molecular orbital plots for **1b**–**7b**.

Table 1: Absorbance properties of **1a**–**6a** and **1b**–**7b** in DMSO.[a]

Compound	λ_{max} (nm)	λ_{onset} (nm)	ε (10^4 M^{-1} cm^{-1})	E_{HOMO}^{DFT} (eV)[b]	E_{LUMO}^{DFT} (eV)[b]	E_{gap}^{DFT} (eV)[b]	E_{gap}^{opt} (eV)[a]
1a	400	447	1.4	−7.72	−4.42	3.30	2.85
2a	400	455	2.1	−7.45	−4.21	3.24	2.71
3a	388	546	0.73	−6.53	−3.73	2.80	2.26
4a	394	436	1.3	−7.24	−3.82	3.42	2.85
5a	407	466	1.7	−7.16	−3.92	3.24	2.67
6a	423	492	2.2	−7.09	−4.08	3.01	2.52
1b	368	377	2.6	−6.99	−2.89	4.10	3.23
2b	377	388	2.8	−6.71	−2.72	3.98	3.20
3b	399	451	3.9	−6.06	−3.05	3.01	2.75
4b	391	443	1.8	−6.38	−2.75	3.63	2.80
5b	357	391	2.4	−6.39	−2.49	3.89	3.17
6b	400	432	4.6	−6.39	−2.72	3.67	2.86
7b	396	398	3.0	−6.75	−2.95	3.80	3.11

[a]All measurements performed at room temperature and 20 μM concentration; [b]Energy values obtained from gas-phase computations using Gaussian 09 at the DFT B3LYP-6-31+G* level.

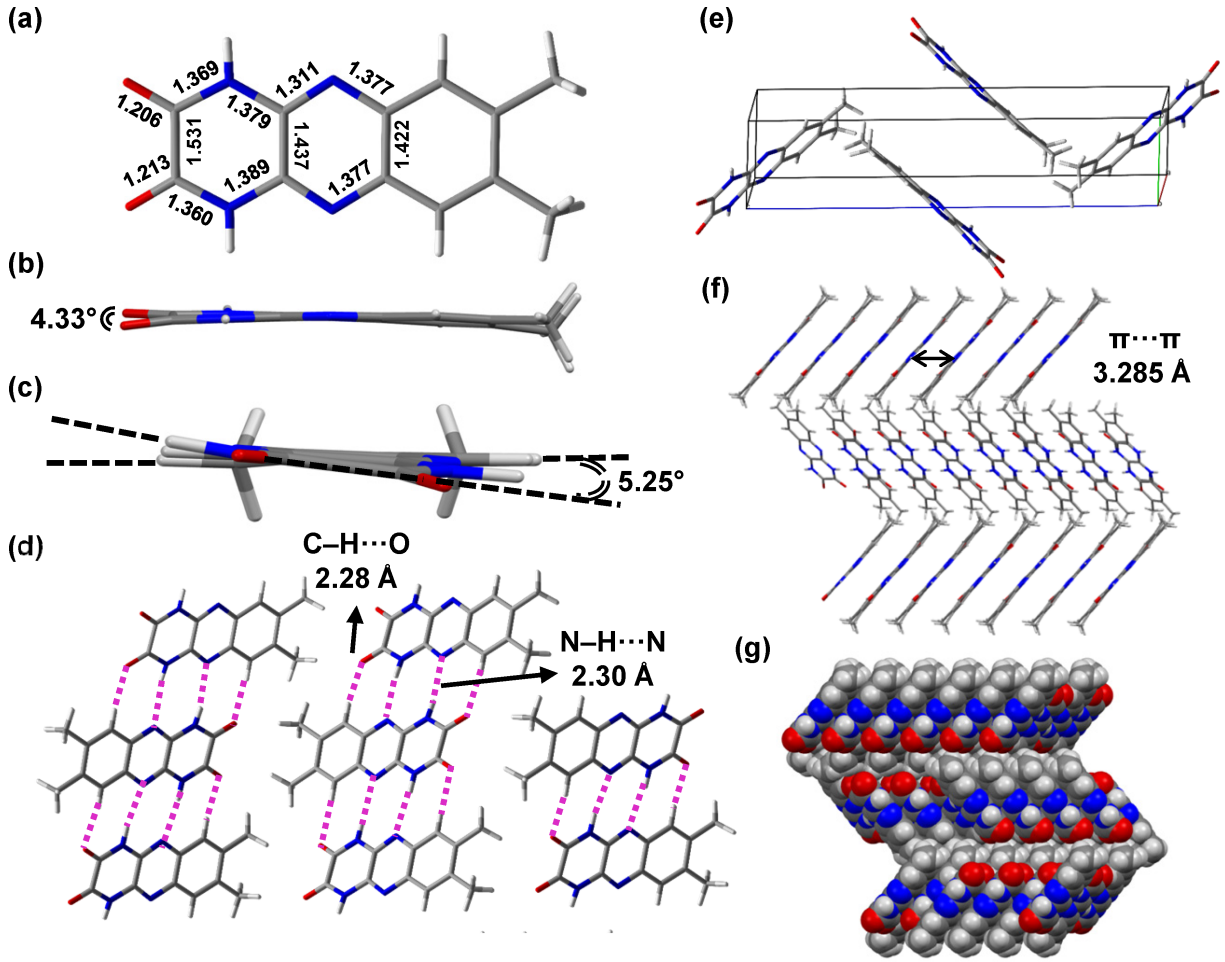

Figure 6: Asymmetric unit of DPQD **2b** with important bond lengths highlighted (a). Torsion angles of 4.33° and 5.25° are associated with the carbonyl groups and rings 1 and 3, respectively (b) and (c). Packing diagram showing the average intermolecular N–H···N and C–H···O=C distances (d). Unit cell comprised of four molecules of **2b** (e). Herringbone packing of **2b** showing the distance between adjacent ring centroids (f). Herringbone backing of **2b** shown as a spacefilling model (g). Atom color code: blue N, gray C, red O, and white H.

100 °C). Single-crystal X-ray analysis of DPQD derivative **2b** further revealed that it adopts a favorable herringbone motif characterized by short π–π distances and extensive intermolecular hydrogen bonding. These structural features are anticipated to promote efficient charge transport. Future work will involve device fabrication and comparison of the DCPQs and DPQDs in this context. Overall, this work contributes to our overarching objective to investigate the influence of hydrogen-bonding functionality on optoelectronic material organization and next-generation organic semiconductor device performance.

Experimental

General methods

Reagents and solvents were purchased from commercial sources and used without further purification unless otherwise specified. THF, ether, CH_2Cl_2, and DMF were degassed in 20 L drums and passed through two sequential purification columns (activated alumina; molecular sieves for DMF) under a positive argon atmosphere. Palladium(II) acetate and anhydrous 1,4-dioxane were purchased from Strem Chemicals or Sigma-Aldrich and used as received. Thin-layer chromatography (TLC) was performed on SiO_2-60 F_{254} aluminum plates with visualization by UV light or staining. Flash column chromatography was performed using Purasil SiO_2-60, 230–400 mesh from Whatman. Routine 300(75) MHz $^1H(^{13}C)$ NMR spectra were recorded on Varian Mercury 300 or Gemini 300 spectrometers. Routine 500(125) MHz $^1H(^{13}C)$ NMR were recorded on an INOVA 500 spectrometer. 2D NMR spectra were recorded using a 600 MHz Varian instrument. Chemical shifts (δ) are given in parts per million (ppm) relative to TMS and refer-

enced to residual protonated solvent ($CDCl_3$: δ_H 7.26 ppm, δ_C 77.23 ppm; DMSO-d_6: δ_H 2.50 ppm, δ_C 39.50 ppm). Abbreviations used are s (singlet), d (doublet), t (triplet), q (quartet), quin (quintet), hp (heptet), b (broad), and m (multiplet). ESI- and ESI-TOF-MS spectra were recorded on a Bruker APEX II FTICR and Agilent 6210 TOF spectrometer, respectively. EI-, CI-, and DIP-CI-MS spectra were recorded on a Thermo Trace GC DSQ (single quadrupole) spectrometer.

Absorbance measurements

Absorbance spectra were measured for 2.5, 5, 10, 15, 20, and 40 μM solutions of the DCPQs and DPQDs on a Cary 100 Bio spectrophotometer using 1 cm quartz cells. All solvents were HPLC grade (purchased from Fisher) and stored over 4 Å molecular sieves. The absorption intensity at λ_{max} was then plotted against the concentration in all cases to confirm, by linearity, that the compounds followed Beer's law. Molar extinction coefficients (ε) were determined from the linear plot for each compound (where $A = \varepsilon bc$).

Computational analysis

Starting geometries were obtained from semi-empirical calculations using the MM2 method as implemented in Chem3D Pro v. 13.0.0.3015 for Windows. The ground state geometries, energies and orbital energies were then obtained from DFT calculations at the B3LYP/6-31+G* level as implemented in Gaussian 09 [38], accessed through the UF High-Performance Computing Center. Frequency calculations were performed at the same computational level, and no imaginary frequencies were found. Molecular orbital plots were made using GaussView v. 5.0.898 from the Gaussian output files.

Thermogravimetric analysis

Thermal gravimetric analysis (TGA) was performed on a TA Instruments TGA Q5000-0121 V3.8 Build 256 at a heating rate of 10 °C/min using 1–3 mg of sample in a 100 μL platinum pan (under nitrogen). The data was analyzed on Universal Analysis 2000 4.4A software.

Synthetic procedures to access dicyanopyrazinoquinoxalines (DCPQs) **1a**–**6a**

Pyrazino[2,3-*b*]quinoxaline-2,3-dicarbonitrile (**1a**)

To a 50 mL round-bottom flask was added DDQ (0.581 g, 2.56 mmol) and CH_2Cl_2 (20 mL). To the suspension was added 5,10-dihydropyrazino[2,3-*b*]quinoxaline-2,3-dicarbonitrile (**8**, 0.300 g, 1.28 mmol) in small portions. The reaction was allowed to proceed overnight at room temperature, after which a pale orange reaction mixture was filtered, washed with copious amounts of CH_2Cl_2 and THF (10 mL), and dried in vacuo to afford a bright orange solid of **1a** (0.264 g, 1.14 mmol, 89%). ^{1}H NMR (600 MHz, DMSO-d_6) δ 8.30–8.31 (dd, J = 3 Hz, J = 6.6 Hz, 2H), 8.49–8.51 (dd, J = 3 Hz, J = 6.6 Hz, 2H); ^{13}C NMR (150 MHz, DMSO-d_6) δ 114.5, 130.4, 136.1, 136.2, 142.7, 147.4; HRMS (DART): $[M + H]^+$ calcd for $C_{12}H_4N_6$, 233.0570; found, 233.0574; $[M + NH_4]^+$, 250.0836; found, 250.0839.

7,8-Dimethylpyrazino[2,3-*b*]quinoxaline-2,3-dicarbonitrile (**2a**)

Compound **2a** was synthesized the same way as **1a** using DDQ (0.581 g, 2.56 mmol), 7,8-dimethyl-5,10-dihydropyrazino[2,3-*b*]quinoxaline-2,3-dicarbonitrile (**9**, 0.300 g, 1.28 mmol) and CH_2Cl_2 (20 mL). The reaction mixture was filtered, washed with copious amounts of CH_2Cl_2, THF (20 mL), and dried in vacuo to give a bright orange solid of **2a** (0.26 g, 1.0 mmol, 87%). ^{1}H NMR (500 MHz, $CDCl_3$) δ 2.70 (s, 6H), 8.21 (s, 2H); ^{1}H NMR (500 MHz, DMSO-d_6) δ 2.66 (s, 6H), 8.27 (s, 2H); ^{13}C NMR (125 MHz, DMSO-d_6) δ 20.1, 114.2, 127.8, 134.6, 142.3, 146.6, 148.7. The proton NMR in chloroform matches the literature value [25]; HRMS (DART): $[M + H]^+$ calcd for $C_{14}H_8N_6$, 261.0883; found, 261.0889; $[M + NH_4]^+$, 278.1149; found, 278.1154.

Aceanthryleno[1,2-*b*]pyrazino[2,3-*e*]pyrazine-11,12-dicarbonitrile (**3a**)

An oven dried sealed tube was charged with 5,6-diaminopyrazine-2,3-dicarbonitrile (**12**) (56.6 mg, 0.353 mmol), 1,2-aceanthrylenedione (56.6 mg, 0.244 mmol) and dry pyridine (3 mL). The resulting orange suspension was heated to 80 °C for 72 hours. After this time, brown solids precipitated out. The tube was adequately cooled, and the solid residue was filtered and washed with copious amounts of methanol, ethyl acetate and dichloromethane, to afford pure red-brown colored amorphous material (36 mg, 0.10 mmol, 41%). The material could be further purified by recrystallization from boiling DMSO to obtain highly insoluble red-brown microcrystalline material. ^{1}H and ^{13}C NMR could not be recorded for the compound **3a** given its extremely poor solubility in common organic solvents. R_f (CH_2Cl_2): 0.75, fluorescent orange spot; HRMS (DART): $[M + NH_4]^+$ calcd for $C_{22}H_8N_6$, 374.1154; found, 374.1155.

Acenaphtho[1,2-*b*]pyrazino[2,3-*e*]pyrazine-9,10-dicarbonitrile (**4a**)

An oven dried sealed tube was charged with 5,6-diaminopyrazine-2,3-dicarbonitrile (**12**) (0.15 g, 0.92 mmol), acenaphthylene-1,2-dione (0.15 g, 0.84 mmol) and glacial acetic acid (20 mL). The resulting pale-yellow suspension was heated to 115 °C for 20 hours with vigorous stirring. After 20 hours, the reaction was cooled, and yellow-gold shimmering particles began to settle out. The mixture was filtered, and the resulting gold-colored solid was recrystallized from hot DMF to obtain

pure compound **4a** (0.12 g, 0.39 mmol, 47%). ^{1}H NMR (500 MHz, $CDCl_3$) δ 8.04–8.06 (t, *J* = 7.5 Hz, 2H), 8.40–8.42 (d, *J* = 8.5 Hz, 2H), 8.71–8.73 (d, *J* = 7 Hz, 2H); ^{13}C NMR could not be obtained due to the poor solubility of the compound; HRMS (DART): $[M + NH_4]^+$ calcd for $C_{18}H_6N_6$, 324.0997; found, 324.0978.

6,7-Diphenylpyrazino[2,3-*b*]pyrazine-2,3-dicarbonitrile (**5a**)

Compound **5a** was synthesized by a modified literature method [31]. To an oven dried sealed tube was added 5,6-diaminopyrazine-2,3-dicarbonitrile (**12**, 306 mg, 1.91 mmol), diphenylethanedione (benzil) (365 mg, 1.74 mmol), glacial acetic acid (7 mL), trifluoroacetic acid (1 mL), and 1,4-dioxane (2 mL). The resulting orange suspension was heated at 110 °C for 48 hours. After completion, the tube was allowed to cool to room temperature and placed in a freezer overnight. Gold-colored crystals of **5a** were collected by filtration and dried in vacuo (430 mg, 1.28 mmol, 74%). ^{1}H NMR (500 MHz, $CDCl_3$) δ 7.41–7.44 (t, *J* = 7.5 Hz, 2H), 7.53–7.56 (t, *J* = 7.5 Hz, 1H), 7.73–7.75 (d, *J* = 8 Hz, 2H); ^{13}C NMR (125 MHz, $CDCl_3$) δ 113.0, 129.2, 130.9, 132.4, 133.8, 136.5, 143.9, 162.8; HRMS (DART): $[M + H]^+$ calcd for $C_{20}H_{10}N_6$, 335.1040; found, 335.1094; $[M + NH_4]^+$, 352.1305; found, 352.1358.

Dibenzo[*f*,*h*]pyrazino[2,3-*b*]quinoxaline-11,12-dicarbonitrile (**6a**)

An oven dried sealed tube was charged with 5,6-diaminopyrazine-2,3-dicarbonitrile (**12**, 0.73 g, 4.6 mmol), phenanthrene-9,10-dione (0.86 g, 4.1 mmol), glacial acetic acid (24 mL), TFA (6 mL) and 1,4-dioxane (12 mL). The resulting suspension was heated to 100 °C for 35 hours. By the end of the reaction, a red shimmering precipitate was observed. The reaction mixture was allowed to cool to room temperature, filtered and washed with copious amounts of dichloromethane and dried to obtain red-brick-colored solid **6a** (1.10 g, 3.30 mmol, 80%). ^{1}H NMR (500 MHz, DMSO-d_6) δ 7.88–7.91 (t, *J* = 7 Hz, 2H), 8.02–8.05 (t, *J* = 7.5 Hz, 2H), 8.83–8.84 (d, *J* = 8 Hz, 2H), 9.21–9.23 (d, *J* = 7 Hz, 2H). The compound was too insoluble for ^{13}C NMR spectroscopic analysis.

Synthesis of dihydropyrazinoquinoxaline diones **1b–7b** (DPQD) from dicyanopyrazinoquinoxalines (DCPQs) **1a–6a**

1,4-Dihydropyrazino[2,3-*b*]quinoxaline-2,3-dione (**1b**)

To a 20 mL round-bottom flask was added pyrazino[2,3-*b*]quinoxaline-2,3-dicarbonitrile (**1a**, 146 mg, 0.628 mmol) and THF (10 mL). To the resulting orange suspension was dropwise added a solution of KOH (353 mg, 6.280 mmol) in water (10 mL) and reacted at room temperature for 3 hours. After this time the light orange solution was diluted with water (50 mL) and acidified with 1 N HCl until a white solid precipitated out. The solids were collected via filtration and dried in an oven (120 °C) for 24 hours. An off-white to pale yellow solid of **1b** was obtained (123 mg, 0.572 mmol, 91%). ^{1}H NMR (600 MHz, DMSO-d_6) δ 7.65–7.67 (dd, *J* = 3.6 Hz, *J* = 6.6 Hz, 2H), 7.84–7.86 (dd, *J* = 3.6 Hz, *J* = 6.6 Hz, 2H), 12.71 (s, 1H); ^{13}C NMR (150 MHz, DMSO-d_6) δ 126.7, 128.0, 137.4, 137.7, 155.6; HRESIMS: $[M + Na]^+$ calcd for $C_{10}H_6N_4O_2$, 237.0388; found, 237.0394.

7,8-Dimethyl-1,4-dihydropyrazino[2,3-*b*]quinoxaline-2,3-dione (**2b**)

Compound **2b** was synthesized with a method similar to that of **1b** using **2a** (97.7 mg, 0.378 mmol), THF (8 mL), and KOH (64 mg, 1.13 mmol) in water (8 mL). After reaction, the red-orange solution was diluted with water (50 mL) and acidified with 1 N HCl until a pink-colored solid precipitated out. The solids were collected via filtration using a fine sintered funnel and dried in an oven to afford off-white solid of **2b** (90 mg, 0.37 mmol, 99%). ^{1}H NMR (500 MHz, DMSO-d_6) δ 2.41 (s, 6H), 7.61 (s, 2H), 12.61 (s, 2H); ^{13}C NMR (150 MHz, DMSO-d_6) δ 19.7, 126.0, 136.1, 136.8, 137.9, 155.6; HRESIMS: $[M + Na]^+$ calcd for $C_{12}H_{10}N_4O_2$, 265.0701; found, 265.0692.

10,13-Dihydroaceanthryleno[1,2-*b*]pyrazino[2,3-*e*]pyrazine-11,12-dione (**3b**)

Compound **3b** was synthesized in the same way as **1b** using compound **3a** (10 mg, 0.03 mmol), THF (4 mL), 1,4-dioxane (1 mL), and KOH (10 equiv) in water (5 mL). The product **3b** was obtained as an orange precipitate after the reaction mixture was poured into 30 mL of ice and neutralized with 1 N HCl. Yield: 6 mg, 0.02 mmol, 67%. ^{1}H NMR (500 MHz, DMSO-d_6) δ 7.56–7.60 (t, *J* = 7.5 Hz, 1H), 7.71–7.74 (t, *J* = 7.5 Hz, 2H), 8.04–8.05 (d, *J* = 7 Hz, 1H), 8.21–8.23 (d, *J* = 8.5 Hz, 2H), 8.76 (s, 1H), 9.00–9.02 (d, *J* = 8.5 Hz, 1H), 12.72 (brs, 2H); ^{13}C NMR (125 MHz, DMSO-d_6 + TFA) δ 123.0, 124.3, 124.9, 126.0, 126.8, 127.9, 128.2, 128.8, 128.9, 129.8, 130.1, 130.4, 130.9, 133.5, 133.8, 134.4, 144.7, 147.0, 155.5, 155.6; HRESIMS: $[M + K]^+$ calcd for $C_{20}H_{10}N_4O_2$, 377.0441; found, 377.0423.

8,11-Dihydroacenaphtho[1,2-*b*]pyrazino[2,3-*e*]pyrazine-9,10-dione (**4b**)

Compound **4b** was synthesized using a method similar to that of **1b** using compound **4a** (102 mg, 0.333 mmol), THF (5 mL), and KOH (187 mg, 3.33 mmol) in water (5 mL). After the addition of KOH, the reaction mixture turned red-brown. After completion, the reaction mixture was diluted with water (10 mL) and acidified with concentrated HCl until a precipitate became apparent. The yellow-orange precipitate was filtered

and washed with copious amounts of water and dried in vacuo (95 mg, 0.300 mmol, 99%). ^{1}H NMR (500 MHz, DMSO-d_6) δ 7.68–7.71 (t, J = 7.5 Hz, 2H), 7.96–7.98 (d, J = 7 Hz, 2H), 7.99–8.01 (d, J = 8.5 Hz, 2H), 11.57 (brs, 1H); ^{1}H NMR (500 MHz, C_6D_6) δ 7.36–7.39 (t, J = 7 Hz, 2H), 7.64–7.65 (d, J = 8.3 Hz, 2H), 7.99–8.00 (d, J = 6.9 Hz, 2H), 12.94 (brs, 1H); ^{13}C NMR (125 MHz, DMSO-d_6) δ 121.9, 128.8, 129.1, 129.2, 130.7 131.3, 134.8, 145.3, 155.5; HRESIMS: $[M + K]^+$ calcd for $C_{16}H_8N_4O_2$, 327.0284; found, 327.0279.

6,7-Diphenyl-1,4-dihydropyrazino[2,3-*b*]pyrazine-2,3-dione (**5b**)

Compound **5b** was synthesized using a method similar to that of **1b** using compound **5a** (236 mg, 0.706 mmol), THF (9 mL), and KOH (400 mg, 7.06 mmol) in water (9 mL). The red solution was diluted with water (10 mL) and acidified with 1 N HCl until an orange precipitate of **5b** was obtained (198 mg, 0.628 mmol, 89%). ^{1}H NMR (500 MHz, DMSO-d_6) δ 7.32 (s, 10H), 12.70 (brs, 2H); ^{13}C NMR (125 MHz, DMSO-d_6) δ 128.5, 128.6, 129.9, 135.2, 138.4, 144.1, 156.1; HRESIMS: $[M + H]^+$ calcd for $C_{18}H_{12}N_4O_2$, 317.1038; found, 317.1021.

10,13-Dihydrodibenzo[*f*,*h*]pyrazino[2,3-*b*]quinoxaline-11,12-dione (**6b**)

Compound **6b** was synthesized similarly to **1b** using compound **6a** (1.11 g, 3.34 mmol, THF (50 mL), and KOH (1.87 g, 33.3 mmol) in water (50 mL). After completion, a yellow precipitate was observed which was filtered and washed with copious amounts of 1 N HCl and diethyl ether. The product **6b** was then dried in vacuo to obtain pale yellow amorphous solid (1.15 g, 3.31 mmol, 99%). ^{1}H NMR (500 MHz, DMSO-d_6) δ 7.60–7.63 (t, J = 7.5 Hz, 2H), 7.66–7.69 (t, J = 8.5 Hz, 2H), 8.71–8.73 (d, J = 8.5 Hz, 2H), 8.98–9.00 (d, J = 8 Hz, 2H); ^{13}C NMR (125 MHz, DMSO-d_6) δ 123.0, 123.8, 127.1, 129.1, 130.0, 132.6, 143.1, 160.4; ^{13}C NMR (150 MHz, DMF-d_7) δ 123.3, 124.0, 127.7, 128.6, 128.8, 129.9, 133.6, 136.5, 155.7; HRESIMS: $[M + H]^+$ calcd for $C_{18}H_{10}N_4O_2$, 315.0881; found, 315.0877.

10,13-Dihydropyrazino[2',3':5,6]pyrazino[2,3-*f*][1,10]phenanthroline-11,12-dione (**7b**)

In a 100 mL three-neck round-bottom flask, compounds **12** (100 mg, 0.624 mmol) and **7e** (150 mg, 0.713 mmol) were added to 15 mL of tetrahydrofuran (THF). Subsequently, a solution of potassium hydroxide in water (15 mL) was added dropwise at room temperature, resulting in a color change from orange to red. The reaction mixture stirred for 72 hours, resulted in the formation of an orange-brown precipitate. The reaction mixture was then filtered, and 1 N HCl was added until orange-red colored solids appeared. The solids were collected via filtration and washed with copious amounts of water and dried in an oven to obtain red-orange product **7b** (120 mg, 0.381 mmol, 61%). ^{1}H NMR (500 MHz, DMSO-d_6) δ 7.78–7.81 (dd, J = 4.5 Hz, 8.5 Hz, 2H), 8.96–8.98 (d, J = 7.5 Hz, 2H), 9.34–9.36 (d, J = 8 Hz, 2H); ^{13}C NMR (125 MHz, DMSO-d_6 + TFA) δ 126.8, 127.8, 136.8, 138.3, 139.0, 147.9, 155.8; HRESIMS: $[M + H]^+$ calcd for $C_{16}H_8N_6O_2$, 317.0787; found, 317.0776.

Supporting Information

Supporting Information File 1

General experimental methods, ^{1}H and ^{13}C NMR, and HRMS spectra of the compounds as well as photophysical, computational and X-ray data.
[https://www.beilstein-journals.org/bjoc/content/supplementary/1860-5397-20-92-S1.pdf]

Acknowledgements

This work is based on Tural N. Akhmedov's doctoral thesis ("Design, Synthesis, and Characterization of Novel N-Heteroacenes for Organic Electronics", University of Florida, 2017). We acknowledge the University of Florida Research Computing facilities for providing computational resources and support that have contributed to the research results reported herein (https://www.rc.ufl.edu). We are thankful to the UF Center for Nuclear Magnetic Resonance Spectroscopy for providing necessary instrumentation, equipment, and support that have contributed to these results.

Funding

R.K.C. and J.X. are grateful to the National Science Foundation (NSF) for supporting this research (R.K.C.: CHE-1057411; R.K.C./J.X.: CHE-1507561). K.A.A. wishes to acknowledge the NSF and the University of Florida for funding of the purchase of the X-ray equipment. The mass spectrometry data has been generated by the Mass Spectrometry Research and Education Center at the University of Florida which is grateful for funding from the National Institutes of Health (NIH S10 OD021758-01A1 and S10 OD030250-01A1). N.G.A. acknowledges funding from the NSF for NMR instrumentation (CHE-1228336).

Author Contributions

Tural N. Akhmedov: conceptualization; data curation; formal analysis; investigation; methodology; validation; visualization; writing – original draft; writing – review & editing. Ajeet Kumar: data curation; investigation; validation; visualization; writing – original draft; writing – review & editing. Daken J. Starkenburg: data curation; formal analysis; investigation;

methodology; validation; visualization; writing – original draft. Kyle J. Chesney: data curation; investigation; methodology; writing – original draft. Khalil A. Abboud: data curation; formal analysis; investigation; visualization. Novruz G. Akhmedov: data curation; formal analysis; investigation; visualization. Jiangeng Xue: conceptualization; formal analysis; funding acquisition; methodology; project administration; resources; supervision; writing – original draft; writing – review & editing. Ronald K. Castellano: conceptualization; formal analysis; funding acquisition; methodology; project administration; resources; supervision; visualization; writing – original draft; writing – review & editing.

ORCID® iDs

Tural N. Akhmedov - https://orcid.org/0009-0007-3559-539X
Ajeet Kumar - https://orcid.org/0000-0002-1480-4785
Daken J. Starkenburg - https://orcid.org/0009-0003-7086-3792
Kyle J. Chesney - https://orcid.org/0000-0002-0479-7251
Khalil A. Abboud - https://orcid.org/0000-0003-3413-9118
Novruz G. Akhmedov - https://orcid.org/0000-0002-4586-2304
Jiangeng Xue - https://orcid.org/0000-0002-0932-3469
Ronald K. Castellano - https://orcid.org/0000-0003-4322-9932

Data Availability Statement

All data that supports the findings of this study is available in the published article and/or the supporting information to this article.

References

1. Gospodinova, N.; Tomšík, E. *Prog. Polym. Sci.* **2015,** *43,* 33–47. doi:10.1016/j.progpolymsci.2014.10.010
2. Chen, J.; Wang, Z.; Deng, Z.; Chen, L.; Wu, X.; Gao, Y.; Hu, Y.; Li, M.; Wang, H. *Front. Chem. (Lausanne, Switz.)* **2023,** *11,* 1200644. doi:10.3389/fchem.2023.1200644
3. Gómez, P.; Georgakopoulos, S.; Más-Montoya, M.; Cerdá, J.; Pérez, J.; Ortí, E.; Aragó, J.; Curiel, D. *ACS Appl. Mater. Interfaces* **2021,** *13,* 8620–8630. doi:10.1021/acsami.0c18928
4. Głowacki, E. D.; Coskun, H.; Blood-Forsythe, M. A.; Monkowius, U.; Leonat, L.; Grzybowski, M.; Gryko, D.; White, M. S.; Aspuru-Guzik, A.; Sariciftci, N. S. *Org. Electron.* **2014,** *15,* 3521–3528. doi:10.1016/j.orgel.2014.09.038
5. Gsänger, M.; Oh, J. H.; Könemann, M.; Höffken, H. W.; Krause, A.-M.; Bao, Z.; Würthner, F. *Angew. Chem., Int. Ed.* **2010,** *49,* 740–743. doi:10.1002/anie.200904215
6. Watanabe, Y.; Yokoyama, D.; Koganezawa, T.; Katagiri, H.; Ito, T.; Ohisa, S.; Chiba, T.; Sasabe, H.; Kido, J. *Adv. Mater. (Weinheim, Ger.)* **2019,** *31,* 1808300. doi:10.1002/adma.201808300
7. Fukagawa, H.; Hasegawa, M.; Morii, K.; Suzuki, K.; Sasaki, T.; Shimizu, T. *Adv. Mater. (Weinheim, Ger.)* **2019,** *31,* 1904201. doi:10.1002/adma.201904201
8. Trinh, C. K.; Abdo, N. I. *J. Mol. Struct.* **2022,** *1269,* 133764. doi:10.1016/j.molstruc.2022.133764
9. Anthony, J. E. *Angew. Chem., Int. Ed.* **2008,** *47,* 452–483. doi:10.1002/anie.200604045
10. Bunz, U. H. F. *Acc. Chem. Res.* **2015,** *48,* 1676–1686. doi:10.1021/acs.accounts.5b00118
11. Bunz, U. H. F.; Engelhart, J. U.; Lindner, B. D.; Schaffroth, M. *Angew. Chem., Int. Ed.* **2013,** *52,* 3810–3821. doi:10.1002/anie.201209479
12. Wang, J.; Chu, M.; Fan, J.-X.; Lau, T.-K.; Ren, A.-M.; Lu, X.; Miao, Q. *J. Am. Chem. Soc.* **2019,** *141,* 3589–3596. doi:10.1021/jacs.8b12671
13. Jonkheijm, P.; Stutzmann, N.; Chen, Z.; de Leeuw, D. M.; Meijer, E. W.; Schenning, A. P. H. J.; Würthner, F. *J. Am. Chem. Soc.* **2006,** *128,* 9535–9540. doi:10.1021/ja061966z
14. Schulze, B. M.; Shewmon, N. T.; Zhang, J.; Watkins, D. L.; Mudrick, J. P.; Cao, W.; Bou Zerdan, R.; Quartararo, A. J.; Ghiviriga, I.; Xue, J.; Castellano, R. K. *J. Mater. Chem. A* **2014,** *2,* 1541–1549. doi:10.1039/c3ta13529b
15. Shewmon, N. T.; Watkins, D. L.; Galindo, J. F.; Zerdan, R. B.; Chen, J.; Keum, J.; Roitberg, A. E.; Xue, J.; Castellano, R. K. *Adv. Funct. Mater.* **2015,** *25,* 5166–5177. doi:10.1002/adfm.201501815
16. Weldeab, A. O.; Kornman, C. T.; Li, L.; Starkenburg, D. J.; Zhao, X.; Fagnani, D. E.; Sadovy, S. J.; Perry, S. S.; Xue, J.; Castellano, R. K. *Org. Mater.* **2021,** *03,* 390–404. doi:10.1055/a-1534-1508
17. Berg, D.; Nielinger, C.; Mader, W.; Sokolowski, M. *Synth. Met.* **2009,** *159,* 2599–2602. doi:10.1016/j.synthmet.2009.09.017
18. Głowacki, E. D.; Leonat, L.; Voss, G.; Bodea, M.-A.; Bozkurt, Z.; Ramil, A. M.; Irimia-Vladu, M.; Bauer, S.; Sariciftci, N. S. *AIP Adv.* **2011,** *1,* 042132. doi:10.1063/1.3660358
19. Irimia-Vladu, M.; Głowacki, E. D.; Troshin, P. A.; Schwabegger, G.; Leonat, L.; Susarova, D. K.; Krystal, O.; Ullah, M.; Kanbur, Y.; Bodea, M. A.; Razumov, V. F.; Sitter, H.; Bauer, S.; Sariciftci, N. S. *Adv. Mater. (Weinheim, Ger.)* **2012,** *24,* 375–380. doi:10.1002/adma.201102619
20. Irimia-Vladu, M.; Kanbur, Y.; Camaioni, F.; Coppola, M. E.; Yumusak, C.; Irimia, C. V.; Vlad, A.; Operamolla, A.; Farinola, G. M.; Suranna, G. P.; González-Benitez, N.; Molina, M. C.; Bautista, L. F.; Langhals, H.; Stadlober, B.; Głowacki, E. D.; Sariciftci, N. S. *Chem. Mater.* **2019,** *31,* 6315–6346. doi:10.1021/acs.chemmater.9b01405
21. Głowacki, E. D.; Irimia-Vladu, M.; Kaltenbrunner, M.; Gsiorowski, J.; White, M. S.; Monkowius, U.; Romanazzi, G.; Suranna, G. P.; Mastrorilli, P.; Sekitani, T.; Bauer, S.; Someya, T.; Torsi, L.; Sariciftci, N. S. *Adv. Mater. (Weinheim, Ger.)* **2013,** *25,* 1563–1569. doi:10.1002/adma.201204039
22. He, Z.; Liu, D.; Mao, R.; Tang, Q.; Miao, Q. *Org. Lett.* **2012,** *14,* 1050–1053. doi:10.1021/ol203404q
23. Lindner, B. D.; Engelhart, J. U.; Märken, M.; Tverskoy, O.; Appleton, A. L.; Rominger, F.; Hardcastle, K. I.; Enders, M.; Bunz, U. H. F. *Chem. – Eur. J.* **2012,** *18,* 4627–4633. doi:10.1002/chem.201103227
24. Takeda, T.; Ikemoto, T.; Yamamoto, S.; Matsuda, W.; Seki, S.; Mitsuishi, M.; Akutagawa, T. *ACS Omega* **2018,** *3,* 13694–13703. doi:10.1021/acsomega.8b01943
25. Nishida, J.-i.; Naraso; Murai, S.; Fujiwara, E.; Tada, H.; Tomura, M.; Yamashita, Y. *Org. Lett.* **2004,** *6,* 2007–2010. doi:10.1021/ol0494010
26. Akhmedov, T. Design, Synthesis, and Characterization of Novel N-Heteroacenes for Organic Electronics. Ph.D. Thesis, University of Florida, Gainesville, FL, USA, 2017.
27. Suzuki, T.; Nagae, Y.; Mitsuhashi, K. *J. Heterocycl. Chem.* **1986,** *23,* 1419–1421. doi:10.1002/jhet.5570230533
28. Richards, G. J.; Hill, J. P.; Okamoto, K.; Shundo, A.; Akada, M.; Elsegood, M. R. J.; Mori, T.; Ariga, K. *Langmuir* **2009,** *25,* 8408–8413. doi:10.1021/la8041633
29. Li, B.-N.; Liu, Y.-Y.; Wang, Y.-P.; Pan, M. *Molecules* **2021,** *26,* 3244. doi:10.3390/molecules26113244

30. He, Z.; Mao, R.; Liu, D.; Miao, Q. *Org. Lett.* **2012,** *14,* 4190–4193. doi:10.1021/ol301854z
31. Richards, G. J.; Hill, J. P.; Subbaiyan, N. K.; D'Souza, F.; Karr, P. A.; Elsegood, M. R. J.; Teat, S. J.; Mori, T.; Ariga, K. *J. Org. Chem.* **2009,** *74,* 8914–8923. doi:10.1021/jo901832n
32. Li, Y.; Liu, T.; Liu, H.; Tian, M.-Z.; Li, Y. *Acc. Chem. Res.* **2014,** *47,* 1186–1198. doi:10.1021/ar400264e
33. Lee, J.-H.; Kim, J.-J. *Phys. Status Solidi A* **2012,** *209,* 1399–1413. doi:10.1002/pssa.201228199
34. Nakayama, K.; Hirose, Y.; Soeda, J.; Yoshizumi, M.; Uemura, T.; Uno, M.; Li, W.; Kang, M. J.; Yamagishi, M.; Okada, Y.; Miyazaki, E.; Nakazawa, Y.; Nakao, A.; Takimiya, K.; Takeya, J. *Adv. Mater. (Weinheim, Ger.)* **2011,** *23,* 1626–1629. doi:10.1002/adma.201004387
35. Sirringhaus, H. *Adv. Mater. (Weinheim, Ger.)* **2009,** *21,* 3859–3873. doi:10.1002/adma.200901136
36. Coropceanu, V.; Cornil, J.; da Silva Filho, D. A.; Olivier, Y.; Silbey, R.; Brédas, J.-L. *Chem. Rev.* **2007,** *107,* 926–952. doi:10.1021/cr050140x
37. Mei, J.; Diao, Y.; Appleton, A. L.; Fang, L.; Bao, Z. *J. Am. Chem. Soc.* **2013,** *135,* 6724–6746. doi:10.1021/ja400881n
38. *Gaussian 09,* Revision D. 01; Gaussian Inc.: Wallingford, CT, 2009.

License and Terms

BEILSTEIN JOURNAL OF ORGANIC CHEMISTRY

Two-fold addition reaction of silylene to C_{60}: structural and electronic properties of a bis-adduct

Masahiro Kako*[1], Masato Kai[1], Masanori Yasui[1], Michio Yamada[2], Yutaka Maeda[2] and Takeshi Akasaka[3]

Full Research Paper

Open Access

Address:
[1]Department of Engineering Science, The University of Electro-Communications, Chofu 182-8585, Japan, [2]Department of Chemistry, Tokyo Gakugei University, Tokyo 184-8501, Japan and [3]TARA Center, University of Tsukuba, Tsukuba 305-8577, Japan

Email:
Masahiro Kako* - m.kako@uec.ac.jp

* Corresponding author

Keywords:
bis-adduct; C_{60}; fullerene; silirane; silylene

Beilstein J. Org. Chem. **2024,** *20,* 1179–1188.
https://doi.org/10.3762/bjoc.20.100

Received: 01 December 2023
Accepted: 30 April 2024
Published: 22 May 2024

This article is part of the thematic issue "Carbon-rich materials: from polyaromatic molecules to fullerenes and other carbon allotropes".

Guest Editor: Y. Yamakoshi

Abstract

The addition reaction of C_{60} with silylene **1**, a silicon analog of carbene, yielded the corresponding bis-adduct **3**. The structure of **3** was determined by single-crystal X-ray structure analysis, representing the first example of a crystal structure of a silirane (silacyclopropane) derivative of fullerenes. Electrochemical measurements confirmed that the redox potentials of **3** are shifted cathodically compared to those of the parent mono-adduct **2**. Density functional theory (DFT) calculations provided the basis for the electronic properties of compound **3**.

Introduction

The chemical functionalization of fullerenes has been exploited extensively from both fundamental and practical perspectives, elucidating their potential applications for biochemistry, nanomaterials sciences, and molecular electronics [1-3]. With the development of research investigating the functionalization of fullerenes, several multiple addition reactions of fullerenes have been investigated [4-8]. For example, earlier reports have described that some functionalization reactions of fullerenes afford bis-adducts with excellent properties as organic photovoltaic materials [9-14]. Furthermore, regioisomerically pure bis-functionalized fullerenes function better as electron acceptors in organic thin-film solar cells than mixtures of the corresponding regioisomers do [12-14]. Therefore, controlling the regioselectivities of multiple functionalizations of fullerenes for the selective synthesis of specific multi-adducts poses an important challenge.

Addition reactions of C_{60} are well known to occur mainly at the 6,6-bonds (junction between two hexagons) rather than at the 5,6-bonds (junction between a pentagon and a hexagon). If the second additions proceed also at the 6,6-bonds, then nine regioisomers are possible for bis-additions, as shown in Figure 1

[4,5]. In addition, when the second addends are identical to the first, the *e′* and *e″* isomers are the same adducts, thereby affording eight possible regioisomers for bis-addition reactions. Hirsch and co-workers reported two-fold additions of C_{60} using the Bingel–Hirsch and the Bamford–Stevens reactions as well as nitrene addition reactions, indicating the formation of regioisomers as anticipated from the possible addition sites in Figure 1 [5]. Diederich and co-workers developed a general methodology using tether-directed remote functionalization for the regioselective formation of multiple adducts of fullerenes [6].

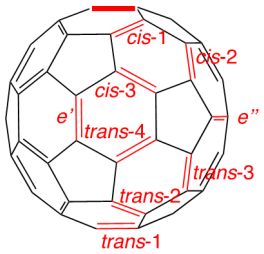

Figure 1: Positional notation of 6,6-bonds in a mono-adduct of C_{60} with the first addition site indicated using a bold line [5].

In our earlier reports, the reactions of C_{60} and C_{70}, with silylene Dip_2Si (**1**, Dip = 2,6-diisopropylphenyl), a silicon analog of carbene, were described as providing silirane (silacyclopropane)-type 6,6-mono-adducts Dip_2SiC_{60} (**2**, Scheme 1) and Dip_2SiC_{70} [15,16]. Furthermore, bis-adducts $(Dip_2Si)_2C_{60}$ and $(Dip_2Si)_2C_{70}$ were obtained as byproducts, but no details of these bis-adducts have been clarified [15,16]. The results demonstrated that the electronic properties of product **2** were altered considerably compared to that of pristine C_{60} mainly because silicon atoms are less electronegative. Electron-donating effects of silyl groups in fullerene derivatives were also rationalized in terms of σ–π conjugations between C–Si σ bonds of the silirane ring and adjacent π-bonds of the fullerene cage [17-20]. Therefore, it is interesting to examine the electronic properties of multi-silylene adducts in comparison with those of **2**. Herein, we report the structural determination and characterization of a bis-silylene adduct **3** of C_{60} based on spectroscopic measurements, X-ray crystallography, electrochemical analyses, and theoretical calculations.

Results and Discussion

Synthesis of bis-silylene adduct 3

The synthesis of the silylene adduct was conducted using a modified literature procedure [15]. A degassed solution of $Dip_2Si(SiMe_3)$ as a silylene precursor and C_{60} in toluene was irradiated by a 125-W low-pressure mercury lamp in a quartz tube for 2 h (Scheme 1). During reaction, the color of the solution turned to dark brown. After the photolysis, the bis-silylene adduct **3** was isolated in 36% yield accompanied by mono-adduct **2** (22% yield) by silica gel flash column chromatography using mixed solvents of hexane/CH_2Cl_2 by changing the ratios of volumes from 10:1 to 3:1. In thin-layer chromatography (TLC) analysis using silica gel, the R_f values are 0.55 for **2** and 0.33 for **3**, respectively, with hexane/CH_2Cl_2 5:1 as solvent mixture. Although several other fractions containing C_{60} derivatives were obtained, their structures are still under investigation because of the difficulty in isolating and purifying those fractions.

To clarify the addition site of **3**, we measured the ultraviolet–visible (UV–vis) spectrum. Fullerene derivatives are well-known to show characteristic absorption spectra depending on the addition pattern. As shown in Figure 2, the spectrum of **3** exhibited an absorption maximum at 515 nm, which is similar to those of the *e′* and *e″* isomers of $C_{60}[C(C_6H_4OMe)_2]_2$ and $C_{60}[C(C_6H_4OMe)_2][NCOOEt]$ [5]. In the case of **3**, the *e′* and

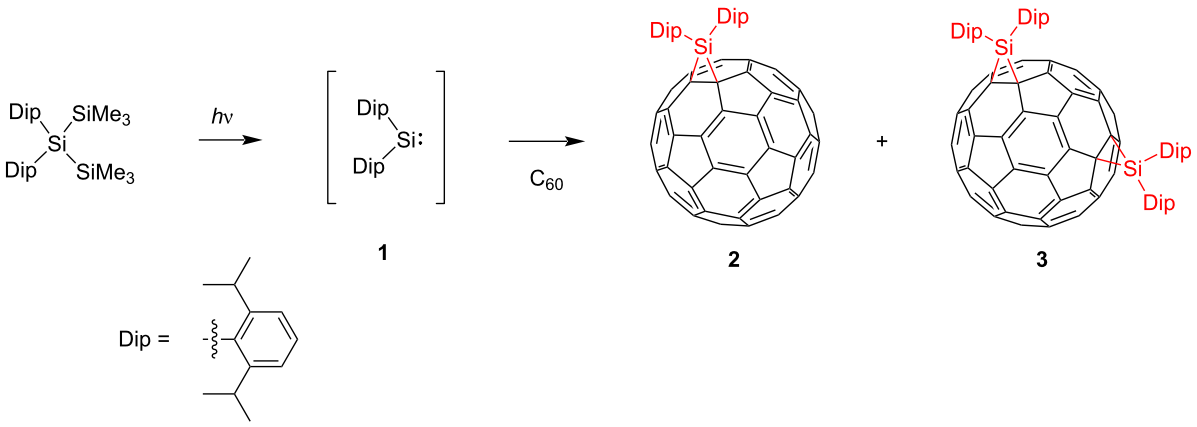

Scheme 1: Synthesis of silylene adducts **2** and **3**.

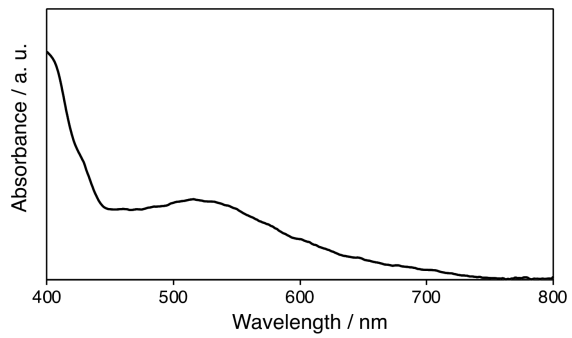

Figure 2: Absorption spectrum of **3** in CH_2Cl_2.

e'' isomers are identical products, and **3** is denoted as the *e* isomer hereinafter.

The ^{1}H NMR spectrum of **3** showed signals of eight doublets and three septets, which were assigned respectively to the methyl and methine groups, along with the aromatic protons (Figure 3). In the ^{13}C NMR spectrum, a total of 43 signals were observed in the low-field region (approximately 160–120 ppm), of which 29 signals are attributed to the C_{60} carbon cage and 14 signals are attributed to the aromatic ring carbon nuclei of the Dip groups (Figure 4). In addition, three sp^3 carbon atoms of the C_{60} carbon cage, eight methyl, and three methine carbon signals of the Dip group were observed. These spectral features

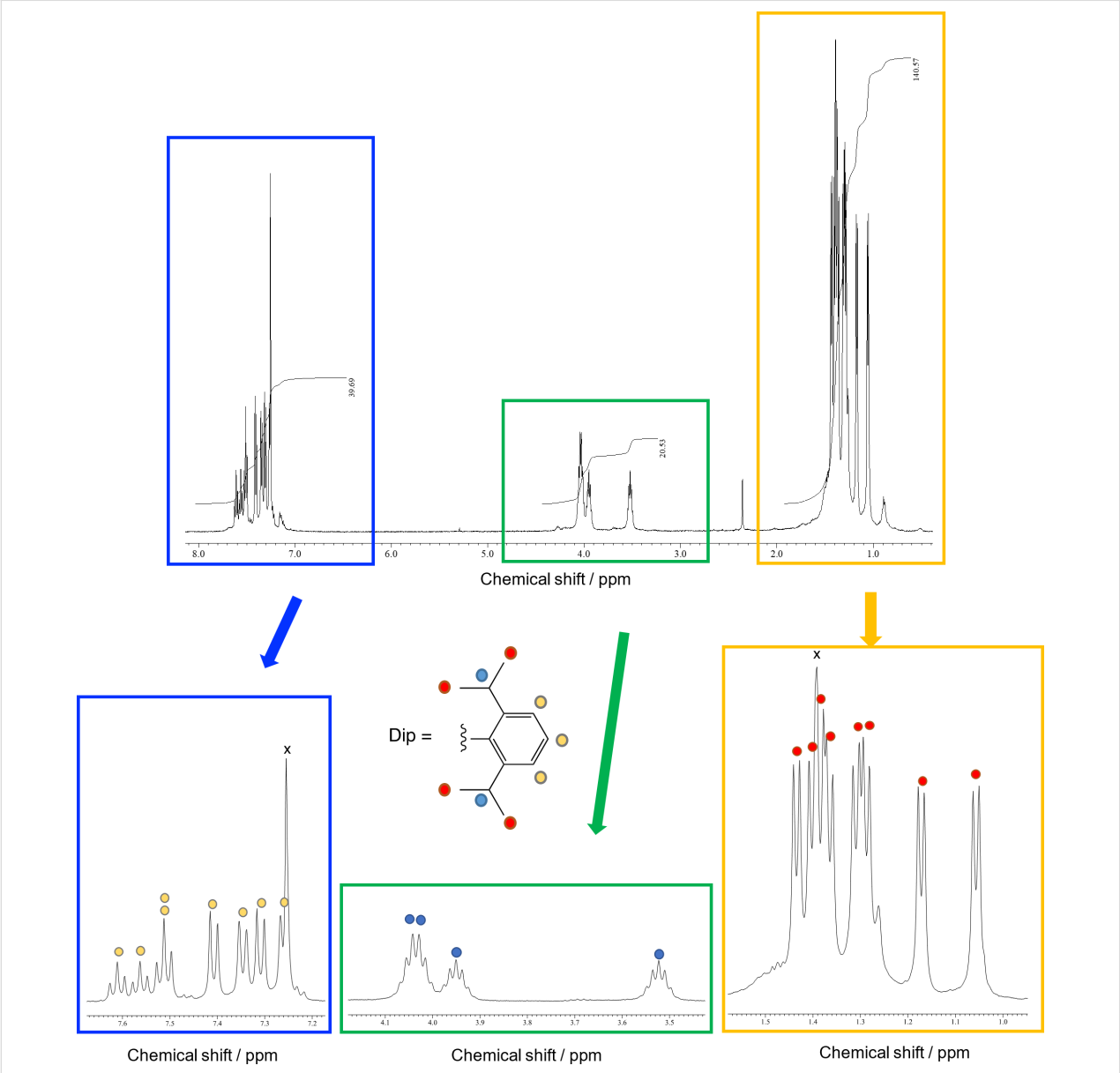

Figure 3: 500 MHz ^{1}H NMR spectrum of **3** in $CDCl_3/CS_2$ 3:1.

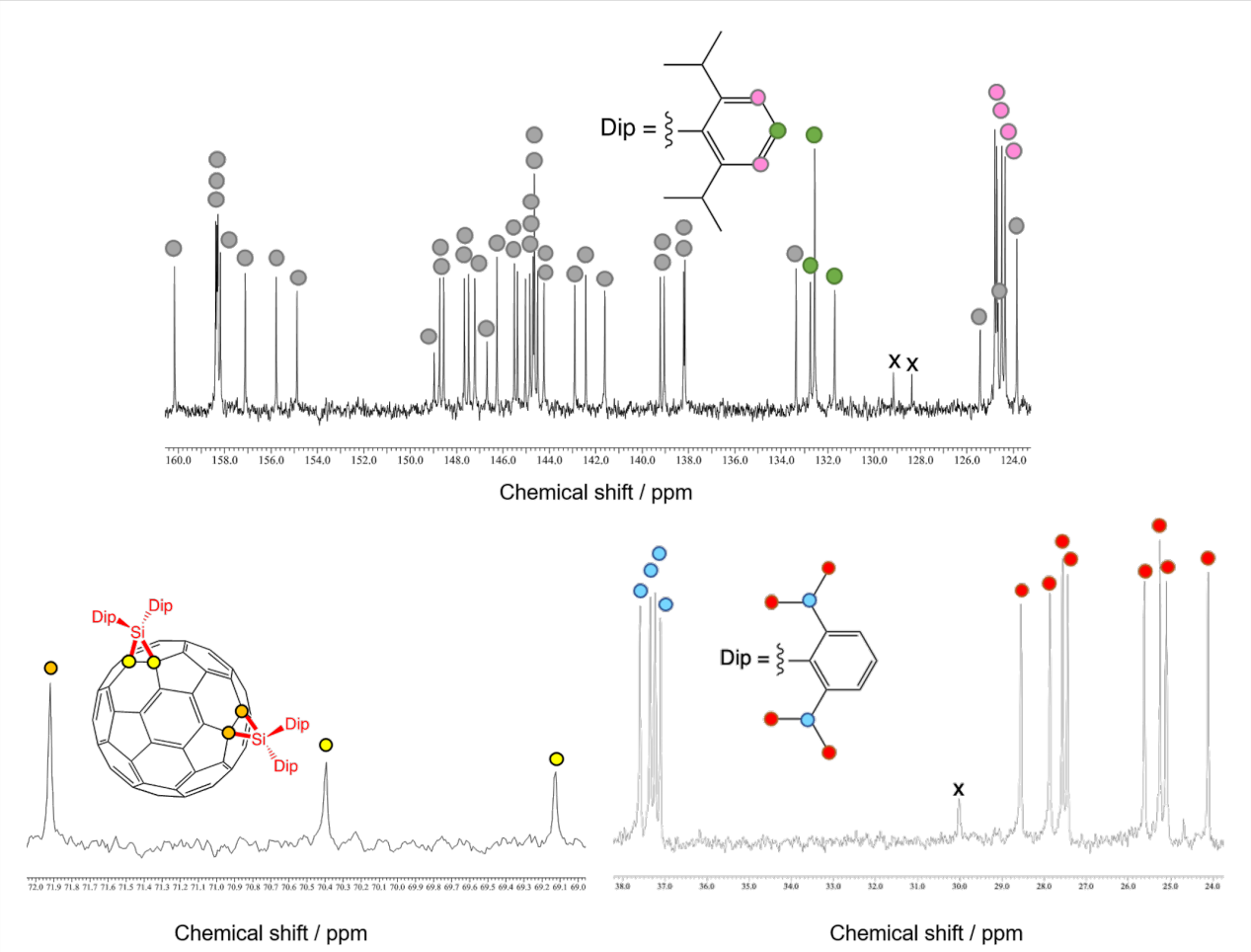

Figure 4: 125 MHz ^{13}C NMR spectrum of **3** in $CDCl_3/CS_2$ 3:1. The signals of sp^2 carbons of C_{60} and quaternary carbons of the Dip groups are indicated by grey circles.

are consistent with the structure of **3** as the *e* isomer of bis-adducts with C_s symmetry. The plane of symmetry includes one silirane ring and bisects another silirane ring perpendicularly.

Unfortunately, the matrix-assisted laser desorption ionization time-of-flight (MALDI-TOF) mass spectrometry of **3** afforded no molecular ion peak expected for adducts derived from Dip_2Si and C_{60} while a base peak at *m*/*z* 720 due to C_{60} was observed probably because of the low stability of radical ions of **3**.

Finally, the structure of **3** was established by single-crystal X-ray structure analysis. The ORTEP diagram of **3** is presented in Figure 5 with the selected bond lengths and angles collected in Table 1. The cage C–C bond lengths of the addition sites are C1–C9: 1.623(2) Å and C21–C40: 1.6282(19) Å, which fall within the range of the corresponding values reported for the crystal structures of methano-derivatives of C_{60} [5,21-33]. It is noteworthy that these C–C bond lengths are longer than those of

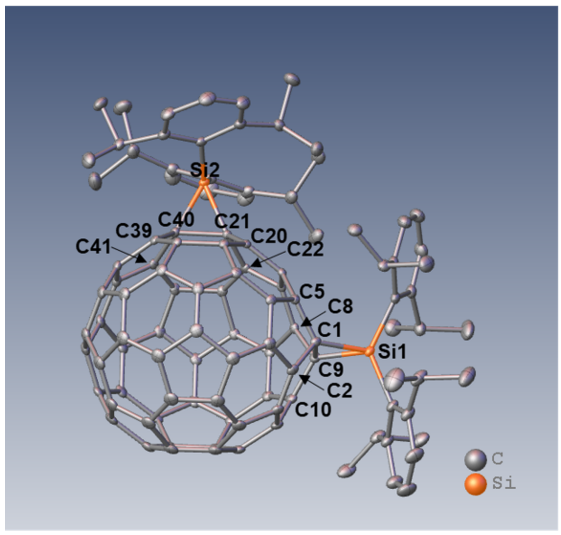

Figure 5: ORTEP drawing of **3** showing thermal ellipsoids at the 50% probability level at 100 K. Hydrogen atoms are omitted for clarity.

Table 1: Selected bond lengths and angles of **3**.

bond length [Å]		bond angle [°]	
C1–C9	1.623(2)	Si1–C1–C9	64.19(7)
Si1–C1	1.8886(15)	C1–Si1–C9	51.04(6)
Si1–C9	1.8796(15)	Si1–C9–C1	64.77(7)
C1–C2	1.495(2)		
C1–C5	1.497(2)		
C8–C9	1.492(2)		
C9–C10	1.498(2)		
C21–C40	1.6282(19)	Si2–C21–C40	64.65(7)
Si2–C21	1.8778(14)	C21–Si2–C40	51.26(6)
Si2–C40	1.8865(15)	Si2–C40–C21	64.10(7)
C20–C21	1.4951(19)		
C21–C22	1.490(2)		
C39–C40	1.4951(19)		
C40–C41	1.4928(19)		

the reported siliranes [34-42], except for rare examples such as 3-(hydroxydimesitylsilyl)-1,1-dimesityl-2,2-bis(trimethylsilyl)-1-silirane [43]. In contrast, we earlier reported the crystal structure of the adduct of $Lu_3N@I_h$–C_{80} with silylene Dep_2Si (Dep = 2,6-diethylphenyl), which was revealed to be a sila-fulleroid structure with the cage C–C separation distance of 2.25 Å at the addition site [44]. On the other hand, the Si–C bond lengths of the silirane ring in **3** are Si1–C1: 1.8886(15) Å, Si1–C9: 1.8796(15) Å, Si2–C21: 1.8778(14) Å, and Si2–C40: 1.8865(15) Å, which are roughly equal to those of the reported siliranes. These results confirm that the two addends in **3** are both silirane structures, which represents the first example of a crystallographic analysis of silirane derivatives of fullerenes.

Theoretical calculations

Hirsch and co-workers reported the bis-functionalization of C_{60} using the Bingel–Hirsch, the Bamford–Stevens reactions, and nitrene addition, indicating that preferential formation of the *e* (*e′* or *e″*) isomers followed by *trans*-3 isomer when at least one of the two addends was sterically demanding [5]. The formation of **3** in the present bis-silylene addition is consistent with those earlier results. To obtain some insight into regioselectivity, we performed density functional theory (DFT) calculations using the B3LYP/6-31G(d) method [45-48]. We first compared the relative stabilities of mono-adducts (Dip_2SiC_{60}) with 6,6-silirane (**2a**), 6,6-sila-fulleroid (**2b**), 5,6-silirane (**2c**), and 5,6-sila-fulleroid (**2d**) structures (Figure 6). The optimized structure of **2a** was found to be more stable than that of **2c** by 19.23 kcal/mol. In contrast, optimization using initial structures of **2b** and **2d** afforded the structures of **2a** and **2c**, respectively. Based on these results, the optimized structures of bis-adduct isomers $\mathbf{3}_{cis\text{-}2}$, $\mathbf{3}_{cis\text{-}3}$, $\mathbf{3}_{e}$, $\mathbf{3}_{trans\text{-}1}$, $\mathbf{3}_{trans\text{-}2}$, $\mathbf{3}_{trans\text{-}3}$, and $\mathbf{3}_{trans\text{-}4}$ were calculated by assuming the 6,6-silirane structures for addition sites. Calculation of $\mathbf{3}_{cis\text{-}1}$ was not conducted because of its sterically clouded structure. Structural parameters around the addition sites of $\mathbf{3}_{e}$ showed rough agreement with the corresponding values of **3** obtained using the X-ray structural analysis (Table 1 and Table S1 in Supporting Information File 1). As shown in Figure 7, few differences in relative energies are

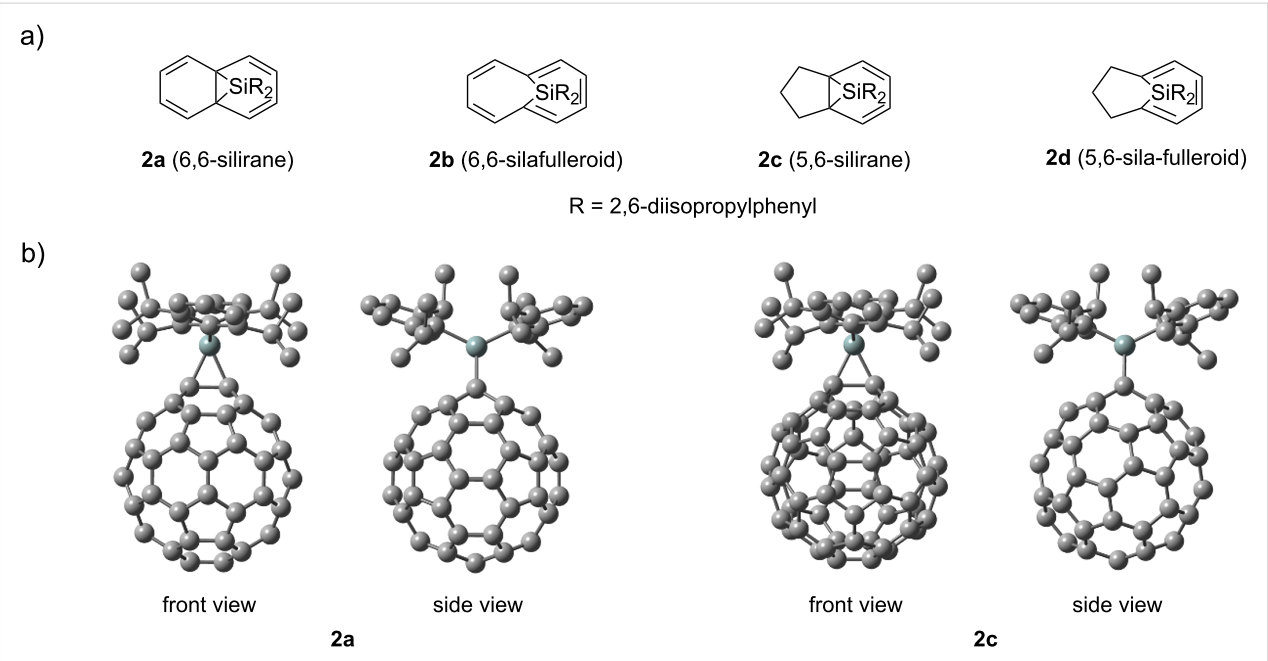

Figure 6: (a) Partial structures of isomers of Dip_2SiC_{60}. (b) Optimized structures of **2a** and **2c**. Hydrogen atoms are omitted for clarity.

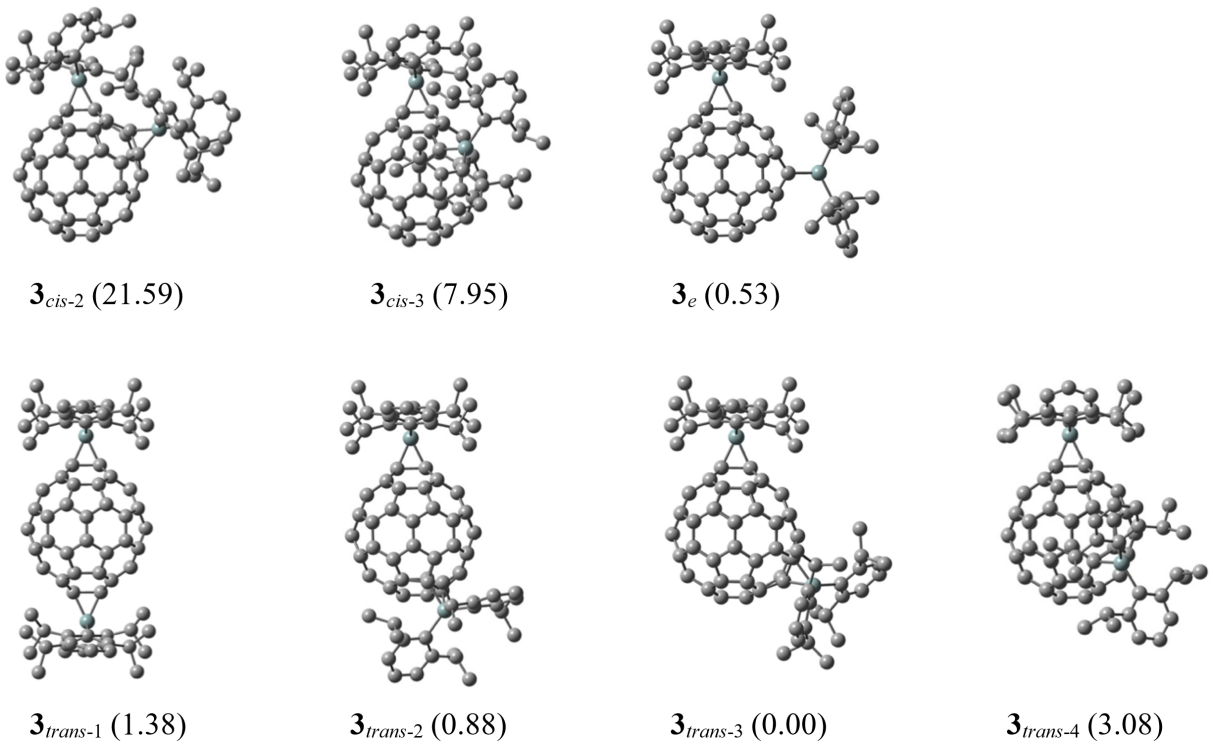

Figure 7: Optimized structures of $\mathbf{3}_{cis\text{-}2}$, $\mathbf{3}_{cis\text{-}3}$, $\mathbf{3}_{e}$, $\mathbf{3}_{trans\text{-}1}$, $\mathbf{3}_{trans\text{-}2}$, $\mathbf{3}_{trans\text{-}3}$, and $\mathbf{3}_{trans\text{-}4}$. Values in parentheses are the relative energies in kcal/mol compared to that of $\mathbf{3}_{trans\text{-}3}$. Hydrogen atoms are omitted for clarity.

apparent among $\mathbf{3}_{e}$, $\mathbf{3}_{trans\text{-}1}$, $\mathbf{3}_{trans\text{-}2}$, $\mathbf{3}_{trans\text{-}3}$, and $\mathbf{3}_{trans\text{-}4}$, although $\mathbf{3}_{cis\text{-}2}$ and $\mathbf{3}_{cis\text{-}3}$ are unstable. Therefore, we next investigated the structural and electronic properties of the calculated mono-adduct **2a** to evaluate its reactivity toward **1**.

The bond lengths of the cage C–C double bonds and the π-orbital axis vector (POAV) [49] of the cage carbon atoms of **2a** are presented in Tables S2 and S3 in Supporting Information File 1. Mean values are given respectively for the identical type of bonds and atoms. The differences in the double bond lengths are negligible, but the *cis*-1, *cis*-2, and *e* bonds are slightly shorter than the other bonds. The POAV values show no marked difference except for the carbons adjacent to the addition site. Therefore, neither the double bond lengths nor the POAV values of **2a** are regarded as affecting the regioselectivity.

The frontier orbitals of **2a** were then examined to elucidate the reactivity in the second silylene addition. The ground states of silylenes are known to be singlet except for a few examples [50,51]. Singlet silylenes have n orbitals as the highest occupied molecular orbitals (HOMOs) that accommodate unshared electron pairs on the silicon atoms, while empty 3p orbitals correspond to the lowest unoccupied molecular orbitals (LUMOs). In addition, silylenes are characterized by both nucleophilic properties based on the high HOMO levels, and electrophilic properties because of the low LUMO levels [50,51]. The Mulliken charge densities of **2s** are also shown in Figure S2 (Supporting Information File 1), which shows that the charge densities are nearly zero on the cage carbon atoms except those adjacent to the addition site. The charge densities of **2a** are regarded as affecting the regioselectivity. Thus, it is suggested that the regioselectivity in the silylene addition could not be estimated by the charge densities of **2a**.

The regioselectivity in the addition reaction of **1** with C_{70} was explained earlier in terms of the interaction between the HOMO of **1** and the LUMO of C_{70} [16]. The reaction mechanism of ethylene with a silylene substituted with thiolate ligands has been studied using theoretical calculations, in which the transition state was ascribed to the donor–acceptor interactions between the HOMO of the silylene and the LUMO of ethylene, and vice versa [42]. For **2a**, the LUMO is largely distributed at the *e′* bonds, followed by the *cis*-2 and *trans*-3 bonds (Figure 8). These results suggest that the formation of **3** may involve the interaction of **1** with the LUMO of **2a**. The HOMO of **2a** is observed mainly around the *cis*-1 and *e″* bonds among the 6,6-bonds, although the *cis*-1 bond would not be susceptible to the

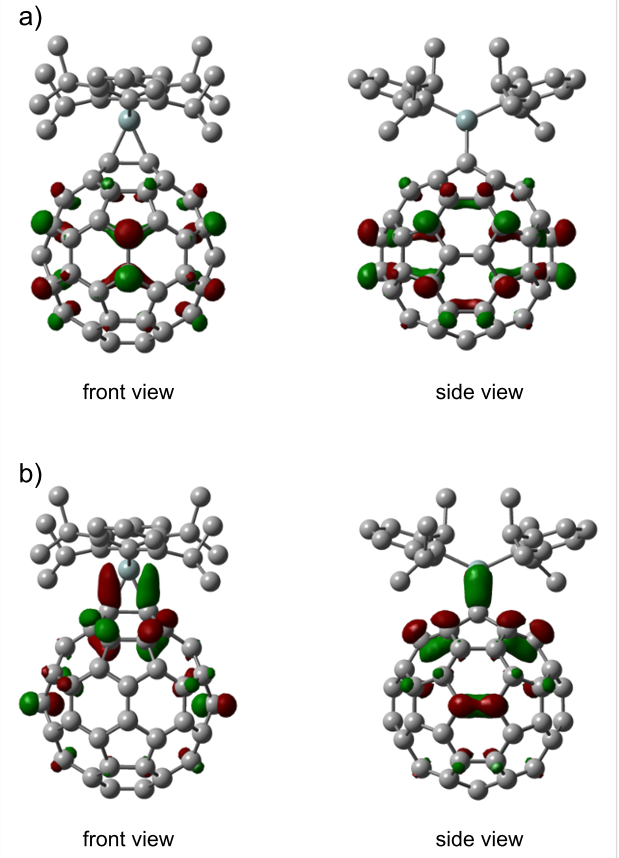

Figure 8: (a) LUMO and (b) HOMO of **2a** calculated at the B3LYP/6-31G(d) level. Hydrogen atoms are omitted for clarity.

second silylene addition because of its steric hindrance. Alternatively, the interaction of the LUMO of **1** with the HOMO of **2a** should be considered.

Electrochemical measurements of 3

Cyclic voltammetry (CV) and differential pulse voltammetry (DPV) measurements were conducted to evaluate the electronic effects of the silylene addends in **3** (Figure 9). The oxidation processes of **3** were shown to be irreversible, probably because of the removal of silylene addends, whereas the electrochemically reversible behavior was observed for the reduction waves. Table 2 presents the redox potentials of **3** obtained by DPV with those of C_{60} and **2**, as reference compounds. Both the reduction (E^{red}) and the oxidation (E^{ox}) potentials of **3** were found to be shifted cathodically compared respectively to those of C_{60} and **2**, indicating the electron-donating effects of the two Dip_2Si groups. It is noteworthy that the first reduction potential of **3** ($E^{red}_1 = -1.52$ V) is the most negative among those of the silylated empty fullerenes [52-56].

The energies of HOMOs and LUMOs of the calculated regioisomers of **3** were compared with those of C_{60} and **2a** (Table 3).

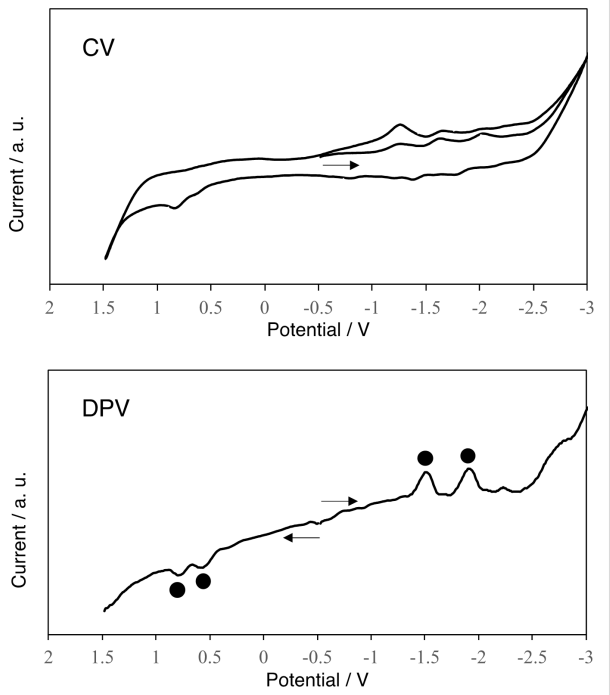

Figure 9: Cyclic voltammograms (CV) and differential pulse voltammograms (DPV) of **3** in *o*-dichlorobenzene containing 0.1 M $(n\text{-Bu})_4NPF_6$. In DPVs, peaks of the adducts are denoted by circles. Potentials are shown in volts relative to the ferrocene/ferrocenium couple. Conditions: glassy carbon working electrode; Pt wire counter electrode; SCE reference electrode; 50 mV/s scan rate.

Table 2: Redox potentials[a] (V) of C_{60}, **2**, and **3**.

compound	E^{ox}_2	E^{ox}_1	E^{red}_1	E^{red}_2
C_{60}		+1.32[b]	−1.15	−1.58
2[b]		+0.71	−1.30	−1.71
3	+0.80	+0.58	−1.52	−1.92

[a]Values obtained by DPV are in volts relative to the ferrocene/ferrocenium couple. [b]Data from ref [54].

The HOMO and LUMO levels of $\mathbf{3}_e$ were both found to be higher than those of C_{60} and **2a**, respectively, which is qualitatively consistent with the shifts in the redox potentials of C_{60}, **2**, and **3**. By contrast, $\mathbf{3}_{cis\text{-}2}$, $\mathbf{3}_{cis\text{-}3}$, $\mathbf{3}_e$, $\mathbf{3}_{trans\text{-}1}$, $\mathbf{3}_{trans\text{-}2}$, $\mathbf{3}_{trans\text{-}3}$, and $\mathbf{3}_{trans\text{-}4}$ were found to have no significant differences in their respective HOMO and LUMO levels, as shown in Table 3.

Conclusion

The bis-silylene adduct **3** was isolated by the two-fold addition of **1** to C_{60}. The spectroscopic and crystallographic analyses established **3** as an *e* isomer of bis-adducts with silirane structures at the 6,6-bonds. In the DFT calculations of mono-adduct **2a**, the LUMO is distributed remarkably around the *e'* bonds,

Table 3: Calculated HOMO/LUMO levels (eV)[a].

compound	HOMO	LUMO
C_{60}	–5.99	–3.23
2a	–5.30	–2.91
3$_{cis\text{-}2}$	–5.14	–2.68
3$_{cis\text{-}3}$	–4.77	–2.62
3$_{e}$	–5.01	–2.61
3$_{trans\text{-}1}$	–4.99	–2.67
3$_{trans\text{-}2}$	–4.97	–2.67
3$_{trans\text{-}3}$	–4.90	–2.58
3$_{trans\text{-}4}$	–4.86	–2.58

[a]B3LYP/6-31G(d).

which are likely to interact with the HOMO of **1** leading to the formation of **3**. Also, the HOMO of **2a** is observed around the *cis*-1 and *e''* bonds, although the *cis*-1 bond would be sterically protected from the second silylene addition. Alternatively, the interaction of the LUMO of **1** with *e''* bonds of **2** should be considered. Electrochemical measurements (CV and DPV) were taken to evaluate the electronic properties of **3**. As expected, the redox potentials of **3** are shown to be shifted cathodically compared to those of C_{60} and **2** because of the electron-donating effect of the two silylene groups. These results are qualitatively consistent with the shifts in the HOMO and LUMO levels calculated respectively for C_{60}, **2**, and **3**.

Experimental

Materials and general method: All chemicals were reagent grade, purchased from commercial suppliers. *o*-Dichlorobenzene (ODCB) was distilled from P_2O_5 under vacuum before use. Toluene was distilled from benzophenone sodium ketyl under dry N_2 prior to use. Reagents were used as purchased unless otherwise specified. The ^{1}H and ^{13}C NMR measurements were conducted on a JEOL ECA-500 spectrometer (JEOL Ltd.). Absorption spectra were measured using a UV-3150 spectrophotometer (Shimadzu Corp.). Cyclic voltammograms and differential pulse voltammograms were recorded on a BAS CV50W electrochemical analyzer (BAS Inc.). The reference electrode was a saturated calomel reference electrode (SCE). The glassy carbon electrode was used as the working electrode, and a platinum wire was used as the counter electrode. All potentials are referenced to the ferrocene/ferrocenium couple (Fc/Fc^+) as the standard. (n-Bu)$_4$NPF$_6$ (0.1 M) in ODCB was used as the supporting electrolyte solution. The cyclic voltammograms were recorded using a scan rate of 50 mV/s. The differential pulse voltammograms were obtained using a pulse amplitude of 50 mV, a pulse width of 50 ms, a pulse period of 200 ms, and a scan rate of 50 mV/s.

Synthesis of 3. A degassed solution of $Dip_2Si(SiMe_3)$ (30 mg) and C_{60} (4.6 mg) in toluene (20 mL) in a quartz tube was irradiated by a 125-W low-pressure mercury lamp for 2 h [15]. After the photolysis, **2** (22% yield) and **3** (36% yield) were isolated by flash column chromatography (SiO_2) using mixed solvents of hexane/CH_2Cl_2 by changing the ratios of volumes from 10:1 to 3:1. TLC analysis (SiO_2, hexane/CH_2Cl_2 5:1) afforded R_f = 0.55 for **2** and R_f = 0.33 for **3**, respectively. Data for compound **3**: ^{1}H NMR ($CDCl_3/CS_2$ 3:1) δ 7.61 (t, J = 7.5 Hz, 1H), 7.56 (t, J = 7.5 Hz, 1H), 7.51 (t, J = 7.5 Hz, 2H), 7.41 (d, J = 7.5 Hz, 2H), 7.35 (d, J = 7.5 Hz, 2H), 7.31 (d, J = 7.5 Hz, 2H), 7.26 (d, J = 7.5 Hz, 2H), 4.04 (sept, J = 7.0 Hz, 2H), 4.03 (sept, J = 7.0 Hz, 2H), 3.95 (sept, J = 7.0 Hz, 2H), 3.52 (sept, J = 7.0 Hz, 2H), 1.43 (d, J = 7.0 Hz, 6H), 1.40 (d, J = 7.0 Hz, 6H), 1.371 (d, J = 7.0 Hz, 6H), 1.365 (d, J = 7.0 Hz, 6H), 1.31 (d, J = 7.0 Hz, 6H), 1.29 (d, J = 7.0 Hz, 6H), 1.17 (d, J = 7.0 Hz, 6H), 1.06 (d, J = 7.0 Hz, 6H); ^{13}C NMR ($CDCl_3/CS_2$ 3:1) δ 160.16 (s, 2C), 158.38 (s, 2C), 158.33 (s, 2C), 158.29 (s, 2C), 158.18 (s, 2C), 157.12 (s, 2C), 155.78 (s, 2C), 154.87 (s, 2C), 148.96 (s, 1C), 148.73 (s, 2C), 148.56 (s, 2C), 147.66 (s, 2C), 147.48 (s, 2C), 147.22 (s, 2C), 146.69 (s, 1C), 146.26 (s, 2C), 145.51 (s, 2C), 145.37 (s, 2C), 145.03 (s, 2C), 144.84 (s, 2C), 144.71 (s, 2C), 144.65 (s, 4C), 144.51 (s, 2C), 144.23 (s, 2C), 142.90 (s, 2C), 142.43 (s, 2C), 141.62 (s, 2C), 139.22 (s, 2C), 139.05 (s, 2C), 138.21 (s, 2C), 138.15 (s, 2C), 133.37 (s, 2C), 132.76 (d, 1C), 132.56 (d, 2C), 131.71 (d, 1C), 125.43 (s, 1C), 124.79 (d, 2C), 124.71 (d, 2C), 124.66 (s, 1C), 124.49 (d, 2C), 124.35 (d, 2C), 123.85 (s, 2C), 71.92 (s, 2C), 70.39 (s, 1C), 69.12 (s, 1C), 37.59 (d, 2C), 37.35 (d, 2C), 37.24 (d, 2C), 37.11 (d, 2C), 28.55 (q, 2C), 27.86 (q, 2C), 27.57 (q, 2C), 27.44 (q, 2C), 25.61 (q, 2C), 25.25 (q, 2C), 25.10 (q, 2C), 24.11 (q, 2C); UV–vis (CH_2Cl_2) λ_{max} 515 nm.

X-ray crystallography of 3: Black plate crystals suitable for X-ray diffraction were obtained using the liquid–liquid bilayer diffusion method with solutions of **3** in CS_2 using hexane as a poor solvent at 0 °C. Single-crystal X-ray diffraction data of **3** were collected on a Rigaku Oxford Diffraction XtaLAB Synergy R DW system with a HyPix detector equipped with a nitrogen-gas flow low-temperature apparatus providing a constant temperature at 100 K. Crystal data for $C_{60}(Dip_2Si)_2$: $C_{108}H_{68}Si_2$: M_r = 1421.87, black plate, 0.11 × 0.16 × 0.025 mm, λ = 0.71073 Å, monoclinic, space group $P2_1/n$ (no. 14), a = 18.3631(3), b = 13.6696 (2), c = 27.6360 (5) Å, β = 92.857 (2)°, V = 6928.5(2) Å^3, T = 99.9(2) K, Z = 4, 67750 reflections measured, 19176 unique (R_{int} = 0.0321), which were used for all calculations, $2\theta_{max}$ = 63.262; min/max transmission = 0.921/1.000 (absorption correction was applied by multi-scan method); The structure was solved using a direct method using olex2.solve 1.5-ac5-018 [57] and was refined with SHELXL-2018 [58]. The final $wR(F_2)$ was 0.1283 (all data),

conventional R_1 = 0.0493 computed for 14459 reflections with $I > 2\sigma(I)$ using 1007 parameters with 0 restraints. Crystallographic computations were performed with Olex2 [59]. CCDC 2311474 (**3**) contains the supplementary crystallographic data for this paper, and is obtainable free of charge from the Cambridge Crystallographic Data Centre.

Computational method. All calculations were conducted using the Gaussian 16 program [60]. Optimized structures were obtained at the B3LYP [45-47] level of theory using basis sets of 6-31G(d) [48].

Supporting Information

Supporting Information File 1

Structural data of **2a** and $\mathbf{3}_e$ obtained by DFT calculations, and Cartesian coordinates of optimized structures.
[https://www.beilstein-journals.org/bjoc/content/supplementary/1860-5397-20-100-S1.pdf]

Supporting Information File 2

Crystallographic information file of **3**.
[https://www.beilstein-journals.org/bjoc/content/supplementary/1860-5397-20-100-S2.cif]

Funding

This work was supported by Grants-in-Aid for Scientific Research (B) (No. 24350019) and (C) (No. 17K05797 and 20K05469) from the Ministry of Education, Culture, Sports, Science, and Technology of Japan.

Author Contributions

Masahiro Kako: conceptualization; supervision; writing – original draft; writing – review & editing. Masato Kai: investigation. Masanori Yasui: investigation. Michio Yamada: investigation; writing – review & editing. Yutaka Maeda: investigation; writing – review & editing. Takeshi Akasaka: conceptualization; writing – review & editing.

ORCID® iDs

Masahiro Kako - https://orcid.org/0000-0002-2669-5870
Masanori Yasui - https://orcid.org/0009-0006-3157-9862
Michio Yamada - https://orcid.org/0000-0002-6715-4202
Yutaka Maeda - https://orcid.org/0000-0003-0502-5621
Takeshi Akasaka - https://orcid.org/0000-0002-4073-4354

Data Availability Statement

All data that supports the findings of this study is available in the published article and/or the supporting information to this article.

References

1. Hirsch, A. *The Chemistry of the Fullerenes;* Thieme: Stuttgart, Germany, 1994. doi:10.1002/9783527619214
2. Taylor, R., Ed. *The Chemistry of the Fullerenes; Advanced Series in Fullerenes*, Vol. 4; World Scientific: Singapore, 1995. doi:10.1142/2790
3. Hirsch, A., Ed. *Fullerenes and related Structures;* Springer: Berlin, Germany, 1999. doi:10.1007/3-540-68117-5
4. Hirsch, A.; Lamparth, I.; Karfunkel, H. R. *Angew. Chem., Int. Ed. Engl.* **1994,** *33,* 437–438. doi:10.1002/anie.199404371
5. Djojo, F.; Herzog, A.; Lamparth, I.; Hampel, F.; Hirsch, A. *Chem. – Eur. J.* **1996,** *2,* 1537–1547. doi:10.1002/chem.19960021211
6. Diederich, F.; Kessinger, R. *Acc. Chem. Res.* **1999,** *32,* 537–545. doi:10.1021/ar970321o
7. Hirsch, A. *Chem. Rec.* **2005,** *5,* 196–208. doi:10.1002/tcr.20047
8. Cerón, M. R.; Echegoyen, L. *J. Phys. Org. Chem.* **2016,** *29,* 613–619. doi:10.1002/poc.3563
9. Brabec, C. J.; Cravino, A.; Meissner, D.; Sariciftci, N. S.; Fromherz, T.; Rispens, M. T.; Sanchez, L.; Hummelen, J. C. *Adv. Funct. Mater.* **2001,** *11,* 374–380. doi:10.1002/1616-3028(200110)11:5<374::aid-adfm374>3.0.co;2-w
10. Lenes, M.; Wetzelaer, G.-J. A. H.; Kooistra, F. B.; Veenstra, S. C.; Hummelen, J. C.; Blom, P. W. M. *Adv. Mater. (Weinheim, Ger.)* **2008,** *20,* 2116–2119. doi:10.1002/adma.200702438
11. Mishra, A.; Bäuerle, P. *Angew. Chem., Int. Ed.* **2012,** *51,* 2020–2067. doi:10.1002/anie.201102326
12. Tao, R.; Umeyama, T.; Kurotobi, K.; Imahori, H. *ACS Appl. Mater. Interfaces* **2014,** *6,* 17313–17322. doi:10.1021/am5058794
13. Wong, W. W. H.; Subbiah, J.; White, J. M.; Seyler, H.; Zhang, B.; Jones, D. J.; Holmes, A. B. *Chem. Mater.* **2014,** *26,* 1686–1689. doi:10.1021/cm404054z
14. Meng, X.; Zhao, G.; Xu, Q.; Tan, Z.; Zhang, Z.; Jiang, L.; Shu, C.; Wang, C.; Li, Y. *Adv. Funct. Mater.* **2014,** *24,* 158–163. doi:10.1002/adfm.201301411
15. Akasaka, T.; Ando, W.; Kobayashi, K.; Nagase, S. *J. Am. Chem. Soc.* **1993,** *115,* 1605–1606. doi:10.1021/ja00057a072
16. Akasaka, T.; Mitsuhida, E.; Ando, W.; Kobayashi, K.; Nagase, S. *J. Chem. Soc., Chem. Commun.* **1995,** 1529–1530. doi:10.1039/c39950001529
17. Bock, H.; Solouki, B. Photoelectron Spectra of Silicon Compounds. In *The Chemistry of Organic Silicon Compounds;* Patai, S.; Rappoport, Z., Eds.; John Wiley & Sons: Chichester, UK, 1989; pp 555–653. doi:10.1002/0470025107.ch9
18. Traylor, T. G.; Hanstein, W.; Berwin, H. J.; Clinton, N. A.; Brown, R. S. *J. Am. Chem. Soc.* **1971,** *93,* 5715–5725. doi:10.1021/ja00751a024
19. Hosomi, A. *Acc. Chem. Res.* **1988,** *21,* 200–206. doi:10.1021/ar00149a004
20. Fleming, I.; Barbero, A.; Walter, D. *Chem. Rev.* **1997,** *97,* 2063–2192. doi:10.1021/cr941074u
21. Osterodt, J.; Nieger, M.; Vögtle, F. *J. Chem. Soc., Chem. Commun.* **1994,** 1607–1608. doi:10.1039/c39940001607
22. Anderson, H. L.; Boudon, C.; Diederich, F.; Gisselbrecht, J.-P.; Gross, M.; Seiler, P. *Angew. Chem., Int. Ed. Engl.* **1994,** *33,* 1628–1632. doi:10.1002/anie.199416281
23. Paulus, E. F.; Bingel, C. *Acta Crystallogr., Sect. C: Cryst. Struct. Commun.* **1995,** *51,* 143–146. doi:10.1107/s0108270194009728
24. Seiler, P.; Isaacs, L.; Diederich, F. *Helv. Chim. Acta* **1996,** *79,* 1047–1058. doi:10.1002/hlca.19960790413

25. Tezuka, Y.; Kawasaki, N.; Yajima, H.; Ishii, T.; Oyama, T.; Takeuchi, K.; Nakao, A.; Katayama, C. *Acta Crystallogr., Sect. C: Cryst. Struct. Commun.* **1996,** *52,* 1008–1010. doi:10.1107/s0108270195013096
26. Cardullo, F.; Seiler, P.; Isaacs, L.; Nierengarten, J.-F.; Haldimann, R. F.; Diederich, F.; Mordasini-Denti, T.; Thiel, W.; Boudon, C.; Gisselhrccht, J.-P.; Gross, M. *Helv. Chim. Acta* **1997,** *80,* 343–371. doi:10.1002/hlca.19970800203
27. Iversen, B. B.; Darovsky, A.; Bolotovsky, R.; Coppens, P. *Acta Crystallogr., Sect. B: Struct. Sci.* **1998,** *54,* 174–179. doi:10.1107/s0108768197012007
28. Rispens, M. T.; Meetsma, A.; Rittberger, R.; Brabec, C. J.; Sariciftci, N. S.; Hummelen, J. C. *Chem. Commun.* **2003,** 2116–2118. doi:10.1039/b305988j
29. Nikawa, H.; Nakahodo, T.; Tsuchiya, T.; Wakahara, T.; Rahman, G. M. A.; Akasaka, T.; Maeda, Y.; Liu, M. T. H.; Meguro, A.; Kyushin, S.; Matsumoto, H.; Mizorogi, N.; Nagase, S. *Angew. Chem., Int. Ed.* **2005,** *44,* 7567–7570. doi:10.1002/anie.200502971
30. Ishitsuka, M. O.; Enoki, H.; Nikawa, H.; Wakahara, T.; Tsuchiya, T.; Akasaka, T.; Liu, M. T. H. *Tetrahedron Lett.* **2007,** *48,* 859–861. doi:10.1016/j.tetlet.2006.11.145
31. Sato, S.; Yamada, M.; Wakahara, T.; Tsuchiya, T.; Ishitsuka, M. O.; Akasaka, T.; Liu, M. T. H. *Tetrahedron Lett.* **2007,** *48,* 6290–6293. doi:10.1016/j.tetlet.2007.07.027
32. Matsuo, Y.; Okada, H.; Maruyama, M.; Sato, H.; Tobita, H.; Ono, Y.; Omote, K.; Kawachi, K.; Kasama, Y. *Org. Lett.* **2012,** *14,* 3784–3787. doi:10.1021/ol301671n
33. Okada, H.; Kawakami, H.; Aoyagi, S.; Matsuo, Y. *J. Org. Chem.* **2017,** *82,* 5868–5872. doi:10.1021/acs.joc.7b00730
34. Delker, G. L.; Wang, Y.; Stucky, G. D.; Lambert, R. L., Jr.; Haas, C. K.; Seyferth, D. *J. Am. Chem. Soc.* **1976,** *98,* 1779–1784. doi:10.1021/ja00423a024
35. Ando, W.; Fujita, M.; Yoshida, H.; Sekiguchi, A. *J. Am. Chem. Soc.* **1988,** *110,* 3310–3311. doi:10.1021/ja00218a056
36. Suzuki, H.; Tokitoh, N.; Okazaki, R. *J. Am. Chem. Soc.* **1994,** *116,* 11572–11573. doi:10.1021/ja00104a049
37. Suzuki, H.; Tokitoh, N.; Okazaki, R. *Bull. Chem. Soc. Jpn.* **1995,** *68,* 2471–2481. doi:10.1246/bcsj.68.2471
38. Ando, W.; Shiba, T.; Hidaka, T.; Morihashi, K.; Kikuchi, O. *J. Am. Chem. Soc.* **1997,** *119,* 3629–3630. doi:10.1021/ja9637412
39. Klapötke, T. M.; Kumar Vasisht, S.; Mayer, P. *Z. Anorg. Allg. Chem.* **2009,** *635,* 2447–2454. doi:10.1002/zaac.200900309
40. Ishida, S.; Iwamoto, T.; Kira, M. *Heteroat. Chem.* **2011,** *22,* 432–437. doi:10.1002/hc.20705
41. Pichaandi, K. R.; Mague, J. T.; Fink, M. J. *J. Organomet. Chem.* **2011,** *696,* 1957–1963. doi:10.1016/j.jorganchem.2010.10.043
42. Lips, F.; Fettinger, J. C.; Mansikkamäki, A.; Tuononen, H. M.; Power, P. P. *J. Am. Chem. Soc.* **2014,** *136,* 634–637. doi:10.1021/ja411951y
43. Ishikawa, M.; Matsuzawa, S.; Sugisawa, H.; Yano, F.; Kamitori, S.; Higuchi, T. *J. Am. Chem. Soc.* **1985,** *107,* 7706–7710. doi:10.1021/ja00311a080
44. Sato, K.; Kako, M.; Suzuki, M.; Mizorogi, N.; Tsuchiya, T.; Olmstead, M. M.; Balch, A. L.; Akasaka, T.; Nagase, S. *J. Am. Chem. Soc.* **2012,** *134,* 16033–16039. doi:10.1021/ja3073929
45. Becke, A. D. *Phys. Rev. A* **1988,** *38,* 3098–3100. doi:10.1103/physreva.38.3098
46. Becke, A. D. *J. Chem. Phys.* **1993,** *98,* 5648–5652. doi:10.1063/1.464913
47. Lee, C.; Yang, W.; Parr, R. G. *Phys. Rev. B* **1988,** *37,* 785–789. doi:10.1103/physrevb.37.785
48. Hehre, W. J.; Ditchfield, R.; Pople, J. A. *J. Chem. Phys.* **1972,** *56,* 2257–2261. doi:10.1063/1.1677527
49. Haddon, R. C. *J. Am. Chem. Soc.* **1997,** *119,* 1797–1798. doi:10.1021/ja9637659
50. Gaspar, P. P.; West, R. Silylenes. In *The Chemistry of Organosilicon Compounds;* Patai, S.; Rappoport, Z., Eds.; John Wiley & Sons: Chichester, UK, 1998; Vol. 2, pp 2463–2568. doi:10.1002/0470857250.ch43
51. Mizuhata, Y.; Sasamori, T.; Tokitoh, N. *Chem. Rev.* **2009,** *109,* 3479–3511. doi:10.1021/cr900093s
52. Suzuki, T.; Maruyama, Y.; Akasaka, T.; Ando, W.; Kobayashi, K.; Nagase, S. *J. Am. Chem. Soc.* **1994,** *116,* 1359–1363. doi:10.1021/ja00083a022
53. Akasaka, T.; Suzuki, T.; Maeda, Y.; Ara, M.; Wakahara, T.; Kobayashi, K.; Nagase, S.; Kako, M.; Nakadaira, Y.; Fujitsuka, M.; Ito, O. *J. Org. Chem.* **1999,** *64,* 566–569. doi:10.1021/jo981689h
54. Wakahara, T.; Han, A.; Niino, Y.; Maeda, Y.; Akasaka, T.; Suzuki, T.; Yamamoto, K.; Kako, M.; Nakadaira, Y.; Kobayashi, K.; Nagase, S. *J. Mater. Chem.* **2002,** *12,* 2061–2064. doi:10.1039/b201118b
55. Maeda, Y.; Aminur Rahman, G. M.; Wakahara, T.; Kako, M.; Okamura, M.; Sato, S.; Akasaka, T.; Kobayashi, K.; Nagase, S. *J. Org. Chem.* **2003,** *68,* 6791–6794. doi:10.1021/jo0344788
56. Han, A. H.; Wakahara, T.; Maeda, Y.; Akasaka, T.; Fujitska, M.; Ito, O.; Yamamoto, K.; Kako, M.; Kobayashi, K.; Nagase, S. *New J. Chem.* **2009,** *33,* 497–500. doi:10.1039/b808119k
57. Bourhis, L. J.; Dolomanov, O. V.; Gildea, R. J.; Howard, J. A. K.; Puschmann, H. *Acta Crystallogr., Sect. A: Found. Adv.* **2015,** *71,* 59–75. doi:10.1107/s2053273314022207
58. Sheldrick, G. M. *Acta Crystallogr., Sect. C: Struct. Chem.* **2015,** *71,* 3–8. doi:10.1107/s2053229614024218
59. Dolomanov, O. V.; Bourhis, L. J.; Gildea, R. J.; Howard, J. A. K.; Puschmann, H. *J. Appl. Crystallogr.* **2009,** *42,* 339–341. doi:10.1107/s0021889808042726
60. *Gaussian 16,* Revision C.01; Gaussian, Inc.: Wallingford, CT, 2019.

License and Terms

BEILSTEIN JOURNAL OF ORGANIC CHEMISTRY

Introduction of peripheral nitrogen atoms to cyclo-*meta*-phenylenes

Koki Ikemoto* and Hiroyuki Isobe*

Letter

Open Access

Address:
Department of Chemistry, The University of Tokyo, Hongo 7-3-1, Bunkyo-ku, Tokyo 113-0033, Japan

Email:
Koki Ikemoto* - kikemoto@chem.s.u-tokyo.ac.jp; Hiroyuki Isobe* - isobe@chem.s.u-tokyo.ac.jp

* Corresponding author

Keywords:
cross coupling; macrocycles; nitrogen doping; UV–vis spectroscopy; X-ray charge density analysis

Beilstein J. Org. Chem. **2024,** *20,* 1207–1212.
https://doi.org/10.3762/bjoc.20.103

Received: 29 February 2024
Accepted: 13 May 2024
Published: 24 May 2024

This article is part of the thematic issue "Carbon-rich materials: from polyaromatic molecules to fullerenes and other carbon allotropes".

Guest Editor: Y. Yamakoshi

Abstract

Cyclo-*meta*-phenylenes doped with nitrogen atoms at the periphery were designed and synthesized. The syntheses of the macrocyclic structures were achieved with one-pot Suzuki–Miyaura coupling to arrange phenylene rings and pyridinylene rings in an alternating fashion. Analyses with UV–vis spectroscopy showed changes in the photophysical properties with nitrogen doping, and X-ray crystallographic analyses experimentally revealed the presence of biased charges on the peripheral nitrogen atoms.

Introduction

Graphitic carbonaceous sheets of graphene continue to attract considerable attention, which lead us to explore structural defects such as heteroatom doping and porous defects for unique properties and functions. For instance, with nitrogen atoms as dopants [1-3], a range of applications, such as electrocatalysis [4] and gas storage [5], has been exploited. Although the locations of nitrogen, in addition to the types, including pyridinic, pyrrolic and graphitic nitrogen, play important roles in determining the properties and functions (Figure 1a), top-down, physical production does not enable control of the doped structures with atomic precision. The bottom-up chemical syntheses of molecular nanocarbons have thus become attractive for controlling the nitrogen-doped structures embedded in large, molecular π-systems [6,7]. As a versatile synthetic strategy for defective molecular nanocarbons, we recently introduced phenine design [8,9], which allowed us to introduce nitrogen dopants, as was demonstrated with nitrogen-doped phenine nanocarbons such as **1** and **2** [10,11]. The nitrogen dopants were introduced in an inward-focused manner to decorate the inner rims of [*n*]cyclo-*meta*-phenylenes ([*n*]CMP) (Figure 1b) and captured other entities such as protons and metal atoms at the porous defect. In this study, the nitrogen dopants were installed in an outward-radiated manner, which expands the structural diversity to exploit the chemistry at the periphery of [*n*]CMP (Figure 1b). Through the use of Suzuki–Miyaura coupling for macrocyclisation, pyridinyl and phenylene rings were assem-

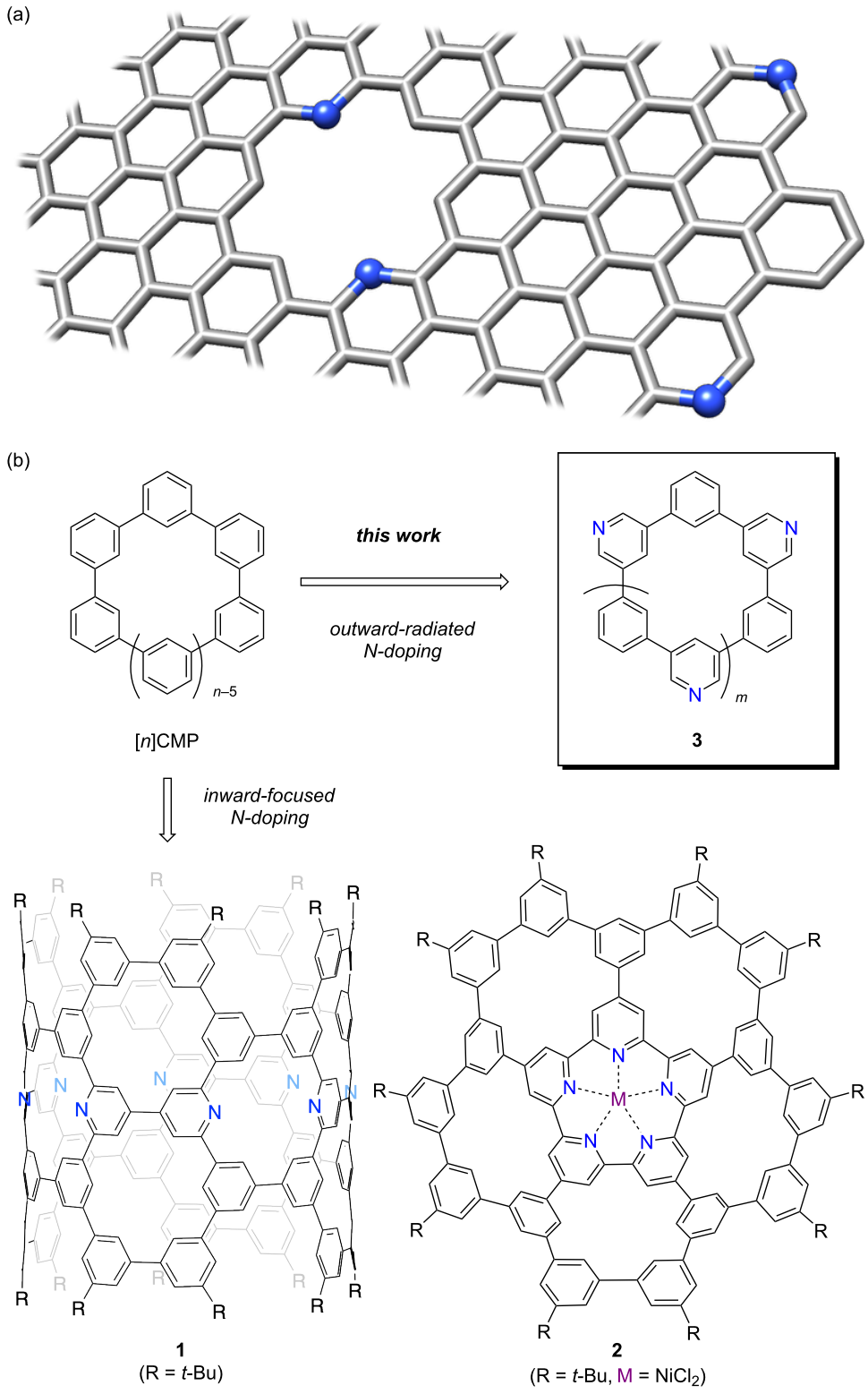

Figure 1: Nitrogen-doped nanocarbons. (a) Schematic illustration of pyridinic nitrogen atoms installed at the interior and periphery of a graphene sheet. (b) Phenine nanocarbon molecules with nitrogen dopants.

bled in an alternating fashion, which afforded nitrogen-doped [*n*]CMPs (**3**) containing outward-radiating nitrogen dopants. The properties and structures were investigated with UV–vis spectroscopy and X-ray crystallography, which revealed the fundamental properties of the nitrogen dopants in the macrocyclic structures.

Results and Discussion

Nitrogen-doped [*n*]CMPs, **3a** and **3b**, were synthesized via one-pot Suzuki–Miyaura coupling [12] (Scheme 1). Previously, we synthesized [*n*]CMPs with inward-focused nitrogen dopants by using Suzuki–Miyaura coupling with $Pd(PPh_3)_4$ as the catalyst [13] and applied this method to outward-radiated congeners in this work. However, a MALDI-TOF MS analysis of the crude mixture showed that macrocyclisation did not complete to afford a complex mixture containing noncyclic, linear oligomers (Figure S1, Supporting Information File 1). After examining the Pd-catalysts, we found that macrocyclisation with $PdCl_2(dppf)\cdot CH_2Cl_2$ worked best and afforded cyclic congeners from N_3-[6]CMP to N_6-[12]CMP (Figure S1, Supporting Information File 1) and isolated N_3-[6]CMP (**3a**) and N_4-[8]CMP (**3b**) in 7% and 3% yields, respectively [14].

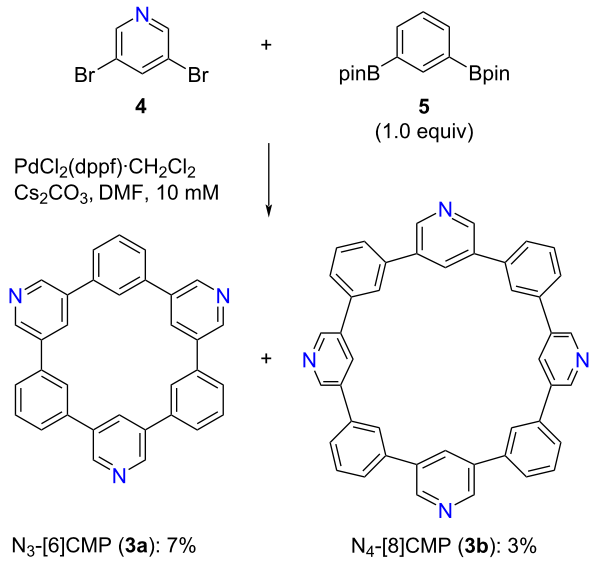

Scheme 1: Syntheses of **3a** and **3b**.

Comparisons of the UV–vis spectra of the doped and undoped congeners revealed dopant-induced changes in the electronic properties. The UV–vis spectra of **3a** and **3b** were recorded in chloroform and are shown in Figure 2, with spectra of the undoped [*n*]CMP congeners shown as references [15]. The nitrogen-doped [*n*]CMPs **3a** and **3b** commonly showed minor yet new absorptions at approximately 280 nm, with major absorptions appearing at 250 nm (Figure 2). As shown with the reference spectra of [6]CMP and [8]CMP, the absorption at 280 nm was absent for the corresponding hydrocarbon congeners. These results showed that the nitrogen-dopants induced novel transitions for photoexcitation.

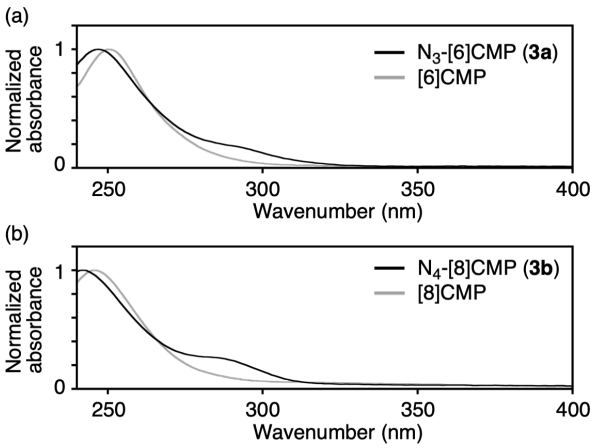

Figure 2: Photophysical properties of **3a** and **3b**. (a) UV–vis spectrum of **3a** in $CHCl_3$. (b) UV–vis spectrum of **3b** in $CHCl_3$. For reference, the spectra of [6]CMP and [8]CMP from the literature are also shown in gray [15].

Crystallographic analyses revealed the structural features of nitrogen-doped [*n*]CMPs. The crystal molecular structures of **3a** and **3b** are shown in Figure 3. The hexagonal macrocyclic structure of **3a** showed a chair-like conformation with alternating biaryl dihedral angles showing +/– values. The octagonal structure of **3b** exhibited a saddle-like conformation with an average dihedral angle of 45.0°, which was slightly larger than that of **3a** (30.4°). The shapes of nitrogen-doped [*n*]CMPs did not deviate from those of hydrocarbon [*n*]CMPs, with similar average dihedral angles (32.4° for [6]CMP and 40.6° for [8]CMP) [15]. Likewise, the crystal packings of **3a** and **3b** resembled those of the hydrocarbon congeners, forming one-dimensional columns of stacked macrocycles (Figure 3b).

The electronic effects of the nitrogen dopants in **3a** were examined with X-ray charge density analyses [10,16]. For the crystal structures shown in Figure 3, we used a standard method with spherical independent atom models (IAM) [17], whereas for the charge density analyses, we used the transferrable aspherical atom models (TAAM) from the Hansen and Coppens formalism [18,19]. The TAAM analysis with parameters from the University at Buffalo pseudoatom databank (UBDB) [20] was performed on XD2016 [21] to obtain an *R* factor of $R(F) = 0.0269$, which was better than that of the IAM on XD2016 with $R(F) = 0.0382$. As shown in Figure 4, the TAAM analysis allowed us

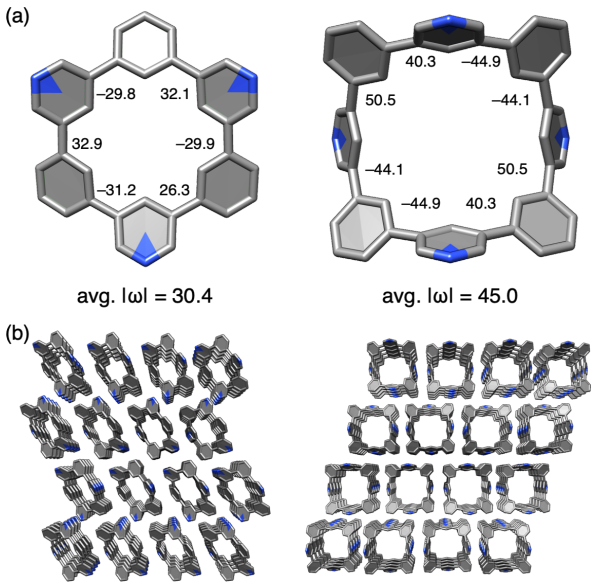

Figure 3: Crystal structures of **3a** and **3b**. (a) Molecular structures. Biaryl dihedral angles (ω) are shown. (b) Packing structures. Chloroform molecules in the crystal of **3b** are omitted for clarity.

to obtain a deformation map that located bonding and lone-pair electron densities of the nitrogen atom (Figure 4a). The analyses also allowed us to visualise experimental electrostatic potential (ESP) maps to reveal the presence of negative potentials on the nitrogen atoms (Figure 4b). For comparison, we performed TAAM analyses of hydrocarbon [6]CMP by reanalysing previous diffraction data [15] and obtained the corresponding ESP maps. A comparison of the ESP maps of **3a** and hydrocarbon [6]CMP showed induction of biased densities by the nitrogen dopants. Similar biased densities were previously found to be critical in determining the packing structures of nitrogen-doped π-systems to make parallel-displaced configurations preferred over T-shaped stackings [22]. In our study, we observed that pyridine–pyridine stacks were preferred in the crystal stacking (Figure 3), which might be attributed to the biased ESPs on the macrocycles.

Finally, we found that nitrogen locations altered chemical characteristics of nitrogen-doped CMPs. Thus, when trifluoroacetic acid (TFA) was added to a solution of **3a** in chloroform, bathochromic shifts in UV spectra were observed, indicating protonation-induced changes in the electronic properties [10]. Because of the weakly acidic nature of pyridinic nitrogen atoms, an excess amount of acid was necessary for this effect to be observed with a maximum equivalent of TFA at 2×10^5, and the absorption band at the longest wavelength gradually shifted as shown in Figure 5a. When we added TFA to a solution of a reference compound **6** having inward-focused nitrogen atoms with a maximum equivalent of TFA at 2×10^5 [13], bathochromic shifts were also observed. However, unlike the case with **3a**, gradual absorption shifts were not observed, and the absorption changed from 299 nm to 320 nm with an isosbestic point at 303 nm as shown in Figure 5b. This observation indicated that the protonation-induced change of UV spectra for **6** involved two equilibrating states, which most likely originated from single protonation at the centre of the CMP pore. On the other hand, the gradual absorption shifts observed with **3a** might thus be ascribed to the presence of multiple protonated species involved in the equilibrium. These results show that the coordination chemistry associated with nitrogen dopants may

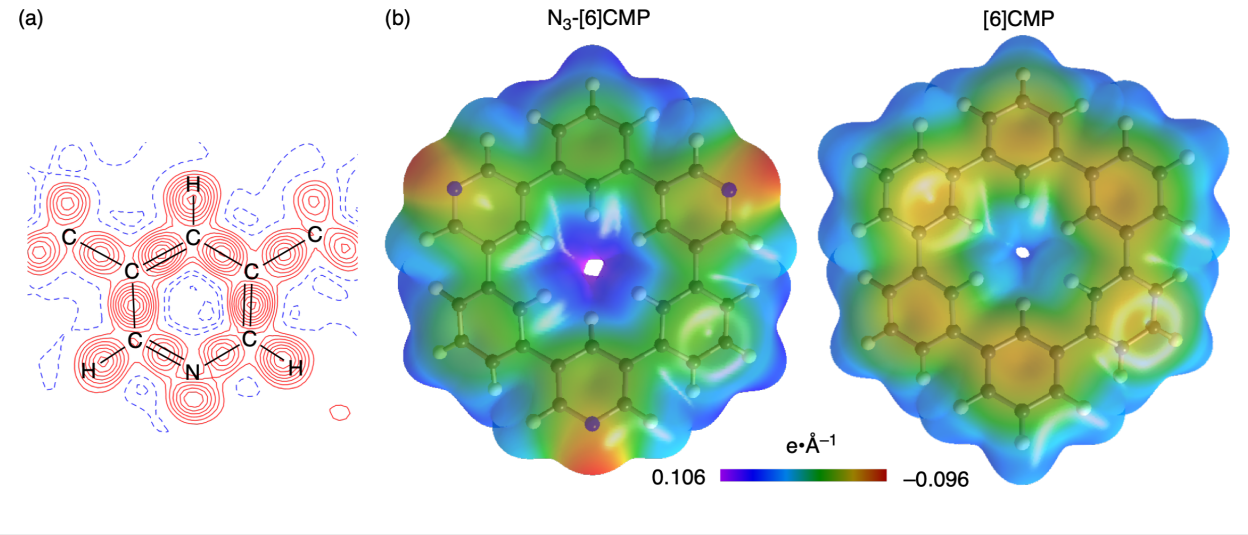

Figure 4: X-ray charge density analyses of **3a** and [6]CMP. (a) Deformation map ($F_o - F_c$) of a pyridine ring in **3a** (contour interval: 0.05 e·Å^{-3}, positive: red, negative: blue). (b) Electrostatic potential maps mapped on the 0.0067 e·Å^{-3} isosurface for the electron density.

well be controlled by the locations and directions of the nitrogen atoms.

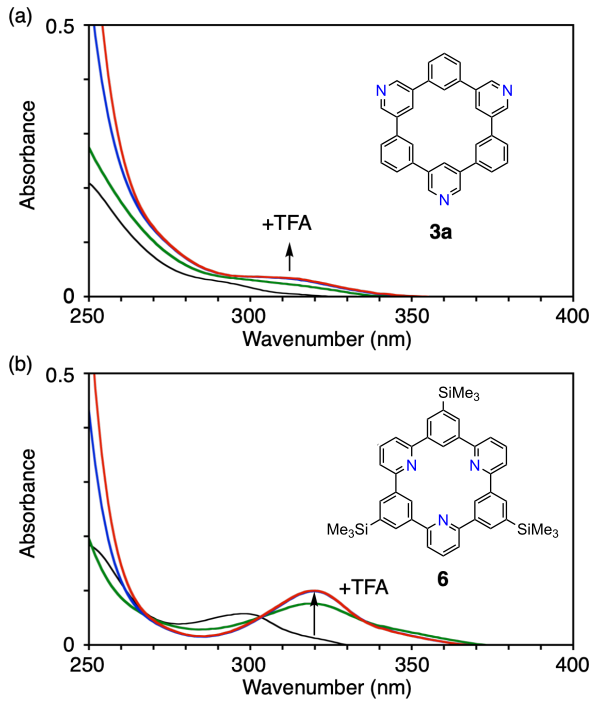

Figure 5: Response towards acid treatment with nitrogen-doped CMPs. (a) Absorption spectra of **3a** ($CHCl_3$, 2.3 × 10^{-6} M) in the absence (black) and presence of trifluoroacetic acid (green: 4.3 × 10^{-2} M, blue: 2.1 × 10^{-1} M, red: 4.2 × 10^{-1} M). (b) Absorption spectra of **6** ($CHCl_3$, 1.9 × 10^{-6} M) in the absence (black) and presence of trifluoroacetic acid (green: 4.3 × 10^{-2} M, blue: 2.1 × 10^{-1} M, red: 4.2 × 10^{-1} M).

Conclusion

Macrocycles with nitrogen atoms doped at the periphery were designed and synthesised, and their electronic properties were experimentally investigated with UV–vis and X-ray charge density analyses. The changes in the UV–vis transitions caused by nitrogen dopants may be useful for designing doped materials for optical applications, and the biased ESPs on the macrocycles should also be considered for material design. Nitrogen-induced π-stacking may also enable exploration of molecular assemblies. The experimental lone-pair electron densities were directed outward in **3a** and could be used as linkers for metal atoms to assemble trigonal pyramidal macrocycles, for instance, in networks of metal organic frameworks [23,24]. Investigations of the nitrogen dopants in molecular nanocarbons should enrich the chemistry of nanocarbons.

Experimental

Syntheses of N_3-[6]CMP (**3a**) and N_4-[8]CMP (**3b**) [14]: A mixture of 3,5-dibromopyridine (**4**, 7.11 g, 30.0 mmol), diborylbenzene (**5**, 9.90 g, 30.0 mmol), $PdCl_2(dppf)·CH_2Cl_2$ (2.50 g, 3.0 mmol), and Cs_2CO_3 (48.9 g, 150 mmol) in 3.0 L of DMF was stirred at 110 °C for 24 h. After the addition of H_2O (2.5 L) and $CHCl_3$ (3.0 L), the precipitate was removed by filtration. The organic layer was separated, dried over Na_2SO_4, and concentrated in vacuo. To eliminate the soluble by-products, the crude material was first washed with $CHCl_3$ (100 mL), and a residue comprising **3a** and **3b** was obtained. The residue was then suspended in $CHCl_3$ (100 mL) and sonicated for 10 min. After separating the solid and the filtrate, each sample was purified as follows: The former was subjected to Soxhlet extraction with $CHCl_3$ overnight to give **3a** in 6% yield (272 mg, 0.592 mmol) after the extraction. The latter was purified by silica gel short path and GPC (column: YMC-GPC T30000-40 + T4000-40 + T2000-40, eluent: $CHCl_3$, flow rate: 30 mL/min) to give **3a** in 1% yield (52.8 mg, 0.115 mmol) and **3b** in 3% yield (118 mg, 0.193 mmol). In total, **3a** was obtained in 7% yield (325 mg, 0.707 mmol). N_3-[6]CMP (**3a**): ^{1}H NMR ($CDCl_3$, 600 MHz) δ 9.05 (d, J = 2.1 Hz, 6H), 8.58 (t, J = 2.1 Hz, 3H), 8.23 (t, J = 2.1 Hz, 3H), 7.89 (dd, J = 7.6, 2.1 Hz, 6H), 7.69 (t, J = 7.6 Hz, 3H); ^{13}C NMR ($CDCl_3$, 150 MHz) δ 146.6 (CH), 138.3, 135.7, 133.9 (CH), 130.2 (CH), 127.5 (CH), 125.9 (CH); HRMS (APCI) (m/z): $[M + H]^+$ calcd. for $C_{33}H_{22}N_3$, 460.1808; found, 460.1808. N_4-[8]CMP (**3b**): ^{1}H NMR ($CDCl_3$, 600 MHz) δ 8.81 (d, J = 1.4 Hz, 8H), 8.13 (t, J = 1.4 Hz, 4H), 7.76 (s, 4H), 7.66–7.73 (m, 12H); ^{13}C NMR ($CDCl_3$, 150 MHz) δ 147.9 (CH), 139.2, 137.0, 133.5 (CH), 129.9 (CH), 127.5 (CH), 127.3 (CH); HRMS (APCI) (m/z): $[M + H]^+$ calcd. for $C_{44}H_{29}N_4$, 613.2387; found, 613.2366.

Supporting Information

Supporting Information File 1

Experimental and copies of spectra.
[https://www.beilstein-journals.org/bjoc/content/supplementary/1860-5397-20-103-S1.pdf]

Supporting Information File 2

Crystallographic data of N_3-[6]CMP (**3a**) analysed by SHELX (CCDC 2335441).
[https://www.beilstein-journals.org/bjoc/content/supplementary/1860-5397-20-103-S2.cif]

Supporting Information File 3

Crystallographic data of N_4-[8]CMP (**3b**) analysed by SHELX (CCDC 2335442).
[https://www.beilstein-journals.org/bjoc/content/supplementary/1860-5397-20-103-S3.cif]

Supporting Information File 4

Crystallographic data of N_3-[6]CMP (**3a**) analysed by XD2016 (CCDC 2335443).
[https://www.beilstein-journals.org/bjoc/content/supplementary/1860-5397-20-103-S4.cif]

Supporting Information File 5

Crystallographic data of [6]CMP analysed by XD2016 (CCDC 2335444).
[https://www.beilstein-journals.org/bjoc/content/supplementary/1860-5397-20-103-S5.cif]

Funding

This study was partly supported by KAKENHI (20H05672, 22H02059).

ORCID® iDs

Koki Ikemoto - https://orcid.org/0000-0003-4186-7156
Hiroyuki Isobe - https://orcid.org/0000-0001-8907-0694

Data Availability Statement

All data that supports the findings of this study is available in the published article and/or the supporting information to this article. The crystallographic data were deposited in the Cambridge Crystallographic Data Centre (CCDC 2335441–2335444). The data can be obtained free of charge from the CCDC via http://www.ccdc.cam.ac.uk/data_request/cif.

References

1. Ayala, P.; Arenal, R.; Rümmeli, M.; Rubio, A.; Pichler, T. *Carbon* **2010,** *48,* 575–586. doi:10.1016/j.carbon.2009.10.009
2. Ćirić-Marjanović, G.; Pašti, I.; Mentus, S. *Prog. Mater. Sci.* **2015,** *69,* 61–182. doi:10.1016/j.pmatsci.2014.08.002
3. Inagaki, M.; Toyoda, M.; Soneda, Y.; Morishita, T. *Carbon* **2018,** *132,* 104–140. doi:10.1016/j.carbon.2018.02.024
4. Paul, D. R.; Koros, W. J.; Liu, R. Y. F.; Hu, Y. S.; Baer, E.; Hiltner, A.; Keith, H. D.; Liu, R. Y. F.; Hiltner, A.; Baer, E.; Cohen, R. E.; Bellare, A.; Albalak, R. J.; Hu, W.; Reiter, G. *Science* **2009,** *323,* 760–764. doi:10.1126/science.1168049
5. Terrones, M.; Kamalakaran, R.; Seeger, T.; Rühle, M. *Chem. Commun.* **2000,** 2335–2336. doi:10.1039/b008253h
6. Stępień, M.; Gońka, E.; Żyła, M.; Sprutta, N. *Chem. Rev.* **2017,** *117,* 3479–3716. doi:10.1021/acs.chemrev.6b00076
7. Wang, X.-Y.; Yao, X.; Narita, A.; Müllen, K. *Acc. Chem. Res.* **2019,** *52,* 2491–2505. doi:10.1021/acs.accounts.9b00322
8. Ikemoto, K.; Isobe, H. *Bull. Chem. Soc. Jpn.* **2021,** *94,* 281–294. doi:10.1246/bcsj.20200284
9. Ikemoto, K.; Fukunaga, T. M.; Isobe, H. *Proc. Jpn. Acad., Ser. B* **2022,** *98,* 379–400. doi:10.2183/pjab.98.020
10. Ikemoto, K.; Yang, S.; Naito, H.; Kotani, M.; Sato, S.; Isobe, H. *Nat. Commun.* **2020,** *11,* 1807. doi:10.1038/s41467-020-15662-6
11. Ikemoto, K.; Harada, S.; Yang, S.; Matsuno, T.; Isobe, H. *Angew. Chem., Int. Ed.* **2022,** *61,* e202114305. doi:10.1002/anie.202114305
12. Miyaura, N.; Yamada, K.; Suzuki, A. *Tetrahedron Lett.* **1979,** *20,* 3437–3440. doi:10.1016/s0040-4039(01)95429-2
13. Xue, J. Y.; Ikemoto, K.; Sato, S.; Isobe, H. *Chem. Lett.* **2016,** *45,* 676–678. doi:10.1246/cl.160218
14. Taka, H.; Izumi, T.; Isobe, H.; Sato, S.; Ikemoto, K.; Xue, J. Cyclic heteroaromatic compounds, organic electronic element material, organic electronic element, and electronic device. WO Pat. Appl. WO2017038642A1, March 9, 2017.
15. Xue, J. Y.; Ikemoto, K.; Takahashi, N.; Izumi, T.; Taka, H.; Kita, H.; Sato, S.; Isobe, H. *J. Org. Chem.* **2014,** *79,* 9735–9739. doi:10.1021/jo501903n
16. Koritsanszky, T. S.; Coppens, P. *Chem. Rev.* **2001,** *101,* 1583–1628. doi:10.1021/cr990112c
17. Sheldrick, G. M. *Acta Crystallogr., Sect. C: Struct. Chem.* **2015,** *71,* 3–8. doi:10.1107/s2053229614024218
18. Hansen, N. K.; Coppens, P. *Acta Crystallogr., Sect. A: Cryst. Phys., Diffr., Theor. Gen. Crystallogr.* **1978,** *34,* 909–921. doi:10.1107/s0567739478001886
19. Brock, C. P.; Dunitz, J. D.; Hirshfeld, F. L. *Acta Crystallogr., Sect. B: Struct. Sci.* **1991,** *47,* 789–797. doi:10.1107/s0108768191003932
20. Dominiak, P. M.; Volkov, A.; Li, X.; Messerschmidt, M.; Coppens, P. *J. Chem. Theory Comput.* **2007,** *3,* 232–247. doi:10.1021/ct6001994
21. Volkov, A., Macchi, P., Farrugia, L. J., Gatti, C., Mallinson, P., Rihter, T., Koritsánszky, T. XD2016 - A Computer Program Package for Multipole Refinement, Topological Analysis of Charge Densities and Evaluation of Intermolecular Energies from Experimental and Theoretical Structure Factors, 2016.
22. Hohenstein, E. G.; Sherrill, C. D. *J. Phys. Chem. A* **2009,** *113,* 878–886. doi:10.1021/jp809062x
23. Furukawa, H.; Cordova, K. E.; O'Keeffe, M.; Yaghi, O. M. *Science* **2013,** *341,* 1230444. doi:10.1126/science.1230444
24. Kitagawa, S.; Kitaura, R.; Noro, S.-i. *Angew. Chem., Int. Ed.* **2004,** *43,* 2334–2375. doi:10.1002/anie.200300610

License and Terms

BEILSTEIN JOURNAL OF ORGANIC CHEMISTRY

Synthesis of indano[60]fullerene thioketone and its application in organic solar cells

Yong-Chang Zhai[1], Shimon Oiwa[1], Shinobu Aoyagi[*2], Shohei Ohno[3], Tsubasa Mikie[3], Jun-Zhuo Wang[1], Hirofumi Amada[1], Koki Yamanaka[1], Kazuhira Miwa[1], Naoyuki Imai[4], Takeshi Igarashi[4], Itaru Osaka[3] and Yutaka Matsuo[*1,5]

Letter

Open Access

Address:
[1]Department of Chemical Systems Engineering, Graduate School of Engineering, Nagoya University, Furo-cho, Chikusa-ku, Nagoya 464-8603, Japan, [2]Department of Information and Basic Science, Nagoya City University, Nagoya 467-8501, Japan, [3]Applied Chemistry Program, Graduate School of Advanced Science and Engineering, Hiroshima University 1-4-1 Kagamiyama, Higashi-Hiroshima, Hiroshima 739-8527, Japan, [4]Institute for Advanced Fusion, Resonac Corporation, 5-1 Okawa-cho, Kawasaki-ku, Kawasaki-shi, Kanagawa 210-0858, Japan and [5]Institute of Materials Innovation, Institutes for Future Society, Nagoya University, Furo-cho, Chikusa-ku, Nagoya 464-8603, Japan

Email:
Shinobu Aoyagi[*] - aoyagi@nsc.nagoya-cu.ac.jp; Yutaka Matsuo[*] - matsuo.yutaka@material.nagoya-u.ac.jp

* Corresponding author

Keywords:
C_{60}; evaporable fullerene derivatives; organic photovoltaics; organic solar cells; thioketone

Beilstein J. Org. Chem. **2024,** *20,* 1270–1277.
https://doi.org/10.3762/bjoc.20.109

Received: 21 February 2024
Accepted: 06 May 2024
Published: 31 May 2024

This article is part of the thematic issue "Carbon-rich materials: from polyaromatic molecules to fullerenes and other carbon allotropes".

Guest Editor: Y. Yamakoshi

Abstract

Evaporable indano[60]fullerene ketone (FIDO) was converted to indano[60]fullerene thioketone (FIDS) in high yield by using Lawesson's reagent. Three compounds with different substituents in *para* position were successfully converted to the corresponding thioketones, showing that the reaction tolerates compounds with electron-donating and electron-withdrawing substituents. Computational studies with density functional theory revealed the unique vibrations of the thioketone group in FIDS. The molecular structure of FIDS was confirmed by single-crystal X-ray analysis. Bulk heterojunction organic solar cells using three evaporable fullerene derivatives (FIDO, FIDS, C_{60}) as electron-acceptors were compared, and the open-circuit voltage with FIDS was 0.16 V higher than that with C_{60}.

Introduction

Fullerene is a carbon allotrope that has attracted significant scientific interest since its discovery by H. W. Kroto in 1985 [1]. Due to their distinctive spherical structure and electron-deficient properties, fullerene derivatives have found applications in various fields, including photovoltaics [2-5], biomedicine [6-8], and electron transporters [9,10]. Organic photo-

voltaic (OPV) and perovskite solar cell (PSC) technologies have proven to be promising candidates for the sustainable use of solar energy, with power conversion efficiency (PCE) improving to 17% for OPVs and over 25% for PSCs in just a few years [11]. Functionalized fullerene derivatives have played an important role both in OPVs as electron acceptors and in PSCs as electron transport layers (ETLs) by efficiently accepting electrons and hindering the transport of holes [12-14].

During the past 10 years, considerable attention has been focused on functional fullerene derivatives with an emphasis on tuning solubility and energy levels. Meanwhile, less attention has been devoted to improving the thermal stability of fullerene derivatives. One well-known example is [6,6]-phenyl-C_{61}-butyric acid methyl ester (PCBM), which is recognized for its excellent solubility in solution-processed OPV fabrication [15]. Films generated through vacuum deposition, on the other hand, exhibit superior quality, have fewer defects, and are eco-friendlier than films produced by spin-casting. However, only a few studies to date have investigated the design of fullerene derivatives with the aim of improving their thermal stability, and more specifically, of designing evaporable fullerene derivatives [16-18]. Recently, we reported on perovskite solar cells fabricated with indano[60]fullerene ketone (FIDO), which was synthesized through fullerene cation chemistry. These cells demonstrated long-term stability and a remarkable PCE of 22.11%, surpassing that of the commonly used C_{60} (20.45%). This improved performance can be attributed to the evaporated amorphous film, which prevents the transformation of the film into a crystalline state during the heating and aging of the devices. Additionally, the ketone structure acts as a Lewis base, resulting in a passivation effect on Pb^{2+} [19].

In this study, we designed and synthesized indano[60]fullerene thioketones (FIDSs) with various *para*-substituents. The vacuum-deposition performance and thermal stability of FIDS were assessed by both normal-pressure and vacuum thermogravimetric analysis (TGA). Additionally, we conducted a comparative analysis of bulk heterojunction (BHJ) organic solar cells using the three evaporable fullerene derivatives investigated in this work.

Results and Discussion

The synthesis of FIDO was performed by fullerene cation chemistry as reported by our group [20-26]. Conversion from ketone to thioketone is usually achieved by using Lawesson's reagent, which tends to form a trimer structure when reacted with indanone without a substituent at the α position [27-29]. Introduction of fullerene at the α position facilitated the successful transformation of ketone to thioketone.

Initially, we adopted the widely reported reaction conditions with 1.5 equiv of Lawesson's reagent and tetrahydrofuran (THF) as solvent. *t*-Bu-FIDO was dissolved in THF by sonication for 30 min. Unfortunately, the results were not fully satisfactory. Considering the poor solubility of fullerene derivatives, toluene, carbon disulfide (CS_2), and *ortho*-dichlorobenzene (*o*-DCB) were tested as solvent. Surprisingly, the conversion from ketone to thioketone did not occur as anticipated. In another attempt, where the amount of Lawesson's reagent was increased to 3 equiv (Table 1, entry 5), the signal of thioketone was observed for the first time by high-performance liquid chromatography (HPLC) and MALDI time-of-flight mass spectrometry. Subsequently, a conversion of 99% was achieved by further increasing the amount of Lawesson's reagent and the reaction temperature. The transformation from ketone to thioketone was confirmed by ^{13}C NMR, which showed a downfield shift from 198 ppm for the carbonyl carbon to 235 ppm for the thiocarbonyl carbon. With the optimized conditions (Table 1, entry 9) in hand, different *para*-substituents were used and the reaction from FIDO to FIDS was found to tolerate both electron-donating and -withdrawing functional groups as shown in Table 2.

It is well known that functional groups with larger steric hindrance can reduce intermolecular forces. Consequently, a *tert*-butyl-functionalized compound (*t*-Bu-FIDS) was chosen for further studies in this work. To identify the formation of the thiocarbonyl group, Fourier transform infrared spectroscopy (FTIR) was conducted as shown in Figure 1a. The carbonyl stretching vibration peak of *t*-Bu-FIDO at 1720 cm^{-1} disappeared, indicating all the *t*-Bu-FIDO was completely consumed. Interestingly, the characteristic vibration peak of thiocarbonyl groups was not observed, which should be located at 1050–1300 cm^{-1} theoretically. Instead, numerous new low-intensity peaks were observed in this region.

To gain a comprehensive understanding of the differences between *t*-Bu-FIDO and *t*-Bu-FIDS, the density functional theory (DFT) method was employed using the B3LYP hybrid functional. The 6-31G* basis set was used for the geometry optimization and frequency calculation. The thiocarbonyl group in FIDS was found to have an out of plane bending vibration, however, the carbonyl group in FIDO showed a strong in-plane stretching vibration as shown in Figure S1 (Supporting Information File 1). Due to the direct connection between the five-membered ring and the fullerene cage, the out of plane bending vibration was easily affected by the fullerene cage vibration. Furthermore, the out-of-plane bending vibration of the thiocarbonyl group was also watched, which also affected the vibration of fullerene cage and benzene ring (Figure S2 and Table S1, Supporting Information File 1). This interesting phenome-

Table 1: Optimization of reaction conditions for the treatment of *t*-Bu-FIDO with Lawesson's reagent.[a]

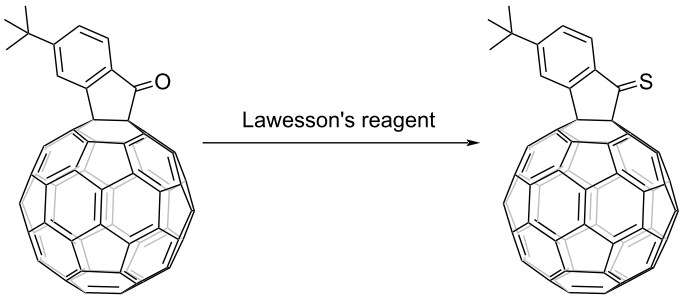

Entry	Equiv	Reaction temperature (°C)	Solvent	Reaction time (h)	Conversion[b] (%)
1	1.5	70	THF	14	NR[c]
2	1.5	50	CS_2	14	NR
3	1.5	70	*o*-DCB	14	NR
4	1.5	100	toluene	14	NR
5	3	100	toluene	14	5
6	3	120	toluene	14	10
7	14	120	toluene	14	50
8	20	120	toluene	14	70
9	20	120	toluene	20	90
10	20	120	*o*-DCB	20	99

[a]All reactions were performed with *t*-Bu-FIDO (50 mg) under N_2 atmosphere. All the solvents (10 mL) were anhydrous. [b]Conversion was estimated from the HPLC peak area ratio. [c]NR = no reaction.

Table 2: Reaction of R-FIDO with Lawesson's reagent.[a]

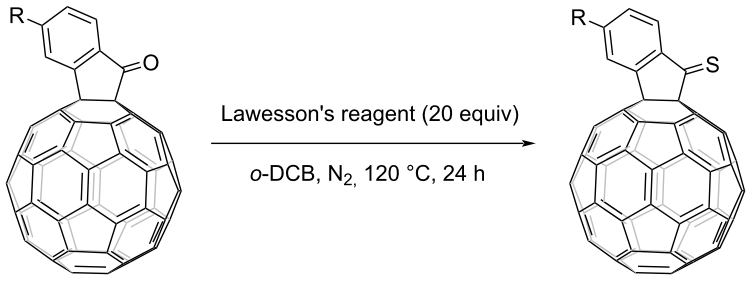

R = H, F, *t*-Bu

Entry	R	Product	Yield[b] (%)	Conversion (%)
1	*t*-Bu	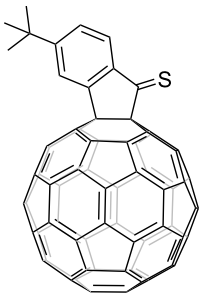	45	99

Table 2: Reaction of R-FIDO with Lawesson's reagent.[a] (continued)

2	F	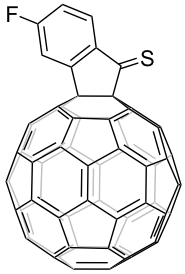	50	90
3	H	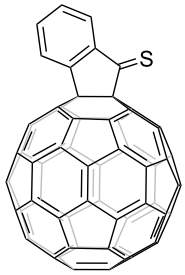	38	95

[a]All reactions were performed in *o*-DCB at 120 °C for 20 h under N_2 atmosphere with FIDO as starting material. The molar ratio of Lawesson's reagent to FIDO was 20:1. [b]Isolated yield.

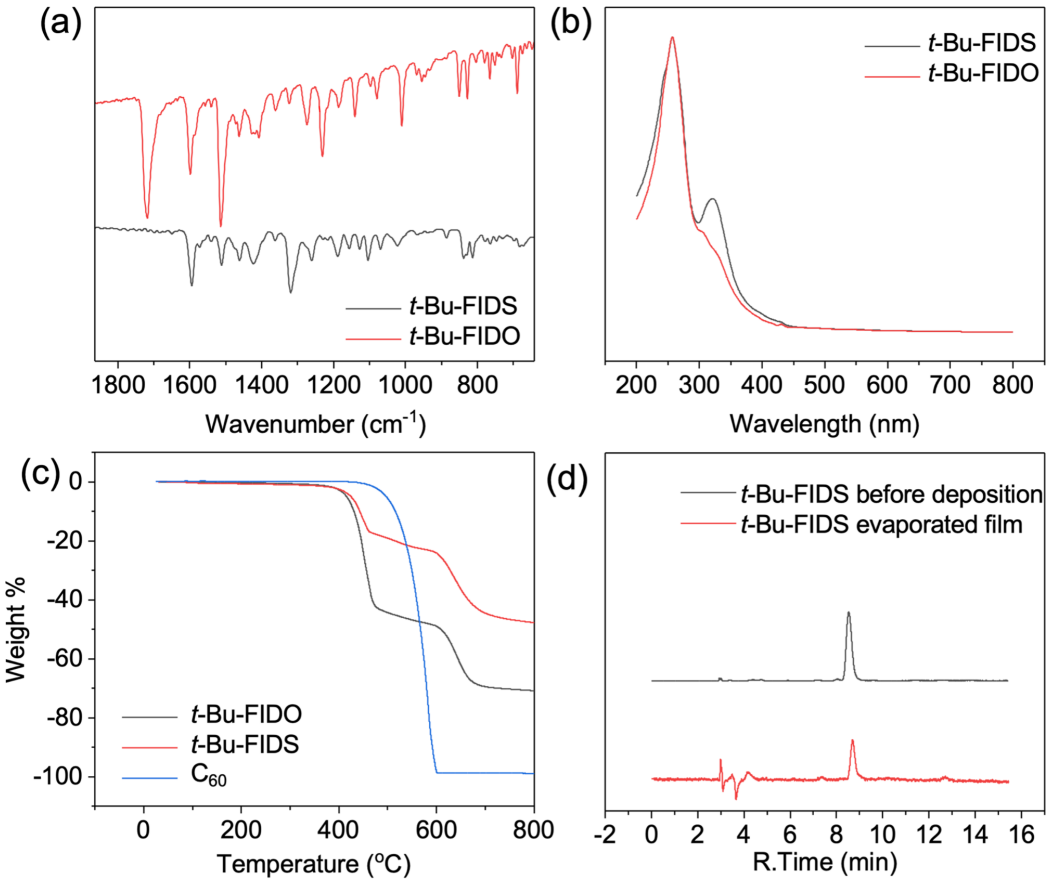

Figure 1: Characterization data. (a) FTIR spectra of *t*-Bu-FIDO and *t*-Bu-FIDS. (b) UV–vis spectra of fullerene derivatives normalized at 270 nm. (c) Vacuum TGA curves of *t*-Bu-FIDO (black), *t*-Bu-FIDS (red), and C_{60} (blue). The measurements were conducted under 0.1 Pa. (d) HPLC analyses before deposition of *t*-Bu-FIDS (black) and of toluene used to rinse the evaporated film of *t*-Bu-FIDS (red).

non may explain the numerous new peaks that formed around 1000 cm^{-1} for *t*-Bu-FIDS.

Ultraviolet–visible (UV–vis) spectroscopy of *t*-Bu-FIDS in *o*-DCB exhibited two prominent UV absorption bands with peaks at 257 nm and 320 nm (Figure 1b). The absorption at 257 nm indicated the integrity of the fullerene cage chromophore. The absorption peak at 320 nm was assigned to the charge transfer band of the C=S bond in *t*-Bu-FIDS, which was stronger than that of the C=O bond in *t*-Bu-FIDO [30]. Interestingly, the maximum absorption band observed in *t*-Bu-FIDO at 432 nm, which is a characteristic feature of 58π-fullerene derivatives with a 1,2-addition pattern, was absent in *t-Bu*-FIDS [31]. Its absence might be due to perturbation caused by the presence of the C=S bond in *t*-Bu-FIDS.

To examine the sublimation behavior of *t*-Bu-FIDS under an environment similar to vacuum deposition, vacuum TGA measurements were performed using a TGA instrument connected to a vacuum pump and heater. The internal pressure of heater was reduced to 0.1 Pa or lower. Figure 1c shows the weight loss of the three fullerene derivatives under vacuum conditions. In contrast to C_{60}, both *t*-Bu-FIDO and *t*-Bu-FIDS exhibited similar two-stage weight-loss curves. The sublimation temperature (T_{sub}) was determined by analyzing the onset of weight loss for these compounds. T_{sub} was lower for *t-Bu*-FIDO and *t-Bu*-FIDS, at 410 °C and 417 °C, respectively, than for $C_{60,}$ which began to sublimate at 460 °C (Table 3). The lower sublimation temperature was attributed to the steric hindrance of the *tert*-butyl groups, which disrupted the π–π stacking between the fullerene cages. The slight difference in sublimation temperature between *t*-Bu-FIDO and *t*-Bu-FIDS might be due to the slightly higher electron density of the sulfur atom compared with the oxygen atom. Additionally, data on the degradation temperature (T_{deg}) obtained by normal-pressure TGA are shown in Table 3 and Figure S3 (Supporting Information File 1). T_{deg} was higher than T_{sub} for all three compounds, indicating their evaporability. Unfortunately, however, the sublimation window ($T_{deg} - T_{sub}$) of *t*-Bu-FIDS was narrower than that of *t*-Bu-FIDO due to the lower T_{deg} of *t*-Bu-FIDS. A *t*-Bu-FIDS film was prepared by vacuum deposition at 0.1 Å/s, as shown in Figure 1d and Figure S4 (Supporting Information File 1). The film was uniform and smooth, with a thickness of approximately 20 nm. The film was rinsed with toluene, and the collected toluene was analyzed by HPLC to check for thermal decomposition during vacuum deposition. The *t*-Bu-FIDS structure remained almost unchanged, but very small amounts of two decomposed products were found at retention times of 7.5 min and 12.5 min. The latter decomposed product is C_{60}, judged from the retention time.

Table 3: Sublimation and degradation temperatures of three evaporable fullerene derivatives.

Compound	T_{sub} (°C)	T_{deg} (°C)
C_{60}	460	–
t-Bu-FIDO	410	474
t-Bu-FIDS	417	450

A single crystal of *t*-Bu-FIDS was grown by liquid–liquid diffusion method (CS_2/EtOH). The crystal structure was successfully analyzed using synchrotron radiation at SPring-8. The crystal exhibited the orthorhombic space group (No. 61) with the D_{2h} point group, and the structure confirmed the 1,2-addition pattern of *t*-Bu-FIDS (Figure 2a,b). The shortest π–π distance between the two fullerene molecules of *t*-Bu-FIDS in a unit cell was 3.14 Å, while that in *t*-Bu-FIDO was 2.974 Å [19]. The C=S bond length was 1.627 Å and was clearly longer than the C=O bond in *t*-Bu-FIDO. We consider that this longer bond length may have caused the higher reactivity and lower degradation temperature of *t*-Bu-FIDS compared with *t*-Bu-FIDO.

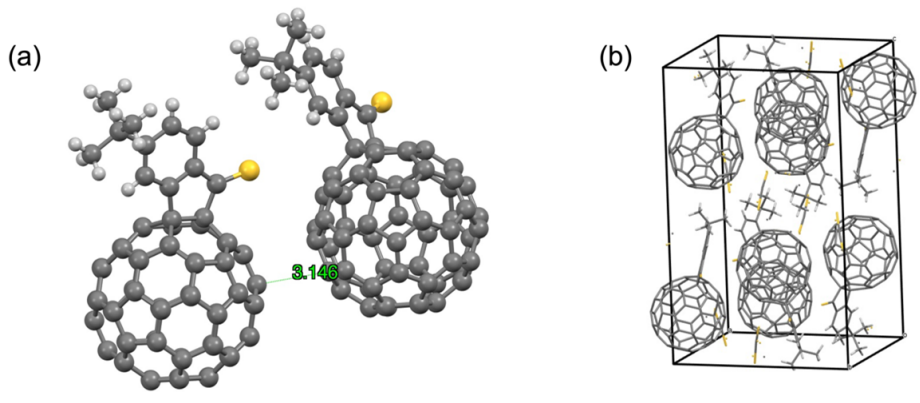

Figure 2: Single-crystal structure of *t*-Bu-FIDS. (a) The π–π distance between two molecules. (b) Crystal packing.

Electron-accepting ability is one of the most important properties for fullerene derivatives, and it is typically described in terms of the energy level of the lowest unoccupied molecular orbital (LUMO). To understand the electron affinity of *t*-Bu-FIDS, cyclic voltammetry was conducted. The cyclic voltammogram of *t*-Bu-FIDS in *o*-DCB showed reversible reduction waves at $E_{1/2}$ = −1.14 V and −1.51 V (vs Fc/Fc^+), as shown in Figure 3. Both the first and second reduction potentials of *t*-Bu-FIDS were higher than those of pristine C_{60}. The LUMO energy of *t*-Bu-FIDS and C_{60} was calculated as −3.62 eV and −3.68 eV, respectively, using the following equation: $E(\text{LUMO}) = -(E_{1/2}^{\text{red1}} + 4.80)$ eV. To compare the electron affinity among the evaporable fullerenes, *t-Bu*-FIDO was also measured in the same solution system and showed a LUMO energy of −3.64 eV, which was slightly deeper than that of *t*-Bu-FIDS.

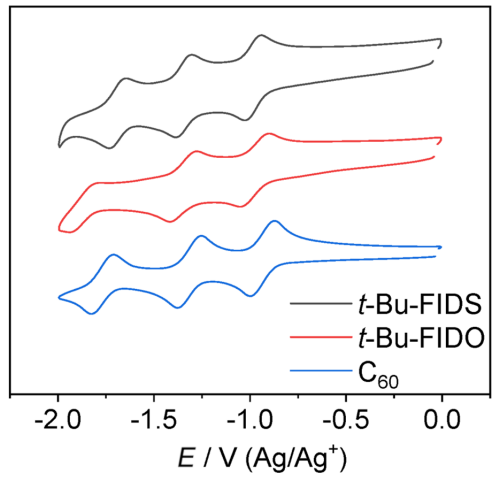

Figure 3: Cyclic voltammograms of fullerene derivatives in *o*-DCB solution containing $Bu_4N^+(CF_3SO_2)_2N^-$ (0.1 M) as supporting electrolyte at 25 °C with a scan rate of 0.05 V/s, for C_{60} (blue), *t*-Bu-FIDO (red), and *t*-Bu-FIDS (black). Glassy carbon, platinum wire, and Ag/Ag^+ electrodes were used as the working, counter, and reference electrodes, respectively.

The use of vacuum-deposited FIDS as the electron transport layer in perovskite solar cells is still being explored. Considering that the open-circuit voltage (V_{OC}) of OPVs is mainly determined by the difference between the HOMO level of the donor and the LUMO level of the acceptor, *t*-Bu-FIDS, with a higher LUMO level than C_{60}, was used to fabricate a solution-processed BHJ OPV device with the donor poly(3-hexylthiophene) (P3HT). For comparison, the two known evaporable fullerenes C_{60} and *t*-Bu-FIDO were chosen. The results are summarized in Figure 4 and Table 4. Benefiting from higher V_{OC},

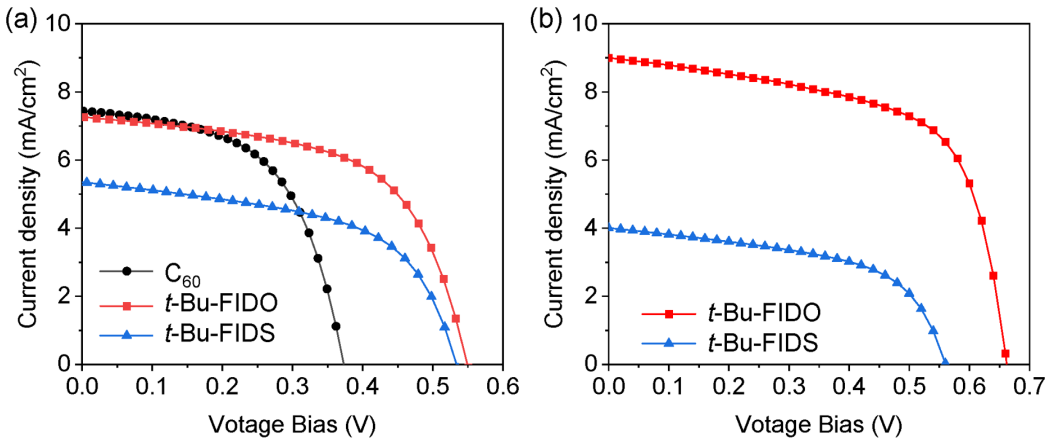

Figure 4: *J–V* curves of BHJ OPV devices. (a) ITO/ZnO/fullerene:P3HT (1:1, w/w)/PEDOT:PSS/Ag. (b) ITO/ZnO/fullerene:PNTz4T (2:1, w/w)/MoO_x/Ag. ITO, indium tin oxide; PEDOT:PSS = poly(3,4-ethylenedioxythiophene) polystyrene sulfonate.

Table 4: Summary of photovoltaic parameters of BHJ OPV devices.

Fullerene	Donor	V_{OC} (V)	J_{SC} (mA/cm^2)	FF	PCE %
C_{60}	P3HT[a]	0.37	7.45	0.55	1.55
t-Bu-FIDO	P3HT	0.55	7.53	0.60	2.47
t-Bu-FIDS	P3HT	0.53	5.39	0.55	1.58
t-Bu-FIDO	PNTz4T[b]	0.66	9.00	0.62	3.71
t-Bu-FIDS	PNTz4T	0.56	4.00	0.54	1.23

[a]ITO/ZnO/fullerene P3HT (1:1, w/w)/PEDOT:PSS/Ag. [b]ITO/ZnO/fullerene:PNTz4T (2:1, w/w)/MoO_x/Ag.

the *t*-Bu-FIDS showed a PCE comparable to that of C_{60}, although the short-circuit current density (J_{SC}) was slightly lower. To further improve the performance of *t*-Bu-FIDO and *t*-Bu-FIDS, the crystalline polymer donor PNTz4T [32] was used. Compared with *t*-Bu-FIDS, *t*-Bu-FIDO achieved 3.71% PCE with larger J_{SC} and higher V_{OC}. With PNTz4T, *t*-Bu-FIDS exhibited low performance, with J_{SC} of only 4 mA/cm^2. This lower V_{OC} may be attributable to a suboptimal BHJ structure between PNTz4T and *t*-Bu-FIDS. Considering the lower J_{SC} performance of *t*-Bu-FIDS with both P3HT and PNTz4T, *t*-Bu-FIDS might not be suitable for BHJ OPV devices.

Conclusion

In summary, we successfully synthesized evaporable indano[60]fullerene thioketones with functional groups at the *para*-position of the benzene ring. Furthermore, we examined the sublimation behavior of three evaporable fullerene derivatives (FIDO, FIDS, C_{60}). the sublimation window of *t*-Bu-FIDS was unfortunately slightly narrower than that of *t*-Bu-FIDO, which we have previously reported. Additionally, we compared the solution-processed OPV performance of the three evaporable fullerene derivatives as electron acceptors. FIDO exhibited the best performance, with V_{OC} that was 0.18 V higher compared with C_{60}. Although FIDS showed a lower performance due to its less-desirable BHJ structure in the OPV, it could still potentially be utilized in perovskite solar cells in the future.

Supporting Information

Supporting Information File 1

Experimental procedures, device fabrication, method of single-crystal growth, device evaluations and characterizations.
[https://www.beilstein-journals.org/bjoc/content/supplementary/1860-5397-20-109-S1.pdf]

Supporting Information File 2

Chemical information file of *t*-Bu-FIDS, CCDC deposition number 2332797.
[https://www.beilstein-journals.org/bjoc/content/supplementary/1860-5397-20-109-S2.cif]

Funding

This work was financially supported by the Japan Society for the Promotion of Science (JSPS) KAKENHI Grant Numbers 21KK0087 and 23H05443. Y.M. thanks the Takahashi Industrial and Economic Research Foundation and the Yashima Environment Technology Foundation for financial support. This work was supported by the Japan Science and Technology Agency (JST SPRING), Grant Number JPMJSP2125. The synchrotron radiation experiment was performed at SPring-8 with the approval of the Japan Synchrotron Radiation Research Institute (JASRI) (Proposal No. 2023A1758).

ORCID® iDs

Shinobu Aoyagi - https://orcid.org/0000-0002-7393-343X
Tsubasa Mikie - https://orcid.org/0000-0003-0532-8905
Takeshi Igarashi - https://orcid.org/0000-0002-3621-6335
Yutaka Matsuo - https://orcid.org/0000-0001-9084-9670

Data Availability Statement

The data that supports the findings of this study is available from the corresponding author upon reasonable request.

References

1. Kroto, H. W.; Heath, J. R.; O'Brien, S. C.; Curl, R. F.; Smalley, R. E. *Nature* **1985,** *318,* 162–163. doi:10.1038/318162a0
2. Yu, G.; Gao, J.; Hummelen, J. C.; Wudl, F.; Heeger, A. J. *Science* **1995,** *270,* 1789–1791. doi:10.1126/science.270.5243.1789
3. Matsuo, Y. *Chem. Lett.* **2012,** *41,* 754–759. doi:10.1246/cl.2012.754
4. Lin, H.-S.; Matsuo, Y. Fullerenes in Photovoltaics. In *Handbook of Fullerene Science and Technology;* Lu, X.; Akasaka, T.; Slanina, Z., Eds.; Springer Nature: Singapore, 2022; pp 851–888. doi:10.1007/978-981-16-8994-9_37
5. Matsuo, Y.; Kawai, J.; Inada, H.; Nakagawa, T.; Ota, H.; Otsubo, S.; Nakamura, E. *Adv. Mater. (Weinheim, Ger.)* **2013,** *25,* 6266–6269. doi:10.1002/adma.201302607
6. Friedman, S. H.; DeCamp, D. L.; Sijbesma, R. P.; Srdanov, G.; Wudl, F.; Kenyon, G. L. *J. Am. Chem. Soc.* **1993,** *115,* 6506–6509. doi:10.1021/ja00068a005
7. Martinez, Z. S.; Castro, E.; Seong, C.-S.; Cerón, M. R.; Echegoyen, L.; Llano, M. *Antimicrob. Agents Chemother.* **2016,** *60,* 5731–5741. doi:10.1128/aac.00341-16
8. Bakry, R.; Vallant, R. M.; Najam-ul-Haq, M.; Rainer, M.; Szabo, Z.; Huck, C. W.; Bonn, G. K. *Int. J. Nanomed.* **2007,** *2,* 639–649.
9. Abe, Y.; Tanaka, H.; Guo, Y.; Matsuo, Y.; Nakamura, E. *J. Am. Chem. Soc.* **2014,** *136,* 3366–3369. doi:10.1021/ja500340f
10. Lenoble, J.; Campidelli, S.; Maringa, N.; Donnio, B.; Guillon, D.; Yevlampieva, N.; Deschenaux, R. *J. Am. Chem. Soc.* **2007,** *129,* 9941–9952. doi:10.1021/ja071012o
11. Wang, D. H.; Park, K. H.; Seo, J. H.; Seifter, J.; Jeon, J. H.; Kim, J. K.; Park, J. H.; Park, O. O.; Heeger, A. J. *Adv. Energy Mater.* **2011,** *1,* 766–770. doi:10.1002/aenm.201100347
12. Heo, J. H.; Han, H. J.; Kim, D.; Ahn, T. K.; Im, S. H. *Energy Environ. Sci.* **2015,** *8,* 1602–1608. doi:10.1039/c5ee00120j
13. Lin, X.; Cui, D.; Luo, X.; Zhang, C.; Han, Q.; Wang, Y.; Han, L. *Energy Environ. Sci.* **2020,** *13,* 3823–3847. doi:10.1039/d0ee02017f
14. Yu, Z.; Yang, Z.; Ni, Z.; Shao, Y.; Chen, B.; Lin, Y.; Wei, H.; Yu, Z. J.; Holman, Z.; Huang, J. *Nat. Energy* **2020,** *5,* 657–665. doi:10.1038/s41560-020-0657-y
15. Ganesamoorthy, R.; Sathiyan, G.; Sakthivel, P. *Sol. Energy Mater. Sol. Cells* **2017,** *161,* 102–148. doi:10.1016/j.solmat.2016.11.024
16. Shibuya, H.; Suk Choi, Y.; Choi, T.; Yun, S.; Moon, J.; Matsuo, Y. *Chem. – Asian J.* **2022,** *17,* e202200609. doi:10.1002/asia.202200609

17. Matsuo, Y.; Ishikawa, S.; Amada, H.; Yokoyama, K.; Shui, Q.-j.; Huda, M.; Ueoka, N.; Lin, H.-S. *Chem. Lett.* **2023,** *52,* 685–687. doi:10.1246/cl.230217
18. Lin, H.-S.; Ma, Y.; Xiang, R.; Manzhos, S.; Jeon, I.; Maruyama, S.; Matsuo, Y. *Commun. Chem.* **2021,** *4,* 74. doi:10.1038/s42004-021-00511-4
19. Shui, Q.-J.; Shan, S.; Zhai, Y.-C.; Aoyagi, S.; Izawa, S.; Huda, M.; Yu, C.-Y.; Zuo, L.; Chen, H.; Lin, H.-S.; Matsuo, Y. *J. Am. Chem. Soc.* **2023,** *145,* 27307–27315. doi:10.1021/jacs.3c07192
20. Yang, X.-Y.; Lin, H.-S.; Matsuo, Y. *J. Org. Chem.* **2019,** *84,* 16314–16322. doi:10.1021/acs.joc.9b02618
21. Lin, H.-S.; Jeon, I.; Chen, Y.; Yang, X.-Y.; Nakagawa, T.; Maruyama, S.; Manzhos, S.; Matsuo, Y. *Chem. Mater.* **2019,** *31,* 8432–8439. doi:10.1021/acs.chemmater.9b02468
22. Lin, H.-S.; Matsuo, Y. *Chem. Commun.* **2018,** *54,* 11244–11259. doi:10.1039/c8cc05965a
23. Yang, X.-Y.; Lin, H.-S.; Jeon, I.; Matsuo, Y. *Org. Lett.* **2018,** *20,* 3372–3376. doi:10.1021/acs.orglett.8b01295
24. Matsuo, Y.; Ogumi, K.; Zhang, Y.; Okada, H.; Nakagawa, T.; Ueno, H.; Gocho, A.; Nakamura, E. *J. Mater. Chem. A* **2017,** *5,* 2774–2783. doi:10.1039/c6ta10319g
25. Zhang, Y.; Matsuo, Y.; Nakamura, E. *Org. Lett.* **2011,** *13,* 6058–6061. doi:10.1021/ol202511u
26. Zhang, Y.; Matsuo, Y.; Li, C.-Z.; Tanaka, H.; Nakamura, E. *J. Am. Chem. Soc.* **2011,** *133,* 8086–8089. doi:10.1021/ja201267t
27. Campaigne, E.; Moss, R. D. *J. Am. Chem. Soc.* **1954,** *76,* 1269–1271. doi:10.1021/ja01634a020
28. Rufanov, K. A.; Stepanov, A. S.; Lemenovskii, D. A.; Churakov, A. V. *Heteroat. Chem.* **1999,** *10,* 369–371. doi:10.1002/(sici)1098-1071(1999)10:5<369::aid-hc5>3.0.co;2-z
29. Ozturk, T.; Ertas, E.; Mert, O. *Chem. Rev.* **2007,** *107,* 5210–5278. doi:10.1021/cr040650b
30. Pandey, M.; Muthu, S.; Nanje Gowda, N. M. *J. Mol. Struct.* **2017,** *1130,* 511–521. doi:10.1016/j.molstruc.2016.10.064
31. Varotto, A.; Treat, N. D.; Jo, J.; Shuttle, C. G.; Batara, N. A.; Brunetti, F. G.; Seo, J. H.; Chabinyc, M. L.; Hawker, C. J.; Heeger, A. J.; Wudl, F. *Angew. Chem., Int. Ed.* **2011,** *50,* 5166–5169. doi:10.1002/anie.201100029
32. Vohra, V.; Kawashima, K.; Kakara, T.; Koganezawa, T.; Osaka, I.; Takimiya, K.; Murata, H. *Nat. Photonics* **2015,** *9,* 403–408. doi:10.1038/nphoton.2015.84

License and Terms

BEILSTEIN JOURNAL OF ORGANIC CHEMISTRY

Metal-free double azide addition to strained alkynes of an octadehydrodibenzo[12]annulene derivative with electron-withdrawing substituents

Naoki Takeda, Shuichi Akasaka, Susumu Kawauchi and Tsuyoshi Michinobu*

Full Research Paper

Open Access

Address:
Department of Materials Science and Engineering, Tokyo Institute of Technology, 2-12-1 Ookayama, Meguro-ku, Tokyo 152-8552, Japan

Email:
Tsuyoshi Michinobu* - michinobu.t.aa@m.titech.ac.jp

* Corresponding author

Keywords:
annulene; click chemistry; polymerization; strain-promoted azide–alkyne cycloaddition

Beilstein J. Org. Chem. **2024,** *20,* 2234–2241.
https://doi.org/10.3762/bjoc.20.191

Received: 30 April 2024
Accepted: 21 August 2024
Published: 04 September 2024

This article is part of the thematic issue "Carbon-rich materials: from polyaromatic molecules to fullerenes and other carbon allotropes".

Guest Editor: Y. Yamakoshi

Abstract

Strain-promoted azide–alkyne cycloaddition (SpAAC) is a powerful tool in the field of bioconjugation and materials research. We previously reported a regioselective double addition of organic azides to octadehydrodibenzo[12]annulene derivatives with electron-rich alkyloxy substituents. In order to increase the reaction rate, electron-withdrawing substituents were introduced into octadehydrodibenzo[12]annulene. In this report, the synthesis of new octadehydrodibenzo[12]annulene derivatives, regioselective double addition of organic azides, and an application to crosslinking polymers are described.

Introduction

The strain-promoted azide–alkyne cycloaddition (SpAAC) is one of the most representative metal-free click chemistry reactions [1-5]. SpAAC has been mainly employed in bioconjugation in the fields of chemical biology and medicinal chemistry due to its high efficiency under physiologically active conditions and the absence of any toxic metal ions. SpAAC is biorthogonal, which allows for the specific labeling and imaging of biomolecules even in living cells and organisms. Recently, a more rapid click reaction was desired and the strain-promoted oxidation-controlled cyclooctyne-1,2-quinone cycloaddition (SPOCQ) was developed and employed in the same fields of chemical biology [6,7]. On the other hand, the use of the SpAAC in materials science was slow. We developed another class of metal-free click chemistry reactions, such as the [2 + 2] cycloaddition–retroelectrocyclization (CA-RE) between electron-rich alkynes and electron-deficient olefins [8]. The [2 + 2] CA-RE click reactions were employed to produce a variety of functional materials, such as nonlinear optical chromophores [9,10], super acceptors [11,12], ion sensing D–A systems [13], and crosslinked polymers [14-17]. Since crosslinking polymers requires high reaction efficiency under mild conditions, developing such reactions is crucial.

We previously reported the regioselective double azide addition to octadehydrodibenzo[12]annulene with hexyloxy substituents (DBA-OHex), which are readily accessible by the oxidative acetylenic coupling of a 1,2-diethynylbenzene derivative (Figure 1) [18]. The chemical stability of DBAs depends on the electronic character of the substituents. Electron-donating alkyloxy groups are known to enhance the stability of DBAs. On the other hand, DBAs substituted with electron-withdrawing groups have been little studied [19], and their chemical stability and physical properties are not well understood. In this paper, a new DBA substituted with ester groups was synthesized, and the double azide addition was comprehensively investigated. Finally, the double azide addition reaction was applied to polymer crosslinking and the mechanical properties of the self-standing polymer films were compared.

Results and Discussion

Strain-promoted azide–alkyne cycloaddition

Octadehydrodibenzo[12]annulene (DBA) with electron-withdrawing carbonyl substituents **5** was prepared from phthalimide (**1**, Scheme 1). Iodination followed by hydrolysis afforded 4,5-diiodophthalic acid (**2**) in 46.7% yield. Esterification with

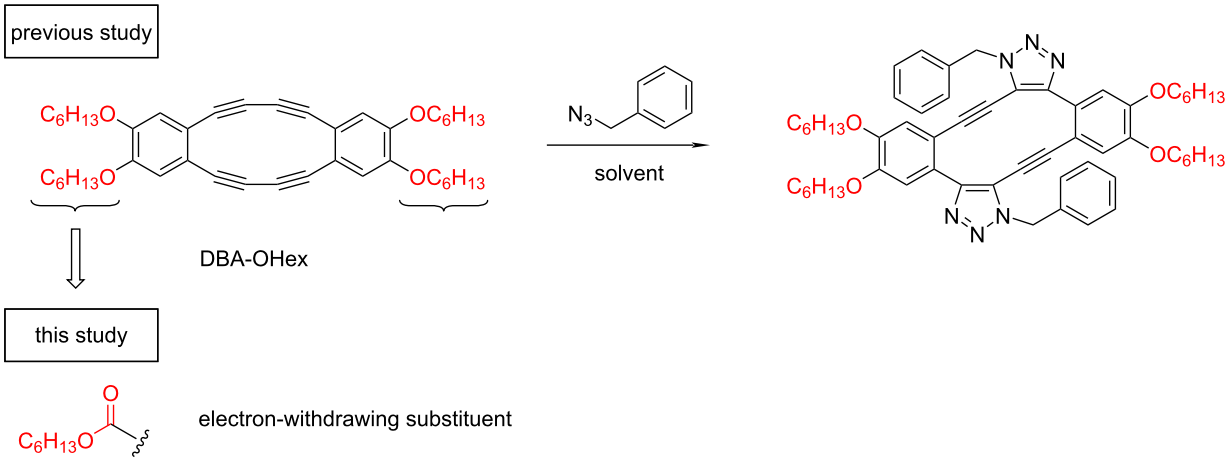

Figure 1: Previously reported regioselective double azide addition to DBA with hexyloxy substituents and molecular design in this study.

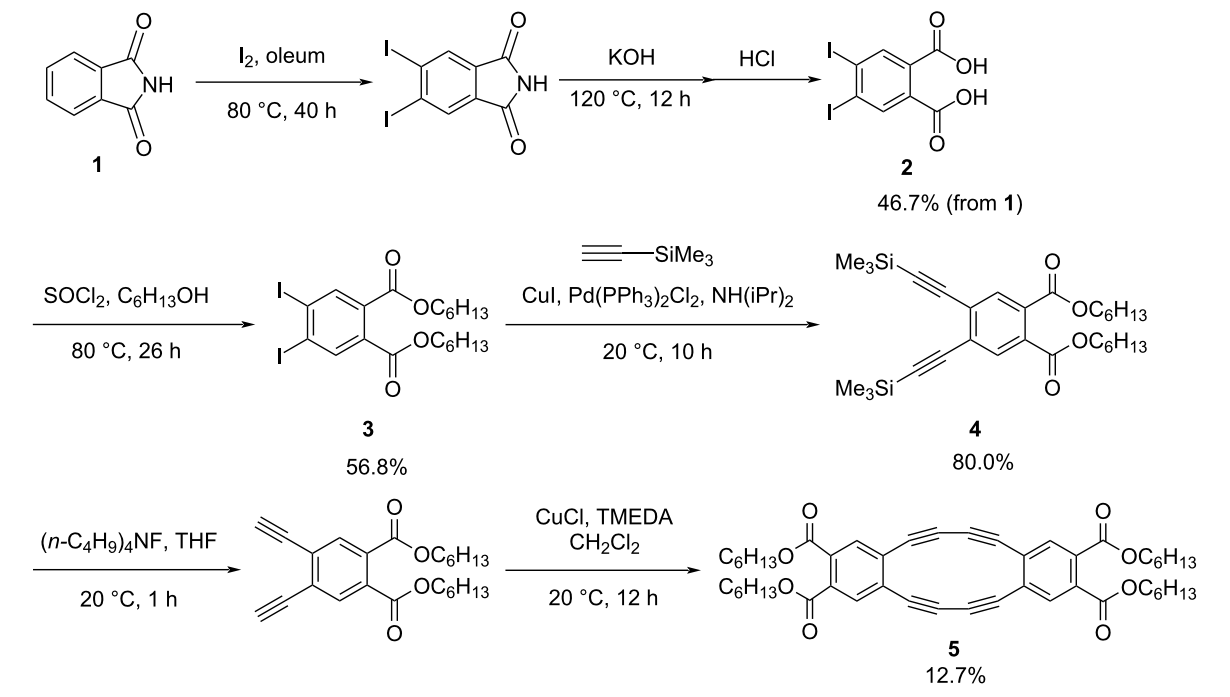

Scheme 1: Synthesis of DBA **5**.

1-hexanol yielded compound **3** in 56.8% yield and the subsequent Sonogashira coupling with trimethylsilylacetylene provided compound **4** in 80.0%. Silyl deprotection with $(n\text{-}C_4H_9)_4NF$ in THF followed by acetylenic oxidative dimerization under Hay conditions produced the desired DBA **5** in 12.7% yield. It should be noted that a thermodynamically more stable trimeric macrocycle was also formed in 17.7%, but it was not isolated and purified because it was outside the scope of this study.

Next, DBA **5** was subjected to the SpAAC with benzyl azide. When two equivalents of benzyl azide were added to a solution of **5** in $CDCl_3$ at a controlled temperature of 30 °C, the reaction slowly proceeded (Figure 2). After 22 h, the original peak

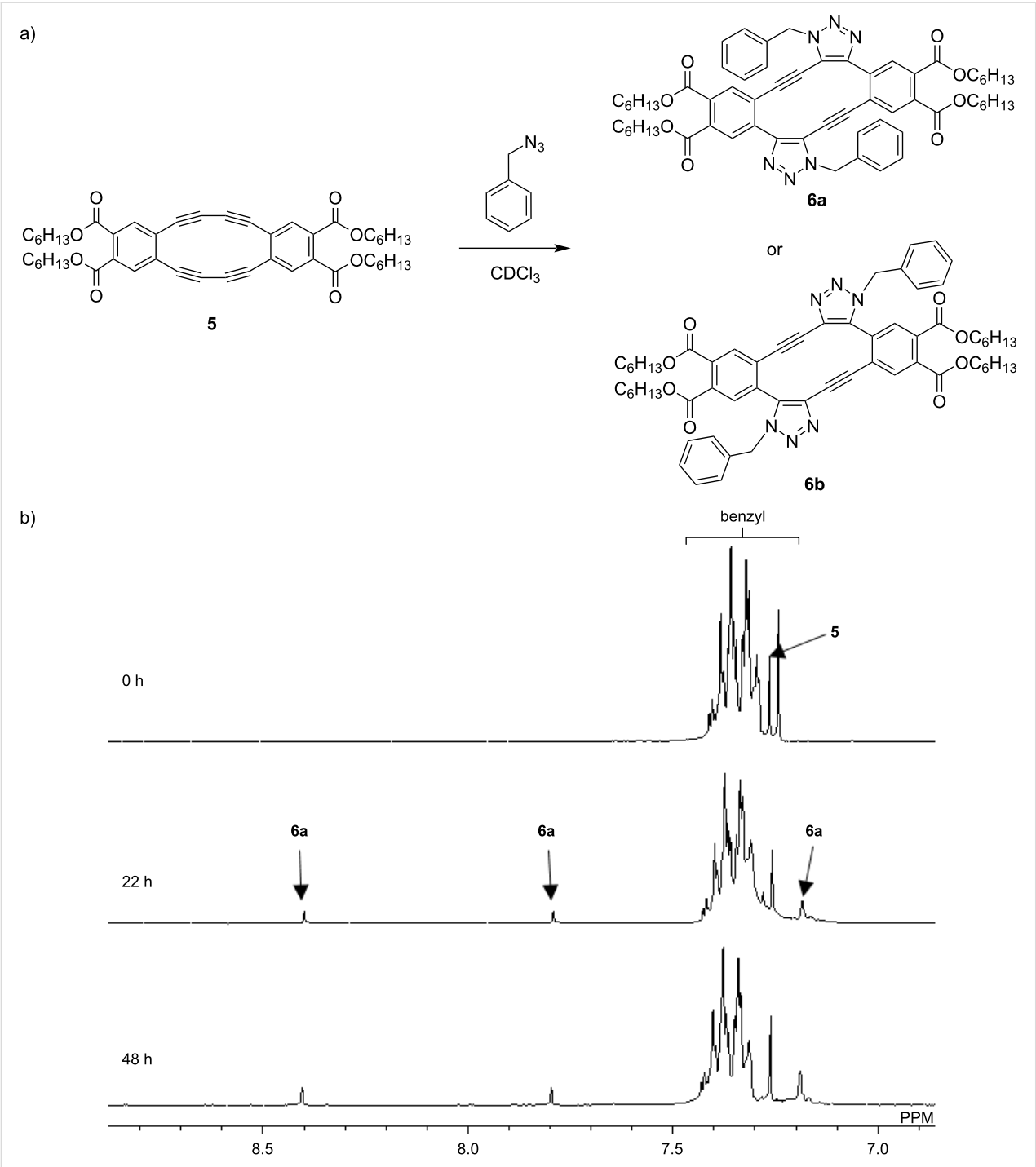

Figure 2: (a) Strain-promoted azide–alkyne cycloaddition between DBA **5** and benzyl azide and (b) ^{1}H NMR spectral change at 30 °C in $CDCl_3$.

ascribed to starting compound **5** decreased, while a set of new peaks appeared at 8.40 ppm, 7.79 ppm, and 7.20–7.18 ppm. Considering the high symmetry, no monoadducts were formed and the regioselective double azide addition occurred. In other words, 1,4-disubstituted-5-ethynyltriazole derivative (in-) (**6a**) or 1,5-disubstituted-4-ethynyltriazole derivative (out-) (**6b**) adducts were formed. To determine the chemical structure of the product, the NOESY measurement was conducted. The NOESY spectrum suggested the intermolecular through-space coupling between two benzene protons (Figure S10 in Supporting Information File 1). This result indicates that the formed double azide adduct is **6a**, which is consistent with our previous report [18].

The double azide addition was further investigated by changing the reaction temperature. The rate constant was determined by the temperature-dependent ^{1}H NMR spectra in $CDCl_3$. The reaction kinetics followed a second-order reaction. Since no monoadducts were formed, the rate-determining step is the first azide addition. Based on this fact, the activation energy (E_a) of the reaction between **5** and benzyl azide in $CDCl_3$, determined by the Arrhenius plots, was 60.9 kJ mol^{-1} (Figure 3). This value was apparently smaller than those previously reported for the reaction between DBA-OHex and benzyl azide (Table S1 in Supporting Information File 1). However, the E_a values were previously measured in DMSO-d_6 and C_6D_6, and it is known that there is a solvent polarity effect on the reactivity of SpAACs. In order to quantitatively compare the reactivity of DBAs with different substituents, the reaction between DBA-OHex and benzyl azide was also monitored in $CDCl_3$. The E_a in $CDCl_3$ was 71.1 kJ mol^{-1} (Table S1 in Supporting Information File 1). This result clearly suggests that DBA **5** with electron-withdrawing substituents has a lower E_a than DBA with electron-donating substituents.

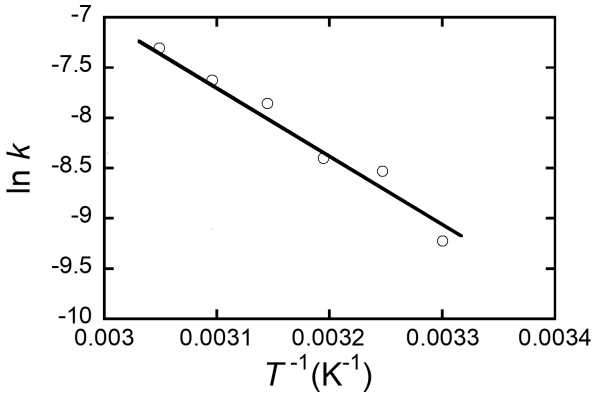

Figure 3: Arrhenius plots of the rate constants for the reaction between **5** and benzyl azide in $CDCl_3$.

DFT calculations

The reaction mechanism was investigated by computational calculations. The reaction mechanism between **5** and benzyl azide was supported by the ωB97X-D/6-31G(d,p) calculations with the CH_2Cl_2 polarizable continuum model (PCM) solvent (Figure 4). The reaction initially started with the addition of benzyl azide to one of the internal alkynes of **5**. Although the benzyl group is situated on the interior side of DBA, a more energetically unstable transition state (in-ts) is generated. However, the resulting monoadduct (in) is more energetically demanding than the counter monoadduct (out) due to steric factors. The second azide addition follows this step. The alkyne, which is diagonally positioned relative to the triazole group, shows the highest reactivity due to its significant distortion. This finding correlates with the experimental observation that no monotriazoles were obtained. During the second azide addition, the orientation of benzyl azide is once more controlled. The benzyl group positioned on the inner side results in a thermodynamically less stable transition state (in-in-ts) compared to that on the outer side (in-out-ts), but the thermodynamically stable final product is a regioselective "in-in" adduct, i.e., compound **6a**.

Optical properties

Absorption and emission spectra of **6a** were measured in CH_2Cl_2 (Figure 5). The conjugation is changed and a highly-twisted macrocyle forms by the double azide addition. Thus, compound **6a** shows an ultraviolet absorption peak at 249 nm (λ_{max}) and no absorption in the visible region was observed. When excited at 249 nm, an emission band at 513 nm (λ_{em}) appeared in the spectrum with a fluorescence quantum yield (Φ) of 7.0%. The absorption and fluorescence spectra were almost independent of solvents. For example, the λ_{em} in $CHCl_3$ and THF was 514 nm (Figure S11 in Supporting Information File 1). The double benzyl azide adduct of DBA-OHex displayed similar absorption and emission spectra with a λ_{max} of 247 nm and λ_{em} of 539 nm in CH_2Cl_2. Since the Stokes shift of the double benzyl azide adduct of DBA-OHex was 21900 cm^{-1} and larger than that of **6a** (20700 cm^{-1}), the Φ was 4.3%. This result suggested that replacing the hexyloxy substituents with electron-withdrawing ones enhanced the fluorescence intensity by approximately 1.6 times.

Crosslinker application

Using the strain-promoted double azide addition feature, DBA **5** was evaluated as a crosslinker for azidated polymers. After **5** (5 mol %) was added to a partially azidated poly(vinyl chloride) (PVC-N_3) (x = 0.11, n = 1000) in THF, the solvent was gradually evaporated on a Teflon boat. The resulting self-standing film became insoluble due to the occurrence of strain-promoted double azide–alkyne cycloaddition (Figure 6a). The mechanical

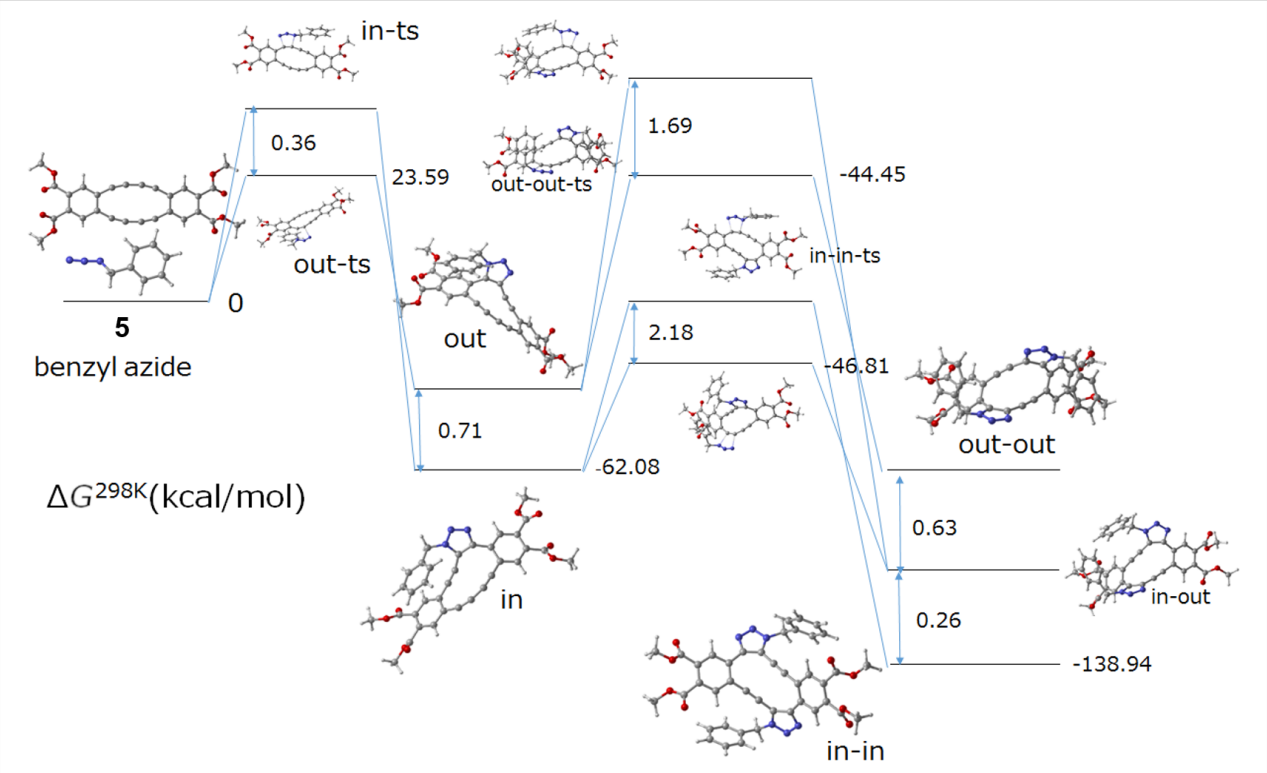

Figure 4: Proposed reaction mechanism for the formation of compound **6a**. Free energy profiles (ΔG_{298} in kJ mol^{-1}) calculated at the ωB97X-D/6-31G(d,p)/PCM (in CH_2Cl_2).

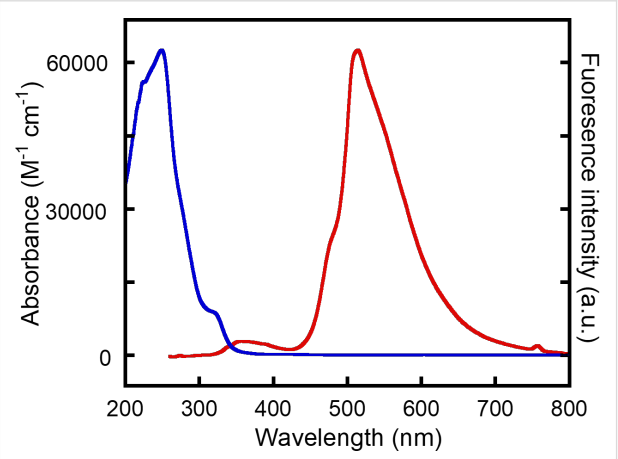

Figure 5: Absorption (blue) and fluorescence (red) spectra of **6a** (2×10^{-5} M) in CH_2Cl_2.

properties of the polymer films were then examined to observe the impact of crosslinking.

A PVC-N_3 film was prepared by a solvent-cast method on a Teflon boat. The strain-stress (S–S) curve of the PVC-N_3 film exhibited a breakdown at the strain of >300% with a gradual increase in the stress (Figure 6b). This film did not display any yielding points (Figure 6c). Interestingly, the crosslinking with **5** dramatically changed the mechanical features. The crosslinked film showed a clear yield point at the strain of about 4% with the maximum stress of 26.3 MPa (Table 1). When the applied stress gradually increased, the film displayed a ductility up to the strain of about 180 MPa. Young's moduli were estimated from the initial slopes of the S–S curves. The Young's modulus significantly increased from 277 MPa to 777 MPa by crosslinking. This result is consistent with the general understanding of covalent crosslinking of linear polymers. The crosslinking points formed by the SpAAC resulted in a rigid film.

Conclusion

Octadehydrodibenzo[12]annulene substituted with electron-withdrawing groups was successfully synthesized. This molecule underwent SpAAC with two equivalents of benzyl azide under mild conditions to quantitatively form the regioselective symmetric bistriazole product. The electron-withdrawing substituents facilitated the reaction progress as compared to the previously reported electron-donating hexyloxy substituents. The addition pattern was experimentally investigated by 2D NMR, which was also supported by DFT calculations. The bistriazole product displayed fluorescence in the visible range with a fluorescence quantum yield of 7.0%. Finally, the developed metal-free click reaction was employed to crosslink a partially azidated poly(vinyl chloride). The crosslinking

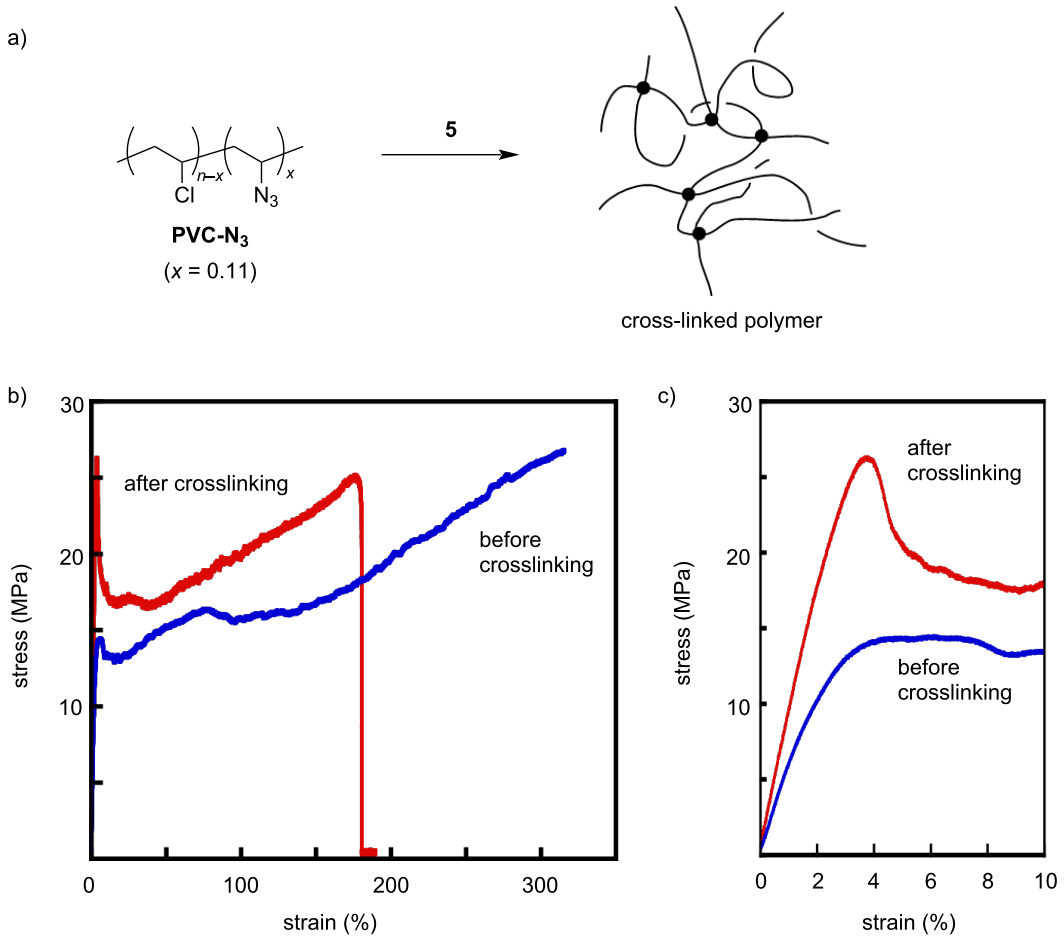

Figure 6: (a) Crosslinking reaction of PVC-N_3 (x = 0.11) with compound **5**. (b,c) Strain-stress curves of PVC-N_3 before (blue) and after (red) crosslinking.

Table 1: Mechanical properties of PVA-N_3 before and after crosslinking.

	Young's modulus (MPa)	Yield stress (MPa)	Maximum fracture stress (MPa)
PVA-N_3 (before crosslinking)	277	14.2	26.8
PVA-N_3 + **5** (after crosslinking)	777	26.3	26.3

proceeded by simply mixing the polymer and crosslinker in THF and evaporating, and the formation of the crosslinked polymer film was confirmed by the strain–stress curves. The developed method is straightforward and has broad applicability, extending to other azidated molecules and polymers.

Experimental

Materials

All reagents are purchased from TCI, Aldrich, and Kanto Chemical Co. Inc., and used as received. 4,5-Diiodophthalic acid was prepared according to a literature method [20]. A partially azidated poly(vinyl chloride) (PVA-N_3) was prepared by stirring poly(vinyl chloride) and NaN_3 in DMF at room temperature overnight.

Measurements

NMR spectra were recorded using a JEOL mode Al300 (300 MHz) at room temperature. Deuterated chloroform was used as the solvent unless otherwise stated. Chemical shifts of NMR were reported in ppm relative to the residual solvent peak

at 7.26 ppm for ^{1}H NMR spectroscopy and 77.6 ppm for ^{13}C NMR spectroscopy. Coupling constants (J) were given in Hz. The resonance multiplicity was described as s (singlet), t (triplet), and m (multiplet). FTIR spectra were recorded on a JASCO FT/IR-4100 spectrometer in the range from 4000 to 600 cm^{-1}. MALDI–TOF mass spectra were measured on a Shimadzu/Kratos AXIMACFR mass spectrometer equipped with a nitrogen laser (λ = 337 nm) and pulsed ion extraction, which was operated at an accelerating potential of 20 kV. THF solutions containing 1 g L^{-1} of a sample, 10 g L^{-1} of dithranol, and 1 g L^{-1} of sodium trifluoroacetate were mixed at a ratio of 1:1:1, and then 1 μL aliquot of this mixture was deposited onto a sample target plate. UV–vis absorption spectra were recorded on a JASCO V-670 spectrophotometer. Fluorescence spectra were recorded on a JASCO FP-8500.

All calculations were carried out using the Gaussian 16 program [21]. The DFT calculations were carried out using the long-range and dispersion-corrected ωB97X-D functional [22]. The 6-31G(d,p) basis set was used for H, C, O, and S atoms [23,24]. The solvent effect of CH_2Cl_2 was taken into account by the polarizable continuum model using the integral equation formalism (IEFPCM) [25] for DFT calculations. The optimized molecular structures were verified by vibrational analysis; equilibrium structures did not have imaginary frequencies and transition-state structures had only one imaginary frequency corresponding to the reaction coordinate.

Synthesis of **6a**

To a solution of **5** in CH_2Cl_2, two equivalents of benzyl azide were added and the mixture was stirred at room temperature for 12 h. Evaporation of the solvent quantitatively yielded the target compound. ^{1}H NMR ($CDCl_3$, 300 MHz, 297 K) δ 8.40 (s, 2H), 7.80 (s, 2H), 7.40–7.18 (m, 10H), 5.53 (s, 4H), 4.34–4.29 (m, 8H), 1.74–1.71 (m, 8H), 1.37–1.32 (m, 24H), 0.92–0.88 (m, 12H); ^{13}C NMR ($CDCl_3$, 75 MHz, 297 K) δ 166.26, 147.55, 135.76, 133.90, 133.67, 133.36, 131.92, 130.83, 128.74, 128.70, 128.34, 120.99, 119.57, 103.11, 82.18, 66.30, 53.55, 31.39, 28.42, 25.54, 22.48, 13.98; FTIR ν (cm^{-1}): 2067 (C≡C), 1730 (C=O); MALDI–TOF MS (dithranol, m/z): [M]$^+$ calcd for $C_{62}H_{70}N_6O_8$, 1026.53; found, 1026.98.

Supporting Information

Supporting Information File 1

Experimental section and kinetic study of the reaction of compound **5** and benzyl azide.
[https://www.beilstein-journals.org/bjoc/content/supplementary/1860-5397-20-191-S1.pdf]

Funding

This work was partially supported by NEDO (grant number 23200050-0), the Amano Institute of Technology, and the Nakatani Foundation.

Acknowledgement

We thank S. Fukushima (Tokyo Institute of Technology) for assisting with organic synthesis.

Author Contributions

Naoki Takeda: investigation. Shuichi Akasaka: investigation; writing – review & editing. Susumu Kawauchi: investigation; writing – review & editing. Tsuyoshi Michinobu: conceptualization; funding acquisition; supervision; writing – original draft.

ORCID® iDs

Shuichi Akasaka - https://orcid.org/0000-0002-6962-4327
Susumu Kawauchi - https://orcid.org/0000-0002-8865-541X
Tsuyoshi Michinobu - https://orcid.org/0000-0001-6948-1189

Data Availability Statement

The data that supports the findings of this study is available from the corresponding author upon reasonable request.

References

1. Xie, S.; Sundhoro, M.; Houk, K. N.; Yan, M. *Acc. Chem. Res.* **2020,** *53,* 937–948. doi:10.1021/acs.accounts.0c00046
2. Krell, K.; Harijan, D.; Ganz, D.; Doll, L.; Wagenknecht, H.-A. *Bioconjugate Chem.* **2020,** *31,* 990–1011. doi:10.1021/acs.bioconjchem.0c00072
3. Kang, X.; Cai, X.; Yi, L.; Xi, Z. *Chem. – Asian J.* **2020,** *15,* 1420–1429. doi:10.1002/asia.202000005
4. Li, K.; Fong, D.; Meichsner, E.; Adronov, A. *Chem. – Eur. J.* **2021,** *27,* 5057–5073. doi:10.1002/chem.202003386
5. Li, X.; Xiong, Y. *ACS Omega* **2022,** *7,* 36918–36928. doi:10.1021/acsomega.2c03931
6. Sen, R.; Escorihuela, J.; van Delft, F.; Zuilhof, H. *Angew. Chem., Int. Ed.* **2017,** *56,* 3299–3303. doi:10.1002/anie.201612037
7. Gahtory, D.; Sen, R.; Kuzmyn, A. R.; Escorihuela, J.; Zuilhof, H. *Angew. Chem., Int. Ed.* **2018,** *57,* 10118–10122. doi:10.1002/anie.201800937
8. Michinobu, T.; Diederich, F. *Angew. Chem., Int. Ed.* **2018,** *57,* 3552–3577. doi:10.1002/anie.201711605
9. Biaggio, I. *Chem. – Eur. J.* **2022,** *28,* e202103168. doi:10.1002/chem.202103168
10. Li, Y.; Tsuboi, K.; Michinobu, T. *Macromolecules* **2010,** *43,* 5277–5286. doi:10.1021/ma100869m
11. Kivala, M.; Boudon, C.; Gisselbrecht, J.-P.; Enko, B.; Seiler, P.; Müller, I. B.; Langer, N.; Jarowski, P. D.; Gescheidt, G.; Diederich, F. *Chem. – Eur. J.* **2009,** *15,* 4111–4123. doi:10.1002/chem.200802563
12. Tu, K.-H.; Wang, Y.; Kiyota, Y.; Iwahashi, T.; Ouchi, Y.; Mori, T.; Michinobu, T. *Org. Electron.* **2020,** *87,* 105978. doi:10.1016/j.orgel.2020.105978

13. Li, Y.; Washino, Y.; Hyakutake, T.; Michinobu, T. *Anal. Sci.* **2017,** *33,* 599–604. doi:10.2116/analsci.33.599
14. Washino, Y.; Michinobu, T. *Phys. Chem. Chem. Phys.* **2016,** *18,* 2288–2291. doi:10.1039/c5cp05180k
15. Fujita, H.; Michinobu, T. *ACS Macro Lett.* **2018,** *7,* 716–719. doi:10.1021/acsmacrolett.8b00365
16. Fujita, H.; Michinobu, T. *Soft Matter* **2018,** *14,* 9055–9060. doi:10.1039/c8sm01986j
17. Fujita, H.; Nihei, N.; Bito, M.; Michinobu, T. *Macromol. Biosci.* **2018,** *18,* 1800336. doi:10.1002/mabi.201800336
18. Fukushima, S.; Ashizawa, M.; Kawauchi, S.; Michinobu, T. *Helv. Chim. Acta* **2019,** *102,* e1900016. doi:10.1002/hlca.201900016
19. Zimmermann, B.; Baranović, G.; Štefanić, Z.; Rožman, M. *J. Mol. Struct.* **2006,** *794,* 115–124. doi:10.1016/j.molstruc.2006.01.049
20. Jiang, J.; Kaafarani, B. R.; Neckers, D. C. *J. Org. Chem.* **2006,** *71,* 2155–2158. doi:10.1021/jo0522198
21. *Gaussian 16;* Gaussian, Inc.: Wallingford, CT, 2016.
22. Chai, J.-D.; Head-Gordon, M. *Phys. Chem. Chem. Phys.* **2008,** *10,* 6615–6620. doi:10.1039/b810189b
23. Krishnan, R.; Binkley, J. S.; Seeger, R.; Pople, J. A. *J. Chem. Phys.* **1980,** *72,* 650–654. doi:10.1063/1.438955
24. McLean, A. D.; Chandler, G. S. *J. Chem. Phys.* **1980,** *72,* 5639–5648. doi:10.1063/1.438980
25. Tomasi, J.; Mennucci, B.; Cammi, R. *Chem. Rev.* **2005,** *105,* 2999–3094. doi:10.1021/cr9904009

License and Terms

BEILSTEIN JOURNAL OF ORGANIC CHEMISTRY

Interaction of a pyrene derivative with cationic [60]fullerene in phospholipid membranes and its effects on photodynamic actions

Hayato Takagi[1], Çetin Çelik[2], Ryosuke Fukuda[1], Qi Guo[3], Tomohiro Higashino[3], Hiroshi Imahori[3,4,5], Yoko Yamakoshi[2] and Tatsuya Murakami[*1,4]

Letter

Open Access

Address:
[1]Department of Biotechnology and Pharmaceutical Engineering, Graduate School of Engineering, Toyama Prefectural University, 5180 Kurokawa, Imizu City, Toyama 939-0398, Japan, [2]Laboratorium für Anorganische Chemie, ETH Zürich, CH-8093 Zürich, Switzerland, [3]Department of Molecular Engineering, Graduate School of Engineering, Kyoto University, Nishikyo-ku, Kyoto 615-8510, Japan, [4]Instutite for Integrated Cell–Material Sciences (iCeMS), Kyoto University, Sakyo-ku, Kyoto 606-8501, Japan and [5]Instutite for Liberal Arts and Sciences (ILAS), Kyoto University, Sakyo-ku, Kyoto 606-8501, Japan

Email:
Tatsuya Murakami[*] - murakami@pu-toyama.ac.jp

* Corresponding author

Keywords:
liposome; π–π interaction; reactive oxygen species; superoxide radical anion

Beilstein J. Org. Chem. **2024,** *20,* 2732–2738.
https://doi.org/10.3762/bjoc.20.231

Received: 12 July 2024
Accepted: 01 October 2024
Published: 30 October 2024

This article is part of the thematic issue "Carbon-rich materials: from polyaromatic molecules to fullerenes and other carbon allotropes".

Associate Editor: C. Stephenson

Abstract

We have reported that upon visible light irradiation, ferrocene-porphyrin-[60]fullerene triad molecules yield long-lived charge-separated states, enabling the control of the plasma membrane potential (V_m) in living cells. These previous studies indicated that the localization of the triad molecules in a specific intra-membrane orientation and the suppression of the photodynamic actions of the [60]fullerene (C_{60}) moiety are likely important to achieve fast and safe control of V_m, respectively. In this study, by mimicking our previous system of triad molecules and living cells, we report a simplified model system with a cationic C_{60} derivative ($catC_{60}$) and a liposome with embedded 1-pyrenebutyric acid (PyBA) to demonstrate that the addition of PyBA was important to achieve fast and safer control of V_m.

Introduction

The [60]fullerene (C_{60}) is known as an excellent electron acceptor [1,2] and is commonly used in organic solar cell applications [3]. Taking advantage of the fact that C_{60} can be an acceptor in photoinduced charge-separation systems, we have previously employed ferrocene-porphyrin-C_{60} triad molecules (Figure 1a) in a biological system to control the plasma mem-

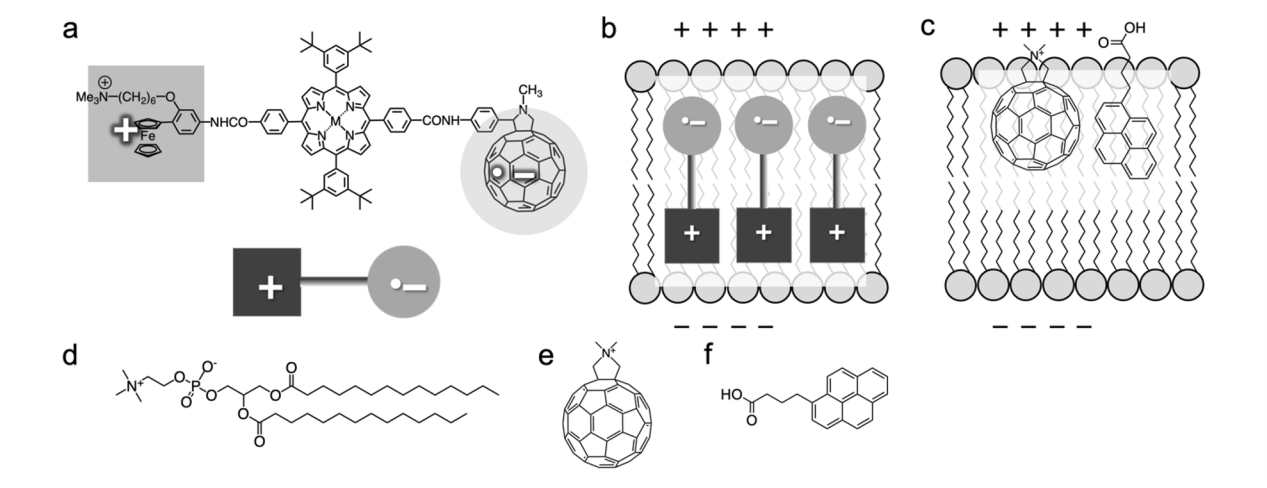

Figure 1: (a) Chemical structure and schematic illustration of the charge-separated state of a triad molecule and (b) control of the membrane potential by the illuminated molecule with a favourable arrangement. (c) Strategy of the present study for controlling both the location and photodynamic actions of a cationic derivative of C_{60} ($catC_{60}$), a simple model compound of the triad molecules, in a membrane via π–π interactions with 1-pyrenebutyric acid (PyBA). (d–f) Chemical structures of 1,2-dimyristoyl-*sn*-glycero-3-phosphocholine (DMPC) (d), $catC_{60}$ (e), and PyBA (f).

brane potential (V_m) of living mammalian neuronal cells under photoirradiation [4-6]. Generally, V_m originates from a difference in electric charge on the two sides of the plasma membrane (approximately 5 nm thickness), with a slight excess of the positive ions inside relative to the negative ions outside. Our ferrocene-porphyrin-C_{60} triad molecule exhibited long-lived charge-separated states under visible light irradiation [7], with the C_{60} species becoming negatively charged while the ferrocene moiety became positively charged (Figure 1a). This charge-separated state can be used to initiate nanoscale electric fields, e.g., V_m. The design of the triad molecules may also help to keep their orientation within the plasma membrane to have the C_{60} moiety located near the outer membrane surface and the ferrocene moiety near the inner membrane surface (Figure 1b). With this favorable arrangement of the molecules, it was expected to trigger a photoinduced change of the V_m that occurs at very fast time scales (less than milliseconds), leading to the (partial) cancellation of the V_m. However, in reality, the change occurred on a minute time scale, indicating that the favorable arrangement was not sufficiently achieved in the plasma membrane.

One of the concerns with our previous triad molecules was photoinduced generation of reactive oxygen species (ROS) [8]. In our more recent study, the reversal of V_m after stopping photoirradiation of our triad molecule was associated with the renewal of the plasma membrane through endocytosis in living cells [6]. These results suggested that the photoinduced change in V_m was caused by some modification – most likely oxidation – of the plasma membrane by the photoexcited triad molecule. Taken together, for the realization of rapid control of V_m using such C_{60}-based molecules in the membrane, the suppression of ROS generation is an important consideration. In this study, we aim to develop a system to achieve a quick V_m control without damaging the membranes by using a C_{60} derivative and a pyrene derivative as a model system for the triad molecules.

C_{60} has been reported to be incorporated into the phospholipid bilayers at the central part of membrane due to its hydrophobicity [9,10]. In contrast, to achieve the favorable arrangement as described above, the C_{60} moiety of the triad molecule needs to be located near the outer membrane surface. To facilitate this arrangement, in this study, we utilized a simplified system (Figure 1c) consisting of (i) liposomes of 1,2-dimyristoyl-*sn*-glyreco-3-phosphocholine (DMPC, Figure 1d), a well-known model of the plasma membrane, (ii) a cationic derivative of C_{60} ($catC_{60}$, Figure 1e) as a replacement of the triad molecules, and (iii) 1-pyrenebutyric acid (PyBA, Figure 1f) as an anchor molecule for $catC_{60}$ to be localized near the surface of phospholipid membranes [11,12]. With this model system, we aimed to examine whether both the intramembrane localization and the photodynamic actions of $catC_{60}$ can be modulated by PyBA.

Results and Discussion

The $catC_{60}$-loaded liposomes ($catC_{60}$-lip) were prepared by hydration of a $catC_{60}$-embedded DMPC film [13] and compared with C_{60}-loaded liposomes (C_{60}-lip) by physicochemical characterizations. When $catC_{60}$ or C_{60} was added to DMPC (in a 1:1 molar ratio to DMPC) the zeta potential of the $catC_{60}$-lip was higher (16 mV) than that of C_{60}-lip (–0.3 mV). Based on the experiments of differential scanning calorimetry analyses with varied amount of $catC_{60}$ or C_{60} (Figure 2a), the addition of $catC_{60}$ caused the disappearance of phase transition of DMPC liposomes in a dose-dependent manner and more efficiently

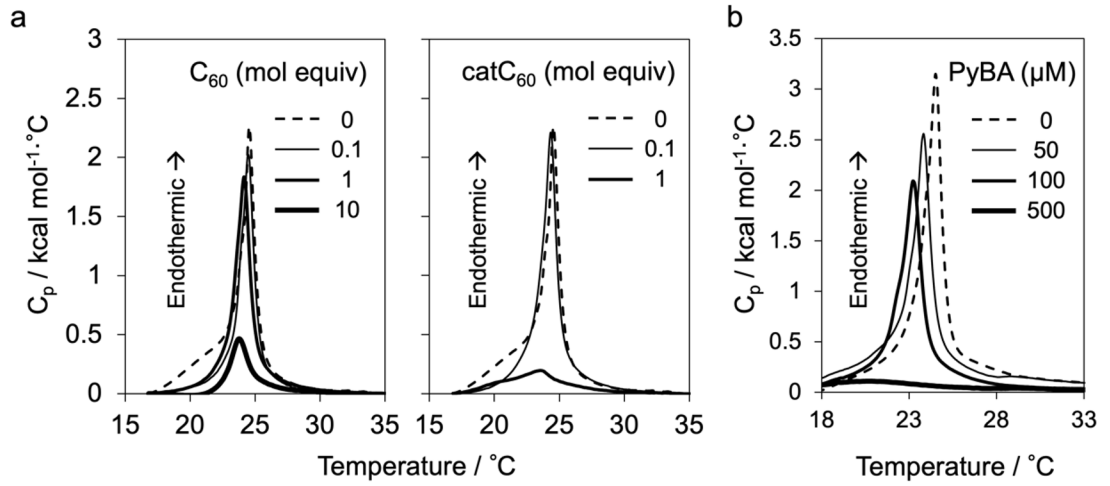

Figure 2: Differential scanning calorimetry analysis for the phase transition of liposomes (1 mM phospholipid). (a) Effect of the addition of C_{60} (left) or a cationic derivative of C_{60} ($catC_{60}$) (right) at various molar equivalents (mol equiv) to the phospholipid of liposomes. (b) Effect of 1-pyrenebutyric acid (PyBA) addition at various concentrations to liposomes without $catC_{60}$ and C_{60}. The gel-to-liquid crystalline phase transition for 1,2-dimyristoyl-*sn*-glycero-3-phosphocholine (DMPC) liposomes was observed at 25 °C. All the measurements were performed with liposome samples dispersed in phosphate-buffered saline (PBS(–)).

than the case with C_{60}. These results suggested that $catC_{60}$ was more likely to localize near the surface of the lipid bilayer of $catC_{60}$-lip than the C_{60} in C_{60}-lip [14]. Similarly, the incorporation of PyBA into the pre-prepared liposomes was tested by zeta potential analysis (–15 mV) and differential scanning calorimetry analysis (Figure 2b), showing a clear dose dependency on the amount of PyBA added.

The absorption spectra of $catC_{60}$-lip and C_{60}-lip were compared in PBS(–) (Figure 3). At two different concentrations, no significant change was observed in $catC_{60}$-lip, whereas broadening and a red shift were observed in C_{60}-lip at higher concentrations (10 mol equiv). These results indicate that $catC_{60}$ was better dispersed in the DMPC membrane than C_{60}. The results also provided some insight into the situation of our previous triad molecule – how the undesired aggregate formation of the triad molecules is reduced during solubilization and cell studies in physiologically relevant media [15].

The interaction between $catC_{60}$ and PyBA in the liposomes was assessed by the fluorescence spectra of PyBA in $catC_{60}$-lip [16]. The $catC_{60}$-lip containing $catC_{60}$ at 0, 5.4, and 54 μM were mixed with PyBA (50 μM) in PBS(–), and the fluorescence spectra were measured. As shown in Figure 4a, the intensity decreased upon increasing the concentration of the $catC_{60}$ in the liposomes, showing the quench of PyBA fluorescence by

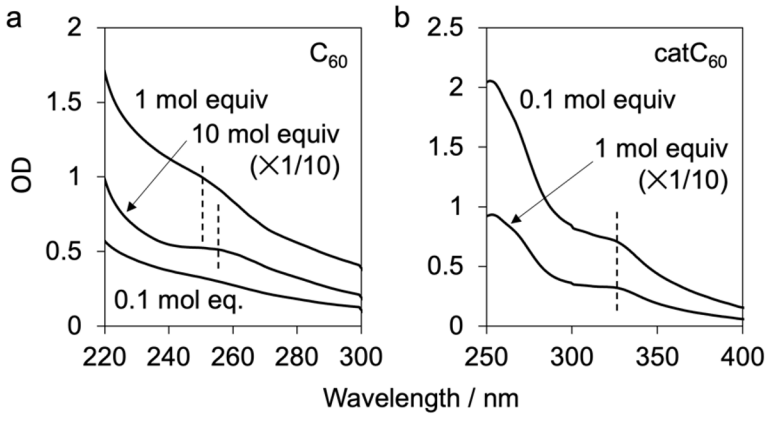

Figure 3: UV–vis absorption spectra of liposomes (1 mM phospholipid) with C_{60} (a) or a cationic derivative of C_{60} ($catC_{60}$) (b) added at various molar equivalents (mol equiv) to phospholipid. The equivalent of C_{60} added in C_{60}-loaded liposomes (C_{60}-lip) was 0.1, 1 and 10 mol equiv, and the equivalent of $catC_{60}$ added to $catC_{60}$-loaded liposomes ($catC_{60}$-lip) was 0.1 and 1 mol equiv. Spectra of 10 mol equiv of C_{60} in (a) and 1 mol equiv of $catC_{60}$ in (b) were measured after 10-fold dilution. The absorption peak positions for C_{60} and $catC_{60}$ are indicated with dotted lines. Liposome samples were dispersed in phosphate-buffered saline (PBS(–)).

$catC_{60}$, presumably by interacting in the liposome membrane. The incomplete quenching after the addition of PyBA at a concentration comparable to that of $catC_{60}$ may be attributed to the presence of unembedded PyBA in the dispersion. To this PyBA-embedded $catC_{60}$-lip system, methanol was added to completely destroy the liposome structures, resulting in the regain of the fluorescence intensity (Figure 4b). The results clearly demonstrate that PyBA interacts with $catC_{60}$ in the DMPC membrane near the surface, at least to some extent, indicating the potential of PyBA acting an anchor molecule to $catC_{60}$ in the liposome membrane. Nevertheless, further study is necessary to gain more insight into their location in the membrane.

The results above indicated the interaction of $catC_{60}$ with PyBA in the DMPC liposome membrane. We anticipated some effect of PyBA on the photoinduced generation of ROS by $catC_{60}$ due to such interaction within the liposome membrane. To investigate such effects, we employed an electron spin resonance (ESR) spin-trapping method to evaluate the generation of ROS by $catC_{60}$ in the absence or presence of PyBA. As spin trapping reagents for the singlet oxygen ($^1O_2$), hydroxyl radical (•OH) and superoxide radical anion (O_2•$^-$); 2,2,6,6,-tetramethyl-4-piperidone (4-oxo-TEMP), 3,4-dihydro-2,3-dimethyl-2*H*-pyrrole 1-oxide (DMPO), and 5-(diethoxyphosphoryl)-5-methyl-1-pyrrolidone-*N*-oxide (DEPMPO) were respectively used (schemes in Figure 5). Our previous study demonstrated that both $^1O_2$ and O_2•$^-$ were generated under irradiation of triad molecules in DMSO/H_2O [8].

Under irradiation by a blue LED (464–477 nm, 23 lm·W^{-1}), significant ESR signals corresponding to the $^1O_2$ adduct of 4-oxo-TEMP (4-oxo-TEMPO) were observed in the dispersion of $catC_{60}$-lip ([$catC_{60}$] = 5 μM) in PBS(–) showing an evidence of energy transfer reaction by the photoexcited $catC_{60}$ (Figure 5a(ii)). In the presence of electron donor (NADH) under photoirradiation, •OH generation was observed as a •OH adduct of DMPO (DMPO-OH, Figure 5b(ii)) revealing that electron transfer reaction was also occurring. Using DEPMPO as a spin trapping reagent, detection of O_2•$^-$ was tried and some radical adducts were detected, but without being clearly identified (Figure 5c(i), (ii)). The reason of the inability of O_2•$^-$ detection is not known at present. Upon addition of dimethyl sulfoxide (DMSO) to this system, an adduct of DEPMPO and •CH_3 (DEPMPO-CH_3), which was presumably generated from the reaction of •OH and DMSO, was clearly observed, further confirming the generation of •OH (Figure 5b(iii)). At the same time, unusually fast conversion of $O_2^{\bullet-}$ to •OH was also suggested in this system.

The results above suggest that $catC_{60}$-lip generated both types of ROS ($^1O_2$ and •OH) via energy transfer and electron transfer mechanisms. The present results are in line with previous studies of photoinduced ROS generation by C_{60} and its derivatives [17-19]. The most important: upon the addition of PyBA to $catC_{60}$-lip, the signal intensities of both types of ROS ($^1O_2$ and •OH) were decreased (Figure 5a(iii), b(iii), c(iv)). These results indicate that PyBA suppresses ROS generation by $catC_{60}$-lip in liposome environment, which would be advantageous for the nanoscale control of V_m by the triad molecules.

Conclusion

In summary, our findings indicate that PyBA can interact with $catC_{60}$ within DMPC liposomes and modestly inhibit the photoinduced generation of ROS by $catC_{60}$. These insights offer

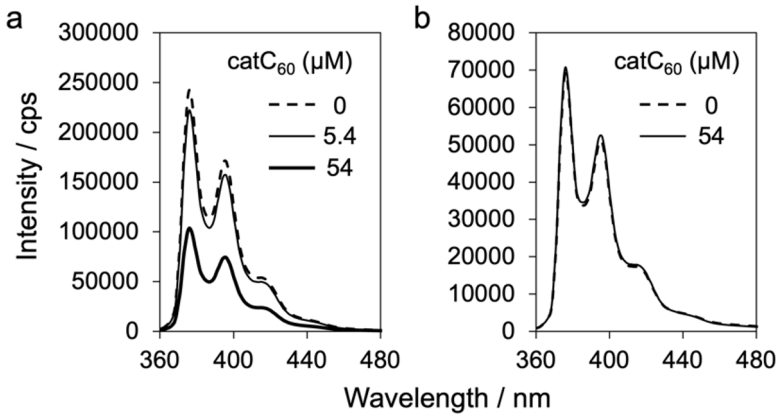

Figure 4: Fluorescence spectra of 1-pyrenebutyric acid (PyBA) in cationic derivative of C_{60} ($catC_{60}$)-loaded liposomes ($catC_{60}$-lip, 1 mM phospholipid) containing $catC_{60}$ at various concentrations. (a) Effect of $catC_{60}$ in liposomes on the fluorescence intensity of PyBA, with concentrations of $catC_{60}$ at 0, 5.4, 54 μM, and PyBA at 50 μM. (b) Fluorescence spectra of $catC_{60}$-lip with 0 and 54 μM $catC_{60}$, treated with 50 μM PyBA, after addition of methanol. Liposome samples were dispersed in phosphate-buffered saline (PBS(–)).

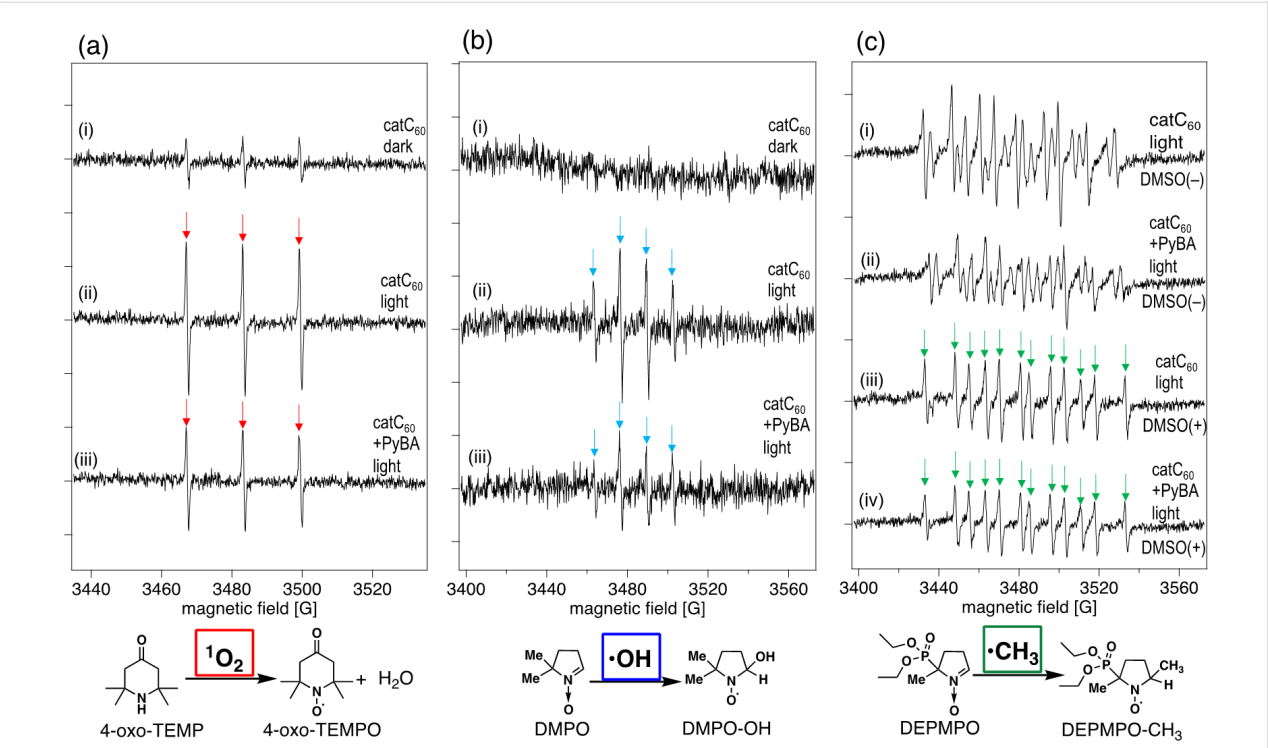

Figure 5: Photoinduced generation of reactive oxygen species (ROS) by cationic derivative of C_{60} ($catC_{60}$)-loaded liposomes ($catC_{60}$-lip) (5 μM $catC_{60}$) in the absence and presence of 1-pyrenebutyric acid (PyBA, 50 μM). (a) X-band electron spin resonance (ESR) spectra of 2,2,6,6,-tetramethyl-4-piperidone (4-oxo-TEMP) adduct with $^1O_2$ generated by $catC_{60}$ under irradiation by a blue LED. Experimental conditions: (i) $catC_{60}$ 5 μM and 4-oxo-TEMP 100 μM, in phosphate-buffered saline (PBS(–)) under dark conditions. (ii) $catC_{60}$ 5 μM and 4-oxo-TEMP 100 μM in PBS(–) under irradiation for 30 min by blue LED lamp. (iii) $catC_{60}$ 5 μM, PyBA 67 μM, and 4-oxo-TEMP 100 μM, in PBS(–) under irradiation for 30 min by blue LED lamp. (b) X-band ESR spectra of 3,4-dihydro-2,3-dimethyl-2*H*-pyrrole 1-oxide (DMPO) adduct with •OH generated by $catC_{60}$ under irradiation by a blue LED. Experimental conditions: (i) $catC_{60}$ 5 μM, β-nicotinamide adenine dinucleotide, reduced disodium salt hydrate (NADH) 8 mM, Fe(II)-diethylenetriaminepentaacetic acid (DETAPAC) 1 mM, and DMPO 100 mM in PBS(–) under irradiation for 30 min by blue LED lamp. (ii) $catC_{60}$ 5 μM, NADH 8 mM, Fe(II)-DETAPAC 1 mM, and DMPO 100 mM in PBS(–) under irradiation for 30 min by blue LED lamp. (iii) $catC_{60}$ 5 μM, PyBA 67 μM, NADH 8 mM, Fe(II)-DETAPAC 1 mM, and DMPO 100 mM in PBS(–) under irradiation for 30 min by blue LED lamp. (c) X-band ESR spectra of 5-(diethoxyphosphoryl)-5-methyl-1-pyrrolidone-*N*-oxide (DEPMPO) adduct with undefined radicals (i, ii) or •CH_3 (iii, iv) generated by $catC_{60}$ under irradiation by a blue LED. Experimental conditions: (i) $catC_{60}$ 5 μM, NADH 8 mM, DETAPAC 1 mM, and DEPMPO 100 mM in PBS(–) under irradiation for 30 min by blue LED lamp. (ii) $catC_{60}$ 5 μM, PyBA 67 μM, NADH 8 mM, DETAPAC 1 mM, and DEPMPO 100 mM in PBS(–) under irradiation for 30 min by blue LED lamp. (iii) $catC_{60}$ 5 μM, NADH 8 mM, DETAPAC 1 mM, and DEPMPO 100 mM in a 4-to-1 (v/v) mixture of PBS(–) and dimethyl sulfoxide (DMSO) under irradiation for 30 min by blue LED lamp. (iv) $catC_{60}$ 5 μM, PyBA 67 μM, NADH 8 mM, DETAPAC 1 mM, and DEPMPO 100 mM in a 4-to-1 (v/v) mixture of PBS(–) and DMSO under irradiation for 30 min by blue LED lamp. In the ESR spectra, signals corresponding to the adducts are indicated with red (4-oxo-TEMPO in a), blue (DMPO-OH in b), and green (DEPMPO-CH_3 in c) arrows.

valuable guidance for the photocontrol of the plasma membrane potential (V_m) using fullerene-containing triad molecules on a millisecond scale.

Experimental

Preparation of liposomes with $catC_{60}$ ($catC_{60}$-lip) or C_{60} (C_{60}-lip)

Liposomes were prepared using a thin-film hydration method. DMPC (NOF AMERICA Corporation, White Plains, NY, USA) was solubilized in ethanol (FUJIFILM Wako Pure Chemical Corporation, Osaka, Japan), and $catC_{60}$, which was synthesized according to a previous report [20], or C_{60} (NOF AMERICA Corporation, White Plains, NY, USA) was solubilized in a 1:4 (vol:vol) mixture of DMSO (Nacalai Tesque Inc., Kyoto, Japan) and toluene (FUJIFILM Wako Pure Chemical Corporation, Osaka, Japan). DMPC in ethanol and $catC_{60}$ or C_{60} in DMSO/toluene were mixed in molar ratios of 1:0, 1:0.1, 1:1, or 1:10, and the solvent was removed using a rotary evaporator (Rotavapor R-300, BÜCHI Labortechnik AG, Switzerland) at 40 °C to prepare the lipid films. The lipid films were then dried overnight in vacuo. Then, the films were hydrated with PBS(–) (137 mM NaCl, 2.68 mM KCl, 8.1 mM Na_2HPO_4, 1.47 mM KH_2PO_4) so that the theoretical value of DMPC concentration was 3 mg/mL, and the resulting suspension was sonicated at 30 °C until the lipid membrane had completely peeled off from the flask. To remove free $catC_{60}$ and C_{60}, the resulting suspension was centrifuged at 20,000*g* at room temperature for 10 min. The supernatant was collected and subjected to more than 20 extrusions using a Mini-Extruder equipped with a

100 nm-pore-size membrane (Croda International Plc. Avanti Polar Lipids, Inc.).

Differential scanning calorimetry (DSC)

DSC was performed using a MicroCal^{TM}PEAQ-DSC System (Malvern Panalytical, Ltd., Malvern, U.K.). Liposomal suspensions of DMPC with or without catC_{60} or C_{60} were dispersed in PBS(–) (1 mM DMPC). Measurements were performed following equilibration at 10 °C at a scan rate of 180 °C/h. Measurements were also performed after mixing of 50, 100 or 500 μM PyBA (Sigma-Aldrich, St. Louis, MI, USA) and DMPC liposomes without catC_{60} or C_{60} followed by dialysis of the mixture against 3 L PBS for 2 h to remove free PyBA. Data analysis, including calculation of the phase transition temperature, was performed using the MicroCal PEAQ-DSC Software.

UV–vis absorption measurement

UV–vis spectra of DMPC liposomes (1 mM DMPC) with or without catC_{60} or C_{60} were measured in PBS(–) using a UV-3600 Plus absorption spectrometer (Shimadzu Corporation, Kyoto, Japan).

Fluorescence measurement

DMPC liposomes containing 0, 5.4, or 54 μM catC_{60} were mixed with PyBA (final concentration of 50 μM) in PBS(–), and the mixture was dialysed against 3 L PBS for 2 h to remove free PyBA. Fluorescence spectra were measured using an RF-6000 spectrofluorometer (Shimadzu Corporation, Kyoto, Japan) (excitation at 341 nm, emission at 360–500 nm) to evaluate the interaction between catC_{60} and PyBA in DMPC membranes. Measurements were also performed after the addition of 10 times the volume of methanol to the liposome samples to liberate catC_{60} and PyBA from the membranes.

ESR measurements for photoinduced $^1O_2$ and $O_2^{\bullet-}$ generation

ESR spectra were recorded on a Bruker EMX, Continuous Wave X-Band EPR spectrometer (Bruker BioSpin GmbH, Rheinstetten, Germany). Suprasil® ESR tubes with a diameter of 4 mm, length of 250 mm and a wall thickness of 0.8 mm were used (SP Wilmad-LabGlass, New Jersey, US). 4-Oxo-TEMP was purchased from ABCR (Karlsruhe, Germany) and purified by sublimation prior to use. The 50 μL Blaubrand® intraMark capillaries were used in the EPR measurements (Brand GMBH, Wertheim, Germany). DEPMPO was bought from Enzo Life Sciences AG (Farmingdale, NY, USA). $FeSO_4$, DETAPAC and NADH was bought from Sigma-Aldrich (St. Louis, Missouri, USA). DMPO was bought from TCI (Tokyo Chemical Industry Co. Ltd., Tokyo, Japan). Irradiation was performed by blue LED light (464–477 nm, 23 lm·W^{-1}) from Lumiflex300 Pro RGB LED Stripes (LUMITRONIX LED-Technik GmbH, Hechingen, Germany) containing 120 LED lamps assembled in an aluminium cylindrical container with a diameter of 8.5 cm. ESR measurements conditions: microwave frequency 9.78 GHz, microwave power 10 mW, receiver gain 5.02×10^4, modulation amplitude 1.00 G, modulation frequency 100 kHz, 3 scan average, sweep time 83.89 s.

$^1O_2$ Generation: All measurements were performed in PBS(–). Ten μL of catC_{60} sample solution (25 μM), 10 μL of 4-oxo TEMP solution (500 mM) and 30 μL of PBS(–) were mixed in a 0.5 mL Eppendorf tube. For the measurement in the presence of PyBA, 10 μL of PyBA solution (335 μM) was added instead of 10 μM of PBS(–). The solution was subjected to O_2 bubbling for 30 seconds and then taken into 50 μL capillary and sealed. The solution was then irradiated with blue LED light for 30 minutes. The capillary was taken into the ESR tube for measurement at room temperature.

$^{\bullet}$OH Generation: All measurements were performed in PBS(–). Ten μL of catC_{60} sample solution (25 μM), 10 μL of Fe(II)-DETAPAC solution (5 mM), 10 μL of DMPO solution (500 mM), 10 μL of NADH (40 mM) and 10 μL PBS(–) were mixed in a 0.5 mL Eppendorf tube. For the measurement in the presence of PyBA, 10 μL of PyBA solution (335 μM) was added instead of 10 μL of PBS(–). The solution was subjected to O_2 bubbling for 30 seconds and then taken into 50 μL capillary and sealed. The solution was irradiated with blue LED light for 30 minutes. The capillary was taken into the ESR tube and ESR spectra were recorded at room temperature.

$O_2^{\bullet-}$ Generation: Measurements were performed in a mixture of DMSO and PBS(–) (1-to-4, v/v). Ten μL of catC_{60} sample solution (25 μM), 10 μL of DETAPAC solution (5 mM), 10 μL of DEPMPO solution (500 mM), 10 μL of NADH (40 mM) and 10 μL of PBS(–) were mixed in a 0.5 mL Eppendorf tube. For the measurement in the presence of PyBA, 10 μL of PyBA solution (335 μM) was added instead of 10 μL of PBS(–). The solution was subjected to O_2 bubbling for 30 seconds and then taken into 50 μL capillary and sealed. The solution was irradiated with blue LED light for 30 minutes. The capillary was taken into the ESR tube and ESR spectra were recorded at room temperature.

Acknowledgements

The authors thank Dr. Ebert from ETH Zurich for his support on ESR measurements.

Funding

This work was financially supported by JSPS KAKENHI Grant Number JP20H05842 [T.M.].

Author Contributions

Hayato Takagi: investigation; writing – original draft; writing – review & editing. Çetin Çelik: investigation; writing – review & editing. Ryosuke Fukuda: data curation; formal analysis; investigation. Qi Guo: investigation. Tomohiro Higashino: project administration; supervision; writing – review & editing. Hiroshi Imahori: project administration; supervision; writing – review & editing. Yoko Yamakoshi: formal analysis; methodology; project administration; supervision; validation; writing – review & editing. Tatsuya Murakami: conceptualization; data curation; formal analysis; funding acquisition; project administration; supervision; validation; writing – original draft; writing – review & editing.

ORCID® iDs

Hayato Takagi - https://orcid.org/0009-0009-3557-9730
Çetin Çelik - https://orcid.org/0000-0001-6132-8710
Ryosuke Fukuda - https://orcid.org/0000-0003-2509-3314
Tatsuya Murakami - https://orcid.org/0000-0001-5199-500X

Data Availability Statement

The data that supports the findings of this study is available from the corresponding author upon reasonable request.

References

1. Sariciftci, N. S.; Smilowitz, L.; Heeger, A. J.; Wudl, F. *Science* **1992,** *258,* 1474–1476. doi:10.1126/science.258.5087.1474
2. Yu, G.; Gao, J.; Hummelen, J. C.; Wudl, F.; Heeger, A. J. *Science* **1995,** *270,* 1789–1791. doi:10.1126/science.270.5243.1789
3. Imahori, H.; Kobori, Y.; Kaji, H. *Acc. Mater. Res.* **2021,** *2,* 501–514. doi:10.1021/accountsmr.1c00045
4. Cai, N.; Takano, Y.; Numata, T.; Inoue, R.; Mori, Y.; Murakami, T.; Imahori, H. *J. Phys. Chem. C* **2017,** *121,* 17457–17465. doi:10.1021/acs.jpcc.7b04466
5. Takano, Y.; Miyake, K.; Sobhanan, J.; Biju, V.; Tkachenko, N. V.; Imahori, H. *Chem. Commun.* **2020,** *56,* 12562–12565. doi:10.1039/d0cc05326k
6. Numata, T.; Fukuda, R.; Hirano, M.; Yamaguchi, K.; Sato-Numata, K.; Imahori, H.; Murakami, T. *Cell. Physiol. Biochem.* **2020,** *54,* 899–916. doi:10.33594/000000277
7. Imahori, H.; Tamaki, K.; Guldi, D. M.; Luo, C.; Fujitsuka, M.; Ito, O.; Sakata, Y.; Fukuzumi, S. *J. Am. Chem. Soc.* **2001,** *123,* 2607–2617. doi:10.1021/ja003346i
8. Takano, Y.; Numata, T.; Fujishima, K.; Miyake, K.; Nakao, K.; Grove, W. D.; Inoue, R.; Kengaku, M.; Sakaki, S.; Mori, Y.; Murakami, T.; Imahori, H. *Chem. Sci.* **2016,** *7,* 3331–3337. doi:10.1039/c5sc04135j
9. Qiao, R.; Roberts, A. P.; Mount, A. S.; Klaine, S. J.; Ke, P. C. *Nano Lett.* **2007,** *7,* 614–619. doi:10.1021/nl062515f
10. Ikeda, A.; Kiguchi, K.; Shigematsu, T.; Nobusawa, K.; Kikuchi, J.-i.; Akiyama, M. *Chem. Commun.* **2011,** *47,* 12095–12097. doi:10.1039/c1cc14650e
11. Jablonski, A. E.; Kawakami, T.; Ting, A. Y.; Payne, C. K. *J. Phys. Chem. Lett.* **2010,** *1,* 1312–1315. doi:10.1021/jz100248c
12. Takeuchi, T.; Kosuge, M.; Tadokoro, A.; Sugiura, Y.; Nishi, M.; Kawata, M.; Sakai, N.; Matile, S.; Futaki, S. *ACS Chem. Biol.* **2006,** *1,* 299–303. doi:10.1021/cb600127m
13. Bangham, A. D.; Standish, M. M.; Watkins, J. C. *J. Mol. Biol.* **1965,** *13,* 238–252. doi:10.1016/s0022-2836(65)80093-6
14. Ikeda, A.; Mae, T.; Ueda, M.; Sugikawa, K.; Shigeto, H.; Funabashi, H.; Kuroda, A.; Akiyama, M. *Chem. Commun.* **2017,** *53,* 2966–2969. doi:10.1039/c7cc00302a
15. Numata, T.; Murakami, T.; Kawashima, F.; Morone, N.; Heuser, J. E.; Takano, Y.; Ohkubo, K.; Fukuzumi, S.; Mori, Y.; Imahori, H. *J. Am. Chem. Soc.* **2012,** *134,* 6092–6095. doi:10.1021/ja3007275
16. Sluch, M. I.; Samuel, I. D. W.; Petty, M. C. *Chem. Phys. Lett.* **1997,** *280,* 315–320. doi:10.1016/s0009-2614(97)01159-7
17. Yamakoshi, Y.; Umezawa, N.; Ryu, A.; Arakane, K.; Miyata, N.; Goda, Y.; Masumizu, T.; Nagano, T. *J. Am. Chem. Soc.* **2003,** *125,* 12803–12809. doi:10.1021/ja0355574
18. Serda, M.; Szewczyk, G.; Krzysztyńska-Kuleta, O.; Korzuch, J.; Dulski, M.; Musioł, R.; Sarna, T. *ACS Biomater. Sci. Eng.* **2020,** *6,* 5930–5940. doi:10.1021/acsbiomaterials.0c00932
19. Liosi, K.; Stasyuk, A. J.; Masero, F.; Voityuk, A. A.; Nauser, T.; Mougel, V.; Solà, M.; Yamakoshi, Y. *JACS Au* **2021,** *1,* 1601–1611. doi:10.1021/jacsau.1c00239
20. Guo, Q.; Ghalei, B.; Qin, D.; Mizutani, D.; Joko, I.; Al-Aziz, H.; Higashino, T.; Ito, M. M.; Imahori, H.; Sivaniah, E. *Chem. Commun.* **2023,** *59,* 10012–10015. doi:10.1039/d3cc02175k

License and Terms

BEILSTEIN JOURNAL OF ORGANIC CHEMISTRY

Surprising acidity for the methylene of 1,3-indenocorannulenes?

Shi Liu[1], Märt Lõkov[2], Sofja Tshepelevitsh[2], Ivo Leito[2], Kim K. Baldridge[1] and Jay S. Siegel[*1]

Full Research Paper

Open Access

Address:
[1]School of Pharmaceutical Science and Technology, Tianjin University, Tianjin, PR China and [2]University of Tartu, Institute of Chemistry, Ravila 14a, Tartu 50411, Estonia

Email:
Jay S. Siegel[*] - siegel@hku.hk

* Corresponding author

Keywords:
acidity; aromatic hydrocarbon; Clar sextet; Loschmidt group element; molecular graph

Beilstein J. Org. Chem. **2024,** *20,* 3144–3150.
https://doi.org/10.3762/bjoc.20.260

Received: 15 August 2024
Accepted: 19 November 2024
Published: 02 December 2024

This article is part of the thematic issue "Carbon-rich materials: from polyaromatic molecules to fullerenes and other carbon allotropes".

Guest Editor: Y. Yamakoshi

Abstract

Quantitative assessment of the first acidity constant (pK_a) for BFC (27.6 in CH_3CN) and FIC (27.8 in CH_3CN) shows the methylene protons to be significantly more acidic than those in related cyclopentadiene (32 in CH_3CN), indene (34 in CH_3CN), or fluorene (37 in CH_3CN) and comparable to the methine of 9-perfluorophenylfluorene (28.14 in CH_3CN). This work reports quantitative pK_a values of BFC and FIC, places those values in a broadened context of CpH-cognate hydrocarbon acidity and presents a Clar–Loschmidt graph perspective to help understand the “surprises”.

Introduction

A classic textbook tetrad linking hydrocarbon acidity to aromatic stabilization energy comprises cyclopentadiene (CpH), indene (InH), fluorene (FlH), and diphenylmethane (DPMH) [1,2], with pK_a values in DMSO equal to 18 [3], 20.1 [3], 22.6 [3], and 32.2 [4], respectively (Scheme 1) [5,6]. The reaction enthalpy for deprotonation of CpH is ca 20 kcal/mol less endothermic than DPMH and ca. 24–27 kcal/mol less endothermic than 1,4-pentadiene (PDH; pK_a ≈ 35 in DMSO) [3], values strikingly similar to the resonance stabilization energy estimated for benzene [7,8]. Furthermore, the trend of pK_a values for CpH, InH, and FlH correlates with the reduction of the aromatic stabilization energy for the anion across the series [1,2]. At first glance, this model supports the notion that the relative pK_a values of cyclopentadienes embedded in polynuclear aromatic hydrocarbons (CpH-PAHs) reflect some general measure of the embedded CpH's aromatic character. In this context, the observation that BFC and FIC (FlH cognates) manifest acidity comparable to CpH, was surprising [9]. This study uses a Clar–Loschmidt graph model to show that the acidity of CpH-PAH is more nuanced [10,11]. Subsequently,

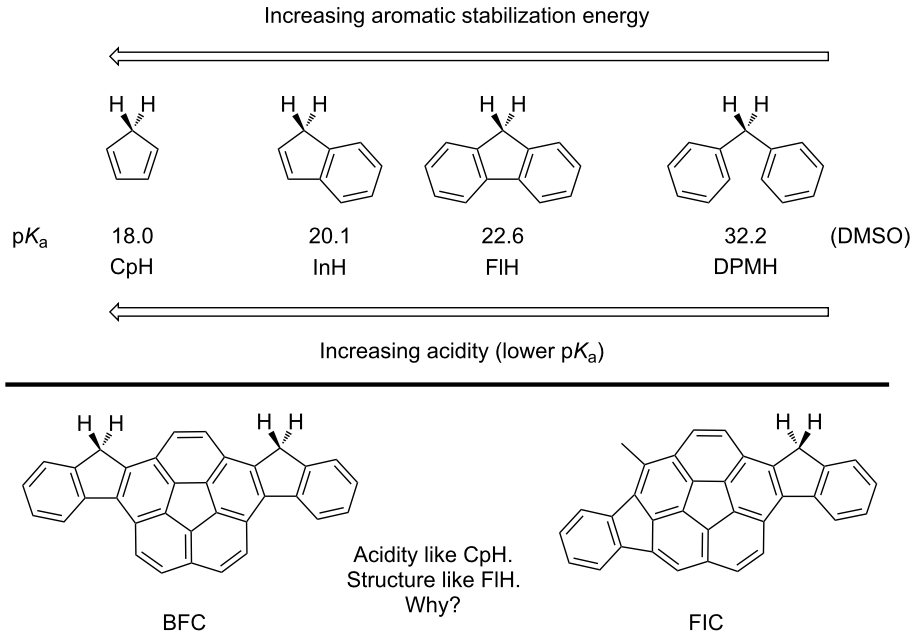

Scheme 1: Aromatic stabilization energy across a series of small aromatics (upper); graphical depiction of the BFC/FIC acidity quandry (lower).

literature and computational examples reveal a leitmotif for CpH-PAH-based redox-active carbon-rich materials.

Results and Discussion

From competitive titrations against 9-C_6F_5-fluorene (pK_a = 28.14 in CH_3CN) [12,13] and (4-Me-C_6F_4)(C_6H_5)CHCN (pK_a = 26.98 in CH_3CN) [12,13] as upper and lower references, respectively, the acidities of BFC (pK_a = 27.6 in CH_3CN) and FIC (pK_a = 27.8 in CH_3CN) could be quantified and ordered relative to a series of organic aromatic acids (Table 1). Rather than falling among the series cyclopentadiene (pK_a = 32 in CH_3CN), indene (pK_a = 34 in CH_3CN), or fluorene (pK_a = 37 in CH_3CN), BFC and FIC rank as stronger acids than CpH in acetonitrile. Extrapolation to DMSO by conversion equations, supports the assertion that BFC and FIC are more acidic than CpH in an "absolute acidity" sense [13].

How odd is such a pK_a value of ca. 14 for a CpH-PAH like BFC or FIC in DMSO? From the initial structural analogy to fluorene there is a substantial 8 pK_a unit difference, which is nearly 11 kcal/mol in ambient reaction free energy. Computations (B97-D/def2-TZVPP(THF)//B97-D/def2-TZVPP(THF)) also predict pK_a values of 14.4 and 14.3 for FIC and BFC in DMSO, respectively, so to the extent that these values are surprising, the problem must mostly come from a distortion of our perspective, and not from any dispute between

Table 1: Relative aromatic hydrocarbon acidities I.

Compound	CH_3CN Cmptl[a]	CH_3CN Exptl/Est[b]	DMSO Cmptl[a]	DMSO Exptl/Est[b]
fluorene	35.0	37[b,c]	21.6	22.6[d]
indene	32.2	34[b,c]	18.8	20.1[d]
cyclopentadiene	29.1	32[b,c]	15.6	18.0[d]
FIC	27.8	27.8[e]	14.4	14.4[b,e]
BFC	28.3	27.6[e]	14.3	14.3[b,e]
9-phenylfluorene	30.8	32[b,c]	17.4	17.9[f]
fluoradene	22.8	23.9[b,c]	9.4	10.5[f]
diphenylmethane	43.4	48[b,c]	29.9	32.2[g]

[a]B97-D/def2-TZVPP(solvent)//B97-D/def2-TZVPP(solvent) referenced to 9-C_6F_5-fluorene (solvent). [b]Estimated using experimental data and correlation equations. [c]Ref. [13]. [d]Ref. [3]. [e]This work. [f]Ref. [5]. [g]Ref. [4].

theory and experiment. If that is the case, then what might be a better perspective to investigate CpH-PAH structures like BIC and FIC?

Let us consider a perspective based on the teachings of Clar and Loschmidt. Clar held the electron sextet as the paragon of aromaticity [14] and Loschmidt considered benzene a "group element" [15]. Combining these perspectives, one can view PAH networks as graphs comprised of Clar–Loschmidt (CL) "elements" [10,16]. For corannulene, a maximum of two CL elements (sextets) are present in any one resonance form. Therefore, applying the CL perspective to BFC and FIC one sees dibenzofluorene (full name 13*H*-dibenzo[*a*,*c*]fluorene) as a cognate, which highlights these compounds to be like a conformationally planar-locked 2,3-diphenylindene (pK_a 17.7 in DMSO [17].

The CL perspective also allows one to create graphs with points representing the aromatic elements, such as, benzene, Cp anion, pyrrole, etc. (Scheme 2, top). Triphenylene is a simple cyclic graph of three benzene elements and their direct connections. A simple modification of the triphenylene graph is the replacement of benzene by Cp anion (Scheme 2, middle). From the CL graph perspective, the anion of cyclopentaphenanthrene is related to that of dibenzofluorene the same way as the Cp anion is related to that of indene. Therefore, cyclopentaphenanthrene should be more acidic than dibenzofluorene, which it is [18]. Monofluorenocorannulene and dibenzofluorene map onto a common CL graph with benzene and indenyl elements (Scheme 2, bottom). These compounds display related electronic structures and are predicted computationally to have similar pK_a values (i.e., show similar acidity).

The extreme of this graph example is the five rim benzene elements and a Cp^- core, pentabenzocorannulene (Scheme 3, upper) [19,20]. Such a CpH derivative should be a very acidic aromatic hydrocarbon, and computations for this study predict its pK_a to be ca 1.1 in DMSO. This high acidity is well seen if

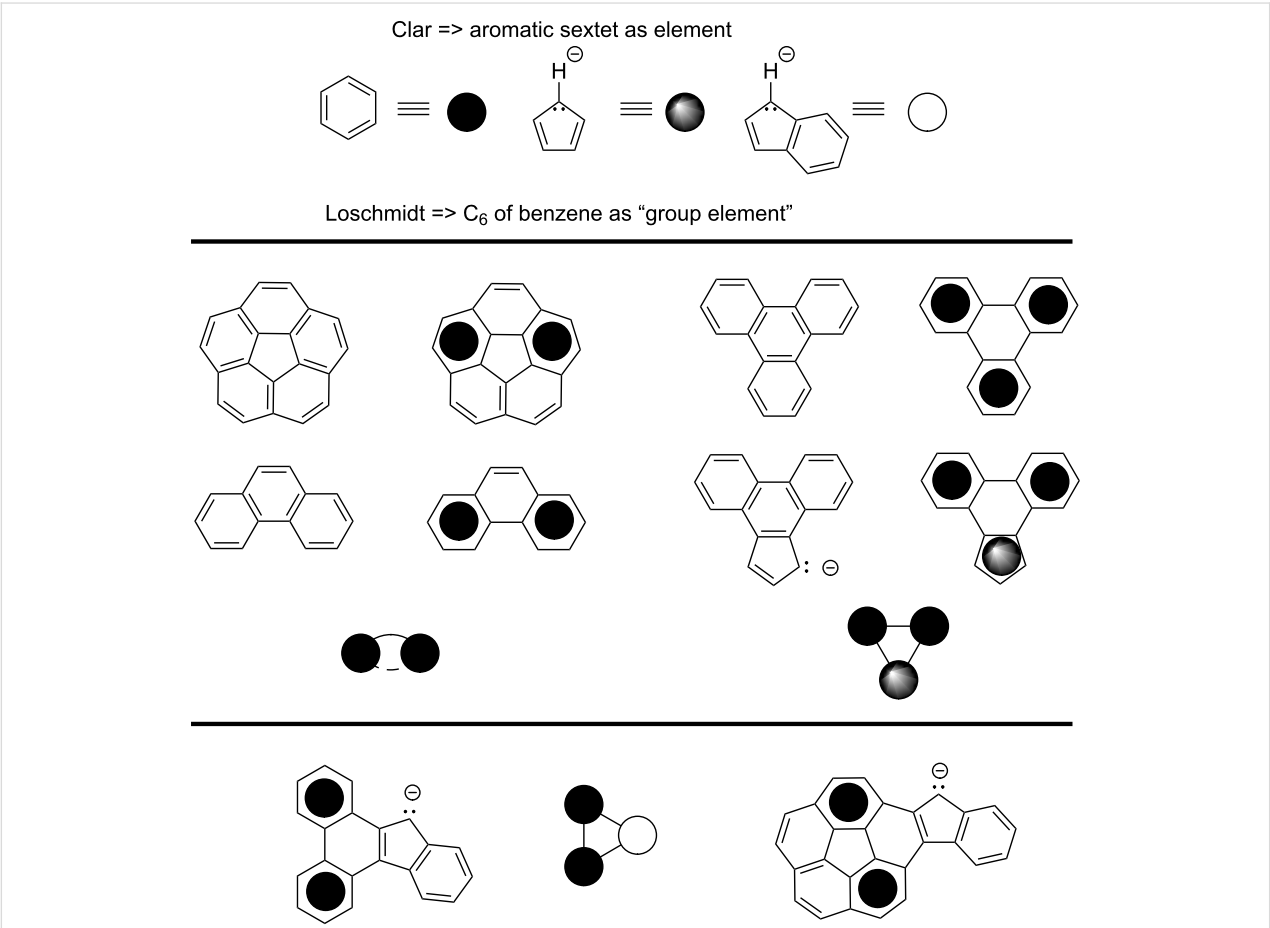

Scheme 2: Clar–Loschmidt graphs: [upper] defining the relationship of the molecular fragment to the graph node (shaded circle) for benzene, Cp anion, and indene anion; [middle], superposition of the graph node onto the molecular fragment and then representation of the nodes in the abstract graph: corannulene above phenanthrene (left); triphenylene above cyclopentaphenanthrene (right); [lower] as with middle but dibenzofluorene (left) and fluorenocorannulene (right).

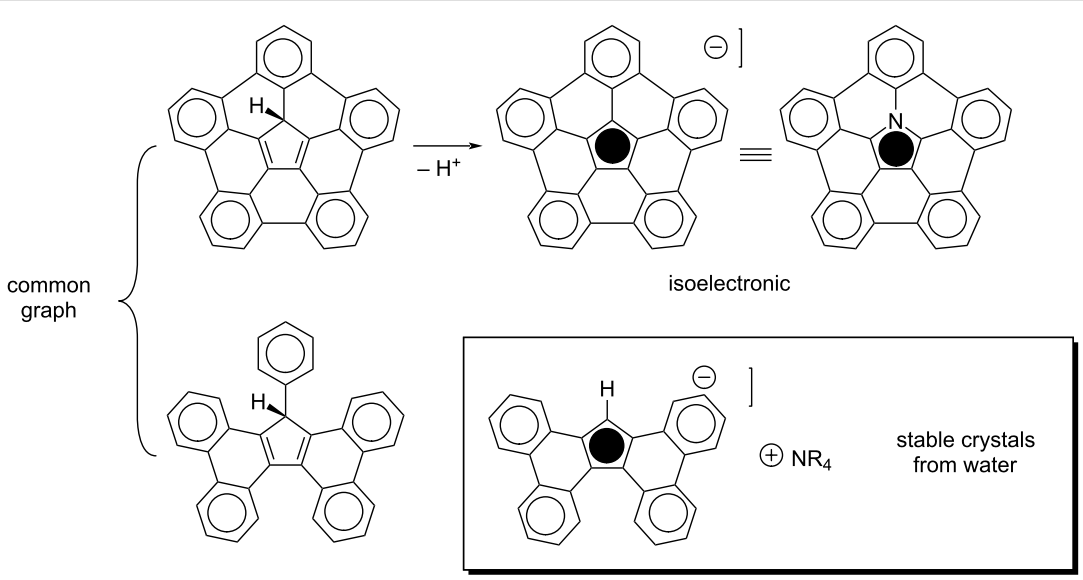

Scheme 3: CL graph perspective on acidic PAH-CpHs; pentabenzocorannulene and pentabenzoazocorannulene (upper); phenyltetrabenzofluorene and tetrabenzofluorene TBF (lower).

one recognizes that, when seen through the CL model, pentabenzocorannulene is more of a well-overlapping pentaphenyl-CpH derivative than a pentabenzocorannulene. Swap out Cp^- by the isolelectronic pyrrole and it becomes clear that pentabenzoazacorannulene is also less of an azocorannulene and more a pentaphenylpyrrole, which explains its ease of synthesis and the physical properties [21,22].

The graph with four benzene elements and a CpH core is evident in the commercially available tetrabenzofluorene, TBF (Scheme 3, lower). The parent and the phenyl TBF derivative were also recently prepared by a mechanochemical Scholl reaction [23-25]. Furthermore, the anion of TBF is stable enough to be easily handled and the crystal structures of a number of common ammonium salts of TBF anion, grown from water, have been reported [26].

Neutral highly acidic compounds tend to deprotonate to form highly stable anions. The air stability of TBF conforms to that model. In contrast, although the dianion of BFC can be generated with *tert*-butoxide under inert atmosphere, in the presence of water it quenches and exposed to oxygen it oxidizes to form the diketone. Access to the dianion of BFC presages an interesting diradical and this was achieved by inclusion of mesityl protecting groups [27]. Extension of the BFC model with thiophene provides further interesting materials [28]. A reasonable corollary to this behavior would assert that derivatives of TBF and pentabenzocorannulene would produce air-stable radical and ionic PAHs, and that coupling such fragments would lead to stable redox-active carbon sheets.

Conclusion

In conclusion, the "surprise" in the surprising pK_a for BIC and FIC was in our expectation of the deprotonated forms as poorly delocalized fluorenyl anions. The CL perspective provided us a different way to look at these compounds and interpret them as phenyl-substituted CpHs, thus reconciling their higher acidity. That perspective led us to a CL graph representation that predicted/rationalized additional acidic CpH-PAHs and sharpened our understanding of an "azacorannulene". Working from graph structures based on chemically stable ("group elementary") nodes is a useful principle in molecular design and chemical synthesis. Such a perspective is important to understand fundamental physical organic molecular properties as well as to predict desirable unforeseen new material designs (e.g., redox-active electrooptical materials).

Methods

pK_a measurements in acetonitrile

The experimental setup and methodology for the pK_a determination of BFC and FIC in acetonitrile was essentially the same as described in detail in previous papers [12,13]. A brief description will follow.

The pK_a determinations in acetonitrile are based on the determinations of differences of pK_a values of two acids. In this case one compound is a reference acid with a previously known pK_a value and the other acid is either FIC or BFC. Both compounds, as well as the references are also separately titrated in order to obtain the UV–vis spectra of the acids in neutral as well as in deprotonated forms.

Then, the same titration is done with a mixture of measured acid (FIC or BFC) and a reference acid. Using the spectral data from the titrations of mixtures the dissociation levels $\alpha = [A^-]/([A^-] + [HA])$ of both acids in all the mixtures formed during titration are calculated and are then in turn used to calculate the differences of pK_a values (ΔpK_a) of FIC or BFC and the used reference acids according the following equation:

$$\Delta pK_a = \log \frac{\alpha_1(1-\alpha_2)}{\alpha_2(1-\alpha_1)}$$

The pK_a values of BFC and FIC are estimated as a result of ΔpK_a measurements against different reference acids.

A Perkin-Elmer Lambda 40 UV–vis spectrophotometer connected with optical fibre cables to an external cell compartment inside a MBraun Unilab glovebox filled with 99.999% pure argon was used for the spectrophotometric titrations. This setup ensured that during all titrations the moisture and oxygen contents in argon were always under 10 ppm during measurements. Triflic acid (Aldrich, 99+%) and phosphazene base P_2-Et (165535-45-5, Aldrich, ≥98%) were used to prepare the acidic and basic titrant solutions, respectively. Acetonitrile (Romil 190 SpS far UV/gradient quality) was used as solvent after drying with molecular sieves (3 Å), which lowered the water content to a range of 2–6 ppm.

Acids with previously published pK_a values in acetonitrile were used as reference acids [12,13]. Usually this kind of ΔpK_a measurements are done against three reference acids but due to the lack of suitable reference acids in the weakly acidic pK_a region in acetonitrile only two reference acids were used. The results are presented in Table 2. We estimate the standard uncertainties of the assigned pK_a values of BFC and FIC as 0.15 pK_a units.

pK_a predictions using correlation analysis

The pK_a values of fluorene, indene, cyclopentadiene, 9-phenylfluorene, and diphenylmethane in acetonitrile were estimated by averaging the values obtained from their experimental pK_a values in DMSO [5] and three correlation equations: equations 2.1 and 2.2 in Ref. [13] and correlation equation composed of experimental pK_a values of 9-C_6F_5-fluorene, octafluorofluorene, fluoradene, (4-Me-C_6F_4)(C_6H_5)CHCN, (C_6F_5)(C_6H_5)CHCN, 9-COOMe-fluorene, and 9-CN-fluorene in acetonitrile [12,13] and DMSO [5]. All these pK_a estimations involve significant extrapolation and the agreement between the estimates obtained from different equations is not good. Therefore, the standard uncertainties of these obtained pK_a estimates are high: 2 pK_a units for fluorene, indene and 9-phenylfluorene, 3 pK_a units for cyclopentadiene (as this acid is very different from the acids used for developing the correlation equations), and 3 pK_a units for diphenylmethane (as very strong extrapolation is involved with this acid) [12,13].

The pK_a values of FIC and BFC in DMSO were estimated from the experimental pK_a values in acetonitrile determined in this study using the average values from the same three equations as above, however, using them in reverse. The standard uncertainty estimates of the pK_a values of FIC and BFC in DMSO are 0.8 pK_a units.

Synthesis

Material used to measure the acidity of compounds BFC and FIC was prepared previously by methods reported in reference [9].

Computational methods

The structural and energetic analyses of the molecular systems for all compounds described in this study were carried out with the B97-D dispersion enabled density functional method [29,30], using an ultrafine grid, together with the def2-TZVPP basis set [31]. Full geometry optimizations were performed and uniquely characterized via second derivatives (Hessian) analysis to establish stationary points and effects of zero point and thermal energy contributions. Effects of solvent employed the COSMO:ab initio continuum method [32,33], using a dielectric as in experiment, and fully optimized using radii of Klamt [34]. Electronic and thermal free energy differences between neutral and anion were compared to a reference pentafluorophenylfluorene, and subsequently converted to pK_a values by dividing by 1.36. Visualization and analysis of structural and property results were obtained using Avogadro [35]. Our group develops

Table 2: Results of pK_a measurements in acetonitrile.

Acid	Reference acid	pK_a (Ref)	ΔpK_a	pK_a (acid)	assigned pK_a
BFC	9-C_6F_5-fluorene	28.14	0.55	27.59	27.6
	(4-Me-C_6F_4)(C_6H_5)CHCN	26.98	–0.78	27.76	
FIC	9-C_6F_5-fluorene	28.14	0.38	27.76	27.8
	(4-Me-C_6F_4)(C_6H_5)CHCN	26.98	–0.94	27.92	

GAMESS [36] and has also contributed to Gaussian software packages, in this work the G09 ES64L-G09RevE.01 version [37] of the latter was used.

Acknowledgements

High-performance computational work was carried out using the supercomputer at SPST Tianjin University.

Funding

Experimental work at Tartu was carried out using the instrumentation at the Estonian Center of Analytical Chemistry (TT4, https://www.akki.ee) and was supported by the Estonian Research Council grant (PRG690) and by the Estonian Ministry of Education and Research (TK210).

ORCID® iDs

Märt Lõkov - https://orcid.org/0000-0003-4484-0864
Sofja Tshepelevitsh - https://orcid.org/0000-0002-7734-9310
Ivo Leito - https://orcid.org/0000-0002-3000-4964
Kim K. Baldridge - https://orcid.org/0000-0001-7171-3487
Jay S. Siegel - https://orcid.org/0000-0002-3226-3521

Data Availability Statement

All data that supports the findings of this study is available in the published article and/or the supporting information of this article.

References

1. Dicks, A. P. *J. Chem. Educ.* **2003,** *80,* 1322–1327. doi:10.1021/ed080p1322
2. Streitwieser, A., Jr. *Molecular Orbital Theory for Organic Chemistry;* Wiley: New York, NY, USA, 1961.
3. Bordwell, F. G.; Drucker, G. E.; Fried, H. E. *J. Org. Chem.* **1981,** *46,* 632–635. doi:10.1021/jo00316a032
4. Bordwell, F. G.; Matthews, W. S.; Vanier, N. R. *J. Am. Chem. Soc.* **1975,** *97,* 442–443. doi:10.1021/ja00835a048
5. Bordwell, F. G. *Acc. Chem. Res.* **1988,** *21,* 456–463. doi:10.1021/ar00156a004
6. Kinoshita, T.; Fujita, M.; Kaneko, H.; Takeuchi, K.; Yoshizawa, K.; Yamabe, T. *Bull. Chem. Soc. Jpn.* **1998,** *71,* 1145–1149. doi:10.1246/bcsj.71.1145
7. Baldridge, K. K.; Siegel, J. S. *J. Phys. Org. Chem.* **2004,** *17,* 740–742. doi:10.1002/poc.819
8. Maier, G. *Chem. Unserer Zeit* **1975,** *9,* 131–141. doi:10.1002/ciuz.19750090502
9. Liu, S.; Roch, L. M.; Allemann, O.; Xu, J.; Vanthuyne, N.; Baldridge, K. K.; Siegel, J. S. *J. Org. Chem.* **2018,** *83,* 3979–3986. doi:10.1021/acs.joc.8b00320
10. Baldridge, K. K.; Siegel, J. S. *Angew. Chem., Int. Ed.* **2013,** *52,* 5436–5438. doi:10.1002/anie.201300625
11. Sritana-Anant, Y.; Seiders, T. J.; Siegel, J. S. *Top. Curr. Chem.* **1998,** *196,* 1–43. doi:10.1007/3-540-69691-1_1
12. Kütt, A.; Leito, I.; Kaljurand, I.; Sooväli, L.; Vlasov, V. M.; Yagupolskii, L. M.; Koppel, I. A. *J. Org. Chem.* **2006,** *71,* 2829–2838. doi:10.1021/jo060031y
13. Kütt, A.; Tshepelevitsh, S.; Saame, J.; Lõkov, M.; Kaljurand, I.; Selberg, S.; Leito, I. *Eur. J. Org. Chem.* **2021,** 1407–1419. doi:10.1002/ejoc.202001649
14. Clar, E. *The Aromatic Sextet;* Wiley: New York, NY, USA, 1972.
15. Loschmidt, J. *Konstitutionsformeln der Organischen Chemie in Graphischer Darstellung;* Wilhelm Engelmann: Leipzig, Germany, 1860.
16. Rigby, S. S.; Stradiotto, M.; Brydges, S.; Pole, D. L.; Top, S.; Bain, A. D.; McGlinchey, M. J. *J. Org. Chem.* **1998,** *63,* 3735–3740. doi:10.1021/jo9711504
17. Bordwell, F. G.; Drucker, G. E. *J. Org. Chem.* **1980,** *45,* 3325–3328. doi:10.1021/jo01304a037
18. Vianello, R.; Maksić, Z. B. *Eur. J. Org. Chem.* **2005,** 3571–3580. doi:10.1002/ejoc.200500153
19. Kanthak, M.; Muth, E.; Dyker, G. *Eur. J. Org. Chem.* **2010,** 6084–6091. doi:10.1002/ejoc.201000821
20. Wu, G.-Y.; Huang, C.-L.; Kang, H.-W.; Ou, W.-T.; Ho, Y.-S.; Cheng, M.-J.; Wu, Y.-T. *Angew. Chem., Int. Ed.* **2024,** *63,* e202408321. doi:10.1002/anie.202408321
21. Yokoi, H.; Hiraoka, Y.; Hiroto, S.; Sakamaki, D.; Seki, S.; Shinokubo, H. *Nat. Commun.* **2015,** *6,* 8215. doi:10.1038/ncomms9215
22. Ito, S.; Tokimaru, Y.; Nozaki, K. *Angew. Chem., Int. Ed.* **2015,** *54,* 7256–7260. doi:10.1002/anie.201502599
23. Báti, G.; Csókás, D.; Stuparu, M. C. *Chem. – Eur. J.* **2024,** *30,* e202302971. doi:10.1002/chem.202302971
24. Hopkinson, A. C.; Lee-Ruff, E.; Maleki, M. *Synthesis* **1986,** 366–371. doi:10.1055/s-1986-31637
25. Schröder, K.; Haase, D.; Saak, W.; Lützen, A.; Beckhaus, R.; Wichmann, S.; Schellenberg, J. *Organometallics* **2006,** *25,* 3824–3836. doi:10.1021/om0602613
26. Frey, O. N.; Stalling, T.; Schlüter, F.; Saak, W.; Schmidtmann, M.; Haase, D.; Beckhaus, R. *Dalton Trans.* **2016,** *45,* 1085–1092. doi:10.1039/c5dt04137f
27. Lu, R.-Q.; Wu, S.; Yang, L.-L.; Gao, W.-B.; Qu, H.; Wang, X.-Y.; Chen, J.-B.; Tang, C.; Shi, H.-Y.; Cao, X.-Y. *Angew. Chem., Int. Ed.* **2019,** *58,* 7600–7605. doi:10.1002/anie.201902028
28. Pedersen, V. B. R.; Jasti, R.; Nielsen, M. B. *ChemPhotoChem* **2024,** *8,* e202400122. doi:10.1002/cptc.202400122
29. Grimme, S. *J. Comput. Chem.* **2006,** *27,* 1787–1799. doi:10.1002/jcc.20495
30. Grimme, S. *J. Chem. Phys.* **2006,** *124,* 034108. doi:10.1063/1.2148954
31. Weigend, F.; Ahlrichs, R. *Phys. Chem. Chem. Phys.* **2005,** *7,* 3297–3305. doi:10.1039/b508541a
32. Baldridge, K. K.; Biggs, B.; Gilbertson, R. D.; Haley, M. M.; Bläser, D.; Boese, R.; Maulitz, A. H.; Siegel, J. S. *Chem. Commun.* **1998,** 1137–1138. doi:10.1039/a801217b
33. Baldridge, K.; Klamt, A. *J. Chem. Phys.* **1997,** *106,* 6622–6633. doi:10.1063/1.473662
34. Klamt, A.; Jonas, V.; Bürger, T.; Lohrenz, J. C. W. *J. Phys. Chem. A* **1998,** *102,* 5074–5085. doi:10.1021/jp980017s
35. Hanwell, M. D.; Curtis, D. E.; Lonie, D. C.; Vandermeersch, T.; Zurek, E.; Hutchison, G. R. *J. Cheminf.* **2012,** *4,* 17. doi:10.1186/1758-2946-4-17
36. Schmidt, M. W.; Baldridge, K. K.; Boatz, J. A.; Elbert, S. T.; Gordon, M. S.; Jensen, J. H.; Koseki, S.; Matsunaga, N.; Nguyen, K. A.; Su, S.; Windus, T. L.; Dupuis, M.; Montgomery, J. A., Jr. *J. Comput. Chem.* **1993,** *14,* 1347–1363. doi:10.1002/jcc.540141112
37. *Gaussian 09,* Revision D01; Gaussian, Inc.: Wallingford, CT, 2009.